UAB

Universitat Autònoma de Barcelona

Universitat Autònoma de Barcelona
Escola d'Enginyeria

UAB

Doctoral Thesis in Electrical Engineering and Telecomunications

High-Bandwidth Graphene Neural Interfaces

Ramon Garcia Cortadella

March 2021

UAB
Universitat Autònoma
de Barcelona

Supervisors: Prof. Dr. Jose A. Garrido and Dr. Anton Guimerà
Tutor: Prof. Dr. David Jimenez
Advanced Electronic Materials and Devices Group

Abstract

Brain function is based on highly complex processes, which remain yet to be described and understood in detail. In the last decades, neuroscience has experienced an accelerated development, prompted by novel neurotechnologies that allow monitoring the dynamics of electrical activity in the brain with a higher spatio-temporal resolution and wider coverage area. However, due to the high complexity of neural networks in the brain, which are composed of strongly interconnected neural populations across large brain regions, we are far from monitoring a significant fraction of neurons mediating complex functions.

In order to investigate large-scale brain dynamics with high spatial resolution several technologies have been extensively used, including functional magnetic resonance imaging (fMRI), voltage-sensitive dye imaging or high sensor-count electrophysiological recordings. However, the temporal resolution of fMRI and optical methods is typically limited to few hertz, almost three orders of magnitude below that of action potentials, and are limited to head-fixed conditions. On the other hand, electrophysiological recordings based on micro-electrode arrays provide a high spatio-temporal resolution, allowing to accurately detect fast dynamics from hundreds of individual neurons simultaneously in freely moving animals. However, neuroelectronic sensing interfaces present a trade-off between spatial resolution and coverage area. Moreover, they present a poor sensitivity in the infra-slow frequency band ($< 0.5\,Hz$), which migh be related to long-range functional connectivity.

In this thesis, a novel technology based on graphene active sensors is presented, which allows to increase the coverage area and spatial resolution of electrophysiological recordings while preserving a high sensitivity in a wide frequency band, from infra-slow to single electrogenic cell activity. This technological development is divided into three main stages; first, a deeper understanding of the intrinsic noise characteristics and frequency response of these sensors is obtained by building on prior graphene sensor technology. In the second stage, a quasi-commercial system based on epi-cortical graphene sensor arrays and a wireless headstage for chronic implantation in rats is shown. Using this system, the reproducibility of the graphene sensor arrays, their long-term stability and their chronic biocompatibility are demonstrated. Furthermore, preliminary evidence is provided for a wide range of novel electrophysiological patterns owing to their sensitivity in the infra-slow frequency band. Finally, in the last stage of this thesis, the focus is centred on the development of new multiplexing strategies to upscale the number of sensors on the neural probes.

These three main development stages have led to the demonstration of the potential of multiplexed graphene sensor arrays for mapping of large-scale brain dynamics in a wide frequency band in freely moving animals over long periods. The combination of these capabilities makes graphene active sensor arrays a promising technology for high bandwidth brain computer interfaces and a unique tool to investigate the role of infra-slow activity on the coordination of higher frequency brain dynamics.

Contents

Preface

Natural evolution has led to the emergence of highly complex biological computing systems. Among them, the human brain is an unparalleled example, which is the cornerstone of human intelligence. However, human intelligence is not only based on the astonishing capabilities of the human brain, but also on our ability to externalize thought via social interaction and the use of technology[1]. Expansion of our computing capabilities beyond those of our own brains has been driven by the evolutionary success of social behaviour and verbal communication. Furthermore, following the emergence of languages, human societies evolved to invent writing systems as an efficient way to store and retrieve information. Writing was a disruptive technological development, which represented a qualitative change in our way to preserve knowledge beyond the existence of individuals.

In the past decades, we have experienced yet another non-incremental change in our capabilities to store and process information by the use of digital computers and new communication protocols such as internet. With the use of portable computers such as smart phones and the use of wireless data transmission technologies[2] our access to data has increased dramatically. However, an important bottleneck in the improvement of our data processing capabilities is the link between our biological brains and external information processing systems. This communication is bidirectional, from computers to the brain via devices such as displays, and from the brain to computers via low bandwidth peripheral devices such as keyboards. Our sensory systems, in particular the visual and auditory systems, are highly optimized to acquire information from the environment and therefore offer a high bandwidth for communication from computers to the brain. On the other hand, the communication between the human brain and computers is currently arguably more constrained. Our main form of natural communication is undeniably speech. Using

verbal languages, we are able to convey information to other human beings with a high bandwidth. Speech is a very efficient way for the brain to transmit internal variables representing abstract, highly processed data from the sensory system, through a physical communication channel to other brains. This highly optimized communication form can be used to transmit information to digital computers as well. In the last decade there has been a huge progress on the development of algorithms for speech recognition and processing[3], which are critical to stablish high bandwidth communication channels between brains and computers. Nevertheless, use of speech to communicate with machines has some drawbacks. An important one is privacy, speaking commands to a machine outloud cannot be used to transmit sensitive information in an environment where others can intercept the messages. Another disadvantage is that verbal communication with machines is not selective and is prone to crosstalk among brain-machine communicating nodes[4]. Natural verbal communication among humans has been optimized by natural evolution to minimize this problem[5], commonly known as the cocktail party problem, but its technological implementation remains elusive. Not to say that the capacity of our brain to filter out noises is also certainly limited. An alternative way to improve the communication between humans and external computing devices could be the use of neuroelectronic interfaces. Implantation of bioelectronic devices on the brain could be used to detect internal cognitive variables encoding e.g. covert speech, which could be then transmitted to digital computers, enabling a high bandwidth and private communication channel. In the last years, important progress has been made in this direction, including the demonstration of the decoding of spoken sentences in human patients[6]. In these first clinical trials, the engineered communication between the human brain and a digital computer is not focused on enhancing cognition, but on enabling patients to recover their ability to speak.

Although the great prospects of speech decoding for the restoration of speech and enhanced brain-machine communication, there is concern in the scientific community, and society in general, that these devices could infringe ethical principles. An example of such concerns is the potential interception of personal information encoded in thoughts[7] or the shaping of thought by the statistical models used to produce speech[8]. In order to avoid such problems it would be critical for a safe technology to ensure that internal cognitive variables used for brain-machine communication can be intentionally articulated by the user, in the same way we control our intentions to speak aloud. In case of neural prosthesis for non-clinical appli-

cations, the ethical concerns are more prominent. Neuroprosthetic speech can be classified as a technology for human enhancement, which is origin of intense debate, rising concerns of human freedom and autonomy, health and safety or equity and societal disruption[9]. While many support the right of choice if no one other than ourselves can be hurt, such technologies should be regulated to prevent potential health problems that ultimately affect others[9]. Similarly, the choice of enhancing oneself could put pressure on others to receive the implants to be successful in a competitive society[9]. Additionally, expensive human enhancement technologies could lead to unfair distribution of the benefits and costs derived from their use. Certainly, stablishing a more efficient communication channel between humans and external computing devices is a technological development that could help patients and users as individuals as well as society as a whole, especially as the costs of mass production drop. However, ethical concerns are currently not elucidated and arguments should be revisited as novel technologies with concrete functionalities and dangers are developed.

Beyond the potential benefits and ethical concerns, the development of neuroelectronic interfaces capable of providing a high bandwidth and safe brain-to-computer communication for speech decoding channel do not yet exist. In the last decade, huge efforts have been dedicated to develop such devices, improving their biocompatibility for chronic use in humans[10, 11] with reduced risk following implantation by using minimally invasive devices. Very recently, a relatively simple neuroelectronic interface was used to demonstrate the decoding of spoken sentences in clinical trials for the restoration of speech in impaired patients[6]. However, this trial was carried out in patients with intact motor abilities, which was central for the decoding. Furthermore, chronic implantation of devices over long periods could lead to complications due to their high invasiveness. In order to improve the biocompatibility in chronic settings of high bandwidth neural interfaces, multiple strategies have been recently proposed both from academic institutions[11–13] as well as from private initiatives[14], which have focused on reducing the footprint of the devices and the trauma caused by their implantation.

In order to effectively detect electrophysiological activity in the brain encoding cognitive variables, it is critical to get sensors in proximity to the nervous tissue. An important fraction of high order functions in the mammalian brain are considered to occur in the cortex, which is the outermost area of the brain and is therefore

relatively accessible to external devices[15]. In order to effectively detect information encoded in the activity of individual neurons, presumably the basic units of processing in the brain[16], it is important to insert electrical sensors into the brain tissue, penetrating through the outermost cortical layers. Intra-cortical devices have demonstrated the potential to detect high dimensionality neural data[17]. However, current technologies still cause significant tissue damage and are prone to failure over chronic time points. Although the use of flexible, ultrathin neural probes is thought to improve their chronic performance[18], it is yet to be demonstrated the final reach of these technologies. Alternatively, surface micro-electrocorticography (μ-ECoG) grids, which are placed on the surface of the cortex, are promising to provide a platform for speech decoding[6] without causing direct trauma on the brain tissue. However, the complexity of the flexible electronic devices required to increase the bandwidth of conformal surface probes has so far limited their use in clinical studies. In this thesis, I present a new technological platform for neuroelectronic sensing interfaces based on graphene solution-gated field-effect transistors (g-SGFETs). These active sensors allow the implementation of multiplexing techniques to increase the number of sensors integrated in neural implants and provide a high sensitivity in a wide frequency band. This technology has a great potential to enable minimally invasive, high bandwidth and flexible neural interfaces for chronic brain-computer communication.

0.1 Significance statement

In this thesis, the current limitations in monitoring the electrical brain activity from large cortical areas with high spatio-temporal resolution and in a wide frequency band are addressed. For this purpose, the use of graphene active sensors is proposed and novel developments achieved by: i), studying the sensitivity of g-SGFETs and their dynamic response *in-vitro*, ii), developing advanced recording systems for proof-of-concept *in-vivo* and iii), demonstrating novel multiplexing strategies. These results have led to the demonstration of high sensor-count probes with improved spatio-temporal resolution and wide frequency band sensitivity (Fig. 0.1). The outcomes of this thesis set a clear path towards the implementation of graphene-based neural probes for the study of wide frequency band brain dynamics across large-scale neural networks in freely moving animals, which is currently not possible with existing methodologies. Based on the results of this PhD thesis, future studies will help to understand the role of infra-slow fluctuations on the coordination of fast brain dynamics that mediate cognition. Furthermore, the initial validation of the biocompatibility and long-term stability of chronically implanted devices confirms the great potential of this technology to implement high bandwidth brain-machine communication.
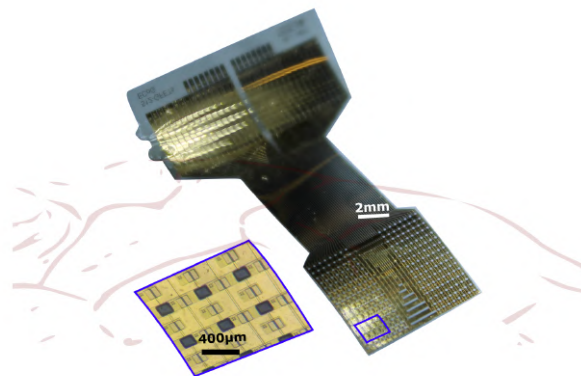
Figure 0.1: Photograph and 512-channel epi-cortical neural probe based on multiplexed active graphene sensor arrays. The inset shows an optical micrograph of the device active area. The active area presents 512 g-SGFETs covering a wide area, accounting for a large fraction of the rat cortical mantle. Multiplexing of graphene sensors reduces the complexity of the connectors, which present only 48 contacts for the 512 channels.

0.2 List of publications and contributions

This doctoral dissertation is based on a compendium of articles. Here, a complete list of the publications derived from this doctoral research is presented. Their significance and my contribution to each of them is briefly described. The contributions from the rest of co-authors can be found on each of the publications unless otherwise stated in the description below. The articles that shall be considered for evaluation of this work are summarized in the main text of this thesis, and are included as reprints of the published works in the appendix. Complementary publications, where I also contributed, are included in the appendix of this dissertation. Although they are not to be evaluated, a summary of each of them is also included in the main text in order give a coherent and complete description of my doctoral research.

Main articles

1. Article I: **Garcia-Cortadella, R.**; Masvidal-Codina, E.; De la Cruz, J. M.; Schäfer, N.; Schwesig, G.; Jeschke, C.; Martinez-Aguilar, J.; Sanchez-Vives, M. V.; Villa, R.; Illa, X.; et al. Distortion-Free Sensing of Neural Activity Using Graphene Transistors. **Small (2020)**

The article I of this compendium represents a central part of the 1st stage of the technological development of my PhD, which is centred on understanding and optimizing the response of graphene active sensors from a single device perspective. In this article, a thorough evaluation of the stationary and dynamic response of graphene active sensors and the effect of non-ideal response on the distortion of neural signals is presented. First, the focus is placed on the characterization of the voltage and frequency dependence of the transfer function of g-SGFETs. Having a detailed model of their response, I could propose a calibration method to correct signal distortion and demonstrated its effectivity on wide-band electrophysiological activity.

This article does not include an author contribution statement. My contribution to this work consisted in proposing the research idea and designing the research plan. I also performed most of the fabrication of devices and characterized their response. I analysed the results and proposed the model of frequency response. I also performed the recordings of local field potential signals *in-vivo* and single cell activity on cardiomyocyte cultures. Finally, I wrote the manuscript. Co-author EMC contributed to propose the research idea, performed the recordings of cortical spreading depression events and contributed to the revision of the manuscript. JMC performed the cell cultures. NS fabricated the devices used for the recording of electrophysiological activity of cardiomyocytes. GS performed the implantation of devices on a rat and contributed to perform the recordings *in-vivo*. CJ, JMA and AG contributed to the development of the electronics and software used for the characterization of devices and electrophysiological recordings. MVSV coordinated the

recording of cortical spreading depression events. RV contributed to coordination of the team that developed the device characterization electronics. XI contributed to the fabrication of g-SGFETs, AS coordinated the recording of local field potentials in rats. AG and JAG contributed to the research idea and extensively revised the manuscript.

2. Article II: **Garcia-Cortadella, R.***; Schwesig, G.*; Jeschke, C.; Illa, X.; Grey, A.; Savage, S.; Stamatidou, E.; Schiessl, I.; Masvidal-Codina, E.; Kostarelos, K.; et al. Graphene Active Sensor Arrays for Long-Term and Wireless Mapping of Wide Frequency-Band Epicortical Brain Activity. **Nature Communications (2021)**.

The article II of this compendium comprises the 2nd stage of the technological development presented in this thesis, which is focused on advanced electrophysiology recording systems based on graphene active sensors. In this work, carried out in collaboration with the neuroscience team led by Prof. Sirota, the company Multi Channels Systems and the nanomedicine team led by Prof. Kostarelos, the high performance of graphene sensing technology *in-vivo* in an operational environment is shown. Here, the sensitivity, reproducibility, stability and biocompatibility of graphene active sensors implanted on the rat cortex is demonstrated. Preliminary evidence of topographically structured modulation of theta, spindle and gamma band power by ISA is also shown. With these results, the potential of the graphene technology for the study of infra-slow activity (ISA) in combination with higher frequency local-field potential (LFP) bands in large cortical areas in behaving rodents is demonstrated.

The contributions from all authors are detailed in the published article. I contributed to all parts of this study, coordinating with the rest of co-authors to perform the experiments and write the manuscript. I proposed, together with my thesis supervisors, the research idea and research plan. I fabricated the neural probes and performed their characterization. I contributed to the development and characterization of the wireless headstage and development of the software for signal acquisition and processing. I performed the electrophysiological recordings in cooperation with co-first author G. Schwesig and I contributed to the analysis of electrophysiological signals, which was led by Prof. Sirota. I wrote the introduction, the results section on the characterization of graphene-based probes and the wireless headstage *in-vitro* as well as *in-vivo*. I also contributed to the writing of results section on the analysis of brain signals and the discussion section.

3. Article III: **Garcia-Cortadella, R.***; Schäfer, N.*; Cisneros-Fernandez, J.; Re, L.; Illa, X.; Schwesig, G.; Moya, A.; Santiago, S.; Guirado, G.; Villa, R.; et al. Switchless Multiplexing of Graphene Active Sensor Arrays for Brain Mapping. **Nano Letters (2020)**.

The article III of this compendium represents an important part of the 3rd stage of technological development of this thesis, which is focused on upscaling the graphene-

based neural probes. Multiplexing strategies are crucial to increase the number of sensors, while keeping a manageable complexity of the connector. In this article, I could show for the first time the operation of graphene sensor arrays in frequency-division multiplexing (FDM) mode. Demonstration of FDM consisted on a detailed characterization of the graphene sensors' response in FDM and non-multiplexed operation for comparison. In order to evaluate the scalability of this strategy I modelled the effect of harmonic distortion, bandwidth limits, cross-talk and heat dissipation in large-scale arrays, showing that this technology can enable up to >1000-channel arrays. Finally, an *in-vivo* proof of concept was demonstrated, showing the sensitivity of FDM-graphene probes in a wide frequency band.

The contribution from all authors is detailed in the published article. I contributed to the proposal of the research plan together with co-first author N. Schaefer and my thesis supervisors, I designed and fabricated the graphene neural probes and I performed the characterization of the devices *in-vitro*. Subsequently, I modelled their response for the analysis on the scalability and I proposed and developed the methodology for cross-talk characterization. I contributed to develop a recording system based on a high speed PXI for proof-of-concept *in-vivo* and the software for data acquisition and processing in collaboration with co-author L. Re. I coordinated with N. Schaefer and G. Schwesig to perform the recording of electrophysiological activity *in-vivo*. I wrote all the parts of the manuscript, which was revised by my thesis supervisors J. A. Garrido and A. Guimerà.

Complementary articles

1. Article S1: Schaefer, N.*; **Garcia-Cortadella, R.***; Calia, A. B.*; Mavredakis, N.; Illa, X.; Masvidal-Codina, E.; Cruz, J. de la; Corro, E. del; Rodríguez, L.; Prats-Alfonso, E.; et al. Improved Metal-Graphene Contacts for Low-Noise, High-Density Microtransistor Arrays for Neural Sensing. **Carbon (2020)**.

The article S1 summarized in this compendium is part of the $1st$ stage of technological development. This article is focused on the understanding and mitigation of low frequency noise (LFN) in g-SGFETs. In this work, a framework to model the relative impact of metal-graphene contact noise with respect to channel noise in g-SGFETs depending on the transistor geometry is presented. Identification of contact noise allows to determine possible causes of increased noise and mitigate its impact by applying ultra-violet ozone treatment on graphene prior to metallization. Furthermore, the effect of ozone treatment on the contacts is modelled, leading to an explanation of the physical origin of contact noise in wafer scale graphene transistors.

The contributions from each author are detailed in the published article. My contribution was on developing the research idea, proposing a research plan and developing the methodology. I contributed to the analysis of the results and I proposed the

model of contact and channel noise contributions as well as the numerical modelling of contact noise. I wrote the part of the manuscript corresponding to contact noise modelling.

2. Article S2: Mavredakis, N.; **Garcia Cortadella, R.**; Bonaccini Calia, A.; Garrido, J. A.; Jiménez, D. Understanding the Bias Dependence of Low Frequency Noise in Single Layer Graphene FETs. **Nanoscale (2018)**.

The article S2 summarized in this compendium is part of the 1st stage of technological development of this dissertation, and in particular it is focused on the understanding of the physical origin of LFN in g-SGFET. In this work, lead by N. Mavredakis, a compact model is presented to describe the bias dependence of LFN in g-SGFET. Modelling of LFN indicates that the dominant sources of noise are trapping-detrapping events of charge carriers in graphene and provides a tool for the modelling of LFN noise in graphene transistors in circuit simulators.

The contribution from each author is not described in the published manuscript. NM contributed to the development of the research idea, he presented the compact model of LFN. He also wrote the manuscript. ABC and I contributed to the development of the research idea and on the design, fabrication and characterization of devices. I also contributed to the identification and modelling of contact noise and to the revision of the original manuscript. Co-authors JAG and DJ contributed to the development of the research idea and to the revision of the original manuscript.

3. Article S3: Schaefer, N.; **Garcia-Cortadella, R.**; Martínez-Aguilar, J.; Schwesig, G.; Illa, X.; Lara, A. M.; Santiago, S.; Hébert, C.; Guirado, G.; Villa, R.; et al. Multiplexed Neural Sensor Array of Graphene Solution-Gated Field-Effect Transistors. **2D Materials (2020)**.

The article S3 summarized in this compendium is part of the 3rd stage of technological development presented in this thesis. Here, the demonstration of time-division multiplexing of g-SGFET arrays using external switching arrays is presented. The performance of the devices in multiplexed operation mode is presented *in-vitro* and it is compared with the performance of g-SGFET in non-multiplexed operation. The concept is also proven *in-vivo*, demonstrating the wide frequency band sensitivity of g-SGFETs in this operation mode. Furthermore, characterization and modelling of crosstalk is performed to discuss the scalability of this technology.

The contributions from each author are not described in the published manuscript. The first author NS made a major contribution, developing the research idea, proposing the research plan, designing and characterizing the neural probes and contributing to the development of the multiplexing system. He also performed the experiments *in-vivo* in collaboration with GS and wrote the manuscript. I contributed to develop the research idea and to the design and characterization of devices. I developed the methodology to characterize cross-talk and contributed to its analysis and modelling. JMA and AGB contributed to develop the multiplexing

electronics. AML, SS and GG contributed to develop the methodology to characterize cross-talk. CH contributed to develop the research idea. RV coordinated the team developing the electronic system. AG and JAG supervised and coordinated the research and revised the original manuscript.

Additional contributions

1. **Severo-Ochoa seed funding project. Title:** Multiplexed intra-cortical probes for wide bandwidth neural sensing. **Principal investigator: Garcia-Cortadella, R.**, **Funding agency:** Severo-Ochoa foundation. **Amount granted:** 8k€. Start: September 2020. End: April 2021.

2. **Patent application** (no. EP20382819) filled by CSIC, ICREA, CIBER and ICN2 in september 2020; concerning an acquisition device to limit leakage current in electrophysiological signal recording using active sensors (pending);

In addition to the aforementioned articles, the work presented in this thesis has contributed to additional publications:

3. Hébert, C.; Masvidal-Codina, E.; Suarez-Perez, A.; Calia, A. B.; Piret, G.; **Garcia-Cortadella, R.**; Illa, X.; Del Corro Garcia, E.; De la Cruz Sanchez, J. M.; Casals, D. V.; et al. Flexible Graphene Solution-Gated Field-Effect Transistors: Efficient Transducers for Micro-Electrocorticography. **Advanced Functional Materials (2017)**.

4. Masvidal-Codina, E.; Illa, X.; Dasilva, M.; Calia, A. B.; Dragojević, T.; Vidal-Rosas, E. E.; Prats-Alfonso, E.; Martínez-Aguilar, J.; De la Cruz, J. M.; **Garcia-Cortadella, R.**; et al. High-Resolution Mapping of Infraslow Cortical Brain Activity Enabled by Graphene Microtransistors. **Nature Materials (2019)**.

5. Mavredakis, N.; Wei, W.; Pallecchi, E.; Vignaud, D.; Happy, H.; Garcia Cortadella, R.; Bonaccini Calia, A.; Garrido, J. A.; Jiménez, D. Velocity Saturation Effect on Low Frequency Noise in Short Channel Single Layer Graphene Field Effect Transistors. **ACS Applied Electronic Materials (2019)**.

6. Mavredakis, N.; Wei, W.; Pallecchi, E.; Vignaud, D.; Happy, H.; **Cortadella, R. G.**; Schaefer, N.; Calia, A. B.; Garrido, J. A.; Jimenez, D. Low-Frequency Noise Parameter Extraction Method for Single-Layer Graphene FETs. **IEEE Trans. Electron Devices (2020)**.

7. Mavredakis, N.; **Garcia-Cortadella, R.**; Illa, X.; Schaefer, N.; Calia, A. B.; Anton-Guimerà-Brunet; Garrido, J. A.; Jiménez, D. Bias Dependent Variability of Low-Frequency Noise in Single-Layer Graphene FETs. **Nanoscale Advances (2020)**.

8. Cisneros-Fernández, J.; Guimerà-Brunet, A.; **Garcia-Cortadella, R.**; Schäfer, N.; Garrido, J. A.; Terés, L.; Serra-Graells, F. A 1024-Channel GFET 10-Bit 5-KHz 36-UW Read-Out Integrated Circuit for Brain UECoG. In **27th IEEE International Conference on Electronics, Circuits & Systems (2020) - Best paper award**.

0.3 Acknowledgements

Chapter 1

An introduction to intracranial neural sensing interfaces

The brain is an organ with a high computational power, which processes sensory information representing physical quantities from the external world and combines it with internal representations of previous experiences to predic future events. Weighting the significance of external inputs allows the brain to define the behaviour of living organisms, which sets a strong influence on the evolution of brain complexity[1]. For human beings, since initial discovery of its function[19], the brain has been mostly understood as a black box, forcing us to speculate and hypothesise on the nature of cognition. Understanding neural computation will have profound epistemological and ontological implications and a huge potential for biomedical applications. In the last decades, important progress has been made on the understanding of brain function[20], leading to major breakthroughs in the field of neural prosthesis[6, 21]. This progress has been prompted by the development of novel neurotechnologies that allow to establish alternative communication channels between the brain and external computing systems.

Neural sensing interfaces are an example of such links, which are used to measure electrical or biochemical variables in the nervous system[11]. These signals, produced by neural activity, can present correlations with external stimulus or, similarly, with internal cognitive variables. Sensing information from physical variables encoded by the human brain can therefore be used to decode internal cognitive variables such as the intention of a subject to undertake particular actions. Different areas of the brain are typically associated with particular cognitive functions. However, as novel technologies allow to detect brain activity in distant regions simultaneously with improved resolution, it is becoming increasingly clear that large-scale neural networks are highly integrated[17]. Therefore, it is currently considered that mapping large brain areas is critical to understand complex brain functions[22] and to improve decoding of neural dynamics for brain-computer interfaces (BCIs).

Furthermore, neural activity must be determined with a high spatial resolution and high sensitivity in all frequency bands potentially involved in neural communication, ideally covering from infra-slow potential fluctuations ($< 0.5\,Hz$) to high frequency activity generated by single neurons. An outstanding approach to map brain activity with high spatio-temporal resolution is the use of electrophysiological techniques based on the detection of electrical signals using voltage-sensitive electronic devices. Typically, microfabricated electrodes are used, which can be arranged into arrays, that are placed in contact with the brain for signal detection. In order to optimize the detection of neural signals, sensor arrays must be placed in direct contact with the surface of the brain tissue (epi-cortically), penetrating into the cortex (intra-cortically) or reaching into deeper brain structures. Making such neural interfaces stable and biocopatible over long periods represents a great challenge from a material science perspective.

This introduction is divided into three blocks. First, the interaction between brain tissue and the implants is described, which is crucial for the long-term stability of implants and must be carefully considered for chronic clinical applications. This section motivates the development of flexible technologies, being flexibility one of the key characteristics for highly biocompatible neural interfaces. Subsequently, recent advances in the translation of novel neurotechnologies into clinical practice are presented, from which the importance of increasing the sensor count, while minimizing their invesiveness is derived. An important challenge ahead for neural sensing interfaces is therefore the integration of a high number of highly sensitive devices on mechanically compliant and biocompatible probes. However, the flexibility requirement narrows down the list of materials available, which must also present demanding functional properties in order to enable the integration of a high number of sensors in neural probes. Following this discussion, the state of the art of high-count neural probes currently used for neuroscientific research or undergoing pre-clinical studies is presented. In the second block of this introduction, the principles of brain-machine communication are presented. Extraction of information from the brain is based on finding correlations between the neural patterns of activity and the cognitive or motor functions of interest, which can be then used for decoding of neural features. A high bandwidth communication therefore requires the use probes with high spatial resolution covering wide brain areas and a wide frequency band to capture the neural responses at different spatio-temporal scales. Here, the basic principles of decoding are presented, starting from high frequency spiking activity, towards lower frequency local field potentials. To conclude, the third block of this introduction presents the state of the art of graphene bioelectronics prior to this thesis. This block is focused on the intrinsic properties of graphene as well as the impact of structural defects on its performance, which will define the actual functionality of graphene-based neural interfaces.

1.1 Neural sensing interfaces

1.1.1 Biocompatibility: device and signal stability

In order to improve the long-term signal stability and reduce the rate of complications after surgical implantation of sensor arrays in the central nervous system (CNS), it is critical to improve the biocompatibility of neural interfaces. The implantation of devices in the brain can have multiple negative effects such as direct trauma, disruption of the brain blood barrier, induction of gliosis or inflammation, which can occur in the acute or chronic timescale[23]. The effect of the devices on the tissue depends on the position of the implant, but also on the mechanical and chemical properties of the materials used. Furthermore, the interaction between tissue and device is bidirectional. Therefore, not only the implant can have negative effects on the tissue, but also the tissue can actively contribute to the device degradation and loss of functionality. In this way, it is critical to develop novel material engineering solutions that minimize the foreign body response (FBR) of the tissue, enhancing not only the tolerability of the implant but also the biological signal stability as well as the device longevity.

The first step to understand the requirements for the implanted materials is to understand in detail the response of the tissue to foreign objects. Although the neuron is the cellular type most commonly associated with the brain, 75 % of its cells are vascular-related or glial cells (oligodendrocytes, astrocytes, and microglia)[24]. While oligodendrocytes are dedicated to axon myelination in the CNS, astrocytes and microglia are the main effectors of the FBR. Astrocytes and microglia have different phenotypes under physiological or pathological conditions. In the physiological state, astrocytes have multiple functions such as mechanical support, control of the chemical environment or buffering of neurotransmitters and ions for modulation of neurons' firing activity[24, 25]. On the other hand, microglia are the resident macrophages in the neural tissue. Upon their activation, for instance mediated via injury, the role of these glial cells changes. In the activated state, astrocytes present enhanced migration, proliferation, hypertrophy in addition to various anabolic changes[24]. Similarly, microglia also increase their proliferation, assume a more compact morphology and upregulate production of lithic enzymes for foreign body degradation. In addition, microglia secrete multiple factors to recruit macrophages and activated microglia as well as pro-inflammatory cytokines. Finally, microglia can secrete various cytotoxic and neurotoxic factors, which can induce neuronal death[24].

These changes in the brain tissue can be acute or chronic depending on their duration. In order to discriminate the acute effects after trauma, some studies have evaluated the response to stab-like wounds[26] (i.e. probe implantation followed by immediate removal). When a needle-like object is inserted in the cortex, it may rupture capillaries, extracellular matrix (ECM) fibres or glial and neuronal cell

membranes, ultimately producing displacement of the tissue and causing a local increase of pressure around the device. Disruption of blood vessels leads to the release of blood cells, activation of platelets, clotting factors and recruitment of macrophages. In turn, accumulation of fluid and necrotic tissue can lead to edema, which is typically observable up to 4 days post-implantation. Finally, microglia and astrocytes in their activated phenotype proliferate around the implant following the insertion. When the acute response declines, these cells typically continue accumulating around the implant, creating a tight cellular sheath in few weeks referred to as glial scar[27], which is not observed in stab-like wounds[26]. The main function of this glial tissue is thought to be the physical separation of the foreign body from the surrounding functional tissue[28]. However, such encapsulation is usually postulated to have detrimental effects on the signal quality and stability[29–31]. Besides the effects of glial scar on the signal attenuation and displacement of neurons from the surrounding tissue, glial cells can have an active role in the neural signal activity by modulating neuronal excitability, synaptic transmission or network activity[25]. Therefore, minimizing both the initial trauma as well as chronic inflammation and formation of the glial scar is critical to detect unperturbed neural activity.

The main strategies to minimize the FBR in the brain are based on the use of flexible and soft materials, engineering the topographical and chemical properties of the material surfaces as well as minimizing the implant footprint and traumatic wound. The mammalian brain is a soft tissue. Its main cellular constituents, neurons and glial cells, are very compliant, with Young moduli on the order of ten to few hundred pascals[32]. These cells are surrounded by the ECM; however, the importance of the ECM on the mechanical properties of the brain is relatively low compared to other soft tissues in the body. The mechanical properties of the brain are consistent with those of a dense colloidal system, with the cellular bodies being the colloids[32, 33]. In between this soft tissue and the skull there are several layers, including the pia mater, the arachnoid and the dura mater. These layers play a protective role against physiological movements, pressure changes and injury. The dura matter presents a thickness of about $0.3 - 0.8\,mm$[34] and a Young modulus of 0.5-1.2MPa[35] in humans, much larger that that of the brain. One interesting approach to achieve highly biocompatible implants is the so-called electronic dura[35], consisting of an epi-cortical neural probe fabricated on a soft and stretchable polymeric substrate, designed to substitute the dura mater and mimic its mechanical properties. These mechanical match reduces the stress and possible friction between the pulsating neural tissue and a more static and rigid implant. Similarly, extremely thin polymeric substrates ($< 10\,\mu m$) also present a lower flexural stiffness[36]. Such thin and flexible objects are not only promising to replace the dura on the surface of the brain, but have also been shown to reduce the FBR[37, 38] when inserted into the cortex, leading to an improved stability of spiking single-unit activity (SUA) detection[39]. In order to insert such flexible devices into the cortex, rather complex insertion methods have been proposed with relative success[14, 39, 40].

In this thesis, the focus is placed on developing high bandwidth biocompatible neural

probes for both epi-cortical as well as intra-cortical neural sensing. Flexibility is critical to reduce the FBR and improve the signal stability in chronic recordings, as well as to conform with the corrugated surface of large cortical areas. Therefore, development of highly flexible neural interfaces has been a central objective of this thesis.

1.1.2 Clinical translation

Implantation of electrical sensor arrays on the human brain for clinical applications has been the focus of intensive research. In the last decades, multiple clinical trials have been carried out seeking to translate advanced neural sensing interfaces into clinical use. One of the most prominent biomedical applications of neural sensing are brain computer interfaces (BCIs) used to restore certain sensory, cognitive or motor functions via the communication between brain and computers. Such applications can be based on electroencephalography (EEG) recordings, placing the sensors on the surface of the scalp, or placing the sensor arrays intracranially, which provides a much higher brain-computer communication bandwidth by enabling the detection of higher frequency activity from local current sources. In such applications, the internal brain variables correlated with the patients' intention to perform a certain action are identified. In some of such applications, the classified intentions are then used to restore the impaired functions, enabling the patients to perform the desired action through electromechanical devices. Examples of these applications include the detection of motor intentions to activate the motion of paralyzed or robotic limbs [21, 41] or the classification of speech intentions to articulate them through a speech synthesizer[6]. Other interesting applications beyond BCIs are the monitoring of brain activity to detect biomarkers related to neural diseases such as epileptic seizures [42] or Parkinson's disease[43]. In recent years, the concept of closed-loop systems that stimulate the nervous tissue for a therapeutic effect based on the detected brain signals has attracted increasing attention[44]. Finally, the sensor arrays can also be used intraoperatively to monitor the brain activity as a response of the electrical stimulation of the tissue [45, 46]. Such mapping enables the determination of the tissue functionality, minimizing brain damage during surgery. While the latter application only requires acute monitoring of the brain activity, all the rest strongly rely on long-term mapping and therefore an excellent chronic biocompatibility and stability of the implants is required.

One of the most successful initiatives toward the clinical application of intracranial BCIs (iBCIs) has been the clinical trial of BrainGate. An initial trial was carried out between 2004 and 2006 in which an array of intra-cortical electrodes were implanted on the motor cortex of 4 tetraplegic patients. This study demonstrated for the first time the ability of patients to move a cursor on a screen with high efficiency over several months[47]. A second clinical trial (BrainGate2) is currently ongoing on 15 participants for the determination of the implant safety as well as establishment of
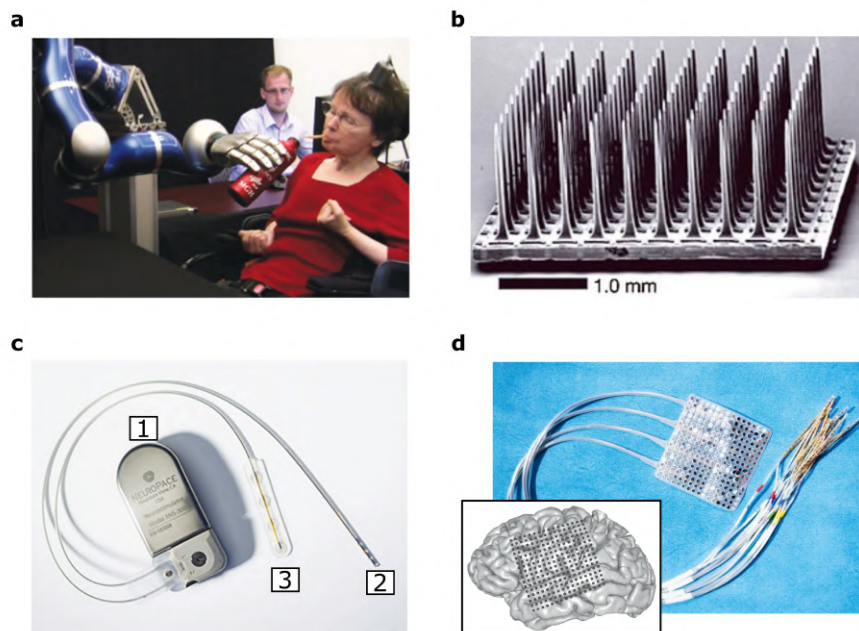
Figure 1.1: a, Participant of the BrainGate2 clinical trial moving a robotic arm controlled by an iBCI. Adapted with permission from Hochberg et. al.[21]. **b,** Utah array consisting of 100 penetrating needles with a Si core coated with platinum, titanium-tungsten and platinum and passivated with Parylene except for the tip. Adapted with permission from Hochberg et. al.[47]. **c,** RNS NeuroPace implant (1), which can be interrogated and programmed wirelessly, is connected to a deep brain stimulation (DBS) electrode (2) and an epi-cortical electrode strip (3). Reprinted with permission from Lee et. al.[48]. **d,** Electrocorticography (ECoG) grid with 256 electrodes (photograph by Noah Berger/UCSF). The inset shows the position of the electrodes on the cortical surface for decoding of spoken sentences. Reprinted with permission from Anumanchipalli et. al.[6].

decoding and evaluation parameters for a larger clinical trial. Initial results have led to some breakthroughs in the field: in 2012 a tetraplegic patient achieved the movement of a robotic arm through her thought[21] (Fig. 1.1a), in 2017 functional electrical stimulation (FES) of muscles was combined with motor cortex monitoring to control the movement of a patient's paralyzed arm[41] and in 2018 the brain mapping technology was used to control a general purpose computer[49]. These achievements are based on the use of a 100-sites intra-cortical array referred to as the Utah array (Fig. 1.1b). The success of this technology stems from its high stability and its sensitivity to record activity from single neurons due to its intra-cortical configuration. Although these devices are the only penetrating cortical sensor arrays that have been approved by the food and drug administration (FDA) for long-term human studies, they are still highly invasive and cause significant tissue damage[50].

Alternatively, the use of less invasive epi-cortical sensor arrays has been explored to detect local field potentials (LFP), which emerge from the superposed activity of a myriad of neurons[51]. An important clinical application of epi-cortical sensor arrays, also referred to as electrocorticography (ECoG) grids, is intraoperative mapping of the brain to localize the seizure foci in epileptical patients[52]. Similarly, ECoG grids are also used in functional brain mapping, where local bipolar stimulation is performed simultaneously with brain mapping in order to detect regions with higher excitability, which can be related to seizure foci[52]. Functional brain mapping is also used during brain tumour surgery to identify functional brain areas to be protected during the resection [53]. The stimulation is used to momentarility impair the function of the stimulated areas while the patient is asked to perform a certain task. However, too low amplitudes would not impair their function and too high aplitudes could affect adjacent areas. During functional brain mapping, ECoG grids can be used to detect the evoked activity induced by the electrical stimulation of the tissue and adjust the stimulation amplitude[53]. Besides the aforementioned applications of ECoG grids, their use for chronic applications has also been investigated. Clinical trials demonstrated the suitability of ECoG grids for the prediction of epileptic seizures[42]; currently, there is a FDA-approved device (RNS system, Fig. 1.1c) for intracranial monitoring of brain activity to predict epileptic seizure and prevent it by stimulation of the seizure foci. This device has demonstrated a safe functioning in a 2-years study, with 230 patients transitioning into a 7-years study[10]. Its chronic and wireless functionality has also enabled the study of cortical evoked responses to spoken sentences in natural ambulatory settings, showing signals selective to phonetic features for over 1.5 years[54]. The actual application of the RNS system for speech restoration is definitely not possible due to its limited bandwidth[54]; however, the results from these chronic studies are encouraging, given that other ECoG grids with a higher bandwidth have demonstrated promising performance for iBCIs in shorter-term implants. Prominent examples include the demonstration of arm and hand movement in a patient with a 28-electrode ECoG array implanted for up to four weeks[55] or decoding of spoken sentences using 256-electrode grids[6, 56] (Fig. 1.1d). Basing neural signal decoding on the LFP or multi unit activity (MUA) instead of single unit activity (SUA) from individual neurons may present the additional advantage of higher signal stability over time[57]. Currently, several clinical trials are undergoing to evaluate the compatibility of ECoGs with long-term BCI applications[58–61]. However, some studies have pointed out at the relatively high probability of complications during implantation[62], which is positively correlated with the total volume of the array or the number of cables connecting the electrodes[62, 63]. In addition, the implant can have an acute or chronic effect on the surrounding tissue, therefore producing changes in the detected signals over time[31]. This evidence confirms that there is still a long way toward a realistic use of high-density, large coverage area ECoG arrays for chronic biomedical applications.

23

1.1.3 High-count sensor arrays

The choice of biocompatible materials strongly constrains the palette of available functional materials[11, 13] that are used in neuroelectronic sensing interfaces. The previous discussion highlighted that one of the most important requirements for neural implants is their flexibility. This characteristic is arguably also one of the most limiting in terms of materials functionality and technology development.

Typically, the sensors used for the detection of electrical activity of neural tissue are macro or micro electrodes coupled to a high input-impedance amplifier. Electrodes typically consist of metallic discs, which are sometimes covered by high-surface area conductive layers to reduce their impedance[64–67]. In a first instance, these devices can be patterned on the substrate of choice by photolithographic methods, including a metallic track to establish a connection with electronic instrumentation for amplification and digitalization of the signals. Nevertheless, following this simple approach, each electrode requires an individual connection, which strongly limits the scalability of the micro-electrode arrays (MEA). Based on this device configuration, the number of sensors can be hardly increased above few hundreds, even for research oriented devices[68] (Fig. 1.2a).

In order to mitigate this problem, multiplexing strategies can be developed to send the signals from multiple sensors through a shared communication channel. However, in order to multiplex signals from an electrode, the front-end amplifier must be placed within each pixel of the array[69]. This local amplification of the signals allows doing time-domain multiplexing of sensors in a column/row addressable matrix, in a similar approach as for readout integrated circuits (ROIC) used in digital cameras. Unfortunately, the fabrication of such a complex circuitry can currently only be achieved using standard silicon microelectronics, limiting their implementation on flexible substrates. Fabrication of multiplexed MEAs on rigid substrates have led to great advances in the field of *in-vitro* sensing of neural activity in slices or cell cultures. Initial demonstrations with over 16 thousand sensors were reported almost two decades ago[70] and since then multiple technical developments have been reported[71, 72] (Fig. 1.2b). Nevertheless, their application for *in-vivo* applications is strongly limited due to their lack of flexibility, which prevents from conforming with the curved brain surface. Alternatively, multiplexing based on silicon nanomembrane transistors on a flexible substrate has been proposed[73], which allows to transduce the voltage signals to current on each pixel using a low impedance buffer silicon transistor (Fig. 1.2c). The main challenge in this direction is to properly insulate the silicon from the biofluids to prevent its fast degradation. Similarly, multiplexed sensor arrays based on organic semiconductors have also been proposed, however, their slow frequency response limits the upscaling of the array[74]. Great efforts have been made to improve these technologies, with novel organic transistor architectures demonstrating an improved frequency response [75] and novel passivation layers enabling 1024 channel sensor arrays based on silicon nanomembranes[76]. However, to date, no multiplexed epi-cortical technology has

demonstrated simultaneously a high sensor count, high sensitivity and long term stability *in-vivo*.
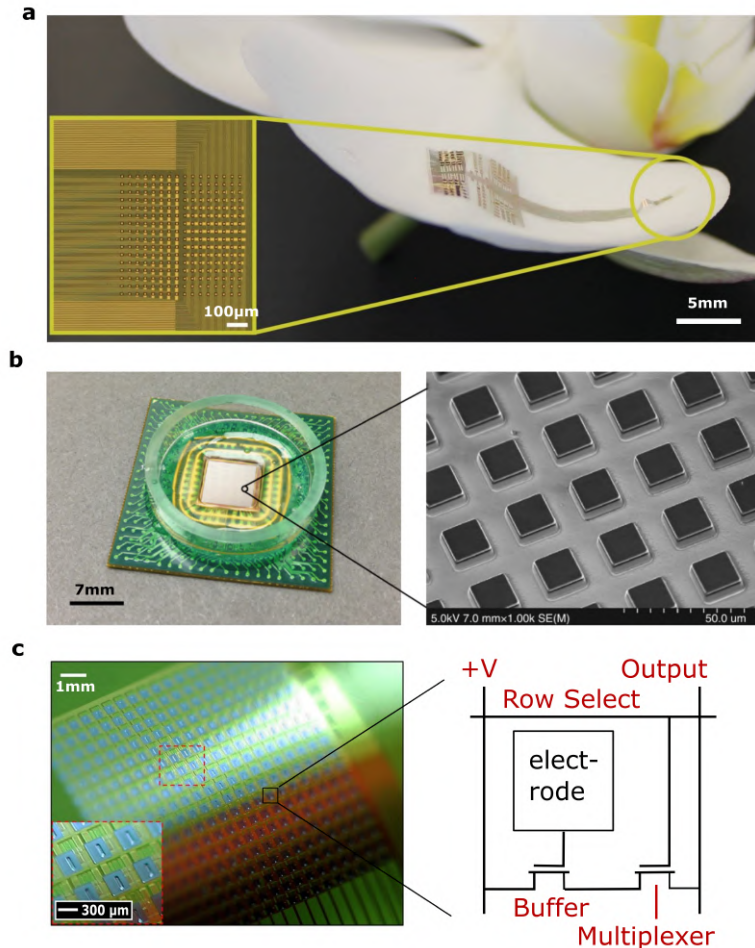
Figure 1.2: a, High-density and highly sensitive NeuroGrid device based on PEDOT:PSS semiconducting polymer on an orchid petal. Adapted with permission from Khodagholy et. al.[68]. **b,** Micro-electrode array based on a silicon complementary metal-oxide-semiconductor (CMOS) rigid technology with 65,536 recording and stimulating electrodes. Reprinted from Tsai et. al.[71]. **c,** Flexible, multiplexed sensor array with 380 recording sites based on Si nanomembrane transistors (left). On the right, the schematic for a single pixel of the array is shown which includes a buffer transistor coupled to an electrode and a switching element. Adapted with permission from Viventi et. al.[73].

Intra-cortical devices present similar challenges; however, in this case rigid devices can be inserted into the brain if their cross-section is small enough to minimize tissue damage. An interesting approach recently reported[77] is based on interfacing a bundle of stiff micro-wires with a high density CMOS-based readout integrated circuit (Fig. 1.3a). Similarly, integrated circuits for signal amplification and

multiplexing can also be fabricated on the base of high density silicon probes[78] (Fig. 1.3b). However, the application of these technologies has been so far limited to animal studies and the number of detected units declines significantly after implantation[79], presumably due to glial scar formation. In order to reduce the FBR, some works have developed flexible intra-cortical probes[18], which must be inserted using bioresorvable stiffener or using temporarily attached rigid shuttles. Minimizing the cross-section of flexible neural probes has been shown effective for monitoring SUA over chronic time points [39](Fig. 1.3c). In order to minimize the tissue damage while maximising the bandwidth of the probes, increasing the number electrodes per thread and controlling the exact insertion position to prevent blood vessels rupture has been proposed[14] (Fig. 1.3d).

From the previous discussion, it is clear that increasing the number of sensing sites on neuroelectronic sensing interfaces has been the focus of intensive research. Detection of SUA from a large number of neurons is expected to be an effective way to increase the bandwidth of neural interfaces. However, detection of intra-cortical activity is certainly more invasive than detection of LFP signals from the surface of the cortex. In the following section, the principles of brain-machine communication are introduced in order to justify the potential of surface probes compared to intra-cortical devices for high bandwidth brain to computer communication.
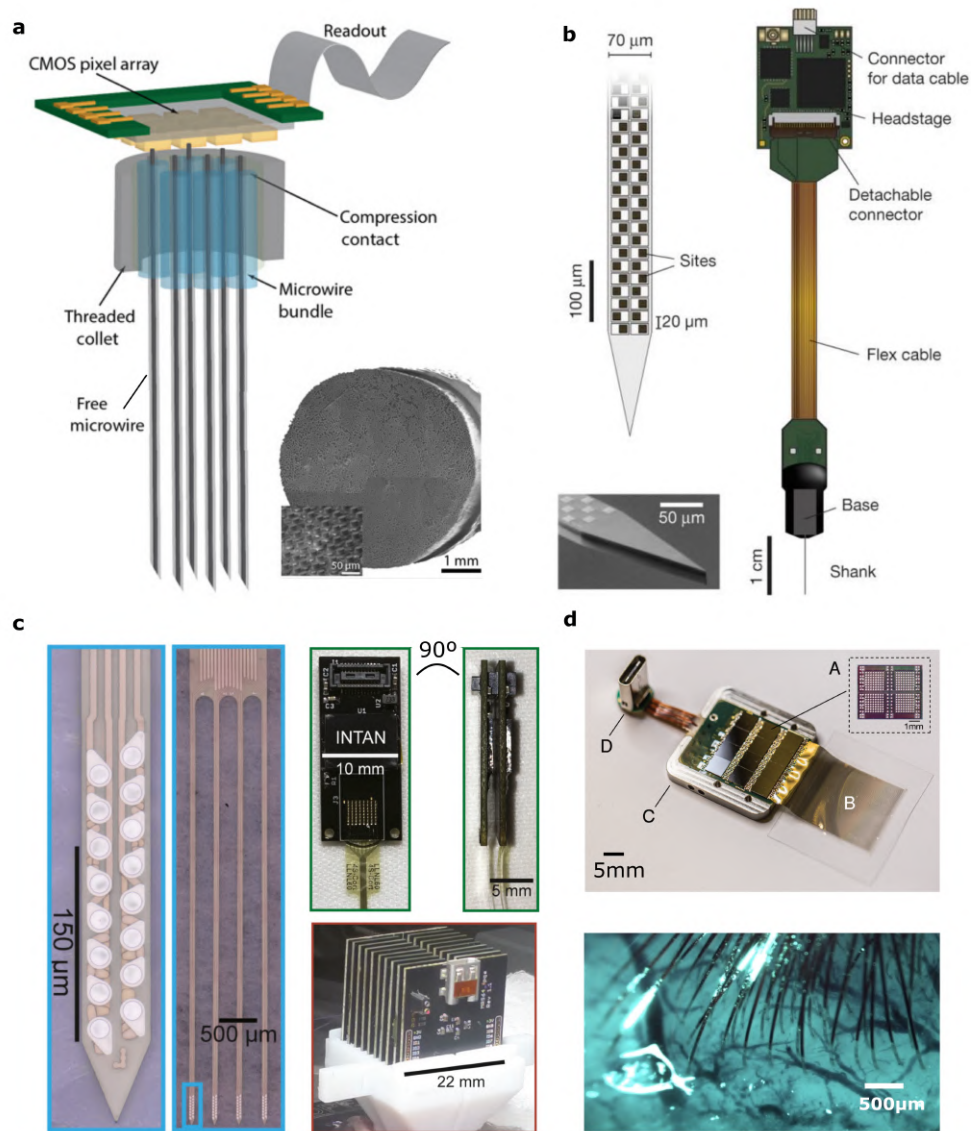
Figure 1.3: a, Schematic of the three-dimensional microwire arrays interfaced with rigid CMOS technology. The inset shows a bundle of microwires for interfacing the CMOS integrated circuit. The other end of the bundle, for interfacing the brain, must have a lower density of microwires to limit tissue damage. Reprinted from Obaid et. al.[77]. **b,** Neuropixel high density intra-cortical Si probe with integrated circuits for digitization and multiplexing of signals on the base of the probe. Printed with permission from Jun et. al.[78]. **c,** 64 channel, 4-shank intra-cortical flexible probes (left) enabling to stack up recording modules (right) up to 1024 channels. Adapted with permission from Chung et. al.[39]. **d,** Neuralink's device with dedicated integrated circuits for data amplification, digitization and processing (A) and up to 3072 sites (96 threads) (B). Up to 12 chips are integrated with the 3072 connectors (C) and data is transmitted through USB-C connector (D). Threads are individually inserted with a robotic system to minimize vascular rupture (bottom). Adapted from Musk et. al.[14]

1.2 Brain machine communication

The final goal of neural sensing interfaces is to provide information about the neural dynamics in the brain, which can be correlated with applied sensory stimuli or controllable cognitive states, such as the intention to perform specific motor actions or the intention to speak. These controllable variables will be referred here as the stimuli, although in particular cases could be motor intentions or other cognitive states controlled by the patient. Representation of such stimuli in the form of neural activity patterns is referred to as neural encoding[80]. If the neural correlates of stimuli are determined in a controlled setting, the neural responses evoked by a particular stimulus can be determined. This knowledge of the neural response can be expressed as the conditional probability of a neural response (r) happening given a particular stimulus (s), which can be expressed as $P[r|s]$. In an analogous, but opposite way, it is also possible to determine the state of the stimuli from their neural correlates in a process referred to as neural decoding. The knowledge about the stimulus when a certain neural response is observed can be expressed as the conditional probability of observing a stimulus given the occurrence of a certain neural response, $P[s|r]$. In this framework, the neural response, which presents an intrinsic variability, and the stimulus are considered stochastic variables. Therefore, neural coding ($P[r|s]$) and neural decoding ($P[s|r]$) are related through the basic identity of probability theory, the Bayes theorem:

$$P[s|r] = P[r|s]P[s]/P[r] \tag{1.1}$$

where the prior stimulus probability density of the stimulus ($P[s]$) and the response ($P[r]$) express the statistical properties of the stimulus and response respectively[80]. In the previous section, we have described the materials and electrical engineering strategies to produce neural sensing interfaces, distinguishing between epi-cortical and intra-cortical devices. Using intra-cortical probes, the extracellular potentials produced by single neurons can be detected. These signals represent the elementary electrical signals in the brain and are responsible, in a great extent, for its information processing capabilities[81]. Here, we maintain this distinction to discuss the process of neural decoding based on signals detected intra-cortically or from the surface of the brain.

1.2.1 Neural encoding and decoding based on spikes

The transmission of action potentials or spikes between neurons through synaptic connections allows the transmission and processing of information in neural networks[81]. Information can be encoded in the form of spike rates and/or timing of spikes[80, 82–84]. Spike rate codes are also referred to as independent-spike codes because no information is contained in the correlation among spikes. On the

other hand, time codes can also referred to as correlation codes, because correlation between spike times carry additional information. Although correlation codes have been shown to encode relevant information in some cases[85, 86], spike rate codes are generally simpler to analyse, and have been shown paramount for sensory and motor information encoding[47, 87–89].

In independent spike codes all the information is assumed to be encoded in the number of action potentials fired per unit of time. The firing rate represents a time dependent neural response ($r(t)$) of stochastic nature[80], with a certain variability among equivalent trials. Part of this variability is presumably intrinsic to the neuronal response[90], and another part might arise from uncontrolled parallel processing by the neuronal units which are not exclusively sensitive to a one-dimensional stimulus[17]. Determining the neural response, it is possible to characterize the term $P[r|s]$, which describes the encoding of information by spike rates. Furthermore, according to Bayes theorem, this information can be used to decode the information encoded by neural responses. In order to determine $P[r|s]$, the stimuli must be controlled while measuring the neural response. Knowing the relationship between stimulus and neural response allows to extract the so-called tuning curve $f(s)$ for particular neurons, which represents the firing rate as a function of the stimulus value. Such curve typically presents a maximum, corresponding to the preferred stimulus and a Gaussian distribution around this maximum[80]. From the uncertainty in $f(s)$ it is possible to determine the probability density distribution of $P[r|s]$. One way to estimate $P[r|s]$ from the tuning curves is assuming that the variability in the spikes number over a trial can be described by a homogeneous Poisson model[80] or more accurate statistical models[91]. Knowing $P[r|s]$, it is then possible to infer, or decode, the applied stimulus applied, for example by choosing the stimulus value corresponding to the maximum of $P[s|r]$ as the stimulus estimate.

This framework allows to decode a stationary stimulus from the average neural response. However, the variables to be decoded are typically time dependent ($s(t)$), and the neural responses are not only selective for a particular stimulus, but also for their dynamics[80]. A methodology to determine the preferred time dependence of the stimulus is called the spike-triggered average stimulus ($C(\tau)$). This function of time represents the average value of the stimulus at a time τ before a spike is generated. Therefore, it can be calculated by averaging $s(t_i - \tau)$, where t_i is the time of occurrence of each spike. If the number of spikes is large enough to estimate the time dependent firing rate ($r(t)$), the spike-triggered average can be calculated from the convolution of $r(t)$ and $s(t)$[80]:

$$C(\tau) = 1/<n> \int_0^T r(t)s(t-\tau)dt \tag{1.2}$$

where T is the time duration of the recording session. $C(\tau)$, similarly to a tuning

curve, describes the relation between the stimulus and the neural response. Therefore, given the knowledge of $C(\tau)$, the firing rate of a characterized neuron can be estimated from the presented stimulus. In turn, knowing the spike-triggered average it is possible to estimate the stimulus from the neural response. However, note that estimating the stimulus from the firing rates on real time is paradoxical. The reason is that the neural response is caused by the stimulus over a certain period preceding the response. Therefore, a certain time lag (τ_0), typically in the range of $100\,ms$, must be introduced between the time the stimulus takes place and its estimation[80?]. The larger the time lag the more accurate the estimation becomes, but the less practical it is for clinical applications. The first step towards constructing an estimate or kernel (K), is to determine how each spike contributes to the stimulus estimate. The contribution of each spike is the spike-triggered average, shifted by τ_0[80]. The convolution of this kernel with the neural response function ($\rho(t)$), defined as a sum of Dirac delta functions at the spike times ($\sum \delta(t - t_i)$), gives an estimate of the controlled dynamical stimulus:

$$s(t - \tau_0) = \int_{-\infty}^{\infty} (\rho(t - \tau) - <r>)C(\tau_0 - \tau)d\tau \tag{1.3}$$
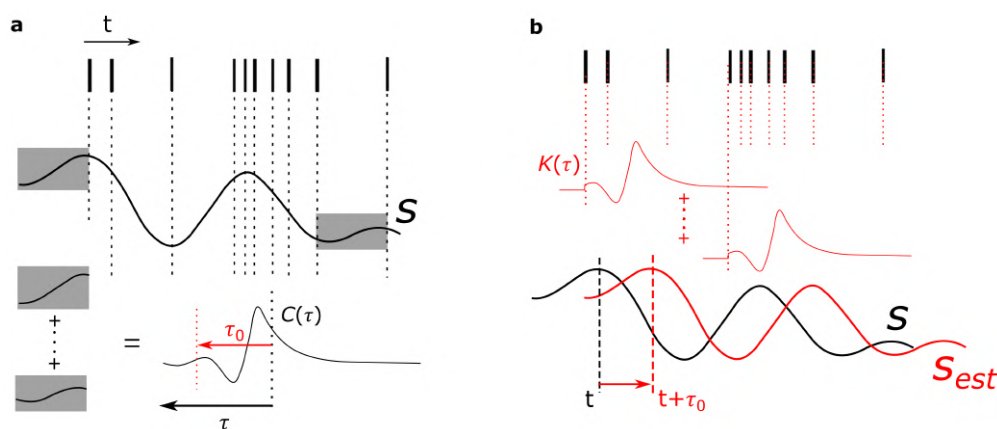
Figure 1.4: a, Schematic representation of spike-triggered average stimulus. The stimulus preceding each spike (represented within the gray boxes) are averaged leading to a preferred stimulus dynamics for the neurons under study. **b,** Using the spike triggered average it is possible to define a kernel for neural decoding. Each spike contributes with a kernel to a delayed stimulus estimate. Figure based on the work by Dayan et. al.[80].

Spike-triggered average can be interpreted as the preferred time dependence of the stimulus which is the most likely to cause a spike. The development of methods based on linear filtering[92, 93] and optimum kernel determination based on spike trains from large neural populations has led to important progress in the field of BCIs, in particular for the motor control of limbs [21, 41, 47]. However, we have previously seen that less-invasive epi-cortical neural probes typically do not have access to the activity of single neurons; instead, they are limited to LFP detection.

In the following section, the relation between single spikes and LFP is discussed in order to justify the potential and limitations of LFP signals for neural decoding.

1.2.2 Origin and decoding of LFP signals

Although action potentials have been detected from the surface of the cortex[68], all practical applications and the vast majority of neuroscientific studies based on surface recordings focus on LFPs because single units are hardly accessible. The reason is that the pia mater physically separates the sensors from the outermost cortical neurons in layer 1, which is sparsely populated by neurons[94]. On the other hand, LFPs emerge from the collective dynamics of neural populations and are therefore easily accessible from the surface of the brain. LFP are correlated with the activity of single neurons and therefore present a great potential for neural decoding. However, their interpretation is complex and a better understanding of their biophysical origin is crucial to improve the efficiency of their decoding.

When neurons in the brain elicit an action potential, ionic currents are generated across the ECM, which cause electrical potential gradients parallel to the charge flow. Constructive interference of currents generated by multiple neurons leads to large amplitude LFP signals that can reach the mV scale. Therefore, the amplitude of LFP activity strongly depends on the synchrony of local current sources (Fig. 1.5a). Slow extracellular currents, such as synaptic currents, are more easily synchronous and therefore they constitute the main contributors to LFP[51]. Similarly, long-lasting Ca^{2+} mediated spikes[95–97] can also affect significantly the LFP. Fast (Na^+) spikes, which last less than $2\,ms$, rarely fire synchronously and therefore have a relatively low, although not always negligible, contribution to LFP[51]. Due to the strong dependence of LFP power on synchrony of local sources, measureable LFP signals usually present oscillatory dynamics[98] that span over a frequency range that covers from infra-slow (< 0.5Hz) to ultra-fast oscillations ($200 - 600$Hz)[98]. Interestingly, higher-frequency components of LFP are usually phase-locked to lower frequency oscillations[99], presumably due to the interplay between excitatory and inhibitory neurons at different time scales[100].

Due to the collective origin of oscillatory LFP signals, they are considered to reflect large-scale brain dynamics[22] and are regarded as fingerprints of neural communication at different spatio-temporal scales[100–102]. Theta oscillations ($4-12\,Hz$)[103] are a well-studied example of oscillatory LFP patterns. Theta oscillations can be measured from the surface of the brain of small mammals such as the rat, although the measured fields are mainly generated in the hippocampus and parahippocampal areas and propagate through the cortex mostly via volume conduction[101]. Firing of pyramidal neurons[104] in the hippocampus at specific phases of the theta rhythm has been found to encode the spatial position of the animal[85], demonstrating the potential importance of LFPs for neural decoding. Another example of widely studied dynamics are gamma oscillations ($30-200\,Hz$), which are also modulated by

hippocampal theta[101]. Gamma oscillations have been observed in multiple neocortical areas during wake and REM sleep states[99] and have been shown to depend on the attention levels to sensory stimuli[105]. The origin of gamma dynamics is considered to be at the interplay between principal excitatory and inhibitory interneurons. When excitatory neurons fire stimulus-elicited action potentials, local inhibitory neurons are activated, which induce the network silencing for a certain period. When the inhibitory effects decline, excitability rises again in a timescale that presumably leads to the gamma oscillation[99, 100]. In this way, afferent excitatory inputs which are out of synchrony with the gamma oscillation in the target neural group would not be as effective in triggering a response[100]. Coherence among neural populations has been therefore proposed as a mechanism coordinating functional connectivity and it might enhance communication between distant neural populations, which is costly in terms of axonal connections[99]. The generation mechanism of gamma activity implies a strong correlation of its power with synchronous SUA in local clusters of neurons in the neocortex[101] (Fig. 1.5b), which in turn are coordinated by lower frequency theta activity. From this perspective, the generation of oscillatory LFP patterns might seem to be a mere epiphenomenon of synchronous action potentials encoding information[51]. However, there is evidence supporting that oscillatory LFP rhythms might have a causal role on spike synchronization via ephaptic effects[106]. Independently of the cause/effect relationship between LFP and spiking activity, it is the correlation of LFP to behaviourally relevant variables that gives useful information for decoding.

Due to the highly localized nature of gamma activity and its correlation with sensory input, it has been extensively investigated for decoding applications. Gamma activity has been used for decoding visual attention and extraction of tuning curves from the visual cortex[107, 108], decoding of attempted motor actions from the sensorimotor cortex[55], determination of complex acoustic signals encoding and their decoding from the superior temporal gyrus[109, 110]. Furthermore, it has been used for the decoding of articulatory kinematic trajectories related to speech from the sensorimotor cortex[6, 111]. As described above, LFP signals can be correlated with local firing rate of neural populations and their coherence among distal regions can be indicative of enhanced communication, showing similar or complementary information to SUA. Strategies for neural decoding from LFP signals are thus, in general, conceptually similar to the SUA-based decoding discussed in the previous section. The first step for neural decoding based on LFP is also defining the neural response feature for decoding. For SUA, the use of the firing rates was described as the most common feature. For LFP instead, the signal power in different frequency bands is generally used. Broad band gamma $(30-200\text{Hz})$ analysis is most commonly used, but in specific cases low frequency components have also been found informative[6, 108, 112]. Having defined the feature of interest, a decoding algorithm can be defined[113]. A common approach is to determine a filter kernel also referred to as the stimulus reconstruction model $(R(t,i))$[109], which is used to estimate the time dependent stimulus $(s_{est}(t))$ by its convolution with the neural

response $(r(f, t, i))$, in an analogous way as in Eq. 1.3(Fig. 1.5c), where i is the index of each sensor.

Compared to SUA, LFPs could provide a better signal stability for chronic applications due to the lower impact of glial scar on the collective LFP than on the local SUA[57, 112, 114]. Furthermore, LFP require a lower sampling rate than SUA (10-fold lower for gamma and down to 1000-fold lower for low-frequency LFP[112]). This reduction in sampling frequency potentially leads to a lower power consumption, which is an important advantage for wearable devices. In order to increase the information bandwidth of a neural probe, its spatial resolution should be improved in order to provide a detailed information of the signals topography[76, 109]. As a downside, an increase in the number of sensors also increases the amount of correlated information and the complexity of the dataset. Therefore, principal component analysis (PCA) is typically used to reduce the dimensionality of the extracted raw data[113]. In addition to increasing the number of sensors, another way to increase the information bandwidth of the neural probe would be to detect novel neural features that are currently not available. An example of such activity is infra-slow activity.

ISA could be an important feature for brain decoding applications due to its extremely low frequency, which could enable ultra-low power neuroprosthetics. Although ISA has been to date seldomly investigated, infra-slow fluctuations of higher frequency LFP bands have been reported[115]; further, ISA has been recently recognized as a possible mediator of brain sub-states[116] via the coordination of the resting state network[117] or modulation of higher frequency activity[118]. Furthermore, ISA has been found to correlate with the infra-slow blood oxygen level dependent (BOLD) signal measured using fMRI[116, 119, 120], which has been the standard method for the study of large-scale brain dynamics in the last decades. fMRI studies have demonstrated the selective activation of distinct brain areas in the infra-slow timescale for particular brain states, stimuli or tasks[116, 121]. However, BOLD has a poor temporal resolution[121] (in the scale of seconds), and electrophysiological methods present a low spatial resolution in the ISA band[122]. Furthermore, fMRI studies are limited to immobile conditions due to the large size of the magnetic resonance scanners, which has prevented the study of ISA correlates of natural behaviour. The combination of these technical hurdles has hindered the simultaneous characterization of infra-slow and high frequency dynamics with high spatial resolution in behaviourally relevant environments. In turn, these limitations have prevented the investigation of neural response features in the ISA band for decoding applications. Development of a novel technology that combines the large-scale coverage and ISA mapping capabilities of fMRI with the high temporal resolution and wearability of electrophysiological recordings would allow to investigate in greater detail the physiological role of ISA and evaluate its use for neural decoding applications. In the following section, graphene bioelectronics are introduced as a promising technology to bridge the gap between large-scale fMRI brain mapping and high spatio-temporal resolution electrophysiological recordings.
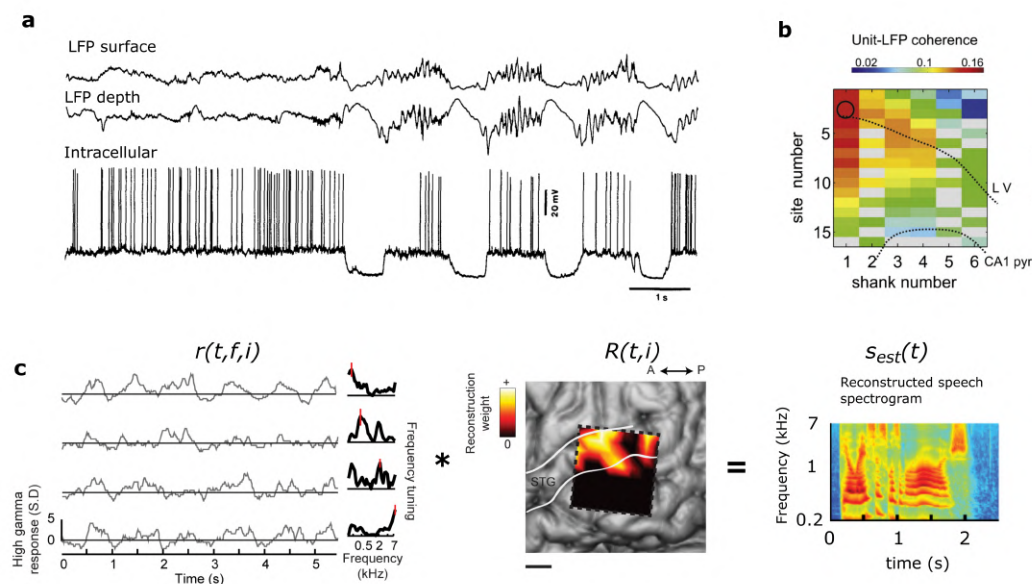
Figure 1.5: a, Recorded LFP signals from the cortical surface (top) and deeper layers (middle) of the motor cortex in an anaesthetized cat. Intracellular trace from a layer 5 pyramidal neuron (bottom). The slow alternation of hyperpolarization and depolarization of intracellular potential is reflected on the slow oscillations on the LFP. Higher spiking rates present a correlation with increased high frequency LFP power. Adapted with permission from Contreras et. al.[123]. Copyright 1995 Society for Neuroscience. **b,** Spatial topography of spike-gamma coherence in the rat hippocampus computed from depth recordings using multi-shank probes. Adapted with permission from Sirota et. al.[101]. **c,** High gamma band power (70–150 Hz, gray curves) induced in a single trial by a certain speech segment. Recordings are from four different electrodes placed in the superior temporal gyrus. The high gamma activity is z-scored and plotted in standard deviation units. Dark black traces on the right-hand side correspond to the frequency tuning curves sorted by peak frequency (marked by red bars) and normalized by maximum amplitude. The high gamma power is convoluted with the reconstruction model $R(t, i)$. The color map in the middle represents the anatomical distribution of fitted weights in the reconstruction model (scale bar is $1\,cm$. The right panel represents the reconstructed speech spectrogram. Adapted from Pasley et. al.[109].

1.3 Graphene bioelectronics

The previous section described the importance of developing highly biocompatible, flexible and ultra-thin neural interfaces. In addition, advanced neural interfaces can benefit from having a high sensor-count and wide frequency bandwidth, ideally from ISA band to SUA, in order to cover the entire frequency range of neural activity. An optimum material for the fabrication of neural sensing technologies should be highly inert, so that it does not degrade over time or causes chemical reactions in the physiologic environment. Additionally, it must be highly flexible and stable in

34

an ultra-thin conformation that can be handled and processed. Finally, in order to implement active sensors, which might solve current challenges in terms of sensor count and frequency bandwidth, an optimal material must present semiconductor or semimetal properties and a high electrical mobility. In this section, graphene is presented as an outstanding candidate to fulfil this challenging set of requirements. A short survey of previous literature on graphene technology is presented in order to describe the initial context of this work and outline the main challenges to move graphene bioelectronics from a promising technology into fully functional devices.

1.3.1 Graphene properties

The remarkable properties of graphene, from a mechanical, chemical and electronic perspective, emerge from the robust sigma bond among sp2-hybridized carbon atoms. These covalent bonds enable the formation of a highly stable two-dimensional hexagonal lattice, which is the building block of multiple carbon allotropes besides graphene[124]. The sigma bonds in graphene represent a closed valence shell, which is responsible for its high stability. On the other hand, the p_z orbitals, perpendicular to the graphene plane, also form covalent bonds but present a half-filled delocalized π-orbital, which is responsible for the electronic properties of graphene[125].

Electronic properties of graphene

The band structure of graphene, governing its electronic properties, can be modelled by considering only the linear combination of its p_z atomic orbitals. The first calculation of the dispersion relation of graphene was based on the tight binding model[126], which, when considering the interactions among nearest and next nearest carbon atom[125] can be expressed as in Eq. 1.4.

$$E_\pm(\boldsymbol{k}) - E_D = \pm t\sqrt{3 + f(\boldsymbol{k})} - t'f(\boldsymbol{k}) \tag{1.4}$$

where, $f(\boldsymbol{k}) = 2cos(\sqrt{3}k_y a) + 4cos(\frac{\sqrt{3}}{2}k_y a)cos(\frac{3}{2}k_x a)$. Here, t and t' stand for the nearest neighbour and the next nearest-neighbour hopping energy, respectively. $\boldsymbol{k}$ represents the momentum of electrons and a the distance among nearest carbon atoms. If the interaction among next nearest neighbours is neglected, the dispersion relation is symmetric for the bonding and antibonding π bands represented by the + and - signs in Eq. 1.4. If a finite value is assigned to t', this symmetry is broken, however the dispersion relation remains highly linear at the $\boldsymbol{K}$ and $\boldsymbol{K'}$ points of the Brillouin zone. At these points of the reciprocal space, the valence and conduction bands merge at an energy referred to as the Dirac energy (E_D). Fig. 1.6 shows the energy dispersion relation and the so-called Dirac cone. Expanding Eq. 1.4 around E_D leads to:
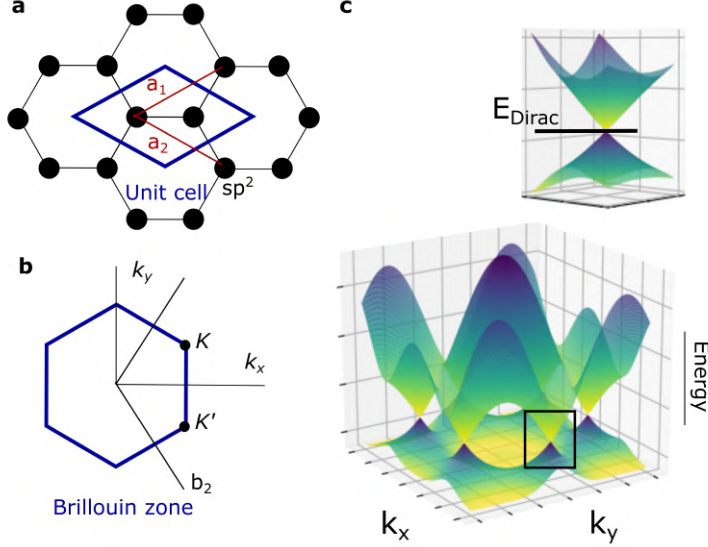
Figure 1.6: a, Crystalline lattice of graphene representing the unit cell and the lattice vectors $a_1 = (3, \sqrt{3})a/2$ and $a_2 = (3, -\sqrt{3})a/2$. **b,** Brillouin zone of graphene and reciprocal-lattice vectors $b_1 = (1, \sqrt{3})2\pi/3a$ and $b_2 = (1, -\sqrt{3})2\pi/3a$. The K and K' points of the Brillouin zone correspond to the position in reciprocal space of the Dirac point. **c,** Band structure of graphene as defined by Eq.1.4. The inset shows the dispersion relation around the Dirac point.

$$E_{\pm}(\boldsymbol{q}) \approx \pm v_F \mid \boldsymbol{q} \mid + O[(q)^2] \tag{1.5}$$

where $\boldsymbol{q}$ is the momentum measured relative to $\boldsymbol{K}$ and $\boldsymbol{K'}$, $O[(q)^2]$ represents the second order of the expansion around the Dirac point at which the Fermi velocity v_F was found equal to $10^6 m/s$[127, 128]. Interestingly, the linearity of the band structure implies that the charge carriers have a vanishing effective mass (m^*) at the Dirac point[128]. However, the average mass of electrons away from the Dirac point increases due to the contribution of the finite effective mass in the transverse direction of the Dirac cone[129]. The electrical mobility of charge carriers in graphene with a finite effective mass is therefore limited to a finite value, dominated by acoustic phonon-electron scattering in the ideal case. This intrinsic limit is predicted to be $2.10^5 \, cm^2/(Vs)$ at room temperature[130]. This extraordinary mobility is one of the main reasons for the interest on graphene for electronic applications. However, in addition to intrinsic sources of scattering, extrinsic scattering mechanisms further limit the mobility of graphene.

A prominent source of extrinsic scattering is the interaction of charge carriers in graphene with the substrate. One such source of scattering are infra-red (IR)-active

remote interfacial phonons (RIP) in the substrate[130], which degrade the mobility in graphene at room temperature down to maximum values of $\sim 4.10^4\,cm^2/(Vs)$ for SiO_2 as well as certain polymeric substrates[130]. Other sources of scattering induced by the substrate such as microscopic corrugations[131] and charged impurities[132] can also attenuate significantly the mobility in graphene. In addition to substrate-induced scattering, structural defects in the graphene lattice can play a detrimental role on the electrical properties of graphene. Structural defects in graphene are typically classified as point defects or one-dimensional defects[133]. In the first group, it is possible to differentiate among Stone-Wales (SW) defects, which occur when rotating a C-C bond by 90° on the graphene plane (Fig. 1.7a), vacancies or adatoms. Point defects typically induce a certain degree of sp3 hybridization in the carbon lattice[133]. SW and vacancies present a reconstruction of the lattice from the original hexagons into a combination of heptagons and pentagons, which present dangling bonds only in case of odd number of carbon atoms missing and relatively high formation energies[133] (Fig. 1.7). A series of experiments determined the effect of point defects and charged impurities on the mobility of graphene on SiO_2, showing that initial values in the order of $10^4\,cm^2/(Vs)$ are attenuated proportionally to the density of both charged as well as uncharged impurities[132, 134]. Similarly, the mobility in graphene has been found to depend on the presence of one-dimensional grain boundaries among crystals, resulting in a low mobility in the range of $10^3\,cm^2/(Vs)$, which can eventually increase up to $2.10^4\,cm^2/(Vs)$ after grain boundary healing treatment[135]. In order to eliminate these extrinsic limits, isolation of high quality graphene samples from the substrate has demonstrated mobility values near to the intrinsic limit, up to $1, 4.10^5\,cm^2/(Vs)$). These record values at room temperature were measured for field-effect transistors based on graphene sheets exfoliated from graphite and subsequently encapsulated between hexagonal boron nitride (hBN) films[136], demonstrating the strong effect of the substrate on the properties of high-mobility graphene samples[137].

Mechanical and chemical stability of graphene

Due to the strong σ bonds among carbon atoms, graphene presents a relatively low density of structural defects and its intrinsic strength is the highest ever measured in any material[139–141]. These mechanical properties make graphene devices on flexible substrates stable; however, the presence of structural defects can have a strong impact on its mechanical and chemical properties. The presence of point defects, in particular SW defects and vacancies, are expected to decrease the failure strain of graphene and slightly decrease its Young's modulus[142]. This prediction has been confirmed experimentally by measuring the breaking strength and elastic modulus of graphene with a controlled level of sp3 defects or vacancies induced by oxygen plasma[143]. Results show that while oxygen adatoms and vacancies have a relatively low impact on the graphene stiffness, the strength of the graphene lattice is significantly compromised by vacancies[143].
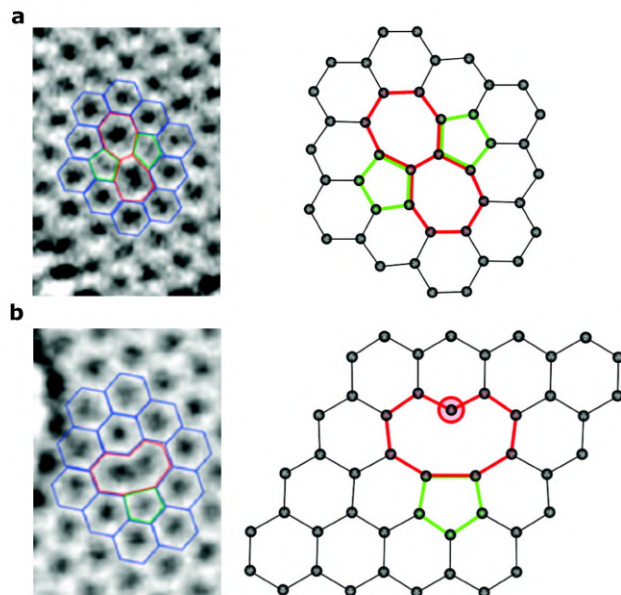
Figure 1.7: a, Transmission electron microscopy (TEM) image of a graphene lattice with a SW defect (left) and its schematic representation (right). **b,** TEM image of a graphene lattice with a single vacancy defect and its schematic representation (right). Panel a and b have been reprinted with permission from Banhart et. al.[133], which in turn was reprinted from Meyer et. al.[138]. Copyright 2008 American Chemical Society.

Similarly, structural defects also affect the chemical properties of graphene by increasing its local reactivity[133]. One example of such increased reactivity described theoretically is the covalent bonding of an hydrogen atom to a carbon in the graphene lattice. The formation energy of such bond in pristine graphene is $1.5\,eV$ while its energy for a SW or a bi-vacancy is 0.3 and $0.93\,eV$ respectively[144]. Interestingly, the chemisorption energy of an additional hydrogen atom is lower than for the first one. However, in the case of defective graphene with SW or vacancy defects, there is an energy barrier after the chemisorption of few hydrogen atoms (Fig. 1.7c). In contrast, in pristine graphene the chemisorption energy of an hydrogen atom decreases monotonically with each hydrogen atom addition[144],suggesting that realistic, imperfect, graphene might present local energy minima preventing the complete degradation of the atomic layer in reactive environments. The oxydation of graphene via the adsorption of hydroxyl groups or the dissociation of O_2 molecules shares certain features with the adsorption of hydrogen atoms; however, the effect of structural defects has not been investigated. While the chemisorption energy for oxygen atoms on pristine graphene presents a global minimum for full coverage[145], for hydroxyl groups it presents a global minimum for 75 % coverage [145]. Nevertheless, graphene does not oxydize in standard atmospheric conditions

at low temperatures ($< 200\,°C$), and the theoretical chemisorption energy for triplet O_2 molecules is very high, suggesting that the singlet O_2 should play a role in the oxydation of graphene[146]. This observation could be critical for the application of graphene devices for neural sensing in chronic settings, where its chemical stability is critical.

Another source of increased reactivity is the presence of charged impurities at the substrate, which locally shift the Dirac energy in graphene, leading to an increase in the density of states and consequently an increased electron-transfer reaction rate to unoccupied electronic states of reactive species[147]. In pristine graphene, the density of charge carriers at the Dirac point should be homogeneous and only different from zero due to thermal fluctuations. However, local changes in the Dirac energy induced by charged impurities lead to the so-called charge puddles[148]. Increased reactivity in graphene with charged impurities has been found to be more prominent in single-layer graphene compared to multi-layer graphene and has been found to be supressed by the use of a h-BN substrate[149].

Opto-electronic properties of graphene

Single layer graphene presents a high optical transmittance because of its monoatomic structure[150]. However, scattering of photons with electrons and phonons in the two-dimensional lattice provide rich information about the number of graphene layers, doping, density of defects or strain. In particular, Raman spectroscopy has been shown to be a powerful tool for non-destructive analysis of graphene properties[151]. Raman spectroscopy is based on the inelastic scattering of photons by phonons. When a photon with energy $\hbar\omega_L$ interacts with the atomic structure it perturbs the energy of electronic states, inducing an oscillation of electrons with frequency ω_L. This excited state is short-lived and it can be followed by either a direct relaxation to the initial state (i.e. elastic scattering) or the interaction with the lattice phonons producing a variation in the energy of the scattered photon $\hbar\omega_S = \hbar\omega_L \pm \hbar\Omega$ (i.e. inelastic or Raman scattering, where $\hbar\Omega$ is the energy of the phonon taking part in the scattering process). Because of energy and momentum conservation and because of the negligible momentum of photons, first-order Raman scattering only probes the phonon states around the Γ point of the Brillouin zone, which corresponds to the E_D. However, scattering of multiple phonons can lead to the characterization of higher momentum phonon states without violation of the momentum conservation selection rule. Raman scattering typically involves multiple intermediate states, including electronic excited states[152]. In addition, the effect of defects in graphene can also modify the momentum of electronic states by electron-defect scattering and therefore enable activate additional Raman modes.

In defect-free single layer graphene, the only one-phonon Raman-active mode is the G-peak at ($\approx 1585\,cm^{-1}$). Another prominent peak appears due to the interaction of two phonons with opposite wave vectors, the 2D-peak at ($\approx 2685\,cm^{-1}$).

The relative intensity and energy of these two modes depends on the doping of graphene[153]. On the other hand, the D and D' band are activated by defects, D-peak for intervalley scattering and D'-peak for intravalley scattering, and allow to characterize the density of structural defects in the graphene lattice and to extract information about the nature of the structural defects. Experimental works have shown that the intensity of the D band is primarily associated with sp^3 hybridization of carbon atoms while the intensity of the D' increases for vacancy type defects[154].

In summary, graphene presents outstanding mechanical, chemical and electrical properties, which arise from its particular crystal structure and atomic orbitals hybridization. While the structure of the graphene lattice governs the properties of pristine graphene, real samples present multiple types of non-idealities, which effectively govern the actual mechanical, chemical and electronic properties. In order to use graphene in technological applications, controlling the presence of structural defects and impurities is therefore paramount. In the following section, the state of the art graphene production and processing techniques are described with the aim of highlighting the main technological challenges and promising strategies to improve the maturity of graphene-based bioelectronics.

1.3.2 Wafer-scale graphene technology

The electrical, mechanical and chemical properties of graphene depend on the structural defects and the presence of impurities in the graphene environment. Therefore, in order to achieve high performance devices it is important to optimize three main aspects of graphene technology; the graphene growth, its transfer onto the final substrate and the microfabrication processes to produce functional graphene devices. In order to move graphene electronics forward into industrial production these three steps must be optimized at a wafer scale to produce high-performance devices with high homogeneity and reproducibility. In addition, the final graphene properties must meet particular specifications for different applications; therefore, an application-oriented development is crucial to reach this technological maturity. In the 1st stage of this thesis, the main focus is placed on thoroughly characterizing and modelling of graphene transistors produced in a wafer-scale in order to evaluate and optimize their performance for bioelectronic applications. In this section, the state of the art large-area graphene technology is surveyed in order to define the context of this thesis.

Graphene can be produced by several methods, including mechanical exfoliation from graphite[155], chemical exfoliation[156], epitaxial growth on SiC[157] or by CVD growth on catalitic metals. The highest quality has been reported for mechanically exfoliated samples, with carrier mobilities up to $1,4.10^5\,cm^2/(Vs)$ at room temperature. However, the trade-off between large scale production and high electrical performance is optimal for CVD growth, with production areas in the

range of tens of inches[158] and carrier mobilities up to $5.10^4\,cm^2/(Vs)$ at room temperature[159]. CVD graphene is therefore the most promising technique for large-area and high quality graphene production[160, 161]. In the CVD growth of graphene, the precursor gas (typically CH_4) is introduced into a chamber with a controlled gas pressure and temperature. The precursor undergoes a reaction in the gas phase to form active species (C_xH_y), which can then diffuse until reaching the catalytic metal surface. The activated carbon species adsorb on the catalytic surface and decompose into carbon atoms and hydrogen, which desorbs from the surface[162]. If the diffusion of activated species in the gas phase is relatively slow, it can be the limiting factor in the growth (i.e. diffusion-limited regime). Otherwise, if the catalysed decomposition rate is the limiting factor, the growth occurs in the reaction-limited regime. Changing the temperature, the gas pressure or the catalytic metal, the growth regime can be tuned. On the other hand, if the catalytic material presents a high carbon solubility, the carbon sources decompose on the surface and the carbon radicals diffuse into the bulk (Fig. 1.8-top). When the temperature is decreased, the dissolved carbon concentration exceeds saturation and aggregates on the metal surface. This growth regime can be employed to produce multilayer graphene samples; however, the growth of SLG cannot be easily controlled. Alternatively, if catalytic metals with very low carbon solubility are used, such as Cu, the carbon radicals formed onto the metal diffuse onto the surface to form the graphene lattice (Fig. 1.8-top). This process is a self-limited growth, which typically leads to a graphene monolayer[162] and it is therefore preferred for large-area SLG growth.
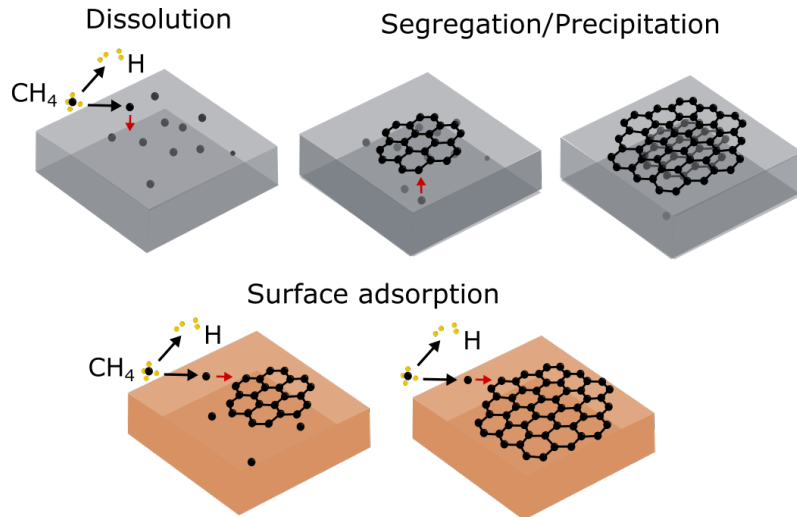

Figure 1.8: Growth mechanism of graphene on catalytic metals with high carbon solubility (top) and self-limited graphene growth on the surface of catalytic metals with low carbon solubility (bottom). Adapted with permission from Li et. al.[163]. Copyright 2009 American Chemical Society.

After the growth on a Cu substrate, the SLG must be transferred onto an insulating

substrate. The transfer process typically requires the use of a support layer, which provides sufficient mechanical strength to minimize cracks on the graphene sheet. A typically used supporting layer material is poly(methyl methacrylate) (PMMA) due to its sufficient strength, insolubility in water and solubility in solvents such as acetone. After depositing the support layer, the Cu substrate must be separated from the graphene layer. This process is typically done by wet etching of Cu. However, other methods such as electrochemical bubbling or dry transfer methods have also been developed[164]. One of the main challenge in the transfer process is the elimination of residues such as support polymer traces, metal residues or trapped water between the graphene and transfer. In order to minimize the presence of polymer residues, paraffin has been recently reported to be a promising alternative to PMMA, with non-covalent affinity to graphene, it leads to a clean surface and high carrier mobilities above $1,4.10^4 \, cm^2/(Vs)$[165] which are close to the limit imposed by substrate induced scattering at room temperature[130]. Similarly, dry transfer using h-BN layer encapsulation, which presents a high van-der-Waals interaction with graphene, has shown successful detachment from the Cu substrate leading to high mobilities for graphene flakes in the order of $5.10^4 \, cm^2/(Vs)$ at room temperature[159].

Finally, after completing the graphene transfer process, the graphene must be patterned and metallic contacts usually defined. This process must be carried out by lithographic methods, using photodefinable resists, which also represent a major source of contamination. Graphene is especially prone to photo-resist residues due to its 2-dimensional nature. First, because of its high surface to volume ratio the effect of surface charges, defects and trap states has a huge impact on the graphene properties. Second, because dry-etching methods typically used to eliminate resist residues from the surface of bulk semiconductors cannot be directly applied in graphene to prevent its etching. Therefore, development of specific cleaning methods and sacrificial layers to protect graphene is required. Cleaning of resist residues by thermal annealing[166–168] or by ultra-violet ozone (UVO)[169] have been explored with relative success. Similarly, recent works reported the use of Cu sacrificial layers to protect graphene against resist residues[170]. In this thesis, the focus is placed on evaluating the technological maturity of devices based on CVD-grown graphene transferred by a standard PMMA-based wet transfer process for neural sensing. Following the characterization and modelling of the graphene biosensors, the presence of resist residues has been found to be often related with performance degradation and diverse procedures have been implemented to optimize the sensitivity of graphene biosensors.

1.3.3 Graphene active sensors

As previously argued, increasing the frequency bandwidth and sensor count of neuroelectronic sensing interfaces is of great importance to measure the electrical activity generated by individual neurons and neural populations in the brain with high

spatio-temporal resolution. As previously introduced, active sensors have emerged as a promising building block for high bandwidth neural interfaces[11, 76, 171–173] because they can be arranged in a multiplexed array[73, 174]. The detection principle of active biosensors is based on the transduction of electrochemical potentials signals in the environment into electric currents from the drain to the source of a transistor[73, 173, 175–178]. Although active sensors present important advantages compared to passive electrodes, their use has been typically constrained by the demanding functional properties of the materials needed for their fabrication, combined with the required biocompatibility and long-term stability. Graphene solution-gated field-effect transistors (g-SGFETs) are a promising technology to satisfy all these challenging requirements. This section, summarizes the basic properties of g-SGFETs, their stationary response and the understanding of low-frequency noise in graphene transistors prior to this thesis.

As introduced in the previous section, the conduction and valence bands in graphene are approximately symmetric and linear around the Dirac energy, where the density of states is minimum. This band structure leads to ambipolar transfer characteristics of graphene field-effect transistors (GFETs), which are approximately symmetric for the hole and electron conduction regimes. The conductance minimum is found at the charge neutrality point (CNP), where the average density of electrons in graphene equals the average density of holes, leading to a transport dominated by the residual carrier density (n_0). n_0 in GFETs takes a finite value due to thermal excitation of carriers and variations in the Dirac energy[179, 180]. Away from the CNP, the density of charge carriers (n) can be approximated as the charging of the gate capacitance (C_{gate}) with respect to the potential at the CNP (U_{CNP})[179] (i.e. $n \propto \sqrt{(U_{gs} - U_{CNP})^2 C_{gate}/e}$).

Due to the high stability of graphene in aqueous environments, the graphene channel in GFETs can be directly exposed to the electrolyte solution in a g-SGFET architecture. The gate capacitance in this configuration is, in a first approximation, given by the double layer capacitance (C_{dl}) that forms at the graphene-electrolyte interface[181]. The double layer consists of a first charged layer in graphene and a second layer of closely packed ions separated by the Debye length, in the nm scale. This short separation leads to a high gate capacitance, which is paramount to effectively transduce electrochemical potentials at the gate into variations of charge carriers. In addition to C_{dl}, the gate capacitance presents an additional term in series due to the low density of states in graphene around the Dirac point. This term, referred to as the quantum capacitance (C_Q)[182, 183], effectively limits the gate capacitance around the CNP. C_Q presents a minimum value at the CNP, which depends on charged impurities n_{imp}[183] and increases proportionally to the potential drop at the quantum capacitance, or chemical potential (U_Q)[183, 184](Eq. 1.6). For $eU_Q \gg kT$[183]:

$$C_Q \approx \frac{2e^2}{\hbar v_F \sqrt{\pi}} \sqrt{\left(\frac{eU_Q}{\hbar v_F \sqrt{\pi}}\right)^2 + n_{imp}} \qquad (1.6)$$

where $U_Q = U_{gs}C_{dl}/(C_{dl} + C_Q))$.

From the dependence of the quantum capacitance on the gate bias (Eq. 1.6), the conductance in graphene can be described as $G_{ds} = \mu e n(U_Q)W/L$, where W and L stand for the width and length of the transistors respectively, μ for the electrical mobility and $n(U_Q) = n_0 + kU_Q^2/2$ [184], neglecting the effect of n_{imp} on C_Q. The complexity in modelling the stationary response of GFETs mostly comes from the non-linear dependence of C_Q on U_{gs}. Additionally, in g-SGFETs the drain-source bias (U_{ds}) is typically in the same order as U_{gs}, due to the high gate capacitance. Therefore, the non-homogeneous effective gating across the graphene channel must be taken into account in order to properly model the g-SGFET response[185, 186]. Implementation of such solution in a compact model compatible with circuit simulation tools provided an accurate description of the current-voltage relation and the charge distribution across the channel, even for channel potentials values close to the Dirac point[186].
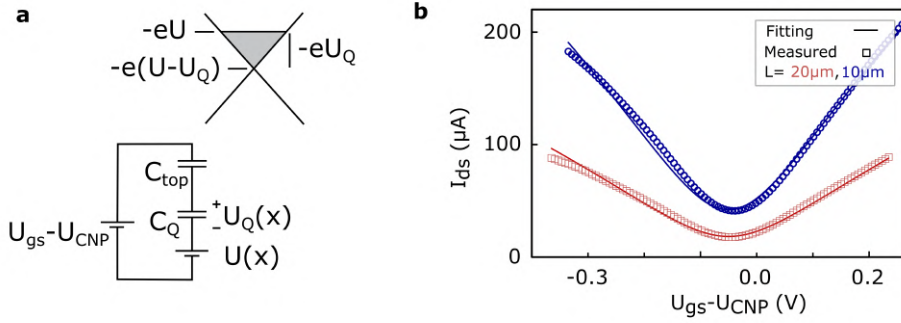
Figure 1.9: a, Equivalent capacitive circuit of a GFET (bottom) and schematic of the dispersion relation in graphene indicating relation between the variables U_Q and U and the position of the Fermi energy relative to the energy at the Dirac point. **b,** Transfer characteristics of g-SGFETs for two different channel lengths. Experimental data (empty symbols) correspond to the average for $n = 16$ g-SGFETs; the fitting (solid line) has been done using the compact model reported in Landauer et. al.[186]. This data corresponds to experiments reported in Schäfer, Garcia-Cortadella and Bonaccini et. al.[187].

Assuming a constant potential along the channel and a voltage independent capacitance, a simplified expression can be derived to describe the current-voltage relation in GFETs, which is accurate in the linear regime of the transfer characteristics. The slope of the current-voltage relation or transconductance (G_m) can be expressed as:

$$G_m = U_{ds} \frac{W}{L} \mu e \frac{dn}{dU_{gs}} \approx U_{ds} \frac{W}{L} \mu C_{gate} \qquad (1.7)$$

From this simplified expression it is clear that the transconductance of GFETs is, in a first approximation, proportional to the electrical mobility in graphene as well as their gate capacitance. Due to the exceptional μ in graphene and the high double-layer capacitance enabled by its high stability in aqueous environments, g-SGFETs present a high transconductance in the range $1 - 4\,mS/V$ for squared transistors, which is about two orders of magnitude higher than that of flexible silicon-nanomembrane transistors[73]. An important technological aspect of transistors, which is critical to maintain a high G_m, is the metal-graphene contact resistance[188, 189]. The metal-graphene contacts are a challenging aspect of graphene technology due to several factors. First, the mismatch between the work function of graphene and metals as well as the low density of states in graphene limit charge transfer[190, 191]. Secondly, the relatively high sheet resistance of graphene, due to its two-dimensional nature, leads to the so-called current crowding effect by which most of the current flows close to the contact end[192, 193]. In order to minimize contact resistance, many works have focused choosing metals that interact more strongly with graphene[190], creating dangling bonds in carbon atoms at the contact [194–197] or reducing the distance between edge carbon atoms and the contact end[136, 198]. Having a low contact resistance is therefore paramount to achieve a high transconductance, and thus an efficient signal transduction.

In sensing systems basd on graphene transducers, the transconductance of the transistors is the first pre-amplification stage. After the electrical potential signals are transduced at the transistor level, the resulting drain-source current signals are further amplified by an external transimpedance amplifier, which converts the current signals back to voltage prior to digitalization. Having high transconductance is therefore critical to pre-amplify small neural signals above the intrinsic noise of the amplifier chain. The higher the transconductance of GFETs, the higher will be the relation between signal and the floor noise of the amplification system. However, active sensors also present an intrinsic noise, typically $1/f$, that limits the sensitivity of the recording system beyond the noise of the amplifiers. The intrinsic sensitivity of g-SGFETs can be determined as the ratio between between G_m and the RMS current noise I_{ds-rms}, which is referred to as the equivalent noise at the gate (U_{gs-rms})[176]. This term is an important figure of merit, and corresponds to the signal amplitude at the gate that equals the RMS noise. In order to improve the sensitivity of g-SGFETs, it is therefore critical to understand the origin of $1/f$ noise in graphene and mitigate its effects.

$1/f$ or flicker noise appears in many kinds of devices and the nature of its generation has traditionally been a controversial topic[199, 200]. Fluctuations in the conductance can arise from changes in the electrical mobility or in the number of charge carriers. In the case of graphene, both contributions have been observed to

be significant in different regimes[201]. On the one hand, fluctuations in the number of charge carriers can occur due to carrier excitation-relaxation events between conduction and trap states in the environment of graphene. On the other hand, mobility fluctuations can occur due to changes in the scattering cross-section of scattering centres[202]. These transitions between different scattering cross-sections, or between trap and conduction states can be characterized by their transition rate, and can be described in the frequency domain by a Lorentzian spectral density function. Below the characteristic frequency, the PSD remains constant while for higher frequencies it presents a $1/f^2$ decay[201, 202]. The superposition of multiple events with different time constants, homogeneously distributed across a particular frequency range, leads to $1/f$ noise[201, 202](Fig. 1.10).
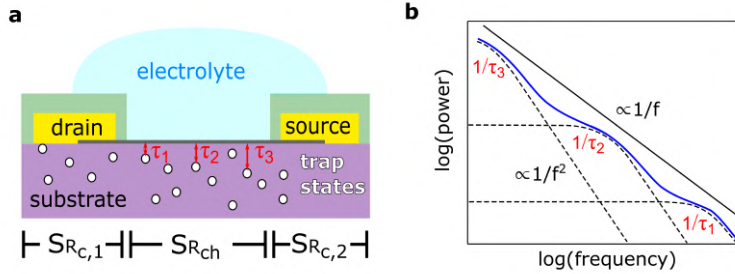
Figure 1.10: a, The charge trap states in the vicinity of graphene generate trapping-detrapping noise with a time constant τ, which depends on the graphene-trap distance[201, 203]. **b,** The power spectral density of trapping-detrapping events presents a Lorentzian distribution, corresponding to a $1/f^2$ decay above the characteristic frequency. Superposition of events with different time constants can lead to a $1/f$ decay.

1.3.4 Chapter outlook: towards high bandwidth graphene neural probes

In this chapter, the rationale behind the need for high bandwidth neural interfaces has been introduced. The bandwidth of a neural sensing interface can be defined as the information per unit time that can be decoded from detected patterns of neural activity. Neural decoding is based on determining the correlation between the controlled cognitive states of interest in a set of training experiments, which are then used to estimate the intentions of the patient in the final clinical application [6, 21, 80]. The communication bandwidth of this neural interface depends on the information contained in the correlation between the cognitive variables of interest and the neural response ($P[s|r]$) which, in turn, depends on the spatio-temporal resolution of the neural features detected. The intracranial implantation of sensor arrays enables the detection of local neural activity with high resolution. However, in order to prevent clinical complications, the implanted devices must be highly biocompatible, mechanically compliant with the soft brain tissue, as well as chemi-

cally and mechanically stable for long-term operation in chronic implants. Clinical translation of neural implants for BCI applications has led to promising results when using high-count sensor arrays, therefore motivating the development of advanced technologies with higher sensor-count and improved long-term biocompatibility and stability[14, 39, 76, 78, 204].

In this thesis graphene active sensor arrays are presented as a promising technology to satisfy the technical requirements for intracranial, high sensor-count neural probes for long-term mapping of brain activity. Graphene is an atom-thick crystalline material that presents a high chemical inertness in aqueous environments[144, 145], a high mechanical strength[141] and a very high electrical mobility[136]. This combination of properties enables the operation of graphene field-effect transistors in a solution-gated architecture, where the brain tissue represents the gate electrode that modulates the conductance of the active graphene sensors. Furthermore, graphene transistors can be arranged in an addressable matrix to enable the multiplexing of large sensor arrays. In order to move graphene-based neural probes from a promising concept to advanced functional systems, this thesis presents three main technology development stages.

In the first stage, the performance of graphene active sensors produced in a wafer-scale is evaluated at the single-device level. The principle of detection is thoroughly investigated; including the origin and mitigation of low-frequency noise, the frequency response of the sensors and the mechanisms of signal distortion. In a second stage, the performance of the sensors is evaluated at the system level, investigating the reproducibility and homogeneity of the arrays and integrating them in a recording systems for a chronic brain mapping in freely moving rats. Finally, novel strategies for the multiplexing of g-SGFETs are presented, which show a great potential for the integration of hundreds of graphene sensors with a high stability, chronic biocompatibility and high sensitivity. The combination of these results makes graphene active sensor arrays a unique tool for the investigation of large-scale brain dynamics and a promising technology for the implementation of high bandwidth brain computer interfaces.

Chapter 2

Single device characterization and modelling:
Wide frequency band sensing

The sensitivity of graphene active sensors is a critical property for neural sensing of low-amplitude extracellular potentials. The sensitivity of g-SGFETs results from the relation between their transconductance and their intrinsic LFN. Therefore, understanding the current-voltage relation of g-SGFETs and the origin of LFN in graphene is paramount to optimize their performance. While the stationary response of g-SGFETs and the intrinsic LFN have been previously investigated, there are still existing gaps in their understanding and technological optimization. The first stage of technological development of this thesis is focused on the study of the performance of g-SGFETs from a single device perspective. First, the relative contribution of the contacts and the channel to LFN has been modelled in order to guide the enginering of devices with low contact noise. Secondly, the effect of non-idealities in the stationary and frequency response of g-SGFETs has been investigated, leading to a deeper understanding of signal distortion mechanisms and the optimization of their sensitivity in a wide frequency band.

2.1 Noise characteristics in graphene transistors

The intrinsic LFN in graphene transistors has been the subject of intense research. The reason is that graphene is particularly promising for analog electronics, due to its high electrical mobility and two-dimensional nature[205]. However, in opposition to digital electronics, applications such as radio-frequency communication[205], chemical[206] and biological sensing[176] or optoelectronic applications[207] are susceptible to LFN. Furthermore, graphene is expected to be particularly prone to LFN due to its high surface to volume ratio, which implies a strong interaction of carriers with trap states and charged impurities in its environment[208]. In addition to the physical mechanism underlying the generation of LFN in graphene transistors resulting from its interaction with the environment, another topic of debate is the role of the metal-graphene contacts in noise generation. Previous works have characterized LFN in GFETs generated at the contacts or in the active graphene channel[208–210] (Fig. 2.1a). In particular, Heller et. al. [209] presented a model of noise in g-SGFETs with a channel noise contribution independent of the contact noise. The former contribution was assumed to be proportional to the transconductance of the g-SGFETs, leading to a noise power generated in the channel proportional to g_m^2[209], as previously derived to describe LFN in silicon transistors[211]. However, this model presented deviations from the experimental data both away from as well as close to the CNP. In order to correct deviations from the model away from the CNP, the authors proposed to introduce a term proportional to I_{ds}^4 describing contact noise. Although the model described most features of the gate bias dependence of LFN in g-SGFET, deviations around the CNP were presumably related to the assumption of homogeneous charge distribution in the graphene channel. Later works addressed the study of contact noise in further detail and proposed that the current crowding effect, which reduces the effective area of the metal-graphene contact, could be the physical origin of high contact noise[210]. However, this explanation implies that contacts with lower resistance (i.e. a shorter current transmission length) would present a higher contact noise, which is not observed. In short, a complete model of low-frequency noise in graphene transistors describing the physical origin of contact noise, the effect of non-homogeneous charge noise in the channel, and the relative contribution of channel and contact sources is still missing.

2.1.1 Contacts noise modelling and mitigation

The 1st complementary article of this thesis addressed the evaluation of the relative contributions from the contacts and the channel to LFN. For this purpose, the current noise power (S_I) generated in g-SGFETs was characterized for a wide range of channel geometries. More details on the fabrication process are provided in the experimental section of the 1st complementary article of this thesis (Appendix B). In order to distinguish between the noise sources at the contacts (S_{R_c}) and in the

channel ($S_{R_{ch}}$), the relation between S_{R_c}, $S_{R_{ch}}$ and S_I was derived. It can be shown that the normalized current noise power (S_I/I^2) is equivalent to the normalized resistance noise power (S_{R_T}/R_T^2), where R_T is the total resistance of the conductor. Assuming that fluctuations in the resistance of the channel and the contacts are uncorrelated, the total power of resistance fluctuations can be expressed as the sum of their individual contributions:

$$\frac{S_I}{I_{ds}^2} = \frac{S_{R_c} + S_{R_{ch}}}{R_T^2} \qquad (2.1)$$

From Eq. 2.1, the geometrical dependence of each of the contributions can be expressed explicitly:

$$\frac{S_I f}{I_{ds}^4} = (k_{R_c}/W^3 + k_{R_{ch}}L/W^3)/U_{ds}^2 \qquad (2.2)$$

where k_{R_c} and $k_{R_{ch}}$ include all the geometry-independent constants, which depend on the physical origin of LFN (this is discussed in detail in the supporting information of the 1st complementary article of this compendium). From Eq. 2.2, it is shown that the dependence of contact and channel noise on the width (W) is the same. Therefore, the relation between the contribution of both terms only depends on the device length (L). On the other hand, the contact noise is shown to be independent of L, while the channel noise term is proportional to L. By measuring the current noise from g-SGFETs with different channel lengths it was possible to show that the noise in g-SGFET fabricated with our standard contact technology, consisting of Ni/Au top-contacts, showed no dependence on L (Fig. 2.1b). This result was consistent with a contact noise dominated response, indicating that the contact technology should be optimized for an optimal sensitivity. This high contact noise was also related to a high contact resistance, in the range of $4\,k\Omega.\mu m$, which was far from previously reported record-low resistance values in the range of $100\,\Omega$[212]. We hypothesised that a high contact resistance, caused by photolithography resist residues accumulated at the graphene surface prior to metallization could be the origin of a high contact resistance as well as LFN.

In order to minimize the level of contamination at the interface, we reproduced a previous work on the use of ultra-violet ozone (UVO)[169] to decrease the contact resistance. In addition to eliminating residues, ozone can also introduce structural defects in graphene, which are considered to enhance charge transfer between the metal and graphene[169, 195, 196]. After ozone treatment, we could validate that contact resistance was significantly reduced to $0.7\,k\Omega.\mu m$. More importantly, when we measured the contact noise in the g-SGFETs with UVO-treated contacts, LFN was significantly attenuated (Fig. 2.1c). This trend was followed by a change in the dependence of the normalized noise with the channel length (Fig. 2.1b, from a contact-dominated dependence to a channel-dominated regime). From this

characterization, it was possible to determine the channel length for which the LFN contribution from untreated contacts equaled the channel noise (dominating in UVO-treated devices). This length was found to be $\sim 50\mu m$, which is a typical value for g-SGFETs used for neural sensing, ranging between $10\,\mu m$ to few $100\,\mu m$. Below this characteristic channel length, g-SGFETs fabricated with the UVO treatment showed a lower intrinsic noise and therefore an improved sensitivity (U_{gs-rms}) (Fig. 2.1d). The evaluation of the normalized current noise $I_{ds-rms}/I_{ds}^2 \propto \sqrt{S_I/I_{ds}^4}$) demonstrates that the improvement in U_{gs-rms} is not only due to an improvement in G_m caused by the R_c reduction, but also by a reduction of the term S_{R_c}. Interestingly, from Eq. 2.1, the previously reported dependence of contact noise on I_{ds} and R_c can be recovered. If R_c is considered voltage independent, which is expected for contacts not modulated by the gate, the only dependence of S_I on U_{gs} corresponds to the term I_{ds}^4 in Eq. 2.2[209]. On the other hand, if the term S_{R_c} is evaluated for contacts modulated by a back gate, the gate bias dependence of the contact noise term is given by the voltage dependence of k_{R_c}, which depends on the physical origin of contact noise. In case of charge trapping-detrapping events, suggested as the dominant source in previous works[210], $k_{R_c} \propto 1/n^2$, leading to:

$$S_{R_c} = (K_B T \lambda N_T/A)R_c^2/n_c^2 \qquad (2.3)$$

where λ is a constant accounting for the tunnelling probability of electrons between graphene and trap states, K_B is the Boltzmann constant, T the temperature and N_T the density of trap states[213] and A the active area of the contact. Assuming a linear relation between R_c and the number of carriers at the contact (n_c), S_{R_c} is proportional to R_c^4. This dependence is the main evidence supporting that high contact noise originates from trapping-detrapping events[210]. However, in previous studies[210], high contact noise was tentatively attributed to the effect of current crowding, presumably due to the small area contributing to charge transfer. Note that if the sheet resistance of graphene under the metal is increased, the current crowding effect is enhanced. Similarly, if the charge transfer from the metal to graphene is optimized, the current crowding effect is also enhanced. Applying the UVO-treatment on the contacts, the contact resistance was shown to decrease due to an enhancement of charge transfer at the metal-graphene interface. Yet, the contact noise also dropped, suggesting that current crowding is not a direct cause of high contact noise in g-SGFETs.

In order to explain the contact noise reduction produced by the UVO-treatment, the metal-graphene contact was simulated using a finite elements model (FEM). The simulation consists of three stacked domains conforming the graphene plane, the charge-transfer plane and the metal electrode. This simulation allowed to determine the current profile along the transmission-line contact (see supporting information in the 1st complementary article of this thesis). The solution of such a transmission-line contact can be easily computed analytically; however, using the

numerical model it was possible to simulate the effect of local fluctuations in the graphene resistance along the contact. Due to the current crowding effect, resistance fluctuations in the graphene sheet close to the channel have a much stronger impact on contact noise that those further inside the contact, where little charge transfer occurs. The differential equation which describes a transmission line contact with non-homogeneous resistance has, to our knowledge, no analytical solution (see supporting information of the 1st complementary article of this thesis). Therefore, in order to compute the effect of local sources of LFN on the overall contact resistance the numerical model was required. For this purpose, the domain representing the graphene sheet was divided into 50 sections and the effect of changes in their sheet resistance $R_{sh,c}$ on the total contact resistance R_c was evaluated for each of them individually (Fig. 2.1a). Following this approach, it was possible to determine the terms $dR_c/dR_{sh,c}(x)$ at each of the partitions, from which the effect of local noise sources on the total contact resistance noise (S_{R_c}) could be calculated. The power of local contributions, weighted by the term $(dR_c/dR_{sh}(x))^2$, was then summed for all partitions, as a discrete approximation of the integral along the contact:

$$fS_{R_c} = \int_0^{L_c} \frac{kR_{sh,c}^2 dx}{W^3} \Big(\frac{dR_c}{dR_{sh,c}(x)} \Big)^2 \tag{2.4}$$

where k stands for the geometry independent terms, which depend on the physical origin of the LFN (see supporting information of the 1st complementary article of this thesis). In order to validate the model, the simulations where repeated after doubling the number of sections of the graphene domain leading to a difference $< 1.1\,\%$. As expected, we could observe that noise sources at the graphene partitions closer to the contact end had a stronger influence on S_{R_c} (Fig. 2.1e). Furthermore, when the conductance through the z-plane (G_z) was enhanced in the model, the simulated contact resistance decreased as expected. This drop is related with a larger relative influence of $R_{sh,c}$, which enhances the current crowding effect, forcing a larger fraction of the current to flow closer to the contact end. Similarly, increasing $R_{sh,c}$, which is also expected to occur with UVO treatment, also enhances the current crowding effect and reduces contact noise (Fig. 2.1f). Interestingly, the numerical solution of the discrete approximation of Eq. 2.4 leads to the conclusion that enhanced current crowding leads to a reduced contact resistance noise. This is consistent with the observation that both contact resistance and noise decrease with the UVO treatment time (Fig. 2.1c). For very long UVO treatment times, it was possible to observe a clear increase in R_c(Fig. 2.1c), presumably associated with an increase in $R_{sh,c}$ not compensated by an increase of G_z. However, the contact noise did not increase significantly, possibly due to the dominance of channel noise. The independence of noise on UVO treatment time is expected to dissapear for longer UVO treatment times, when the increase of R_c in Eq. 2.3 or the increase in mobility fluctuation noise at the contacts dominates over the channel noise contribution.
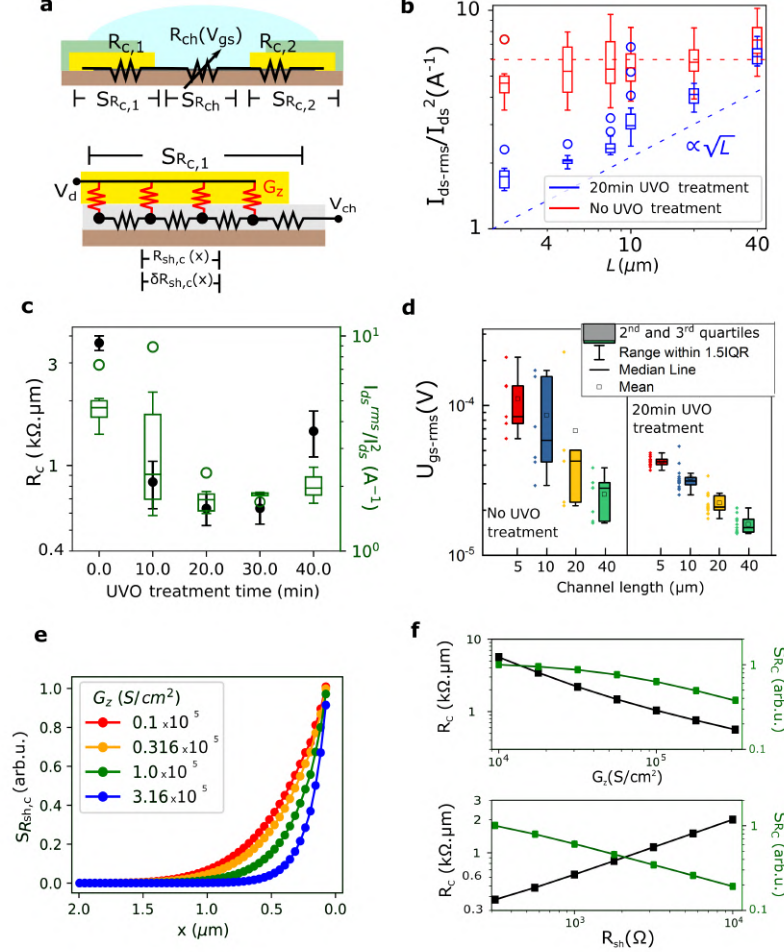
Figure 2.1: a, Schematic of the g-SGFET (top) and the metal-graphene contact (bottom). The contact (R_c) and channel (R_{ch}) resistance present fluctuations with a power S_{R_c} and $S_{R_{ch}}$ respectively. The electrical response of contacts is described by a transmission line model, where the term G_z represents the conductance per unit area at the metal-graphene interface and R_{sh_c} the sheet resistance of graphene under the metal. Contact noise is presumably generated by local resistance fluctuations in R_{sh_c}. **b,** I^{ds-rms}/I_{ds}^2, which is proportional to S_I/I_{ds}^4, shown for different channel lengths and for both ozone-treated and untreated devices. Number of non-treated g-SGFETs is 66 and number of treated g-SGFETs is 61. Minimum number of g-SGFET per L value is 5. **c,** R_c and I_{ds-rms}/I_{ds}^2 for different ozone treatment times. The noise values correspond to $L = 2, 5\,\mu m$, with a minimum of 4 g-SGFETs per treatment time. The R_c values are obtained from 66, 54, 61, 35 and 31 g-SGFETs for the UVO treatment times 0, 10, 20, 30 and 40 minutes respectively. **d,** U_{gs-rms} for different channel lengths, for ozone-treated and untreated devices. Scatter plot indicates the individual values for each g-SGFET **e,** Simulated local noise ($S_{R_{sh,c}}$) contributions to S_{R_c} along the contact for different G_z values.**f,** Simulated R_c and S_{R_c} for different G_z and $R_{sh,c}$. Figure adapted with permission from Schäfer, Garcia-Cortadella and Bonaccini-Calia et. al.[214].

2.1.2 Understading the bias dependence of channel noise

Having understood in greater detail the origin of contact noise, its relative contribution with respect to channel noise and how to mitigate it, the next step was to investigate the physical origin of channel noise and model its bias dependence. This issue was addressed in the 2nd complementary article presented in this thesis (Appendix B). In this work, the LFN in g-SGFETs with different channel lengths was characterized for different bias conditions (U_{gs} and U_{ds}). The first objective of the study was to understand the gate bias dependence of the normalized current noise (S_I/I_{ds}^2). This term has been reported to show a peculiar V-shape dependence with U_{gs} close to the CNP[215], which changes to an M-shape when the gate bias range is extended[216]. However, this behaviour is not described by typically used models of LFN in semiconductors, such as the phenomenological Hooge model[217]:

$$\frac{S_{I_{ds}}f}{I_{ds}^2} = \frac{\alpha_H}{nA} \tag{2.5}$$

where α_H is an scaling factor and A the device area, or the McWhorther model, which describes the LFN generated by charge trapping-detrapping events:

$$\frac{S_{I_{ds}}f}{I_{ds}^2} = \frac{K_B T \lambda N_T}{An^2} \tag{2.6}$$

which holds if the contact resistance contribution can be neglected. Note that both typically used models in Eq. 2.5 and Eq. 2.6 predict an increase of LFN close the CNP, where n is minimal. However, LFN in graphene shows an opposite dependence with n, showing a local minima at the CNP. In order to describe the resulting M-shape, previous works proposed the use of a term $\propto g_m$[209], which has also been used for the modelling of charge noise in silicon transistors[211] under constant charge noise along the channel. However, the validity of this model to describe the bias dependence close to the CNP is not clear. The relation between fluctuations in the drain-source current ($\delta_{I_{ds}}$) and the charge fluctuations in graphene ($\delta_{Q_{gr}}$) can be expressed as follows:

$$\frac{\delta_{I_{ds}}}{I_{ds}} = \frac{1}{N_{gr}} \frac{\delta Q_{gr}}{\delta Q_t} \delta N_t \tag{2.7}$$

where N_{gr} and Q_{gr} stand for the number of carriers in graphene and the charge accumulated in graphene respectively. N_t and Q_t stand for the number of trapped carriers and the trapped charge respectively. Rewriting Eq. 2.7, it is possible to show that the normalized current noise can be expressed as proportional to a term g_m/I_{ds}, under the assumption of homogeneous charge along the channel.

$$\frac{\delta_{I_{ds}}}{I_{ds}} = \frac{e}{Q_{gr}}\frac{\delta Q_{gr}}{\delta U_{gs}}\frac{\delta U_{gs}}{\delta Q_t}\delta Nt = \frac{eg_m}{I_{ds}}\frac{\delta U_{gs}}{\delta Q_{gr}}\frac{\delta Q_{gr}}{\delta Q_t}\delta N_t \tag{2.8}$$

where the term δN_t represents the fluctuations in the number of carriers trapped, which can be expanded as $\sqrt{k_B T \lambda N_T / A}$. However, the term $\delta U_{gs}/\delta Q_t$ also presents a certain bias dependence. If we assume $C_Q >> C_{dl}$, which holds away from the CNP, then $\frac{\delta U_{gs}}{\delta Q_{gr}} \approx 1/C_{dl}$ and $\delta Q_{gr}/\delta Q_t \approx 1$ as assumed in previous literature[209]. Under this assumption, the bias dependence of charge noise in graphene is given by the term g_m/I_{ds}. However, this assumption does not hold close to the CNP[185, 218], where the term $\delta Q_{gr}/\delta Q_t$ will modulate the bias dependence of the normalized noise. Therefore, deviations from the g_m/I_{ds} relationship occur due to the effect of the quantum capacitance, which limits the graphene charging around the CNP. According to charge conservation law, any change in the charge accumulated in trap states must be compensated by an opposite change in the charge accumulated in graphene or at the double layer(i.e. $\delta Q_{gr} + \delta Q_{dl} + \delta Q_t = 0$) (see supporting information in the 2nd complementary article of this thesis). In turn, $\delta Q_{gr} = -C_Q \delta U_Q$ and $\delta Q_{dl} = -C_{dl}\delta U_Q$. Thus, it is possible to rewrite δQ_{gr} and δQ_t in Eq. 2.8 as:

$$\frac{\delta_{I_{ds}}}{I_{ds}} = \frac{1}{N_{gr}}\frac{C_Q}{C_Q + C_{dl}}\delta N_t \tag{2.9}$$

Assuming that $C_Q \propto U_Q$ (i. e. neglecting the effect of impurities in Eq. 1.6 for simplicity) one can integrate over U_Q to obtain the dependence of Q_{gr} on the applied potential, $Q_{gr} = ekU_Q^2/2 + \rho_0$, where ρ_0 represents the residual charge. Given that $C_Q < C_{dl}$ close to the CNP, the bias dependence of Eq. 2.9 can be approximated as:

$$\frac{\delta_{I_{ds}}}{I_{ds}} = \frac{ekU_Q}{\left(kU_Q^2/2 + \rho_0\right)}\delta N_t \tag{2.10}$$

where k is the constant defining the relation between C_Q and U_Q defined in Eq. 1.6.

If the residual charge tends to zero, then the bias dependence in Eq. 2.10 is simply $1/U_Q$, which does not explain the M-shape. However, if ρ_0 takes a finite value, the normalized noise becomes propoortional to U_Q around the CNP, explaining the observed M-shape (Fig. 2.2a). Note that in cases of very low ρ_0, a Λ-shape is expected, which has been sometimes reported for low U_{ds} values[219]. In fact, ρ_0 mainly results from charge inhomogeneities, which can origin from charge puddles[220] or, similarly, by U_{ds} values close to U_{gs}. This is exactly the case close to the CNP; however, note that the model presented in Eq. 2.10 still does not take into account charge inhomogeneities along the channel. In order to take this effect into account it is necessary to first have a model of the electrostatic response of the g-SGFET. This allows to extract the profile of U_Q along the channel and therefore to calculate the magnitude of local sources of noise. For this purpose, it is possible to
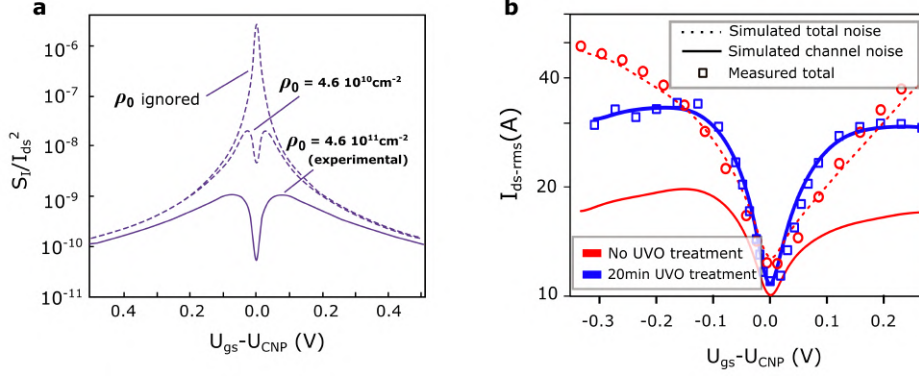
Figure 2.2: a, Effect of residual charge (ρ_0) on the bias dependence of LFN in g-SGFETs. from Mavredakis et. al[213] with permission from The Royal Society of Chemistry. **b,** V-shape bias dependence of contact noise dominated characteristics for g-SGFETs with standard contact technology and M-shape bias dependence observed in g-SGFETs with optimized contacts by ozone treatment. Contact noise term model assumes that R_c is voltage independent, leading to a term $\propto I_{ds}^4$[187] and the channel noise is modelled with the compact model presented in Mavredakis et. al.[213]. Figure reprinted with permission from Schäfer, Garcia-Cortadella and Bonaccini et. al.[187].

use the previously introduced compact model[184, 186] (see Fig. 1.9), which can be solved analytically and can be therefore easily integrated in circuit simulators. Knowing $U_Q(x)$ it is then possible to calculate the contributions from local noise sources on the drain-to-source current in a procedure previously described for silicon transistors[221] and translated to the GFETs case by N. Mavredakis[213] (see the 2nd complementary article of this thesis). Assuming that all local noise sources are uncorrelated, the contribution from multiple channel sections can be integrated. The noise in a particular channel section, between x and $x + \Delta x$, can be modelled as a current source (δI_n) connected in parallel with the resistance of the section ΔR (Norton equivalent) and in series with the remaining noiseless part of the transistor. The conductance of the noiseless part of the transistor tends to G_{ds} due to the infinitesimal length of the noise local sources. Therefore, the current fluctuations generated by the local source at the drain can be expressed as:

$$\delta_{I_{nD}} = G_{ds}\Delta R \delta I_n \tag{2.11}$$

which can be integrated along the channel to describe the total current noise:

$$S_{ID} = \int_0^L G_{ds}^2 \Delta R^2 \frac{\delta I_n^2(\omega, x)}{\Delta x} dx \tag{2.12}$$

where $G_{ds}^2 \Delta R^2 = (\Delta x/L)^2$. Combining Eq. 2.12 and Eq. 2.9 it is possible write down the integral that describes the current noise in the whole range of U_{gs} and U_{ds}.

Changing the integration variable from x to the U_Q, it is possible to solve equation 2.12 analytically, taking into account the electrostatic changes in the channel conductance as derived from the previously reported compact model[184, 186]. The resulting model represents a physics-based description of the bias dependence of the noise characteristics of GFETs and accurately describes the effect of the quantum capacitance and non-homogeneous charge along the graphene channel. This accurate description of channel noise could be combined with the model of contact noise to describe LFN in g-SGFETs for different contact technologies. Fitting of the noise characteristics for transistors with non-treated and with UVO-treated contacts confirmed the change from a contact dominated regime to a channel noise dominated regime (Fig. 2.2b). Note that I_{rms}^{ds} in Fig. 2.2b is not normalized, therefore it does not directly represent the noise sources S_{R_c} and $S_{R_{ch}}$. These results represent a complete modelling of the noise characteristics in g-SGFETs, which accurately describes the contributions from distinct local sources and provides new insights into the physical origin of low-frequency noise in graphene devices.

2.2 Distortion mechanisms in graphene active sensors

The transduction factor that relates the amplitude of voltage signals applied at the gate with the drain-souce current changes can be, in a first aproximation, modelled by a constant transconductance. However, the relation between the output current and input voltage, or transfer function, might present a significant voltage and frequency dependence. Recent results have evidenced the importance of detecting neural activity of high amplitude and with wide band frequency components, from infra-slow to single unit activity using g-SGFETs[222]. Large amplitude voltage fluctuations, typically occuring in the low frequency range of LFP, could eventually lead to harmonic distortion caused by a voltage-dependent transfer function. Further, recording of neural signals in a wide frequency band could lead to phase-amplitude distortion. In addition, a frequency dependence of the transfer function could lead to loss of sensitivity in particular frequency bands. The 1st main article of this thesis (Appendix A), presents a detailed characterization and modelling of the stationary and dynamic response of g-SGFETs aiming to understand the mechanisms of signal distortion in graphene transducers.

2.2.1 Voltage-dependent transfer function

Harmonic distortion can appear in any amplifying system due to a voltage-dependent gain. In the specific case of g-SGFETs, the voltage dependence of G_m introduced by non-linearities in the $I_{ds} - U_{gs}$ curves will lead to harmonic distortion of the signals, which can be modelled from the Taylor expansion of the $I_{ds} - U_{gs}$.

$$I_{ds}(t) = I_{ds}\big\|_{U_{gs0}} + \frac{dI_{ds}}{dU_{gs}}\bigg\|_{U_{gs0}} A_{sig}sin(2\pi ft) + \frac{1}{2!}\frac{d^2I_{ds}}{dU_{gs}^2}\bigg\|_{U_{gs0}} \frac{A_{sig}^2}{2}sin(4\pi ft) + ...$$

$$\frac{1}{3!}\frac{d^3I_{ds}}{dU_{gs}^3}\bigg\|_{U_{gs0}} \frac{A_{sig}^3}{4}sin(6\pi ft)$$

$$(2.13)$$

Where A_{sig} stands for the amplitude of the transduced signal, f its frequency and U_{gs0} the gate bias under stationary conditions. This description has been previously proposed and evaluated for the harmonic distortion in a theoretical GFET model[223]. However, predicted distortion levels have not been compared with experimentally obtained values. Therefore, validating the relation between nonlinearities in the $I_{ds}-U_{gs}$ curves and harmonic distortion experimentally is required to understand and optimize the operation of graphene transducers.

For this purpose, the stationary response of g-SGFETs ($I_{ds-DC} = I_{ds}|_{U_{gs0}}$) and their dynamic response (I_{ds-sig}) to a $10\,Hz$ pure tone applied at the gate were measured under different gate bias conditions (Fig. 2.3a). From I_{ds-sig}, the amplitude of the transduced signal could be determined together with the generated high order harmonics. Fig. 2.3b shows the measured bias dependence of the first three harmonics as well as the predicted values from the Taylor expansion of the stationary $I_{ds}-U_{gs}$ curves. These results show the close agreement between the measured harmonic distortion and the values derived from the stationary response, which holds for a wide range of signal amplitudes (see the 1st main article of this thesis). Having validated the stationary model of harmonic distortion, it is possible to compute a map representing the signal-to-distortion ratio (SDR) over a wide U_{gs} and A_{sig} range (Fig. 2.3c). This figure of merit can be used to evaluate the impact of distortion on the signal quality. The SDR presents a maximum at $U_{gs}-U_{CNP} \approx \pm 100\,mV$, where the stationary transfer characteristics are most linear. Fig. 2.3c also reveals the drop of SDR for higher A_{sig} values. This dependence is explained by the linear, quadratic and cubic relationship of the 1st, 2nd and 3rd order harmonics, respectively, with A_{sig} (see supporting information of the 1st main article). The SDR map can guide the selection of the optimum bias conditions in terms of harmonic distorion; however, LFN is typically considered to be the dominant source of signal degradation. In order to compare the impact of harmonic distortion and of LFN on the signal quality, one can evaluate the distortion-to-noise ratio (DNR). Fig. 2.3d shows the DNR for the noise integrated in a one-decade frequency band (i.e. 4-40Hz). The $0\,dB$ contour line indicates the parameters for which distortion and noise contribute with the same power to the degradation of signal quality. These results highlight the importance of choosing a right gate bias to minimize the impact of harmonic distortion, especially for large amplitude signals.
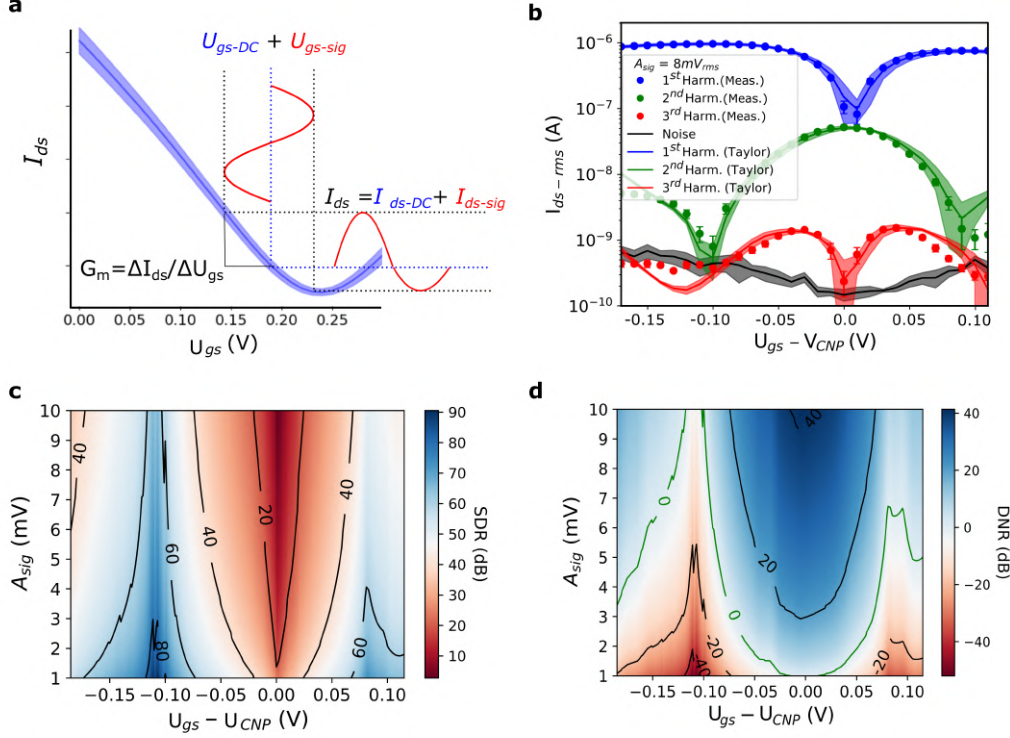
Figure 2.3: a, Typical transfer characteristics of a g-SGFETs. G_m is indicated as $\Delta I_{ds}/\Delta U_{gs}$. **b,** RMS amplitude of the 1st, 2nd and 3rd order harmonics extracted from the PSD of the measured I_{ds} (dots) and from the Taylor expansion of the transfer characteristics (solid lines). Error bars and filled areas show the standard deviation (for 4 g-SGFETs). The noise is evaluated from the power spectrum at $28\,Hz$ (slightly below $3f_{sig}$). The measured and calculated harmonics correspond to a $10\,Hz$ signal with an amplitude of $8\,mV_{RMS}$. **c,** Evaluation of the signal-to-distortion ratio (in dB) in the A_{sig}-U_{gs} parameter map. The solid lines indicate the contour lines of the SDR every $20\,dBs$. **d,** Distortion-to-noise ratio (in dB); the contour lines represented by solid lines every $20\,dBs$. The maps in panel c and d are calculated using the Taylor expansion of the stationary $I_{ds} - U_{gs}$ curves fited to the experimental data. Figure adapted from Garcia-Cortadella et. al.[224].

2.2.2 Frequency-dependent transfer function

The frequency response of g-SGFETs has been typically assumed to be approximately constant up to high frequencies due to the high electrical mobility of graphene. However, the dynamics of the graphene-electrolyte might present slow time constants due to poor ion mobilities or slow transitions in the occupation of trap states in the graphene environment [225, 226]. In addition, displacement currents through parasitic capacitances can result in an attenuation of the tranduced signals[227]. In the 1st main article of this thesis, the frequency response in g-SGFET has been characterized with the aim to propose and validate an equivalent

circuit and its analytical transfer function.

For this purpose, the frequency response of g-SGFETs in the frequency range between $0.4\,Hz$ and $200\,kHz$ was measured. Fig. 2.4a shows the module and phase of the frequency response as well as the g_m computed from the stationary $I_{ds}-U_{gs}$ curves (where $g_m \equiv G_m/U_{ds}$, see Eq. 1.7). In the measured frequency response, three regimes can be distinguished (Fig. 2.4a). First, in the $0.4\,Hz$-$3\,kHz$ range it is possible to observe a fractional-order attenuation of the transconductance with frequency (i. e. a constant slope in log-scale) and an approximately constant phase deviation few degrees from 180 (expected in the holes conduction regime). In the $3\,kHz$-$40\,kHz$ range, another regime can be observed for low ionic concentrations (Fig. 2.4a), which presents an abrupt attenuation of the gain with frequency ($\sim 1/f$). This attenuation of the magnitude is followed by a negative shift of the phase. Finally, the high frequency regime ($> 40\,kHz$) is characterized by an increase of the magnitude and phase of the transconductance.
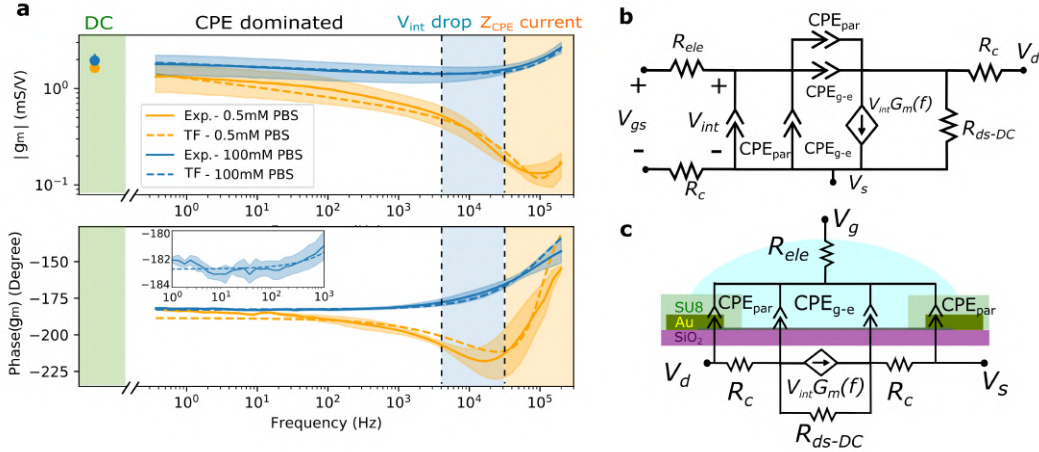
Figure 2.4: a, Bode diagram of g-SGFETs (for 4 g-SGEFTs). Three different response regimes are displayed together with the G_m extracted from the DC characteristics: CPE dominated regime, a regime where the g_m drops with approximately $1/f$ and finally a g_m increase due to capacitive currents. The experimental data corresponds to the average of 4 g-SGFETs. The fitting of the data using the analytical transfer function (TF) from Eq. 2.15 is represented by the dashed lines. The filled area indicates de standard deviation. **b,.** Small signal model of the g-SGFET frequency response. The gate-to-source bias (U_{gs}) and the drain voltage (U_d) are defined. The voltage drop at the graphene-electrolyte interface is defined as U_{int}. The CPE_{g-e} represents the constant phase element (CPE) describing the non-ideal capacitive behavior of the graphene-electrolyte interface. The CPE describing the leakage through parasitic elements is defined as CPE_{par}. The resistance of the electrolyte (R_{ele}) and the contact resistance of the g-SGFET (R_c) are also defined. The dynamic response of the g-SGFET is modelled by the current source ($U_{int}G_m(f)$) and its stationary response is modelled by the resistance in parallel R_{ds-DC}. **c,** The equivalent circuit shown in c. is drawn on a schematic of the g-SGFET to illustrate the physical origin of each element. Figure adapted from Garcia-Cortadella et. al.[224].

Having identified the different regimes of dynamic response, a small signal model can be proposed (see Fig. 2.4b,c). In the proposed model, the graphene-electrolyte interface is not modelled as an ideal capacitor, as typically proposed in standard models[185, 227], but as a constant phase element (CPE_{g-e}), which is commonly required to describe the response of a double-layer capacitance [228, 229]. In the particular case of the graphene-electrolyte interface, the CPE behaviour has been previously reported in impedance measurements[229]. The equivalent circuit in Fig. 2.4b,c also includes the resistance of the electrolyte R_{ele} and the contacts R_c in series with the graphene-electrolyte interface. The stationary response of the g-SGFET is modelled by the resistance R_{ds-DC}, while the dynamic response can be modelled by a current source with an amplitude $U_{int}G_m(f)$, where U_{int} stands for the effective voltage drop at the graphene-electrolyte interface. Finally, an additional CPE is added in parallel with CPE_{g-e} to account for any parasitic capacitance of the device (CPE_{par}). From the proposed equivalent circuit it is possible to derive an analytical expression, describing the frequency response of g-SGFETs.

$$G_m(f) = \left.\frac{dI_{ds}}{dU_{int}}\right|_{U_{ds}} \frac{dU_{int}}{dU_{gs}} + G_{m,eff} \tag{2.14}$$

The first factor on the right hand side of Eq. 2.14 corresponds to the intrinsic tranconductance of the g-SGFETs. Its frequency dependence results from the CPE behaviour of the graphene-electrolyte interface ($dI_{ds}/dU_{int}|_{U_{ds}} = kC_{CPE_{g-e}}(f)$). The second factor in Eq. 2.14 results from the contribution of the resistance in series R_s with the g-SGFET (i.e. R_c plus R_{ele}) and CPE_{par} in parallel with the transistor, which lead to a voltage divider and the corresponding attenuation of U_{int} at high frequencies. The last term in Eq. 2.14 accounts for the measured increase of the g_m magnitude at high frequencies. This term represents the direct contribution from displacement currents through CPE_{g-e} and CPE_{par}, from the drain to the gate. This contribution is not result of the field-effect modulation, and can be therefore regarded as an effective transconductance ($G_{m,eff}$). Expressing the frequency dependence of the terms in Eq. 2.14 explicitly, the following transfer function is obtained:

$$G_m(f) = \pm \frac{Q_{g-e}}{(2\pi f)^{1-\alpha}} e^{i\frac{\pi}{2}(\alpha_{g-e}-1)} \frac{1}{1 + 2R_s[Q_{g-e}(2\pi f)^{\alpha_{g-e}} e^{i\frac{\pi}{2}\alpha_{g-e}} + Q_{par}(2\pi f)^{\alpha_{par}} e^{i\frac{\pi}{2}\alpha_{par}}]}$$

$$... + Q_{g-e}(2\pi f)^{\alpha_{g-e}} e^{i\frac{\pi}{2}\alpha_{g-e}} + Q_{par}(2\pi f)^{\alpha_{par}} e^{i\frac{\pi}{2}\alpha_{par}}$$

$$\tag{2.15}$$

where α_{g-e} and α_{par} are the CPE ideality factors for CPE_{g-e} and CPE_{par} respectively and Q_{g-e}, Q_{par} represent the magnitude of the same CPEs. The derived

analytical transfer function has been used to fit the experimentally obtained frequency response (Fig. 2.4a). All the main features of the frequency response are properly captured, supporting the validity of the proposed model. The understanding of the frequency response provided by this model represents a strong basis for the improvement of the sensitivity of g-SGFETs at high frequencies. Furthermore, the derived transfer function can be used to define a calibration procedure to correct the phase-amplitude distortion produced by the non-ideal dynamic response of g-SGFETs (see section3.2.2). The derived transfer function in Eq. 2.15, the CPE-dominated regime extends to arbitrarily low frequencies, predincting a rather constant transconductance for low frequencies. This response of the active graphene sensors is radically different from the response of micro-electrodes coupled to high input-impedance amplifiers[122], as recently revealed by Masvidal-Codina et. al. [222]. This advantage is expected to be valid for all FET-based sensor technologies with stable transfer characteristics; however, experimental proof has been only shown for graphene active sensors, which present a particularly high chemical inertness[222]. Signal detection based on the field-effect mechanism therefore allows to prevent the signal distortion and gain loss observed for small passive sensors at low frequencies. However, at high frequencies, g-SGFETs present a significant transconductace drop, which should be corrected by engineering an optimized graphene-electrolyte interface.

2.3 Chapter outlook: Improving the high frequency sensitivity

Following the characterization and modelling of the non-ideal frequency response of g-SGFETs, its optimization was addressed. The fractional order attenuation of g_m, which can be explained from the CPE behaviour of the graphene-electrolyte interface, has been shown to depend on the conductivity of the electrolyte as well as on the presence of contaminants on the graphene surface[229]. In order to investigate the effect of contaminants on the frequency response of g-SGFETs, a new fabrication process has been explored in which the graphene channel is protected against resist residues and other contaminants[170]. The protective layer consists of a Cu film, which is deposited by electron-beam evaporation after the transfer of graphene onto the final substrate. The Cu sacrificial layer can be etched using ammonium persulfate after completing the fabrication, allowign to remove all the contaminants accumulated on the Cu film (Fig. 2.5a). More details on the standard fabrication process can be found in the experimental section in the 1st main article of this thesis.

The graphene quality before Cu deposition and after Cu etching was evaluated with Raman spectroscopy. Fig. 2.5b shows the distribution of D-band intensity to G-band intensity ratio, related to structural defects in graphene[152]; after Cu etching, a bimodal distribution is observed. This feature might be related to defects
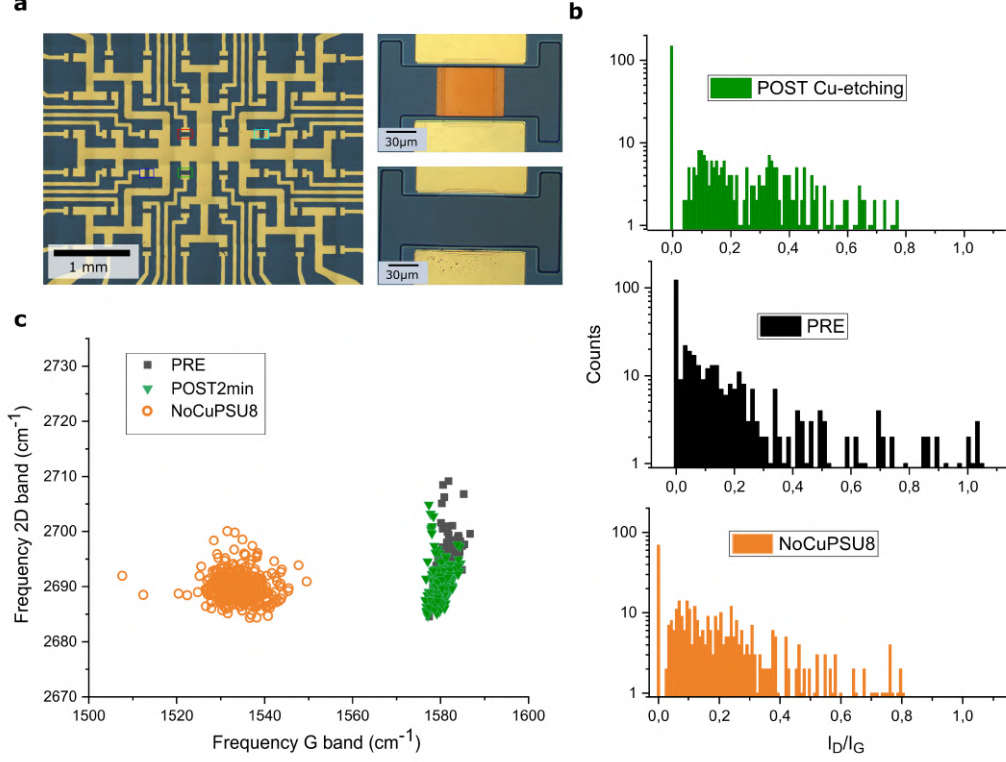
Figure 2.5: a, Optical micrograph of the g-SGFET array used for Cu-protection characterization. GFET with a Cu sacrificial layer during fabrication before (left) and after (right) Cu removal by ammonium persulfate etching. **b,** D/G Raman band intensity ratio before Cu deposition (black), after Cu-etching (green) and after passivation in control devices without Cu protection (orange). **c,** Frequency of the 2D-band Raman shift vs G-band shift in graphene before Cu deposition (PRE), after Cu etching for 2 min (POST2min), as well as in non-protected control devices after SU8 passivation (NoCuPSU8).

induced by Cu or oxygen adatoms or hydroxyl groups induced by the oxidant etching solution[133]. However, the D/G intensity distribution after Cu etching presents a higher fraction of Raman spectra with an undetectable D-peak compared to the standard technology. This leads to a lower median of the D/G distribution in Cu-protected devices compared to the standard SU-8 passivated devices (0.11 and 0.15 respectively). Fig. 2.5c shows the frequency of the 2D-band and G-band, which indicates the doping and strain in graphene[230]. Importantly, in devices protected with Cu during fabrication, it is possible to observe a doping level close to the as-transferred graphene, in strong contrast with the standard technology, where the accumulated residues lead to a strong doping.

Following Raman spectroscopy, the electrical performance of the g-SGFETs protected with Cu was characterized and compared to control devices fabricated following the standard process. Comparison of U_{CNP} for both procedures confirms

the reduced doping of graphene in the Cu-protected transistors (see boxplot in Fig. 2.6a, n between 22 and 25 for all devices). The drain-source current in Cu-protected devices is higher (Welch's t-test, $p = 1, 2.10^{-23}$) and presents a lower resistance at the CNP. In terms of transconductance, Cu-protected devices present a larger mean value $\mu = -0.146 mS/V$ compared to control devices $\mu = -0.123 mS/V$ (Welch's t-test, $p = 2, 7.10^{-11}$) but non-significant differences in equivalent noise at the gate (Welch's t-test, $p = 0.62$). Most importantly, Cu-protected g-SGFETs showed a much better frequency response, as shown in the Bode diagram in Fig. 2.6b. Interestingly, the g_m module in Cu-protected devices presents a fractional-order ($\propto 1/f^{\alpha}$) attenuation, with a factor $\alpha = 0.022$ for PBS $10\,mM$, lower than in previously characterized devices fabricated without Cu-protection (0.03 for PBS $100\,mM$ and 0.1 for PBS $0.5\,mM$).
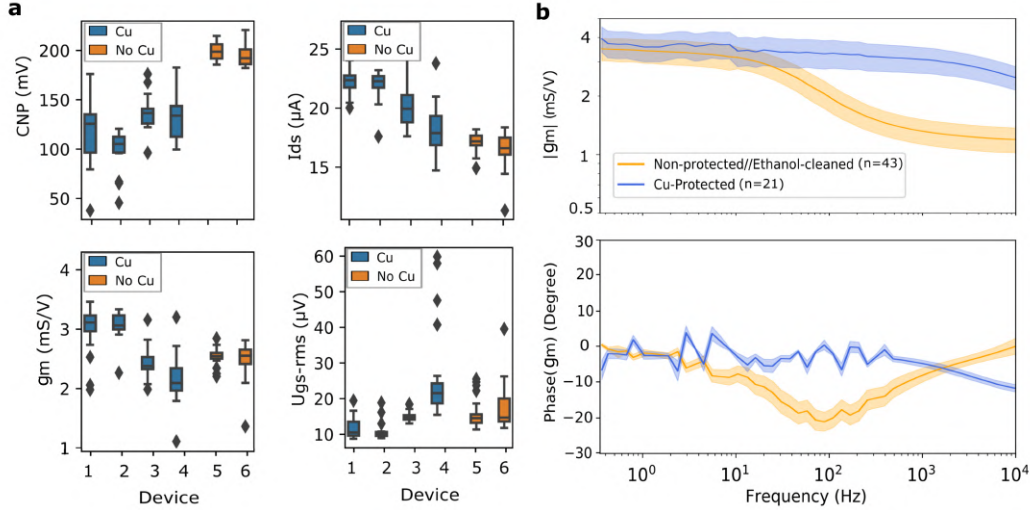
Figure 2.6: a, Static electrical response parameters are shown for different devices fabricated either using the Cu sacrificial layers or the standard process (n between 20 and 24 g-SGFETs for each device). I_{ds}, G_m and U_{gs-rms} are extracted at $U_{gs} - U_{CNP} = -0.1V$. **b,** Frequency response of Cu-protected and control devices fabricated following the standard method without Cu sacrificial layers. Magnitude (top) and phase (bottom) shown a much constant transconductance with a phase closer to zero for protected devices.

The results obtained during the 1st stage of this thesis, and summarized in chapter 2, provide a deeper understanding of the origin of LFN in g-SGFET as well as the effect of non-linearities in their transfer characteristics and transconductance drop at high frequencies. This understanding has guided the development of novel fabrication methodologies that can be applied to improve the sensitivity of g-SGFETs, such as UVO treatment of the contacts for the mitigation of contact noise[187] or the protection of the graphene channel with Cu films to improve their sensitivity at high frequencies (unpublished). Together, these improvements are deemed crucial for the miniaturization of g-SGFETs while preserving a high sensitivity, which can open the door to the detection of SUA using graphene sensors.

Chapter 3

System evaluation in an operational environment: Chronic implants in freely moving animals

Application of graphene bioelectronics for neural sensing primarily relies on the performance of the individual sensors, which has been the focus of the previous chapter. However, in order to provide reliable tools for neuroscience and biomedical engineering, they must be integrated in a functional system and its performance demonstrated in an operational environment. Characterization of the performance of g-SGFETs from a system perspective should include an evaluation of the reproducibility and homogeneity of graphene sensor arrays, characterization of their long-term stability and biocompatibility as well as development of dedicated amplification electronics. Finally, their applicability should be demonstrated by recording electrophysiological signals with improved performance. In the 2nd main article of this thesis, this challenge is tackled by developing and characterizing an advanced wireless recording system and by demonstrating its applicability to a chronic cortical recording in a freely behaving animal.

3.1 Recording system design and characteristics

In order to demonstrate the actual performance of graphene active sensors for neural sensing, a recording system based on a quasi-commercial, wireless headstage and 64 g-SGFET neural probes was developed. This system was developed in collaboration with Multi Channel Systems GmbH, adapting their commercial wireless headstage for passive sensor arrays. This adaptation consisted in modifying the amplification layer of the commercial system, which also includes a digitalization and wireless data transmission layer (see Fig. 3.1a, more details are provided in the supporting information of the 2nd main article of this thesis). The g-SGFETs in the neural probes were designed with a size of $100\,\mu m$x$100\,\mu m$ and an intersite separation of $400\,\mu m$ for mesoscale epi-cortical LFP analysis[231] (Fig. 3.1a). More details on the fabrication process of these neural probes can be found in the methods section of the2^{nd} main article of this thesis (see Appendix A).

3.1.1 Homogeneity and sensitivity of graphene active sensors

Development of high-count neural recording systems based on graphene active sensors requires a thorough evaluation of the homogeneity and reproducibility of the graphene technology. Two of the main challenges in the development of graphene technology have typically been the production of high quality single-layer graphene (SLG) and its transfer onto the required substrate. In the last decade, development on these areas has concentrated many efforts both from academic institutions as well as from industry[160, 162]. In the 2nd main article of this thesis, it is demonstrated that the quality of commercially available single-layer graphene produced by CVD and transferred onto polymeric substrates is currently high enough to enable a reproducible fabrication of g-SGFET arrays with high performance and yield.

Fig. 3.1b shows the g_m of nine neural probes, each of them containing 64 g-SGFETs. These probes were randomly selected from three wafers, all of them processed in independent batches. It is possible to observe a high homogeneity and yield in terms of g_m, with $99\,\%$ of channels showing a g_m above 0.7 times the median, and a high median value compared to competing active sensor technologies[73, 75, 172]. In Fig. 3.1c, the equivalent noise at the gate of the same neural probes is shown. Although U_{gs-rms} presents a larger dispersion than g_m, it is possible to identify 3 out of 9 probes with $96\,\%$ of the sensors showing a U_{gs-rms} below $10\,\mu V$. The discrepancy in the homogeneity of g_m and U_{gs-rms} suggest that these two parameters are not directly proportional, as one could expect from the dependence of U_{gs-rms} on the variability of the density of trap states[232]. The histograms in Fig. 3.1b,c show the distribution of g_m and U_{gs-rms} for the neural probe #3, which was subsequently implanted for the *in-vivo* study. The dispersion in the transconductance can be corrected by calibrating the neural signals (see section 3.2.2). Therefore, the truly limiting factor in terms of homogeneity of the g-SGFET arrays is the equivalent

noise at the gate. U_{gs-rms} presents a log-normal distribution[232, 233] with a mean of $4.13\,\mu V$ and a standard deviation of $1.14\,\mu V$ (excluding the outlier indicated in Fig. 3.1c-left). These results show that graphene-based neural probes produced in a wafer-scale process present a promising homogeneity and high sensitivity for neural sensing.
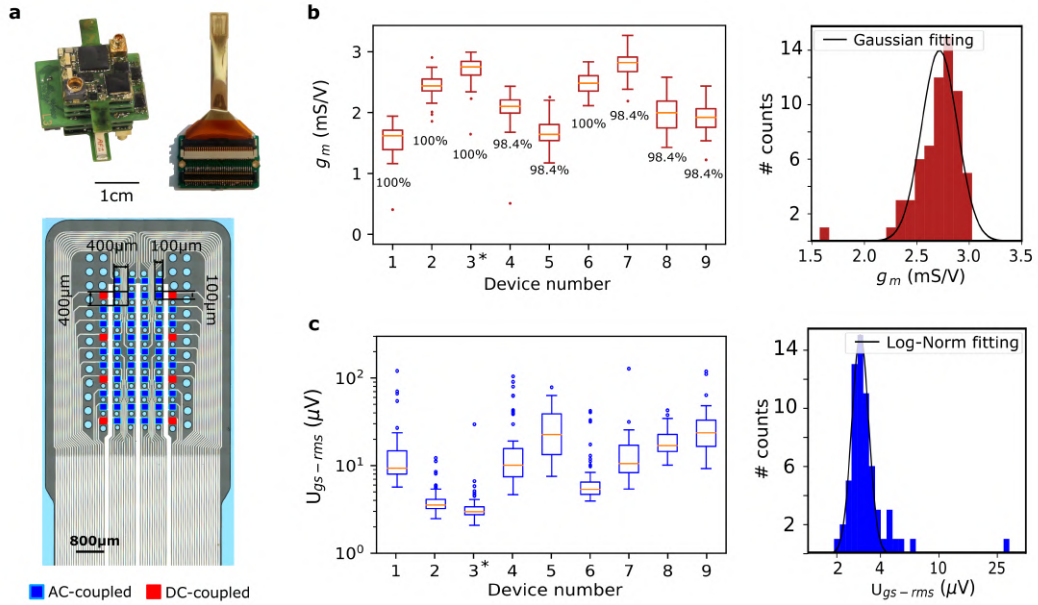
Figure 3.1: a, Photograph of the wireless headstage designed for these experiments (top-left) and a 64 g-SGFET array mounted on a customized connector (bottom-left) and zoomed image of the probe active area (right). The red squares indicate the 8 g-SGFETs on the array, which are connected to the 8 DC-coupled channels of the headstage. **b,** Left: boxplot of gm for nine randomly selected probes from three different wafers produced in independent batches. The yield in terms of gm above 70 % of the median is indicated. Right: histogram of g_m for the 64 g-SGFETs of probe #3 and Gaussian fit of the histogram excluding the outliers shown in the boxplot. **c,** Left: boxplot for U_{gs-rms} measured in the $1 - 10\,Hz$ frequency range and plotted for the same neural probes evaluated in panel b. Right: histogram of U_{gs-rms} for the 64 transistors in probe #3 and log-normal fit of the histogram excluding the outliers shown in the boxplot. All probes consisting of 64 g-SGFETs. The boxes extend from the lower to the upper quartiles, with a line at the median. The whiskers extend 1.5 times the inter-quartile range and the data points beyond the whiskers are indicated by a dot. Figure adapted with permission from Garcia-Cortadella and Schwesig et. al.[234]

3.1.2 Characteristics of the quasi-commercial system for wireless recording

An important challenge in the implementation of graphene active sensor arrays for neural sensing is the development of dedicated electronics for the amplification and

digitalization of the signals. The operation of g-SGFETs requires the acquisition of the stationary currents (I_{ds-DC}) in order to determine the optimal U_{gs} with respect to U_{CNP} and to detect low frequency components of the signal, which would otherwise be filtered[222]. Acquisition of the full-band signal using graphene active sensors has been shown to enable the detection of large amplitude infra-slow brain activity with high fidelity[222]; however, their sensitivity in this frequency band has not been quantified. The amplification of the signals in the infra-slow frequency band could be limited by LFN sources from the transimpedance amplifiers and the voltage references. Furthermore, the amplification of full-band signals, containing large stationary offsets, is challenging for the analog-to-digital converter (ADC). In order to digitalize signals with such a large dynamic range, while minimizing quantization noise, a two-stage amplifier was implemented. The first stage amplifies the full-band signal, while a second stage further amplifies the high-pass filtered signal to fill the full scale of the ADC. In order to enable the selection of the DC or AC coupled signals from the first and second stage respectively, a multiplexer was implemented (see the 2nd main article of this thesis). In order to minimize power consumption and, therefore, battery weight and volume of the headstage, only 8 of the 64 channels included a multiplexer and therefore only 8 of the channels allowed DC-coupling.

In order to validate that the sensitivity of the recording system is not limited by the noise of the amplification and digitalization chain, the PSD of the output noise was characterized. Fig. 3.2a presents the PSD of the equivalent noise at the gate ($S_{U_{gs}}$), defined as S_I/G_m^2. The central part of the spectrum, from roughly $0.05\,Hz$ to $10\,Hz$, is dominated by the $1/f$ intrinsic noise of the graphene transistors. For frequencies below $0.05\,Hz$, the DC-coupled channels show a slight increase above the $1/f$ noise, which can be attributed to the contribution of additional noise sources in the amplification chain (see the supporting information of the 2nd main article of this thesis). Above $10\,Hz$ the noise spectra also present a significant increase above the $1/f$ decay, caused by the quantization noise, which is more pronounced in DC-coupled channels. The impact of extrinsic noise sources can be determined by integrating $S_{U_{gs}}$ in different frequency bands. Fig. 3.2b shows the integrated noise for all g-SGFETs in probe #3. The three maps show that the system presents a rather constant sensitivity per frequency decade in a wide frequency range. Although the DC-coupled channels present a higher noise in the $20-200\,Hz$ band, all sensors (except for an outlier) present a $U_{gs-rms} < 15\,\mu V$. These results demonstrate the high sensitivity of the system in a wide frequency band and the low impact of extrinsic flicker noise in the ISA band. Importantly, smaller g-SGFETs are expected to present a higher intrinsic noise, therefore, recording systems based on g-SGFET with areas below $100\,\mu m$x$100\,\mu m$ are expected to exhibit the intrinsic sensitivity of g-SGFETs in the ISA band. This is in contrast with the case of passive micro-electrodes, where the gain attenuation at low frequencies is more prominent for smaller areas[122, 222].
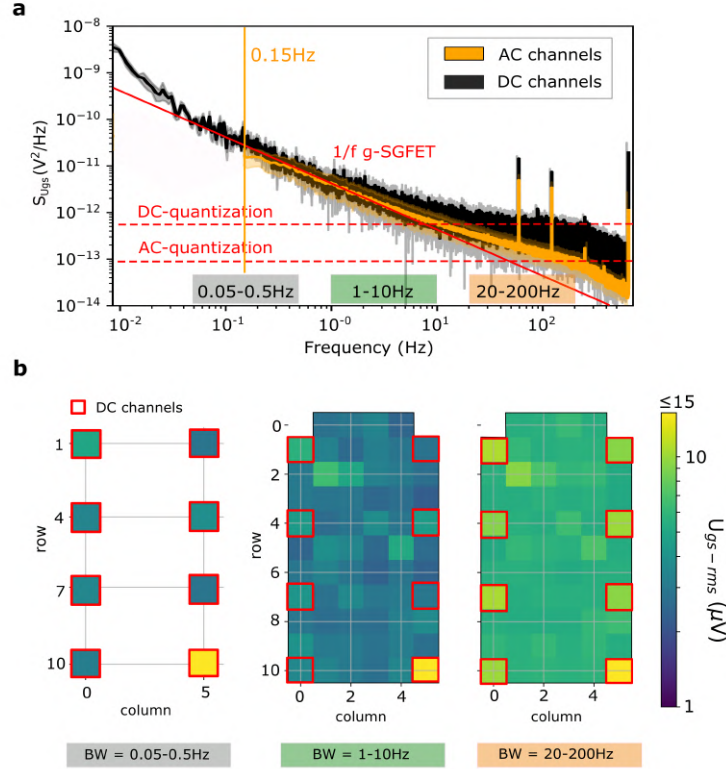
Figure 3.2: a, Power spectral density (PSD) of the noise from DC channels (black) and AC channels (orange) in probe #3 presented in Fig. 3.1. The $1/f$ dependence is represented by the solid red line. The vertical orange line indicates the hardware high-pass filter applied to AC channels at $0.15\,Hz$. The quantization noise of the DC and AC channels is indicated by the horizontal dashed red lines. **b,** Representation of the U_{gs-rms} for all g-SGFETs in probe #3 shown for different bandwidths; $0.05 - 0.5\,Hz$ band for the DC-channels (left), $1 - 10\,Hz$ band (middle), and $20 - 200\,Hz$ (right). The position of the g-SGFETs on the array connected to DC-channels of the headstage is indicated by the red squares. Figure adapted with permission from Garcia-Cortadella and Schwesig et. al.[234].

3.2 Chronically implanted epi-cortical devices *in-vivo*

Following the characterization of the recording system *in-vitro*, a neural probe was chronically implanted on the cortex of a Long Evans rat to demonstrate its *in-vivo* applicability (see the 2nd main article of this thesis). These experiments were carried out in collaboration with Gerrit Schwesing and Prof. Sirota from Ludwig-Maximillians-Universität. The implanted device allowed to evaluate the long-term stability of g-SGFETs *in-vivo*, determining the degradation of the graphene sensors as well as the impact of changes in the surrounding tissue on the signal quality. Furthermore, non-functional graphene devices were developed by collaborators in order to test the biocompatibility of graphene-based epi-cortical probes in acute as

well as chronic conditions. Finally, the graphene active sensor arrays were used for the mapping of wide frequency band brain activity in a freely moving rat, demonstrating the potential of this technology for the mapping of ISA and its correlation with high frequency LFP activity.

3.2.1 Longitudinal evaluation of sensitivity *in-vivo*

The long-term stability of neural probes is a critical factor for the investigation of brain dynamics as well as for the development of chronic neuroprosthetics. Pristine graphene has shown excellent chemical stability due to its sp2 hybridization[133]. However, dangling bonds at edges, grain boundaries, atomic vacancies or reconstructions in the atomic lattice increase the reactivity of graphene, which might lead to the increase of the defects density over time. Furthermore, there could be mechanical causes of performance degradation such as the detachment of graphene from the substrate or bending-induced strain on the graphene lattice and metal contacts. Finally, the encapsulation of the device by the glial scar could lead to an attenuation of the signal, in particular at high frequencies. Changes in the graphene-electrolyte interface can also cause doping of graphene, leading to drifts in the measured DC-coupled signals. Such drifts can be confused with electrophysiological infra-slow signals and ultimately change the effective gate bias of the transistors, leading to a drop of the sensitivity. Having a controllable doping and a homogeneous CNP among sensors is therefore necessary to maintain a good performance of the array over time.

Fig. 3.3a shows the evolution of the transfer characteristics of the DC-coupled channels over four weeks after implantation of the neural probe. The observed shift of the CNP is presumably due to the adsorption of charged chemical species present in the environment or changes in the reference potential (see supporting information of the 2nd main article of this thesis). The accumulated drift in the CNP during the first $24\,h$ of recording reached approximately $50\,mV$, however, this drift could be corrected on a daily basis without affecting significantly the sensitivity of the system (see the 2nd main article of this thesis). In addition to changes in the doping of graphene, it was possible to monitor the change in the g_m and U_{gs-rms} of the DC-coupled g-SGFETs over 4 weeks (Fig. 3.3b). These results demonstrate that the sensitivity of g-SGFETs remains within a functional range for at least four weeks. In order to determine the fraction of working g-SGFETs, the signals detected in AC-coupled channels were analysed. The PSD at high frequencies ($> 200\,Hz$) is dominated by the flicker noise of g-SGFETs due to the transient nature and low amplitude of high frequency neural oscillations. Therefore, evaluation of the noise at high frequencies allowed to determine the evolution of flicker noise in g-SGFETs *in-vivo*. Fig. 3.3c shows the integrated current noise estimated from this measurement for all g-SGFETs in the implanted array (see supporting information of the 2nd main article of this thesis). From the evaluation of the output noise

level it was also possible to estimate the percentage of working g-SGFETs over the course of the chronic implant (see Fig. 3.3c). Finally, the frequency response of the g-SGFETs was also determined *in-vivo* in order to evaluate the impact of potential device encapsulation by the glial scar on the signal quality. For this purpose, two Pt-Ir electrodes were implanted on both sides of the neural probe (see inset in Fig. 3.3d) and $1\,\mu A$ amplitude pure tone signal at different frequencies was applied using a current source. Fig. 3.3d shows the magnitude of $g_m(f)$ for different days after implantation of the neural probe normalized by the mean magnitude at $1\,Hz$. Note that the fractional order attenuation of the magnitude reported in PBS is also observed *in-vivo* with an slightly larger decay of $\sim 1/f^{0.1}$. However, the decay factor is approximately constant over time, indicating that there is not a significant increase in the electrical impedance in series with the graphene-electrolyte interface due to device encapsulation (see section 2.2).

3.2.2 Voltage and frequency dependent signal calibration

Graphene active sensors transduce voltage signals at the gate into current signals between drain and source. In order to interpret the neural signals correctly, the measured currents must be converted back to units of volts by dividing the measured current signal by the transconductance of the g-SGFETs. In a first approximation, the stationary transconductance can be used. However, as described in section 2.2, neural signals with a large amplitude can be distorted by the voltage dependence of the transfer function. Similarly, signals at different frequencies will be amplified with a different factor and errors in the phase might be introduced as a result of a frequency dependent transfer function. In order to correct such distortions, a method has been proposed in the 1st main article of this thesis, which takes into account the voltage and frequency dependence of the transfer function.

In the first place, in order to correct the harmonic distortion introduced by the graphene active sensors, it is possible to interpolate the measured full-band signals into the non-linear transfer curves of each g-SGFET. In order to determine the effect of this calibration method on the attenuation of high order harmonics, a high-amplitude test-signal was applied on the gate of g-SGFETs and the amplitude of high order harmonics was compared for the standard calibration using a constant G_m and the interpolated signals. Fig. 3.4a shows the amplitude of the 2nd order harmonic, which is significantly attenuated in the bias range of lower SDR (see the 1st main article of this thesis for more details). Following the correction of harmonic distortion, the signals can be further processed in order to correct the frequency dependence of the transfer function. Fig. 3.4b shows the magnitude and phase of the transfer function measured *in-vivo* using the methodology described above (see section 3.2.1). Fitting of the measured response with the analytical function presented in Eq. 2.14 shows a close agreement with a response dominated by the CPE behaviour of the graphene-electrolyte interface. This response leads to an
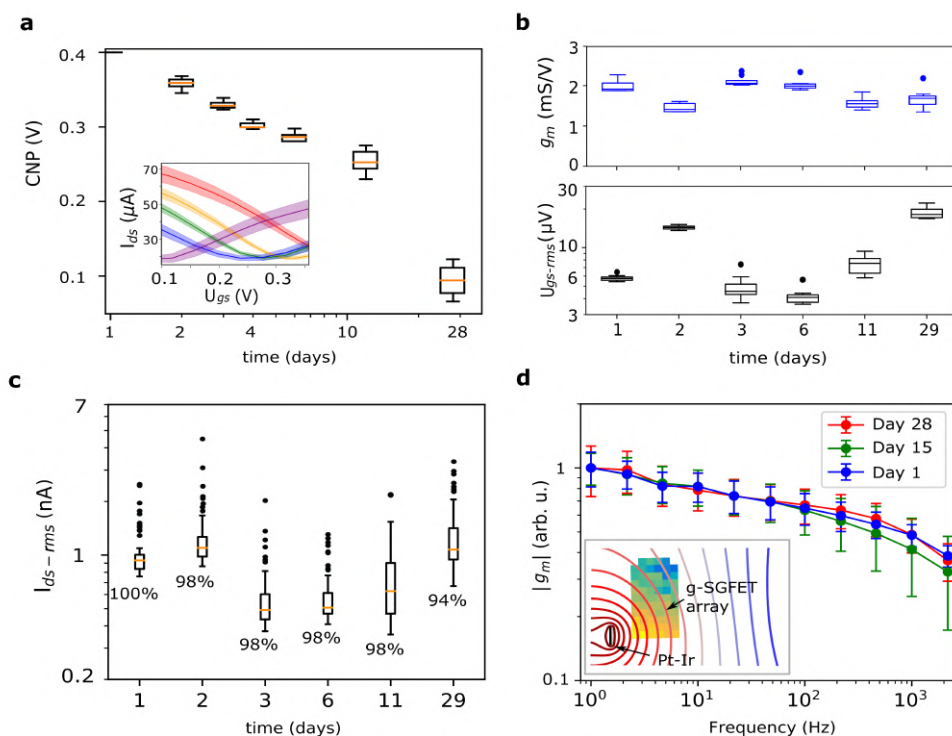
Figure 3.3: a, CNP vs time over 4 weeks. The inset shows the $I_{ds} - U_{gs}$ curves. Mean and standard deviation for $n = 7$ g-SGFETs (1 outlier was excluded from the dataset). **b,** g_m (top) and U_{gs-rms} (bottom) measured over 4 weeks post-implantation; g_m was obtained from the I_{ds}–U_{gs} curves of the DC-coupled channels ($n = 7$ g-SGFETs, 1 outlier was excluded from the dataset). **c,** Current noise over 4 weeks after implantation ($n = 64$ g-SGFETs). The numeric values indicate the yield of working devices. The boxes in panels a-c extend from the lower to the upper quartiles, with a line at the median. The whiskers extend 1.5 times the inter-quartile range and the data points beyond the whiskers are indicated by a dot. **d,** Average and standard deviation of the frequency-dependent transconductance ($\|g_m\|(f)$) shown for different days after the implantation ($n = 10$ g-SGFETs). The inset shows the approximate position of the Pt-Ir electrode close to the array, the simulated equipotential contour lines in a conductive plane and the relative signal amplitude measured by each of the g-SGFETs in the array. Figure adapted with permission from Garcia-Cortadella and Schwesig et. al.[234].

approximately constant phase of the transfer function in the typical frequency range of LFP signals. The analytical transfer function has been implemented numerically following Oustaloup's method which synthetizes the TF by the recursive distribution of $(2N+1)$ zeros and poles[235], which can be easily implemented digitally for real-time calibration of the neural signals (see the supporting information of the 1st main article of this thesis).
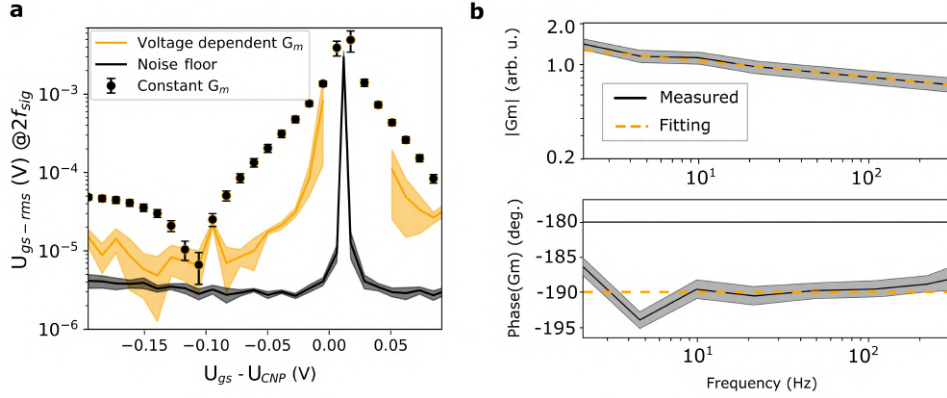
Figure 3.4: a, Amplitude of the 2nd harmonic in the equivalent voltage at the gate for $A_{sig} = 8\,mV_{rms}$, showing the values calibrated using a constant transconductance (dots) and using the interpolation into the transfer characteristics (solid orang line). The solid black line shows the average intrinsic noise of the g-SGFET measured at $17\,Hz$ and $23\,Hz$ (i.e. $3\,Hz$ below and above $2f_{sig}$). The errorbars and filled area show the standard deviation for $n = 4$ g-SGFETs. **b,** Frequency response measured *in-vivo* usign bipolar current stimulation. The filled area shows the standard deviation (for $n = 4$ g-SGEFTs) and the orange dashed line the fitting using the derived transfer function ($\alpha_{g-e} = 0.9$). Figure adapted with permission from Garcia-Cortadella et. al.[224].

3.2.3 Biocompatibility of graphene neural probes

In order to assess the applicability of g-SGFET arrays for long-term monitoring of brain activity, it is critical to assess the biocompatibility of graphene-based neural probes *in-vivo*. For this purpose, a cohort of Sprague Dawley rats were implanted with non-functional devices comprising a large area covered by graphene, platinum or PI (Fig. 3.5a), or had the full surgery without the implantation of any device (sham control). A cohort of naïve animals who underwent no intervention were also used as a control. Subsequently, the immunohistochemical response of the tissue was investigated over three time points; 2 weeks, 6 weeks and 12 weeks post-implantation (see the 2nd main article of this thesis). This work was conducted by collaborators in the University of Manchester (see author contributions in section 0.2).

Evaluation of the inflammatory response was carried out by performing immunohistochemical analysis for activated microglia and an enzyme-linked immunosorbent assay (ELISA) of blood and brain tissue for a panel of four inflammatory cytokines. Evaluation of cytokines in blood serum presented no significant differences at any of the timepoints or for any materials implanted (see supporting information of the 2nd main article of this thesis). Cytokine levels in brain tissue presented significantly higher values for graphene and platinum devices at the 2 weeks timepoint, when compared to the contralateral control. At the 6 weeks timepoint there was still a significant difference in two of the four tested cytokines for graphene and

platinum devices compared to the control. However, by 12 weeks after implantation, there was no significant expression of any cytokine for any material (see Fig. 3.5b and the supporting information of the 2nd main article of this thesis for the complete dataset). In order to confirm these results, activated microglia were manually counted following an Iba-1 immunofluorescent staining (Fig. 3.5c). Fig. 3.5d shows the percentage of activated microglia, which is significantly increased in all the devices as well as in the sham control. Similarly to cytokine levels, at the 12 weeks timepoint the percentage of activated microglia was back to the baseline level. These results indicate that the tissue response to graphene devices is transient and comparable to the platinum clinical standard. The increased level of activated microglia in the sham control indicates that their activation could be more susceptible to the surgical procedure and probe insertion, while inflammation measured by the cytokine levels in the brain could be primarily affected by the properties of the implanted material.
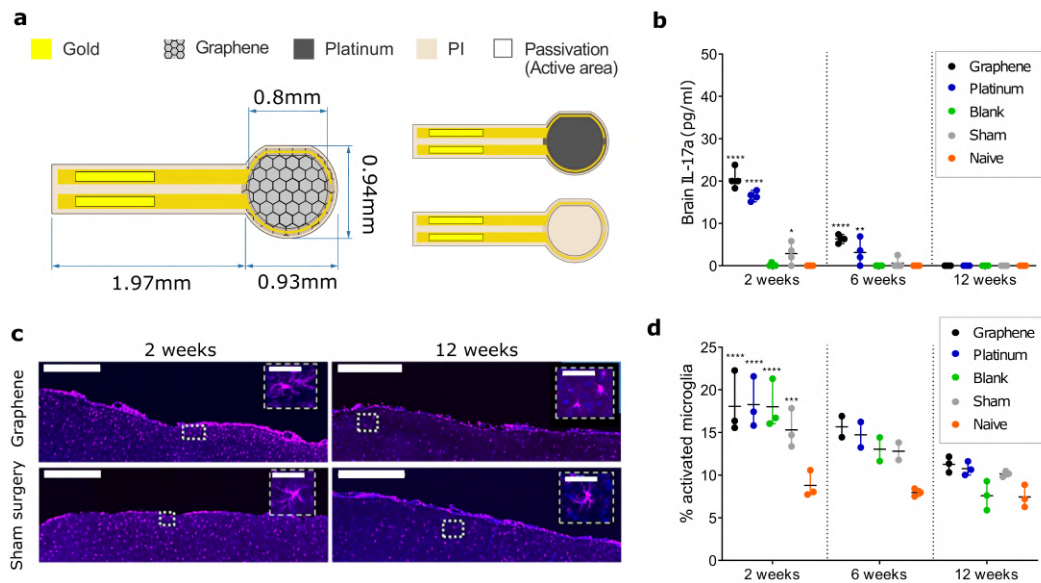
Figure 3.5: **a,** Schematic of the g-SGFET prototype with an enlarged graphene area developed for biocompatibility testing *in-vivo*. **b,** Inflammatory marker IL-17a in the brain tissue for all groups and timepoints. Evaluated for $n = 4$ animals after 2 and 6 weeks, and $n = 3$ animals at 12 weeks. **c,** Iba-1 immunoflourescent staining to assess activation status of microglia at the surgical site obtained from 40 sections per animal. Scale bar equals $500\,\mu m$ ($50\,\mu m$ at the insets). **d,** Microglial activation state, expressed as a percentage of total microglial presence in the site surrounding the electrodes. $n = 3$ animals at 2 and 12 weeks, $n = 2$ animals (or 3 for the contralateral hemisphere) at 6 weeks. Bars in panels b and d indicate the mean and range of data point. In panels b and d two way ANOVA test with Dunnett's multiple comparison to the naïve control within each timepoint with $n = 3$ or larger: **, *** and **** indicate $p = 0.015$, $p = 0.007$, $p = 0.0016$ and $p < 0.0001$ respectively. Figure adapted with permission from Garcia-Cortadella and Schwesig et. al.[234].

74

3.2.4 Long-term monitoring of wide frequency bandwidth brain activity

In order to demonstrate the performance of the system in an operational environment, the cortical dynamics of the Long Evans rat with the implanted g-SGFET array were monitored during natural behaviour. The main advantage of non-multiplexed graphene active sensor arrays with respect to passive electrodes is their sensitivity in the ISA band. ISA has recently attracted increasing attention due to its unique neurophysiological basis[236] and its relation to resting-state networks[117, 119, 237, 238] and to brain states[116, 118, 237, 239]. Therefore, it is paramount to demonstrate that the sensitivity of graphene active sensors in the typical LFP band is sufficient to capture typical patterns of brain activity related to distinct brain states. In order to take full advantage of the sensitivity of g-SGFETs, the long-term stability demonstrated in section 3.2.1 becomes particularly relevant to detect ISA events across sparse brain-state transitions with sufficient statistical power. For this purpose, the motion of the animal was tracked during the electrophysiological recordings for up to $24\,h$ uninterruptedly, except for sporadic battery replacement (Fig. 3.6a,b). The electrophysiological recordings allowed to detect the wide frequency band LFP activity that clearly reflected slow-wave (SW) states, theta states and sparsely occurring high-voltage spindles (HVS)[240, 241] (Fig. 3.6c-top). The combination of the activity states and electrophysiological data was used to classify the brain state of the animal among slow-wave sleep (SWS), rapid eye movement (REM) sleep, Awake Theta (AwT) and Awake Non-Theta (AwNT) as described in the 2nd main article of this thesis and illustrated in the example shown in Fig. 3.6c. During most of the hours of the recording all four sleep/wake states were present, as expected from the polyphasic nature of rat sleep[242].

Following the classification of brain states, the relation between ISA patterns and higher frequency LFP activity could be investigated. In the first place, the infra-slow fluctuations associated with HVS events were analysed. Fig. 3.7a shows the HVS-triggered averaged of the signals monitored in the 8 DC-coupled channels of the system. Benefiting from the long-term stability of the system, a large number of HVS events could be detected during immobility (IMM) ($n = 566$ events), and more sparsely during REM ($n = 92$ events), which is typically not associated with HVS. The infra-slow patterns associated with HVS presented a clear phase reversal from anterior to posterior sites, which was preserved across brain states (i.e. during IMM and REM sleep states) and illustrates the importance of resolving the spatial topography of ISA dynamics. While the ISA component associated with HVS events did not present significant differences in distinct brain states, the higher frequency components of HVS did present significant differences in their spectral peak frequency and power between IMM and REM sleep (see Fig. 3.7b and the 2nd main article of this thesis). Following on the analysis of state dependent ISA patterns, we investigated the modulation of physiologically established oscillatory dynamics by the ISA phase. Interestingly, we found the modulation of hippocam-
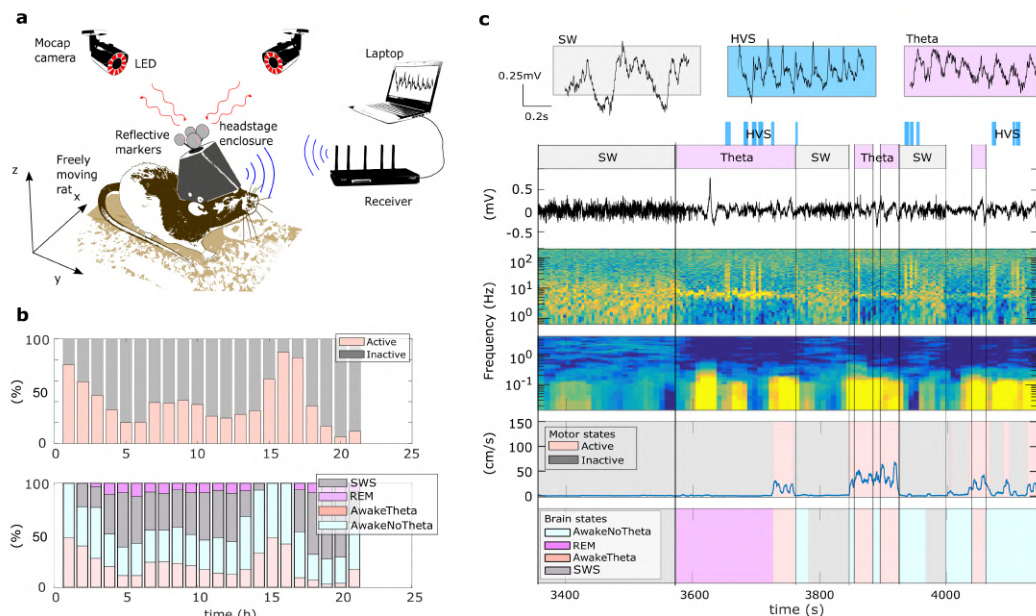
Figure 3.6: a, Illustration of the rat with the untethered recording system implanted. The headstage and the 3D-printed frame to hold it are covered by a 3D-printed enclosure. On top, the position markers of the motion capture (Mocap) system are fixed, which reflect light back to the Mocap cameras placed in the room. The neural signals transduced by the graphene sensors are digitized and transmitted wirelessly to the signal receiver, which is connected to a computer for signal recording. **b,** Top: percentage of time in the active vs inactive state (interruptions to replace the battery not included). Bottom: percentage of time the rat was in each main brain state. **c,** The spectrogram and raw LFP signal of an illustrative channel is displayed for distinct brain states (top); slow-wave (SW), high-voltage spindles (HVS) and Theta. Movement speed is displayed along with classification of motor state (middle) and brain states (bottom). Figure adapted with permission from Garcia-Cortadella and Schwesig et. al.[234].

pal theta by the epi-cortical ISA phase during REM sleep (see Fig. 3.7c-right), which presented a clear spatial topography as shown in Fig. 3.7c-left. Similarly, the power in the spindle band $(10 - 14\,Hz)$ was modulated by the ISA during SWS (see the 2nd main article of this thesis). Subsequently, we also investigated the state-specific changes in the ISA band power; as an example Fig. 3.7d shows the averaged spectrogram in the $0.0015 - 4\,Hz$ band triggered in the transition between SWS and REM sleep. Note that the ISA power increases in the REM state in opposition to the power in the SW band. This observation supports previous evidence on the unique neurophysiological basis of ISA[236]. Finally, the performance of the graphene active sensor arrays to detect high frequency band activity was addressed. Due to the fractional order drop of transconductance with frequency and the impact of quantization noise, it is important to determine the functionality of the system in the high frequency band. Analysis of gamma activity showed that

the power of gamma in the range of $60 - 120\,Hz$ was modulated by the ISA phase, proving the sensitivity of the system at high frequencies and providing new insights into the electrophysiology of ISA. Similarly, the power in the high-gamma range of $120 - 150\,Hz$ was modulated by the phase of theta oscillations as expected from previous works[101]. To conclude the investigation of high-frequency oscillations, the relationship between broad range gamma ($60 - 200\,Hz$) and sparsely occurring rearing events was analysed. Fig. 3.7f shows the average spectrogram triggered in the rear onset. While the gamma in the $60 - 70\,Hz$ band presented a power increase, high gamma activity in the range of $120 - 200\,Hz$ presented a clear power increase, which could be identified at the single trial level (see the 2nd main article of this thesis). These results demonstrate the capabilities of the graphene active sensors to detect diverse gamma oscillators. Although future research is needed to replicate these results in a larger cohort of animals, these long-term recordings allowed to detect a large number of sparsely occurring physiological patterns and behavioural events, which enabled a detailed quantitative analysis of the relation between ISA and physiologically established oscillatory dynamics in freely behaving animals.
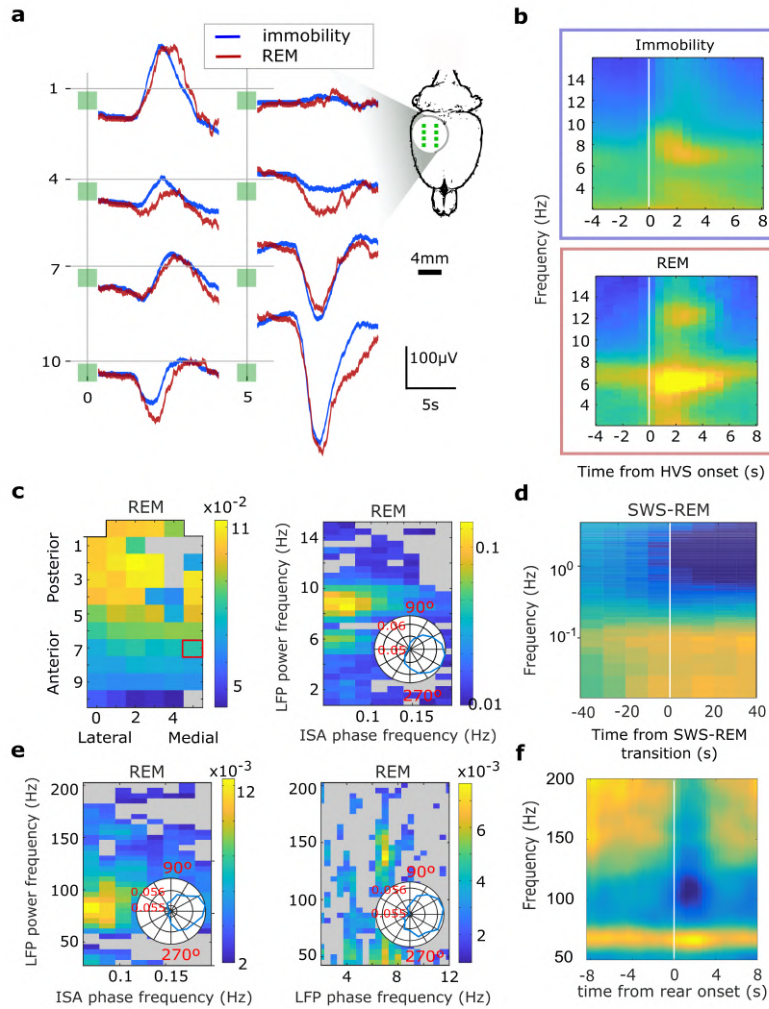
Figure 3.7: a, Average DC LFP traces triggered on HVS onset during immobility and REM sleep (channels arranged as in Fig. 3.2b), inset showing anatomical localization of DC ECoG recording sites. **b,** Average AC LFP spectrograms triggered on HVS onset during immobility (top) and REM sleep (bottom). The spectrograms correspond to anterior positions on the array. **c,** Left: topography of ISA phase modulation of LFP power in theta band during REM. ISA phase derived from DC channel marked with a red square. Right: color-coded strength of modulation of LFP power across slow frequency range (y-axis) for one channel by the phase of ISA across $0.05 - 0.2 \, Hz$ range derived from one DC channel (see left panel) during REM sleep. Inset, circular plot of LFP theta power with respect to respective ISA phase. **d,** Average $0.015 - 4 \, Hz$ spectrogram for one DC channel triggered on REM episode onsets (n=44). **e,** Color-coded strength of modulation of LFP power across gamma frequency range (y-axis) for one channel by the phase of ISA across $0.05 - 0.2 \, Hz$ range derived from one DC channel (left panel) and by the phase of LFP in the slow frequency range (right panel) during REM. Inset, circular plot of LFP gamma power with respect to respective (ISA or theta) phase. **f,** Average spectrogram for high frequency range of LFP on posterior channel triggered on rear onset ($n = 162$). Figure adapted with permission from Garcia-Cortadella and Schwesig et. al.[234].

78

3.3 Chapter outlook: Improved technology for chronic, wide frequency band recordings

Demonstration of the wide frequency band sensitivity of g-SGFETs and their applicability in freely moving rodents in a chronic setting has important implications. Recording of ISA with a high spatial resolution has been so far limited to head-fixed experiments[116] either using optical methods[243] or fMRI studies[116, 121]. In addition, both of these methods are limited in temporal resolution to the infra-slow band. Therefore, graphene active sensor arrays present unique properties for the simultaneous detection of infra-slow and higher frequency LFP signals with high spatial resolution and in freely moving animals. Having stablished the sensitivity of g-SGFET arrays in a wide frequency LFP band, two technological aspects should be addressed. First, the capability of the g-SGFETs to detect single-unit activity, which remained unresolved due to the planar design of the neural probes used in this study. Secondly, the stability of g-SGFETs *in-vivo* might be compromised by extrinsic causes of instabilities, mainly failure of the SU-8 passivation layer. Therefore, optimization of the passivation layers might significantly improve the long-term stability reported in the present study.

Following the implementation of Cu-protected g-SGFETs to improve their frequency response (section 2.3), it is possible to investigate the passivation of Cu-protected g-SGFETs with non-photodefinable passivation layers. Replacement of SU-8 by polyimide could significantly improve the long-term stability of graphene sensors while providing an improved sensitivity in the high frequency band. For this purpose, intra-cortical graphene neural probes were designed and fabricated following the protection of the channel by Cu thin films. Having a Cu-protective layer, it becomes possible to pattern a non-photodefinable passivation layer with non-selective dry etching methods without damaging graphene. In order to demonstrate the potential of Cu-protected g-SGFETs to detect spikes, the graphene sensors were fabricated on a narrow polyimide thread for intra-cortical recording and a waveform generator was used to apply spike-like activity of relatively low amplitude for *in-vitro* testing of the devices. Following this approach, artificial spike-like signals with an amplitude of $\sim 100\,\mu V$ could be reliably detected Fig. 3.8a. The improved sensitivity is the high frequency range can be attributed to the approximately constant $|g_m|(f)$ up to $> 1\,kHz$ (Fig. 3.8b) achieved with the protection of the graphene channel with Cu sacrificial layers. Integration of the intrinsic $1/f$ from the g-SGFETs in different frequency bands, yields a constant I_{ds-rms} per frequency decade up to at least $10\,kHz$ (Fig. 3.8c). Combined with the constant G_m at high frequencies it leads to a constant U_{gs-rms} per frequency decade for Cu-protected graphene sensors. In contrast, devices fabricated with the standard fabrication proces present an increase of the equivalent noise at the gate in the SUA frequency band (Fig. 3.8d,e). More information about the standard fabrication process is provided in the experimental section of the 1st main article of this thesis

(Appendix A). Future experiments should address the evaluation of the sensitivity of g-SGFETs in the SUA frequency band *in-vivo* and development of large-scale graphene sensor arrays for intra-cortical recording of neural activity.
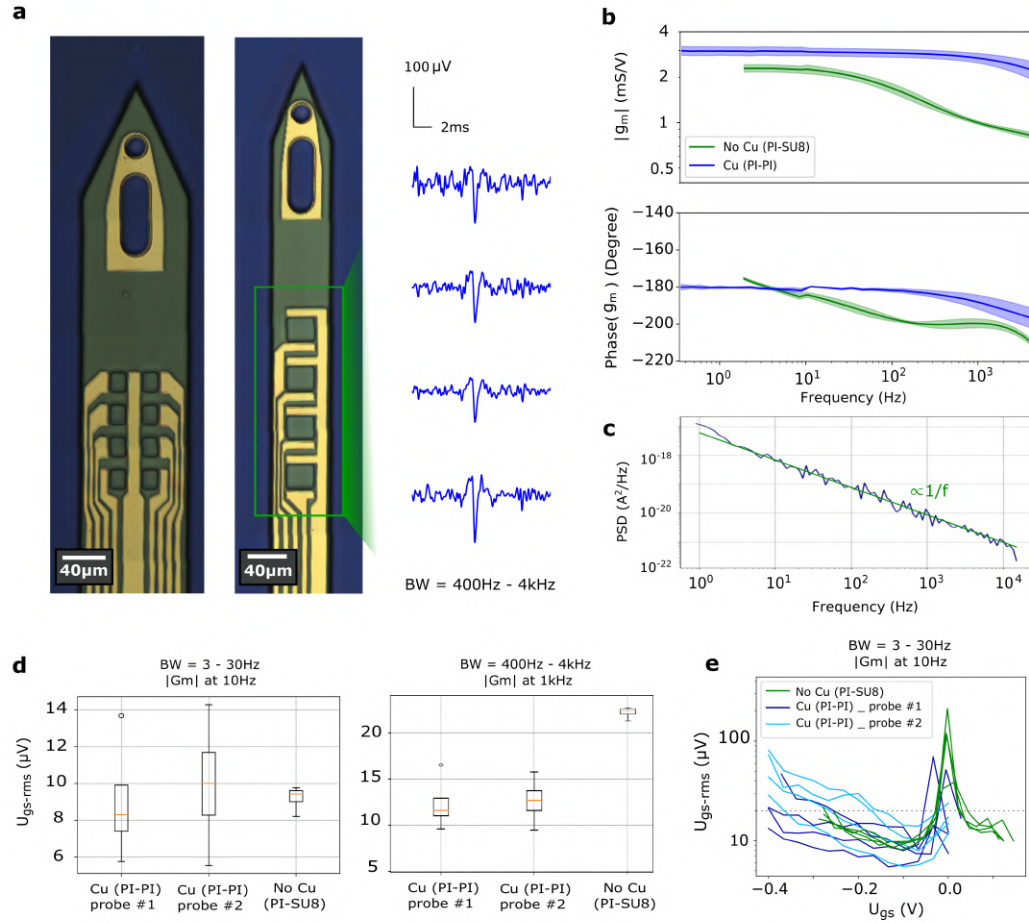
Figure 3.8: a, Optical micrograph of a 4 channel ($25\,\mu m\ x\ 25\,\mu m$ g-SGFETs) in a $70\,\mu m$ wide shank and 8 channels ($15\,\mu m\ x\ 15\,\mu m$) in a $100\,\mu m$ wide shank passivated with polyimide. Right: Artificial signals corresponding to hippocampal spikes with $\sim 100\,\mu V$ amplitude detected with $25\,\mu m\ x\ 25\,\mu m$ g-SGFETs in PBS. The holes in the tip could be used for insertion using a customized rigid shuttle. **b,** Frequency response of the polyimide-polyimide fabricated using Cu sacrificial layers and polyimide-SU8 devices without Cu protection. The improvement in the frequency response achieved with Cu sacrificial layers (Fig. 2.6) holds for polyimide-polyimide devices (n=8 g-SGFETs) with geometry $25\,\mu m\ x\ 25\,\mu m$. **c,** Current power spectral density of a representative Cu-protected polyimide-polyimide g-SGFET and the fitting of $1/f$. **d,** Integrated equivalent noise at the gate in the $3-30\,Hz$ range calculated with $|G_m|@10\,Hz$ (left) and integrated in the $400\,Hz$-$4\,kHz$ range calculated with $|G_m|@1\,kHz$ (right) for Cu-protected and non-protected devices. **e,** Equivalent RMS noise at the gate (U_{gs-rms}) integrated in the $3-30\,Hz$ band for Cu-protected and unprotected devices.

In summary, the thorough *in-vitro* and *in-vivo* evaluation of the sensing and long-term recording capabilities of graphene active-sensors from a system perspective demonstrates the maturity of this technology and supports its application for the study of ISA without sacrificing the detection of high frequency neural dynamics. In this direction, we have successfully evaluated ISA patterns during distinct brain states and their correlation with higher frequency oscillations. These results represent an important step towards the broad implementation of graphene active-sensor arrays for neuroscience research, offering a stable and biocompatible sensing technology for long-term mapping of wide frequency band epi-cortical brain activity during spontaneous behaviour.

One potential disadvantage of g-SGFET arrays compared to fMRI and optical methods for the study of ISA is the coverage area. Upscaling sensor arrays is typically constrained by the difficulty in connecting each sensor to an individual macroscopic connector. However, g-SGFETs are also promising to implement multiplexing strategies, which allow transmitting the signals from multiple sensors through a shared micro-wire. The combination of wide frequency band sensitivity of g-SGFETs and their operation in multiplexed mode would raise graphene active sensor arrays as a unique tool for the study of large-scale brain dynamics. In the following section, novel strategies for g-SGFET array multiplexing are presented.

Chapter 4

Multiplexed graphene neural probes:
Large-scale brain mapping

Previous sections have discussed how graphene active sensors allow a high sensitivity in a wide frequency band in addition to a high biocompatibility and long-term stability. Furthermore, g-SGFETs can be arranged in addressable arrays, which together with their expected drain-source frequency response, raises them as promising candidates as a building block for multiplexed sensor arrays. This chapter presents two strategies for the multiplexing of graphene sensor arrays, which do not need on-site flexible switches. The first strategy is based on time-division multiplexing (TDM) in which the drain bias U_{ds} is applied sequentially to all columns of the g-SGFET array, dividing the sampling resources of the readout circuits among all columns. In this mode, the switching among columns is performed externally, using rigid silicon-based transistors. In a second approach, the use of frequency-division multiplexing (FDM) is proposed, in which a carrier signal with a particular frequency is applied on each column, continuously biasing all the g-SGFETs on the array. In this mode, the graphene transistors operate as mixers, multiplying the carrier signals by the transduced neural signals, leading to their amplitude modulation (AM). Following the FDM strategy, each readout circuit amplifies the signals from all g-SGFETs in continuous time, with each column of the array modulated at different carrier frequencies. This chapter summarizes a proof-of-concept for each of these multiplexing modes, focusing on their performance and scalability.

4.1 Time-Division Multiplexing of graphene transistors

Time-division multiplexing of neural signals detected by active sensor arrays has been previously proposed[11, 69, 76, 174]. However, state of the art multiplexed sensor arrays are currently limited by the properties of the flexible semiconductors used, which present a limited switching speed, a limited long-term stability and/or a poor sensitivity. Graphene-based active sensors have demonstrated a high stability *in-vivo* and present a high electrical mobility, which is critical for high-speed operation. However, due to the gap-less nature of its band structure, graphene cannot be used to produce switching devices. To date, all proposed approaches for multiplexing of active sensors on flexible substrates rely on the use of on-site switching elements on the neural probe to select the biasing of particular columns in the array[11, 69, 76, 174]. The use of switches is unavoidable in TDM operation, however, in the 3rd complementary article of this thesis (Appendix B), the use of graphene transistors in combination with external switching arrays is presented as a promising alternative to the use of on-site switches. This section summarizes the results from this article together with recent results on the scalability of TDM.

4.1.1 Validation of the time-division multiplexing principle

For the operation of g-SGFET arrays in TDM, a system based on discrete electronic components was developed to multiplex arrays of up to 16x16 g-SGFETs (Fig. 4.1a). The developed system comprises of a data acquisition system (DAQ-card from National Instruments) for signal digitalization and control of the source and gate bias. An external switching array, consisting of MOSFET silicon transistors, is controlled by the digital outputs of the DAQ-card to switch among the columns of the array. The front-end electronics consist of two amplification stages: first, a transimpedance amplifier with a low-pass filter at $10\,kHz$ and, second, a stage consisting of a high-pass filter at $0.1\,Hz$ and a voltage amplifier (see Fig. 4.1a). Using this system, the sensitivity of 8x8 g-SGFET arrays could be evaluated *in-vitro* as well as *in-vivo*[187] (see the 3rd complementary article of this thesis). Fig. 4.1b shows the detection of a signal generated *in-vitro* representing an electrocardiogram pattern, detected in TDM mode and in standard static acquisition mode, which show comparable signal quality. Following the characterization *in-vitro*, g-SGFETs arrays in TDM operation were benchmarked against commercial μ-ECoG arrays on the cortex of an anaesthetized Long-Evans rat[187] (see the 3rd complementary article of this thesis). The spectrogram in Fig. 4.1c shows the comparison between a signal detected with a g-SGFET of $50\,\mu m$ x $50\,\mu m$ in TDM mode and the signal detected in the contralateral hemisphere with a Neuronexus commercial electrode array ($100\,\mu m$-diameter circular platinum electrodes). The spectrograms reveal a similar signal to noise ratio for both systems in the measured frequency range. Furthermore, multiplexing of g-SGFETs in TDM mode preserves the sensitivity of g-SGFETs in the infra-slow frequency band. Fig. 4.1d shows the detection of a

cortical spreading depression (CSD), triggered following the procedure described in previous literature[222], and its propagation across the cortical area under the multiplexed sensor array. These results demonstrate the potential of TDM graphene neural probes for studying the topography of wide frequency-band LFP dynamics on the surface of the brain.
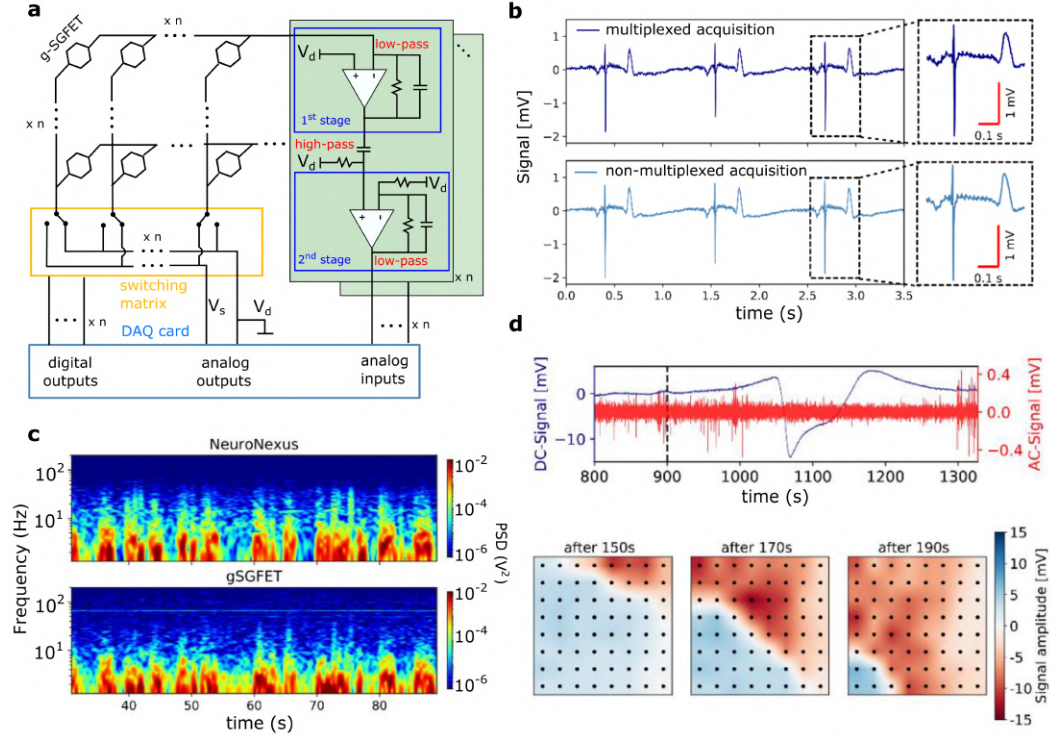

Figure 4.1: a, Schematic of the main components of the TDM system, consisting of the 256 g-SGFET array, a front-end signal amplifier, an external switching matrix and a data acquisition (DAQ-card) system. **b,** Electrocardiogram pattern generated artificially using a low noise waveform generator and detected using g-SGFETs in TDM operation (top) and in static acquisition (bottom). **c,** Spectrogram of neural signals in the typical LFP frequency range from the cortex of an anaesthetized rat. Signals detected with a commercial electrode from Neuronexus (top) or using g-SGFETs in TDM operation (bottom). **d,** DC-coupled signal detected with a g-SGFET in TDM operation (left-axis) and high-pass filtered signal ¿0.1Hz (right axis) during the occurrence of a cortical spreading depression (top). Propagation of a CSD across the cortex under the μ-ECoG grid (bottom).

One of the main disadvantages of TDM based on external switching, in comparison to other technologies incorporating on-site switches, is that the impedance of the sensors cannot be controlled externally. This relatively low impedance leads to an increased susceptibility to crosstalk among columns and rows. When the source potential (U_s) is applied on a particular column, it generates a drain-source current through all g-SGFETs sharing this column. In a first approximation, the current flowing to the readout channels at the rows level contains only the neural signals

detected by g-SGFETs in the selected column. However, the presence of parasitic resistance at the metal tracks due to their finite conductance, generates a common-mode voltage, which results in crosstalk among g-SGFETs in the same column or row. Measurement and simulation of this coupling confirmed that the crosstalk level among g-SGFETs in the same column or row is equal to the ratio between the track resistance and the g-SGFET resistance. Understanding the origin of crosstalk guided the design of the neural probes to present a minimal track resistance, lowering the signal-to-crosstalk level to 40dB. Moreover, having an accurate model of its generation, it is possible to correct the crosstalk level in a calibration process, as described in section 4.2.3 and the supporting information of 3rd main article of this thesis (Appendix A).

4.1.2 Scalability of TDM graphene neural probes

Having demonstrated the good performance of g-SGFETs in TDM and having understood the origin and magnitude of crosstalk, the next step is to upscale the sensor count on the neural probes. For this purpose, we have designed and fabricated 16x16 graphene sensor arrays on a flexible substrate (see Fig. 4.2a), following the process described in the methods section of the 3rd complementary article of this thesis. This design offers a high density of sensors capable of covering a relatively large area of the cortex of the rat or mouse brain with high spatial resolution. The active sensors have a reduced area of $50\,\mu m$ x $50\,\mu m$, in comparison to the devices presented in the chapter 3, which is expected to slightly increase their intrinsic noise. Characterization of the g-SGFETs revealed an average sensitivity in the range of $20\,\mu V$ RMS, and a high yield, with $99\,\%$ of the sensors presenting a sensitivity below $80\,\mu V$. However, the system exhibited an increase in the U_{gs-rms} at high frequencies (Fig. 4.2c). This increase is caused by the contribution at high frequencies of white noise sources. These noise sources are increasingly dominant for larger-scale arrays due to two main reasons. Firstly, sources of noise from the amplifiers and voltage references are amplified with a gain factor that is inversely proportional to the impedance of the sensor array (see supporting information of the 2nd main article of this thesis). Due to the lack of on-site switches, the impedance of the array drops as the number of sensors is increased, enhancing the amplification of extrinsic noise sources. The second reason for an increased high frequency noise is the downsampling of the acquired signal in TDM. This downsampling implies that the frequency of the antialiasing filter, which eliminates high-frequency noise, must be higher than the final sampling frequency per channel. Downsampling the signal without a proper antialiasing filter leads to folding of high frequency noise into the frequency band of operation by aliasing. This folding effectively increases the floor noise of the system. Therefore, the larger the number of columns in the array, the larger the floor noise of the system will be.

Fig. 4.3a shows the output current in a row for a 16x16 g-SGFET array using the acquisition system presented in Fig. 4.1. The sampling rate (F_s) in each row was
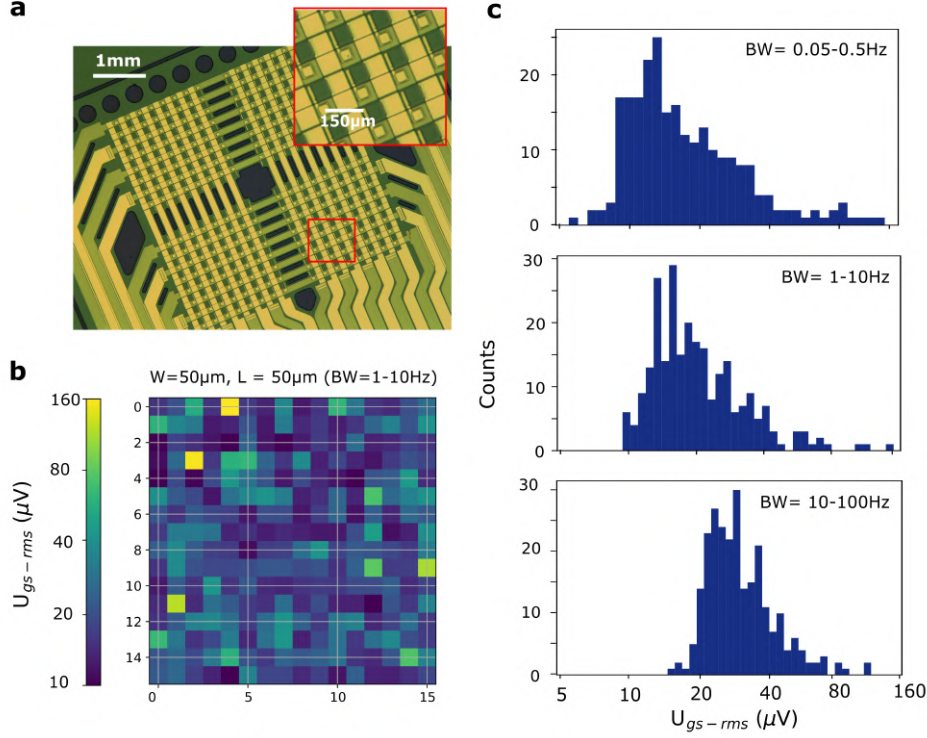
Figure 4.2: **a,** Optical micrograph of a 16x16 g-SGFET array. **b,** Color-map of the equivalent noise at the gate (U_{gs-rms}) in the $1 - 10\,Hz$ band for the g-SGFET array in panel b. **c,** Histogram representing the distribution of the sensitivity of the g-SGFETs in a 16x16 sensor array in the $0.05 - 0.5\,Hz$ band (top), the $1 - 10\,Hz$ frequency band (middle) and in the $10 - 100\,Hz$ band (bottom).

equal to $62.5\,kHz$; however, switching among columns occurred every 20 samples ($T_{sw} = 320\,\mu s$), in order to allow for the stabilization of the g-SGFETs response. The slow stabilization observed in Fig. 4.3a can be attributed to a transient capacitive current, which produces an offset in the multiplexed signals. The cause of this capacitive current is presumably the voltage pulse applied from drain to source during switching among columns, which produces the charging of the graphene-electrolyte interface capacitance. The resulting source-to-gate current adds to the measured drain-to-source current. However, this capacitive contribution does not attenuate the amplification of the signal by field-effect, as shown in Fig. 4.3b, leading to an intact transconductance. After stabilization, the sampling rate per sensor was equal to the switching rate (F_{sw}) divided by the number of columns (16 in this case), resulting in a downsampling to $F_{s-ch} = 195\,Hz$ per sensor. Fig. 4.3c represents the aforementioned frequencies together with the antialiasing filter, which must be above F_{sw}. Therefore, part of the high-frequency noise between F_{s-ch} and F_{sw} (bandwidth of x16 for 16 columns) will be folded into the band of operation,

increasing the floor noise level and introducing high frequency pick up noise by aliasing. Fig. 4.3d shows the PSD of the noise for a particular channel of the array when taking only the last sample of each period between switching events T_{sw}, or by averaging multiple samples. These results show how averaging of samples within T_{sw} mitigates aliasing of high frequency noise. Nevertheless, part of the effect of aliasing is intrinsic to the TDM operation mode and will occur even using on-site switches. Fig. 4.3e shows the average PSD for 256 g-SGFETs characterized in static operation or in TDM mode. It is possible to see that although the sensitivity in the low frequency range is approximately equal, the floor noise in TDM mode is higher, approaching a 16-fold increase with respect to the static acquisition when averaging multiple samples within T_{sw}.

Having characterized the response of high-count sensor arrays in TDM mode, it is clear that the readout circuits and voltage references for biasing the devices must present a very low noise level in addition to very high sampling speed. In order to optimize TDM of high-count sensor arrays, it is therefore convenient to develop an application specific integrated circuit (ASIC), which can be embedded in a lightweight, implantable headstage for freely moving rodents. Collaboration with the group led by Prof. Serra-Graells at the Microelectronics National Center (CNM-IMB) led to the design of an ASIC for the operation of up to 32x32 g-SGFET arrays in TDM[244] (Fig. 4.4). In order to reduce the floor noise of the system, the ASIC incorporates a correlated double sampling stage[244], which effectively filters out the noise from the transimpedance amplifier below a characteristic frequency of $100\,kHz$. Moreover, the ASIC includes a programmable resistance array for offset cancelation. The importance of offset cancelation stems from the fact that the amplification chain must be DC-coupled in order to detect infra-slow activity and to acquire the transfer curve of the g-SGFETs, which is required for gain calibration *in-vivo*. However, the static current in g-SGFET represents a large offset, which increases very significantly the dynamic range of the measured current. One possible solution is to include two amplification stages, as presented in Fig. 4.1, the first providing the DC-coupled signal and the second providing the high-pass filtered signal. However, this solution is not optimal as it duplicates the sampling requirements for the ADC. Furthermore, the high-pass filter in the AC-coupled channel can induce additional crosstalk around its cut-off frequency. Using the programmable resistance array of the ASIC[244], it is possible to keep the DC-coupling in the amplifiers while reducing the dynamic range of the signal (Fig. 4.4). The proposed circuit subtracts the required current before the transimpedance amplifier stage and, therefore, allows to operate the g-SGFETs with a much higher U_{ds}, which is an important advantage to increase the signal amplitude above the floor noise of the system.

In order to test the sensitivity of the ASIC-based system, the dependence of G_m and U_{gs-rms} on U_{ds} was first evaluated. Operating the g-SGFETs with U_{ds} in the range of the gate bias (i. e. $0-0.4\,V$) causes a non-homogeneous charge distribution along the channel, due to the effective gating induced by the potential gradient
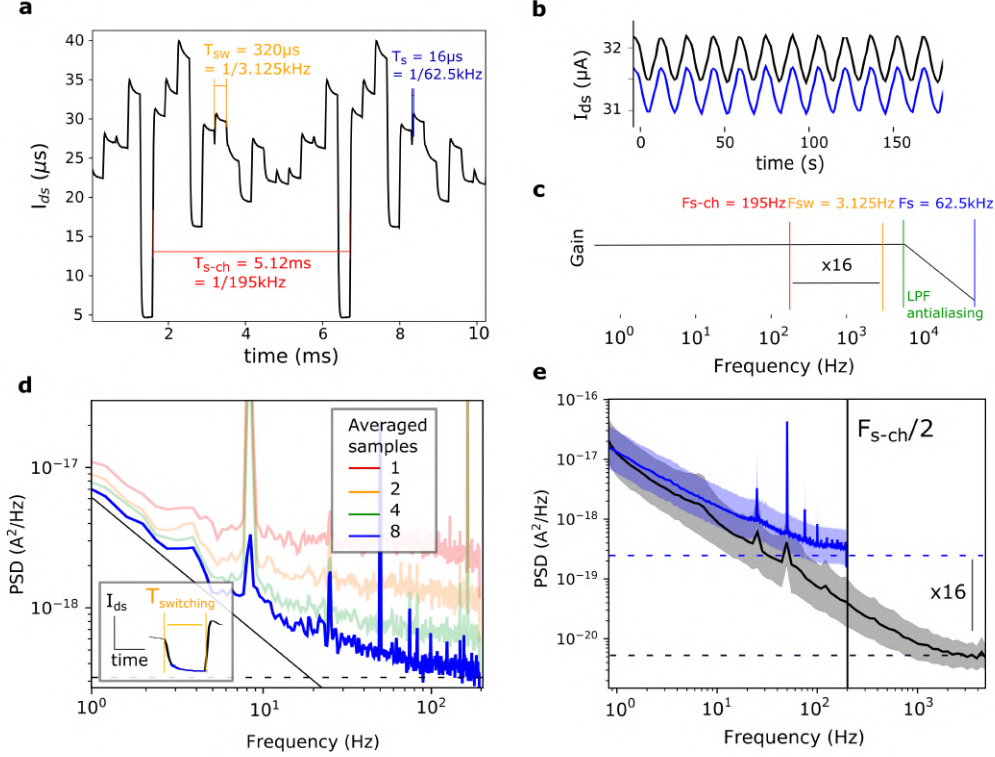
Figure 4.3: a, Output current from a row of a 16x16 g-SGFET array. Sampling period (T_s), switching period (T_{sw}) and the sampling period per recording channel (T_{s-ch}) are indicated. **b,** Demultiplexed signal from a single recording channel by taking the last sample in each switching period or by taking the first sample, after stabilization of the low-pass filter. **c,** Representation of the sampling frequency (F_s), switching frequency (F_{sw}), sampling frequency per channel (F_{s-ch}) and the low-pass filter cut-off in the frequency domain. **d,** PSD of the demultiplexed signal from one g-SGFET obtained by taking the last sample in each switching period or by averaging multiple samples. **e,** Average PSD from all 256 g-SGFETs in the array measured sequentially at maximum sampling frequency (black) or measured in TDM mode and averaging 8 samples per switching period. The filled area indicates de standard deviation.

along the channel. Such non-linearities imply that the gradient of the quasi-Fermi level driving the current is non-homogeneous. In turn, regions of the channel with a lower gradient are expected to have a lower contribution to the transconductance. In order to evaluate the linearity of the g-SGFETs response with U_{ds}, the g-SGFETs were biased at $U_{gs} = 0.18\,V$ (approximately $-0.1\,V$ from the CNP) in a wide U_{ds} range, from 0.05 to 0.4 V. Fig. 4.5a reveals that G_m and I_{ds-rms} scale linearly with U_{ds}, leading to a flat U_{gs-rms} in a wide U_{ds} range. This linearity in the sensitivity of the system is only compromised at low U_{ds} values, where the low G_m prevents the transduction of signals above the floor noise.
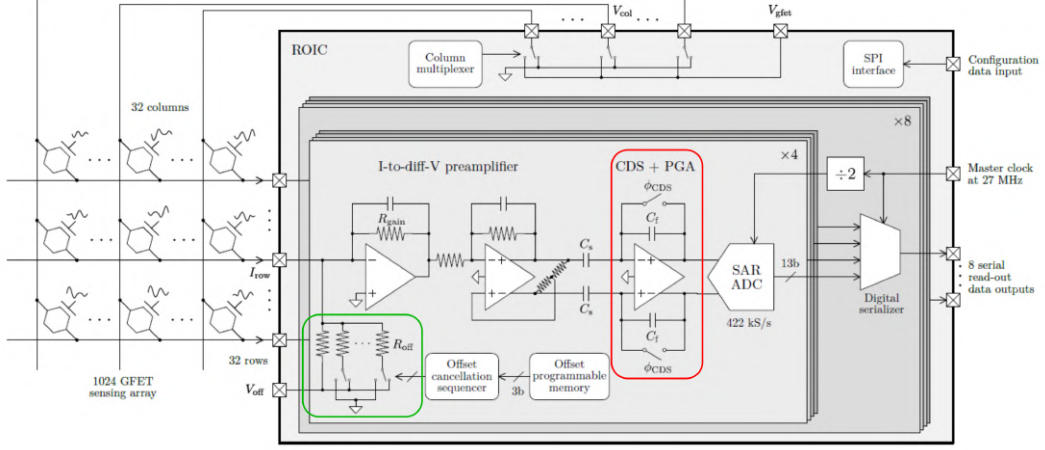
Figure 4.4: Main components of the ASIC system, consisting of a front-end signal amplifier and a switching matrix. A correlated double sampling stage (marked in red) for noise cancelation and a programmable resistance array (marked in green) for offset cancelation are implemented. Copyright IEEE. Adapted, with permission, from Cisneros-Fernandez et. al., "A 1024-Channel GFET 10-bit 5-kHz 36-μW Read-Out Integrated Circuit for Brain μECoG, Nov. 2020[244].

Having determined the linearity of the g-SGFETs response with U_{ds}, the sensitivity of the ASIC-based system was evaluated. For this purpose, we used a test-ASIC with the number of readout channels reduced to four. For the characterization, large-scale probes of 16x16 g-SGFET arrays were used in order to test the operation of the system under real conditions, which includes a low impedance of the array. Evaluation of the sensitivity of the system in the low frequency range confirmed that the LFN of the g-SGFETs dominates in this band (Fig. 4.5b) allowing to detect signals of relatively low amplitude (100 μV_{pk}, see Fig. 4.5c). Fig. 4.5d presents the PSD of the equivalent signal at the gate for a 10 μV_{pk}, 10 Hz, pure tone signal applied at the gate. The PSD indicates the frequency range in which the flicker noise of the g-SGFETs dominates. In this frequency range ($< 20\,Hz$), the sensitivity of the system is equal to the intrinsic sensitivity of the graphene sensors (i.e. $\sim 30\,\mu V$ per frequency decade) for a $U_{ds} = 0.2\,V$. Above this frequency, the RMS noise per frequency decade will increase proportionally with the frequency. Although these results are promising for the detection of LFP activity up to the low-gamma range ($30 - 60\,Hz$) with large-scale probes, detection of higher frequency activity, from high gamma to action potentials would be constrained by the noise of the amplifiers. In order to improve the high frequency sensitivity, frequency-division multiplexing could be implemented. As discussed in the next section, FDM does not imply the downsampling of the acquired data and therefore does not cause aliasing of high-frequency noise into the band of operation.
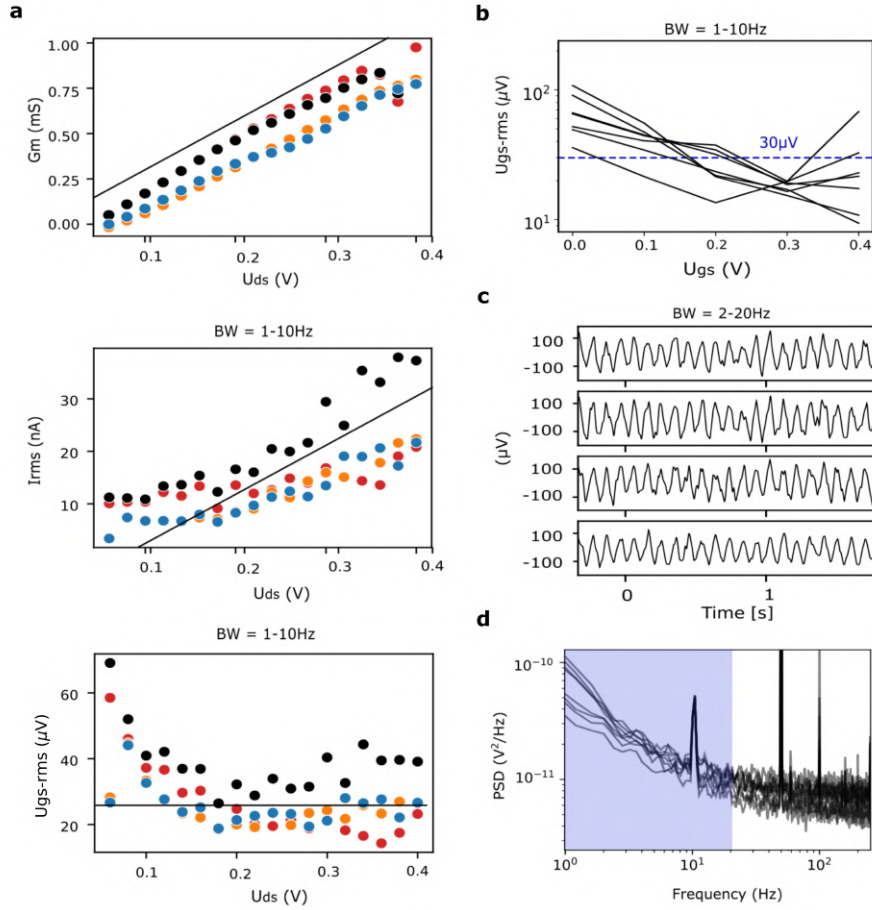
Figure 4.5: a, Dependence of G_m, I_{rms} and U_{gs-rms} on U_{ds}. **b,** U_{gs-rms} vs U_{gs} in the $1-10\,Hz$ band, demonstrating the high sensitivity of the ASIC-GFET system in the low frequency range. **c,** Signal recorded with the ASIC-GFET system while a applying a $100\,V-peak$ pure tone at $10\,Hz$. **d,** PSD of the output current measured during the application of a pure tone, $10\,\mu V_{pk}$, $10\,Hz$ signal on the gate. PSD calculated from the signal recorded over $150\,s$. The frequency band where the $1/f$ noise of the g-SGFETs dominates is marked in blue.

4.2 Frequency-Division Multiplexing of graphene transistors

FDM represents a novel strategy for the multiplexing of neural signals, which allows mapping the brain activity at high frequencies without downsampling the acquired data. In the 3rd main article of this thesis (Appendix A), the performance of graphene sensors in FDM operation was characterized for the first time and benchmarked against the standard acquisition with g-SGFETs in static mode. In order to demonstrate the applicability of the sensor arrays *in-vivo*, a recording system based on a high speed acquisition system was developed. In this work, the scalability of FDM was also addressed by studying the effects of non-linearities in the output characteristics, the drain-source frequency response of g-SGFETs at high frequencies, the effect of crosstalk and the effect of heat dissipation in large-scale arrays.

4.2.1 Frequency-division multiplexing principle

The electrical response of graphene active sensors can be modelled, as described in section 2.2.2, by a stationary response term proportional to the static conductance of the transistor G_{ds-DC}, and by a dynamic term depending on the signal applied at the gate and the transconductance ($U_{sig}G_m$). In the typical operation mode discussed so far (i.e. DC mode), the drain-source bias is constant; thus the only time dependence in the dynamic response of the g-SGFETs is given by U_{sig}. However, in FDM (also referred to as amplitude modulation - AM mode), the drain-source bias is a pure tone carrier signal ($U_{carrier}(t)$). Therefore, the dynamic response of the g-SGFET is expressed as the product $U_{carrier}(t)(g_m U_{sig}(t) + G_{ds-DC})$ (Fig. 4.6a).

The multiplication of $U_{carrier}$ and U_{sig} produces the folding of their frequencies. In the frequency domain this folding means a peak at the carrier frequency (f_c) (with an amplitude proportional to G_{ds-DC}), and two side bands at $f_c - f_{sig}$ and $f_c + f_{sig}$ containing the neural information (with an amplitude proportional to $U_{sig}G_m$) (Fig. 4.6b-left). This mixed signal can then be demodulated in a lock-in amplifier (Fig. 4.6b-middle), producing the folding of the side bands back to the baseband frequency (Fig. 4.6b-right), with the DC-offset corresponding to the stationary component of I_{ds}. Applying different carrier frequencies on each column of the array, it is possible to demodulate each carrier signal independently at the row level and to recover the neural signals detected in each of the sensors (see Fig. 4.6c).
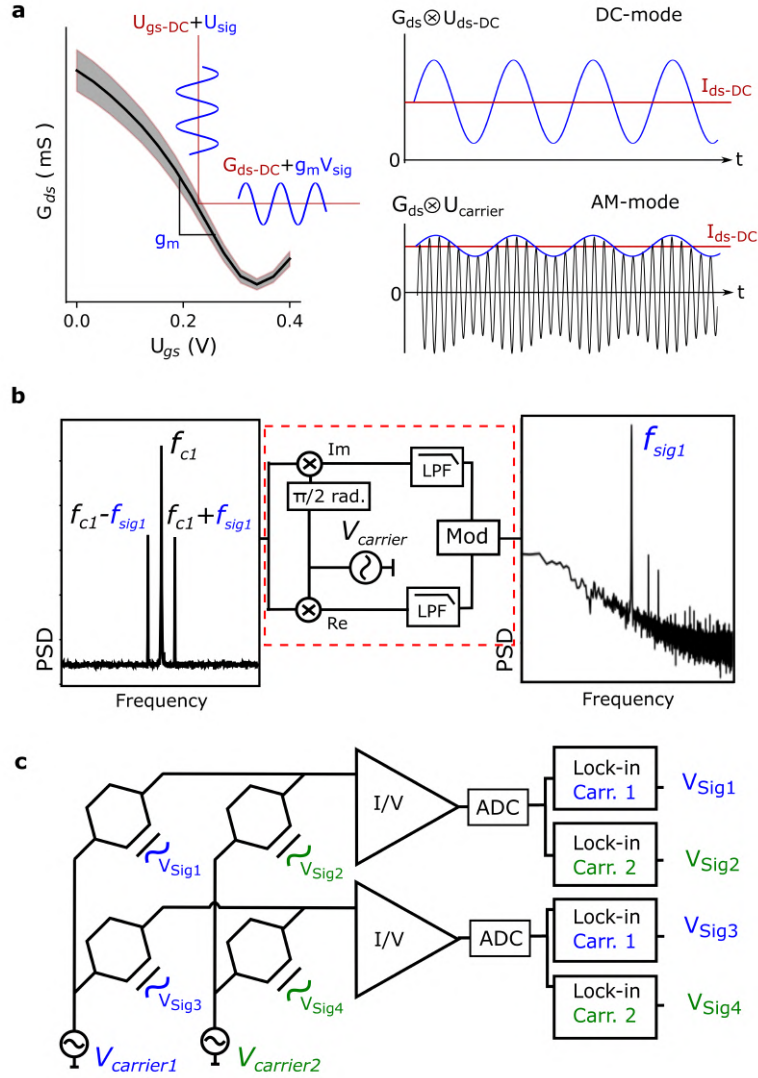
Figure 4.6: **a,** Typical $G_{ds} - U_{gs}$ curve of g-SGFETs. The definition of normalized transconductance (g_m) as the slope of the $G_{ds} - U_{gs}$ curve, is indicated in the graph. The g-SGFETs acts as a multiplier of the drain-to-source voltage and the signal at the gate. The resulting I_{ds} in the DC and AM modes is illustrated. **b,** The signal folded by the carrier is shown in the frequency domain (left). Demodulation scheme (middle): the multiplication of the modulated signal by an oscillator at the carrier frequency of interest and the $\pi/2$ radians phase shifted oscillator allows to recover the module of the signal in the baseband (right). **c,** Basic schematic of the addressable g-SGFET array, which allows modulating the signals at the gate of different g-SGFETs with different carrier frequencies. The mixed signals, containing multiple carrier frequencies, are demodulated after current-to-voltage conversion and digitization. Figure adapted with permission from Garcia-Cortadella and Schäfer et. al.[245].

4.2.2 *In-vitro* characterization of FDM graphene neural probes

In order to validate the performance of g-SGFETs in AM mode, multiplexed arrays of up to 4x8 sensors were fabricated (see the 3rd main article of this compendium). For the characterization of the FDM sensor arrays and their operation *in-vivo*, a recording system based on a PXIe for high sampling speed and a custom built front-end amplifier for current-voltage conversion was developed (see the supporting information of the 3rd main article of this thesis). The sensitivity of the graphene sensor arrays in the AM mode was then characterized and compared with the sensitivity in DC mode. The transconductance of the transistors can be characterized from the demodulated stationary $I_{ds} - U_{gs}$ curves or by applying signals of various frequencies at the gate and measuring the demodulated dynamic response. Fig. 4.7a presents the frequency dependent transfer function obtained following the latter strategy. The obtained transfer function is compared with the response in DC mode. The effective transconductance increase at high frequencies, previously described in section 2.2.2, which corresponds to displacement currents between gate and source, is not present in the AM mode. The reason is that capacitive currents are not concequence of the field-effect modulation of the graphene conductance, and therefore are not modulated by the carrier signal. Similarly, extrinsic sources of LFN from the amplifiers are not modulated and therefore do not contribute to signal degradation. Following the characterization of the transfer function in AM mode, the I_{ds-rms} noise was determined in order to compare the U_{gs-rms} in DC and AM mode. The results shown in Fig. 4.7b demonstrate that the sensitivity of g-SGFETs in both operation modes are approximately equivalent, presenting only a slight difference in its U_{gs} dependence. This difference presumably arises from the changes in the effective gating in both modes (see supporting information of the 3rd main article of this thesis). In turn, the effective gating is also responsible for non-linearities in the output characteristics of g-SGFETs, introduced by the dependence of G_{ds} on U_{ds}. These non-linearities lead to a certain harmonic distortion of the carrier signals that introduces high order harmonics at frequencies multiple of f_c (Fig. 4.7c). In this way, harmonic distortion will constrain the selection of carrier frequencies: high order harmonics must not lie within the frequency band of operation. Thereby, the frequency of all carriers must be below the 2nd order harmonic of the carrier with the lowest frequency (Fig. 4.7c). In addition, the Nyquist frequency ($F_s/2$) must be above the 2nd order harmonic of the highest frequency carrier to prevent folding of the 3rd harmonic into the band of operation by aliasing. Finally, another aspect that might constrain the selection of carrier frequencies is the drain-source frequency response of g-SGFETs. The graphene-electrolyte interface can be modelled as a transmission line circuit consisting of distributed capacitive and resistive elements[218], which leads to a parallel current path through the electrolyte at high frequencies. However, due to the relatively high mobility of g-SGFETs compared to other active sensors[173], the cut-off frequency is expected at relatively high frequencies. Fig. 4.7d confirms that the current leakage through the electrolyte is only significant for frequencies above $\sim 500\,kHz$ for channel lengths above $100\,\mu m$.
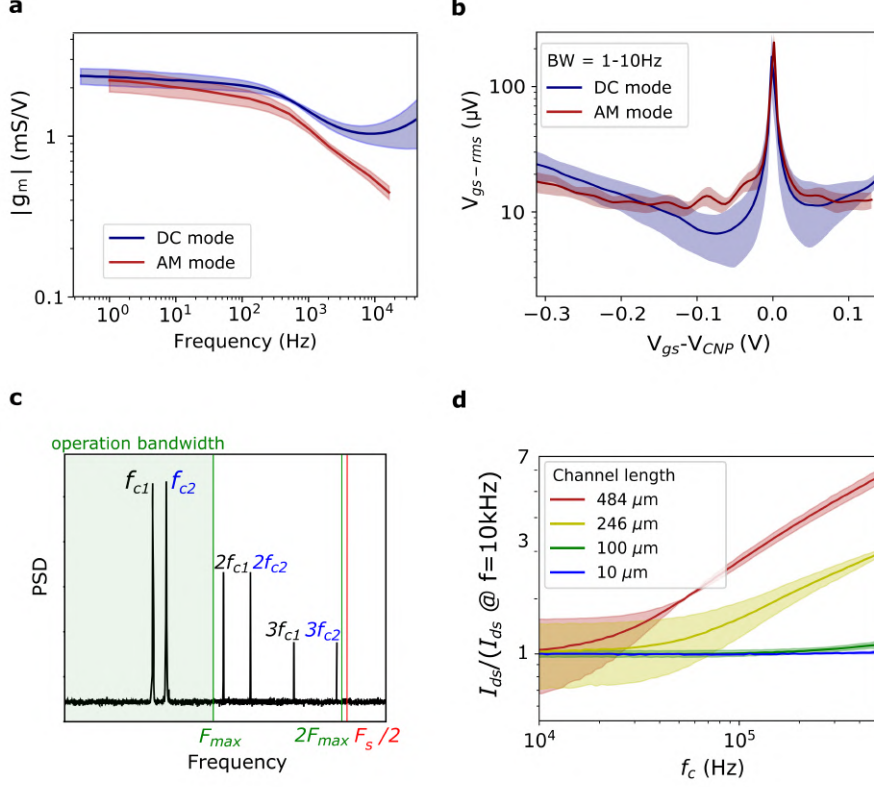
Figure 4.7: a, Magnitude of g_m over frequency of the signal applied at the gate is shown for the two modes. The response was measured in a 2x2 g-SGFET array. **b,** U_{gs-rms} for an integration bandwidth of $1-10\,Hz$ measured in the AM and DC modes; measurements performed with a 3x3 g-SGFET array. **c,** Two carrier signals and their 2nd and 3rd order harmonics are represented in the frequency domain. The frequency which defines the bandwidth of operation (F_{max}) and the position of the Nyquist frequency ($F_s/2$) with respect to F_{max} are indicated by the vertical lines. **d,** The I_{ds} normalized by its value at $10\,kHz$ is shown for different channel lengths. The filled area represents the standard deviation ($n = 3$). Figure adapted with permission from Garcia-Cortadella and Schaefer et. al.[245].

4.2.3 Scalability of FDM graphene neural probes

Considering the ultimate goal of enabling the upscaling of graphene sensor arrays, investigating the scalability of FDM graphene neural probes is critical. The constrains in the carrier frequency selection described in the previous section are limiting factors in the scalability of this technique (see the 3rd main article of this compendium). However, more constraining aspects might be crosstalk or the requirements for high-speed data acquisition system.

In FDM, no switching among sensors is required. Although this feature bears a clear advantage for ease of fabrication of the neural probes, it prevents from doing on-

94

site switching of the sensors and can therefore lead to an increased susceptibility to crosstalk. In order to understand and mitigate crosstalk in FDM g-SGFET arrays, we developed a method to selectively bias individual g-SGFETs on the array and apply signals locally (see Fig. 4.8a and supporting information of the 3rd main article of this thesis). This method, based on ink-jet printing of solid polyelectrolyte gates on individual g-SGFETs, allowed determining the crosstalk level under different bias conditions. Fig. 4.8b shows the signal amplitude and the crosstalk peaks measured in a 3x3 g-SGFET array using this approach. These results confirm that g-SGFETs in the same column or in the same row present an equivalent crosstalk, while the rest of sensors in the array present a much higher signal-to-crosstalk ratio. Besides, the gate bias dependence of the crosstalk level is proportional to $R_s/R_{g-SGFET}$, as theoretically predicted (see supporting information of the 3rd main article of this thesis), where R_s is the resistance in series with the g-SGEFTs. Given that both the resistance in series with all g-SGFETs and the impedance of the g-SGFETs can be measured experimentally, it is possible to mathematically correct the crosstalk among sensors. This correction requires to solve the system of linear equations schematized in Fig. 4.8c. Knowing the measured signals represented by $M(t)$ and the inverse of the k matrix, which represents the coupling factors among g-SGFET, it is possible to determine the matrix S corresponding to the unperturbed signals at the gate (see supporting information of the 3rd main article of this thesis). Fig. 4.8b,c shows the resulting crosstalk level after applying this correction procedure: it leads to a signal-to-crosstalk ratio of $52\,dB$ approaching the values achieved using on-site switches [73].

One important advantage of FDM compared to TDM is that it acquires the signals in quasi-continuous time, without having to share the sampling speed among active columns. Therefore, there are not problems derived from aliasing of high frequency noise. Nevertheless, continuous biasing of all columns leads to the superposition of the current from all columns of the array. This fact limits the maximum amplitude of each carrier and therefore may limit the transduced signal amplitude. In order to optimize the amplitude of the carriers, the phase of the carriers must be carefully selected to prevent constructive periods with high amplitudes (Fig. 4.8d). Using this technique, a high sensitivity, dominated by the intrinsic noise of the g-SGFETs, could be demonstrated up to $100\,Hz$ using 4 carriers and a modest 12-bits ADC (Fig. 4.8e). Finally, the continuous biasing of all g-SGFETs might lead to a relatively high power consumption and therefore a high heat dissipation into the brain tissue. In order to estimate the temperature increase produced by a 1024-channel system, a FEM simulation was implemented. Assuming a thermal conductivity of the human brain cortex of $0.5\,W/m.K$ [246], considering that the temperature of the brain is unperturbed $5\,cm$ away from the array and neglecting the effects of convection or heat dissipation by blood vessels, an upper bound for the temperature increase can be found. For a single g-SGFET, the temperature increase was found to be $0.005\,°C$ while for 1024 g-SGFET arrays, the maximum temperature increase in the center of the array was $0.013\,°C$ (see supporting information of the 3rd main article of this

thesis). These values are much lower than the typical temperature increase allowed in optogenetic studies, which is in the order of $2 - 0.2\,^{\circ}C$[247].

4.2.4 *In-vivo* characterization of FDM graphene neural probes

Having determined the sensitivity of FDM graphene neural probes *in-vitro*, the *in-vivo* performance of the neural probes was evaluated by recording electrical activity from the cortex of an anaesthetized Long Evans rat using 4x8 FDM graphene neural probes. With this experiment, the performance of FDM neural probes in an operational environment could be evaluated, including the implementation of software for real time signal demodulation and visualization, the protocol for acquisition of signals with a maximum sensitivity, the wide frequency-band sensitivity of the sensors and the effect of crosstalk on the mapping of epi-cortical brain dynamics.

In order to maximize the sensitivity of the neural probes, the transfer curves were first obtained *in-vivo* for low carrier amplitudes. After selecting the optimal gate bias, typically close to the CNP, the carrier amplitude was swept in order to determine the linear-response range (not saturating the ADC), allowing to maximize the carrier amplitudes (see the 3rd main article of this thesis for more details). Following this procedure, the sensitivity of the graphene transistors to high-frequency LFP activity was evaluated by measuring visually evoked potentials. The graphene sensors, directly placed on the primary visual cortex V1, detected a sharp response with a short delay from the trigger (Fig. 4.9a,b), while sensors placed further away from V1 presented a lower response and extended delay (Fig. 4.9b), which is consistent with previous literature[171]. Fig. 4.9a presents the signal before and after crosstalk correction, which do not differ significantly, indicating that 4x8 probes present a low crosstalk among sensors (see the supporting information of the 3rd main article of this thesis). Having characterized the sensitivity of the FDM graphene neural probes for high frequency LFP signals, the sensitivity of the system in the infra-slow frequency range was also investigated. For this purpose, a CSD was triggered by injecting KCl into the brain cortex following the procedure described previously[222]. Fig. 4.9c shows the signal from channel in position (4,5) filtered in the $1 - 50\,Hz$ frequency band (blue) together with the wide frequency band signal in the $0.001 - 50\,Hz$ band. It is possible to clearly observe the typical infra-slow depolarization associated with CSD events and the associated suppression of spontaneous LFP activity during the depolarization wave. Fig. 4.9d illustrates the position of KCl injection and the g-SGFET array on the rat cortex. The triggered CSD propagated from anterior to posterior areas covered by the sensor array are precisely captured in Fig. 4.9e, demonstrating the capabilities of FDM graphene neural probes to study topography of wide-band oscillatory dynamics in the brain.
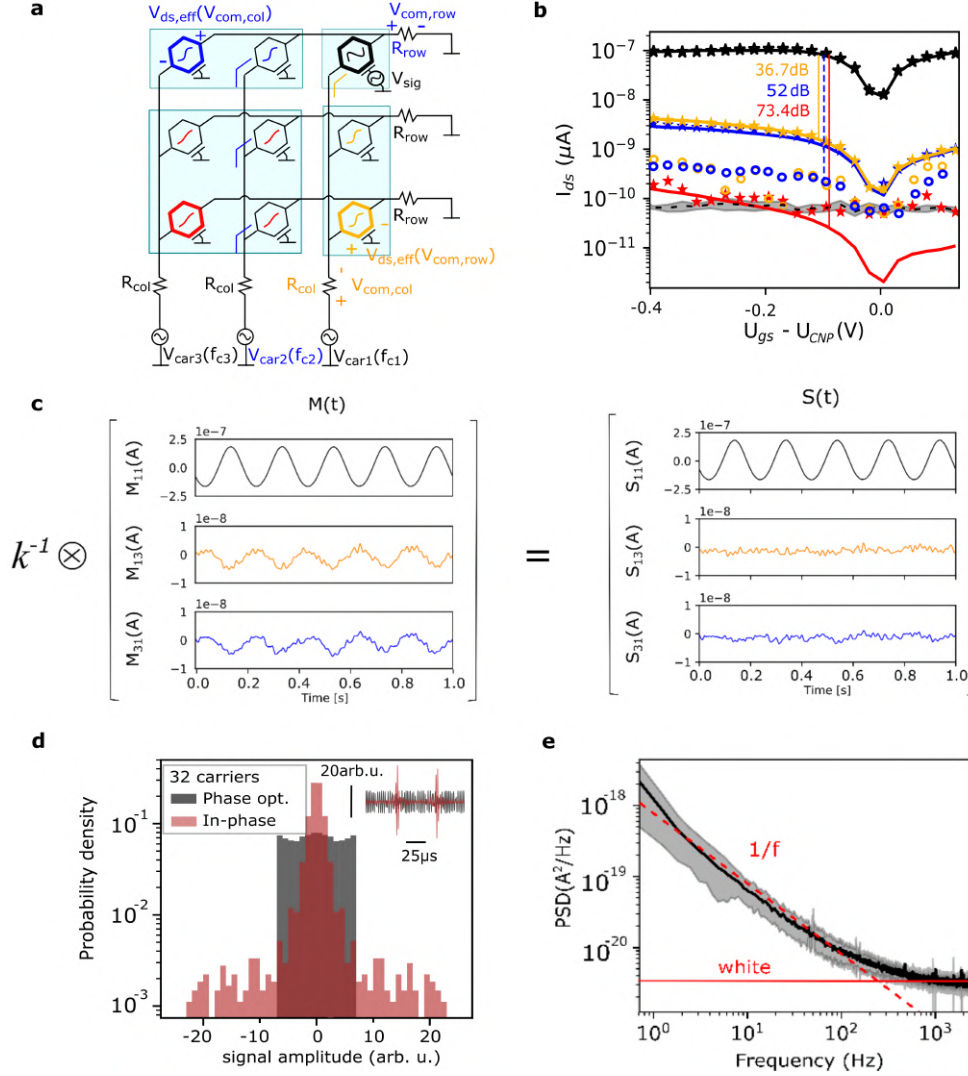
Figure 4.8: a, Equivalent circuit of a 3×3 g-SGFET array. The metal track resistance of the columns and rows is modeled by R_{col} and R_{row} respectively. Each column is biased with a different carrier (U_{car1}, U_{car2}, and U_{car3}). Common voltage oscillations ($U_{com,col}$ and $U_{com,row}$) produce changes in $U_{ds,eff}$. The light blue area indicates the position of four polyelectrolyte gates printed on a 3×3 array. **b,** Response to a $5\,Hz$ signal measured in different g-SGFETs on a 3x3 array for different U_{gs} values. The color of the symbols and lines indicate the position of the corresponding g-SGFET in the 3x3 array shown in part a. The solid lines indicate the fitting by the analytical model. The noise (dashed black line) was measured at $7\,Hz$. The empty blue and orange circles indicate the crosstalk level after correction. The signal-to-crosstalk values (in dB) corresponding to uncorrected, corrected and second order crosstalk are marked by the vertical lines. **c,** Signal measured in different g-SGFETs before (left) and after (right) crosstalk correction. The black line corresponds to the g-SGFET where the signal was applied using printed polyelectrolyte gates. The orange and blue line correspond to g-SGFETs in the same column and row, respectively. **d,** Histogram of 32 superposed carriers with phase optimization to minimize the peak-to-peak amplitude (black), and with all carriers in phase (red). The inset shows a fragment of the resulting signals. **e,** Average power spectral density measured in a 4x8 g-SGFET array. The $1/f$ noise of the g-SGFETs and the white noise from the DAQ are indicated. Figure adapted with permission from Garcia-Cortadella and Schaefer et. al.[245].
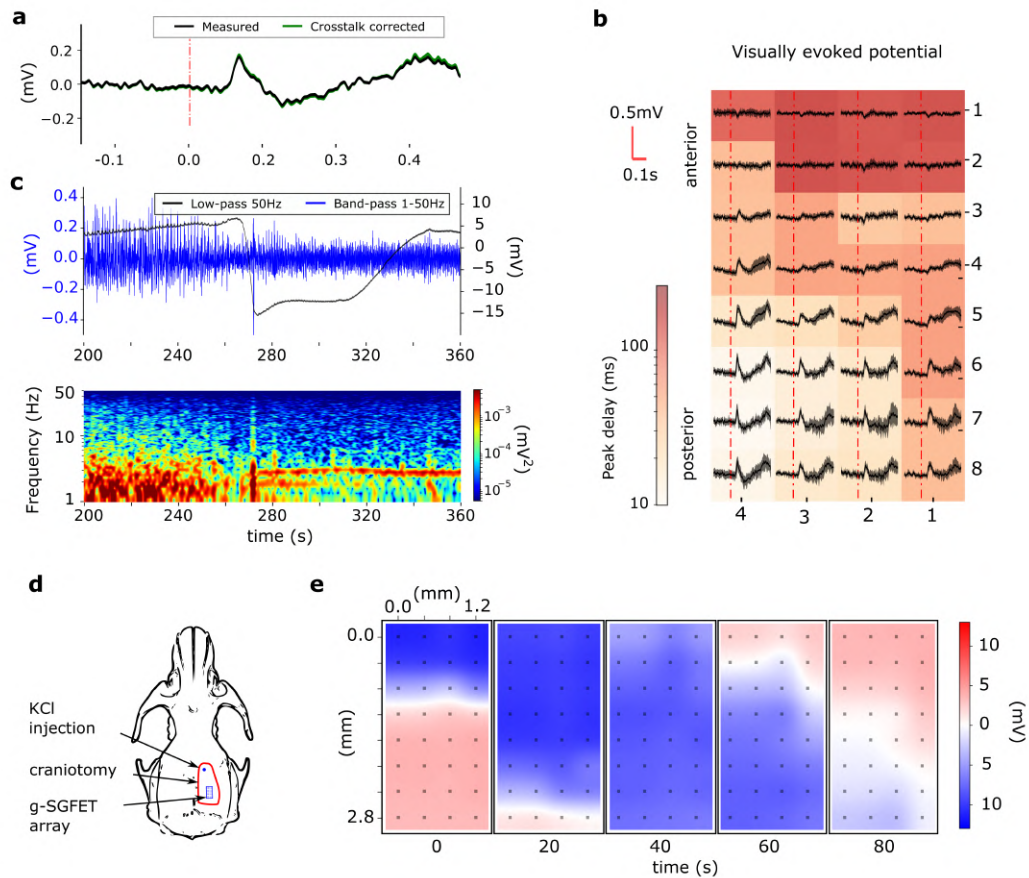
Figure 4.9: a, Visually-evoked potential averaged over 10 consecutive events shown for a g-SGFET placed on the lower-left corner of the array before (black) and after (green) crosstalk correction. **b,** Visually-evoked potential averaged over 10 consecutive events for all g-SGFETs on the 4x8 array. The colour map represents the delay between stimulus and the peak of the response. **c,** CSD event recorded in a single g-SGFET. The top graph shows the activity in the 1-50Hz band (blue, left axis) and the wide-band activity (0.001-50Hz) (black, right axis). The corresponding spectrogram in the 1-50Hz band is shown below. **d,** Illustration of a rat skull indicating the position of the craniotomy, the g-SGFET array and the place of KCl injection to trigger a CSD event. **e,** The colour maps indicate the signal amplitude in each of the g-SGFETs on the array at different times during the CSD propagation. Figure adapted with permission from Garcia-Cortadella and Schaefer et. al.[245].

4.3 Chapter outlook: Upscaling of multiplexed g-SGFET arrays

This chapter has discussed the use of g-SGFETs as a building block of multiplexed sensor arrays for neural sensing. Frequency-division and time-division multiplexing using external switching arrays enable the operation of large-scale sensor arrays with a reduced complexity of the connectors while preventing the use of on-site switching devices. Investigation of the frequency response of g-SGFET arrays and crosstalk in multiplexed arrays has revealed that neural probes based on graphene transistors could be upscaled up to 32x32 sensing sites (see the 3rd main article and the 3rd complementary article of this thesis). For the operation of such large-scale probes, the use of a dedicated ASIC is required in order to optimize the operation of the multiplexed arrays and miniaturize the dimensions of the recording system. Preliminary results on TDM have demonstrated the high performance of an ASIC to record neural signals in the LFP range, from ISA to the gamma band. Nevertheless, detection of neural activity in higher frequency bands remains challenging. The main reason is that operation of the multiplexed probes in TDM implies downsampling of the acquired data, producing aliasing of high-frequency noise into the frequency band of operation. In order to mitigate this problem, the ASIC developed for TDM incorporates offset subtraction to enable a higher g-SGFET transconductance and implements a correlated double-sample to lower the floor noise of the transimpedance amplifier. In order to circumvent the intrinsic limitations of TDM, FDM could be used, allowing to prevent aliasing of high-frequency noise by acquiring the signals from all sensors simultaneously. As a downside, the continuous acquisition of all sensors simultaneously implies the superposition of all carrier signals on each row, leading to an output current with a large dynamic range. Digitalization of signals with such a large dynamic range with high resolution is challenging for the ADC. Therefore, quantization noise is the main expected source of noise at high frequencies for FDM sensor arrays. In order to mitigate this problem, it is critical to implement the phase optimization of all carrier signals, as presented in the 3rd main article of this thesis. In addition, an advanced system for the operation of sensor arrays in FDM should include carrier cancelation techniques to subtract part of the output current.

Having demonstrated the capabilities of TDM and FDM and their potential for the operation of large-scale neural probes, the focus was placed on upscaling the g-SGFET arrays to 512 sensors for pre-clinical research in rats. Fig. 4.10a,b shows the design of the 32x16 neural probes. The tip of the probe contains two active areas comprised of 16x16 g-SGFET arrays each. This neural probe covers a large fraction of the cortical surface of the rat brain bilaterally (Fig. 4.10a,b) with a separation among g-SGFETs of $282\,\mu m$ and sensors size of $100\,\mu m$ x $100\,\mu m$. The neural probe also includes holes in the PI structure with a pitch of $400\,\mu m$, which improves the contact of the sensors with the brain surface by enabling the flow of

fluids during implantation. Furthermore, the holes are sufficiently large to enable the insertion of intra-cortical probes, which are crucial to study the depth profile in particularly interesting spots of the epi-cortical grid. In between the two active areas of the neural probe, there is a narrow path for the tracks corresponding to the rows of the array, which covers the area on top of the longitudinal fissure of the brain.

In order to characterize the devices, the discrete electronics system presented in the 3rd complementary article was modified to include 32 acquisition channels and to selectively switch among up to 32 columns. The distribution of the 512 channels into 32 rows and 16 columns was chosen in order to take advantage of the 32 readout circuits. This layout increases the speed of the sequential characterization of multiple columns and is expected to be optimum for the operation of multiplexed arrays using both FDM as well as TDM. The electrical characterization of the devices revealed a high homogeneity and yield. The g_m of the devices is represented in Fig. 4.10c, which presents only 6 outliers ($\sim 1\%$) that have been excluded from the graph. In Fig. 4.10d the position of these outliers on the array and the distribution of g_m at a particular bias point ($0.25\,V$) is shown for all 512 g-SGFETs. Note that with this layout, the 512-channel probes have a simple connector with 32+16 contacts, which does not represent anymore the bottleneck for the scalability of the sensor arrays.

The demonstration of g-SGFET arrays multiplexed in TDM and FDM, together with the fabrication of large-scale sensor arrays with a high yield and homogeneity represent an important step towards the implementation of high-count sensor arrays for high bandwidth graphene neural interfaces. In the following stages of research, the large-scale graphene sensor arrays, operated with the ASIC presented in this chapter could provide a unique tool for the investigation of brain activity in freely moving animals and the development of advanced brain-computer interfaces.

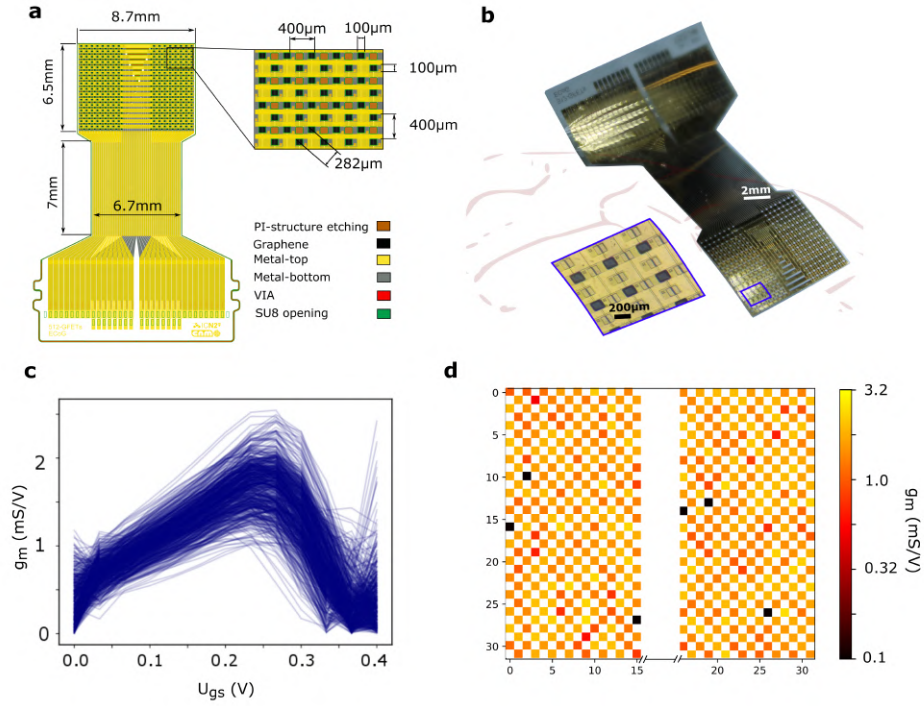**Figure 4.10: a**, Layout of a 512-channel array. The inset shows the position of sensors and holes in the structure of the probe. **b,** Photograph of the neural probe. The inset shows an optical micrograph of the active area of the neural probe. **c,** g_m vs U_{gs} for 506 out of 512 g-SGFETs (6 outliers are not shown). **d,** Color-map representation of g_m at a particular bias point $U_{gs} = 0.25\,V$.

Chapter 5

Future research and conclusions

This PhD thesis has presented graphene active sensors as a biocompatible and stable building block for high bandwidth neural interfaces. The improvement in communication bandwidth of these devices is achieved by demonstrating their sensitivity in a wide frequency band and by developing multiplexing strategies that enable a higher sensor-count. From these results, there are two main research fields in which graphene sensor arrays can have a strong impact. First, high-count epi-cortical sensor arrays are currently not commercially available and have not been extensively used for research in animal models. Therefore, μ-ECoG arrays with hundreds of sensing sites based on graphene can provide new insights into large-scale brain dynamics. In this direction, it is particularly interesting to investigate the correlation of ISA with higher frequency bands. Secondly, graphene active sensors have shown a promising biocompatibility and long-term stability *in-vivo* that makes them very attractive for chronic neuroprosthesis. Optimization of large-scale sensor arrays to comply with regulatory guidelines for human applications implies improvement of the passivation layers and use of novel leakage limiting strategies. In this chapter, these two future stages of research are described in greater detail.

5.1 Wide frequency band, large-scale brain activity in freely moving animals

One of the objectives of this thesis has been to develop graphene active sensor arrays to overcome current limitations in basic electrophysiology. For this purpose, the focus has been centered on increasing the spatio-temporal resolution of large-area sensor arrays and providing access to a wide frequency band, including ISA. Having developed reliable recording systems for proof-of-concept electrophysiology, it has been possible to demonstrate the performance of graphene active sensors to resolve the topography of wide frequency band LFP, from ISA to high-gamma. In

this section, the current understanding on the physiology of infra-slow brain activity, in terms of its correlation with higher frequency rhythms and its biophysical origin, are first discussed. Secondly, the preliminary observations reported in this thesis on large-scale and wide frequency band brain activity are summarized with the aim of discussing promising future experiments.

In the study of neural dynamics across large-scale networks, fMRI has become a standard in the last few decades[121]. The widespread use of fMRI stems from its non invasiveness and its high spatial resolution in large areas, that allowed to identify networks of increased functional connectivity and their activation under particular brain states, stimuli or tasks[116, 121, 248]. However, fMRI presents certain fundamental and practical limitations for the study of brain dynamics. In the first place, the BOLD signals are infra-slow in nature and do not represent a direct measure of neural activity, making it more difficult to interpret the results[121, 249, 250]. This feature is of particular interest for our discussion, given that infra-slow electrical activity detected by graphene sensors might allow to connect fMRI results with their electrophysiological correlates. Secondly, fMRI is limited to head-fixed conditions; therefore, ISA detected with graphene active sensors might provide access to currently non-accessible infra-slow dynamics in freely moving animals.

BOLD activity has a neurovascular origin[250, 251], which in turn is linked to the electrical activity of neurons[248, 252] via their consumption of glucose, which causes the regulation of vasodilation[251]. This coupling leads to a certain correlation of BOLD signals with LFP and spiking activity[120, 248, 252]. However, this correlation is not direct, as evidenced from their distinct coupling in different frequency bands. The higher correlations have been observed between BOLD and gamma activity[120, 253, 254], suggesting that it originates from the metabolic consequences of postsynaptic currents[254]. On the other hand, its correlation with spiking activity or LFP in the alpha $(8 - 13\,Hz)$ and beta $(13 - 30\,Hz)$ bands has been found lower[120, 253, 254], or even negative in the delta and theta bands[255]. Similarly, previous works have demonstrated the correlation between ISA and BOLD signals[117, 119, 236, 238], which could present a common physiological cause, although it has been reported that their correlation presents a certain time dependence[238]. Recent works on the biophysical origin of ISA have found supporting evidence, through simulation, that ISA could originate on the dynamics of ion concentrations that are regulated by Na^+ and K^+ pumps, glial K^+ buffering, as well as excitatory and inhibitory synaptic currents[256]. In turn, re-establishing ion gradients through active pumping is expected to cause fluctuations in the BOLD signal[256]. This mechanism could explain the correlation between ISA and the BOLD signal; however, further studies on the effects of ion concentrations on the generation of ISA and its neurovascular coupling should be carried out to elucidate their correlation. In order to expand our understanding on the physiological role of ISA, its correlation with higher frequency activity should be resolved with high spatio-temporal resolution in freely behaving animals and the underlying current sources resolved with high-density depth probes.

The chapter 3 of this thesis presents preliminary evidence showing distinct patterns of ISA across the cortex of the rat brain. These results include brain state-dependent ISA patterns that modulate higher frequency bands, which are shown for the first time with high spatial resolution. In particular, a strong modulation of theta power by ISA-phase was observed during REM sleep in a rat model, which presented a clear topography, consistent with the location of underlying theta current generators in the hippocampus. These results suggest the presence of global ISA dynamics that co-modulate limbic and cortical circuits. Based on these preliminary results, it would be promising to analyse the modulation of theta power by ISA-phase during awake theta states. Its modulation might explain an important fraction of variability in theta power observed during exploratory behaviour. Similarly, spindle band activity was also modulated by ISA phase during slow-wave sleep, but with a much weaker coupling, which might reflect the activity from more strongly modulated thalamo-cortical subcircuits. Additionally, it was also possible to observe modulation of gamma activity with the ISA phase, which in turn adds further support to the wide frequency band sensitivity of our graphene-based recording system. At present, topography of gamma modulation by ISA-phase has not been explored in this thesis or in any previous works. However, due to the local nature of gamma generation on superficial cortical layers[257], and the modulation of gamma activity by ISA reported in this thesis, it is reasonable to expect gamma activity clusters to be modulated by ISA. Such modulations might be very diverse depending on the gamma-oscillator frequency, cortical area and the ongoing brain state. Additionally, it would be also promising to explore if gamma generators modulated by hippocampal theta (measured via volume conduction) are also modulated by ISA under REM sleep and awake theta states. Finally, phase locking of high frequency ($> 0.5\,Hz$) oscillations to different phases of ISA, or a spatial structure in the ISA-phase, could reflect coordinated activation of distinct cortical areas in an infra-slow timescale[100, 254].

In future stages of research, it would be particularly useful to investigate the topography of ISA on the cortical surface in a larger cohort of rodents under freely moving conditions and with an increased spatial resolution. For these experiments, the 512-channel epi-cortical sensor arrays presented in this thesis could be used for a large bi-lateral brain coverage (Fig. 4.10). Fig. 5.1a,b shows a preliminary experiment done by collaborators Nathan Schäfer and Gerrit Schwesig in which a 256-channel array was implanted on the rat cortex with a large bilateral coverage. In this case, acquisition of the neural activity was carried out using the discrete electronics system presented in this thesis. Therefore, recordings were susceptible to aliasing of high-frequency noise and a rather thick bundle of wires was required to transmit the analog signals to the front-end electronics. Nevertheless, results are promising, showing LFP trajectories with high sensitivity and spatial resolution (Fig. 5.1a). Integration of the ASIC characterized in this thesis, which operates in TDM with improved noise characteristics, in a compact headstage would be highly advantageous to reduce the constrains in the movement of the animals. Fig. 5.1b,c show

the packaged ASIC on the chip carrier PCB and a second layer of the headstage containing the FPGA implementing the communication between the ASIC and a general-purpose computer. This system would allow to replicate preliminary results with even higher sensor counts and improved wide frequency band sensitivity.
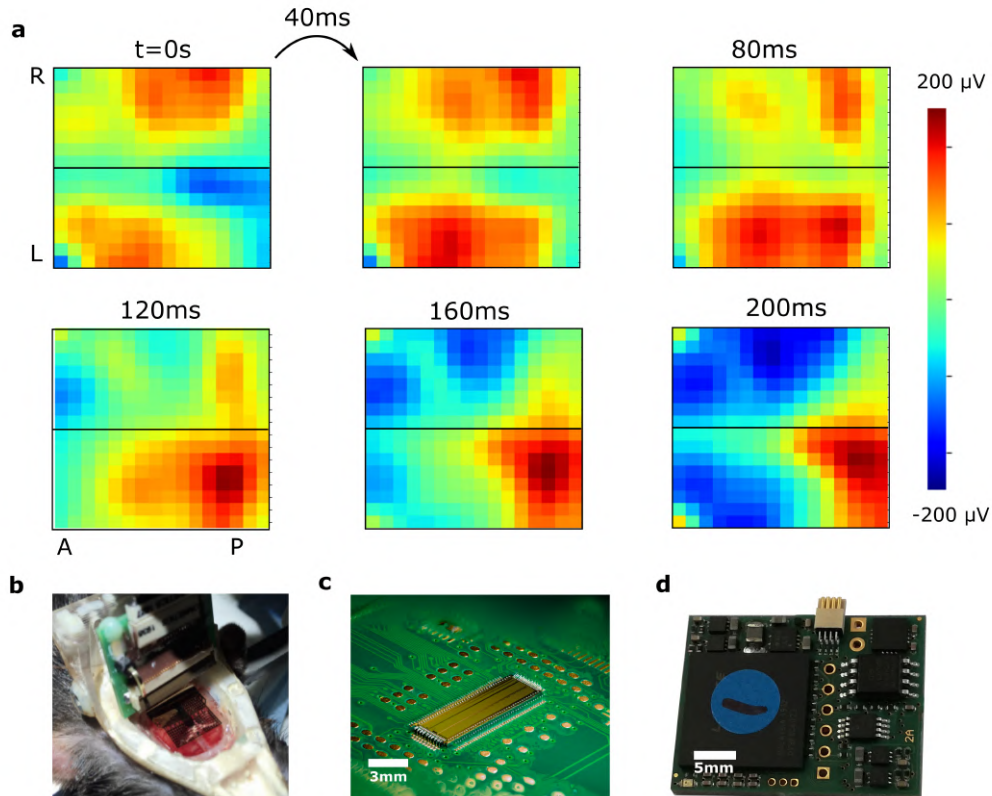

Figure 5.1: a,. Trajectories of LFP in the $4 - 11\,Hz$ band detected from the surface of a freely moving rat using a 256 g-SGFET array covering a large fraction of cortical surface on both hemispheres (see panel b). Spatial Gaussian filtering of the data has been applied with a standard deviation of 1 pixel using scipy python package. Anterior (A)/posterior (P) axis and the right (R)/left(L) hemispheres are labelled next to the spatial maps. **b,** Photograph of a 256 g-SGFET epi-cortical graphene neural probe covering both hemispheres of the rat cortex. Picture taken in an experiment by Gerrit Schwesig and Nathan Schäfer. **c,** Packaged ASIC on the xip carrier PCB by the group of integrated circuits and systems (ICAS) at the National Microelectronics Center of Barcelona (CNM-IMB). **d,** The headstage layer containing the field programmable gate array (FPGA) to communicate the digital output of the ASIC to a general purpose computer. Headstage designed by Multichannel Systems MCS GmbH.

In order to investigate the biophysical origin of ISA, it would be also interesting to detect SUA and wide frequency band LFP across cortical laminae and in deeper brain structures. For this purpose, the same methodology stablished for epi-cortical

recordings could be followed, but now implanting intra-cortical graphene probes. Recently, efforts have dedicated to develop high-density multishank probes for resolving wide frequency band activity with high spatial resolution. Alternatively, insertion of single-shank neural probes on particularly interesting spots identified from surface mapping could also be very informative. Based on these recordings, it should be possible to determine the laminar structure of ISA and its physiological origin. For the determination of ISA generators, independent component analysis (ICA) of current-source density (CSD) maps should be performed[258]. In turn, detection of coherent spiking activity in distinct cortical and hippocampal layers could allow to determine the relationship between LFP modulation by ISA and the functional connectivity among distinct neuronal circuits.

The study of the relation between infra-slow and higher frequency LFP bands using electrophysiological measurements, with high spatio-temporal resolution, in freely behaving animals is completely unexplored. Therefore, its characterization has a great potential to provide novel insights into the generation and physiologic role of ISA across brain states, including active behaviour. A detailed determination of their relationship could have a strong impact on the understanding of the role of ISA on the coordination of large-scale brain dynamics, with important implications on the study of f-MRI brain mapping in humans and for fundamental brain electrophysiology. This research could prompt the study of ISA across multiple experimental conditions, such as distinct behavioural paradigms or using pathological animal models, which can provide a better understanding of pathological states and identification of novel biomarkers.

5.2 Clinical translation of high bandwidth graphene neural interfaces

High bandwidth graphene neural interfaces, presenting a high sensitivity in the ISA band, a high sensor-count and a high biocompatibility and stability represent a promising technology for chronic clinical applications. ISA detected with high spatial resolution represents a neural feature that could provide additional information for neural decoding in iBCIs. In this thesis, preliminary data has been shown indicating that ISA modulation of higher frequency bands is spatially structured and brain-state dependent. Modulation of higher frequency activity by ISA could imply the representation of spatially filtered high frequency activity at lower frequencies, which could be advantageous for reducing power consumption in wearable neuroprosthesis. Alternatively, ISA could also contain orthogonal components to the higher frequency LFP patterns on the brain surface, and might therefore provide additional information for neural decoding. Analysis of spatial maps of LPF signals, such as those presented in Fig. 5.1a, could be performed to extract principal components across multiple time scales leading to an increased communication bandwidth for iBCIs.

Having demonstrated the performance of g-SGFETs in multiplexed operation, their translation to safe neural implants requires the prevention of leakage currents. This is typically an important disadvantage of active sensors with respect to passive electrodes, due to active biasing and the low impedance of the amplifiers. However, following the proof-of-concept experiments in FDM, an additional advantage of operation in AM compared to the DC mode was noticed, which can solve this limitation. Due to the modulation of the g-SGFETs at high frequencies in AM mode, it is possible to place a capacitor in series with the transimpedance amplifier (C_d), which does not attenuate the high frequency carrier signal and the side bands containing the brain signals, but prevents eventual DC leakage currents (Fig. 5.2).
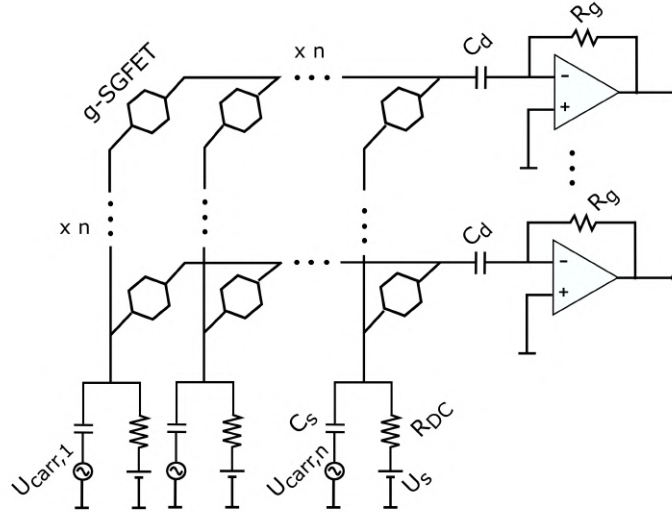

Figure 5.2: Equivalent circuit of a FDM array with decoupled DC bias. The gate to source bias is given by U_s which is followed by a high value resistor R_{DC} which limits eventual leakage currents to the brain. The carrier signals ($U_{carr,1}$ to $U_{carr,n}$) can be applied on all columns, which present C_s in series to decouple the DC component from the GFET. C_d decouple the DC component from the transimpedance amplifier. Figure adapted from patent application EP20382819[259].

Having this decoupling, it is possible to apply a DC potential at the source (U_s) in order to bias the g-SGFET at the optimal U_{gs} and add a large resistance (R_{DC}) in series to prevent DC currents (Fig. 5.2). The gate bias is then defined by the voltage divider between R_{DC} and the Faradic resistance of the graphene-electrolyte interface, which is typically above the $100\,M\Omega$[218]. In case of device failure, R_{DC} would limit the leakage current flowing from the device into the brain. Due to the high Faradic resistance of graphene, R_{DC} can take values in the order of $100\,k\Omega$, limiting leakage currents to the μA range. Finally, note the presence of C_s, which allows to decouple the DC component of the carrier signal source. This safety measure is very relevant for the translation of the graphene active sensors into

clinical use. This concept has been recently presented as a patent application[259] and collaborators within the BrainCom project have recently developed a second ASIC operating in FDM mode[260] in order to apply this technique in large-scale g-SGFET arrays.

In addition to control the leakage current in case of device failure, use of improved passivation layers is critical to ensure low leakage currents during stable operation of the devices and their long-term stability. In this thesis, the use of g-SGFET arrays passivated with SU-8 photodefinable resist has been shown in a chronic setting, demonstrating the relatively high stability of the devices. Nevertheless, it is known that SU-8 is prone to failure in aqueous environments due to permeation of water and delamination from the substrate. Failure of SU-8 passivation is likely the main cause of performance degradation observed *in-vivo*. In order to improve the stability of devices, a new fabrication process has been developed in the frame of this thesis to passivate g-SGFETs with non-photodefinable materials (see chapter 3). The proposed process allows to etch the passivation layers non-selectively by protecting the graphene channel with a thin Cu layer, which can be selectively etched after the fabrication is completed. This process has been demonstrated with the use of non-photodefinable PI, which presents a higher tensile strength than SU-8 and shows stable mechanical properties in PBS [261, 262]. Furthermore, demonstration of the use of non-photodefinable passivation materials opens the door to further improvements in the technology. It is known that polymeric passivation layers present a significant permeation to water that can lead to current leakage[13, 262] and also corrosion of the metal lines. In order to prevent such corrosion, the use of inorganic passivation layer has been proposed, which present much lower permeation to water[13]. As a downside, inorganic materials are typically more fragile, and thin films are prone to present pinholes and cracks[13]. In order to ensure a lower permeability to water and ions while preventing a high leakage current through cracks, the combination of inorganic and organic materials could be implemented. In this direction, it has been shown that certain inorganic layers can enhance the adhesion between metals and polymeric passivation layers[263]. Development of such advanced passivation technologies is expected to drastically improve the long-term stability of g-SGFETs.

The demonstration of DC-decoupled operation and improved passivation layers would be very promising towards the clinical translation of graphene neural probes. In order to test devices in a model closer to the human brain, an animal model with similar characteristics in terms of size and physiology should be used. For this purpose, new experiments in minipigs are planned within the BrainCom project. Fig. 5.3a shows the schematic of a 512-channel probe designed for implantation in the minipig. Note that the wafer scale production of graphene devices allows the fabrication of neural probes in the few-centimetres scale with large active areas. Furthermore, the implantation in a minipig requires long traces at the base of the probe in order to allow the connection through the thick skull to a headstage implanted on the scalp of the animal. The tail of the probe must be relatively narrow

in order to minimize the dimensions of the opening in a chronic setting. This feature is radically different in rat models due to their particularly strong immune system, but it must be taken into account for the translation of the technology to human use. In order to minimize the resistance of the metal tracks in such large devices, metal lines are distributed in the two levels separated by PI. Large animals, such as the minipig, represent a great model to implement ultra high-count neural interfaces covering large cortical areas with thousands of sensing sites. Fig. 5.3b shows a preliminary design of a headstage for minipigs comprising multiple ASIC layers in a stackable design (courtesy of Christoph Jschke, MCS), which could enable the recording from up to 4096 sensors simultaneously.
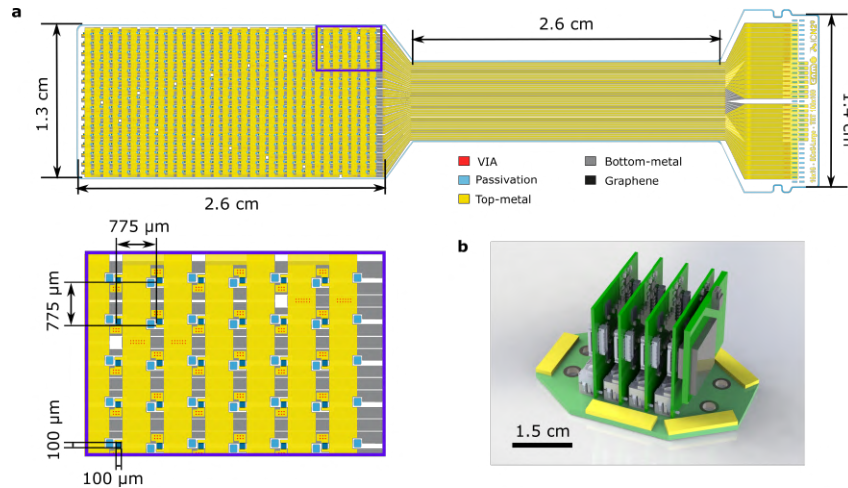

Figure 5.3: a, Schematic of a 512 g-SGFET epi-cortical graphene neural probe to cover with high resolution a large area of the cortical surface of the minipig. A relatively long and narrow tail is required. The inset shows the active area of the array in greater detail. The $100\,\mu m$ x $100\,\mu m$ g-SGFETs are separated by $755\,\mu m$. Every two vertical tracks are connected together to an horizontal metal line in the bottom metal level through VIA holes (red). **b,** Schematic of a multi ASIC headstage for implantation of multiple graphene probes simultaneously. Four ASIC carrier layers can be observed in addition to an FPGA layer for data communication. Multiple connectors to the large-scale neural probes are placed on the edges of the PCB (coloured in yellow). Headstage design by Christoph Jeschke in Multichanel Systems MCS GmbH.

5.3   Conclusions

In this doctoral thesis, high-bandwidth graphene-based neural interfaces have been developed and validated in a pre-clinical environment. In the first stage of technological development, the sensitivity of g-SGFETs at a single device level has been studied and optimized. This research has led to a deeper understanding of low-frequency noise generation in graphene transistors and the effect on non-ideal

transfer function on the distortion of transduced signals. This knowledge has led to the improvement of the sensitivity of graphene-based neural sensors by mitigating the noise generated at the contacts and improving the frequency response of the graphene-electrolyte interface at high frequencies. In a second development stage, graphene active sensor arrays have been integrated in recording systems for electrophysiology in order to demonstrate the performance of these sensor arrays at the system level in an operational environment. For this purpose, a recording system based on 64 g-SGFET probes and a wireless headstage has been developed. Using this system, the reproducibility, wide frequency band sensitivity, long-term stability and biocompatibility could be demonstrated, leading to the observation of preliminary evidence for various electrophysiological phenomena. These observations include the spatial structure of theta and spindle band activity modulation by ISA, the infra-slow correlates of HVS or the ISA power changes in the SWS to REM sleep states transition. Finally, in order to fully exploit the capabilities of active sensors, we have developed novel multiplexing strategies that allow to upscale the neural probes up to at least 512 recording channels. The large-scale probes present a high homogeneity and sensitivity. Operation of multiplexed arrays in TDM has been demonstrated using an ASIC to optimize the performance of the recording systems. Furthermore, FDM is proposed as novel multiplexing strategy to maximize the sensitivity of the recording systems at high frequencies and prevent the risk of current leakage to the brain. Together, these results demonstrate the potential of graphene active sensor arrays for the study of large-scale brain dynamics across a wide frequency band and for the implementation of chronic, high bandwidth, brain computer interfaces.

Bibliography

[1] G. Buzsáki, *The brain from the inside out.* Oxford University Press, 2019.

[2] M. Shafi, A. F. Molisch, P. J. Smith, T. Haustein, P. Zhu, P. De Silva, F. Tufvesson, A. Benjebbour, and G. Wunder, "5G: A tutorial overview of standards, trials, challenges, deployment, and practice," *IEEE Journal on Selected Areas in Communications*, vol. 35, no. 6, pp. 1201–1221, 2017.

[3] R. Matarneh, S. Maksymova, V. V. Lyashenko, and N. V. Belova, "Speech Recognition Systems: A Comparative Review," *IOSR Journal of Computer Engineering*, vol. 19, no. 5, pp. 71–79, 2017.

[4] Y. min Qian, C. Weng, X. kai Chang, S. Wang, and D. Yu, "Past review, current progress, and challenges ahead on the cocktail party problem," *Frontiers of Information Technology and Electronic Engineering*, vol. 19, no. 1, pp. 40–63, 2018.

[5] L. M. Miller, "Shaken, not stirred: Emergence of neural selectivity in a "cocktail party"," *Neuron*, vol. 77, no. 5, pp. 806–809, 2013.

[6] G. K. Anumanchipalli, J. Chartier, and E. F. Chang, "Speech synthesis from neural decoding of spoken sentences," *Nature*, vol. 568, no. 7753, pp. 493–498, 2019.

[7] S. Rainey, S. Martin, A. Christen, P. Mégevand, and E. Fourneret, "Brain Recording, Mind-Reading, and Neurotechnology: Ethical Issues from Consumer Devices to Brain-Based Speech Decoding," *Science and Engineering Ethics*, vol. 26, no. 4, pp. 2295–2311, 2020.

[8] H. Maslen and S. Rainey, "Control and Ownership of Neuroprosthetic Speech," *Philosophy and Technology*, pp. 1–21, 2020.

[9] F. Allhoff, P. Lin, J. Moor, and J. Weckert, "Ethics of human enhancement: 25 questions & answers," *Studies in Ethics, Law, and Technology*, vol. 4, no. 1, 2010.

[10] G. K. Bergey, M. J. Morrell, E. M. Mizrahi, A. Goldman, D. King-Stephens, D. Nair, S. Srinivasan, B. Jobst, R. E. Gross, D. C. Shields, G. Barkley,

V. Salanova, P. Olejniczak, A. Cole, S. S. Cash, K. Noe, R. Wharen, G. Worrell, A. M. Murro, J. Edwards, M. Duchowny, D. Spencer, M. Smith, E. Geller, R. Gwinn, C. Skidmore, S. Eisenschenk, M. Berg, C. Heck, P. Van Ness, N. Fountain, P. Rutecki, A. Massey, C. O'Donovan, D. Labar, R. B. Duckrow, L. J. Hirsch, T. Courtney, F. T. Sun, and C. G. Seale, "Long-term treatment with responsive brain stimulation in adults with refractory partial seizures," *Neurology*, vol. 84, no. 8, pp. 810–817, 2015.

[11] P. Jastrzebska-Perfect, S. Chowdhury, G. D. Spyropoulos, Z. Zhao, C. Cea, J. N. Gelinas, and D. Khodagholy, "Translational Neuroelectronics," *Advanced Functional Materials*, vol. 30, no. 29, p. 1909165, 2020.

[12] BrainCom, "BrainCom : Collaborative research project, Neurorehabilitation - BrainCom," 2020.

[13] E. Song, J. Li, S. M. Won, W. Bai, and J. A. Rogers, "Materials for flexible bioelectronic systems as chronic neural interfaces," *Nature Materials*, vol. 19, no. 6, pp. 590–603, 2020.

[14] E. Musk and Neurolink, "An integrated brain-machine interface platform with thousands of channels," *bioRxiv*, p. 703801, 2019.

[15] S. Jacobson and E. Marcus, "Higher cortical functions," in *Neuroanatomy for the neuroscientist*, pp. 375–395, Springer, 2008.

[16] A. M. Zador, "The basic unit of computation," *Nature Neuroscience*, vol. 3, no. 1167, 2000.

[17] C. Stringer, M. Pachitariu, N. Steinmetz, C. B. Reddy, M. Carandini, and K. D. Harris, "Spontaneous behaviors drive multidimensional, brainwide activity," *Science*, vol. 364, no. 6437, 2019.

[18] F. He, R. Lycke, M. Ganji, C. Xie, and L. Luan, "Ultraflexible Neural Electrodes for Long-Lasting Intracortical Recording," *iScience*, vol. 23, no. 8, 2020.

[19] G. Charles, "Neuroscience, Early history of," in *Encyclopedia of Neuroscience, Adelman, George (ed.), birkhäuser verlag ag*, pp. 843–847, 1987.

[20] C. M. Altimus, B. J. Marlin, N. E. Charalambakis, A. Colón-Rodriquez, E. J. Glover, P. Izbicki, A. Johnson, M. V. Lourenco, R. A. Makinson, J. McQuail, I. Obeso, N. Padilla-Coreano, and M. F. Wells, "The next 50 years of neuroscience," *Journal of Neuroscience*, vol. 40, no. 1, pp. 101–106, 2020.

[21] L. R. Hochberg, D. Bacher, B. Jarosiewicz, N. Y. Masse, J. D. Simeral, J. Vogel, S. Haddadin, J. Liu, S. S. Cash, P. Van Der Smagt, and J. P. Donoghue, "Reach and grasp by people with tetraplegia using a neurally controlled robotic arm," *Nature*, vol. 485, no. 7398, pp. 372–375, 2012.

[22] B. Pesaran, M. Vinck, G. T. Einevoll, A. Sirota, P. Fries, M. Siegel, W. Truccolo, C. E. Schroeder, and R. Srinivasan, "Investigating large-scale brain dy-

namics using field potential recordings: Analysis and interpretation," *Nature Neuroscience*, vol. 21, no. 7, pp. 903–919, 2018.

[23] M. Jorfi, J. L. Skousen, C. Weder, and J. R. Capadona, "Progress towards biocompatible intracortical microelectrodes for neural interfacing applications," *Journal of Neural Engineering*, vol. 12, no. 1, p. 011001, 2015.

[24] V. S. Polikov, P. A. Tresco, and W. M. Reichert, "Response of brain tissue to chronically implanted neural electrodes," *Journal of Neuroscience Methods*, vol. 148, no. 1, pp. 1–18, 2005.

[25] J. W. Salatino, K. A. Ludwig, T. D. Kozai, and E. K. Purcell, "Glial responses to implanted electrodes in the brain," *Nature Biomedical Engineering*, vol. 1, no. 11, pp. 862–877, 2017.

[26] R. Biran, D. C. Martin, and P. A. Tresco, "Neuronal cell loss accompanies the brain tissue response to chronically implanted silicon microelectrode arrays," *Experimental Neurology*, vol. 195, no. 1, pp. 115–126, 2005.

[27] D. H. Szarowski, M. D. Andersen, S. Retterer, A. J. Spence, M. Isaacson, H. G. Craighead, J. N. Turner, and W. Shain, "Brain responses to micro-machined silicon devices," *Brain Research*, vol. 983, no. 1-2, pp. 23–35, 2003.

[28] J. N. Turner, W. Shain, D. H. Szarowski, M. Andersen, S. Martins, M. Isaacson, and H. Craighead, "Cerebral astrocyte response to micromachined silicon implants," *Experimental Neurology*, vol. 156, no. 1, pp. 33–49, 1999.

[29] A. Prasad and J. Sanchez, "Quantifying Long-Term Microelectrode Array Functionality Using Chronic in Vivo Impedance Testing," *Journal of neural engineering*, vol. 9, no. 2, p. 026028, 2012.

[30] N. F. Nolta, M. B. Christensen, P. D. Crane, J. L. Skousen, and P. A. Tresco, "BBB leakage, astrogliosis, and tissue loss correlate with silicon microelectrode array recording performance," *Biomaterials*, vol. 53, pp. 753–762, 2015.

[31] F. T. Sun, S. Arcot Desai, T. K. Tcheng, and M. J. Morrell, "Changes in the electrocorticogram after implantation of intracranial electrodes in humans: The implant effect," *Clinical Neurophysiology*, vol. 129, no. 3, pp. 676–686, 2018.

[32] S. P. Lacour, G. Courtine, and J. Guck, "Materials and technologies for soft implantable neuroprostheses," *Nature Reviews Materials*, vol. 1, no. 10, pp. 1–14, 2016.

[33] K. Pogoda, L. Chin, P. C Georges, F. J Byfield, F. Bucki, R. Kim, M. Weaver, R. G Wells, C. Marcinkiewicz, and P. A Janmey, "Compression Stiffening of Brain and Its Effect on Mechanosensing by Glioma Cells," *New journal of physics*, vol. 16, no. 7, pp. 1367–2630, 2014.

[34] A. N. Bashkatov, E. A. Genina, Y. P. Sinichkin, V. I. Kochubey, N. A. Lako-dina, and V. V. Tuchin, "Glucose and Mannitol Diffusion in Human Dura Mater," *Biophysical Journal*, vol. 85, no. 5, pp. 3310–3318, 2003.

[35] I. R. Minev, P. Musienko, A. Hirsch, Q. Barraud, N. Wenger, E. M. Moraud, J. Gandar, M. Capogrosso, T. Milekovic, L. Asboth, R. F. Tor-res, N. Vachicouras, Q. Liu, N. Pavlova, S. Duis, A. Larmagnac, J. Vörös, S. Micera, Z. Suo, G. Courtine, and S. P. Lacour, "Electronic dura mater for long-term multimodal neural interfaces," *Science*, vol. 347, no. 6218, pp. 159–163, 2015.

[36] Z. Suo, E. Y. Ma, H. Gleskova, and S. Wagner, "Mechanics of rollable and fold-able film-on-foil electronics," *Applied Physics Letters*, vol. 74, no. 8, pp. 1177–1179, 1999.

[37] J. K. Nguyen, D. J. Park, J. L. Skousen, A. E. Hess-Dunning, D. J. Tyler, S. J. Rowan, C. Weder, and J. R. Capadona, "Mechanically-compliant intra-cortical implants reduce the neuroinflammatory response," *Journal of Neural Engineering*, vol. 11, no. 5, p. 056014, 2014.

[38] P. Moshayedi, G. Ng, J. C. Kwok, G. S. Yeo, C. E. Bryant, J. W. Fawcett, K. Franze, and J. Guck, "The relationship between glial cell mechanosensitiv-ity and foreign body reactions in the central nervous system," *Biomaterials*, vol. 35, no. 13, pp. 3919–3925, 2014.

[39] J. E. Chung, H. R. Joo, J. L. Fan, D. F. Liu, A. H. Barnett, S. Chen, C. Geaghan-Breiner, M. P. Karlsson, M. Karlsson, K. Y. Lee, H. Liang, J. F. Magland, J. A. Pebbles, A. C. Tooker, L. F. Greengard, V. M. Tolosa, and L. M. Frank, "High-Density, Long-Lasting, and Multi-region Electrophysio-logical Recordings Using Polymer Electrode Arrays," *Neuron*, vol. 101, no. 1, pp. 21–31.e5, 2019.

[40] I. D. Dryg, M. P. Ward, K. Y. Qing, H. Mei, J. E. Schaffer, and P. P. Irazoqui, "Magnetically inserted neural electrodes: Tissue response and functional life-time," *IEEE Transactions on Neural Systems and Rehabilitation Engineering*, vol. 23, no. 4, pp. 562–571, 2015.

[41] A. B. Ajiboye, F. R. Willett, D. R. Young, W. D. Memberg, B. A. Murphy, J. P. Miller, B. L. Walter, J. A. Sweet, H. A. Hoyen, M. W. Keith, P. H. Peckham, J. D. Simeral, J. P. Donoghue, L. R. Hochberg, and R. F. Kirsch, "Restoration of reaching and grasping movements through brain-controlled muscle stimulation in a person with tetraplegia: a proof-of-concept demon-stration," *The Lancet*, vol. 389, no. 10081, pp. 1821–1830, 2017.

[42] M. J. Cook, T. J. O'Brien, S. F. Berkovic, M. Murphy, A. Morokoff, G. Fabinyi, W. D'Souza, R. Yerra, J. Archer, L. Litewka, S. Hosking, P. Light-foot, V. Ruedebusch, W. D. Sheffield, D. Snyder, K. Leyde, and D. Himes, "Prediction of seizure likelihood with a long-term, implanted seizure advisory

system in patients with drug-resistant epilepsy: A first-in-man study," *The Lancet Neurology*, vol. 12, no. 6, pp. 563–571, 2013.

[43] S. J. Groiss, L. Wojtecki, M. Sudmeyer, and A. Schnitzler, "Deep brain stimulation in Parkinson-s disease," *Therapeutic Advances in Neurological Disorders*, vol. 2, no. 6, pp. 379–391, 2009.

[44] J. K. Krauss, N. Lipsman, T. Aziz, A. Boutet, P. Brown, J. W. Chang, B. Davidson, W. M. Grill, M. I. Hariz, A. Horn, M. Schulder, A. Mammis, P. A. Tass, J. Volkmann, and A. M. Lozano, "Technology of deep brain stimulation: current status and future directions," *Nature Reviews Neurology*, vol. 17, no. 2, pp. 75–87, 2021.

[45] F. Pittau, P. Mégevand, L. Sheybani, E. Abela, F. Grouiller, L. Spinelli, C. M. Michel, M. Seeck, and S. Vulliemoz, "Mapping epileptic activity: Sources or networks for the clinicians?," *Frontiers in Neurology*, vol. 5, no. NOV, 2014.

[46] T. Saito, Y. Muragaki, T. Maruyama, M. Tamura, M. Nitta, and Y. Okada, "Intraoperative functional mapping and monitoring during glioma surgery," *Neurologia Medico-Chirurgica*, vol. 55, no. 1, pp. 1–13, 2014.

[47] L. R. Hochberg, M. D. Serruya, G. M. Friehs, J. A. Mukand, M. Saleh, A. H. Caplan, A. Branner, D. Chen, R. D. Penn, and J. P. Donoghue, "Neuronal ensemble control of prosthetic devices by a human with tetraplegia," *Nature*, vol. 442, no. 7099, pp. 164–171, 2006.

[48] B. Lee, M. N. Zubair, Y. D. Marquez, D. M. Lee, L. A. Kalayjian, C. N. Heck, and C. Y. Liu, "A Single-Center Experience with the NeuroPace RNS System: A Review of Techniques and Potential Problems," *World Neurosurgery*, vol. 84, no. 3, pp. 719–726, 2015.

[49] P. Nuyujukian, J. Albites Sanabria, J. Saab, C. Pandarinath, B. Jarosiewicz, C. H. Blabe, B. Franco, S. T. Mernoff, E. N. Eskandar, J. D. Simeral, L. R. Hochberg, K. V. Shenoy, and J. M. Henderson, "Cortical control of a tablet computer by people with paralysis," *PLOS ONE*, vol. 13, no. 11, p. e0204566, 2018.

[50] E. Fernández, B. Greger, P. A. House, I. Aranda, C. Botella, J. Albisua, C. Soto-Sánchez, A. Alfaro, and R. A. Normann, "Acute human brain responses to intracortical microelectrode arrays: Challenges and future prospects," *Frontiers in Neuroengineering*, vol. 7, no. 24, 2014.

[51] G. Buzsáki, C. A. Anastassiou, and C. Koch, "The origin of extracellular fields and currents-EEG, ECoG, LFP and spikes," *Nature Reviews Neuroscience*, vol. 13, no. 6, pp. 407–420, 2012.

[52] T. H. Schwartz, T. Yang, and S. Hakimian, "Seminars in Epileptology Intraoperative ElectroCorticoGraphy (ECog): indications, techniques, and utility in epilepsy surgery," *Epileptic Disord*, vol. 16, no. 3, pp. 271–280, 2014.

[53] W. O. Tatum, J. H. McKay, K. ReFaey, A. M. Feyissa, D. Ryan, A. Ritaccio, E. Middlebrooks, K. Yelvington, G. Roth, E. Acton, S. Grewal, K. Chaichana, and A. Quinones-Hinojosa, "Detection of after-discharges during intraoperative functional brain mapping in awake brain tumor surgery using a novel high-density circular grid," *Clinical Neurophysiology*, vol. 131, no. 4, pp. 828–835, 2020.

[54] V. R. Rao, M. K. Leonard, J. K. Kleen, B. A. Lucas, E. A. Mirro, and E. F. Chang, "Chronic ambulatory electrocorticography from human speech cortex," *NeuroImage*, vol. 153, pp. 273–282, 2017.

[55] W. Wang, J. L. Collinger, A. D. Degenhart, E. C. Tyler-Kabara, A. B. Schwartz, D. W. Moran, D. J. Weber, B. Wodlinger, R. K. Vinjamuri, R. C. Ashmore, J. W. Kelly, and M. L. Boninger, "An Electrocorticographic Brain Interface in an Individual with Tetraplegia," *PLoS ONE*, vol. 8, no. 2, p. e55344, 2013.

[56] J. G. Makin, D. A. Moses, and E. F. Chang, "Machine translation of cortical activity to text with an encoder–decoder framework," *Nature Neuroscience*, vol. 23, no. 4, pp. 575–582, 2020.

[57] G. Sharma, N. Annetta, D. Friedenberg, T. Blanco, D. Vasconcelos, A. Shaikhouni, A. R. Rezai, and C. Bouton, "Time Stability and Coherence Analysis of Multiunit, Single-Unit and Local Field Potential Neuronal Signals in Chronically Implanted Brain Electrodes," *Bioelectronic Medicine*, vol. 2, no. 1, pp. 63–71, 2015.

[58] NCT03698149, "ECoG BMI for Motor and Speech Control - Full Text View - ClinicalTrials.gov."

[59] NCT02224469, "First Study With a Brain Implant to Help Locked-in Patients Communicate at Home - Full Text View - ClinicalTrials.gov."

[60] NCT00912041, "BrainGate2: Feasibility Study of an Intracortical Neural Interface System for Persons With Tetraplegia - Full Text View - ClinicalTrials.gov."

[61] NCT00264810, "RNS® System Pivotal Study - Full Text View - ClinicalTrials.gov."

[62] C. H. Wong, J. Birkett, K. Byth, M. Dexter, E. Somerville, D. Gill, R. Chaseling, M. Fearnside, and A. Bleasel, "Risk factors for complications during intracranial electrode recording in presurgical evaluation of drug resistant partial epilepsy," *Acta Neurochirurgica*, vol. 151, no. 1, pp. 37–50, 2009.

[63] G. C. Wiggins, K. Elisevich, and B. J. Smith, "Morbidity and infection in combined subdural grid and strip electrode investigation for intractable epilepsy," *Epilepsy Research*, vol. 37, no. 1, pp. 73–80, 1999.

[64] S. F. Cogan, "Neural Stimulation and Recording Electrodes," *annual reviews Biomedical Engineering*, vol. 10, pp. 275–309, 2008.

[65] S. Gawad, M. Giugliano, M. Heuschkel, B. Wessling, H. Markram, U. Schnakenberg, P. Renaud, and H. Morgan, "Substrate arrays of iridium oxide microelectrodes for in vitro neuronal interfacing," *Frontiers in Neuroengineering*, vol. 2, 2009.

[66] D. Khodagholy, T. Doublet, M. Gurfinkel, P. Quilichini, E. Ismailova, P. Leleux, T. Herve, S. Sanaur, C. Bernard, and G. G. Malliaras, "Highly Conformable Conducting Polymer Electrodes for In Vivo Recordings," *Advanced Materials*, vol. 23, no. 36, pp. H268–H272, 2011.

[67] Y. Lu, H. Lyu, A. G. Richardson, T. H. Lucas, and D. Kuzum, "Flexible Neural Electrode Array Based-on Porous Graphene for Cortical Microstimulation and Sensing," *Scientific Reports*, vol. 6, no. 1, pp. 1–9, 2016.

[68] D. Khodagholy, J. N. Gelinas, T. Thesen, W. Doyle, O. Devinsky, G. G. Malliaras, and G. Buzsáki, "NeuroGrid: Recording action potentials from the surface of the brain," *Nature Neuroscience*, vol. 18, no. 2, pp. 310–315, 2015.

[69] M. E. J. Obien, K. Deligkaris, T. Bullmann, D. J. Bakkum, and U. Frey, "Revealing neuronal function through microelectrode array recordings," *Frontiers in Neuroscience*, vol. 9, no. JAN, p. 423, 2015.

[70] B. Eversmann, M. Jenkner, F. Hofmann, C. Paulus, R. Brederlow, B. Holzapfl, P. Fromherz, M. Merz, M. Brenner, M. Schreiter, R. Gabl, K. Plehnert, M. Steinhauser, G. Eckstein, D. Schmitt-Landsiedel, and R. Thewes, "A 128 × 128 CMOS Biosensor Array for Extracellular Recording of Neural Activity," *IEEE Journal of Solid-State Circuits*, vol. 38, no. 12, pp. 2306–2317, 2003.

[71] D. Tsai, D. Sawyer, A. Bradd, R. Yuste, and K. L. Shepard, "A very large-scale microelectrode array for cellular-resolution electrophysiology," *Nature Communications*, vol. 8, no. 1, pp. 1–11, 2017.

[72] J. Abbott, T. Ye, L. Qin, M. Jorgolli, R. S. Gertner, D. Ham, and H. Park, "CMOS nanoelectrode array for all-electrical intracellular electrophysiological imaging," *Nature Nanotechnology*, vol. 12, no. 5, pp. 460–466, 2017.

[73] J. Viventi, D. H. Kim, L. Vigeland, E. S. Frechette, J. A. Blanco, Y. S. Kim, A. E. Avrin, V. R. Tiruvadi, S. W. Hwang, A. C. Vanleer, D. F. Wulsin, K. Davis, C. E. Gelber, L. Palmer, J. Van Der Spiegel, J. Wu, J. Xiao, Y. Huang, D. Contreras, J. A. Rogers, and B. Litt, "Flexible, foldable, actively multiplexed, high-density electrode array for mapping brain activity in vivo," *Nature Neuroscience*, vol. 14, no. 12, pp. 1599–1605, 2011.

[74] W. Lee, D. Kim, J. Rivnay, N. Matsuhisa, T. Lonjaret, T. Yokota, H. Yawo, M. Sekino, G. G. Malliaras, and T. Someya, "Integration of Organic Electrochemical and Field-Effect Transistors for Ultraflexible, High Temporal Resolu-

tion Electrophysiology Arrays," *Advanced Materials*, vol. 28, no. 44, pp. 9722–9728, 2016.

[75] C. Cea, G. D. Spyropoulos, P. Jastrzebska-Perfect, J. J. Ferrero, J. N. Gelinas, and D. Khodagholy, "Enhancement-mode ion-based transistor as a comprehensive interface and real-time processing unit for in vivo electrophysiology," *Nature Materials*, vol. 19, no. 6, pp. 679–686, 2020.

[76] C. H. Chiang, S. M. Won, A. L. Orsborn, K. J. Yu, M. Trumpis, B. Bent, C. Wang, Y. Xue, S. Min, V. Woods, C. Yu, B. H. Kim, S. B. Kim, R. Huq, J. Li, K. J. Seo, F. Vitale, A. Richardson, H. Fang, Y. Huang, K. Shepard, B. Pesaran, J. A. Rogers, and J. Viventi, "Development of a neural interface for high-definition, long-term recording in rodents and nonhuman primates," *Science Translational Medicine*, vol. 12, no. 538, 2020.

[77] A. Obaid, M. E. Hanna, Y. W. Wu, M. Kollo, R. Racz, M. R. Angle, J. Müller, N. Brackbill, W. Wray, F. Franke, E. J. Chichilnisky, A. Hierlemann, J. B. Ding, A. T. Schaefer, and N. A. Melosh, "Massively parallel microwire arrays integrated with CMOS chips for neural recording," *Science Advances*, vol. 6, no. 12, p. eaay2789, 2020.

[78] J. J. Jun, N. A. Steinmetz, J. H. Siegle, D. J. Denman, M. Bauza, B. Barbarits, A. K. Lee, C. A. Anastassiou, A. Andrei, Ç. Aydın, M. Barbic, T. J. Blanche, V. Bonin, J. Couto, B. Dutta, S. L. Gratiy, D. A. Gutnisky, M. Häusser, B. Karsh, P. Ledochowitsch, C. M. Lopez, C. Mitelut, S. Musa, M. Okun, M. Pachitariu, J. Putzeys, P. D. Rich, C. Rossant, W.-l. Sun, K. Svoboda, M. Carandini, K. D. Harris, C. Koch, J. O'Keefe, and T. D. Harris, "Fully integrated silicon probes for high-density recording of neural activity," *Nature*, vol. 551, no. 7679, pp. 232–236, 2017.

[79] A. L. Juavinett, G. Bekheet, and A. K. Churchland, "Chronically implanted neuropixels probes enable high-yield recordings in freely moving mice," *eLife*, vol. 8, 2019.

[80] P. Dayan, "Neural Encoding I: Firing Rates and Spike Statistics BT - Theoretical Neuroscience," *Theoretical Neuroscience*, p. 460, 2005.

[81] B. B. Averbeck, P. E. Latham, and A. Pouget, "Neural correlations, population coding and computation," *Nature Reviews Neuroscience*, vol. 7, no. 5, pp. 358–366, 2006.

[82] R. Q. Quiroga and S. Panzeri, *Principles of neural coding.* 2013.

[83] C. I. Petkov and D. Bendor, "Neuronal Mechanisms and Transformations Encoding Time-Varying Signals," *Neuron*, vol. 91, no. 4, pp. 718–721, 2016.

[84] A. Azarfar, N. Calcini, C. Huang, F. Zeldenrust, and T. Celikel, "Neural coding: A single neuron's perspective," *Neuroscience and Biobehavioral Reviews*, vol. 94, pp. 238–247, 2018.

[85] G. Dragoi and G. Buzsáki, "Temporal Encoding of Place Sequences by Hippocampal Cell Assemblies," *Neuron*, vol. 50, no. 1, pp. 145–157, 2006.

[86] C. Geisler, D. Robbe, M. Zugaro, A. Sirota, and G. rgy Buzsá ki, "Hippocampal place cell assemblies are speed-controlled oscillators," *Proceedings of the National Academy of Sciences*, vol. 104, no. 19, pp. 8149–8154, 2007.

[87] C. M. Niell, "Cell Types, Circuits, and Receptive Fields in the Mouse Visual Cortex," *Annual Review of Neuroscience*, vol. 38, pp. 413–431, 2015.

[88] M. N. Geffen, B. M. Broome, G. Laurent, and M. Meister, "Neural Encoding of Rapidly Fluctuating Odors," *Neuron*, vol. 61, no. 4, pp. 570–586, 2009.

[89] W. Sun and D. L. Barbour, "Rate, not selectivity, determines neuronal population coding accuracy in auditory cortex," *PLOS Biology*, vol. 15, no. 11, p. e2002459, 2017.

[90] G. Deco, E. T. Rolls, and R. Romo, "Stochastic dynamics as a principle of brain function," *Progress in Neurobiology*, vol. 88, no. 1, pp. 1–16, 2009.

[91] W. Bair, C. Koch, W. Newsome, and K. Britten, "Power Spectrum Analysis of Bursting Cells in Area MT in the Behaving Monkey," *The Journal of Neuroscience*, vol. 74, no. 5, pp. 2870–2892, 1994.

[92] F. Gabbiani and C. Koch, "Coding of Time-Varying Signals in Spike Trains of Integrate-and-Fire Neurons with Random Threshold," *Neural Computation*, vol. 8, no. 1, pp. 44–66, 1996.

[93] W. Wu, Y. Gao, E. Bienenstock, J. P. Donoghue, and M. J. Black, "Bayesian population decoding of motor cortical activity using a Kalman filter," *Neural Computation*, vol. 18, no. 1, pp. 80–118, 2006.

[94] S. Muralidhar, Y. Wang, and H. Markram, "Synaptic and cellular organization of layer 1 of the developing rat somatosensory cortex," *Frontiers in Neuroanatomy*, vol. 7, 2014.

[95] J. Schiller, Y. Schiller, G. Stuart, B. Sakmann, and A. Zellphysiologie, "Calcium action potentials restricted to distal apical dendrites of rat neocortical pyramidal neurons," *Journal of Physiology*, vol. 505, no. 3, pp. 605–616, 1997.

[96] F. Helmchen, K. Svoboda, W. Denk, and D. W. Tank, "In vivo dendritic calcium dynamics in deep-layer cortical pyramidal neurons," *Nature Neuroscience*, vol. 2, no. 11, pp. 989–996, 1999.

[97] M. Suzuki and M. E. Larkum, "Dendritic calcium spikes are clearly detectable at the cortical surface," *Nature Communications*, vol. 8, no. 276, 2017.

[98] G. Buzsáki and A. Draguhn, "Neuronal olscillations in cortical networks," *Science*, vol. 304, no. 5679, pp. 1926–1929, 2004.

[99] G. Buzsáki, *Rhythms of the Brain*. Oxford University Press, 2006.

[100] P. Fries, "Rhythms for Cognition: Communication through Coherence," *Neuron*, vol. 88, no. 1, pp. 220–235, 2015.

[101] A. Sirota, S. Montgomery, S. Fujisawa, Y. Isomura, M. Zugaro, and G. Buzsáki, "Entrainment of Neocortical Neurons and Gamma Oscillations by the Hippocampal Theta Rhythm," *Neuron*, vol. 60, no. 4, pp. 683–697, 2008.

[102] M. Siegel, T. H. Donner, and A. K. Engel, "Spectral fingerprints of large-scale neuronal interactions," 2012.

[103] A. Goyal, J. Miller, S. E. Qasim, A. J. Watrous, H. Zhang, J. M. Stein, C. S. Inman, R. E. Gross, J. T. Willie, B. Lega, J. J. Lin, A. Sharan, C. Wu, M. R. Sperling, S. A. Sheth, G. M. McKhann, E. H. Smith, C. Schevon, and J. Jacobs, "Functionally distinct high and low theta oscillations in the human hippocampus," *Nature Communications*, vol. 11, no. 1, pp. 1–10, 2020.

[104] R. H. Masland, "Primer Neuronal cell types," *Current Biology*, vol. 14, no. 13, pp. 497–500, 2004.

[105] P. Fries, J. H. Reynolds, A. E. Rorie, and R. Desimone, "Modulation of oscillatory neuronal synchronization by selective visual attention," *Science*, vol. 291, no. 5508, pp. 1560–1563, 2001.

[106] C. A. Anastassiou, R. Perin, H. Markram, and C. Koch, "Ephaptic coupling of cortical neurons," *Nature Neuroscience*, vol. 14, no. 2, pp. 217–224, 2011.

[107] J. Liu and W. T. Newsome, "Local Field Potential in Cortical Area MT: Stimulus Tuning and Behavioral Correlations," *Journal of Neuroscience*, vol. 26, no. 30, pp. 7779–7790, 2006.

[108] M. Esghaei and M. R. Daliri, "Decoding of Visual Attention from LFP Signals of Macaque MT," *PLoS ONE*, vol. 9, no. 6, p. 100381, 2014.

[109] B. N. Pasley, S. V. David, N. Mesgarani, A. Flinker, S. A. Shamma, N. E. Crone, R. T. Knight, and E. F. Chang, "Reconstructing speech from human auditory cortex," *PLoS Biology*, vol. 10, no. 1, 2012.

[110] N. Mesgarani, C. Cheung, K. Johnson, and E. F. Chang, "Phonetic feature encoding in human superior temporal gyrus," *Science*, vol. 343, no. 6174, pp. 1006–1010, 2014.

[111] J. Chartier, G. K. Anumanchipalli, K. Johnson, and E. F. Chang, "Encoding of Articulatory Kinematic Trajectories in Human Speech Sensorimotor Cortex," *Neuron*, vol. 98, no. 5, pp. 1042–1054.e4, 2018.

[112] A. Jackson and T. M. Hall, "Decoding Local Field Potentials for Neural Interfaces," *IEEE TRANSACTIONS ON NEURAL SYSTEMS AND REHABILITATION ENGINEERING*, vol. 25, no. 10, 2017.

[113] D. J. Warren, S. Kellis, J. G. Nieveen, S. M. Wendelken, H. Dantas, T. S. Davis, D. T. Hutchinson, R. A. Normann, G. A. Clark, and V. John Mathews, "Recording and decoding for neural prostheses," *Proceedings of the IEEE*, vol. 104, no. 2, pp. 374–391, 2016.

[114] R. A. Andersen, S. Musallam, and B. Pesaran, "Selecting the signals for a brain-machine interface," *Current Opinion in Neurobiology*, vol. 14, no. 6, pp. 720–726, 2004.

[115] D. A. Leopold, "Very Slow Activity Fluctuations in Monkey Visual Cortex: Implications for Functional Brain Imaging," *Cerebral Cortex*, vol. 13, no. 4, pp. 422–433, 2003.

[116] B. O. Watson, K. B. Hengen, S. L. Gonzalez Andino, and G. J. Thompson, "Cognitive and Physiologic Impacts of the Infraslow Oscillation," *Front. Syst. Neurosci*, vol. 12, 2018.

[117] T. Hiltunen, J. Kantola, A. Abou Elseoud, P. Lepola, K. Suominen, T. Starck, J. Nikkinen, J. Remes, O. Tervonen, S. Palva, V. Kiviniemi, and J. M. Palva, "Infra-Slow EEG Fluctuations Are Correlated with Resting-State Network Dynamics in fMRI," *Journal of Neuroscience*, vol. 34, no. 2, pp. 356–362, 2014.

[118] S. Vanhatalo, J. M. Palva, M. D. Holmes, J. W. Miller, J. Voipio, and K. Kaila, "Infraslow oscillations modulate excitability and interictal epileptic activity in the human cortex during sleep," *Proceedings of the National Academy of Sciences of the United States of America*, vol. 101, no. 14, pp. 5053–5057, 2004.

[119] W. J. Pan, G. J. Thompson, M. E. Magnuson, D. Jaeger, and S. Keilholz, "Infraslow LFP correlates to resting-state fMRI BOLD signals," *NeuroImage*, vol. 74, pp. 288–297, 2013.

[120] Y. Nir, L. Fisch, R. Mukamel, H. Gelbard-Sagiv, A. Arieli, I. Fried, and R. Malach, "Coupling between Neuronal Firing Rate, Gamma LFP, and BOLD fMRI Is Related to Interneuronal Correlations," *Current Biology*, vol. 17, no. 15, pp. 1275–1285, 2007.

[121] N. K. Logothetis, "What we can do and what we cannot do with fMRI," *Nature*, vol. 453, no. 7197, pp. 869–878, 2008.

[122] M. J. Nelson, P. Pouget, E. A. Nilsen, C. D. Patten, and J. D. Schall, "Review of signal distortion through metal microelectrode recording circuits and filters," *Journal of Neuroscience Methods*, vol. 169, no. 1, pp. 141–157, 2008.

[123] D. Contreras and M. Steriade, "Cellular basis of EEG slow rhythms: A study of dynamic corticothalamic relationships," *Journal of Neuroscience*, vol. 15, no. 1 II, pp. 604–622, 1995.

[124] A. Hirsch, "The era of carbon allotropes," *Nature Materials*, vol. 9, no. 11, pp. 868–871, 2010.

[125] A. H. Castro Neto, F. Guinea, N. M. R. Peres, K. S. Novoselov, and A. K. Geim, "The electronic properties of graphene," *Reviews of Modern Physics*, vol. 81, no. 109, 2009.

[126] P. R. Wallace, "The band theory of graphite," *Physical Review*, vol. 71, no. 9, pp. 622–634, 1947.

[127] M. S. Dresselhaus and G. Dresselhaus, "Intercalation compounds of graphite," *Advances in Physics*, vol. 51, no. 1, pp. 1–186, 2002.

[128] K. S. Novoselov, A. K. Geim, S. V. Morozov, D. Jiang, M. I. Katsnelson, I. V. Grigorieva, S. V. Dubonos, and A. A. Firsov, "Two-dimensional gas of massless Dirac fermions in graphene," *Nature*, vol. 438, pp. 197–200, 2005.

[129] C. K. Ullal, J. Shi, and R. Sundararaman, "Electron mobility in graphene without invoking the Dirac equation," *American Journal of Physics*, vol. 87, no. 4, pp. 291–295, 2019.

[130] J. H. Chen, C. Jang, S. Xiao, M. Ishigami, and M. S. Fuhrer, "Intrinsic and extrinsic performance limits of graphene devices on SiO 2," *Nature Nanotechnology*, vol. 3, no. 4, pp. 206–209, 2008.

[131] M. I. Katsnelson and A. K. Geim, "Electron scattering on microscopic corrugations in graphene," *Philos Trans A Math Phys Eng Sci*, vol. 366, no. 1863, pp. 195–204, 2008.

[132] J. H. Chen, C. Jang, S. Adam, M. S. Fuhrer, E. D. Williams, and M. Ishigami, "Charged-impurity scattering in graphene," *Nature Physics*, vol. 4, no. 5, pp. 377–381, 2008.

[133] F. Banhart, J. Kotakoski, and A. V. Krasheninnikov, "Structural Defects in Graphene," *ACS Nano*, vol. 5, no. 1, pp. 26–41, 2011.

[134] J. H. Chen, W. G. Cullen, C. Jang, M. S. Fuhrer, and E. D. Williams, "Defect scattering in graphene," *Physical Review Letters*, vol. 102, no. 23, p. 236805, 2009.

[135] K. Balasubramanian, T. Biswas, P. Ghosh, S. Suran, A. Mishra, R. Mishra, R. Sachan, M. Jain, M. Varma, R. Pratap, and S. Raghavan, "Reversible defect engineering in graphene grain boundaries," *Nature Communications*, vol. 10, no. 1, 2019.

[136] L. Wang, I. Meric, P. Y. Huang, Q. Gao, Y. Gao, H. Tran, T. Taniguchi, K. Watanabe, L. M. Campos, D. A. Muller, J. Guo, P. Kim, J. Hone, K. L. Shepard, and C. R. Dean, "One-dimensional electrical contact to a two-dimensional material.," *Science (New York, N.Y.)*, vol. 342, no. 6158, pp. 614–7, 2013.

[137] C. R. Dean, A. F. Young, I. Meric, C. Lee, L. Wang, S. Sorgenfrei, K. Watanabe, T. Taniguchi, P. Kim, K. L. Shepard, and J. Hone, "Boron nitride substrates for high-quality graphene electronics," *Nature Nanotechnology*, vol. 5, no. 10, pp. 722–726, 2010.

[138] J. C. Meyer, C. Kisielowski, R. Erni, M. D. Rossell, M. F. Crommie, and A. Zettl, "Direct imaging of lattice atoms and topological defects in graphene membranes," *Nano Letters*, vol. 8, no. 11, pp. 3582–3586, 2008.

[139] A. K. Geim and K. S. Novoselov, "The rise of graphene," *Nature Materials*, vol. 6, no. 3, pp. 183–191, 2007.

[140] F. Liu, P. Ming, and J. Li, "Ab initio calculation of ideal strength and phonon instability of graphene under tension," *Physical Review B - Condensed Matter and Materials Physics*, vol. 76, no. 6, p. 064120, 2007.

[141] C. Lee, X. Wei, J. W. Kysar, and J. Hone, "Measurement of the elastic properties and intrinsic strength of monolayer graphene," *Science*, vol. 321, no. 5887, pp. 385–388, 2008.

[142] R. Ansari, S. Ajori, and B. Motevalli, "Mechanical properties of defective single-layered graphene sheets via molecular dynamics simulation," *Superlattices and Microstructures*, vol. 51, no. 2, pp. 274–289, 2012.

[143] A. Zandiatashbar, G. H. Lee, S. J. An, S. Lee, N. Mathew, M. Terrones, T. Hayashi, C. R. Picu, J. Hone, and N. Koratkar, "Effect of defects on the intrinsic strength and stiffness of graphene," *Nature Communications*, vol. 5, no. 1, pp. 1–9, 2014.

[144] D. W. Boukhvalov and M. I. Katsnelson, "Chemical functionalization of graphene with defects," *Nano Letters*, vol. 8, no. 12, pp. 4374–4379, 2008.

[145] D. W. Boukhvalov and M. I. Katsnelson, "Modeling of Graphite Oxide," *Journal of the American Chemical Society*, vol. 130, no. 32, pp. 10697–10701, 2008.

[146] D. W. Boukhvalov and M. I. Katsnelson, "Chemical functionalization of graphene," *Journal of Physics Condensed Matter*, vol. 21, no. 34, p. 344205, 2009.

[147] R. Sharma, J. H. Baik, C. J. Perera, and M. S. Strano, "Anomalously large reactivity of single graphene layers and edges toward electron transfer chemistries," *Nano Letters*, vol. 10, no. 2, pp. 398–405, 2010.

[148] S. Samaddar, I. Yudhistira, S. Adam, H. Courtois, and C. B. Winkelmann, "Charge Puddles in Graphene near the Dirac Point," *Physical Review Letters*, vol. 116, no. 12, p. 126804, 2016.

[149] M. Yamamoto, T. L. Einstein, M. S. Fuhrer, and W. G. Cullen, "Charge inhomogeneity determines oxidative reactivity of graphene on substrates," *ACS Nano*, vol. 6, no. 9, pp. 8335–8341, 2012.

[150] R. R. Nair, P. Blake, A. N. Grigorenko, K. S. Novoselov, T. J. Booth, T. Stauber, N. M. Peres, and A. K. Geim, "Fine structure constant defines visual transparency of graphene," *Science*, vol. 320, no. 5881, p. 1308, 2008.

[151] A. C. Ferrari, "Raman spectroscopy of graphene and graphite: Disorder, electron-phonon coupling, doping and nonadiabatic effects," *Solid State Communications*, vol. 143, no. 1-2, pp. 47–57, 2007.

[152] A. C. Ferrari and D. M. Basko, "Raman spectroscopy as a versatile tool for studying the properties of graphene," *Nature Nanotechnology*, vol. 8, no. 4, pp. 235–246, 2013.

[153] A. Das, S. Pisana, B. Chakraborty, S. Piscanec, S. K. Saha, U. V. Waghmare, K. S. Novoselov, H. R. Krishnamurthy, A. K. Geim, A. C. Ferrari, and A. K. Sood, "Monitoring dopants by Raman scattering in an electrochemically top-gated graphene transistor," *Nature Nanotechnology*, vol. 3, no. 4, pp. 210–215, 2008.

[154] A. Eckmann, A. Felten, A. Mishchenko, L. Britnell, R. Krupke, K. S. Novoselov, and C. Casiraghi, "Probing the nature of defects in graphene by Raman spectroscopy," *Nano Letters*, vol. 12, no. 8, pp. 3925–3930, 2012.

[155] K. S. Novoselov, A. K. Geim, S. V. Morozov, D. Jiang, Y. Zhang, S. V. Dubonos, I. V. Grigorieva, and A. A. Firsov, "Electric field in atomically thin carbon films," *Science*, vol. 306, no. 5696, pp. 666–669, 2004.

[156] K. Parvez, S. Yang, X. Feng, and K. Müllen, "Exfoliation of graphene via wet chemical routes," *Synthetic Metals*, vol. 210, pp. 123–132, 2015.

[157] J. Kim, C. Bayram, H. Park, C. W. Cheng, C. Dimitrakopoulos, J. A. Ott, K. B. Reuter, S. W. Bedell, and D. K. Sadana, "Principle of direct van der Waals epitaxy of single-crystalline films on epitaxial graphene," *Nature Communications*, vol. 5, no. 1, pp. 1–7, 2014.

[158] S. Bae, H. Kim, Y. Lee, X. Xu, J. S. Park, Y. Zheng, J. Balakrishnan, T. Lei, H. Ri Kim, Y. I. Song, Y. J. Kim, K. S. Kim, B. Özyilmaz, J. H. Ahn, B. H. Hong, and S. Iijima, "Roll-to-roll production of 30-inch graphene films for transparent electrodes," *Nature Nanotechnology*, vol. 5, no. 8, pp. 574–578, 2010.

[159] L. Banszerus, M. Schmitz, S. Engels, J. Dauber, M. Oellers, F. Haupt, K. Watanabe, T. Taniguchi, B. Beschoten, and C. Stampfer, "Ultrahigh-mobility graphene devices from chemical vapor deposition on reusable copper," *Science Advances*, vol. 1, no. 6, p. e1500222, 2015.

[160] A. Zurutuza and C. Marinelli, "Challenges and opportunities in graphene commercialization," *Nature Nanotechnology*, vol. 9, no. 10, pp. 730–734, 2014.

[161] Deji Akinwande; Li Tao; Qingkai Yu; Xiaojing Lou; Peng Peng; Duygu,

"Large-Area Graphene Electrodes: Using CVD to facilitate applications in commercial touchscreens, flexible nanoelectronics, and neural interfaces.," *IEEE nanotechnology magazine*, vol. 9, no. 3, pp. 6 – 14, 2015.

[162] B. Deng, Z. Liu, and H. Peng, "Toward Mass Production of CVD Graphene Films," *Advanced Materials*, vol. 31, no. 9, p. 1800996, 2019.

[163] X. Li, W. Cai, L. Colombo, and R. S. Ruoff, "Evolution of graphene growth on Ni and Cu by carbon isotope labeling," *Nano Letters*, vol. 9, no. 12, pp. 4268– 4272, 2009.

[164] L. Ma, W. Ren, and H. Cheng, "Transfer Methods of Graphene from Metal Substrates: A Review," *Small Methods*, vol. 3, no. 7, p. 1900049, 2019.

[165] W. S. Leong, H. Wang, J. Yeo, F. J. Martin-Martinez, A. Zubair, P. C. Shen, Y. Mao, T. Palacios, M. J. Buehler, J. Y. Hong, and J. Kong, "Paraffin-enabled graphene transfer," *Nature Communications*, vol. 10, no. 1, pp. 1–8, 2019.

[166] Z. Cheng, Q. Zhou, C. Wang, Q. Li, C. Wang, and Y. Fang, "Toward intrinsic graphene surfaces: A systematic study on thermal annealing and wet-chemical treatment of SiO2-supported graphene devices," *Nano Letters*, vol. 11, no. 2, pp. 767–771, 2011.

[167] Y. C. Lin, C. C. Lu, C. H. Yeh, C. Jin, K. Suenaga, and P. W. Chiu, "Graphene annealing: How clean can it be?," *Nano Letters*, vol. 12, no. 1, pp. 414–419, 2012.

[168] A. Yulaev, G. Cheng, A. R. Hight Walker, I. V. Vlassiouk, A. Myers, M. S. Leite, and A. Kolmakov, "Toward clean suspended CVD graphene," *RSC Advances*, vol. 6, no. 87, pp. 83954–83962, 2016.

[169] W. Li, Y. Liang, D. Yu, L. Peng, K. P. Pernstich, T. Shen, A. R. Hight Walker, G. Cheng, C. A. Hacker, C. A. Richter, Q. Li, D. J. Gundlach, and X. Liang, "Ultraviolet/ozone treatment to reduce metal-graphene contact resistance," *Applied Physics Letters*, vol. 102, no. 18, p. 183110, 2013.

[170] A. Hugo, *Capteurs biologiques à base de transistors graphène à grille liquide.* PhD thesis, 2020.

[171] C. Hébert, E. Masvidal-Codina, A. Suarez-Perez, A. B. Calia, G. Piret, R. Garcia-Cortadella, X. Illa, E. Del Corro Garcia, J. M. De la Cruz Sanchez, D. V. Casals, E. Prats-Alfonso, J. Bousquet, P. Godignon, B. Yvert, R. Villa, M. V. Sanchez-Vives, A. Guimerà-Brunet, and J. A. Garrido, "Flexible Graphene Solution-Gated Field-Effect Transistors: Efficient Transducers for Micro-Electrocorticography," *Advanced Functional Materials*, vol. 28, no. 12, p. 1703976, 2018.

[172] D. Khodagholy, T. Doublet, P. Quilichini, M. Gurfinkel, P. Leleux, A. Gh-estem, E. Ismailova, T. Hervé, S. Sanaur, C. Bernard, and G. G. Malliaras, "In vivo recordings of brain activity using organic transistors," *Nature Communications*, vol. 4, no. 1, pp. 1–7, 2013.

[173] J. Rivnay, S. Inal, A. Salleo, R. M. Owens, M. Berggren, and G. G. Malliaras, "Organic electrochemical transistors," *Nature Reviews Materials*, vol. 3, no. 2, pp. 1–14, 2018.

[174] W. Lee, D. Kim, J. Rivnay, N. Matsuhisa, T. Lonjaret, T. Yokota, H. Yawo, M. Sekino, G. G. Malliaras, and T. Someya, "Integration of Organic Electro-chemical and Field-Effect Transistors for Ultraflexible, High Temporal Resolution Electrophysiology Arrays," *Advanced Materials*, vol. 28, no. 44, pp. 9722–9728, 2016.

[175] P. Fromherz, A. Offenhäusser, T. Vetter, and J. Weis, "A neuron-silicon junction: A Retzius cell of the leech on an insulated-gate field-effect transistor," *Science*, vol. 252, no. 5010, pp. 1290–1293, 1991.

[176] L. H. Hess, M. Seifert, and J. A. Garrido, "Graphene transistors for bioelectronics," *Proceedings of the IEEE*, vol. 101, no. 7, pp. 1780–1792, 2013.

[177] H. Fang, K. J. Yu, C. Gloschat, Z. Yang, E. Song, C. H. Chiang, J. Zhao, S. M. Won, S. Xu, M. Trumpis, Y. Zhong, S. W. Han, Y. Xue, D. Xu, S. W. Choi, G. Cauwenberghs, M. Kay, Y. Huang, J. Viventi, I. R. Efimov, and J. A. Rogers, "Capacitively coupled arrays of multiplexed flexible silicon transistors for long-term cardiac electrophysiology," *Nature Biomedical Engineering*, vol. 1, no. 3, pp. 1–12, 2017.

[178] G. D. Spyropoulos, J. N. Gelinas, and D. Khodagholy, "Internal ion-gated organic electrochemical transistor: A building block for integrated bioelectronics," *Science Advances*, vol. 5, no. 2, p. eaau7378, 2020.

[179] I. Meric, M. Y. Han, A. F. Young, B. Ozyilmaz, P. Kim, and K. L. Shepard, "Current saturation in zero-bandgap, top-gated graphene field-effect transistors," *Nature Nanotechnology*, vol. 3, no. 11, pp. 654–659, 2008.

[180] J. Martin, N. Akerman, G. Ulbricht, T. Lohmann, J. H. Smet, K. Von Klitzing, and A. Yacoby, "Observation of electron-hole puddles in graphene using a scanning single-electron transistor," *Nature Physics*, vol. 4, no. 2, pp. 144–148, 2008.

[181] J. d. P. P. Atkins, P. W. Atkins, *Physical Chemistry*. 2014.

[182] S. Luryi, "Quantum capacitance devices," *Applied Physics Letters*, vol. 52, no. 6, pp. 501–503, 1988.

[183] J. Xia, F. Chen, J. Li, and N. Tao, "Measurement of the quantum capacitance of graphene," *Nature Nanotechnology*, vol. 4, no. 8, pp. 505–509, 2009.

[184] D. Jiménez, "Explicit drain current, charge and capacitance model of graphene field-effect transistors," *IEEE Transactions on Electron Devices*, vol. 58, no. 12, pp. 4377–4383, 2011.

[185] C. Mackin, L. H. Hess, A. Hsu, Y. Song, J. Kong, J. A. Garrido, and T. Palacios, "A Current–Voltage Model for Graphene Electrolyte-Gated Field-Effect Transistors," *IEEE Transactions on Electron Devices*, vol. 61, no. 12, pp. 3971–3977, 2014.

[186] G. M. Landauer, D. Jimenez, and J. L. Gonzalez, "An Accurate and Verilog-A Compatible Compact Model for Graphene Field-Effect Transistors," *IEEE Transactions on Nanotechnology*, vol. 13, no. 5, pp. 895–904, 2014.

[187] N. Schaefer, R. Garcia-Cortadella, J. Martínez-Aguilar, G. Schwesig, X. Illa, A. M. Lara, S. Santiago, C. Hébert, G. Guirado, R. Villa, A. Sirota, A. Guimerà-Brunet, and J. A. Garrido, "Multiplexed neural sensor array of graphene solution-gated field-effect transistors," *2D Materials*, vol. 7, no. 2, p. 025046, 2020.

[188] K. N. Parrish and D. Akinwande, "Impact of contact resistance on the transconductance and linearity of graphene transistors," *Appl. Phys. Lett*, vol. 98, p. 183505, 2011.

[189] A. Hsu, H. Wang, K. K. Kim, J. Kong, and T. Palacios, "Impact of graphene interface quality on contact resistance and RF device performance," *IEEE Electron Device Letters*, vol. 32, no. 8, pp. 1008–1010, 2011.

[190] S. M. Song, J. K. Park, O. J. Sul, and B. J. Cho, "Determination of work function of graphene under a metal electrode and its role in contact resistance," *Nano Letters*, vol. 12, no. 8, pp. 3887–3892, 2012.

[191] A. D. B. Filippo Giubileo, "The role of contact resistance in graphene field-effect devices," *Progress in Surface Science*, vol. 92, no. 3, pp. 143–175, 2017.

[192] P. Zhang, Y. Y. Lau, and R. M. Gilgenbach, "Analysis of current crowding in thin film contacts from exact field solution," *Journal of Physics D: Applied Physics*, vol. 48, no. 47, p. 475501, 2015.

[193] K. L. Grosse, M. H. Bae, F. Lian, E. Pop, and W. P. King, "Nanoscale Joule heating, Peltier cooling and current crowding at graphene-metal contacts," *Nature Nanotechnology*, vol. 6, no. 5, pp. 287–290, 2011.

[194] W. S. Leong, C. T. Nai, and J. T. L. Thong, "What Does Annealing Do to Metal–Graphene Contacts?," *Nano Letters*, vol. 14, no. 7, pp. 3840–3847, 2014.

[195] W. S. Leong, H. Gong, and J. T. L. Thong, "Low-Contact-Resistance Graphene Devices with Nickel-Etched-Graphene Contacts," *ACS Nano*, vol. 8, no. 1, pp. 994–1001, 2014.

[196] H.-Y. Park, W.-S. Jung, D.-H. Kang, J. Jeon, G. Yoo, Y. Park, J. Lee, Y. H. Jang, J. Lee, S. Park, H.-Y. Yu, B. Shin, S. Lee, and J.-H. Park, "Extremely Low Contact Resistance on Graphene through n-Type Doping and Edge Contact Design," *Advanced Materials*, vol. 28, no. 5, pp. 864–870, 2016.

[197] J. T. Smith, A. D. Franklin, D. B. Farmer, and C. D. Dimitrakopoulos, "Reducing Contact Resistance in Graphene Devices through Contact Area Patterning," *ACS Nano*, vol. 7, no. 4, pp. 3661–3667, 2013.

[198] D. W. Yue, C. H. Ra, X. C. Liu, D. Y. Lee, and W. J. Yoo, "Edge contacts of graphene formed by using a controlled plasma treatment," *Nanoscale*, vol. 7, no. 2, pp. 825–831, 2015.

[199] F. N. Hooge, "1/f noise," *Physica B+C*, vol. 83, no. 1, pp. 14–23, 1976.

[200] E. Milotti, "1/f noise: a pedagogical review," *arXiv:physics*, 2002.

[201] A. A. Balandin, "Low-frequency 1/f noise in graphene devices," *Nature Nanotechnology*, vol. 8, no. 8, pp. 549–555, 2013.

[202] A. P. Dmitriev, M. E. Levinshtein, and S. L. Rumyantsev, "On the Hooge relation in semiconductors and metals," *Journal of Applied Physics*, vol. 106, no. 2, p. 024514, 2009.

[203] M. Lax, "Fluctuations from the nonequilibrium steady state," *Reviews of Modern Physics*, vol. 32, no. 1, pp. 25–64, 1960.

[204] D. Khodagholy, J. N. Gelinas, Z. Zhao, M. Yeh, M. Long, J. D. Greenlee, W. Doyle, O. Devinsky, and G. Buzsáki, "Organic electronics for high-resolution electrocorticography of the human brain," *Science Advances*, vol. 2, no. 11, p. e1601027, 2016.

[205] F. Schwierz, "Graphene transistors," *Nature Nanotechnology*, vol. 5, pp. 487–496, 2010.

[206] F. Yavari and N. Koratkar, "Graphene-based chemical sensors," *Journal of Physical Chemistry Letters*, vol. 3, no. 13, pp. 1746–1753, 2012.

[207] F. Bonaccorso, Z. Sun, T. Hasan, and A. C. Ferrari, "Graphene photonics and optoelectronics," *Nature Photonics*, vol. 4, no. 9, pp. 611–622, 2010.

[208] G. Liu, S. Rumyantsev, M. S. Shur, and A. A. Balandin, "Origin of 1/f noise in graphene multilayers: Surface vs. volume," *Applied Physics Letters*, vol. 102, no. 9, p. 093111, 2013.

[209] I. Heller, S. Chatoor, J. Männik, M. A. G. Zevenbergen, J. B. Oostinga, A. F. Morpurgo, C. Dekker, and S. G. Lemay, "Charge Noise in Graphene Transistors," *Nano Letters*, vol. 10, no. 5, pp. 1563–1567, 2010.

[210] P. Karnatak, T. P. Sai, S. Goswami, S. Ghatak, S. Kaushal, and A. Ghosh,

"Current crowding mediated large contact noise in graphene field-effect transistors," *Nature Communications*, vol. 7, no. 1, pp. 1–8, 2016.

[211] G. Ghibaudo, "On the theory of carrier number fluctuations in MOS devices," *Solid State Electronics*, vol. 32, no. 7, pp. 563–565, 1989.

[212] W. Wang, J. L. Collinger, A. D. Degenhart, E. C. Tyler-Kabara, A. B. Schwartz, D. W. Moran, D. J. Weber, B. Wodlinger, R. K. Vinjamuri, R. C. Ashmore, J. W. Kelly, and M. L. Boninger, "An Electrocorticographic Brain Interface in an Individual with Tetraplegia," *PLoS ONE*, vol. 8, no. 2, p. e55344, 2013.

[213] N. Mavredakis, R. Garcia Cortadella, A. Bonaccini Calia, J. A. Garrido, and D. Jiménez, "Understanding the bias dependence of low frequency noise in single layer graphene FETs," *Nanoscale*, vol. 10, no. 31, pp. 14947–14956, 2018.

[214] N. Schaefer, R. Garcia-Cortadella, A. B. Calia, N. Mavredakis, X. Illa, E. Masvidal-Codina, J. de la Cruz, E. del Corro, L. Rodríguez, E. Prats-Alfonso, J. Bousquet, J. Martínez-Aguilar, A. P. Pérez-Marín, C. Hébert, R. Villa, D. Jiménez, A. Guimerà-Brunet, and J. A. Garrido, "Improved metal-graphene contacts for low-noise, high-density microtransistor arrays for neural sensing," *Carbon*, vol. 161, pp. 647–655, 2020.

[215] G. Liu, W. Stillman, S. Rumyantsev, Q. Shao, M. Shur, and A. A. Balandin, "Low-frequency electronic noise in the double-gate single-layer graphene transistors," *Appl. Phys. Lett*, vol. 95, p. 33103, 2009.

[216] G. Xu, C. M. Torres, Y. Zhang, F. Liu, E. B. Song, M. Wang, Y. Zhou, C. Zeng, and K. L. Wang, "Effect of Spatial Charge Inhomogeneity on 1/f Noise Behavior in Graphene," *Nano Letters*, vol. 10, no. 9, pp. 3312–3317, 2010.

[217] F. Hooge, "1/f Noise Sources," in *Advanced Experimental Methods For Noise Research in Nanoscale Electronic Devices*, pp. 3–10, Kluwer Academic Publishers, 2006.

[218] S. Drieschner, A. Guimerà, R. G. Cortadella, D. Viana, E. Makrygiannis, B. M. Blaschke, J. Vieten, and J. A. Garrido, "Frequency response of electrolyte-gated graphene electrodes and transistors," *Journal of Physics D: Applied Physics*, vol. 50, no. 9, p. 095304, 2017.

[219] S. Takeshita, S. Matsuo, T. Tanaka, S. Nakaharai, K. Tsukagoshi, T. Moriyama, T. Ono, T. Arakawa, and K. Kobayashi, "Anomalous behavior of 1/f noise in graphene near the charge neutrality point," *Appl. Phys. Lett*, vol. 108, p. 103106, 2016.

[220] S. Samaddar, I. Yudhistira, S. Adam, H. Courtois, and C. B. Winkelmann,

"Charge Puddles in Graphene near the Dirac Point," *Physical Review Letters*, vol. 116, no. 12, p. 126804, 2016.

[221] C. Enz and E. Vittoz, *Charge-Based MOS Transistor Modeling: The EKV Model for Low-Power and RF IC Design.* John Wiley & Sons, Ltd, 2006.

[222] E. Masvidal-Codina, X. Illa, M. Dasilva, A. B. Calia, T. Dragojević, E. E. Vidal-Rosas, E. Prats-Alfonso, J. Martínez-Aguilar, J. M. De la Cruz, R. Garcia-Cortadella, P. Godignon, G. Rius, A. Camassa, E. Del Corro, J. Bousquet, C. Hébert, T. Durduran, R. Villa, M. V. Sanchez-Vives, J. A. Garrido, and A. Guimerà-Brunet, "High-resolution mapping of infraslow cortical brain activity enabled by graphene microtransistors," *Nature Materials*, vol. 18, no. 3, pp. 280–288, 2019.

[223] S. Rodriguez, A. Smith, S. Vaziri, M. Ostling, M. C. Lemme, and A. Rusu, "Static Non-linearity in Graphene Field Effect Transistors," *IEEE Transactions on Electron Devices*, vol. 61, no. 8, pp. 3001–3003, 2014.

[224] R. Garcia-Cortadella, E. Masvidal-Codina, J. M. De la Cruz, N. Schäfer, G. Schwesig, C. Jeschke, J. Martinez-Aguilar, M. V. Sanchez-Vives, R. Villa, X. Illa, A. Sirota, A. Guimerà, and J. A. Garrido, "Distortion-Free Sensing of Neural Activity Using Graphene Transistors," *Small*, vol. 16, no. 16, p. 1906640, 2020.

[225] H. Wang, Y. Wu, C. Cong, J. Shang, and T. Yu, "Hysteresis of Electronic Transport in Graphene Transistors," *ACS Nano*, vol. 4, no. 12, pp. 7221–7228, 2010.

[226] M. Winters, E. Ö. Sveinbjörnsson, and N. Rorsman, "Hysteresis modeling in graphene field effect transistors," *Journal of Applied Physics*, vol. 117, no. 7, p. 074501, 2015.

[227] C. Mackin, E. McVay, T. Palacios, C. Mackin, E. McVay, and T. Palacios, "Frequency Response of Graphene Electrolyte-Gated Field-Effect Transistors," *Sensors*, vol. 18, no. 2, p. 494, 2018.

[228] E. Barsoukov and J. R. Macdonald, *Impedance Spectroscopy.* Hoboken, NJ, USA: John Wiley & Sons, Inc., 2005.

[229] J. Sun and Y. Liu, "Unique Constant Phase Element Behavior of the Electrolyte–Graphene Interface," *Nanomaterials*, vol. 9, no. 7, p. 923, 2019.

[230] J. E. Lee, G. Ahn, J. Shim, Y. S. Lee, and S. Ryu, "Optical separation of mechanical strain from charge doping in graphene," *Nature Communications*, vol. 3, no. 1, pp. 1–8, 2012.

[231] E. F. Chang, "Towards large-scale, human-based, mesoscopic neurotechnologies.," *Neuron*, vol. 86, no. 1, pp. 68–78, 2015.

[232] N. Mavredakis, R. G. Cortadella, X. Illa, N. Schaefer, A. B. Calia, Anton-Guimerà-Brunet, J. A. Garrido, and D. Jiménez, "Bias dependent variability of low-frequency noise in single-layer graphene FETs," *Nanoscale Advances*, vol. 2, no. 11, pp. 5450–5460, 2020.

[233] B. J. W. Shlesinger and Michael, "The Noise in Natural Phenomena," *American Scientist*, vol. 78, no. 1, pp. 40–45, 1990.

[234] R. Garcia-Cortadella, G. Schwesig, C. Jeschke, X. Illa, A. L. Gray, S. Savage, E. Stamatidou, I. Schiessl, E. Masvidal-Codina, K. Kostarelos, A. Guimerà-Brunet, A. Sirota, and J. A. Garrido, "Graphene active sensor arrays for long-term and wireless mapping of wide frequency band epicortical brain activity," *Nature Communications*, vol. 12, no. 1, pp. 1–17, 2021.

[235] A. Oustaloup, F. Levron, B. Mathieu, and F. Nanot, "Frequency-band complex noninteger differentiator: characterization and synthesis," *IEEE Transactions on Circuits and Systems I: Fundamental Theory and Applications*, vol. 47, no. 1, pp. 25–39, 2000.

[236] A. Mitra, A. Kraft, P. Wright, B. Acland, A. Z. Snyder, Z. Rosenthal, L. Czerniewski, A. Bauer, L. Snyder, J. Culver, J. M. Lee, and M. E. Raichle, "Spontaneous Infra-slow Brain Activity Has Unique Spatiotemporal Dynamics and Laminar Structure," *Neuron*, vol. 98, no. 2, pp. 297–305.e6, 2018.

[237] A. Mitra, A. Z. Snyder, E. Tagliazucchi, H. Laufs, and M. E. Raichle, "Propagated infra-slow intrinsic brain activity reorganizes across wake and slow wave sleep," *eLife*, vol. 4, p. 10781, 2015.

[238] J. K. Grooms, G. J. Thompson, W. J. Pan, J. Billings, E. H. Schumacher, C. M. Epstein, and S. D. Keilholz, "Infraslow Electroencephalographic and Dynamic Resting State Network Activity," *Brain Connectivity*, vol. 7, no. 5, pp. 265–280, 2017.

[239] A. C. Kelly, L. Q. Uddin, B. B. Biswal, F. X. Castellanos, and M. P. Milham, "Competition between functional brain networks mediates behavioral variability," *NeuroImage*, vol. 39, no. 1, pp. 527–537, 2008.

[240] A. Kandel and G. Buzséki, "Cellular-synaptic generation of sleep spindles, spike-and-wave discharges, and evoked thalamocortical responses in the neocortex of the rat," *Journal of Neuroscience*, vol. 17, no. 17, pp. 6783–6797, 1997.

[241] A. Kandel and G. Buzsáki, "Cerebellar neuronal activity correlates with spike and wave EEG patterns in the rat," *Epilepsy Research*, vol. 16, no. 1, pp. 1–9, 1993.

[242] R. Stephenson, J. Lim, S. Famina, A. M. Caron, and H. B. Dowse, "Sleep-wake behavior in the rat: Ultradian rhythms in a light-dark cycle and continuous bright light," *Journal of Biological Rhythms*, vol. 27, no. 6, pp. 490–501, 2012.

[243] A. W. Chan, M. H. Mohajerani, J. M. LeDue, Y. T. Wang, and T. H. Murphy, "Mesoscale infraslow spontaneous membrane potential fluctuations recapitulate high-frequency activity cortical motifs," *Nature Communications*, vol. 6, 2015.

[244] J. Cisneros-Fernández, A. Guimerà-Brunet, R. Garcia-Cortadella, N. Schäfer, J. A. Garrido, L. Terés, and F. Serra-Graells, "A 1024-Channel GFET 10-bit 5-kHz 36-uW Read-Out Integrated Circuit for Brain uECoG," in *27th IEEE International Conference on Electronics, Circuits & Systems*, 2020.

[245] R. Garcia-Cortadella, N. Schäfer, J. Cisneros-Fernandez, L. Re, X. Illa, G. Schwesig, A. Moya, S. Santiago, G. Guirado, R. Villa, A. Sirota, F. Serra-Graells, J. A. Garrido, and A. Guimerà-Brunet, "Switchless Multiplexing of Graphene Active Sensor Arrays for Brain Mapping," *Nano Letters*, vol. 20, no. 5, pp. 3528–3537, 2020.

[246] J. W. Valvano, J. R. Cochran, and K. R. Diller, "Thermal conductivity and diffusivity of biomaterials measured with self-heated thermistors," *International Journal of Thermophysics*, vol. 6, no. 3, pp. 301–311, 1985.

[247] S. F. Owen, M. H. Liu, and A. C. Kreitzer, "Thermal constraints on in vivo optogenetic manipulations," *Nature Neuroscience*, vol. 22, no. 7, pp. 1061–1065, 2019.

[248] M. D. Fox and M. E. Raichle, "Spontaneous fluctuations in brain activity observed with functional magnetic resonance imaging," *Nature Reviews Neuroscience*, vol. 8, no. 9, pp. 700–711, 2007.

[249] H. Lu, S. Jaime, and Y. Yang, "Origins of the Resting-State Functional MRI Signal: Potential Limitations of the "Neurocentric" Model," *Frontiers in Neuroscience*, vol. 13, no. 1136, p. 23, 2019.

[250] P. J. Drew, "Vascular and neural basis of the BOLD signal," *Current Opinion in Neurobiology*, vol. 58, pp. 61–69, 2019.

[251] S.-G. Kim and S. Ogawa, "Biophysical and physiological origins of blood oxygenation level-dependent fMRI signals," *Journal of Cerebral Blood Flow & Metabolism*, vol. 32, no. 7, pp. 1188–1206, 2012.

[252] N. K. Logothetis, J. Pauls, M. Augath, T. Trinath, and A. Oeltermann, "Neurophysiological investigation of the basis of the fMRI signal," *Nature*, vol. 412, no. 6843, pp. 150–157, 2001.

[253] R. Scheeringa, P. Fries, K. M. Petersson, R. Oostenveld, I. Grothe, D. G. Norris, P. Hagoort, and M. C. Bastiaansen, "Neuronal Dynamics Underlying High- and Low-Frequency EEG Oscillations Contribute Independently to the Human BOLD Signal," *Neuron*, vol. 69, no. 3, pp. 572–583, 2011.

[254] R. Scheeringa and P. Fries, "Cortical layers, rhythms and BOLD signals," *NeuroImage*, vol. 197, pp. 689–698, 2019.

[255] J. Niessing, B. Ebisch, K. E. Schmidt, M. Niessing, W. Singer, and R. A. Galuske, "Neuroscience: Hemodynamic signals correlate tightly with synchronized gamma oscillations," *Science*, vol. 309, no. 5736, pp. 948–951, 2005.

[256] G. P. Krishnan, O. C. González, and M. Bazhenov, "Origin of slow spontaneous resting-state neuronal fluctuations in brain networks," *Proceedings of the National Academy of Sciences*, vol. 115, no. 26, pp. 6858–6863, 2018.

[257] E. A. Buffalo, P. Fries, R. Landman, T. J. Buschman, and R. Desimone, "Laminar differences in gamma and alpha coherence in the ventral stream," *Proceedings of the National Academy of Sciences*, vol. 108, no. 27, pp. 11262–11267, 2011.

[258] Y. Senzai, A. Fernandez-Ruiz, and G. Buzsáki, "Layer-Specific Physiological Features and Interlaminar Interactions in the Primary Visual Cortex of the Mouse," *Neuron*, vol. 101, no. 3, pp. 500–513.e5, 2019.

[259] A. Guimera-Brunet, L. Re Blanco, E. Masvidal-Codina, R. Villa Sanz, X. Illa Vila, J. A. Garrido Ariza, N. Schaefer, and R. Garcia-Cortadella, "Acquisition device to limit the leakage curren in electrophysiological signal recording devices," 2020.

[260] J. Cisneros-Fernandez, M. Dei, L. Teres, and F. Serra-Graells, "Switch-Less Frequency-Domain Multiplexing of GFET Sensors and Low-Power CMOS Frontend for 1024-Channel μECoG," in *2019 IEEE International Symposium on Circuits and Systems (ISCAS)*, pp. 1–5, IEEE, 2019.

[261] B. Rubehn and T. Stieglitz, "In vitro evaluation of the long-term stability of polyimide as a material for neural implants," *Biomaterials*, vol. 31, no. 13, pp. 3449–3458, 2010.

[262] C. Hassler, T. Boretius, and T. Stieglitz, "Polymers for neural implants," *Journal of Polymer Science Part B: Polymer Physics*, vol. 49, no. 1, pp. 18–33, 2011.

[263] J. S. Ordonez, C. Boehler, M. Schuettler, and T. Stieglitz, "Improved polyimide thin-film electrodes for neural implants," in *Proceedings of the Annual International Conference of the IEEE Engineering in Medicine and Biology Society, EMBS*, vol. 2012, pp. 5134–5137, Annu Int Conf IEEE Eng Med Biol Soc, 2012.

Chapter 6

Appendix A: main articles

Contents

FULL PAPER

Distortion-Free Sensing of Neural Activity Using Graphene Transistors

Ramon Garcia-Cortadella, Eduard Masvidal-Codina, Jose M. De la Cruz, Nathan Schäfer, Gerrit Schwesig, Christoph Jeschke, Javier Martinez-Aguilar, Maria V. Sanchez-Vives, Rosa Villa, Xavi Illa, Anton Sirota, Anton Guimerà, and Jose A. Garrido*

Graphene solution-gated field-effect transistors (g-SGFETs) are promising sensing devices to transduce electrochemical potential signals in an electrolyte bath. However, distortion mechanisms in g-SGFET, which can affect signals of large amplitude or high frequency, have not been evaluated. Here, a detailed characterization and modeling of the harmonic distortion and non-ideal frequency response in g-SGFETs is presented. This accurate description of the input–output relation of the g-SGFETs allows to define the voltage- and frequency-dependent transfer functions, which can be used to correct distortions in the transduced signals. The effect of signal distortion and its subsequent calibration are shown for different types of electrophysiological signals, spanning from large amplitude and low frequency cortical spreading depression events to low amplitude and high frequency action potentials. The thorough description of the distortion mechanisms presented in this article demonstrates that g-SGFETs can be used as distortion-free signal transducers not only for neural sensing, but also for a broader range of applications in which g-SGFET sensors are used.

1. Introduction

Graphene has attracted much attention for its application on sensing due to its high carrier mobility,[1] chemical stability,[2] high stretchability,[3] and transparency.[3–5] Many applications have been explored, and more are under study, in which active graphene sensors are used to transduce the physical property of

interest into an electrical signal. Prominent examples include biochemical sensors,[6–8] gas sensors,[9,10] pH sensors,[11,12] ion sensors,[13] or transducers of electrical potential for neural interfaces.[14–17] The latter, has recently attracted increasing attention due to the potential of graphene solution-gated field-effect transistors (g-SGFETs) to record infra-slow[18] brain activity with a high spatial resolution.[19] This capability opens the door to full-band neural activity sensing from large amplitude infra-slow oscillations to small amplitude but faster signals such as local field potentials (LFPs) or action potentials (APs).

In g-SGFETs, the graphene channel is in contact with an electrolyte, which comprises the gate of the g-SGFET (see **Figure 1**a). The electrochemical potential in the electrolyte can therefore be regarded as the gate-to-source voltage (V_{gs}), which couples with the channel through the graphene–electrolyte interface capacitance (C_{int}).[20,21] The electric field at the interface produces a change in the number of charge carriers in the graphene channel and therefore a variation in the drain-to-source current ($I_{ds–sig}$) for a constant drain-to-source bias (V_{ds}). These current changes are proportional to the signal at the gate ($V_{gs–sig}$) and to the transconductance (G_m) (see Figure 1b),

R. Garcia-Cortadella, J. M. De la Cruz, N. Schäfer, Prof. J. A. Garrido
Catalan Institute of Nanoscience and Nanotechnology (ICN2)
CSIC and BIST
Campus UAB, Bellaterra, Barcelona 08193, Spain
E-mail: joseantonio.garrido@icn2.cat
E. Masvidal-Codina, J. Martinez-Aguilar, Dr. R. Villa,
Dr. X. Illa, Dr. A. Guimerà
Instituto de Microelectrónica de Barcelona
IMB-CNM (CSIC)
Esfera UAB, Bellaterra 08193, Spain
G. Schwesig, Prof. A. Sirota
Bernstein Center for Computational Neuroscience Munich
Munich Cluster of Systems Neurology (SyNergy)
Faculty of Medicine
Ludwig-Maximilians Universität München
Planegg-Martinsried 82152, Germany

The ORCID identification number(s) for the author(s) of this article can be found under https://doi.org/10.1002/smll.201906640.

DOI: 10.1002/smll.201906640

C. Jeschke
Multi Channel Systems (MCS) GmbH
Reutlingen 72770, Germany

J. Martinez-Aguilar, Dr. R. Villa, Dr. X. Illa, Dr. A. Guimerà
Centro de Investigación Biomédica en Red en Bioingeniería
Biomateriales y Nanomedicina (CIBER-BBN)
Madrid 50018, Spain

Prof. M. V. Sanchez-Vives
Institut d'Investigacions Biomèdiques August Pi i Sunyer (IDIBAPS)
Barcelona 08036, Spain

Prof. M. V. Sanchez-Vives, Prof. J. A. Garrido
ICREA
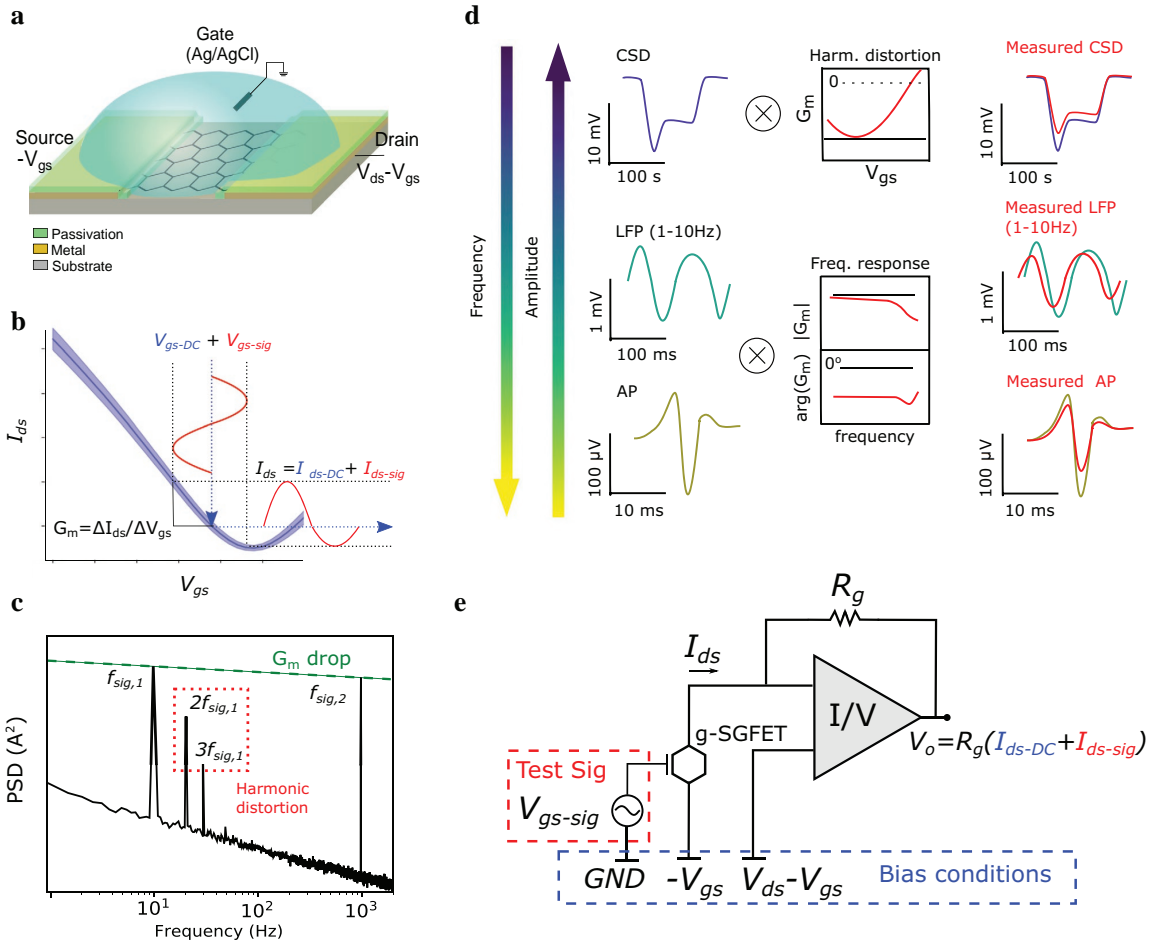Pg. Lluís Companys 23, Barcelona 08010, Spain

135

Figure 1. a) Drawing of a g-SGFET showing the graphene channel, metal contacts, SU8 passivation, electrolyte gate, and reference electrode together with the applied bias. b) Typical transfer characteristics of a g-SGFET. G_m is indicated as $\Delta I_{ds}/\Delta V_{gs}$. c) Typical PSD of the distorted output signal of a g-SGFET. The two tones $f_{sig,1} = 10$ Hz and $f_{sig,2} = 1$ kHz illustrate the effect of transconductance attenuation at higher frequencies. The effect of harmonic distortion on the 10 Hz signal results in the appearance of the harmonic components at $f = 2f_{sig}$ and $3f_{sig}$. d) Representation of a typical CSD event, LFP in the 1–10 Hz band and an AP. The original electrophysiological signal is multiplied by the G_m of the device which might present a V_{gs} dependence (centre-top), producing harmonic distortion shown in red (top-right), or a non-ideal frequency response (center-bottom), producing frequency response distortion of the detected signals. e) Circuit diagram of the custom built electronic setup used for the characterization of g-SGFETs and recording of electrophysiological activity. The reference electrode is set at ground (GND), $-V_{gs}$ is applied between gate and source and $V_{ds}-V_{gs}$ between gate and drain. The current I_{ds} is preamplified by the current-to-voltage converter (I/V).

which represents the input-output relation of the g-SGFET, also referred to as its transfer function. The G_m in g-SGFETs is, in a first approximation, proportional to the electrical mobility of graphene and C_{int} per unit area;[22] therefore presenting no dependence on the area of the active channel. This is the main cause for the improved sensitivity of g-SGFETs in the infra-slow frequency band in comparison with conventional micro-electrodes.[23]

Despite the great potential of g-SGFETs for full-band neural activity monitoring and other applications in sensing, the signal distortion introduced by these transducers remains a key aspect, which has been so far largely underestimated. Signal distortion can appear in any amplifying system due to several reasons,

including voltage-dependent gain, which leads to harmonic distortion, frequency-dependent gain that leads to different amplification of various frequency components and phase distortion due to a non-null imaginary part of the gain. In the specific case of the g-SGFET, a voltage or frequency dependence of G_m will lead to signal distortion. In the first place, non-linearities in the I_{ds}–V_{gs} curves, lead to a dependence with V_{gs} and therefore to harmonic distortion of the signal (see Figure 1b,c). The amplitude of the harmonics introduced can ideally be derived from the Taylor expansion of the I_{ds}–V_{gs} curves. This description has been previously presented and evaluated for a graphene field-effect transistor (GFET) analytical model.[24] However, theoretically predicted parameters have never been compared

to experimentally measured distortion levels in GFETs. Validating the relation between non-linearities in the I_{ds}–V_{gs} curves and harmonic distortion is critical to understand and mitigate its effect on the sensing capabilities of g-SGFETs. On the other hand, the transfer function or G_m also shows a dependence with the signal frequency (f_{sig}), as illustrated in Figure 1c, and a non-null imaginary part, introducing frequency response distortion. A detailed characterization of the frequency response is the first step toward the derivation of a complete analytical transfer function to describe the distortions introduced by a non-ideal frequency response in g-SGFETs.

While harmonic distortion is expected to affect more strongly signals of large amplitude, the frequency response is expected to affect more prominently signals with higher frequency components. Due to the wide range of amplitudes and frequencies found in sensing of full-band neural activity, this application is expected to be particularly sensitive to signal distortion. To show the impact of non-ideal response on the sensing capabilities of g-SGFETs, we have measured full-band electrophysiological activity on the rat cortex and in a cell culture. Figure 1d illustrates the effect of distortion on the different signals measured, from large amplitude and low frequency cortical spreading depression (CSD) events (Figure 1d-top) to high frequency and low amplitude APs (Figure 1d-bottom). In order to recover the equivalent signal at the gate ($V_{gs–sig}$), the measured $I_{ds–sig}$ has to be calibrated by using the inverse of the transfer function. If voltage and frequency dependence of the transfer function, as well as its imaginary part are taken into account, the inverse transfer function will correct the distortions in the output signal, leading to the distortion-free input signal. In order to anticipate changes in the transfer function of the g-SGFET under different conditions and prevent defective calibration, the phenomena involved in signal distortion must be properly understood.

The characterization and modeling of the g-SGFET response reported in this work comprises an important step toward the mitigation of signal distortion in g-SGFETs. On the one hand, the theoretical understanding provided, represents a solid basis for the improvement of the linearity and frequency dependence of the g-SGFET response. On the other hand, the calibration procedure presented represents a method for the acquisition of quasi-distortion-free signals using g-SGFET transducers, with special potential for the sensing of full-band neural activity.

2. Results and Discussion

In this section, the characterization of harmonic distortion and frequency response of g-SGFETs is presented. The measurements have been performed using g-SGFETs on a flexible polyimide substrate (see Experimental Section for details on the fabrication procedure). The devices have been immersed in a phosphate buffered solution (PBS) bath and the gate bias has been applied using an Ag/AgCl reference electrode. The stationary response of the g-SGFETs ($I_{ds–DC}$) and their dynamic response ($I_{ds–sig}$) have been characterized under different V_{gs} bias conditions (see Figure 1e). The quasi-DC current and the alternating current signals have been decoupled in order to adapt their dynamic range to fill the full scale of the analog-to-digital converters (see Experimental Section for more details).

2.1. Characterization of Harmonic Distortion

Harmonic distortion, caused by the voltage dependence of the transfer function in g-SGFET is the result of non-linearities in the I_{ds}–V_{gs} curves. Ideally, GFETs present a particularly linear I_{ds}–V_{gs} relation around their conduction minimum,[25] also referred to as the charge neutrality point (CNP). However, there are various factors that can introduce non-linearities in the response of GFETs.[22] For instance, the resistance between the metal contacts and the graphene channel limits the conductance of the transistor, which can eventually result in a curved I_{ds}–V_{gs} relation away from the CNP. On the other hand, the conductance minimum at the CNP should ideally be perfectly sharp, only limited by thermal fluctuations of charge carriers. However, any inhomogenous doping of the graphene channel, for instance, due to substrate inhomogeneities, can lead to a broadening of the CNP.[26]

Harmonic distortion is commonly characterized by applying test signal and measuring the higher order harmonics generated by signal distortion. In Figure 1c, harmonic distortion is represented in the frequency domain where harmonics at frequencies multiple of f_{sig} can be distinguished. In this section, the harmonic distortion introduced by the g-SGFETs is experimentally determined following this methodology, that is, applying a pure tone signal at the gate ($V_{gs–sig}$) and measuring the amplitude of higher order harmonics. Besides, harmonic distortion is also calculated from the Taylor expansion of the stationary I_{ds}–V_{gs} curves. The 0th order term of the Taylor expansion corresponds to the DC current $I_{ds–DC}$ and the 1st order term represents the linear conversion of the signal at the gate. The 2nd and 3rd order terms of the Taylor expansion represent the 2nd and 3rd order harmonics produced by the curvature and changes in the curvature of the I_{ds} versus V_{gs} curves respectively. Comparing the harmonic distortion levels obtained following these two approaches can be used to validate the stationary description of harmonic distortion, which is critical to correct harmonic distortion in a calibration process.

In **Figure 2**a,b, this comparison is shown for signals of different amplitudes (A_{sig} = 2, 4, and 8 mV$_{rms}$) in a wide V_{gs} range for a frequency of 10 Hz. An excellent agreement between the measured and calculated values is shown for the 1st and 2nd order harmonics in the whole V_{gs} and A_{sig} range. For the 3rd order harmonic this validation is only shown for the A_{sig} = 8 mV_{rms} due to the contribution from the 1/f noise of the g-SGFET, which masks the low amplitude 3rd harmonic for small A_{sig} values (see Figure 2b and Supporting Information S1).

Once we have validated the calculation of harmonic distortion by the Taylor expansion of the I_{ds}–V_{gs} curves, it is possible to calculate the signal-to-distortion ratio (SDR) (i.e., the 1st order harmonic amplitude over the sum of 2nd and 3rd order harmonics) for any combination of A_{sig} and V_{gs} bias conditions (see Figure 2c). The SDR is a figure of merit that can be used to evaluate the impact of distortion on the signal quality. The SDR presents a maximum at V_{gs}–$V_{CNP} \approx \pm100$ mV, where the
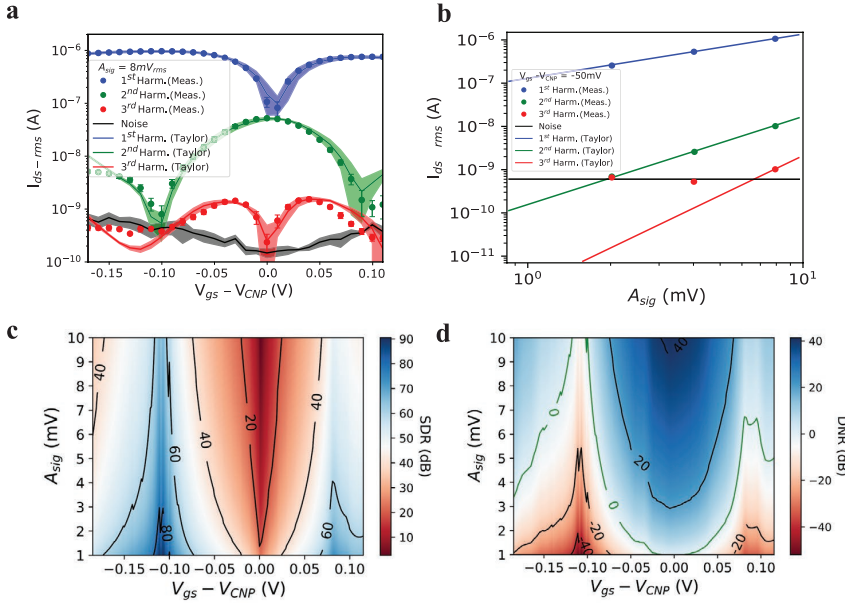
Figure 2. a) 1st, 2nd, and 3rd harmonics rms-amplitude extracted from the power spectrum of the measured I_{ds} (dots) and from the Taylor expansion of the transfer characteristics (solid lines). Error bars and filled areas show the standard deviation (for 4 g-SGEFTs). The noise is evaluated from the power spectrum at 28 Hz (i.e., slightly below $3f_{sig}$). The measured and calculated harmonics correspond to a 10 Hz signal with an amplitude of 8 mV_{rms}. b) The harmonics obtained experimentally for different signal amplitudes (2, 4, and 8 mV_{rms}) are displayed (dots) together with the calculated values derived from the Taylor expansion. The standard deviation of the measured data with for 4 g-SGEFTs is smaller than the radius of the dots used to display the data. The data was evaluated at $V_{gs}-V_{CNP} = -0.05$ V. c) Evaluation of SDR (in dB) in the A_{gs}–V_{gs} parameter map. The solid lines indicate the contour lines of the SDR every 20 dBs. d) Distortion-to-noise ratio (in dB) and the contour lines represented by solid lines every 20 dBs. The maps in (c,d) are calculated using the Taylor expansion of the stationary I_{ds}–V_{gs} curves.

linearity of the I_{ds}–V_{gs} curve is maximal. The SDR exhibits a minimum close to the CNP due to the abrupt drop of transconductance and the increase of the 2nd order harmonic amplitude. Besides, Figure 2c also reveals that the SDR increases with decreasing A_{sig} values. This dependence is explained by the linear, quadratic, and cubic relationship of the 1st, 2nd and 3rd order harmonics, respectively with A_{sig} (see Supporting Information S1). Another useful way to represent the impact of the harmonic distortion on the signal quality is to compare it to the intrinsic $1/f$ noise of the g-SGFET, which is usually considered to limit the signal quality in g-SGFETs.[14,27] Figure 2d shows the distortion-to-noise ratio (DNR) for the noise integrated in a one-decade frequency band (i.e., 4–40 Hz). The DNR presents its minimum at $V_{gs}-V_{CNP} \approx \pm 100$ mV, its maximum at the CNP and it decreases, as expected, with A_{sig}. The 0 dB contour line indicates the parameters for which distortion and noise will contribute with the same power to the degradation of signal quality (see Supporting Information S1 for more details). These results highlight the importance of choosing a right gate bias to minimize the impact of harmonic distortion on the signal quality, especially for large amplitude signals. The methodology followed here for the validation of the stationary model of harmonic distortion in g-SGFETs could be extended to other types of GFET based devices. The SDR and DNR maps can be applied

to other sensor types by a proper rescaling the V_{gs} and A_{sig} axes. The V_{gs} axis can be rescaled by the ratio between the gate capacitance of any sensor and the graphene–electrolyte interface capacitance of the devices reported here.[20] The A_{sig} axis can also be rescaled in the same manner for any GFET-based device in which a small voltage signal applied at the gate is detected.

2.2. Characterization and Modeling of the Frequency Response

In addition to harmonic distortion, non-idealities in the frequency response can also limit the recording capabilities of g-SGFETs. Deviations from a frequency-independent transconductance might appear due to for instance a slow charging of the graphene–electrolyte interface capacitance or a slow filling and depletion of trap states in the graphene environment.[28,29] In addition, displacement currents through parasitic capacitances at the graphene–electrolyte interface can also result in the attenuation of the signal.[30] Here, we have characterized the frequency dependence of the magnitude and phase of the g-SGFETs transfer function. The aim of this section is to propose and validate an equivalent circuit and its analytic transfer function, which fully describes the frequency response of the g-SGFETs in a wide range of signal frequencies and under different experimental conditions. Having such a complete model, a calibration method could be proposed to correct signal distortions introduced by the frequency response of g-SGFETs.

For this purpose, the response of g-SGFETs to input signals ranging from 0.4 Hz to 200 kHz has been measured (see Experimental Section for more details). This characterization has been performed for different electrolyte concentrations in order to show the effect that changing the electrolyte (e.g., to physiological medium) could cause on the frequency response. **Figure 3**a shows the experimentally-obtained module and phase of the transfer function (Bode diagram) compared with the G_m extracted from the stationary I_{ds}–V_{gs} curves. The Bode diagrams in Figure 3a correspond to the frequency response in a bath with two different ionic concentrations. Apart from the stationary response, they present three regimes of frequency response, each of them represented by a colored region. The 0.4 Hz to 3 kHz range corresponds to a regime characterized by a slight attenuation of the transconductance with an approximately constant slope (in log-scale) and an approximately
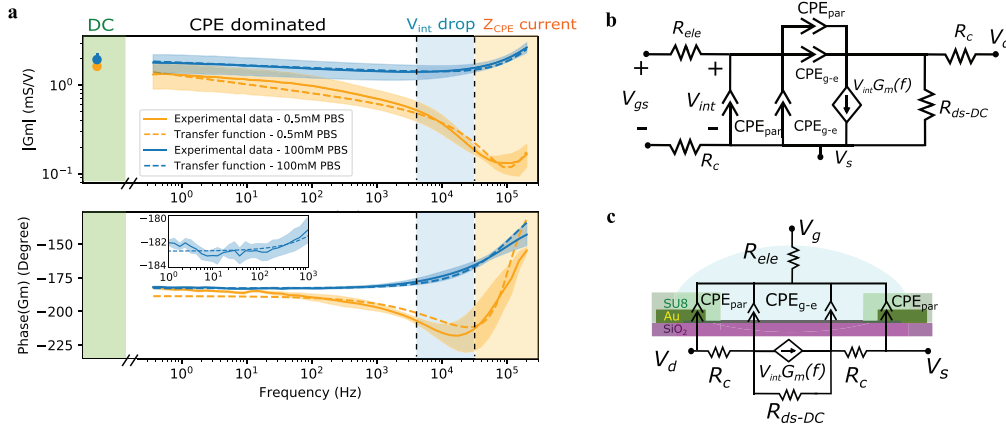
Figure 3. a) Bode diagram of g-SGFETs (for 4 g-SGEFTs). Three different response regimes are displayed together with the G_m extracted from the DC characteristics: CPE dominated regime, a regime where the G_m drops with approximately $1/f$ and finally a G_m increase due to capacitive currents. b) Small signal model of the g-SGFET frequency response. The gate-to-source bias bias (V_{gs}) and the drain voltage (V_d) are defined. The voltage drop at the graphene–electrolyte interface is defined as V_{int}. The CPE_{g-e} represents the constant phase element (CPE) describing the non-ideal capacitive behavior of the graphene–electrolyte interface. The CPE describing the leakage through parasitic elements is defined as CPE_{par}. The resistance of the electrolyte (R_{ele}) and the contact resistance of the g-SGFET (R_c) are defined. The dynamic response of the g-SGFET is modelled by the current source ($V_{int}G_m(f)$) and its stationary response is modelled by the resistance in parallel R_{ds-DC}. c) The equivalent circuit shown is drawn on a schematic of the g-SGFET to illustrate the physical origin of each element.

constant phase deviating few degrees from 180° (expected in the holes conduction regime). In the 3–40 kHz range, another regime can be observed, in this case only for the low ionic concentration experiment, which consists of an abrupt attenuation of the gain with frequency ($\approx 1/f$). The attenuation in magnitude goes along with a negative shift of the phase. Finally, a high frequency regime (above 40 kHz) is characterized by an increase of both the magnitude and phase of the transconductance.

Having identified these three regimes of frequency response, it is now possible to propose a small signal model of the g-SGFET (see Figure 3b,c). In the proposed equivalent circuit, the graphene–electrolyte interface is not modeled as an ideal capacitor, as done in standard models,[22] but instead as a constant phase element (CPE_{g-e}) which is commonly required to properly describe the response of a double-layer capacitance.[31,32] Although CPEs are often used in electrochemical impedance modeling, its physical origin is still a topic under discussion.[33,34] In the particular case of the graphene–electrolyte interface it has been previously reported in impedance measurements.[32] The equivalent circuit in Figure 3b,c also includes the resistance of the electrolyte R_{ele} and the contacts R_c in series with the graphene–electrolyte interface. The V_{gs} applied causes a voltage drop at the graphene–electrolyte interface (V_{int}) which is transduced by the g-SGFET. The conversion of AC signals at the gate is modeled by a current source element $V_{int}G_m(f)$ while the DC current flowing through the g-SGFET is modelled by the element R_{ds-DC}. Finally, an additional CPE, CPE_{par}, is added in parallel with CPE_{g-e} to account for parasitic capacitances in the device. Possible parasitic elements might originate in a capacitive coupling of the electrolyte with the metal lines in the device, caused by an excessively thin or defective passivation of the metal lines. Using this equivalent circuit, we can derive an analytic expression which describes the frequency dependent transfer function of the g-SGFET.

$$G_m\left(f\right) = \left.\frac{dI_{ds}}{dV_{int}}\right|_{V_{ds}} \frac{dV_{int}}{dV_{gs}} + G_{m,eff} \tag{1}$$

The first factor on the right hand side of Equation (1) corresponds to the intrinsic transconductance, and it presents a frequency dependence that results from the non-ideal capacitive behavior of the interface,[35] that is, $dI_{ds}/dV_{int}|_{V_{ds}} = kC_{CPE_{g-e}}(f)$ (see Supporting Information S2 for more details). The second factor in Equation (1) results from the contribution of the resistance in series (R_s) with the g-SGFET (i.e., R_c plus R_{ele}) and CPE_{par} in parallel with the transistor, which are responsible for the attenuation of the signal at the interface V_{int} with frequency[22] (see Supporting Information S2 and S3). The last term in Equation (1) has to be included to account for the measured increase of the transconductance at high frequencies. When a signal is applied at the gate, the CPE_{g-e} and CPE_{par} elements represent a direct current path between gate and the g-SGFET contacts. The impedance of these CPE elements characterizes this capacitive current, which adds-up to the drain-to-source current. This contribution is not result of the field-effect coupling, and can be therefore regarded as an effective transconductance (G_{meff}) term. Above a certain frequency, this capacitive contribution to the current measured at the drain is expected to dominate the frequency response, as shown in Figure 3a. The frequency dependence of the terms in Equation (1) can be expressed explicitly as shown in the Supporting Information S2.

Figure 3a shows the fitting of the experimentally obtained frequency response (magnitude and phase) with the transfer function derived using the equivalent circuit of Figure 3b (fitting parameters can be found in the Supporting Information S2). All the main features of the frequency response described previously are properly captured. The close match between experimental data and the derived $G_m(f)$ validates the proposed

equivalent circuit. The understanding of the frequency response provided by this model represents a strong basis for future improvements of the g-SGFET response (see Supporting Information S4). Furthermore, the derived transfer function can be used to set a calibration procedure to cancel signal distortions introduced by the non-ideal frequency response of the g-SGFETs.

2.3. Calibration of Harmonic Distortion Using the Non-Linear Stationary I_{ds}–V_{gs} Curve

We have previously discussed that harmonic distortion can degrade the signal quality significantly, especially for signals with large amplitudes and for not optimum gate bias conditions. Under these conditions, correction of the harmonic distortion by a proper calibration methodology can be critical. The conversion of measured signals in current (I_{ds-sig}) back to an equivalent voltage at the gate (V_{gs-sig}) is commonly done using a constant factor, that is, the voltage-independent G_m of the GFETs, which is estimated at the bias point of operation.

However, following this approach harmonic distortion is rescaled together with the original signal, but not corrected. In order to correct harmonic distortion we propose to interpolate the measured I_{ds-sig} into the I_{ds}–V_{gs} curves (see Supporting Information S5).

In order to validate this calibration procedure, which takes into account the voltage dependence of G_m, we have quantified the attenuation of the 2nd harmonic after calibration. **Figure 4**a shows the 2nd harmonic of a pure tone signal applied at the gate after calibration using a constant G_m or by interpolating into the I_{ds}–V_{gs} curves. Using the interpolation method, we can obtain a very effective attenuation of the distortion, confirmed by the observation that the 2nd harmonic drops to values very close to the noise level (black line). Yet, the amplitude of the second order harmonic increases significantly around the CNP due to the loss of transconductance and inaccuracies in the determination of the I_{ds}–V_{gs} curves. Another possible source of deviation from an ideal correction of harmonic distortion is the frequency dependence of G_m (see Supporting Information S6). This calibration procedure could be applied to any sensor that detects a voltage fluctuation applied at the gate.
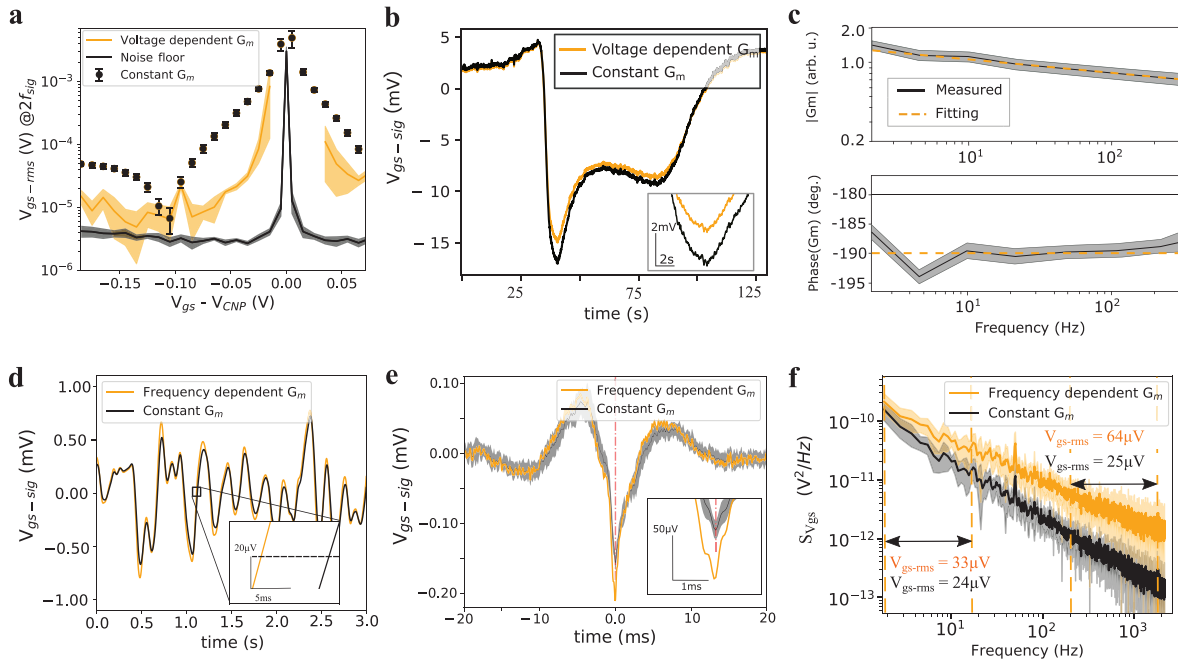

Figure 4. a) Amplitude of the second harmonic in the equivalent voltage at the gate for $A_{sig} = 8mV_{rms}$, showing the values calibrated using a constant transconductance (dots) and using the interpolation into the transfer characteristics (solid orange line). The solid black line shows the average intrinsic noise of the g-SGFET measured at 17 and 23 Hz (i.e., 3 Hz below and above $2f_{sig}$). The errorbars and filled area show the standard deviation for 4 g-SGFETs. b) A CSD signal recorded from the cortex of a rat calibrated with the non-linear transfer characteristics and distorted according to static non-linearities far and close to the CNP. c) Frequency response measured in vivo of the g-SGFETs used for the recording of LFP signals. The filled area shows the standard deviation (for 4 g-SGEFTs) and the orange dashed line the fitting using the derived transfer function ($\alpha = 0.88$). d) A LFP signal recorded from the cortex of a rat (see Experimental Section) is shown in the 1–10 Hz bandwidth. The signal calibrated using a constant G_m is shown in black while the signal calibrated using the derived transfer function is plotted in orange. e) Average of 15 APs recorded from a HL-1 cardiomyocyte. The filled area shows the standard deviation and the orange line the calibrated signal using the derived TF. The frequency response for this device is shown in the Supporting Information S4. f) PSD of the equivalent voltage noise at the gate obtained from calibrating with a constant G_m (black) or interpolating into the transfer characteristics (orange). The V_{gs-rms} indicates the rms of the PSD withing the dashed vertical lines.

In order to show the impact of harmonic distortion on relevant electrophysiologic data, CSD events have been recorded in a headfixed rat model (see Experimental Section and ref. [15]). These signals are especially prone to harmonic distortion because of their large amplitude. Figure 4b shows the electrophysiological signal recorded using a g-SGFET for a V_{gs}–V_{CNP} = −0.04 V and subsequently calibrated using a constant G_m (black line) or by interpolation of the signal into the I_{ds}–V_{gs} curves (orange line). The results show that harmonic distortion modifies the amplitude of the CSD signals, reaching changes of ≈ 1.5 mV (i.e., ≈10% of the total amplitude) in a V_{gs} range where g-SGFETs present an otherwise proper performace (see Supporting Information S5 for more details).

2.4. Calibration of LFP Activity and APs Using the Inverse Transfer Function

The dependence of G_m on the non-ideal double layer capacitance of the graphene–electrolyte interface makes the response of the g-SGFETs to change with frequency even at low frequencies. Small deviations from ideality can cause relatively large changes in the G_m amplitude and phase. Signals showing a wide band activity such as LFPs, with frequency components ranging from ≈1 Hz to ≈200 Hz,[36,37] will present a more pronounced distortion of the signal shape produced by different amplification of various frequency components. In addition, phase distortion might cause defective phase determination in LFPs.[23] To show the impact of non-ideal frequency response on actual physiologic data, LFPs have been recorded in vivo on the rat cortex using epicortical g-SGFET flexible probes (see Experimental Section) and APs have been recorded from a HL-1 cell culture on a g-SGFET array fabricated on a SiO_2 rigid substrate (see Experimental Section).

In order to calibrate the electrophysiological data, the frequency response of the g-SGFETs under in vivo conditions and in the culture medium must be known. Figure 4c shows the frequency response of the g-SGFETs measured on the rat cortex (see Experimental Section), while the response of the g-SGFETs in the culture medium is shown in Supporting Information S4. In the frequency range relevant for the recording of LFPs and APs, the Bode plots show a frequency response dominated by the CPE behavior described previously. In this regime, the $G_m(f)$ can be approximated by $G_m(f = 1 \text{ Hz})/f^{1-\alpha}$ (see fitting in Figure 4c and the Supporting Information S7 for a description of the numerical implementation of the frequency dependent transfer function).

The impact of such distortions can be shown by calibrating the recorded signals using the inverse of the fitted $G_m(f)$. Figure 4d shows an LFP signal (in the 1–10 Hz frequency band) calibrated using a frequency-independent G_m and using the frequency dependent transfer function of the g-SGFETs in the in vivo conditions. The non-ideal frequency response causes changes in the signal amplitude as well as phase shifts of ≈10°. Similarly, Figure 4e shows an average of 15 APs recorded in an in vitro cardiomyocyte culture. In the case of the APs, neglecting the effect of frequency response leads to a significant error in the amplitude determination (an underestimation

of ≈30% of the actual amplitude) due to the high frequency of these signals.

Finally, G_m loss at high frequencies will cause loss of signal-to-noise ratio that cannot be corrected by calibration. Figure 4f shows the effect of G_m loss on the power spectral density (PSD) of the calibrated noise ($S_{V_{gs}}$). The understimation in the noise power made by using a constant G_m for calibration can be quantified by integrating the PSD in different frequency bandwidths (see Figure 4f), leading to different values of equivalent noise at the gate ($V_{gs–rms}$).

These results emphasize the importance of understanding and improving the frequency response of g-SGFETs, especially for sensing high frequency and low amplitude signals. It is also shown the importance of characterizing the frequency response of the g-SGFETs in the environment used for the final application, in our case on the brain cortex, for a proper calibration of the signal.

3. Conclusion

In summary, this work provides a detailed characterization and modeling of the signal distortion mechanisms in g-SGFETs, describing their impact on the recording capabilities of these devices. The effect of distortion on electrophysiological signals has been evaluated in a wide frequency and amplitude range. It has been shown that non-linearities in the I_{ds}–V_{gs} curves can have a significant impact on the amplitude and shape determination of large amplitude signals, such as spreading depression events. This distortion can be corrected by a calibration procedure which takes into account the voltage dependence of G_m. On the other hand, the non-ideal frequency response of g-SGFETs results in a significant effect on the amplitude determination of LFPs and APs as well as on the phase extraction for LFPs. These distortions can be calibrated using the frequency dependent transfer function presented in this work, following a similar approach as previously proposed for microelectrodes when a frequency independent gain cannot be obtained.[23]

In spite of performing a proper calibration of the signal, conventional microelectrodes introduce dramatic SNR loss at infra-slow frequencies.[23] Alternatively, g-SGFETs present a high G_m at low frequencies, allowing to record infra-slow neural activity with a high sensitivity. This high G_m slightly drops as the frequency is increased, therefore producing a progressive loss of SNR. Eliminating the frequency dependence of G_m is thus a clear strategy toward improving the already outstanding sensitivity of g-SGFETs at high frequencies. The understanding of the g-SGFET response provided in this work sets the ground to their frequency response as well as to mitigate harmonic distortion by operating the devices at optimum bias conditions. Finally, and more importantly, the calibration procedures presented in this work have been shown effective to correct the impact of signal distortion on the recording capabilities of g-SGFETs. These results demonstrate the potential of g-SGFETs as a highly sensitive, distortion-free platform, not only for full-band neural sensing, but also for a broader range of applications in which g-SGFET sensors are used.

4. Experimental Section

Fabrication of g-SGFETs: Arrays of g-SGFETs were fabricated on a 10 µm thick polyimide (PI-2611, HD MicroSystems) film spin coated on a Si/SiO$_2$ 4″ wafer and baked at 350 °C. A first metal layer (10 nm Ti/100 nm Au) was deposited by electron-beam vapor and then structured by a lift-off process. Afterward, the graphene grown by chemical vapor deposition on Cu was transferred (process done by Graphenea S.A.). Graphene was then patterned by oxygen plasma (50 SCCM, 300 W for 1 min) in a reactive ion etching after protecting the graphene in the channel region with HIPR 6512 (FujiFilm) positive photoresist. After the graphene etching, a second metal layer was patterned on the contacts following the same procedure as for the first layer. The lift-off was followed by annealing in ultra-high vacuum consisting a temperature ramp from room temperature to 300 °C. Subsequently, the transistors were insulated with a 3-µm-thick photodefinable SU-8 epoxy photoresist (SU-8 2005 Microchem), keeping uncovered the active area of the transistors channel and the contacting pads. The polyimide substrate was structured in a reactive ion etching process using a thick AZ9260 positive photoresist (Clariant) layer as an etching mask. The neural probes were then peeled off from the wafer and placed in a zero insertion force connector to be interfaced with the custom electronic instrumentation described below. Finally, the devices were rinsed for 2 min in ethanol to eliminate remaining resist residues on the graphene channel.

Electrical Characterization in PBS: To measure the DC and AC accurately, the electrical current from drain to source was pre-amplified in a first amplification stage with a "low" 10^4 gain. The pre-amplified signal was then low-pass filtered and subtracted from the pre-amplified signal, thus canceling its low frequency (i.e., DC level) components. The resulting signal could therefore be further amplified and low-pass (anti-aliasing) filtered in a second stage with an additional 10^2 gain factor. A custom built circuit was used for the amplification of the current signals, which were digitalized using an NI DAQCard in all characterization procedures in vitro.

For the characterization of harmonic distortion, the DC and AC components of the signal were measured. The 1st, 2nd, and 3rd order harmonics of a 10 Hz signal applied at the gate were determined from the output of the second amplification stage while the stationary I_{ds}–V_{gs} curves used to calculate harmonic distortion were obtained from the first amplification stage.

The frequency response was characterized by applying a composed signal on the electrolyte containing the superposition of sine waves (12 frequencies per decade with a peak amplitude of 1 mV) in the bandwidth of interest (i.e., 0.4 Hz–200 kHz). Different concentrations of PBS (0.05× and 10×) were used in order to assess the effect of the electrolyte conductivity on the frequency response, where the composition of PBS 1× is 10 mM Na$_2$HPO$_4$, 1.8 mM KH$_2$PO$_4$, 2.7 mM KCl, and 137 mM NaCl. The signal from the first amplification stage was used to have access to a wider frequency bandwidth (from 0.35 Hz to 200 kHz).

Ethical Approval and Animal Handling: All experimental procedures were conducted in accordance with the European Union guidelines on protection of vertebrates used for experimentation (Directive 2010/63/EU of the European Parliament and of the Council of September 22, 2010). The experiments for the recording of CSD events were approved by the ethics committee of the Hospital Clinic de Barcelona. Rats were kept under standard conditions (room temperature 23±1 °C, 12:12 h light–dark cycle, lights on at 08:00), with food (A04, Harlan) and water available ad libitum. Experiments for the recording of LFP were in accordance with the German Law for Protection of Animals (TierSchG), and were approved by the local authorities (ROB-55.2-2532.Vet_02-16-170). Rats were kept under standard conditions (room temperature 22±2 °C, 12:12 h light–dark cycle, lights on at 10:00), with food (V1534-000, SSNIFF) and water available ad libitum.

Recording of CSD Events in a Rat Model and Calibration of Harmonic Distortion: The procedure followed has been thoroughly described previously.[19] The data from one of the rats used in this previous study had been used for evaluating the effect of harmonic distortion on infra-slow CSD signals.

The adult Wistar rats used for this study were deeply anaesthetized with isoflurane (4% induction, 1–3% maintenance) and all pressure and incision points were infiltrated with local anesthetic lidocaine. A craniotomy was performed on the left hemisphere (centered at 43 mm anterior-posterior (AP) and 42.5 mm medio-lateral (ML) and was 6 mm AP by 4.5 mm ML in size). An additional craniotomy was performed on the prefrontal cortex to administer 5 mM KCl to induce CSD events. An Ag/AgCl electrode pellet was inserted in temporal muscle and used as reference both for recordings and for the measurement of the transistor transfer curve.

The DC signals from the first amplification stage and bias control were managed by a data acquisition system (National Instruments USB-6353). On the other hand, the AC signals from the second amplification stage were directly acquired by a commercial electrophysiological recording system consisting of a programmable gain amplifier (Multichannel Systems) and digitizer interface (CED 1401 and Spike2 software, Cambridge Electronic Design). The DC and AC bands were sampled at 1 Hz and 5 kHz respectively. Before the beginning of the recordings, the transfer curve of the g-SGFET was measured in situ.

Recording of LFP Activity on the Rat Cortex: An adult Long–Evans rat was used for the measurement of LFP signals in this study. The rat, weighing 580 g, was deeply anaesthetized with MMF (midazolam 2 mg kg^{-1}, medetomidin 0.15 mg kg^{-1}, fentanyl 0.005 mg kg^{-1}). Starting 1 h after MMF induction isoflurane was supplemented for maintenance at 1% and metamizol was given at 110 mg kg^{-1}. The posterior-dorsal area of the head was shaved, the skin locally disinfected with povidone-iodine and subcutaneously infiltrated with local anesthetic bupivacaine. Subsequently the skin was incised and the dorsal skull cleaned carefully by blunt dissection. The dried skull was covered with UV-curing adhesive OptiBond (Kerr) and a 3D printed base ring was anchored to skull with screws and Metabond cement (Parkell).

Symmetric craniotomies with a maximum width of 5 mm were performed bilaterally, extending between +2 mm and −8 mm with respect to bregma in the anterior–posterior axis.

The dura mater was incised and removed within these craniotomies. A further craniotomy of 1 × 1 mm was performed over the cerebellum. All craniotomies were covered with prepolymerized PDMS (Sylgard 184, Dow Corning, USA) with mixing ratio 1:10 and sealed with Vetbond (Animal Care Products, USA). The skin margins around the implant were sutured and the implant closed with a protective cap.

After 1 week of recovery the g-SGFET array was implanted under isofluran anesthesia (5% induction 1% maintenance). After partial opening and sideward flapping of the polymer covering the right hemisphere the array was placed onto the pial surface positioned such as to cover the posterior aspect of the right hemisphere (approximately −7 to −2 mm from bregma). In addition two Pt–Ir wires were implanted at either side of the g-SGFET array. One proximal to the array, the other distally on the opposing hemisphere. The polymer cover was flapped back into position with the flexible cable of the g-SGFET array leaving through the remaining slit. A second PDMS cover was used to cover both the incised polymer and array, anchored to the skull with Vetbond and Evoflow (Ivoclar Vivadent, Liechtenstein) and sealed with silicon gel 3–4680 (Dow Corning, USA).

An Ag/AgCl electrode was placed in contact with the cerebellum as a reference for the recording of LFP as well as the curves and frequency response for calibration of the neural signals.

The recordings were performed using a custom built data acquisition system with capabilities to switch between the output of the 1st and the 2nd amplification stages. The former was used for the acquisition of LFP activity while the latter was used for the determination of the curves needed for calibration.

Characterization of Frequency Response In Vivo for Calibration of LFP: The frequency response of the g-SGFETs had been observed to depend on the ion concentration in the electrolyte. For this reason, the frequency response had to be properly determined in vivo for subsequent calibration of detected neural activity.

To obtain the frequency response in vivo, two Pt–Ir wires were implanted at either side of the g-SGFET array. The two Pt–Ir wires

were then connected to a current signal generator to perform a bipolar current stimulation at different frequencies. The current signal generator was decoupled from the recording system in order to avoid any current to leak through the g-SGFETs. The amplitude of the current signal was 1 µA which was small for causing ephaptic effects. The amplitude of stimulation was decreased by twofold to validate that the measured G_m dropped by the same factor. The signal was applied in current to avoid any effect of the electrode and tissue impedances on the amplitude of the signal at different frequencies. By imposing a current, the amplitude in volts at the g-SGFETs site was expected to be constant with frequency. The drawback of this approach was that the amplitude in volts of the signal applied was not known and therefore the extracted magnitude of the Bode must be expressed in arbitrary units.

The parameters of the analytic transfer function which describe the frequency response could be obtained by fitting the Bode plot. The only parameter that cannot be obtained from this fitting was the scaling factor or transconductance at $f = 1$ Hz. However, this parameter could be obtained from the first derivative of the static I_{ds}–V_{gs} curves with small uncertainty as shown in Figure 3a. Having all the extracted parameters, it was possible to define the inverse $G_m(f)$, which could be then used to calibrate the data recorded in vivo.

Culture of HL-1 Cardiomyocytes and Recording of APs: The HL-1 cell line was obtained from the LSU Health Sciences Center New Orleans, USA. Cells were culture on Claycomb medium supplemented with 10% FBS, penicillin/streptomycin (100 U mL^{-1}:100 µg mL^{-1}), and L-glutamine (2 mM) on a flask coated with fibronectin/gelatin and incubated at 37 °C with 5% CO_2. The culture medium was exchanged daily and supplemented with fresh norepinephrine 0.1 mM. When the cells were beating, they were subcultured on new flask or on the g-SGFET arrays as needed. To do so, cells were detached from the flask using trypsin and after a few minutes' incubation at 37 °C the enzymatic activity was neutralized using twice the volume of culture media. The solution containing the cells was centrifuged at 120 g for 2 min and the supernatant was aspired before re-suspending the cells on fresh culture media. The cells were seeded then on the desired substrate. To prepare them for culture, the g-SGFET were sterilized in 70% ethanol for 15 min, rinsed several times with PBS, and coated with fibronectin/gelatine for at least 2 h. Then the fibronectin/gelatine was aspired and the device was rinsed again with PBS. Experiments were performed 48–72 h after subculture.

All chemicals were bought from Sigma-Aldrich unless otherwise noted. The APs recording was performed using the home-built system schematized in Figure 1e and described before. The signals were digitized from the second amplification (band-pass filtered) stage. The transistors were operated at a constant source-drain and gate voltage. Signals were recorded at a sampling frequency of $F_s = 20$ kHz and digitally band-pass filtered from 55 Hz to 4 kHz after digitalization. The same setup used for the characterization of the g-SGFETs in a PBS bath was used for the recording of electrophysiological signals from the cell culture. The output from the 1st amplification stage was used for the determination of the transfer characteristics while the output from the 2nd stage was used for the recording of recording of APs. The frequency response was determined following the same approach as for its characterization in a PBS bath.

Supporting Information

Supporting Information is available from the Wiley Online Library or from the author.

Acknowledgements

Conflict of Interest

The authors declare no conflict of interest.

Keywords

[1] L. Banszerus, M. Schmitz, S. Engels, J. Dauber, M. Oellers, F. Haupt, K. Watanabe, T. Taniguchi, B. Beschoten, C. Stampfer, *Sci. Adv.* **2015**, *1*, e1500222.

[2] F. Banhart, J. Kotakoski, A. V. Krasheninnikov, *ACS Nano* **2011**, *5*, 26.

[3] R. R. Nair, P. Blake, A. N. Grigorenko, K. S. Novoselov, T. J. Booth, T. Stauber, N. M. R. Peres, A. K. Geim, *Science* **2008**, *320*, 1308.

[4] D. W. Park, A. A. Schendel, S. Mikael, S. K. Brodnick, T. J. Richner, J. P. Ness, M. R. Hayat, F. Atry, S. T. Frye, R. Pashaie, S. Thongpang, Z. Ma, J. C. Williams, *Nat. Commun.* **2014**, *5*, 5258.

[5] D. Kuzum, H. Takano, E. Shim, J. C. Reed, H. Juul, A. G. Richardson, J. de Vries, H. Bink, M. A. Dichter, T. H. Lucas, D. A. Coulter, E. Cubukcu, B. Litt, *Nat. Commun.* **2014**, *5*, 5259.

[6] B. R. Goldsmith, L. Locascio, Y. Gao, M. Lerner, A. Walker, J. Lerner, J. Kyaw, A. Shue, S. Afsahi, D. Pan, J. Nokes, F. Barron, *Sci. Rep.* **2019**, *9*, 434.

[7] J. Peña-Bahamonde, H. N. Nguyen, S. K. Fanourakis, D. F. Rodrigues, *J. Nanobiotechnol.* **2018**, *16*, 75.

[8] R. Hajian, S. Balderston, T. Tran, T. deBoer, J. Etienne, M. Sandhu, N. A. Wauford, J.-Y. Chung, J. Nokes, M. Athaiya, J. Paredes, R. Peytavi, B. Goldsmith, N. Murthy, I. M. Conboy, K. Aran, *Nat. Biomed. Eng.* **2019**, *3*, 427.

[9] W. Tian, X. Liu, W. Yu, *Appl. Sci.* **2018**, *8*, 1118.

[10] W. Yuan, G. Shi, *J. Mater. Chem. A* **2013**, *1*, 10078.

[11] Y. Zhu, C. Wang, N. Petrone, J. Yu, C. Nuckolls, J. Hone, Q. Lin, in *2015 28th IEEE Int. Conf. on Micro Electro Mechanical Systems (MEMS)*, IEEE, Estoril **2015**, pp. 869–872.

[12] B. Mailly-Giacchetti, A. Hsu, H. Wang, V. Vinciguerra, F. Pappalardo, L. Occhipinti, E. Guidetti, S. Coffa, J. Kong, T. Palacios, *J. Appl. Phys.* **2013**, *114*, 084505.

[13] K. Maehashi, Y. Sofue, S. Okamoto, Y. Ohno, K. Inoue, K. Matsumoto, *Sens. Actuators, B* **2013**, *187*, 45.

[14] C. Hébert, E. Masvidal-Codina, A. Suarez-Perez, A. B. Calia, G. Piret, R. Garcia-Cortadella, X. Illa, E. D. C. Garcia, J. M. De la Cruz Sanchez, D. V. Casals, E. Prats-Alfonso, J. Bousquet, P. Godignon, B. Yvert, R. Villa, M. V. Sanchez-Vives, A. Guimerà-Brunet, J. A. Garrido, *Adv. Funct. Mater.* **2018**, *28*, 1703976.

[15] B. M. Blaschke, N. Tort-Colet, A. Guimerà-Brunet, J. Weinert, L. Rousseau, A. Heimann, S. Drieschner, O. Kempski, R. Villa, M. V. Sanchez-Vives, J. A. Garrido, *2D Mater.* **2017**, *4*, 025040.

[16] K. Kostarelos, M. Vincent, C. Hebert, J. A. Garrido, *Adv. Mater.* **2017**, *29*, 1700909.

[17] L. H. Hess, C. Becker-Freyseng, M. S. Wismer, B. M. Blaschke, M. Lottner, F. Rolf, M. Seifert, J. A. Garrido, *Small* **2015**, *11*, 1703.

[18] E. J. W. van Someren, in *Proc. of the 26th Int. Summer School of Brain Research*, Elsevier, Amsterdam **2010**.

[19] E. Masvidal-Codina, X. Illa, M. Dasilva, A. B. Calia, T. Dragojević, E. E. Vidal-Rosas, E. Prats-Alfonso, J. Martínez-Aguilar, J. M. De la Cruz, R. Garcia-Cortadella, P. Godignon, G. Rius, A. Camassa, E. D. Corro, J. Bousquet, C. Hébert, T. Durduran, R. Villa, M. V. Sanchez-Vives, J. A. Garrido, A. Guimerà-Brunet, *Nat. Mater.* **2019**, *18*, 280.

[20] S. Drieschner, A. Guimerà, R. G. Cortadella, D. Viana, E. Makrygiannis, B. M. Blaschke, J. Vieten, J. A. Garrido, *J. Phys. D: Appl. Phys.* **2017**, *50*, 095304.

[21] M. D. Stoller, C. W. Magnuson, Y. Zhu, S. Murali, J. W. Suk, R. Piner, R. S. Ruoff, *Energy Environ. Sci.* **2011**, *4*, 4685.

[22] C. Mackin, L. H. Hess, A. Hsu, Y. Song, J. Kong, J. A. Garrido, T. Palacios, *IEEE Trans. Electron Devices* **2014**, *61*, 3971.

[23] M. J. Nelson, P. Pouget, E. A. Nilsen, C. D. Patten, J. D. Schall, *J. Neurosci. Methods* **2008**, *169*, 141.

[24] S. Rodriguez, A. Smith, S. Vaziri, M. Ostling, M. C. Lemme, A. Rusu, *IEEE Trans. Electron Devices* **2014**, *61*, 3001.

[25] K. A. Jenkins, D. B. Farmer, S.- J. Han, C. Dimitrakopoulos, S. Oida, A. Valdes-Garcia, *Appl. Phys. Lett.* **2013**, *103*, 173115.

[26] S. Samaddar, I. Yudhistira, S. Adam, H. Courtois, C. B. Winkelmann, *Phys. Rev. Lett.* **2016**, *116*, 126804.

[27] I. Heller, S. Chatoor, J. Männik, M. A. G. Zevenbergen, J. B. Oostinga, A. F. Morpurgo, C. Dekker, S. G. Lemay, *Nano Lett.* **2010**, *10*, 1563.

[28] M. Winters, E. Ö. Sveinbjörnsson, N. Rorsman, *J. Appl. Phys.* **2015**, *117*, 074501.

[29] H. Wang, Y. Wu, C. Cong, J. Shang, T. Yu, *ACS Nano* **2010**, *4*, 7221.

[30] C. Mackin, E. McVay, T. Palacios, *Sensors* **2018**, *18*, 494.

[31] *Impedance Spectroscopy* (Eds:E. Barsoukov, J. R. Macdonald), John Wiley & Sons, Inc., Hoboken, NJ **2005**.

[32] J. Sun, Y. Liu, *Nanomaterials* **2019**, *9*, 923.

[33] C.-H. Kim, S.-I. Pyun, J.-H. Kim, *Electrochim. Acta* **2003**, *48*, 3455.

[34] W. H. Mulder, J. H. Sluyters, T. Pajkossy, L. Nyikos, *J. Electroanal. Chem. Interfacial Electrochem.* **1990**, *285*, 103.

[35] C. H. Hsu, F. Mansfeld, *Corrosion* **2001**, *57*, 747.

[36] G. Buzsáki, B. O. Watson, *Dialogues Clin. Neurosci.* **2012**, *14*, 345.

[37] G. Buzsáki, C. A. Anastassiou, C. Koch, *Nat. Rev. Neurosci.* **2012**, *13*, 407.

WILEY-VCH

Supporting Information

Distortion-Free Sensing of Neural Activity Using Graphene Transistors

Ramon Garcia-Cortadella, Eduard Masvidal-Codina, Jose de la Cruz, Nathan Schäfer, Gerrit Schwesig, Christoph Jeschke, Javier Martinez-Aguilar, Maria V. Sanchez-Vives, Rosa Villa, Xavi Illa, Anton Sirota, Anton Guimerà and Jose A. Garrido*

S1. Comparison of calculated harmonic distortion with experimental data

As mentioned in the introduction of the main text, harmonic distortion introduced by the GFETs can, in principle, be calculated from the Taylor expansion of the $I_{ds} - V_{gs}$ curves (**Equation (S1)**). The expansion to the 3rd order can be expressed as follows:

$$I_{ds} = I_{ds}|_{V_{gso}} + \frac{dI_{ds}}{dV_{gs}}\bigg|_{V_{gso}} A_{sig}\sin(2\pi ft) + \frac{1}{2!}\frac{d^2I_{ds}}{dV_{gs}^2}\bigg|_{V_{gso}} \frac{A_{sig}^2}{2}\sin(4\pi ft) + \frac{1}{3!}\frac{d^3I_{ds}}{dV_{gs}^3}\bigg|_{V_{gso}} \frac{A_{gsig}^3}{4}\sin(6\pi ft)$$

(S1)

where A_{sig} represents the amplitude of the small signal applied at the gate V_{gs-sig} (see Figure 1b) in the main text.

Figure 2a in the main text shows the agreement between measured harmonic distortion and the values calculated from the stationary $I_{ds} - V_{gs}$ curves for a signal amplitude $A_{sig} = 8mV_{rms}$. Here the agreement for the other measured signal amplitudes ($A_{sig} = 4$ and $2\ mV_{rms}$) is also shown for a

WILEY-VCH

wide V_{gs} range. The noise level (in this case at $2f_{sig}$ or frequency of the second harmonic) is displayed in **Figure S1**a and S1b. Figure S1c shows, the rms noise integrated in the 4-40Hz bandwidth, which was used to calculate the DNR displayed in Figure 2d. Figure S1d shows the S/(D+N) ratio, a figure of merit that can be defined to show the impact of distortion on the signal quality for a wide $V_{gs} - A_{sig}$ range. The rms noise shown in Figure S1c was also used to calculate the S/(D+N) ratio.
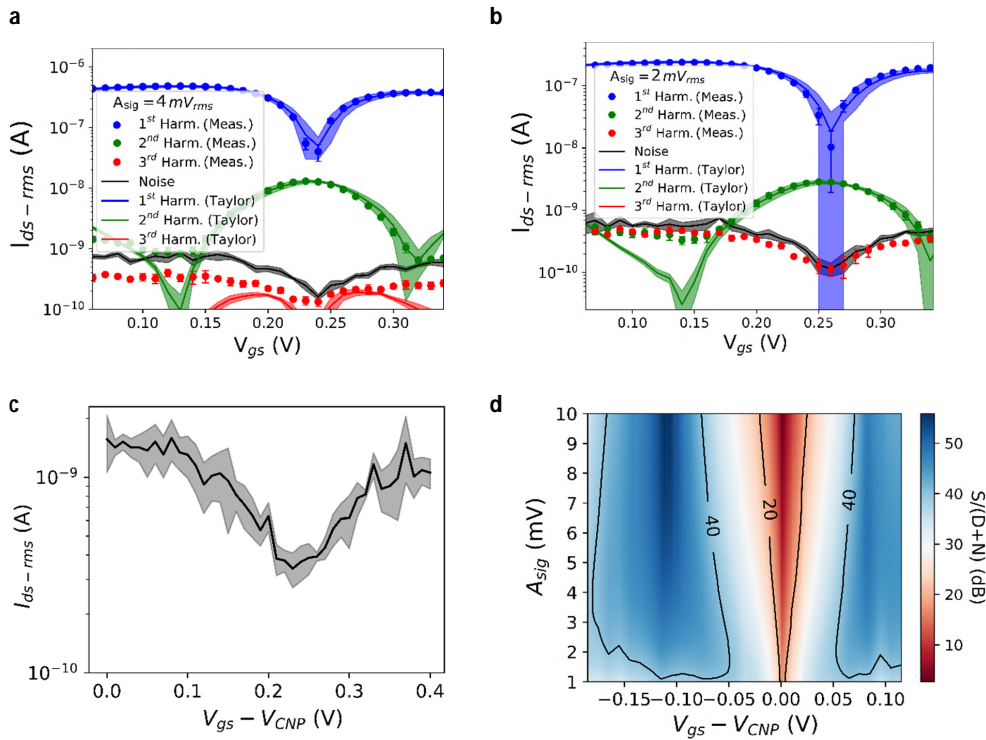
Figure S1: a) 1st, 2nd, and 3rd harmonics rms-amplitude extracted from the power spectrum of the measured I_{ds-sig} (dots-errorbar) and from the Taylor expansion of the $I_{ds} - V_{gs}$ curves (solid lines-filled area) for a signal amplitude A_{sig} of $4mV_{rms}$.. Error bars and filled area shows the standard deviation (for 4 g-SGFETs). The noise is evaluated from the power spectrum at 18Hz (i.e. slightly below $2f_{sig}$). b) The same as part a) for a signal amplitude A_{sig} of $2mV_{rms}$. c) The integrated noise in the 4-40 Hz is shown. These values were used to calculate the DNR in Figure 2d of the main text and Figure S1d. d) Signal to distortion plus noise in a wide $V_{gs} - A_{sig}$ range.

WILEY-VCH

S2. Derivation of analytic transfer function

The derivation of the analytic transfer function describing the frequency response of the g-SGFETs is summarized in the main text. Here, the frequency dependence of the terms in Equation (1) of the main text are expressed explicitly.

The first factor in Equation (1) $(dI_{ds}/dV_{int}|_{V_{ds}})$, referred to as the intrinsic transconductance of the g-SGFET expresses how an electrical potential at the graphene-electrolyte interface couples with the channel conductivity, producing changes in the drain-to-source current. This term is therefore proportional to the capacitance of the interface, which is usually considered independent of the frequency, as expressed in **Equation (S2)**.

$$G_m = \left.\frac{dI_{ds}}{dV_{int}}\right|_{V_{ds}} = V_{ds}\frac{W}{L}\mu\, C_{int} \tag{S2}$$

where W and L stand for the width and length of the channel respectively, and μ for the charge carriers electrical mobility. If the interface capacitance does not present an ideal capacitive behavior, but a constant phase element (CPE)-like response, a frequency dependent equivalent capacitance can be derived. Equating the imaginary part of the CPE impedance with the impedance of a pure capacitance the following equivalent capacitance (C_{CPE}) has been presented previously:[1]

$$C_{CPE} = \frac{Q_0}{\omega^{1-\alpha}}\left(\sin(\alpha\pi/2) - i\cos(\alpha\pi/2)\right)$$

$$\tag{S3}$$

Where Q_0 is the inverse of the impedance at $1\,rad/s$ and $(-\frac{\alpha\pi}{2})$ is the constant angle of its impedance in radians. Substituting **Equation (S3)** for C_{int} in Equation S2, the term regarded as "CPE dominated" in Equation (1) of the main text can be derived.

The second factor in Equation (1) of the main text (dV_{int}/dV_{gs}) represents the effect of the voltage divider composed by the impedance of the graphene-electrolyte interface and the resistance in series (R_s) which includes the contact resistance of the GFET (R_c) and the resistance of the electrolyte (R_{ele}). In addition, if there is a parasitic impedance in parallel with the graphene-electrolyte interface, it must be taken into account to calculate the attenuation of voltage drop at the interface (V_{int}) with respect to the signal applied (V_{gs}). This parasitic impedance could be dominated by either leakage through the metal contacts accidentally exposed to the electrolyte or through the capacitive coupling of the metal tracks with the electrolyte through the 2 μm thick passivation layer.

WILEY-VCH

A similar explanation to this cut-off frequency has been reported before.[2] This attenuation factor or voltage divider can be therefore expressed as:

$$\frac{dV_{int}}{dV_{gs}} = \frac{Z_{CPE_{g-e}}//Z_{CPE_{par}}}{Z_{CPE_{g-e}}//Z_{CPE_{par}} + 2R_s}$$

(S4)

where the factor of 2 multiplying R_s comes from the definition of CPE_{g-e} and CPE_{par} in the equivalent circuit shown in Figure 3 of the main text. Writing the frequency dependence in **Equation (S4)** explicitly:

$$\frac{dV_{int}}{dV_{gs}} = \frac{1}{1 + 2\,R_s\left[Q_{g-e}(2\pi f)^{\alpha_{g-e}}e^{i\frac{\pi}{2}\alpha_{g-e}} + Q_{par}(2\pi f)^{\alpha_{par}}e^{i\frac{\pi}{2}\alpha_{par}}\right]}$$

(S5)

Finally, an additional term contributes positively to the gain at high frequencies. The high interface capacitance causes a direct capacitive current between gate and source through the channel as well as through CPE_{par}. These capacitive currents are distributed to drain and source equally. This contribution can be expressed as:

$$G_{m_{eff}}(f_{sig}) = 1/(2Z_{CPE}) + 1/(2Z_{CPE_{par}})$$

(S6)

writing the frequency dependence of **Equation (S6)** explicitly, the last term in Equation (1) of the main text can be derived:

$$G_{m_{eff}}(f_{sig}) = Q_{g-e}(2\pi f)^{\alpha_{g-e}}e^{i\frac{\pi}{2}\alpha_{g-e}} + Q_{par}(2\pi f)^{\alpha_{par}}e^{i\frac{\pi}{2}\alpha_{par}}$$

(S7)

Merging Equation (1) in the main text, **Equation** (S3), (S5) and **(S7)**, the frequency dependence of the transfer function for g-SGFETs can be expressed as:

WILEY-VCH

$$G_m(f) = \pm k \frac{Q_{g-e}}{(2\pi f)^{1-\alpha}} e^{i\frac{\pi}{2}(\alpha_{g-e}-1)} \frac{1}{1 + 2R_s \left[Q_{g-e}(2\pi f)^{\alpha_{g-e}} e^{i\frac{\pi}{2}\alpha_{g-e}} + Q_{par}(2\pi f)^{\alpha_{par}} e^{i\frac{\pi}{2}\alpha_{par}} \right]}$$

$$+ Q_{g-e}(2\pi f)^{\alpha_{g-e}} e^{i\frac{\pi}{2}\alpha_{g-e}} + Q_{par}(2\pi f)^{\alpha_{par}} e^{i\frac{\pi}{2}\alpha_{par}}$$

(S8)

where $\pm$ takes the positive value in the electron conduction regime and negative in the hole conduction regime (producing a 180° degrees phase shift). Q_{g-e} and Q_{par} stand for the inverse of the impedance at 1 rad/s for the terms CPE_{g-e} and CPE_{par} respectively. **Equation (S8)** describes the effect of the CPE behavior on the frequency response, which causes a drop of G_m with frequency to a fractional order (i.e. $G_m(f) \propto f^{1-\alpha_{g-e}}$). In this regime, the phase of the transfer function depends on α as $\pi/2 \, (\alpha - 1)$. The second factor in the first term of Equation S8 describes the drop of V_{int} with frequency, which is responsible for a drop in the $G_m(f)$ magnitude together with a negative phase shift. Finally, the second term in Equation S8, corresponding to capacitive currents through CPE_{g-e} and CPE_{par}, which produce an increase in the $G_m(f)$ magnitude and a positive phase shift.

Fitting of the experimentally obtained Bode plot can be used to extract the relevant parameters modelling the frequency response of the g-SGFETs. The following table summarizes the parameters extracted from the fitting shown in Figure 3a of the main text:

	PBS 100mM	PBS 0.5mM
Q_{g-e}	$1.8\mu F s^{\alpha-1}/cm^2$	$1.6\mu F s^{\alpha-1}/cm^2$
$Area$	$10^{-8}m^2$	$10^{-8}m^2$
α_{g-e}	0.97	0.905
$k\,[V_{ds}\mu W/L]$	$5.10^{-3}m^2/s$	$4.10^{-3}m^2/s$
Q_{par}	$8nF s^{\alpha-1}$	$8nF s^{\alpha-1}$
α_{par}	0.65	0.6
R_s	$3k\Omega$	$240k\Omega$

Table S1: Parameters extracted from the Bode plot fitting in Figure 3a of the main text.

WILEY-VCH

S3. Effect of transistor geometry on the harmonic distortion

The data presented in the main text validates the stationary model of harmonic distortion for single layer graphene SGFETs. A width=length=100μm was chosen for these experiments. If the width of the g-SGFETs is increased, the drain-source current will increase proportionally. However, the ratio between the contact resistance and the channel resistance remains constant. Therefore, the $I_{ds} - V_{gs}$ curves for different widths are equivalent except for a V_{gs}–independent multiplicative factor. This constant factor results into a linear increase of all terms in Equation S1 and therefore the SDR remains unchanged. On the other hand, if the length of the channel is shortened, the contact resistance will have a stronger impact on the curvature of the $I_{ds} - V_{gs}$ curves. **Figure S2**a shows the amplitude of the 1st harmonic for different channel lengths. These values have been obtained from the measured stationary $I_{ds} - V_{gs}$ curves using Equation S1, for a signal amplitude of 10mVpk. Figures S2b and S2c show the 2nd and 3rd harmonic amplitude respectively for the same devices and Figure S2d shows their SDR. A trend towards the increase of SDR for longer channels can be observed, which can be attributed to the lower impact of the contact resistance on the stationary response of the g-SGFETs. These results can be compared with those presented in the main text. The validity of the stationary model in devices of different lengths is expected to hold as long as the CPE regime dominates the frequency response as for the W=L=100μm devices shown in the main text. Figure 1 shows the frequency response for g-SGFETs with different channel lengths, demonstrating the CPE dominated response below ~30kHz. Only above this frequency, changes in the length produce changes in the frequency response as expected from the derived transfer function in Supplementary information S2.
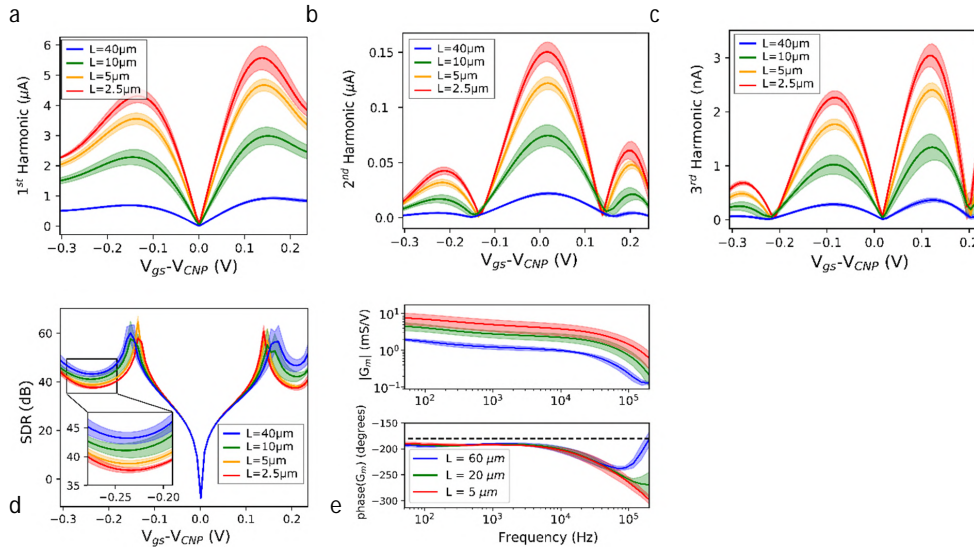
WILEY-VCH

Figure S2: Effect of the channel length on harmonic distortion: a. 1st harmonic, **b.** 2nd harmonic and **c.** 3rd harmonic calculated from the measured stationary response for g-SGFETs of different lengths. **d.** SDR calculated from data in parts **a-c**. In all plots, the mean is indicated by the solid lines and the standard deviation by the filled area. 7 g-SGFET were measured for L=40μm and L=10μm, 3 g-SGFETs were measured for L=5μm and L=2.5μm. **e.** Frequency response of g-SGFETs with different channel lengths measured in 10mM PBS. 7 g-SGFET were measured for L=60μm and L=5μm, 3 g-SGFETs were measured for L=20μm.

S4. Effect of carrier mobility in graphene on the harmonic distortion

Different density of defects in the graphene lattice might produce changes in the mobility, which in turn, might result in different harmonic distortion levels. Lower mobilities, imply a higher channel resistance and therefore it is expected that devices with lower mobilities present a higher SDR. To validate this intuition, we have used a numerical model of the g-SGFET[2] implemented in Matlab. **Figure S3**a shows the $I_{ds} - V_{gs}$ curves simulated for the parameters in **Table S2**, which include multiple mobility values. The simulation corresponding to a mobility of 1550 cm^2/Vs fits the data for the 40 μm x40 μm transistors. Figure S3b shows the Raman spectra measured in these devices, demonstrating a relatively low D/G ratio, which indicates the density of defects. Figure S3c shows the SDR for different mobilities, confirming that a lower mobility increases the SDR due to a higher channel resistance.
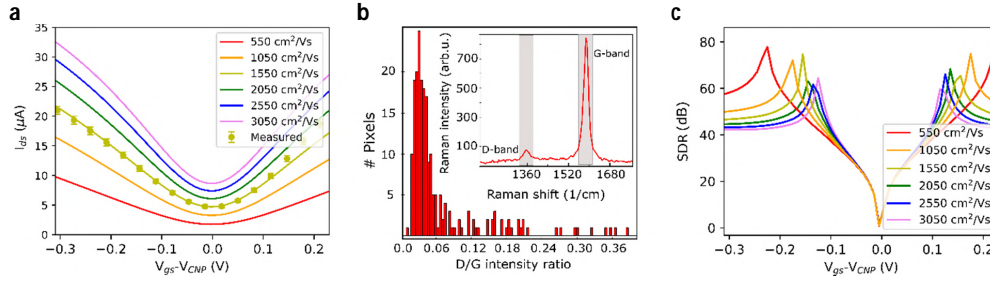
151

WILEY-VCH

Figure S3: Effect of the carrier mobility on harmonic distortion: a. $I_{ds} - V_{gs}$ characteristics measured (dot) for 50 µm x 50 µm g-SGFETs and simulated for different carrier mobilities (line). **b.** Histogram showing the distribution of the ration between Raman D-band and G-band. The inset shows the Raman spectrum for a specific point and indicates the position oft he D and G bands. **c.** SDR simulated for different carrier mobilities.

R_c [kΩ.µm]	W [µm]	L [µm]	µ [cm²/Vs]	n_{imp} [1/m²]	n_0 [1/m²]	C_{dl} [µF/cm²]	U_{CNP} [V]
7.5	40	40	550	4.10^{11}	4.10^{11}	2	0
			1050				
			1550				
			2050				
			2550				
			3050				

Table S2: Parameters used for the simulation of the stationary response of the g-SGFETs for different carrier mobilities.

S5. Effect of leakage through metal contacts exposed to the electrolyte

The signal attenuation at high frequencies due to the voltage divider between CPE_{g-e} and R_s might be affected by the parasitic capacitance from a poor insulation of the metal contacts of the g-SGFETs. In order to determine whether this is the case or the impedance of the graphene-electrolyte interface dominates the attenuation in the transconductance, two sets of devices, with and without a

WILEY-VCH

part of the metal contacts exposed to the electrolyte have been characterized. The access length (L_{access}), which is defined as the distance between the end of the metal-graphene contacts and the uninsulated graphene channel can be defined as negative (i.e. -2 μm) in the first case and positive (1.5 μm) in the second. In **Figure S4**, the frequency response for these two types of device is shown. First, it can be observed that at low frequencies (below $10kHz$) the CPE behavior dominates the frequency response with a α = 0.89 (PBS concentration was equal to 0.5mM). In a second place, it can be observed that in the $3kHz - 40kHz$ band, the attenuation due to the previously described voltage divider dominates the frequency response. In this frequency range, the attenuation is more pronounced for the $L_{access} = -2\mu m$ due to increased parasitic currents.

It is interesting to note that despite the voluntary exposure of the metal contacts to the electrolyte, the frequency response is not dominated by the V_{int} drop term in the frequency bandwidth of interest for neural sensing (i.e. $< 10kHz$). The action potentials shown in Figure 4e in the main text were recorded with the devices corresponding to the Bode plot in Figure S4b (for $L_{access} = -2\mu m$).
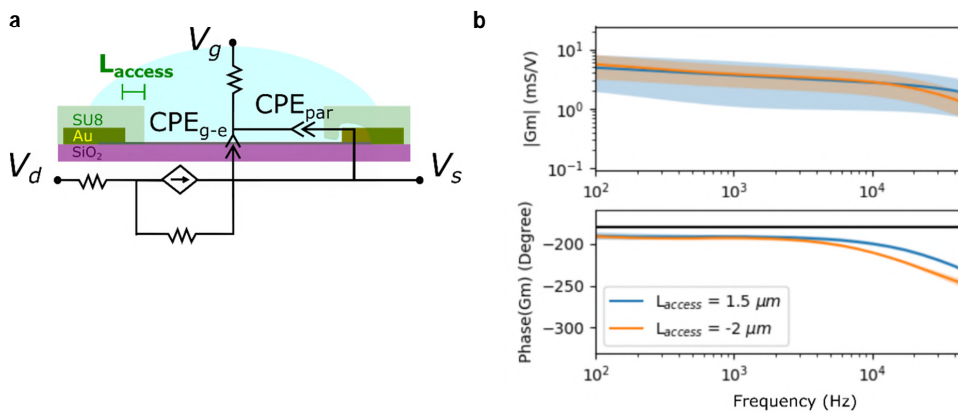
Figure S4: a) The equivalent circuit for the small signal model of the g-SGFET is schematized, indicating the meaning of L_{access}. b) The Bode representation for two different groups of g-SGFETs: with ($L_{access} = 1.5\mu m$) and without ($L_{access} = -2\mu m$) access region. The filled area indicates the standard deviation (for 4 g-SGFETs). The devices with $L_{access} = -2\mu m$ were used for HL-1 AP recording.

WILEY-VCH

S6. Effect of impurities on the frequency response

It has been previously speculated that impurities on the graphene channel might play a crucial role in the CPE behavior of the graphene-electrolyte interface.[3] This dependence on the surface charge could also explain the dependence of the CPE behavior with the ionic concentration in the environment. **Figure S5**a shows the frequency response of a macroscopic g-SGFETs where the graphene was not processed after the transfer (i.e. the channel of the g-SGFET consists of the complete graphene layer transferred on the substrate and the passivation was done manually using epoxy). This device shows a flat frequency response, with a phase of $-180°$ (corresponding to the holes conduction regime). The increase of the G_m magnitude and phase for frequencies above $10Hz$ can be attributed to the capacitive currents described in the main text, which present a much larger contribution in this case due to the large area of the device (i.e. $5mm \, x \, 5mm$). The effect of contamination can also be observed from the effect of cleaning with ethanol the finalized devices fabricated using photolithographic means (see Figure S5b). The pronounced loss of G_m magnitude due to contamination is followed by an increased hysteresis in the $I_{ds} - V_{gs}$ curves and a doping of graphene which results in an increased minimum number of charge carriers and displacement of the CNP. The sign of the hysteresis (i.e. increase/decrease of the current for an increasing/degreasing voltage) confirms that it is caused by a slow charging of the interface capacitance.[4,5]
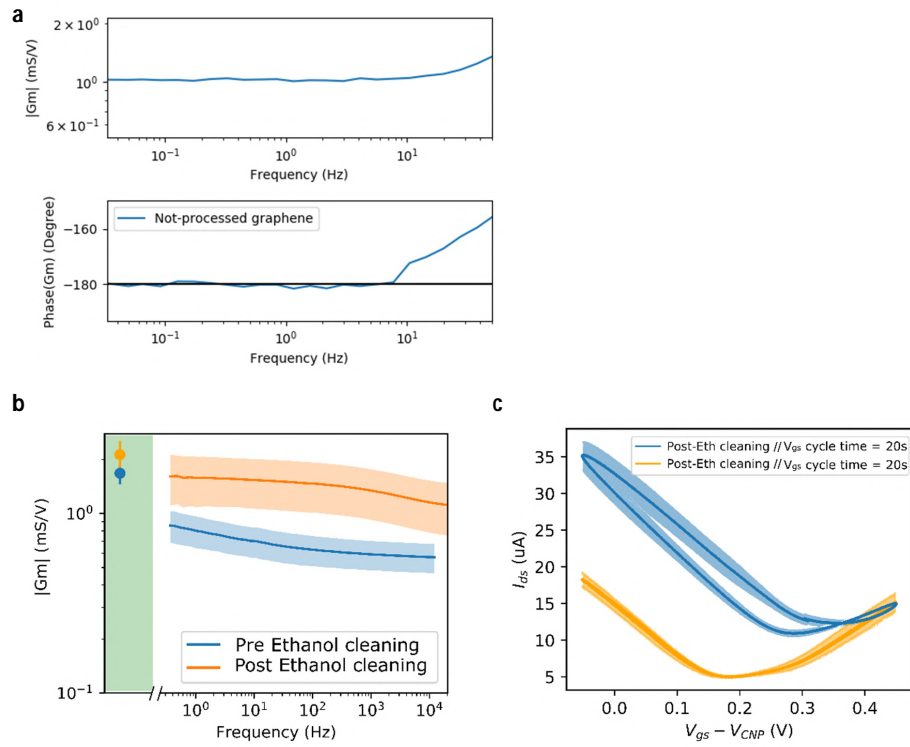
Figure S5: a) Bode representation of the macroscopic (unprocessesed) g-SGFET frequency response. b) Magnitude of the G_m over frequency for the processed g-SGFETs before and after cleaning with ethanol (for 4 g-SGFETs). c) Effect of cleaning with ethanol on the $I_{ds} - V_{gs}$ curves of the g-SGFETs. The filled area in all graphs indicates the standard deviation (for 4 g-SGFET).

WILEY-VCH

S7. Correction of harmonic distortion by interpolation into the $I_{ds} - V_{gs}$ curve

The schematic shown in **Figure S6**a illustrates the interpolation approach used to calibrate the signals. The distorted signal (dashed-red line) when interpolated into the $I_{ds} - V_{gs}$ curve is rescaled and the harmonic distortion simultaneously corrected. The resulting signal is shown by the solid-red line. The effect of calibration on the amplitude of the second harmonic is shown in Figure S6b for two different A_{sig} values. The three vertical lines in Figure S6b indicate the bias conditions for the spectra shown in Figure S6c. In Figure S6c it is possible to see that the increase of amplitude at $2f_{sig}$ around the CNP is due to calibrated noise level with small transconductance. The effectivity of the calibration method is also confirmed by showing the SDR (after calibration) on top of the A_{sig}-V_{gs} parameter map from Figure 2c in the main text. It is shown that the SDR is approximately flat over a wide V_{gs} range and its dependence with A_{sig} is effectively canceled.

The measured CSD events have been calibrated following the interpolation method. Afterwards, the calibrated signal corresponding to a quasi-distortion free signal has been artificially distorted for different V_{gs} values to show the effect of bias on the signal distortion (see Figure S6e). It is possible to observe a transition from a signal amplitude underestimation (for V_{gs} far away from the CNP) to a signal amplitude overestimation (close to the CNP). Figure S6f shows the difference in the CSD amplitude obtained by calibrating with a constant G_m and with the interpolation method. The error made in the signal amplitude determination by using a constant G_m becomes zero around $V_{gs} - V_{CNP} \approx -110mV$ where the impact of distortion is minimal as shown in Figure S6b and S6d.
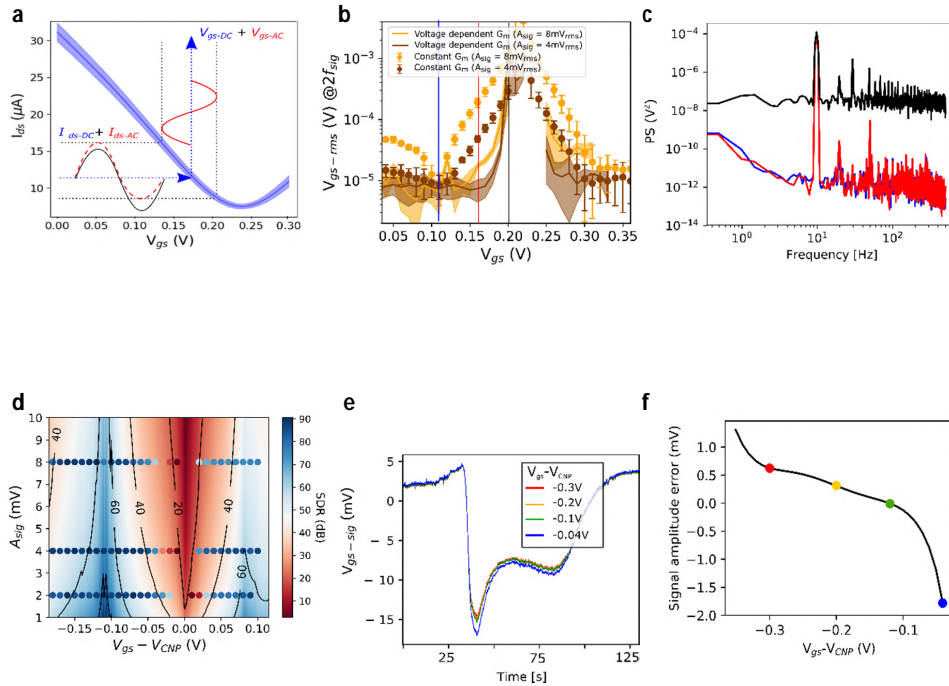
WILEY-VCH

Figure S6: a) Scheme of the calibration approach. Input signal in current is interpolated into the $I_{ds} - V_{gs}$ curve leading to a calibrated signal in voltage with the harmonic distortions corrected. b) The amplitude of the second harmonic in the equivalent voltage at the gate is shown for $A_c = 8mV$ and $4mV$ and calibrated using a constant G_m (dots) and using the interpolation into the $I_{ds} - V_{gs}$ curves (solid lines). The errorbars and filled area show the standard deviation for 4 g-SGFETs. c) Spectra at different representative V_{gs} values (marked by vertical lines in part b). The high SDR ratio close to the CNP appears due to an increase in the equivalent noise at the gate rather than an increase of higher orders. d) The SDR shown in Figure 2d is now plotted with the SDR after calibration with the non-linear $I_{ds} - V_{gs}$ curves. e) Effect of harmonic distortion on the recording of CSDs for different bias conditions. f) The error in the amplitude of the CSD due to harmonic distortion is shown for different V_{gs} values. The colored dots indicate the bias conditions corresponding to the CSD curves in part e).

S8. Limits in the static model of harmonic distortion

The slow charging of the graphene-electrolyte interface capacitance leads to a hysteretic response of the $I_{ds} - V_{gs}$ curve as shown in Figure S5c. The impact of the hysteresis on the harmonic signal distortion, which is related to a non-ideal frequency response, can be better evaluated by measuring

harmonic distortion at different frequencies. To evaluate the impact of the non-ideal frequency response on the harmonic distortion, the comparison between measured harmonic distortion and calculated values from the Taylor expansion of the $I_{ds} - V_{gs}$ curve has been performed for a $1kHz$ pure tone. **Figure S7**a shows the result of this comparison; it is possible to observe a discrepancy between the DC and AC-derived values. This deviation for the 1st harmonic (corresponding to the applied signal) is proportional to the drop observed in the magnitude of the frequency dependent transfer function (ΔG_m shown in Figure S7a and S7b). Interestingly, the 2nd harmonic and the 3rd harmonic drop by the same factor (ΔG_m) squared and cubed respectively. This attenuation corresponds to divide the signal at the interface (V_{int}) by a factor ΔG_m. The close match between the actual distortion and the values extracted from the DC characteristics after correcting the signal amplitude indicates that the hysteretic response does not change significantly the harmonic distortion (Figure S7c), but only the effective signal at the gate V_{int}.

This deviation from the stationary response, however, has a small impact for the calibration of electrophysiological signals. Signals with a large amplitude of few mV are typically in the slow frequency range and therefore close to the stationary response. A deviation from the transconductance of the measured $I_{ds} - V_{gs}$ curve and the actual transconductance at the frequency of the signals will cause a second order error in the signal amplitude determination.
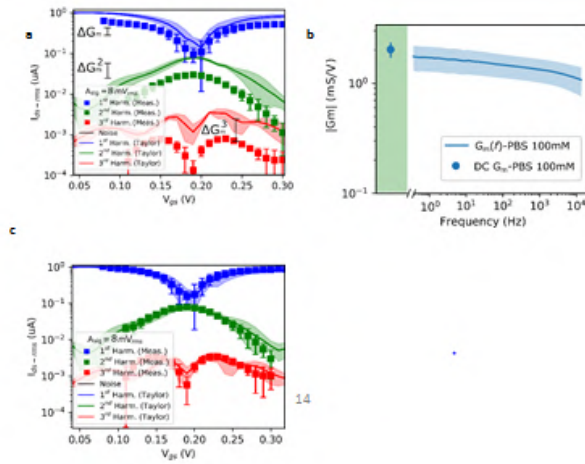
WILEY-VCH

Figure S7: a) Comparison of signal amplitude, 2nd and 3rd order harmonics amplitude extracted from the Taylor expansion of the static $I_{ds} - V_{gs}$ curve and measured by applying a 1kHz pure tone signal at the gate. b) Magnitude of the G_m over frequency and DC G_m of the g-SGFETs used for the characterization of harmonic distortion shown in graph (a) and (c). c) Comparison of AC-derived harmonic distortion and the values extracted from the Taylor expansion of the $I_{ds} - V_{gs}$ curve corrected with the the frequency drop of C_{CPE} at 1kHz. The errorbars and filled area in all graphs show the standard deviation for 4 g-SGFETs.

S9. Numerical implementation of the analytic transfer function

To implement the transfer function of fractional order it has to be approximated as a higher (and integer) order system which mantains a constant phase over a certain bandwidth.[6] **Figure S8** shows the approximation of the transfer function using Oustaloup's method which synthetizes the TF by the recursive distribution of (2N + 1) zeros and poles.[7] This method gives an accurate description of the non-integer order TF within a defined bandwidth [ω_b, ω_h] (see Figure S8). In addition, it has the advantage over other modelling tools that its digital implementation for real-time applications is given in a straight forward manner from its finite number of zeros and poles.
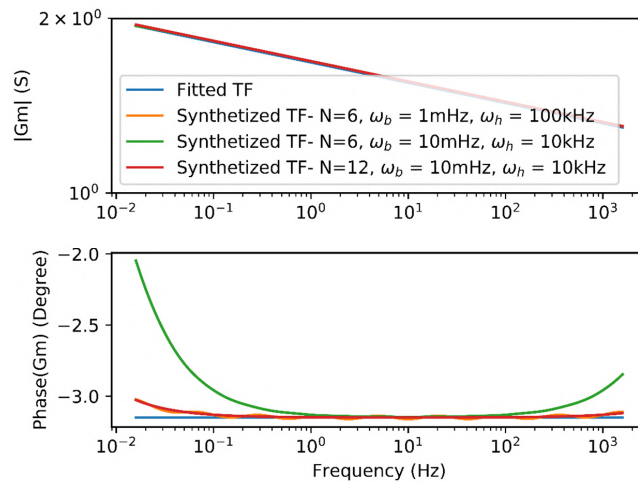
Figure S8: Analytical transfer function (blue) and approximated TF using Oustaloup's method for different bandwidths and number of poles and zeros.

References

[1]   C. H. Hsu, F. Mansfeld, *CORROSION* **2001**, *57*, 747.

[2]   C. Mackin, L. H. Hess, A. Hsu, Y. Song, J. Kong, J. A. Garrido, T. Palacios, *IEEE Trans. Electron Devices* **2014**, *61*, 3971.

[3]   J. Sun, Y. Liu, *Nanomaterials* **2019**, *9*, 923.

[4]   H. Wang, Y. Wu, C. Cong, J. Shang, T. Yu, *ACS Nano* **2010**, *4*, 7221.

[5]   M. Winters, E. Ö. Sveinbjörnsson, N. Rorsman, *J. Appl. Phys.* **2015**, *117*, 074501.

[6]   S. Das, I. Pan, *Fractional Order Signal Processing*, Springer Berlin Heidelberg, Berlin, Heidelberg, **2012**.

[7]   A. Oustaloup, F. Levron, B. Mathieu, F. M. Nanot, *IEEE Trans. Circuits Syst. I Fundam. Theory Appl.* **2000**, *47*, 25.
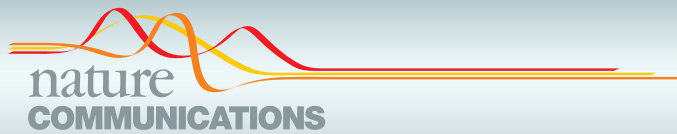
ARTICLE

Check for updates

Graphene active sensor arrays for long-term and wireless mapping of wide frequency band epicortical brain activity

R. Garcia-Cortadella[1,9], G. Schwesig[2,9], C. Jeschke[3], X. Illa [4,5], Anna L. Gray[6], S. Savage[6], E. Stamatidou[6], I. Schiessl [7], E. Masvidal-Codina[4,5], K. Kostarelos [1,6], A. Guimerà-Brunet[4,5], A. Sirota[2✉] & J. A. Garrido [1,8✉]

Graphene active sensors have demonstrated promising capabilities for the detection of electrophysiological signals in the brain. Their functional properties, together with their flexibility as well as their expected stability and biocompatibility have raised them as a promising building block for large-scale sensing neural interfaces. However, in order to provide reliable tools for neuroscience and biomedical engineering applications, the maturity of this technology must be thoroughly studied. Here, we evaluate the performance of 64-channel graphene sensor arrays in terms of homogeneity, sensitivity and stability using a wireless, quasi-commercial headstage and demonstrate the biocompatibility of epicortical graphene chronic implants. Furthermore, to illustrate the potential of the technology to detect cortical signals from infra-slow to high-gamma frequency bands, we perform proof-of-concept long-term wireless recording in a freely behaving rodent. Our work demonstrates the maturity of the graphene-based technology, which represents a promising candidate for chronic, wide frequency band neural sensing interfaces.

[1] Catalan Institute of Nanoscience and Nanotechnology (ICN2), CSIC and BIST, Campus UAB, Bellaterra, 08193 Barcelona, Spain. [2] Bernstein Center for Computational Neuroscience Munich, Faculty of Medicine, Ludwig-Maximilians Universität München, Planegg-Martinsried, Germany. [3] Multi Channel Systems (MCS) GmbH, Reutlingen, Germany. [4] Instituto de Microelectrónica de Barcelona, IMB-CNM (CSIC), Esfera UAB, Bellaterra, Spain. [5] Centro de Investigación Biomédica en Red en Bioingeniería, Biomateriales y Nanomedicina (CIBER-BBN), Madrid, Spain. [6] Nanomedicine Lab, National Graphene Institute and Faculty of Biology, Medicine & Health, University of Manchester, Manchester, UK. [7] Division of Neuroscience and Experimental Psychology, School of Biological Sciences, Faculty of Biology, Medicine and Health, University of Manchester, Manchester M13 9PT, UK. [8] ICREA, Pg. Lluís Companys 23

ncreasing the bandwidth of neuroelectronic interfaces in terms of spatial resolution and sensitivity in a wide frequency range is a major and ongoing challenge in neural engineering. In the last decades, large efforts have been dedicated to the development of neural sensing interfaces with high sensor-count on conformal substrates[1–10], which are required for highly biocompatible intracranial neural probes[11–14]. In this line, active sensors have emerged as a promising building block for high-bandwidth neural interfaces[4,6,15–19] because they can be arranged in a multiplexed array[2,4,6–9] enabling high sensor-count probes. The detection principle of active sensors is typically based on the modulation of the conductivity of a transistor channel, which is electrically coupled with the biological environment through its gate[8,9,15,18,20–22], producing a local signal pre-amplification. Although active sensing technologies present substantial advantages over conventional micro-electrode arrays, their implementation is currently limited by the demanding material properties required. In order to achieve long-term and highly sensitive neural recordings, materials for active sensing are expected to exhibit semiconducting or semimetallic properties, a high electrical mobility and low intrinsic noise, in addition to a high stability, easy integration in flexible substrates and biocompatibility. Some active sensors based on organic semiconductors and thin Si nanomembranes have exhibited promising performance, with novel transistor architectures[17,22] and insulating technologies[4,14] improving their performance in some typically constrained aspects such as their frequency response or their long-term stability. Graphene-based active sensors are another promising candidate to meet these requirements due to the flexibility of graphene[23,24], its high expected stability[25] and biocompatibility[26,27], as well as its electronic properties, including a high mobility of charge carriers[28,29]. Graphene solution-gated field-effect transistors (g-SGFETs) have demonstrated a high sensitivity for the detection of local field potentials[15] (LFP), as well as a high performance in multiplexed operation[6,7]. In addition, g-SGFETs have recently demonstrated a high sensitivity for the mapping of infra-slow (<0.5 Hz) brain activity (ISA)[30–32] with high spatial resolution[6,7,33,34].

ISA has recently attracted increasing attention due to its unique neurophysiological basis[30] and its relation to resting state networks[31,35–37] and to brain states[36,38–40]. To date, ISA has been typically studied using full-band electroencephalography (fb-EEG)[41,42]. However, increasing spatial resolution of ISA monitoring by using small size electrodes is ultimately limited by the dependence of the amplifier gain on the impedance of the electrodes used. This dependence leads to signal-to-noise loss and signal distortion[43] at low frequencies. For this reason, studies of ISA with high spatial resolution have been typically restricted to indirect measurement methods such as functional magnetic resonance imaging[31,37], optical methods[44] or the analysis of infra-slow changes of signal power at higher frequencies[45]. G-SGFETs, as active sensors, transduce the electrochemical potential signals in the brain (V_{sig}) into drain-to-source current (I_{ds}) signals (see Fig. 1a). The amplitude of the transduced signals is proportional to the transconductance (g_m), defined as the slope of the I_{ds}–V_{gs} curves divided by V_{ds} (see Fig. 1b). g_m is proportional to the gate capacitance per unit area (intensive property) and to the W/L ratio of transistor, but not to its active area[17,46–49]. Signal detection based on the field-effect mechanism, therefore, allows to prevent the signal distortion and gain loss observed for small passive sensors in the infra-slow frequency band. This advantage is expected to be valid for all FET-based sensor technologies with stable transfer characteristics, however, experimental proof has been only shown for g-SGFETs, which present a particularly high

physiological role with an improved spatial resolution. However, in order to advance in the actual application of g-SGFET arrays, several technical aspects remain to be thoroughly evaluated.

In this article, we present a sensing system composed of a flexible 64-channel g-SGFET array and a wireless headstage (Fig. 1c–f and supplementary information S1), which we use to demonstrate the maturity of this technology in terms of long-term and wide frequency band recording capabilities in freely moving animals from a system perspective. First, the focus is placed on the assessment of the in vitro characteristics of the system; including the yield and homogeneity of the graphene sensors, their intrinsic noise and the impact of the data-acquisition (DAQ) system on the sensitivity of these devices. Second, critical aspects for their chronic application in vivo have been resolved; including the stability of the graphene doping, the long-term stability of the g-SGFETs sensitivity and their acute, as well as chronic biocompatibility. Finally, we have applied this methodology to monitor the epicortical local field potentials (LFP) in a freely moving rat model simultaneously with its three-dimensional (3D)-position during long sessions of up to ~24 h. The combination of behavioral and electrophysiological data has been used to assess the capabilities of the wireless recording system to monitor brain dynamics across unperturbed alternation of brain states and validate its sensitivity to detection of high-frequency oscillations associated with sparse behavioral events. As an illustration of unique features of the g-SGFET recording we provide a first case demonstration of infra-slow topographically specific and brain-state invariant pattern associated with high-voltage spindles (HVS). Furthermore, we find changes in infra-slow signal power between slow wave sleep (SWS) and rapid eye movement (REM) sleep and identify the modulation of theta oscillations and sleep spindles by the phase of the DC-signal infra-slow dynamics during REM and SWS, respectively. The results reported here demonstrate that neural probes based on graphene active sensor arrays represent a mature technology, with a high sensitivity, stability and biocompatibility, which allows to chronically map wide frequency band epicortical brain dynamics in freely behaving animals.

Results

Homogeneity and sensitivity of graphene active sensor technology. For the implementation of graphene active sensor arrays as a readily available tool for neuroscientific research, the maturity of large-scale, flexible graphene electronics is critical. Two of the main challenges in the development of these technologies have typically been the production of high-quality single-layer graphene (SLG) and its transfer onto the required substrate. The development of wafer-scale methods to produce SLG has concentrated many efforts and investment in the last decade[50], recently leading to important progress on the growth of graphene by chemical-vapor deposition (CVD)[51]. Here, we show that the quality of commercially available single-layer graphene produced by CVD and transferred on a flexible polymeric substrate (spin-coated on a 4-inch Si wafer) is high enough to enable the fabrication of g-SGFET arrays with a homogeneous good performance both in terms of g_m and electrical low-frequency noise.

Figure 2a shows the boxplot for the g_m of nine neural probes, each of them containing 64 g-SGFETs (with a size of 100×100 μm^2 chosen for mesoscale epicortical LFP analysis[10]). These probes were randomly selected from three wafers, all of them processed in independent batches (see "Methods" for fabrication details). It is possible to observe a high homogeneity and yield in
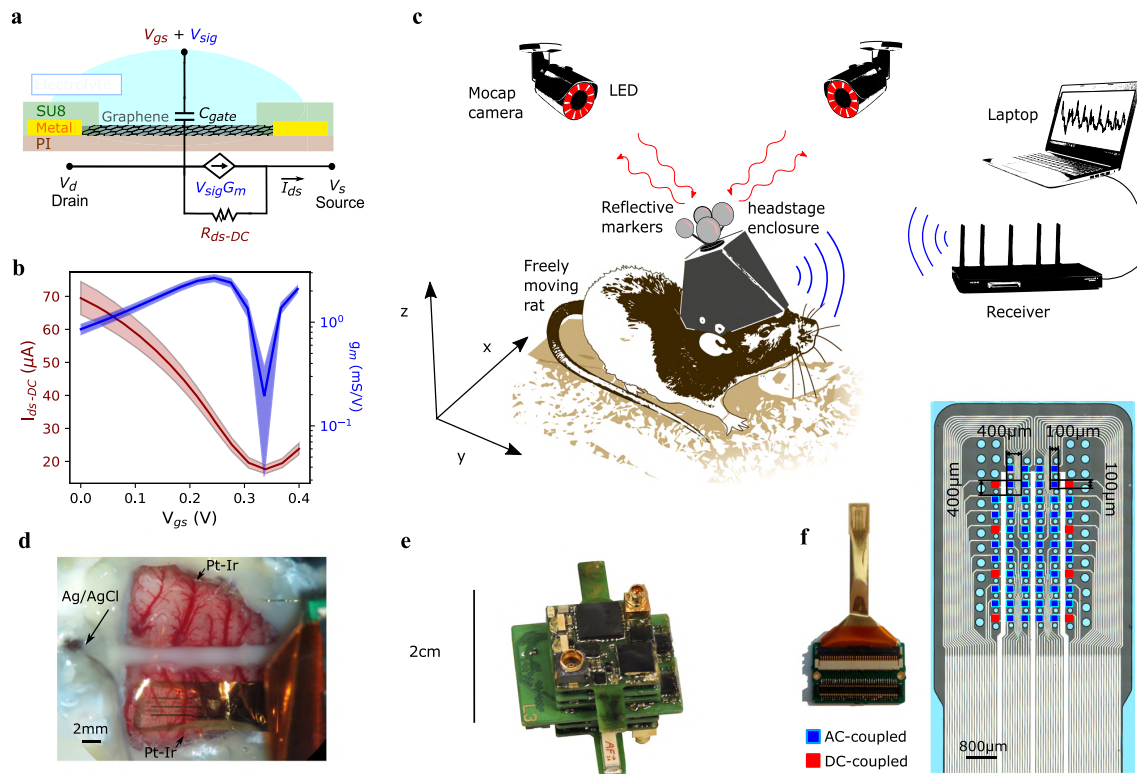
Fig. 1 Graphene active sensor arrays for chronic, wireless monitoring of wide frequency band epicortical neural activity. a Schematic of a g-SGFET and its equivalent circuit. The small-signal transduction from voltage to current is modeled by the current source $G_m V_{sig}$, where $G_m \equiv dI_{ds}/dV_{gs}$. The DC current is modeled by the R_{ds} element. **b** Average stationary transfer characteristics of 8 g-SGFETs (left axis) and the g_m of 64 g-SGFETs (right axis). The filled area indicates the standard deviation. **c** Illustration of the rat with the untethered recording system implanted. The headstage and the 3D-printed frame to hold it are covered by a 3D-printed enclosure. On top, the position markers of the motion capture (Mocap) system are fixed, which reflect light back to the Mocap cameras placed in the room. The neural signals transduced by the graphene sensors are digitized and transmitted wirelessly to the signal receiver, which is connected to a computer for signal recording. **d** g-SGFET array placed on the rat cortex; the position of the reference electrode in contact with the cerebellum and two Pt-Ir electrodes at either side of the g-SGFET array are marked with arrows. **e** Photograph of the wireless headstage designed for these experiments. **f** Photograph of the 64 g-SGFET array mounted on a customized connector (left) and zoomed image of the probe active area (right). The red squares indicate the g-SGFETs on the array, which are connected to the headstage inputs with DC capabilities.

g_m, 1.9 mS/V, is relatively high with respect to flexible silicon FETs[8] and comparable with typical organic transistor values[17,52] due to the high electrical mobility and gate capacitance of g-SGFETs. In Fig. 2b the equivalent noise at the gate ($V_{gs\text{-rms}}$) of the same devices is shown (see supplementary information S2). $V_{gs\text{-rms}}$ is an important figure of merit to evaluate the sensitivity of the sensors[47], which is defined as the ratio between the integrated current noise ($I_{ds\text{-rms}}$) of the transistor and its transconductance. Although this parameter presents a larger dispersion than g_m, it is possible to identify 3 out of 9 probes with 96% of the g-SGFETs showing a $V_{gs\text{-rms}}$ below 10 μVrms, suggesting that the measured noise is not directly related to g_m. In fact, low-frequency noise in graphene has been reported to originate from charge trapping-detrapping events[53], which makes noise directly proportional to the density of traps and thus, sensitive to impurities in the environment of graphene. Figures 2c, d show the distribution of g_m and $V_{gs\text{-rms}}$, respectively, for the probe #3 labeled with an asterisk in Fig. 2a. The dispersion in the transconductance of the g-SGFETs can be taken into account in the calibration of the neural signals, correcting dispersion in the signal amplification. Therefore, the truly limiting factor in terms

a mean of 4.13 μVrms and a standard deviation of 1.14 μVrms (excluding the outliers shown in Fig. 2b). These results show that graphene-based neural probes prepared using a 4-inch wafer-scale fabrication process can be obtained with a high homogeneity and sensitivity. Additionally, upscaling of the fabrication process to an industrial scale is expected to further improve the homogeneity of g-SGFETs characteristics, especially in terms of the contamination-dependent charge noise[47,53].

Wireless headstage design and characteristics. Another aspect that contributes to the sensitivity of the recording system is the noise introduced by the headstage in the amplification and digitization process. The amplification of the wide frequency band activity requires a DC-coupled system, which implies the digitization of signals with large DC-offsets. In order to digitize signals with such a large dynamic range and minimize quantization noise, a two-stage transimpedance amplifier has been implemented (see schematic in Fig. 2e). The first stage converts the I_{ds} currents from the g-SGFETs into voltage, which contains a wide frequency band signal, including the infra-slow frequency components of I_{ds}. In the second amplification stage (see Fig. 2e), the
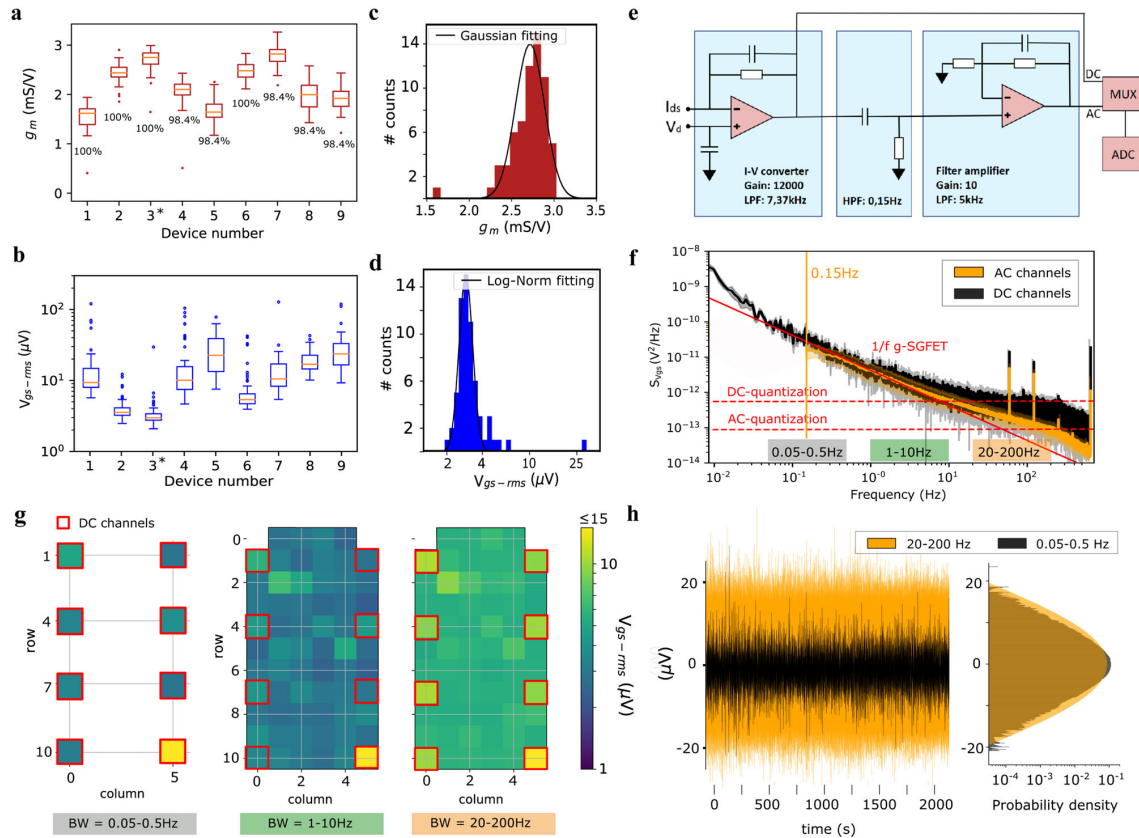
Fig. 2 Evaluation of system sensitivity. a Boxplot of g_m for nine randomly selected probes from three different wafers produced in independent batches. The yield in terms of g_m above 70% of the median is indicated. **b** Boxplot for $V_{gs\text{-rms}}$ measured in the 1–10 Hz frequency range, plotted for the same neural probes evaluated in part **a**. All probes consisting of 64 g-SGFETs. The boxes extend from the lower to the upper quartiles, with a line at the median. The whiskers extend 1.5 times the inter-quartile range and the data points beyond the whiskers are indicated by a dot. **c** Histogram of g_m for the 64 g-SGFETs of probe #3 (labeled in panel **a**) and Gaussian fit of the histogram excluding the outliers shown in panel **a**. **d** Histogram of $V_{gs\text{-rms}}$ for the 64 transistors in probe #3 (see panel **b**) and log-normal fit of the histogram excluding the outliers shown in panel **b**. **e** Equivalent circuit of the wireless headstage. **f** Power spectral density (PSD) of the noise from DC channels (black) and AC channels (orange) in probe #3. The 1/f dependence is represented by the solid red line. The vertical orange line indicates the hardware high-pass filter applied to AC channels at 0.15 Hz. The quantization noise of the DC and AC channels is indicated by the horizontal dashed red lines. **g** Representation of the $V_{gs\text{-rms}}$ for all g-SGFETs in probe #3 shown for different bandwidths; 0.05-0.5 Hz band for the DC-channels (left), 1–10 Hz band (middle), and 20–200 Hz (right). The position of the g-SGFETs on the array connected to DC-channels of the headstage is indicated by the red squares. **h** Time domain representation of the noise spectra shown in part **f** and **g** (DC-channels filtered in the 0.05–0.5 Hz band and AC channels in the 20–200 Hz band). Signal from eight channels are overlapped.

dynamically choose between a DC or AC coupling for each channel, a multiplexer has been added to switch between the output of the first and the second stages, see Fig. 2e. Multiplexers have been implemented in only 8 of the 64 channels in order to minimize power consumption and, therefore, battery weight and volume of the dedicated wireless headstage.

Having a relatively high transconductance is important in order to pre-amplify the signals above the noise floor of the transimpedance amplifiers. However, active sensors typically present an intrinsic 1/f noise, which scales with the drain-to-source current[47]. Therefore, $V_{gs\text{-rms}}$ is a more suitable figure of merit to evaluate the sensitivity of active sensors. In order to validate that the sensitivity of the recording system is limited by the intrinsic noise of the active sensors, it is paramount to evaluate the impact of the amplification electronics on the sensitivity of the system in a wide frequency band. The noise level

$(S_{V_{gs}}(f))$, defined as the PSD of the current noise over the transconductance (see Fig. 2f). The central part of the spectrum, from roughly 0.05 Hz to 10 Hz, is dominated by the 1/f intrinsic noise of the graphene transistors[53]. For frequencies below 0.05 Hz, the DC-channels show a slight increase above the 1/f noise, which is attributed to the contribution of additional noise sources in the amplification chain, leading to slightly larger $V_{gs\text{-rms}}$ values in the 0.005–0.05 Hz band (see supplementary information S2). Above 10 Hz the noise spectra present a significant increase above the 1/f noise, caused by the quantization noise of the headstage amplifiers, which is more pronounced in DC-channels. The $S_{V_{gs}}(f)$ integrated in different frequency bands is shown in Fig. 2g for all channels on the neural probe #3. The three maps demonstrate the similarity of the sensitivity of the system in the different ranges, with only a significant increase in the 20–200 Hz band. In this band, the noise of the DC-channels exceeds

ARTICLE

The digitization noise for AC channels might be decreased by further optimizing the gain of the second amplification stage. However, the intrinsic noise of the amplifier is expected to dominate for large amplification gains. In order to better illustrate the constant sensitivity over frequency, Fig. 2h shows the time domain representation of the noise signal filtered in the ISA band (0.05–0.5 Hz) and the high-frequency band (20–200 Hz). The histogram plotted next to the time-domain representation of both signals shows their probability density distribution, which demonstrates the similarity of their variance, as expected from the integration of a 1/f spectrum in these frequency bands. Note that the apparently lower amplitude in the time-domain representation of the infra-slow noise is due to the different timescales of 1/f noise in both frequency bands, but not due to a different signal variance.

These results show the high sensitivity of the system in a wide frequency band, with $V_{gs\text{-}rms}$ below 5 μV in the infra-slow frequency band. In the design of the headstage, we have considered the compromise between reaching maximum sensitivity in the high-frequency range and minimizing the power consumption of the DC-coupled recording system with a relatively high channel count. Smaller g-SGFETs are expected to present a higher intrinsic noise (see supplementary information S2), as expected for any active or passive sensor. Therefore, our results indicate that the sensitivity of g-SGFETs in the infra-slow frequency is not affected by the amplification electronics for sensor areas below 100×100 μm. This is in strong contrast with ISA detection using passive electrodes, for which the gain loss and signal distortion is expected to increase for smaller sensor dimensions. These results demonstrate the limits and the scalability of the g-SGFET technology towards higher density arrays with ISA detection capabilities.

Signal stability and sensitivity over time. Once the performance of the graphene transistors and the headstage is properly assessed, the stability of the g-SGFETs in an in vivo chronic setting needs to be evaluated in order to ensure the reliability of the recording system.

The I_{ds}–V_{gs} curves of the g-SGFETs describe the relationship between the measured drain-to-source current and the electrochemical potential at the graphene-electrolyte interface. The minimum in I_{ds} occurs at a particular gate voltage, referred to as the charge neutrality point (CNP), which is also related to a minimum in the sensitivity of the device (see Fig. 1a). The CNP corresponds to the bias conditions for which the Fermi energy in the graphene channel is, on average, closest to the energy with a minimum density of states (i.e., the Dirac point)[55]. The V_{gs} overpotential required to reach this energy depends on the doping[56] of the graphene channel, as well as on the electrochemical potential of the reference electrode. Therefore, instabilities in any of these two parameters will produce a shift of the transfer characteristics in the V_{gs} axis. In turn, this shift implies that I_{ds} will present a drift and that the sensitivity of the g-SGFETs might vary over time for a constant V_{gs} overpotential. Having a controllable doping of the g-SGFET and a homogeneous CNP among sensors is, therefore, of paramount importance to maintain a good sensitivity of the sensor array.

Figure 3a shows the evolution of the transfer characteristics over 4 weeks after implantation of the neural probe (see "Methods" for implantation details). The observed shift in the CNP is presumably due to a combination of factors, including desorption of contaminants by electrochemical cleaning of the graphene-electrolyte interface[57], adsorption of charged

information S3). However, from these results it is not possible to distinguish among all different contributions. The accumulated drift in the CNP measured during the first 24 h of recording reaches approximately 50 mV, with a maximum change rate of ~20 mV/h in the first hour (see supplementary information S3). Figure 3b shows the measured signal in two DC-coupled channels (high-pass filtered at 1 mHz) during the first 2 h of recording. Figure 3c shows the amplitude-phase relationship between these two DC-coupled channels in the 0.005–0.05 Hz band (see "Methods" section). The left panel shows the amplitude-phase coupling measured in PBS, while the right panel shows the equivalent results in vivo. The in vivo signals exhibit fluctuations with a much larger amplitude than the signals recorded in PBS, ruling out the transistor 1/f noise and the headstage noise as the origin of these infra-slow oscillations. Further, the in vivo signals recorded in the 0.005–0.05 Hz band present fluctuations in anti-phase, which confirm that neither instabilities in the reference electrode nor adsorption/desorption of chemical species on graphene are responsible for these fluctuations. To conclude this discussion, Fig. 3d shows the effect of drifts in the graphene doping on the $V_{gs\text{-}rms}$ of graphene sensors. These results demonstrate that their sensitivity does not change significantly due to the accumulated drifts during up to 24 h if the initial bias is selected properly. Therefore, daily tracking of the CNP and readjustment of the V_{gs} overpotential back to optimum values is enough to keep a constant sensitivity over long-term monitoring of the brain dynamics.

In addition to changes in the doping of graphene, the transconductance and noise of the g-SGFETs might vary over time due, for instance, to the creation of defects in the graphene lattice. Pristine graphene has shown excellent chemical stability due to its sp2 hybridization[25]. However, dangling bonds at edges, grain boundaries, atomic vacancies or reconstructions in the atomic lattice increase the reactivity of graphene, which might lead to the creation of defects over time[25]. In addition, there might be mechanical causes of performance degradation such as detachment of graphene from the substrate or bending-induced strain on the graphene lattice and metal-graphene contacts. Another possible cause of sensitivity degradation could be the encapsulation of the device by glial scar tissue[58]. This layer of tissue can be modeled as an electrical impedance in series with the graphene-electrolyte interface[59], which can eventually lead to a degraded frequency response of the g-SGFETs.

In order to track changes in the sensitivity over time in a chronic implant, the g_m extracted from the I_{ds}–V_{gs} curves and the $V_{gs\text{-}rms}$ were periodically measured for the 8 DC-coupled channels over 4 weeks. Figure 3e shows that g_m remained approximately constant, suggesting that there are no major creation of defects in the graphene channel in the in vivo environment. Similarly, the $V_{gs\text{-}rms}$ shows only a slight increase in the last days. Figure 3f shows the current noise ($I_{ds\text{-}rms}$) for all the 64 channels measured at 200 Hz over 4 weeks. At this frequency, it is possible to estimate changes in the sensitivity of the recording system due to the low average power of high-frequency neural signals (see supplementary information S4). The numeric values displayed in Fig. 3f indicate the percentage of g-SGFETs working (see supplementary information S4). The frequency response of the transconductance ($g_m(f)$) has also been measured in vivo over 4 weeks after implantation. For this purpose, two Pt-Ir electrodes were implanted on both sides of the g-SGFET array (see inset in Fig. 3g) and 1 μA amplitude pure tone signals of different frequencies were applied using a current source. Figure 3g shows the magnitude of $g_m(f)$ for different days after implantation of
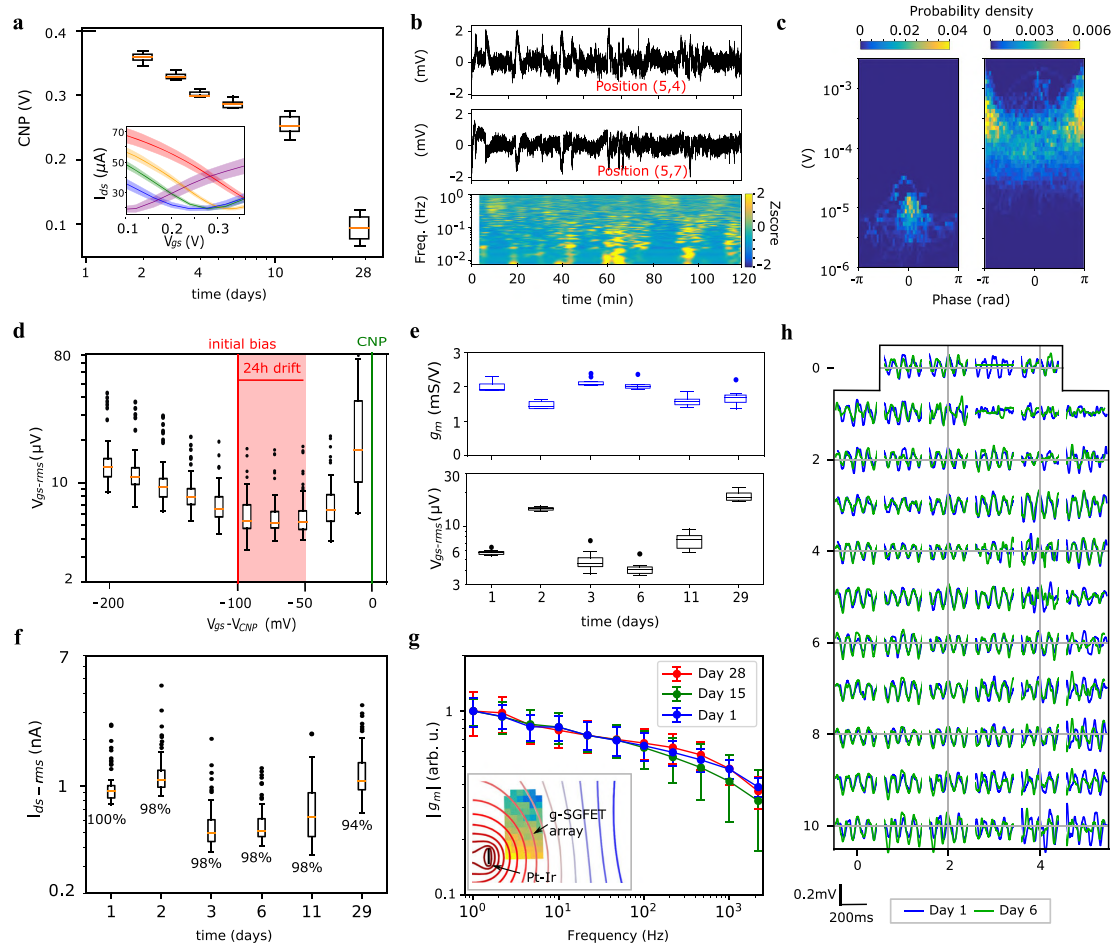
Fig. 3 g-SGFET stability in-vivo. a CNP vs. time over 4 weeks. The inset shows the I_{ds}–V_{gs} curves. Mean and standard deviation for $n = 8$ g-SGFETs (1 outlier excluded). **b** Signal from two DC-coupled channels. Indicated positions corresponding to map in panel **h**. The spectrogram of channel (5,7) is shown (bottom). **c** The phase-amplitude relation between the channels in panel **b**, for the noise measured in the beaker (left) and for the signals measured in vivo (right). **d** Boxplot of $V_{gs\text{-}rms}$ vs. shifts in the effective gating (V_{gs}–V_{CNP}) of the 64 g-SGFETs. The colored area indicates the measured drift in the CNP referred to a Ag/AgCl electrode during the first 24 h of recording. The initial bias and the CNP are indicated by the red and green vertical lines respectively. **e** g_m (top) and $V_{gs\text{-}rms}$ (bottom) measured over 4 weeks post implantation; g_m was obtained from the I_{ds}–V_{gs} curves of the DC-coupled channels ($n = 8$ g-SGFETs, 1 outlier excluded). **f** Current noise over 4 weeks after implantation ($n = 64$ g-SGFETs). The numeric values indicate the yield of working devices (see supplementary information S4). The boxes in panels **a** and **d–f** extend from the lower to the upper quartiles, with a line at the median. The whiskers extend 1.5 times the inter-quartile range and the data points beyond the whiskers are indicated by a dot. **g** Average and standard deviation of the frequency-dependent transconductance ($|g_m|$ (f)) shown for different days after the implantation ($n = 10$ g-SGFETs). The inset shows the approximate position of the Pt-Ir electrode close to the array, the simulated equipotential contour lines in a conductive plane and the relative signal amplitude measured by each of the g-SGFETs in the array (see supplementary information S5). **h** Signals measured by all g-SGFETs on the array during a state of increased theta activity on day 1 and day 6 after implantation.

approximately constant slope (in a log-log scale) follows a fractional order attenuation (i.e., approximately $\propto 1/f^{0.1}$), which has been recently attributed to the non-ideal capacitive response of the graphene-electrolyte interface[34]. A calibration method to correct such transconductance variation has also been proposed[34]. The evolution of the frequency response does not show major changes in the slope of the g_m attenuation, indicating that there is not a significant increase in the electrical impedance in series with the graphene-electrolyte interface due to device encapsulation[60]. To conclude, Fig. 3g shows the recorded neural activity in a state of increased theta power in day 1 and day 6 after

greater detail, by studying a large animal cohort, the stability of the biological signal over time, a critical aspect in electrophysiology research and for the long-term performance of brain-computer interfaces[61,62]. Furthermore, the polymers used as a substrate and passivation layers could be modified to reduce the moisture absorption[14,63] and displace the neutral plane of the device at the position of the graphene channel (see "Methods" section). Yet, the results presented in this section reveal a promisingly stable performance over time, which sets a lower bound for the stability of g-SGFETs in a chronic implant environment. Besides, from a system perspective, we show that g-
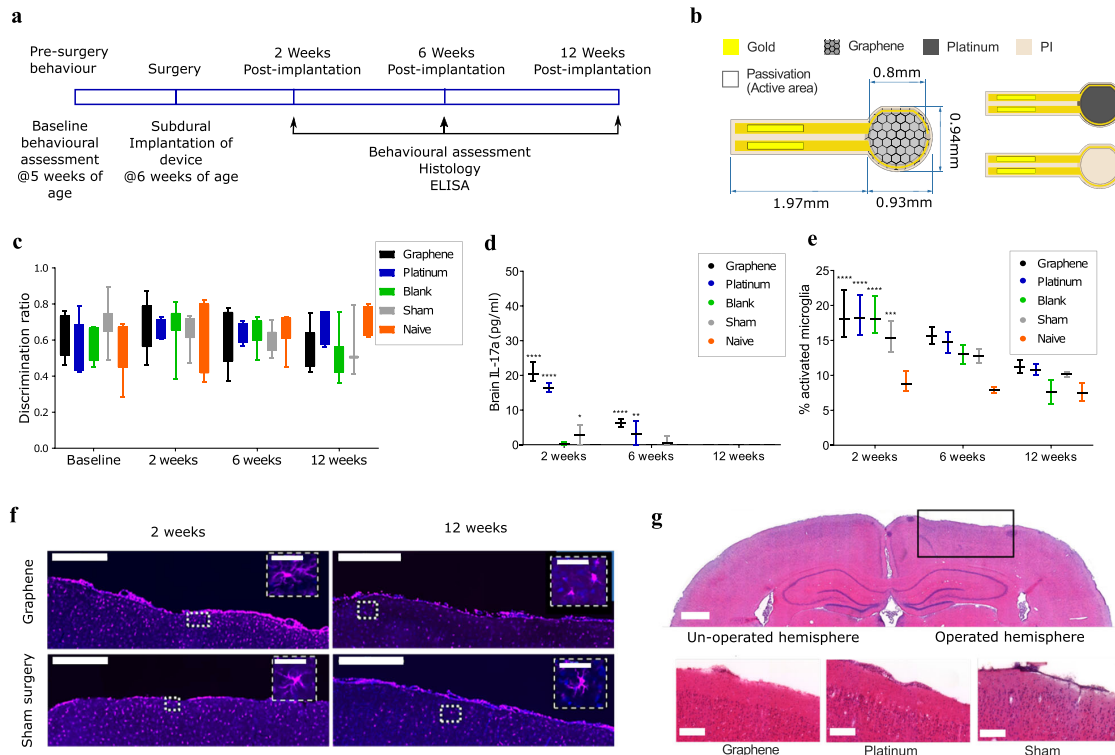
Fig. 4 Biocompatibility testing of non-functional g-SGFET vs. control devices. a The timeline describes the procedures carried out on animals during the biocompatibility study. **b** Schematic of the high-surface area g-SGFET prototype developed for biocompatibility testing in-vivo. **c** Discrimination ratio from NOR test over different days after implantation (see "Methods" section). For all five groups tested, the discrimination ratio was above 0.5 at all timepoints. Evaluated for $n = 7$ animals per group at all timepoints, except 12 weeks which had $n = 3$ (sham), $n = 4$ (platinum and naive) and $n = 7$ (blank). The boxes from the lower to the upper quartile, while whiskers represent minimum and maximum values. **d** Inflammatory marker IL-17a in the brain tissue for all groups and timepoints. Evaluated for $n = 4$ animals after 2 and 12 weeks, and $n = 3$ animals at 12 weeks. **e** Microglial activation state, expressed as a percentage of total microglial presence in the site surrounding the electrodes. $n = 3$ animals at 2 and 12 weeks, $n = 2$ animals (or 3 for the contralateral hemisphere) at 6 weeks. Bars in panels **d** and **e** indicate the mean and range of data point. **f** Iba-1 immunoflourescent staining to assess activation status of microglia at the surgical site obtained from 40 sections per animal. Scale bar equals 500 μm (50 μm at the insets). **g** Haemotoxylin and Eosin staining at 2 weeks post implantation shows there is no structural damage to the cortical layers directly at the device implantation site. Forty sections at 25 μm per animal were imaged. Scale bar equals 1 mm (top) and 200 μm (bottom). In panels **d** and **e** two-way ANOVA test with Dunnett's multiple comparison to the naive control within each timepoint with $n = 3$ or larger: *, **, ***, and **** indicate $p = 0.015$, $p = 0.007$, $p = 0.0016$, and $p < 0.0001$, respectively.

Biocompatibility of graphene devices following subacute and chronic implantation. In order to assess the applicability of g-SGFET arrays for the long-term monitoring of brain activity under natural behavior we have also investigated the biocompatibility of graphene-based epicortical devices. For this purpose, animals were implanted with one of three devices onto the parietal cortex of the brain, or had the full surgery without the implantation of any device (sham control). A cohort of naive animals who had no intervention were used as a control. Three time points were chosen to assess tissue response: 2 weeks, 6 weeks, and 12 weeks post implantation (Fig. 4a). Non-functional devices were custom-designed with an enlarged surface area of CVD graphene, in order to maximize exposure of the material to the brain tissue (see Fig. 4b for device dimensions). The experiments were designed following the guidance from the ISO 10993 standard, which details the biological evaluation of medical devices. Ethylene oxide sterilization was applied prior to implantation[64]. After implantation, the immunohistochemical response of the tissue and potential effects on the behavior were investigated.

significant differences in the discrimination ratio were found in animals implanted with any device at any of the timepoints (Fig. 4c). The inflammatory response of the tissue was evaluated using two main techniques: ELISA of blood or brain tissue for a panel of inflammatory cytokines, and immunohistochemical analysis of brain tissue for cells associated with inflammation. ELISA was performed for four cytokines: interleukin-6 (IL-6), interleukin-17a (IL-17a), interferon gamma (IFN-γ), and tumor necrosis factor alpha (TNF-a). In blood serum, there were no significant differences between any of the materials at any timepoints (see Fig. S6). For cytokine expression in brain tissue, significantly higher levels of all four cytokines in both graphene and platinum devices were found at the 2 weeks timepoint, when compared with the contralateral hemisphere control. Whilst release of these factors is typically intended to prevent further damage to the CNS tissue, prolonged expression can be detrimental. By 6 weeks post implantation, there was still a significant elevation of both IL17a and IFN-γ for graphene and platinum devices vs. control expression, and by week 12, there

adverse tissue response to graphene is transient in nature, comparable to the current clinical standard and specific to the implantation site, with no observed systemic complications.

To confirm the ELISA data, manual counting of the activation state of microglial cells was also performed to assess the inflammatory state within the brain. Microglial cells are always present within the brain, but their morphology serves as an indicator of the inflammatory state within the brain[62]. Expression of activated microglia was increased at both the 2 weeks and 6 weeks post implantation timepoints, and this activation was present to a significant level at 2 weeks post implantation in all four treatment groups when compared with the contralateral hemisphere. However, similar to the ELISA, the activation of microglia had returned to baseline levels by 12 weeks, indicating no prolonged inflammatory reaction to the devices (Fig. 4e, f and Fig. S8). TUNEL cell counting was also performed, to assess any cell death within the tissue as a result of the implantation of devices. At 2 weeks post implantation, there was a significant increase in the number of TUNEL-positive cells for both graphene and sham surgery groups. However, by 6 weeks there was no evidence of cell death, which was also true at 12 weeks (Fig. S9). Finally, there was no obvious morphological changes seen with haemotoxylin and eosin staining. There was an appearance of sunken cortex in some brains, however, this was due to perfusion fixation with the glass window in place, and there was no effect on the thickness of the cortical layers below the implantation site, as shown in Fig. 4g.

Overall, both cytokine expression and histological analysis of the brain area at the implantation site showed an acute reaction to the implantation of devices. However, this was not specific to the graphene devices, even though an enlarged surface area of graphene was used in order to maximize the material specific response. By 6 weeks, the reaction showed clear signs of amelioration, and by 12 weeks, there was no detectable reaction to the devices using any technique. Graphene and Pt devices showed a similar level of microglia activation compared to "blank" devices, while the latter shows much smaller presence of inflammatory markers than for Graphene or Pt. These results suggest that microglia activation is more strongly associated with surgical procedure and probe insertion, while inflammation is primarily affected by the device material. In this way, functional sensor arrays, which present a much lower graphene area, are expected to cause an inflammation closer to that caused by "blank" devices. In addition, according to NOR test, graphene devices did not affect significantly the animal behavior neither in acute nor chronic timepoints. Based on these results, graphene-based devices presented adequate biocompatibility for chronic implantation, comparable to the equivalent platinum-based devices.

Long-term monitoring of wide frequency band epicortical brain activity during natural behavior. During the longitudinal in vivo assessment of the g-SGFET sensitivity, we recorded epicortical brain activity in a freely behaving rat for up to 24 h. Throughout the recording period, the 3D-motion of the animal was tracked with a motion capture (Mocap) system (see "Methods" section and Fig. 5a). The conjunctive recording of animal motion and wide frequency band epicortical signals was used to classify brain states and behavioral states over the recording period. In turn, this classification was used to support two main purposes. First, to validate the ability of the graphene-based wireless recording system to perform long-term stable recordings in freely moving rat across multiple brain states, and test its

the LFP dynamics related to spontaneous behavior. The analysis of the relationships between epicortical brain activity and freely moving behavior was performed over timescales enabled by the wireless recording system. This capability is critical for the study of sparsely occurring behavior events, as well as ISA patterns over distinct brain states.

Brain states were classified through a combination of spectral features in the epicortical LFP signal and motor data. In this way we distinguished the following classes: slow wave sleep (SWS), REM sleep (REM), Awake Theta (AwT), and Awake Non-Theta (AwNT). Figure 5b illustrates the criteria for the brain states classification, described in detail in the "Methods" section. First, slow wave (SW) states, showing increased power in the 1–25 Hz band, and Theta states were identified (see Fig. 5b). The behavior of the animal was then classified in either active or inactive periods from the motion tracking data (see Fig. 5b and "Methods" section). During inactive motor behavior, SW states were classified as SWS except in direct proximity to HVS events, while Theta states were categorized as REM if directly preceded by SWS. On the other hand, Theta states occurring during active behavior were classified as AwT and SW states as AwNT. Finally, periods not assigned to Theta or SW states were classified as AwNT regardless of the behavior of the animal. During the majority of recording hours all four sleep/wake states were expressed at least once in line with the polyphasic nature of rat sleep[66–68]. Their relative prominence however varied substantially over the course of the recording day paralleling the changes observed in motor states (Fig. 5c), in line with circadian rhythmicity.

Classification of brain states is typically based on the delta, alpha-beta and theta frequency bands (see "Methods" section), reflecting fast-time scale state-specific network dynamics. However, some recent research highlighted the role of infra-slow dynamics in the regulation of brain sub-states[40], via modulation of higher LFP frequency bands during sleep[39,45,69] and dynamic coordination and segregation of the resting state[35,70]. These results show the potential importance of ISA for a complete classification and study of brain-states. The graphene-based recording system presented here represents an ideal tool for the study of cortical ISA signals with a high accuracy and spatial resolution in freely behaving animals. The spectrogram in Fig. 5b illustrates changes of the spectral power for frequencies between 0.015 and 4 Hz over the transition between SWS and REM. It is possible to observe clear increase in the ISA-band power following the transition from SWS to REM, even at the single trial level (see Fig. 5b). Taking advantage of the long-term recording capabilities of our system, we could sample 44 of such sparsely occurring SWS-REM (REM duration longer than 40 s) state transitions within a 24 h period. Besides, the spatial mapping of ISA enabled by the g-SGFET technology allows to resolve the topographic region-specific modulation of ISA at the SWS-REM state transition (see supporting information S12). Interestingly, delta-band power, associated with slow oscillations, and infra-slow power showed changes in opposite directions between SWS and REM sleep. While delta band power expectedly decreases from SWS to REM, associated with desynchronized cortical state, infra-slow power increases in REM (see Figs. 5d, e and Fig. S12 and statistical analysis in "Methods").

In order to further illustrate the wide frequency band sensitivity of the recording system, we quantified the strength of modulation of LFP power in the slow frequency range (1–15 Hz) by the phase of the ISA activity during REM and SWS. Interestingly, ISA phase significantly modulated theta power (8–9 Hz) during REM sleep (Fig. 5f-left) and spindle band
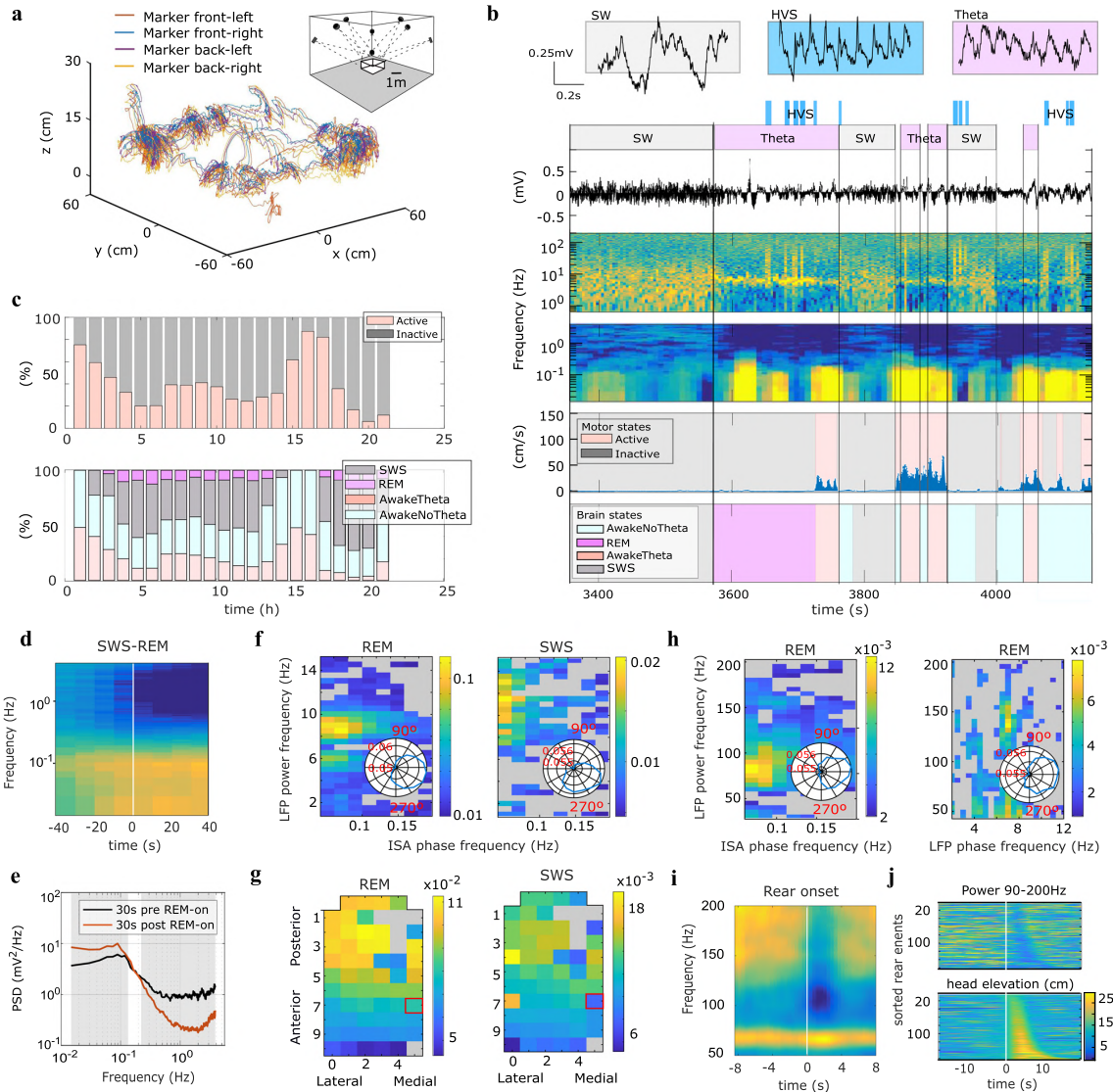
　　　　　　　　　　　　　　　　　　　ARTICLE

Fig. 5 Infra-slow to high-gamma correlates of sleep and behavioral states. a 3D trajectories of the head position of the rat. The inset shows a scheme of the position of the Mocap. **b** The spectrogram and raw LFP signal of an illustrative channel is displayed for distinct brain states (top); slow-wave (SW), high-voltage spindles (HVS) and Theta. Movement speed is displayed along with classification of motor state (middle) and brain states (bottom). **c** Top: percentage of time in the active vs. inactive state (interruptions to replace the battery not included). Bottom: percentage of time the rat was in each main brain state. **d** Average 0.015–4 Hz spectrogram for one DC channel triggered on REM episode onsets ($n = 44$). **e** Median PSD across SWS-REM transition episodes ($n = 44$) for 30 s periods pre and post REM onset. Shaded area marks frequency bins with significant difference ($p < 0.05$, permutation test). **f** Color-coded strength of modulation of LFP power across slow frequency range (*y*-axis) for one channel by the phase of ISA across 0.05–0.2 Hz range derived from one DC channel (see panel **g**) during REM sleep (left) and SWS (right) states. Gray color indicates nonsignificant modulation. Insets show circular plot of LFP power in theta/spindle band as a function of ISA phase. **g** Color-coded topographic maps of ISA phase modulation of LFP power in theta band during REM (left) and spindle band during SWS (right). ISA phase derived from DC channel marked with a red square. **h** Color-coded strength of modulation of LFP power across gamma frequency range (*y*-axis) for one channel by the phase of ISA across 0.05–0.2 Hz range derived from one DC channel (left) and by the phase of LFP in the slow frequency range rhythm (right) during REM. Inset, circular plot of LFP gamma power with respect to respective (ISA or theta) phase. **i** Average spectrogram for high-frequency range of LFP on posterior channel triggered on rear onset ($n = 162$). **j** Head elevation (bottom) and high gamma power (top, same channel as in **i**) color-coded and centered on rearing onset shown for all events sorted by duration of rear event.

to SWS, and the ISA phase of maximal LFP power differed between states being close to the peak (~340°) in REM and ascending phase (~300°) in SWS. Taking advantage of the

of LFP power across cortex, with both theta power during REM and spindle power during SWS showing strongest modulation in posterior part of the array (Fig. 5g). While theta oscillations

entorhino-hippocampal circuits[71,72], sleep spindles are generated by rhythmic currents of thalamo-cortical projections to granular cortical layers[73]. The fact that power of hippocampal theta and cortical spindle band is modulated by the phase of ISA derived from cortical surface likely reflects global infra-slow dynamics that co-modulates both limbic and cortical circuits. While the topographic profile of theta power (Fig. 5g) modulation by ISA phase is consistent with anatomical localization of underlying hippocampal theta current generators, stronger modulation of the spindle power on posterior cortical areas might reflect anatomical thalamo-cortical subcircuits that are more strongly co-modulated by ISA dynamics than derived from epicortical DC signal. Finally, we tested whether g-SGFETs SNR is sufficient to detect fluctuations in the high-frequency LFP dynamics at different time scales and to this end quantified the strength of modulation of broad range gamma power (30–200 Hz) by both ISA phase and theta rhythm phase during REM sleep. Gamma power in in the range of 60-120 Hz was modulated by the ISA phase reaching maximum power at the peak of the ISA (~10°) (Fig. 5h-left) and, consistently with published work based on intracranial recordings[73], high gamma (120–150 Hz) power was modulated by theta phase (Fig. 5h-right).

Having established that we can record state-selective epicortical signals with g-SGFETs across a range of brain/motor states, we subsequently went on to demonstrate applicability of the technique for linking behavior and cortical physiology. To this end we focused on a specific and sparsely occurring spontaneous behavior, rearing on the hindlimbs. Rearing is a exploratory behavior in rodents, which is context- and stress-sensitive[74,75], has been hypothesized to support sampling of distal landmarks for construction of a cognitive model of the surrounding environment[75,76] and is implicated in modulation of cortico-hippocampal interactions in theta and gamma frequencies[76,77]. In general, due to the sporadic and spontaneous occurrence of rearing events their neural physiology has been less widely investigated with conventional recording methods compared to task-specific trained motor actions. Technologies that combine long-term recording stability, high spatial resolution, wireless methodology and precise 3D-tracking of animal behavior, as presented here, open the door to investigating this class of phenomena with a great level of detail. Therefore, we took advantage of the presented technology to collect a large number of individual spontaneous rearing events during a full 24 h period. Evaluating the signature of rearing on the gamma epicortical activity band is of additional interest for our study, since it can be used to illustrate the capabilities of the g-SGFETs in the high-frequency LFP range. In order to robustly detect rearing episodes we took advantage of the continuous 3D tracking, detecting rearing events ($n = 163$) based on head elevation above ground (see "Methods" and supplementary information S6). While rearing events occurred throughout the recording period, expression of rearing activity was highly variable across the day, as with overall motor activity, ranging from 250 s to 0 s spent rearing per hour (mean 43.8 ± 12.1 s, supplementary information S10). Additionally, rearing events expressed variability in terms of height (mean $250,6 \pm 2.7$ mm, see Fig. 5j and Fig. S10d) and duration (mean 5.7 ± 2.8 s, see Fig. S10e).

Having detected this set of spontaneous rearing episodes we proceeded to analyze the power spectra of epicortical LFP, which showed distinct rearing-associated changes in brain signals for specific frequency ranges. Rearing was associated with the suppression of epicortical high-frequency (90–200 Hz) activity

on more frontal channels of our array (see supplementary information S11). In strong contrast no such suppression was observed in the gamma band between 60 and 70 Hz (see Fig. 5i and supplementary information S11).

Subsequently, we took advantage of the infra-slow recording capability of g-SGFET arrays to characterize topographic infra-slow and spectral AC epicortical signals associated with rare highly synchronous high-voltage spindle (HVS) oscillations[78,79], as the most likely cortical dynamics associated with large infra-slow currents, similar to those shown during epileptiform activity in development[80]. Consistent with previous studies[78,79], HVS occurrence was associated primarily with alert immobility states (IMM) (566 events, Fig. 6a), where IMM is defined as the intersection between inactive and awake states. Benefiting from the long-term unperturbed recording allowed by our system we could also sample significant number of HVS events during REM sleep (92 events), where they coexisted with hippocampal theta oscillations visible on posterior derivations (Fig. 6b). While median duration of HVS events was comparable in immobility and REM sleep (~5 s, Fig. 6c-top), the rate of detected HVS events varied across the recorded 24 h period, (Fig. 6c-bottom). Interestingly, HVS during both brain states were associated with transient infra-slow fluctuations as visible in single examples (Fig. 6a, b) and average profiles (Fig. 6d, e). Specifically, positive (putative source) and negative (putative sink) infra-slow transients in, respectively, posterior and frontal positions on the array coincided in duration (median 5 s) with oscillatory dynamics of HVS (Fig. 6c, d, e). Topographic profiles of spectral peak power of HVS were comparable for both states and showed maximal increase to baseline in frontal derivations overlaying sensory-motor cortex (Fig. 6f). REM-associated HVSs were, on average, slower and larger in power than immobility-associated ones (Wilcoxon ranksum test, $p < 1e-19$ for power and $p < 1e-8$ for frequency, Fig. 6g). In contrast, spatial structure and magnitude of infra-slow fluctuations associated with HVS as expressed by positive fluctuations on posterior and negative fluctuation on frontal DC channels, were comparable for both states (Wilcoxon ranksum test between IMM and REM, $p = 0.5$ for posterior peak magnitude and $p = 0.9$ for frontal trough magnitude, Fig. 6h).

Although future work is required to replicate these observations in a large cohort of animals, our long-term recordings enabled detailed quantitative analysis of rare physiological patterns and illustrate the power of this technology. Because of their sparse, strongly state dependent occurrence and distribution over a wide frequency band these events illustrate the class of phenomena whose functional study necessitates the integration of neural-behavioiral measurements with both high spatio-temporal resolution and large spatio-temporal span in freely moving animals, as enabled by our wireless electrophysiology system.

Discussion

Graphene active-sensor arrays represent an emerging technology in neural engineering, which has recently demonstrated a strong potential for the production of high-count sensor arrays[6,7], as well as for wide frequency band neural sensing[33]. In this article, we have presented a detailed characterization of various technical aspects required for their actual application, such as the homogeneity in the performance of the graphene sensors, the specifications required for a dedicated headstage, the limits in the sensitivity of g-SGFETs or their chronic stability and biocompatibility in vivo and demonstrated lines of investigation enabled by their technical characteristics.

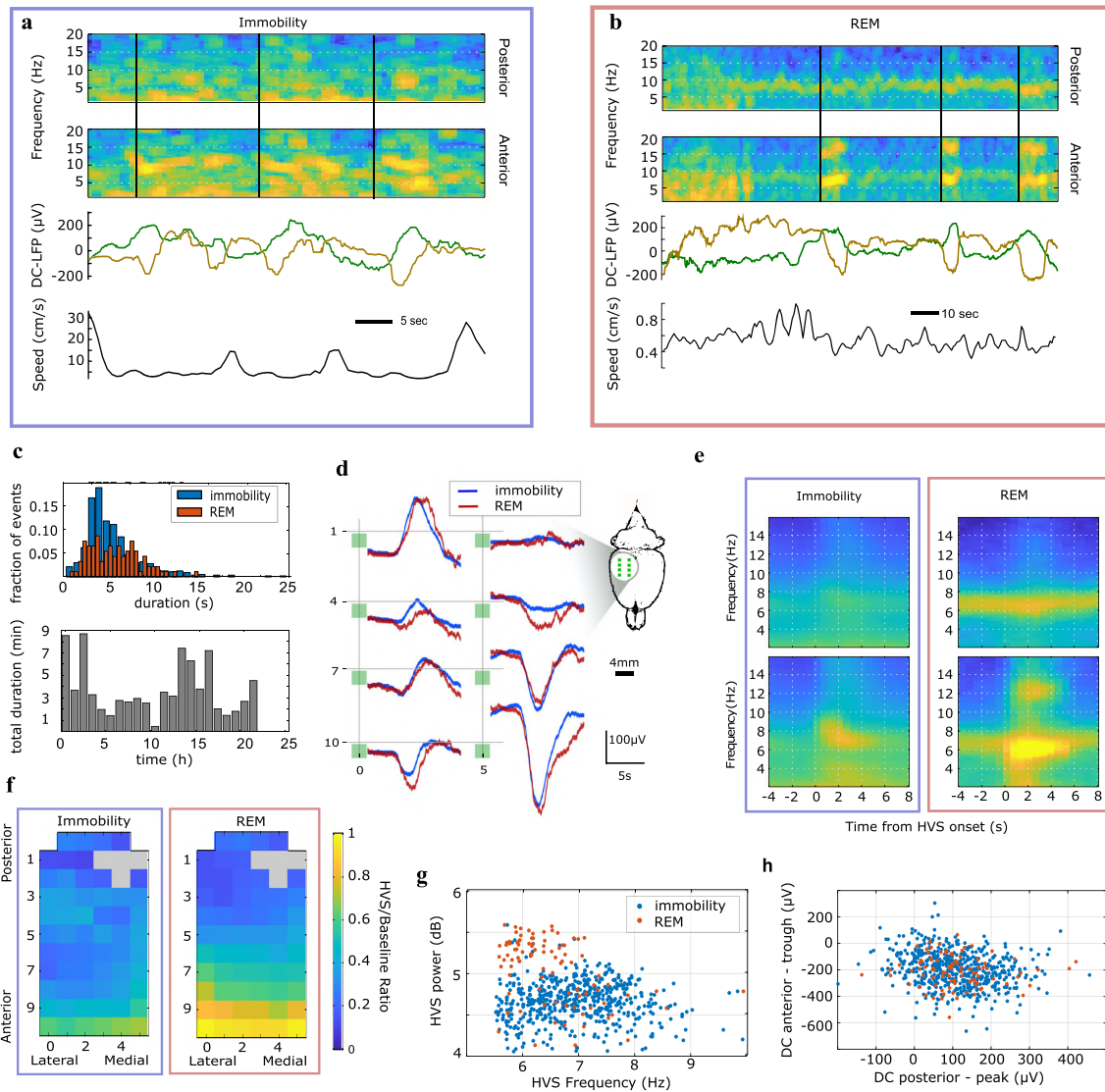In the first place, we have demonstrated the high yield and

ARTICLE

Fig. 6 Topography of AC and DC dynamics associated with high-voltage spindles. a, **b** examples of HVS events during immobility (**a**) and REM sleep (**b**). Spectrograms at posterior (top) and anterior (middle) positions on the array visualize dynamics of HVS (vertical lines at onsets) and ongoing oscillatory dynamics (low-frequency synchrony in IMM, theta oscillation in REM). Bottom two panels show DC LFP signals from posterior (green) and anterior (brown) positions on the array and head speed. **c** Distribution of duration of single HVS events for immobility and REM (top) and total hourly duration of HVS across recorded period (bottom). **d** Average DC LFP traces triggered on HVS onset during immobility and REM sleep (channels arranged as in Fig. 2g-left, inset showing anatomical localization of DC ECoG recording sites). **e** Average AC LFP spectrograms triggered on HVS onset during immobility (left) and REM sleep (right). The spectrograms at posterior (top) and anterior (bottom) positions on the array contrasting spectral content associated, respectively, with theta (posterior) and HVS (anterior) oscillations. Pseudo-color, spectral power (a.u.). **f** Topographic maps of change, relative to baseline, in HVS power at peak oscillation frequency during immobility (left) and REM sleep (right). **g** Distributions of power and peak frequency of individual HVS during immobility (blue) and REM sleep (red). **h** Distribution of DC fluctuation magnitude at posterior lateral and frontal medial derivations for single HVS during immobility and REM (color code as in **g**).

represents an important milestone towards the production of graphene-based neural probes at an industrial scale. On another front, the application of graphene transistors for neural sensing also requires the development of specific electronic equipment for biasing the sensors and converting the measured drain-to-source currents into equivalent voltage signals at the gate. In this study, we

process on the sensitivity of the recording system. In this way, we have identified the challenges in the design of full-band amplifiers given specific energy and weight constrains for wireless applications. Furthermore, using a dedicated headstage we have demonstrated that the sensitivity of graphene active sensors in the ISA band is not significantly affected by the rest of the data-

to adsorption of charged molecules on the graphene channel or drifts in the electrode reference potential. These drifts were easily eliminated with a high pass filter at 1 mHz; however, future experiments could explore the functionalization of the graphene channel and use of alternative reference electrodes to maintain a more stable doping level.

Moreover, we have demonstrated the stability of the graphene sensors in vivo by characterizing their sensitivity over 4 weeks. In order to determine the stability of the signal quality we have also evaluated the signals induced by bipolar stimulation in the LFP frequency band, demonstrating a rather stable frequency response over time. These results suggest that the impedance of glial tissue surrounding the implant does not significantly affect the sensitivity of the g-SGFETs in vivo. To conclude the characterization of the device stability, we have evaluated the biocompatibility of graphene devices over 12 weeks via behavioral and histological markers. These results demonstrate an acute foreign body response comparable to platinum-based devices, which returns to values close to those of control animals 12 weeks after implantation. The demonstration of the graphene biocompatibility and long-term stability in a chronic implant represents another important turning point towards the large-scale production of graphene-based neural probes.

The experimental validation of this technology opens up many opportunities for electrophysiology studies in which having access to unconstrained behavior and multichannel recordings with sensitivity in a wide frequency band is relevant. In this study, we have shown quasi-continuous monitoring of brain activity in long recording sessions of up to 24 h, which allowed us to acquire large samples of neural activity across unperturbed behavioral and brain states. In combination with 3D-tracking, the wireless technology allowed us to explore the relation between neural activity patterns and behavior events, which occur sparsely over time, with sufficient statistical power. In particular, analyzing epicortical LFP signals with respect to rearing behavior we observed differential modulation of the 60–70 Hz gamma and 90–200 Hz high gamma range. While high-frequency activity between 90 and 200 Hz was consistently suppressed in a topographic manner, no such suppression was observed for the 60–70 Hz range, pointing towards distinct behavioral selectivity of underlying circuit mechanisms. The determination of frequency-specific power modulation in the gamma range, even for single rearing events, demonstrates the high sensitivity of the system in the high-frequency spectrum of the LFP.

In the low-frequency range, we found that infra-slow power <0.2 Hz increased significantly across DC sites during REM sleep episodes compared to SWS and thus showed the opposite state dependence than power in the slow oscillation band (1–4 Hz). Interestingly, infra-slow dynamics modulated power of theta and gamma rhythm during REM and with lower strength, power of sleep spindles during SWS. While modulation of LFP power in theta, beta and gamma bands by ISA phase derived from BOLD signal and DC EEG has been shown in humans[81,82] and recently in anesthetized rats[70], the present result is the first demonstration of interaction between physiologically established oscillatory dynamics, theta, spindle and gamma oscillations, and ECoG-derived ISA in freely moving rodent. Consistent with published intracranial work[73], volume conducted hippocampal theta measured at the cortical surface also modulated cortical gamma power, thus demonstrating that the developed technology is sufficiently sensitive to characterize known gamma dynamics.

While power of ISA modulating sleep spindle oscillations power during SWS was much lower than that during REM, a related hypersynchronous thalamo-cortical rhythm, HVS, was

large statistical sample of events. The rate of occurrence during different brain states could be determined over a 24 h period, highlighting their occurrence also outside the awake resting state in which they are commonly reported to be selectively occurring. Specifically, we found them prominently expressed during REM sleep[83]. Having established this bimodal state specificity, we analyzed HVS events separately for awake immobility and REM sleep. Topographic analysis of the HVS peak power demonstrated that sensory-motor cortical preponderance for these oscillations is comparable for these two states. In contrast, the large sample size of events in both states allowed to identify a significant difference in both frequency content and power of the HVS between these two brain states. Furthermore, the capabilities to simultaneously map ISA patterns allowed to determine the distinct topographic structure of spatially specific infra-slow frequency components associated with HVS, showing phase-reversal across anterio-posterior axis. Importantly, these ISA features were conserved between REM-sleep and awake immobility, highlighting that the underlying origin of the DC signal is related to the HVS event itself and is independent of the brain state.

Future work is required to replicate the presented results in a large cohort of animals, follow them longitudinally and relate the surface pattern to intra-laminar and subcortical theta, spindle, gamma[77] and HVS[84] generators. Although we have focused the attention on epicortical ISA patterns, analyzing their correlation with ISA dynamics across cortical laminae could provide important insights into the origin and implications of ISA. A promising strategy in this direction is to combine the epicortical arrays presented here with graphene-based depth probes[33]. Future chronic recordings of depth and large-scale LFP signals across behaviors and behavioral states in freely moving unconstrained animals will lay the foundation for a new qualitative step in the brain dynamics investigation from infra-slow to very fast frequencies[72], contributing to our understanding of the origins of ISA dynamics in the context of resting states and default mode networks and its links to faster brain dynamics.

In summary, the thorough in vitro and in vivo evaluation of the sensing and long-term recording capabilities of graphene active sensors from a system perspective demonstrates the maturity of this technology and supports its application for the study of ISA without sacrificing high-frequency LFP components. In this direction, we have successfully evaluated ISA patterns during distinct brain states and the correlation of high-frequency oscillations with specific sparsely occurring behaviors. Our results represent an important step towards the broad implementation of graphene active-sensor arrays for neuroscience research, offering a stable and biocompatible sensing technology for long-term mapping of wide frequency band epicortical brain activity during spontaneous behavior.

Methods

Fabrication of g-SGFET arrays. Arrays of g-SGFETs and devices for biocompatibility were fabricated on a 10 μm thick polyimide (PI-2611, HD Micro-Systems) film spin coated on a Si/SiO$_2$ 4" wafer and baked at 350 °C. Polyimide was chosen as a substrate due to its thermoxidative stability, high mechanical strength, insulating properties and chemical resistance[63,85], as well as its expected biocompatibility and previously reported stability for chronic implants[4,5]. A first metal layer (10 nm Ti/100 nm Au) was deposited by electron-beam vapor on a previously photodefined-negative AZ 5412E (Clariant, Germany) and then structured by a lift-off process. Afterwards, the graphene grown by chemical-vapor deposition on Cu was transferred (process done by Graphenea s.a.). In platinum devices for biocompatibility studies, another photolithography, metal evaporation and lift-off followed the first one. Graphene was then patterned by oxygen plasma (50 sccm, 300 W for 1 min) in a reactive ion etching (RIE). The photodefinable resist used to protect the graphene in the channel region was HIPR 6512, chosen to minimize the level of contamination. After the graphene etching, a second metal layer was

Subsequently, the transistors were insulated with a 3-μm-thick photodefinable SU-8 epoxy photoresist (SU-8 2005 Microchem), keeping uncovered the active area of the transistors channel. The SU-8 photoresist was chosen as insulating material because it is photodefinable and because its use in chronic implants has been previously reported[86],[87]. The use of a photodefinable passivation polymer is required in the current graphene technology because etching of the passivation layer would also etch the underlying graphene channel. The polyimide substrate was structured in a reactive ion etching process using a thick AZ9260-positive photoresist (Clariant) layer as an etching mask. The neural probes were then peeled off from the wafer and placed in a zero insertion force connector to be interfaced with our custom electronic instrumentation. Finally, the devices were rinsed in ethanol to eliminate remaining resist residues on the graphene channel.

Phase-amplitude coupling evaluation. The signal inversion observed between channels in the infra-slow frequency band (0.005–0.05 Hz) was quantitatively evaluated by calculating the probability density of a signal amplitude as a function of its phase with respect to a second signal. In order to estimate the phase between the two signals the Hilbert transform of each of them was computed using the python library scipy and the difference between their phase calculated. A two-dimensional histogram was then used to express the probability density of the signal amplitude in the amplitude-phase space (Fig. 3c).

Ethical approval and animal handling. The experiments in-vivo were in accordance with the European Union guidelines on protection of vertebrates used for experimentation (Directive 2010/63/EU of the European Parliament and of the Council of 22 September 2010). Electrophysiological experiments with Long Evans rats were carried out under the German Law for Protection of Animals (TierSchG) and were approved by the local authorities (ROB-55.2-2532.Vet_02-16-170). Experimental procedures using Sprague Dawley rats for biocompatibility assessment were carried out according to the United Kingdom Animals (Scientific Procedures) Act, 1986 and approved by the Home Office and the local Animal Ethical Review Group, University of Manchester. Rats were kept under standard conditions (room temperature 22 ± 2 °C, 12:12 h light–dark cycle, lights on at 10:00), with food and water available ad libitum.

Implantation of the graphene-sensor arrays for electrophysiological measurements. As described previously in Garcia-Cortadella et. al.[34], an adult Long Evans rat, weighing 580 g, was anaesthetized with MMF (Midazolam 2 mg/kg, Medetomidin 0.15 mg/kg, Fentanyl 0.005 mg/kg). 1 h after, MMF induction Isoflurane was supplemented at 1% to maintain the rat anaesthetized and Metamizol was given at 110 mg/kg. The posterior-dorsal area of the head was shaved, the skin locally disinfected with Povidone-iodine and subcutaneously infiltrated with local anesthetic Bupivacaine. The skin was then incised and the dorsal skull cleaned carefully by blunt dissection. The dried skull was covered with UV-curing adhesive Optibond (Kerr) and a 3D-printed base ring was anchored to skull with screws and Metabond cement (Parkell).

Symmetric craniotomies with a maximum width of 5 mm were performed bilaterally, extending between +2 mm and −8 mm with respect to Bregma in the anterior-posterior axis. The dura mater was incised and removed within these craniotomies. A further craniotomy of 1 × 1 mm was performed over the cerebellum. All craniotomies were covered with prepolymerized polydimethylsiloxane (PDMS) (Sylgard 184, Dow Corning, USA) with mixing ratio 1:10 and sealed with Vetbond (Animal Care Products, USA). The skin margins around the implant were sutured and the implant closed with a protective cap.

After 1 week of recovery the g-SGFET array was implanted under Isofluran Anesthesia (5% induction 1% maintenance). After partial opening and sidewards flapping of the polymer covering the right hemisphere the array was placed onto the pial surface positioned such as to cover the posterior aspect of the right hemisphere (ca −7 to −2 mm from bregma). In addition, two Pt-Ir wires were implanted at either side of the g-SGFET array. One proximal to the array, the other distally on the opposing hemisphere. The polymer cover was flapped back into position with the flexible cable of the g-SGFET array leaving through the remaining slit. A second PDMS cover was used to cover both the incised polymer and array, anchored to the skull with Vetbond and Evoflow (Ivoclar Vivadent, Liechtenstein) and sealed with silicon gel 3-4680 (Dow Corning, USA). Finally, an Ag/AgCl electrode was placed in contact with the cerebellum as a reference for the recording of neural activity.

Implantation of the graphene, platinum, and PI devices for biocompatibility evaluation. Sprague Dawley rats (200–280 g) were anesthetized using isoflurane inhalation (typically at 3.5% for induction and between 1.5 and 2.5% for maintenance) in 100% oxygen. The top of the animal's head was shaved and the animal was positioned within a stereotactic frame with tooth and ear bar fixation. Animals were placed on a heated blanket, with a pulse oximeter attached to the foot and a rectal probe inserted to monitor body temperature. Viscotears liquid gel (Bausch & Lomb, UK) was applied to the eyes for protection during the procedure. Depth of

skin removed to expose the skull but not the temporal muscle. The periosteum was removed using a bone scraper. The skin around the perimeter of the removed tissue was glued to the bone using Vetbond tissue adhesive (3 M, UK). A craniotomy (~4 mm x 6 mm) was performed using a high speed surgical micro drill. Lambda was used as a posterior reference for the craniotomy, which was positioned at least 1 mm lateral to the midline, to avoid the sagittal sinus. The drilling region was rinsed regularly with saline to prevent heat damage. Once the bone around the border of the craniotomy was sufficiently thin, all bone shavings and other debris were removed using compressed air and the bone flap was gently removed. The cortical surface was kept moist using Ringer's solution. A fine needle with the tip bent at a 90° angle was used to gently lift the dura away from the cortical surface and another needle was used to create a slit in the dura, carefully positioned to avoid blood vessels. A pocket was created by lifting the dura next to the opening using fine forceps and the device was carefully placed on the cortical surface. The dura was then repositioned to hold the device in place. A glass window (UQG Optics, UK) of the appropriate size was positioned to fill the craniotomy and was fixed in place using dental cement (Superbond C&B, Prestige Dental). The animals received a subcutaneous injection of 0.9% saline (1 ml) and were placed in a recovery cage until the anesthetic had worn off.

Behavioral testing for biocompatibility evaluation. All animals had pre-surgical behavioral baselines taken at the age of 5 weeks. One week later, all animals were assigned to one of five groups; graphene electrode, platinum electrode, blank electrode, sham surgery (no electrode implanted), or naive (no surgery). Animals were then tested at one or two timepoints—2 weeks, 2 and 6 weeks, or 6 and 12 weeks post-surgery. Timepoints were chosen in line with ISO 10993 definitions; where prolonged exposure is classified >24 h but <30 days, and permanent exposure is defined as >30 days (ISO 10993-6:2007).

Prior to the first exposure to NOR rats were placed into the empty arenas the day before testing for 20 min with their cage mates for acclimatization purposes. The square Plexiglas boxes (measuring 52 cm by 52 cm at the base with a height of 30 cm) had a white floor and black walls. Animals were acclimatized to the NOR arena before experiments began by placing them into the arena for 3 min while there were no objects within the arena. The NOR test comprises a training and testing trial, separated by an inter-trial period. In the training session, two identical objects were placed within the arena, such as two bottles of the same shape and size. In the testing session, two new objects were placed in the arena, one object identical to that during the training session, and one completely new object, such as a can. For training sessions, animals were placed in the arena and allowed to explore for 3 min, before returning to the home cage. Animals were left in the home cage for 30 min, before being placed into the arena for the testing session, again remaining in the arena to freely explore for 3 min. The time the animal spent interacting with the objects was measured in both the training and testing trials. In a healthy animal, the animal should spend more time interacting with the novel object during the testing session. Ideally these tests should not be used >3 times for any animal, and therefore animals in the 12 week implantation group were tested for NOR at baseline and then at 6 and 12 weeks post implantation. All other animals were tested at every selected timepoint available before sacrifice.

Videos of NOR test trials were manually scored by blinded researchers using an online stopwatch (http://jackrrivers.com/program/). Animals were classed as interacting with an object if their nose or paws touched the object. The amount of time spent interacting with the two objects was analyzed, and a discrimination ratio was determined by dividing time spent interacting with the novel object with time spent interacting with the known object. A discrimination ratio >0.5 indicated an animal had a preference for the novel object, a sign of normal cognition.

Tissue collection and processing. At 2 weeks, 6 weeks or 12 weeks post implantation of devices, animals were culled using an appropriate method for the type of subsequent analysis. For histology, animals underwent perfusion fixation using heparinised saline, followed by 4% paraformaldehyde (PFA; Sigma-Aldrich, UK; 441244) in phosphate-buffered saline (Sigma-Aldrich, UK; D8537). Tissue was stored a minimum of 24 h in PFA, transferred to a sucrose solution for 48 h, and frozen before cryosectioning 40 sections at 25 μm per animal. Cryosections were stained for one of three markers: (i) ionized calcium binding adaptor molecule 1 (Iba1) to quantify microglial population, (ii) terminal deoxynucleotidyl transferase dUTP nick-end labeling (TUNEL) staining to assess apoptosis, or (iii) haemotixylin and eosin (H&E) to assess gross morphology of the brain tissue. Tissue sections were blocked in 5% goat serum in PBS with 0.1% triton-X, before incubation with Iba1 primary antibody (1:200, 019-19741, Wako) overnight. A goat anti-rabbit Alexa 594 secondary antibody (1:1000, A11012, Invitrogen) was used for visualization. For immunofluorescently stained tissue, a DAPI counterstain was performed before slides were mounted using ProLong Gold mountant (P10144, ThermoFisher).

For TUNEL staining, the manufacturer's instructions were followed using a DeadEnd™ Colorimetric TUNEL System (G7360, Promega). Following diaminobenzidine (DAB) visualization of the TUNEL staining, slides were counterstained using methyl green (0.1% w/v aqueous solution, Alfa Aesar). H&E

Slides were imaged using the 3D Histec Pannoramic250 slide scanner, and images analyzed using CaseViewer (Version 2.2, 3DHistech Ltd). TUNEL-positive cells were counted and averaged across the cortical surface in forty 25 μm sections per hemisphere. Microglial cells were individually classified into one of four morphologies; Grade 0 (resting/ramified), Grade 1 (de-ramifying/re-ramifying), Grade 2 (activated/ameboid) or Grade 3 (clustered & activated) as previously described[88]. Activation was determined as a percentage of total microglial cells, which were either Grade 3 or 4.

For ELISA, animals were culled by rising concentration of CO_2, before cardiac puncture was performed to extract blood. Brain tissue was extracted, snap frozen in liquid nitrogen, and stored at −80 °C until further use. The extracted blood was collected in a blood collection tube (Vacutainer, Becton Dickson, UK) and allowed to clot at room temperature for 15–30 min. The tube was centrifuged at 5000RPM for 10 min at 4 °C, and the resulting serum supernatant was collected and stored at −80 °C until further use. There were insufficient serum samples to be run from the naive control group, so this group was excluded from analysis. Brain tissue was lysed by addition of liquid nitrogen and grinding the tissue to create a powder, to which NP-40 lysis buffer (150 mM NaCl, 50 mM Tric-Cl, 1% Nonidet P40 substitute, Fluka, pH adjusted to 7.4) containing protease and phosphatase inhibitor (Halt™ Protease and Phosphatase Inhibitor Cocktail, ThermoFisher Scientific) was added to the tissue. Samples were centrifuged at 5000RPM for 10 min, and the supernatant stored at −80 °C until further use. ELISA kits for four cytokines were used, IL-17a (437904, Biolegend), IFN-γ (439007, Biolegend), TNF-α (438204, Biolegend), and IL-6 (437107, Biolegend). Manufacturer instructions were followed for all four kits.

Motion capture and behavioral states classification. The rat was recorded for up to 24 h during spontaneous behavior in a recording arena of 100×100 cm to which it was prehabituated. During the recording session it had ad libitum access to food and water. The battery of the wireless system was exchanged once every 6 h. A motion capture (Mocap) system (Optitrack) using passive reflective markers and 8 cameras was used to track the motion of the animal head in three-dimensional space. Four reflective markers were anchored to the protective cap and their position averaged to infer the position in 3D and orientation of the head. Instantaneous headspeed in 3D was computed as time derivative of the modulus of the spatial coordinates. Motive 2.2 software was used for the analysis of Mocap data.

For the classification of the behavior as active or inactive, periods where headspeed exceeded 100 mm/s were labeled as active. In a second step active periods shorter than 5 seconds were skipped while gaps in active periods shorter than 5 s were concatenated with the neighboring active state. Timepoints, that did not fall under this definition of active, were labeled as inactive. The ratio of active and inactive periods varied substantially across total recording period (between 6.6% and 88.0% active per hour, mean $40.2\% \pm 4.7\%$ active per hour).

Rear events were defined as short elevations of the head to heights that necessitate the animal to stand on its hindlimbs. After visual inspection of z elevations throughout the recordings a threshold of 200 mm elevation from ground was determined to effectively separate punctuate rearing onsets/offsets from ongoing height variations at lower z positions (see supplementary information S10). While active and inactive states were defined as mutually exclusive, rear events were considered to be a substrate of the active motor state.

Neural signals processing and analysis. The wireless headstage was controlled using Multi Channel Experimenter 2.12.1 software and the recorded data was converted to HDF5 format using Multi Channel Data Manager 1.13.1. Neural data was calibrated according to the transconductance of g-SGFETs using Python 2.7 scripts and exported to Neuroscope software for data exploration (see data and code availability statement). Analysis of neural signals was carried out using Matlab 2016b scripts (see code availability statement).

Brain states classification. Two channels of the epicortical array were chosen for the separation of brain states. One channel was selected from the posterior area of the array, putatively overlying the hippocampal formation and exhibiting prominent theta oscillations. A second channel was selected from the frontal area, recording from the region and neighborhood of somatosensory cortex, where high-voltage spindles are expressed most prominently. Power spectra were computed on whitened LFP signals in the range from 1 to 200 Hz using multitaper methods using 4-s windows in sliding 0.5 s steps. First, slow wave (SW) states were identified as periods were the z-score of the summed power of delta (1–4 Hz), alpha-beta ranges (10–25 Hz) exceeded −0.1. Gaps shorter than 5 s were concatenated with neighboring periods.

SW states coinciding with inactive motor state and >10 s temporal distance from the last preceding high-voltage spindle (HVS) event were defined as slow wave sleep (SWS). Following previous literature we assumed incompatibility between HVS and deep slow wave sleep in unanaesthetized Long Evans rats[84]. HVS are close in frequency to theta oscillations, but differ markedly in their expression of multiple higher harmonics due to their strongly non-sinusoidal waveshape.

was calculated and subsequently z-scored. Periods with z-score values exceeding 0.7 were labeled HVS. Candidate HVS periods shorter than 1 s were skipped to minimize false positives from occasional sharp single wave transients of undetermined physiological nature. Spectral profiles of the individual HVS events were post-hoc classified to remove artifact contamination. Onset and offset of peak power, instantaneous frequency and power of the first spectral peak were extracted from each event.

Theta states were defined based on the ratio between power in the theta (5–9.5 Hz) and delta (2–4 Hz) ranges on the theta reference channel. Gaps shorter than 10 s were concatenated with neighboring Theta periods. Theta coinciding with an Inactive motor state was labeled Inactive Theta. All Inactive Theta periods that were preceded by a SW state within 1 s and which were longer than 5 seconds were considered REM sleep. All remaining Theta periods were considered Awake Theta. Finally, all periods that were neither SWS nor REM nor Awake Theta were defined as Awake Nontheta. It should be noted that the existence of low amplitude microstates during NREM sleep has been described previously[89]. It remains to be determined to which degree a subset of periods with low amplitude in the SW range assigned to Awake-Nontheta in this study maps onto states defined as low activity sleep microstates by Miyawaki and colleagues[89].

All states were considered to be mutually exclusive with the exception of HVS, which was considered an event occurring during but not interrupting ongoing background states. Therefore, for each HVS episode the brain states immediately preceding and following were merged if they belonged to the same state. All spectral analysis was performed using custom-developed Matlab implementation of multitaper estimate[90]. Analysis of the g-SGFET performance was done in Python. ISA brain dynamics analysis was limited to immobility and REM sleep, for which potential influence of motion artifacts on the infra-slow fluctuations could be discarded.

Statistical analysis. For the evaluation of the yield and homogeneity of the g-SGFETs performance, 9 neural probes with 64 g-SGFETs each were characterized in vitro. This data is plotted in the boxplots in Fig. 2, the boxes extend from the lower to the upper quartiles, with a line at the median. The whiskers extend 1.5 times the inter-quartile range and the data points beyond the whiskers are indicated by a dot. The longitudinal evaluation of g-SGFETs stability in-vivo was performed with one 64-channel array implanted on the cortex of a rat. The boxplots shown in Fig. 3 are defined as those in Fig. 2. In panels a and e of Fig. 3, the statistical sample are all 8 g-SGFET connected to the DC-coupled channels of the headstage. Panels d and f of Fig. 3 correspond to all 64 g-SGFETs on the array. Finally, panel g shows the normalized response of the 10 g-SGFETs on the positions under the highest induced electric field during bipolar stimulation.

For biocompatibility assessment, three device types; platinum, graphene, and polyimide (blank) were fabricated. The rats in each of these groups were implanted with one of the three device types on the parietal cortex of the brain. A fourth group of animals had the full surgery without the implantation of any device (sham control) and a fifth group (naive) had no surgery. For NOR testing, the number of rats used was $n = 7$ for all groups at all timepoints, except 12 weeks, which had $n = 3–7$ depending on the group. For cytokine detection in the brain tissue, the number of rats was $n = 4$ at 2 and 6 weeks, and $n = 3$ at 12 weeks post implantation. For microglial activation, the number of rats was $n = 3$ at 2 and 12 weeks and $n = 2$ at 6 weeks (or 3 for the contralateral hemisphere). In all cases, the contralateral hemisphere was also evaluated as a control. Data where $n = 3$ or higher were analyzed using a two-way ANOVA to compare all timepoints and interventions. Dunnett's multiple comparisons were then performed at each timepoint comparing each surgical intervention to the control. $*p < 0.05$, $**p < 0.005$, $***p < 0.001$, $****p < 0.0001$ are indicated for each surgical intervention in Fig. 4.

The measurement of gamma activity modulation during rearing was evaluated for 163 rearing events measured in the course of a 24 h recording. HVS were also measured during the same 24 h recording. Five-hundred sixty-six events were detected during immobility and 92 events during REM sleep. Differences in spectral content of HVS during distinct states (IMM and REM) was evaluated by a Wilcoxon ranksum test (the p-values are indicated in the main text). The electrophysiological data shown corresponds to one rat. The large statistical sample of events allows illustrating the capabilities of the graphene-based technology, however, the interpretation of these results should be subject to variability across measurements and animals.

The modulation of ISA power by REM state vs. SWS was evaluated in two ways: first, for the period directly around the state transition (−30 to 30 s around the REM onset). Second, we evaluated the ISA power in both states over their entire duration, not only in the SWS-REM transition. ISA power comparison between REM vs. SWS states was restricted to the 44 REM episodes lasting more than 40 s (see Supplementary Information S12B). To test for frequency-specific changes across the state transition we compared the distributions of median spectral power across trials for the 30 s pre vs. post SWS-REM transition for each frequency bin. Significance was assessed by permutation test for each frequency bin ($n = 1000$ permutations, see Fig. 5d example channel and Supplementary Information S12C for all working DC channels). Increase of ISA and concurrent decrease of 1–4 Hz power during SWS-REM transition is significant after permutation test ($n = 1000$

ARTICLE

distributions of the integrated power in the ISA (0.01–0.1 Hz) band in SWS and REM states using Wilcoxon rank sum test (see Fig. 5e, test results for each channel in Supplementary Information S12D).

Modulation of the LFP power by the DC signal-derived ISA and LFP phase was quantified using instantaneous fast frequency power-weighted resultant length of the instantaneous slow frequency phase vectors normalized by mean LFP power in the respective band[72] for which magnitude reflects the strength of LFP power modulation to a preferred phase of the ISA or LFP. ISA and LFP phase and LFP power were computed as angle and absolute value of the analytical signal of the respective AC and DC channel signals that were band-pass filtered, with 0.04 and 0.4 Hz bandwidth, respectively. Significance of the modulation was tested based on 1000 surrogate phase-power pairs randomly shifted with respect to each other by up to 100 s. Resulting empirical p-value was corrected following false-discovery-rate control procedure at the error rate of 0.001. For constructing topographic maps of theta and spindle power band modulation we used mean modulation strength for the LFP power band 8–9 Hz (theta) and 10–14 Hz (spindle band), and the ISA phase frequency of 0.05-0.1 Hz computed for every AC channel (LFP power) and one fronto-medial DC channel (ISA phase).

Reporting summary. Further information on research design is available in the Nature Research Reporting Summary linked to this article.

Data availability
Device characterization and raw electrophysiological data examples are available in GIN repository with the identifier (https://doi.org/10.12751/g-node.4zw2lt). The complete electrophysiological dataset is available from the corresponding author upon reasonable request. Source data are provided with this paper.

Code availability
Custom code for the analysis of devices characterization is provided in GIN repository with the identifier (https://doi.org/10.12751/g-node.4zw2lt). The complete code for analysis of electrophysiological data is available from the corresponding author upon request.

References
1. Khodagholy, D. et al. NeuroGrid: Recording action potentials from the surface of the brain. *Nat. Neurosci.* **18**, 310–315 (2015).
2. Lee, W. et al. Integration of organic electrochemical and field-effect transistors for ultraflexible, high temporal resolution electrophysiology arrays. *Adv. Mater.* **28**, 9722–9728 (2016).
3. Khodagholy, D. et al. Organic Electronics for High-resolution Electrocorticography of the Human Brain. *Sci. Adv.* **2**, 11 (2016).
4. Chiang, C.-H. et al. Development of a neural interface for high-definition, long-term recording in rodents and nonhuman primates. *Sci. Transl. Med.* **12**, eaay4682 (2020).
5. Chung, J. E. et al. High-Density, long-lasting, and multi-region electrophysiological recordings using polymer electrode arrays. *Neuron* **101** (21-31), e5 (2019).
6. Garcia-Cortadella, R. et al. Switchless multiplexing of graphene active sensor arrays for brain mapping. *Nano Lett.* acs.nanolett.0c00467. https://doi.org/10.1021/acs.nanolett.0c00467 (2020)
7. Schaefer, N. et al. Multiplexed neural sensor array of graphene solution-gated field-effect transistors. *2D Mater.* **7**, 025046 (2020).
8. Viventi, J. et al. Flexible, foldable, actively multiplexed, high-density electrode array for mapping brain activity in vivo. *Nat. Neurosci.* **14**, 1599–1605 (2011).
9. Fang, H. et al. Capacitively coupled arrays of multiplexed flexible silicon transistors for long-term cardiac electrophysiology. *Nat. Biomed. Eng.* **1**, 0038 (2017).
10. Chang, E. F. Towards large-scale, human-based, mesoscopic neurotechnologies. *Neuron* **86**, 68–78 (2015).
11. Lacour, S. P., Courtine, G. & Guck, J. Materials and technologies for soft implantable neuroprostheses. *Nat. Rev. Mater.* **1**, 1–14 (2016).
12. Nguyen, J. K. et al. Mechanically-compliant intracortical implants reduce the neuroinflammatory response. *J. Neural Eng.* **11**, 056014 (2014).
13. Moshayedi, P. et al. The relationship between glial cell mechanosensitivity and foreign body reactions in the central nervous system. *Biomaterials* **35**, 3919–3925 (2014).
14. Song, E., Li, J., Won, S. M., Bai, W. & Rogers, J. A. Materials for flexible

15. Hébert, C. et al. Flexible graphene solution-gated field-effect transistors: efficient transducers for micro-electrocorticography. *Adv. Funct. Mater.* 1703976. https://doi.org/10.1002/adfm.201703976 (2017).
16. Jastrzebska-Perfect, P. et al. Translational neuroelectronics. *Adv. Funct. Mater.* https://doi.org/10.1002/adfm.201909165 (2020)
17. Cea, C. et al. Enhancement-mode ion-based transistor as a comprehensive interface and real-time processing unit for in vivo electrophysiology. *Nat. Mater.* **19**, 679–686 (2020).
18. Khodagholy, D. et al. In vivo recordings of brain activity using organic transistors. *Nat. Commun.* **4**, 1575 (2013).
19. Rivnay, J. et al. Organic electrochemical transistors. *Nat. Rev. Mater.* **3**, 1–14 (2018).
20. Dankerl, M. et al. Diamond transistor array for extracellular recording from electrogenic cells. *Adv. Funct. Mater.* **19**, 2915–2923 (2009).
21. Fromherz, P., Offenhäusser, A., Vetter, T. & Weis, J. A neuron-silicon junction: a Retzius cell of the leech on an insulated-gate field-effect transistor. *Science (80-.).* **252**, 1290–1293 (1991).
22. Spyropoulos, G. D., Gelinas, J. N. & Khodagholy, D. Internal ion-gated organic electrochemical transistor: a building block for integrated bioelectronics. *Sci. Adv.* **5**, eaau7378 (2020).
23. Lee, C., Wei, X., Kysar, J. W. & Hone, J. Measurement of the elastic properties and intrinsic strength of monolayer graphene. *Science (80-.).* **321**, 385–388 (2008).
24. Zandiatashbar, A. et al. Effect of defects on the intrinsic strength and stiffness of graphene. *Nat. Commun.* **5**, 1–9 (2014).
25. Banhart, F., Kotakoski, J. & Krasheninnikov, A. V. Structural defects in graphene. *ACS Nano* **5**, 26–41 (2011).
26. Bendali, A. et al. Purified neurons can survive on peptide-free graphene layers. *Adv. Healthc. Mater.* **2**, 929–933 (2013).
27. Kostarelos, K., Vincent, M., Hebert, C. & Garrido, J.A. Graphene in the Design and Engineering of Next-Generation Neural Interfaces. *Adv. Mater.* **29**, 42 (2017).
28. Balasubramanian, K. et al. Reversible defect engineering in graphene grain boundaries. *Nat. Commun.* **10**, 1090 (2019).
29. Banszerus, L. et al. Ultrahigh-mobility graphene devices from chemical vapor deposition on reusable copper. *Sci. Adv.* **1**, e1500222 (2015).
30. Mitra, A. et al. Spontaneous infra-slow brain activity has unique spatiotemporal dynamics and laminar structure. *Neuron* **98**, 297–305.e6 (2018).
31. Pan, W.-J., Thompson, G. J., Magnuson, M. E., Jaeger, D. & Keilholz, S. Infraslow LFP correlates to resting-state fMRI BOLD signals. *Neuroimage* **74**, 288 (2013).
32. Krishnan, G. P., González, O. C. & Bazhenov, M. Origin of slow spontaneous resting-state neuronal fluctuations in brain networks. *Proc. Natl Acad. Sci. USA.* https://doi.org/10.1073/pnas.1715841115 (2018)
33. Masvidal-Codina, E. et al. High-resolution mapping of infraslow cortical brain activity enabled by graphene microtransistors. *Nat. Mater.* **18**, 280–288 (2019).
34. Garcia-Cortadella, R. et al. Distortion-free sensing of neural activity using graphene transistors. *Small* 1906640. https://doi.org/10.1002/smll.201906640 (2020)
35. Hiltunen, T. et al. Infra-Slow EEG fluctuations are correlated with resting-state network dynamics in fMRI. *J. Neurosci.* **34**, 356–362 (2014).
36. Mitra, A., Snyder, A. Z., Tagliazucchi, E., Laufs, H. & Raichle, M. E. Propagated infra-slow intrinsic brain activity reorganizes across wake and slow wave sleep. *Elife* **4**, e10781 (2015).
37. Grooms, J. K. et al. Infraslow electroencephalographic and dynamic resting state network activity. *Brain Connect.* **7**, 265–280 (2017).
38. Kelly, A. M. C., Uddin, L. Q., Biswal, B. B., Castellanos, F. X. & Milham, M. P. Competition between functional brain networks mediates behavioral variability. *Neuroimage* **39**, 527–537 (2008).
39. Vanhatalo, S. et al. Infraslow oscillations modulate excitability and interictal epileptic activity in the human cortex during sleep. *Proc. Natl Acad. Sci.* **101**, 5053–5057 (2004).
40. Watson, B. O., Hengen, K. B., Gonzalez Andino, S. L. & Thompson, G. J. Cognitive and physiologic impacts of the infraslow oscillation. *Front. Syst. Neurosci.* **12**, 44 (2018).
41. Vanhatalo, S., Voipio, J. & Kaila, K. Full-band EEG (FbEEG): an emerging standard in electroencephalography. *Clin. Neurophysiol.* **116**, 1–8 (2005).
42. Kovac, S., Speckmann, E.-J. & Gorji, A. Uncensored EEG: the role of DC potentials in neurobiology of the brain. *Prog. Neurobiol.* **165–167**, 51–65 (2018).
43. Nelson, M. J., Pouget, P., Nilsen, E. A., Patten, C. D. & Schall, J. D. Review of signal distortion through metal microelectrode recording circuits and filters. *J. Neurosci. Methods* **169**, 141–157 (2008).
44. Chan, A. W., Mohajerani, M. H., LeDue, J. M., Wang, Y. T. & Murphy, T. H. Mesoscale infraslow spontaneous membrane potential fluctuations

45. Leopold, D. A. Very slow activity fluctuations in monkey visual cortex: implications for functional brain imaging. *Cereb. Cortex* **13**, 422–433 (2003).

46. Mackin, C. et al. A current–voltage model for graphene electrolyte-gated field-effect transistors. *IEEE Trans. Electron Devices* **61**, 3971–3977 (2014).

47. Schaefer, N. et al. Improved metal-graphene contacts for low-noise, high-density microtransistor arrays for neural sensing. *Carbon N. Y.* **161**, 647–655 (2020).

48. Rivnay, J. et al. High-performance transistors for bioelectronics through tuning of channel thickness. *Sci. Adv.* **1**, e1400251 (2015).

49. Masvidal-Codina, E. et al. High-resolution mapping of infraslow cortical brain activity enabled by graphene microtransistors. *Nat. Mater.* **18**, 280–288 (2019).

50. Zurutuza, A. & Marinelli, C. Challenges and opportunities in graphene commercialization. *Nat. Nanotechnol.* **9**, 730–734 (2014).

51. Deng, B., Liu, Z. & Peng, H. Toward mass production of CVD graphene films. *Adv. Mater.* **31**, 1800996 (2019).

52. Khodagholy, D. et al. High transconductance organic electrochemical transistors. *Nat. Commun.* **4**, 1–6 (2013).

53. Mavredakis, N., Garcia Cortadella, R., Bonaccini Calia, A., Garrido, J. A. & Jiménez, D. Understanding the bias dependence of low frequency noise in single layer graphene FETs. *Nanoscale* **10**, 14947–14956 (2018).

54. West, B. J. & Shlesinger, M. The noise in natural phenomena. *Am. Sci.* **78**, 40–45 (1990).

55. Neto, A. H. C., Guinea, F., Peres, N. M. R., Novoselov, K. S. & Geim, A. K. The electronic properties of graphene. *Rev. Mod. Phys.* https://doi.org/10.1103/RevModPhys.81.109 (2007).

56. Pinto, H. & Markevich, A. Electronic and electrochemical doping of graphene by surface adsorbates. *Beilstein J. Nanotechnol.* **5**, 1842–1848 (2014).

57. Fu, W. et al. Biosensing near the neutrality point of graphene. *Sci. Adv.* **3**, e1701247 (2017).

58. Prodanov, D. & Delbeke, J. Mechanical and biological interactions of implants with the brain and their impact on implant design. *Front. Neurosci.* **10**, 11 (2016).

59. Prasad, A. & Sanchez, J. C. Quantifying long-term microelectrode array functionality using chronic in vivo impedance testing. *J. Neural Eng.* **9**, 026028 (2012).

60. Degenhart, A. D. et al. Histological evaluation of a chronically-implanted electrocorticographic electrode grid in a non-human primate. *J. Neural Eng.* **13**, 046019 (2016).

61. Sun, F. T., Arcot Desai, S., Tcheng, T. K. & Morrell, M. J. Changes in the electrocorticogram after implantation of intracranial electrodes in humans: The implant effect. *Clin. Neurophysiol.* **129**, 676–686 (2018).

62. Salatino, J. W., Ludwig, K. A., Kozai, T. D. Y. & Purcell, E. K. Glial responses to implanted electrodes in the brain. *Nat. Biomed. Eng.* **1**, 862–877 (2017).

63. Hassler, C., Boretius, T. & Stieglitz, T. Polymers for neural implants. *J. Polym. Sci. Part B Polym. Phys.* **49**, 18–33 (2011).

64. Mendes, G. C. C., Brandão, T. R. S. & Silva, C. L. M. Ethylene oxide sterilization of medical devices: A review. *Am. J. Infect. Control* **35**, 574–581 (2007).

65. Huang, C., Irwin, M. G., Wong, G. T. C. & Chang, R. C. C. Evidence of the impact of systemic inflammation on neuroinflammation from a non-bacterial endotoxin animal model. *J. Neuroinflammation* **15**, 147 (2018).

66. Stephenson, R., Lim, J., Famina, S., Caron, A. M. & Dowse, H. B. Sleep-wake behavior in the rat: Ultradian rhythms in a light-dark cycle and continuous bright light. *J. Biol. Rhythms* **27**, 490–501 (2012).

67. Vyazovskiy, V. V., Achermann, P. & Tobler, I. Sleep homeostasis in the rat in the light and dark period. *Brain Res. Bull.* **74**, 37–44 (2007).

68. Trachsel, L., Tobler, I. & Borbely, A. A. Sleep regulation in rats: effects of sleep deprivation, light, and circadian phase. *Am. J. Physiol. -Regul. Integr. Comp. Physiol.* **251**, R1037–R1044 (1986).

69. Lecci, S. et al. Coordinated infraslow neural and cardiac oscillations mark fragility and offline periods in mammalian sleep. *Sci. Adv.* **3**, e1602026 (2017).

70. Thompson, G. J. et al. Phase-amplitude coupling and infraslow (<1 Hz) frequencies in the rat brain: relationship to resting state fMRI. *Front. Integr. Neurosci.* **8**, 41 (2014).

71. Sirota, A. et al. Entrainment of neocortical neurons and gamma oscillations by the hippocampal theta rhythm. *Neuron* **60**, 683–697 (2008).

72. Pesaran, B. et al. Investigating large-scale brain dynamics using field potential recordings: analysis and interpretation. *Nat. Neurosci.* **21**, 903–919 (2018).

73. Sirota, A. & Buzsáki, G. Interaction between neocortical and hippocampal networks via slow oscillations. *Thalamus Relat. Syst.* **3**, 245–259 (2007).

74. Sturman, O., Germain, P. L. & Bohacek, J. Exploratory rearing: a context- and stress-sensitive behavior recorded in the open-field test. *Stress* **21**, 443–452 (2018).

75. Lever, C., Burton, S. & O'Keefe, J. Rearing on hind legs, environmental novelty, and the hippocampal formation. *Rev. Neurosci.* **17**, 111–133 (2006).

76. Barth, A. M., Domonkos, A., Fernandez-Ruiz, A., Freund, T. F. & Varga, V.

77. Sirota, A. et al. Entrainment of neocortical neurons and gamma oscillations by the hippocampal theta rhythm. *Neuron* **60**, 683–697 (2008).

78. Kandel, A. & Buzséki, G. Cellular-synaptic generation of sleep spindles, spike-and-wave discharges, and evoked thalamocortical responses in the neocortex of the rat. *J. Neurosci.* **17**, 6783–6797 (1997).

79. Kandel, A. & Buzsáki, G. Cerebellar neuronal activity correlates with spike and wave EEG patterns in the rat. *Epilepsy Res.* **16**, 1–9 (1993).

80. Voipio, J., Tallgren, P., Heinonen, E., Vanhatalo, S. & Kaila, K. Millivolt-scale DC shifts in the human scalp EEG: evidence for a nonneuronal generator. *J. Neurophysiol.* **89**, 2208–2214 (2003).

81. Pan, W. J., Thompson, G. J., Magnuson, M. E., Jaeger, D. & Keilholz, S. Infraslow LFP correlates to resting-state fMRI BOLD signals. *Neuroimage* **74**, 288–297 (2013).

82. Grooms, J. K. et al. Infraslow electroencephalographic and dynamic resting state network activity. *Brain Connect.* **7**, 265–280 (2017).

83. Lazic, K., Ciric, J. & Saponjic, J. Sleep spindle dynamics during NREM and REM sleep following distinct general anaesthesia in control rats and in a rat model of Parkinson's disease cholinopathy. *J. Sleep Res.* **28**, e12758 (2019).

84. Kozák, G., Földi, T. & Berényi, A. Spike-and-wave discharges are not pathological sleep spindles, network-level aspects of age-dependent absence seizure development in rats. *eNeuro* **7**, ENEURO.0253-19.2019 (2020).

85. Rubehn, B. & Stieglitz, T. In vitro evaluation of the long-term stability of polyimide as a material for neural implants. *Biomaterials* **31**, 3449–3458 (2010).

86. Lu, H. et al. SU8-based micro neural probe for enhanced chronic in-vivo recording of spike signals from regenerated axons. In *Sensors, 2006 IEEE,* 66–69 (IEEE, 2006).

87. Márton, G. et al. A multimodal, SU-8-platinum-polyimide microelectrode array for chronic in vivo neurophysiology. *PLoS ONE* **10**, e0145307 (2015).

88. Al-Ahmady, Z. S. et al. Selective liposomal transport through blood brain barrier disruption in ischemic stroke reveals two distinct therapeutic opportunities. *ACS Nano* **13**, 12470–12486 (2019).

89. Miyawaki, H., Billeh, Y. N. & Diba, K. Low activity microstates during sleep. *Sleep* **40**, zsx066 (2017).

90. Mitra, P. P. & Pesaran, B. Analysis of dynamic brain imaging data. *Biophys. J.* **76**, 691–708 (1999).

Author contributions

R.G.C. fabricated the graphene sensor arrays and performed their characterization in vitro, he characterized the headstage and contributed to the recording and analysis of electrophysiological activity. G.S. developed the implantation methodology and did the surgery. He also contributed to electrophysiological signals recording and analysis. C.J. designed the wireless headstage and software for the operation of active sensor arrays. X. I. contributed to the design and fabrication of the neural probes. A.G., S.S., I.S., and E.S. performed the experiments for the biocompatibility study. E.M. fabricated and tested the devices for the biocompatibility study. K.K., S.S., and A.G., designed and interpreted the biocompatibility data. K.K. and S.S. overall coordinated the team for the biocompatibility study. A.G.B. contributed to the design of the recording system. A.S. coordinated the experiments for electrophysiological data-acquisition and contributed to the analysis of electrophysiological signals. J.A.G. coordinated the team in the ICN2 for the fabrication of the sensor arrays. R.G.C., G.S., S.S., A.S., and J.A.G. wrote the manuscript.

Competing interests

Patent application (no. P201831068) filled by CSIC, ICREA, CIBER, ICN2, and IDI-BAPS; concerning a graphene transistor system for measuring electrophysiological sig-

ARTICLE

Additional information

Supplementary Materials

Graphene active sensor arrays for long-term and wireless mapping of wide frequency band epicortical brain activity

R. Garcia-Cortadella[1*], G. Schwesig[2*], C. Jeschke[3], X. Illa[4,5], Anna L. Gray[6], S. Savage[6], E. Stamatidou[6], I. Schiessl[7], E. Masvidal-Codina[4,5], K. Kostarelos[6,1], A. Guimerà-Brunet[4,5], A. Sirota [2†] and J. A. Garrido[1,8†]

[1] Catalan Institute of Nanoscience and Nanotechnology (ICN2), CSIC and BIST, Campus UAB, Bellaterra, 08193 Barcelona, Spain.

[2] Bernstein Center for Computational Neuroscience Munich, Faculty of Medicine, Ludwig-Maximilians Universität München, Planegg-Martinsried, Germany.

[5] Multi Channel Systems (MCS) GmbH, Reutlingen, Germany.

[4] Instituto de Microelectrónica de Barcelona, IMB-CNM (CSIC), Esfera UAB, Bellaterra, Spain.

[5] Centro de Investigación Biomédica en Red en Bioingeniería, Biomateriales y Nanomedicina (CIBER-BBN), Madrid, Spain.

[6] Nanomedicine Lab, National Graphene Institute and Faculty of Biology, Medicine & Health, University of Manchester, Manchester, UK

[7] Division of Neuroscience and Experimental Psychology, School of Biological Sciences, Faculty of Biology, Medicine and Health, University of Manchester, Manchester M13 9PT, United Kingdom

[8] ICREA, Pg. Lluís Companys 23, 08010 Barcelona, Spain.

* These authors contributed equally to this work

† Corresponding author: joseantonio.garrido@icn2.cat (J.A.G.), sirota@biologie.uni-muenchen.de (A.S.)

S1. Specifications of wireless recording system

The wireless system developed by Multichannel systems (MCS) to bias and record from the graphene active sensor arrays consists of two amplification stages followed by a multiplexer to select the output from the first (DC-channel) or second stage (AC-channel). Subsequently the signals are digitized and transmitted in the 2.4GHz band to the receivers (W2100-RE-AO from MCS). The communication between receivers and the computer is done by the interface board (MCS-IFB-in-vitro from MCS). The software used to communicate with the interface board is the commercial software Multi Channel Experimenter. To control the bias conditions V_{gs} and V_{ds} of the active graphene sensors a specific software has been developed, which also allows to quickly extract the $I_{ds} - V_{gs}$ needed to control changes in the charge neutrality point (CNP) of the graphene transistors. The following table summarizes the technical specifications of the wireless system. Fig. S1 shows the dimensions of the wireless headstage, which is connected to a flexible PCB (orange component). The flexible PCB is connected to the headstage on one side and to a PCB containing a zero-insertion-force (ZIF) connector on the other side. The connection between the flexible and rigid PCBs is done by a Molex connector. The flexible PCB eases the alignment of the neural probe on the desired location on the cortex.

DC-Channel count	8
AC-Channel count (with DC enabled)	64 (56)
Input Frequency Range AC (DC)	0.15 Hz – 5 kHz (DC – 7.35kHz)
Maximum input current AC (AC)	+/- 11.5 µA (+/- 115 µA)
Gain AC (DC)	120000 (12000)
Wireless transmission range	5m (depending on environment 10-15m)
OpAmps consumption	52.8mA
ADCs (at Fs = 20kHz) consumption	16mA
RF-Chips consumption	116mA
Battery 3.7V/700mAh duration	~6h
Battery 3.7V/700mAh charging time	~1h
Battery 3.7V/700mAh weight	15g
Headstage weight	7.9g
Flex-PCB weight	0.5g
Weight of 3D printed base ring, headstage support and protective cap	15g

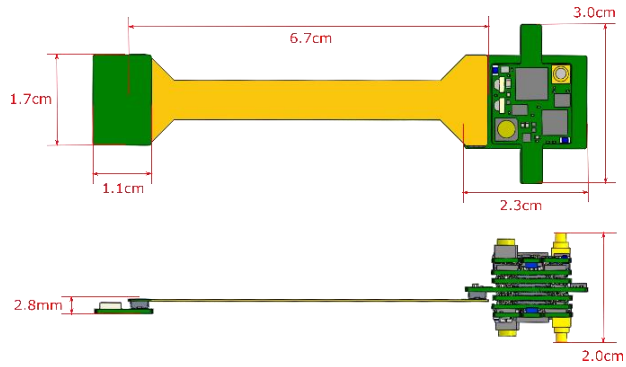**Table S1. Technical specifications of the wireless system**

Figure S1. Dimensions of the wireless headstage and connectors. The green component on the left represents a small PCB containing a ZIF connector to the neural probe and a Molex connector to the flexible PCB (orange component). The component on the right represents the wireless headstage

S2. Intrinsic 1/f noise and headstage noise

The equivalent voltage noise spectrum at the gate is shown in Fig. S2A for g-SGFETs connected to DC and AC- coupled channels of the headstage. In the central part of the spectrum (~0.05-10Hz) the 1/f trend corresponding to the intrinsic noise of the g-SGFETs dominates. The intrinsic noise is expected to present a $1/\sqrt{A}$ dependence[1], where A stands for the area of the active part of the graphene channel. Here we have validated that the expected trend holds for the technology presented in this article. Having this validation it is possible to extrapolate the results from this work to devices with different areas. Fig. S2B shows V_{gs-rms} measured for g-SGFETs of different areas fabricated on a flexible PI substrate following the procedure detailed in the Methods section. Note that the values displayed in Fig. 2 of the main text for an area of 100x100 μm^2 match with the trend observed in Fig. S2B.

The intrinsic noise of the g-SGFETs in the infra-slow ($< 0.5 Hz$) frequency bandwidth is expected to follow the same 1/f trend as in the rest of the frequency spectrum[2]. However, the low frequency noise from other components of the recording system might contribute significantly in this frequency band. Fig. S2D (top) shows a schematic for the transimpedance amplifier in the first amplification stage, and Fig. S2D (bottom) shows the noise sources in this circuit. The voltage source (V_{ds}) as well as the op-amp present several sources of noise. Fluctuations in V_{ds} are common for all the g-SGFETs and would therefore cause coherent noise in all the channels. Conversely, each channel has an independent op-amp and therefore the noise from this source is expected to be uncorrelated among channels. Table S2 shows the contributions from each of these noise sources, separated between coherent and non-coherent. Fig. S2C shows the coherence between two DC-coupled channels connected to a 2kΩ resistance (red) and to g-SGFETs (black). In the central frequency range, the coherence in the noise of different channels is larger when a resistance is connected instead of the g-SGFETs. The reason is that the intrinsic noise of g-SGFETs is completely uncorrelated among different sensors. At higher and lower frequencies, the coherence increases, presumably due to the effect of quantization noise and correlated noise sources respectively. Finally, Fig. S2E shows the power spectral density measured in DC-coupled channels connected to g-SGFETs in the ISA band (0.005-0.4Hz). The noise below 0.05Hz is shown to clearly deviate from the 1/f trend, indicating a significant contribution of low-frequency noise sources from the headstage. Nevertheless, integrating the noise spectrum in the 0.005-0.05Hz shows that the rms noise increases only by roughly a factor of 2 as compared to the intrinsic noise values shown in Fig. 2 of the main text (see Fig. S2F).
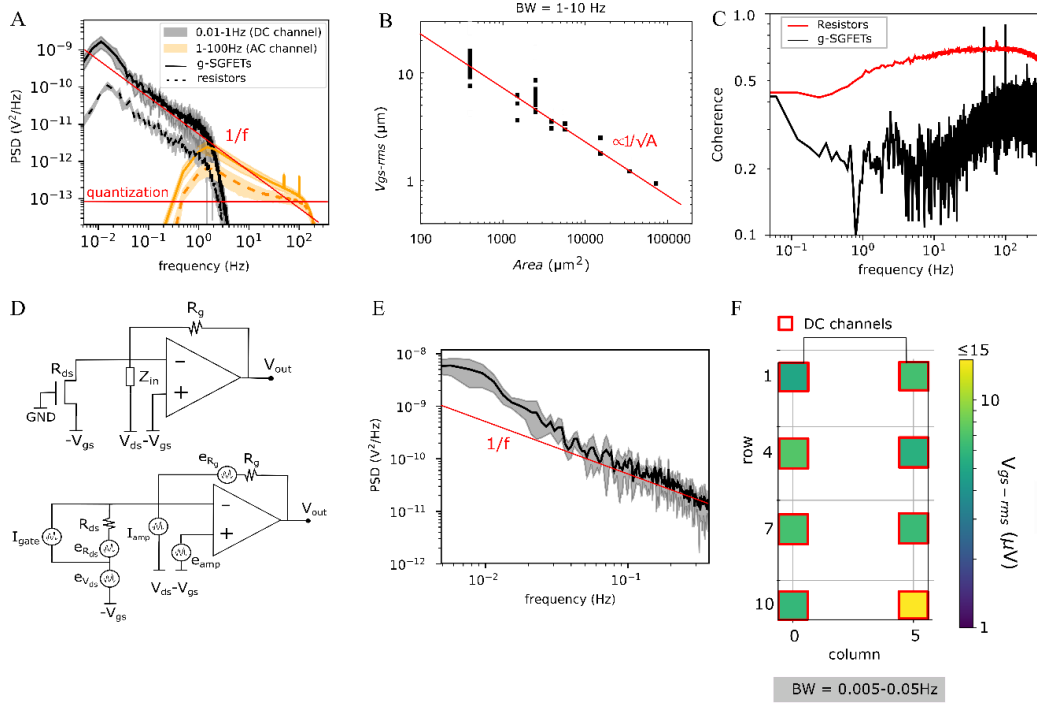
Figure S2. Intrinsic graphene noise and low-frequency contributions from the headstage. (A), Power spectral density of signals from DC-coupled channels (black) and AC channels (orange) measured for g-SGFETs in the beaker (solid) and for 2kΩ resistors (dashed). The red lines indicate the 1/f trend corresponding to intrinsic noise and quantization noise. **(B),** The intrinsic noise of g-SGFETs ($V_{gs\text{-}rms}$ in the 1-10Hz) versus the area of the channel is plotted. The red line indicates the $1/\sqrt{A}$ dependence. **(C),** The coherence for a DC-coupled channel is shown for a resistor (red) and for a g-SGFET (black). **(D),** The equivalent circuit of the g-SGFET connected to the transimpedance amplifier is shown (top) together with the equivalent circuit for the expected noise sources (bottom). **(E),** The power spectral density for the DC-coupled channels with g-SGFETs connected is shown in the infra-slow frequency band. The 1/f trend is indicated by a red line. **(F),** The integrated noise ($V_{gs\text{-}rms}$) in the 0.005-0.05Hz band is shown for all the 8 g-SGFETs connected to DC-coupled channels of the headstage.

Non-coherent noise sources	Coherent noise sources
$V_{out-Rds} = \sqrt{R_{ds}4K_BT}\dfrac{R_g}{R_{ds}}$	$V_{out-Vds} = e_{vds}\dfrac{R_g}{R_{ds}}$
$V_{out-Rg} = \sqrt{R_g4K_BT}$	
$V_{out-Iamp} = I_{amp}R_g$	$V_{out-Igate} = g_m e_{gate}R_g$
$V_{out-eamp} = e_{amp}\dfrac{R_g + R_{ds}}{R_{ds}}$	

Table S2: Output voltage noise produced by coherent and non-coherent noise sources in the amplification chain.

S3. Signal stability

The shift in the CNP presumably caused by adsorption/desorption of charged chemical species on the graphene channel and changes in the reference electrode potential cause very slow drifts of the measured signal. Fig. S3A shows the measured signal *in-vivo* over the first 24h of recording. The observed drift shows an initial rate of ~20mV/h during the first 1-2 hours, which afterwards tends to stabilize. Fig. S3A also shows the high-pass filtered signal above 1mHz, in which the drift is not observed.

Besides long-term changes in the doping of the graphene channel and the reference electrode potential, the reference electrode might present short term instabilities, which could lead to an uncontrolled biasing of the graphene transistor. The use of stainless steel screws to fix the implant on the skull and simultaneously provide a reference potential is a common practice in electrophysiology[3]. However, controlling the bias of active sensors requires the application of a controlled overpotential, in contrast to conventional electrode-based electrophysiological measurements. In this work, it was found that stainless steel screws do not provide a stable reference potential for the operation of g-SGFETs, which might be caused by a poor contact with the dura. In order to circumvent this problem we have used an Ag/AgCl electrode implanted in direct contact with the cerebellum.

The transfer characteristics obtained using a stainless-steel screw in the skull as reference electrode presented inconsistencies for different V_{gs} sweep rates. The stabilization of I_{ds} after changing the gate voltage was very slow causing a defective acquisition of the I_{ds} - V_{gs} curves. Fig. S3B shows the transfer curves for this type of reference electrode obtained by changing V_{gs} at two different rates (2s/step and 40s/step). The differences between the two curves demonstrate that the stationary conditions are not reached. An important drift of the current can be observed which explains the discrepancies between sweep rates in Fig. S5C. In order to eliminate these drifts, an Ag/AgCl electrode was implanted on the cerebellum. Fig. S5D shows the close match between the transfer characteristics obtained for different V_{gs} sweep rates using a Ag/AgCl electrode. Fig. S5E shows the I_{ds} over time during the V_{gs} sweep for this reference electrode, demonstrating a much faster stabilization. These results demonstrate that Ag/AgCl allows to accurately control the bias of the graphene channel during operation *in-vivo*.
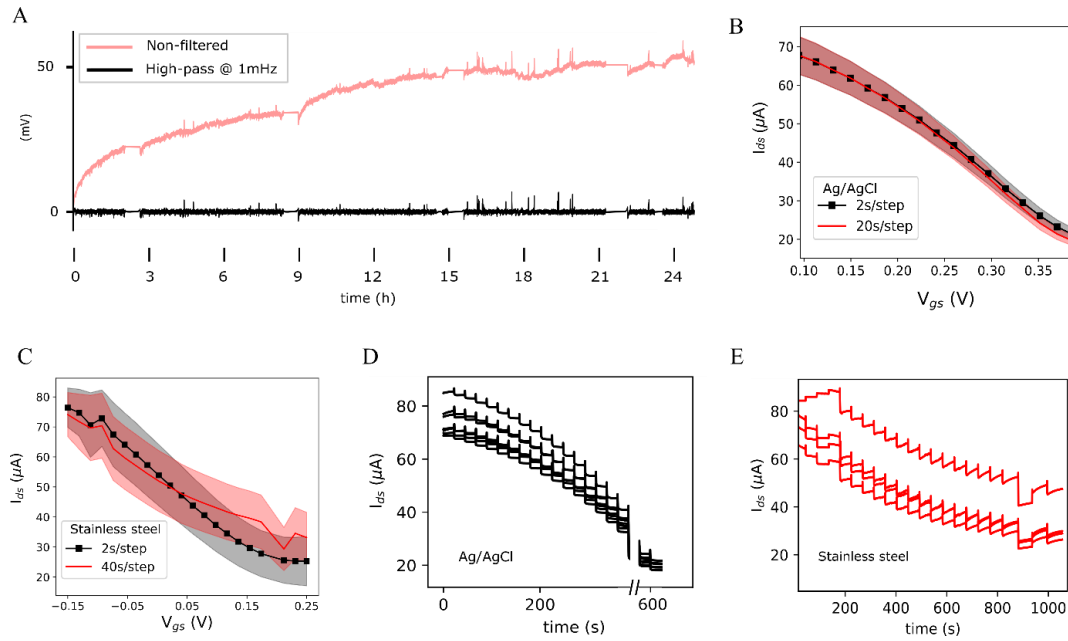
Figure S3. Signal stability. (A), The signal for a DC-coupled channel during the first 24h of recording *in-vivo* is shown in pink and the high pass filtered signal (>1mHz) is plotted in black. **(B),** $I_{ds} - V_{gs}$ curves measured applying two different sweep rates using a Ag/AgCl implanted on the cerebellum (n=7 g-SGFETs). One outlier removed. **(C),** $I_{ds} - V_{gs}$ curves measured applying two different sweep rates using a stainless steel screw implanted on the skull (n=4 g-SGFETs). Solid lines in panels (B) and (C) represent the mean and the error bands the standard deviation. **(D,E),** The I_{ds} over time during a V_{gs} sweep rate of 20s using an Ag/AgCl in contact with the cerebellum **(D)** and a sweep rate of 40s per step and using a stainless steel screw **(D)**is shown. The discontinuity in panel D corresponds to an interruption in the applied voltage (see Source Data file).

S4. Determination of intrinsic noise in g-SGFETs over time

The noise performance of the g-SGFETs is susceptible to degradation over long-term implantation. In order to evaluate the equivalent evolution of intrinsic noise over time the noise power must be measured. Due to the presence of neural activity detected by the g-SGFETs, the *in-vivo* determination of the noise power must be estimated from a frequency band in which, on average, the power of neural activity is below the power of 1/f noise. Fig. S6 shows the PSD of the calibrated signal (i.e. equivalent signal at the gate) for all the g-SGFETs in the array for day 1 and day 11 after the implantation. It is possible to see that above a certain frequency, the power of neural activity goes below the 1/f from the intrinsic noise of the g-SGFET and the quantization noise from the ADC. In order to determine the evolution of the intrinsic noise of the g-SGFETs we measured the power density at 200Hz over time. Assuming a 1/f response the intrinsic noise of the g-SGFET can be estimated for any frequency band of interest. Note that this noise value will always be equal or larger than the actual intrinsic noise of the g-SGFETs due to possible contributions from the quantization noise or neural signal power. Fig. 3f and 3g of the main text show the V_{gs-rms} and I_{ds-rms} values in the 1-10Hz frequency band estimated following this approach. Note that the V_{gs-rms} values obtained *in-vivo* are close to the ones extracted in PBS, indicating the accuracy of this estimation.

Finally, the orange line in Fig. S4 shows the PSD for a broken g-SGFET. When the transistor degrades and the channel breaks, no current can flow through the transistor. Therefore, the flicker noise from the g-SGFETs does not contribute significantly and only the noise from the amplifiers in open circuit remains (see supplementary information S2). This causes a significant drop in the noise as shown in Fig. S4, which is a clear indicator that the channel has broken. Fig. 3F in the main text shows the yield of g-SGFETs working over time based on this indicator.
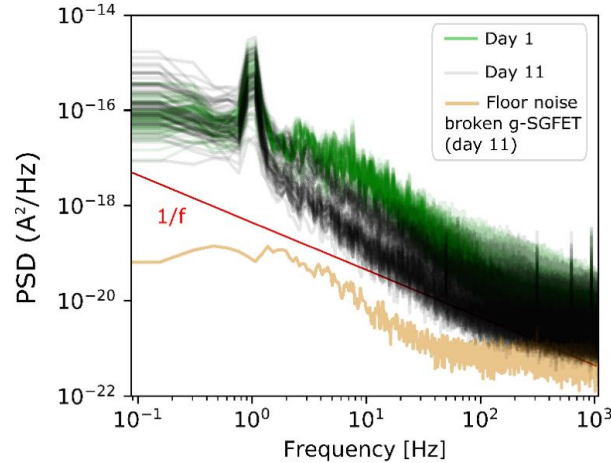

Figure S4. Power spectral density of I_{ds} measured *in-vivo*. The PSD for all 64 g-SGFETs in the array is shown for day 1 and day 11 after the implantation. The red line indicate the 1/f trend. The orange line corresponds to the PSD of a channel which resistance has increased dramatically, probably due to breaking of the graphene sheet.

S5. Frequency response of the g-SGFETs

The magnitude and phase of the transconductance over frequency have been measured *in-vivo*. A certain attenuation of the gain magnitude with an approximately constant slope in a log-log has been observed, which has been previously reported[1]. This slope can be described from the fractional order of constant phase element (CPE) that models the non-ideally capacitive response of the graphene-electrolyte interface. The drop in the magnitude of g_m with frequency presents a $1/f^{1-\alpha}$, where alpha is the ideality factor of the CPE element. This element also introduces a phase delay in the transduced signal of $\pi/2\,(\alpha-1)$, as shown in Fig. S5. Deviations from this model can be observed above $\sim 100 Hz$. This positive shift of the phase has been previously reported when capacitive currents from the electrolyte gate to the drain and source of the g-SGFETs occur[1].
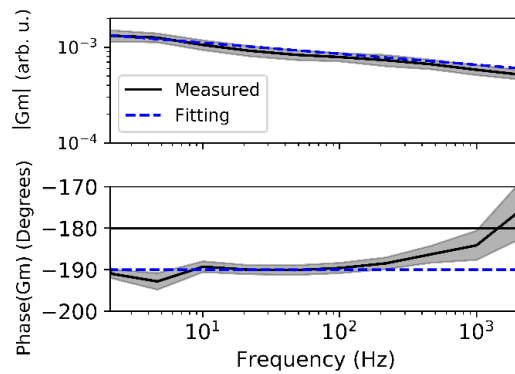
Figure S5. Transconductance over frequency of g-SGFETs in the first day after implantation. The graph on top shows the magnitude of the transconductance while the bottom plot presents the phase of the transconductance (solid line corresponds to the mean and error bands indicate the standard deviation, n=10 g-SGFETs).

S6. Cytokine levels in serum
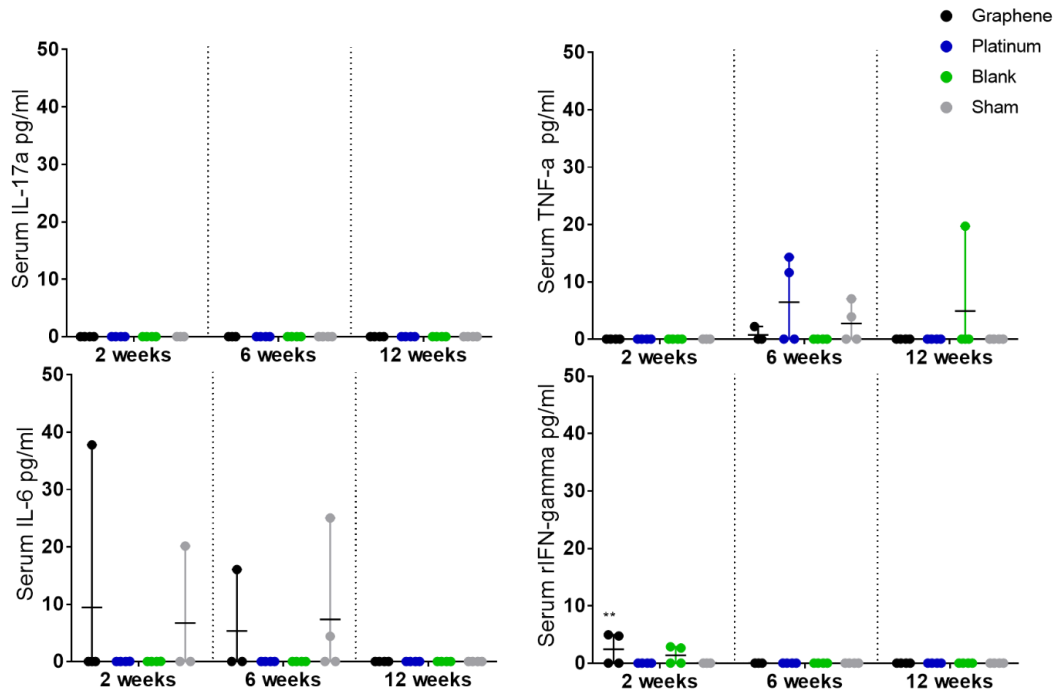
Figure S6. Inflammatory cytokine levels expressed in serum from animals implanted with devices or control animals. Over the four inflammatory markers analysed, IL-17a, TNF-α, IFN-γ and IL-6, there was a significantly higher expression of TNF-α at 2 weeks post implantation for graphene devices compared to sham controls. By 6 weeks this reaction had subsided. No other cytokines showed any significant difference at any timepoint. Bars in panels d and e indicate the mean and range of data point. Two-way ANOVA with Dunnett's multiple comparisons test, compared to sham control for all timepoints. ** indicates p= 0.006.

S7. Cytokine levels in brain tissue
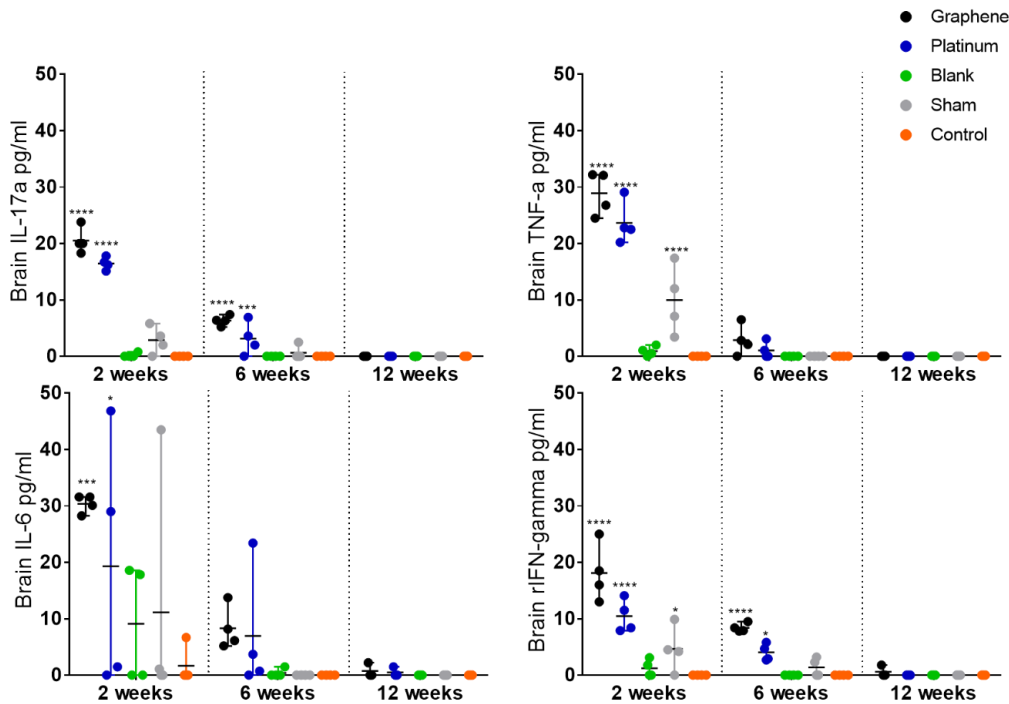
Figure S7. Inflammatory cytokine levels expressed in brain tissue at the surgical site. Over the four inflammatory markers analysed, IL-17a, TNF-α, IFN-γ and IL-6, there was a significantly higher expression at 2 weeks post implantation for graphene and platinum devices compared to naïve animal controls. By 6 weeks, this expression was still significant for both IL-17a and IFN-γ, however by 12 weeks this reaction had subsided. n=4 at 2 and 6 weeks, n=3 at 12 weeks. Bars in panels d and e indicate the mean and range of data point. Two-way ANOVA with Dunnett's multiple comparisons test, compared to naïve control for all timepoints. In all panels, **** indicates p<0.0001. For IL-17a, *** indicates p=0.0016. For IL-6, * and *** indicate p = 0.045 and p = 0.0006 respectively. For rIFN-gamma, * indicates p = 0.012 (for 2 weeks timepoint) and p =0.035 (for 6 weeks timepoint).

S8. Immunoflourescent staining
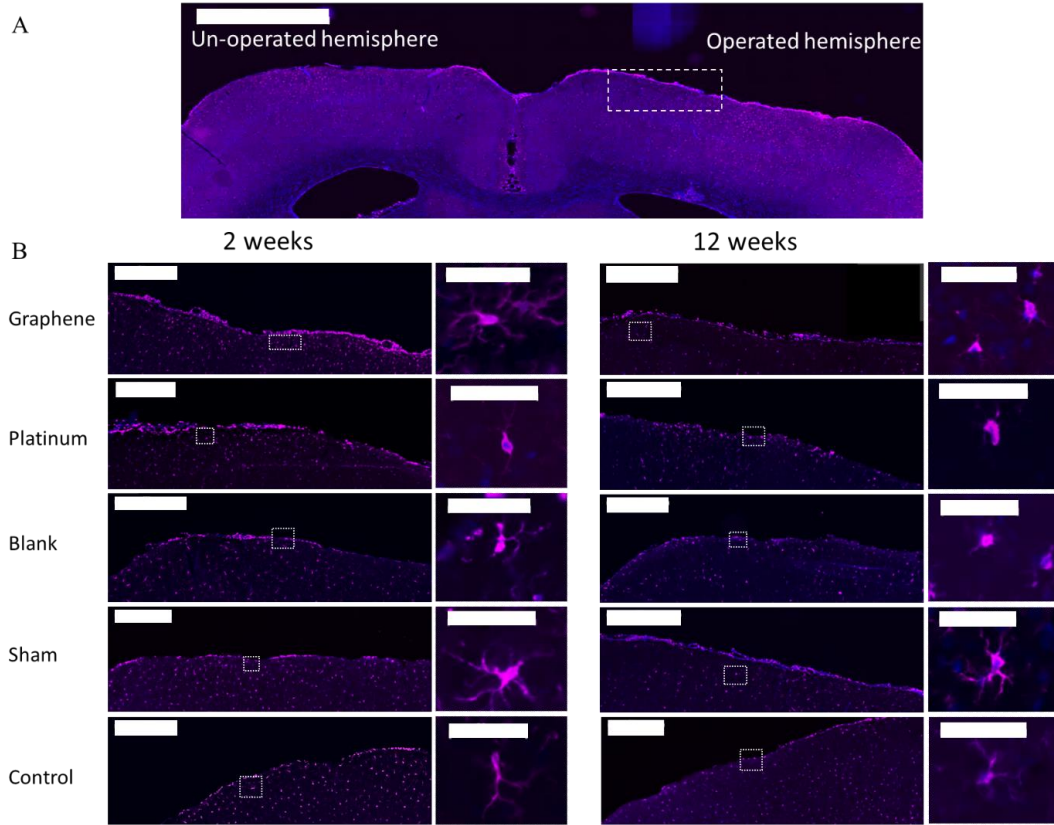
Figure S8. Iba-1 immunoflourescent staining to assess activation status of microglia at the surgical site. (A), Microglial cells were counted for both the operated hemisphere, and the unoperated hemisphere. Scale bar corresponds to 2mm. **(B)**, Exemplar images, taken from the highlighted region in panel A. Left column corresponding to the 2 weeks timepoint and left column to the 12 weeks timepoint. Areas highlighted with white dashed lines are shown with higher magnification. Scale bars correspond to 500μm and 50μm for left and right images respectively within each timepoint.

S9. TUNEL cell counting
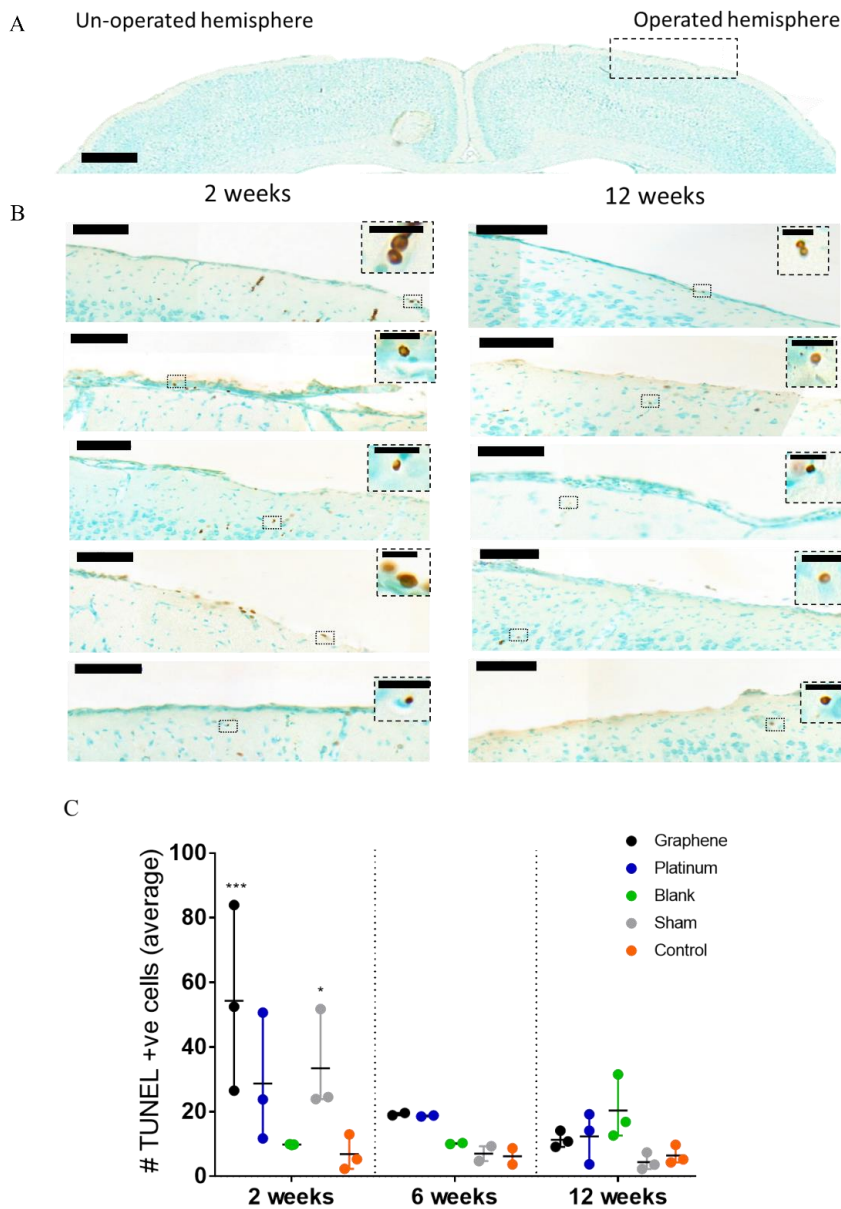
Figure S9. TUNEL positive cell counts from the cortical surface at the implantation site of devices. **(A),** A gross morphological map of the cortex, outlining where representative images were taken from. Scale bar corresponds to 1mm. **(B)** Representative images of TUNEL positive cells counted across 40 sections of the brain per animal. Scale bar corresponds to 100μm (20 μm for the insets). **(C),** The average counts of TUNEL positive cells at the cortex showed that graphene based devices showed a significant increase in apoptosis in the acute period after implantation, as did the shame operated controls, compared with counts of the contralateral hemisphere. By 12 weeks, there was no significant elevation in apoptosis in the surgical area. n=3 for 2 and 12 week timepoints, n=2 for 6 week timepoints. Bars in panels d and e indicate the mean and range of data point. Two-way ANOVA with Dunnett's multiple comparisons test, compared to contralateral hemisphere for 2 and 12 weeks. * indicates p=0.034, *** indicates p=0.0002,

S10. Rearing event detection

Head elevation of the animal varied widely between 20 and ca 330 mm above ground. The distribution of all head elevation values during the 22h recording displayed marked peaks due to distinct long duration behavioral states (like lying on ground, sitting, walking). In contrast the animal spent only very few time points with its head elevated to more than 200 mm above ground. As can be seen in the time-domain (Fig S10A) these timepoints correspond to repeated very shortlived elevations occurring intermittently during active behavior. Elevations of the head beyond 200 mm from ground were therefore labelled as rearing events.
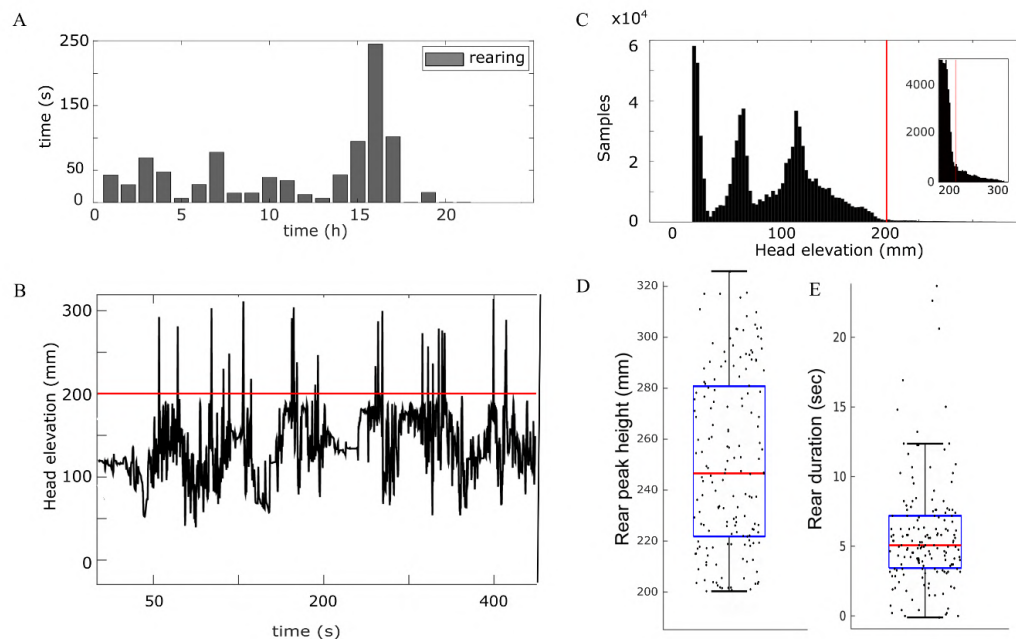
Figure S10. Detection of rearing events. (A), Time spend on rearing over time. **(B),** Example time series of head elevation illustrating the transient and discrete occurrence of rearing events (denoted by *), elevation threshold used for rear detection marked in red. **(C),** Histogram of head elevation during 22h continuous recording period. Threshold for rear event detection marked in red. Zoom-in of same distribution shown in inset. **(D),** distribution of maximum heights for all individual rear events (mean 250,6 ± 2.7 mm). **(E),** distribution of rearing duration for all rear events (mean 5.7 ± 2.8 s). The boxes in panels D and E extend from the lower to the upper quartiles, with a line at the median. The whiskers extend 1.5 times the inter-quartile range and all individual data points are indicated by a dot.
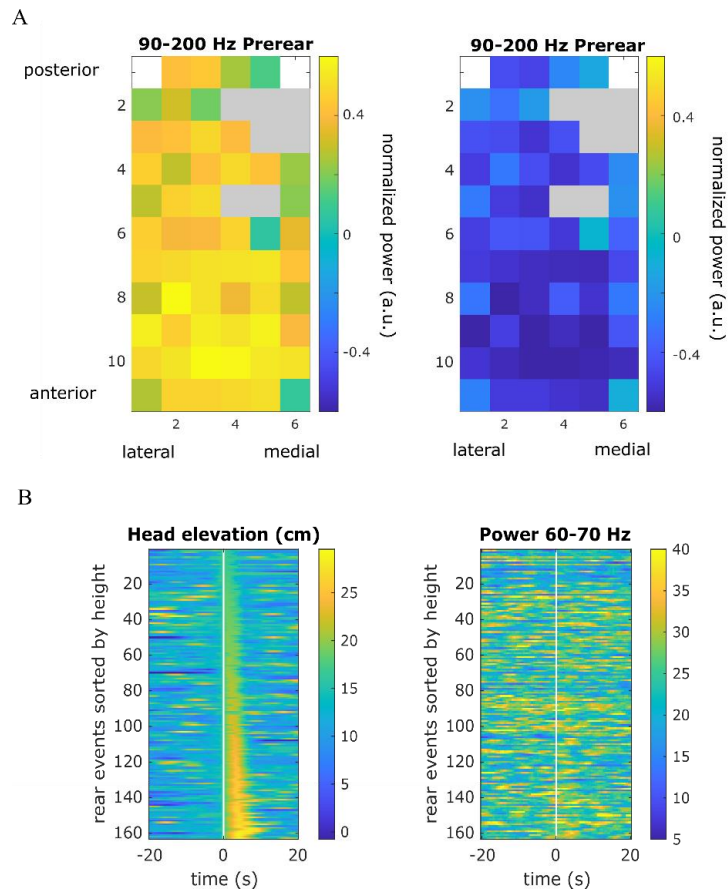
S11. Modulation of high-gamma activity during rearing

Figure S11. Evaluation of gamma modulation during rearing events. (A), Spatial map of normalized power in the high gamma band for pre-rear (-4s to 0s from rear onset) (left) and rear (0s to 4s from rear onset) (right) **(B)** Head elevation for each rear height event sorted by rear duration (left) and spectral power in 60-70 Hz band for each trial extracted from the same channel as in Fig. 5i, sorted by rear height (right).

S12. Slow and infra-slow power in the SWS-REM transition
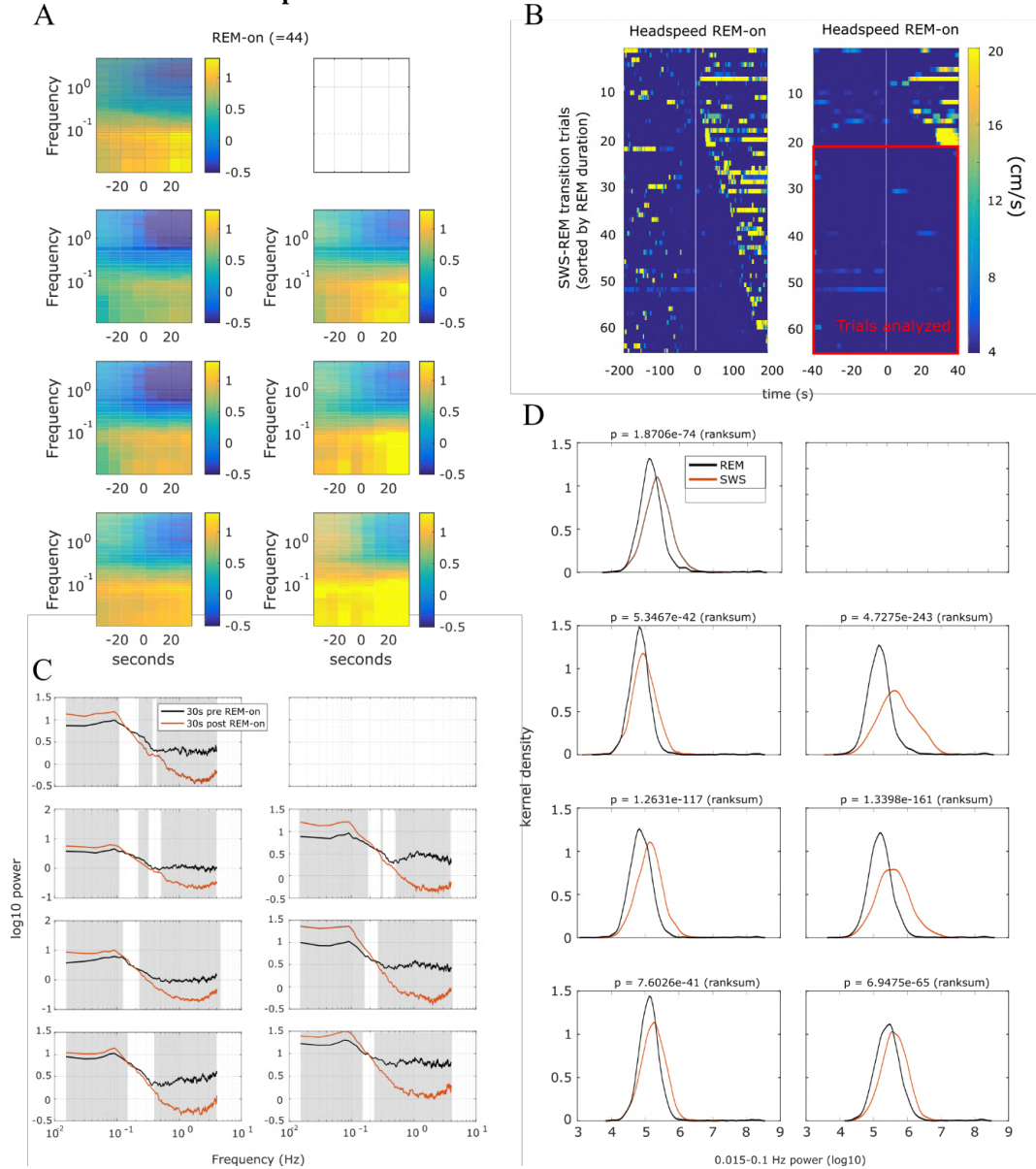
S12. Infra-slow vs slow oscillation band power during SWS/REM sleep: (A), Average spectrogram triggered on REM onsets (n=44) for 7 DC channels with high signal to noise. **(B),** Head speed in the SWS to REM transition for all detected events (left). On the right plot the same data is shown for a shorter time window, where the REM events with duration longer than 40s (n=44) can be identified. **(C),** Median PSD computed for the 30s pre and post REM onsets. Colored area indicates statistically significant difference (two-sided permutation test n=1000 permutations, p<0.05), one channel showing unstable signal is removed. n=44 state transitions. **(D),** Kernel density estimates for the integrated power in 0.01-0.1Hz band during SWS and REM state. p-value for the two-sided Wilcoxon ranksum test are indicated.

References

(1)   Mitra, P. P.; Pesaran, B. Analysis of Dynamic Brain Imaging Data. *Biophys. J.* **1999**, *76* (2), 691–708. https://doi.org/10.1016/S0006-3495(99)77236-X.

(2)   Milotti, E. 1/f Noise: A Pedagogical Review. **2002**.

(3)   Gage, G. J.; Stoetzner, C. R.; Richner, T.; Brodnick, S. K.; Williams, J. C.; Kipke, D. R. Surgical Implantation of Chronic Neural Electrodes for Recording Single Unit Activity and Electrocorticographic Signals. *J. Vis. Exp.* **2012**, No. 60. https://doi.org/10.3791/3565.

Switchless Multiplexing of Graphene Active Sensor Arrays for Brain Mapping

Ramon Garcia-Cortadella,[∇] Nathan Schäfer,[∇] Jose Cisneros-Fernandez, Lucia Ré, Xavi Illa, Gerrit Schwesig, Ana Moya, Sara Santiago, Gonzalo Guirado, Rosa Villa, Anton Sirota, Francesc Serra-Graells, Jose A. Garrido,* and Anton Guimerà-Brunet*

ACCESS | Metrics & More | Article Recommendations | Supporting Information

ABSTRACT: Sensor arrays used to detect electrophysiological signals from the brain are paramount in neuroscience. However, the number of sensors that can be interfaced with macroscopic data acquisition systems currently limits their bandwidth. This bottleneck originates in the fact that, typically, sensors are addressed individually, requiring a connection for each of them. Herein, we present the concept of frequency-division multiplexing (FDM) of neural signals by graphene sensors. We demonstrate the high performance of graphene transistors as mixers to perform amplitude modulation (AM) of neural signals *in situ*, which is used to transmit multiple signals through a shared metal line. This technology eliminates the need for switches, remarkably simplifying the technical complexity of state-of-the-art multiplexed neural probes. Besides, the scalability of FDM graphene neural probes has been thoroughly evaluated and their sensitivity demonstrated *in vivo*. Using this technology, we envision a new generation of high-count conformal neural probes for high bandwidth brain machine interfaces.

KEYWORDS: *Multiplexing, graphene, active sensors, bioelectronics, neural sensing*
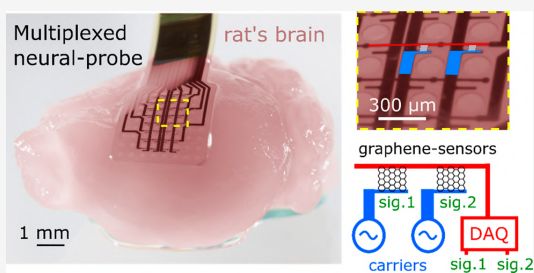
Over the last decades, progress in neurotechnology has enabled a deeper understanding of brain functions such as motor control[1,2] or speech processing and synthesis.[3,4] In turn, these insights have prompted the realization of technological breakthroughs in the field of brain-computer interfaces (BCIs) such as partial restoration of movement[5] or decoding of speech from neural activity.[6] Cortical functions involved in such tasks often emerge from the integration of information in distinct brain regions, yet local activity from small groups of neurons carries essential information for neural coding.[7] Therefore, combining the coverage of large brain areas with high sensor density (i.e., high sensor count) is paramount for both neuroscientific and biomedical applications.[8−10] In this sense, one of the main limitations in current neurotechnologies originates in the need of individually connecting each sensing element to a signal amplifier. This constrain implies having as many conductive lines as sensors in the neural probes, which imposes a trade-off between sensor density and coverage area. One way to overcome this constrain is to perform multiplexing among sensors which allows the transmission of multiple signals over a shared wire.

State-of-the-art sensing technologies for neuroscientific research are mostly based on micro electrode arrays, which can be embedded either in a narrow shank for intracortical mapping[11−14] or in a planar configuration.[8,15−18] Intracortical electrode arrays can be fabricated on rigid substrates,[19] therefore enabling the incorporation of integrated-circuits (ICs) on the probes[12] to amplify and multiplex the measured signals. However, planar arrays on rigid substrate are not conformal with the surface of the brain and are therefore limited to *in vitro* studies.[16−18] Alternatively, flexible electro-corticography (ECoG) arrays are conformal, enabling the detection of local field potentials[20] (LFP) from the surface of the brain.[8,15] ECoGs represent an interesting technology for biomedical applications, since they could be applied to extract a similar information than that obtained with intracortical probes[21,22] but with the additional advantage of lower invasiveness. Nevertheless, the flexible substrate strongly limits the use of nanofabrication methodologies and available materials to fabricate integrated circuits on the neural probe, thus restricting the implementation of *in situ* signal amplification for time-division multiplexing (TDM) of neural
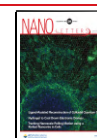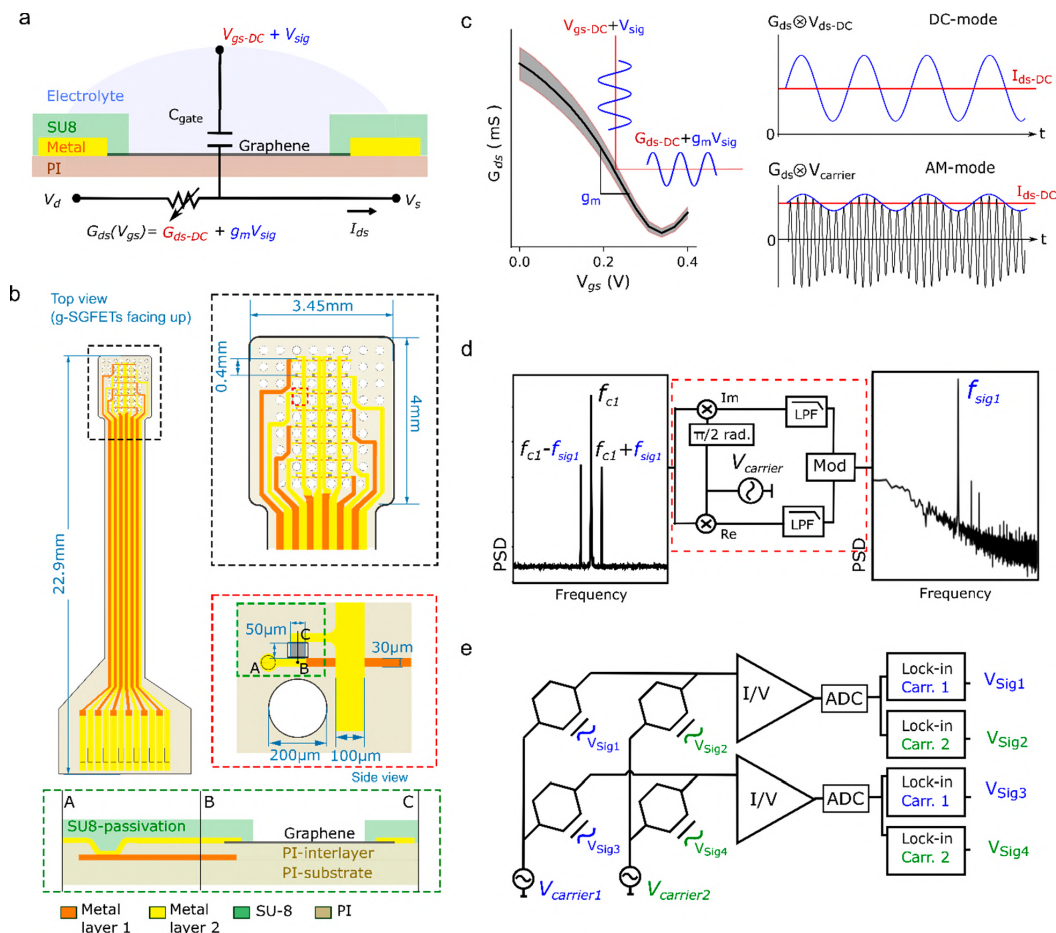
Figure 1. Frequency-domain multiplexing of g-SGFET arrays (a) Equivalent circuit of the g-SGFET together with an illustration of the device. (b) Schematic of the neural probe layout. On the left, the whole probe is displayed. A zoom-in of the probe tip is shown on the top-right image. The orange/yellow colors represent the first/second metal layers, separated by a 2 μm thick polyimide layer. A zoom-in of a single pixel is shown within the red dashed-line square. The bottom schematic depicts a side view of the g-SGFET, showing the connection between the first and second metal layer through a VIA hole in the PI. (c) Typical $G_{ds}-V_{gs}$ curve of g-SGFETs. The filled area represents the standard deviation ($n = 8$). The definition of normalized transconductance (g_m) as the slope of the $G_{ds}-V_{gs}$ curve is indicated in the graph. The g-SGFETs acts as a multiplier of the drain-to-source voltage and the signal at the gate. The resulting I_{ds} in the DC and AM modes is illustrated. (d) The signal folded by the carrier is shown in the frequency domain (left). Demodulation scheme (middle): the multiplication of the modulated signal by an oscillator at the carrier frequency of interest and the $\pi/2$ radians phase-shifted oscillator allows the recovery of the module of the signal in the baseband (right). (e) Basic schematic of the addressable g-SGFET array, which allows modulating the signals at the gate of different g-SGFETs with different carrier frequencies. The mixed signals, containing multiple carrier frequencies, are demodulated after current-to-voltage conversion and digitization.

signals.[23] Flexible materials have been proposed to perform switching among active sensors in an addressable array configuration, including organic semiconductors[24] or ultrathin silicon layers.[25] However, organic semiconductors present an insufficient mobility for high-speed operation, which is critical to achieve high sampling speed for a large number of sensors, and the high complexity of ultrathin silicon technology on flexible substrates limits its widespread application.

Herein, we present a novel approach that uses frequency-division multiplexing (FDM) of graphene solution-gated field-effect-transistors (g-SGFETs) in order to eliminate the need for on-site switches and to reduce the fabrication complexity of high-count neural probes. In this approach, neural signals

detected by different graphene active sensors on the array are amplitude modulated (AM) by different carrier signals, allowing the transmission of multiple signals through a shared communication channel. We present the fabrication of g-SGFET arrays on an addressable column/row matrix configuration to demonstrate their high performance for FDM operation *in vivo*, sensing wide-band neural activity from the surface of the rat brain. Besides, we carefully assess the scalability of this technique, demonstrating the operation of g-SGFETs for a wide range of carrier frequencies, the low impact of crosstalk, and the requirements for an application specific integrated circuit (ASIC) to operate large-scale flexible arrays. The simplification of the technological complexity,
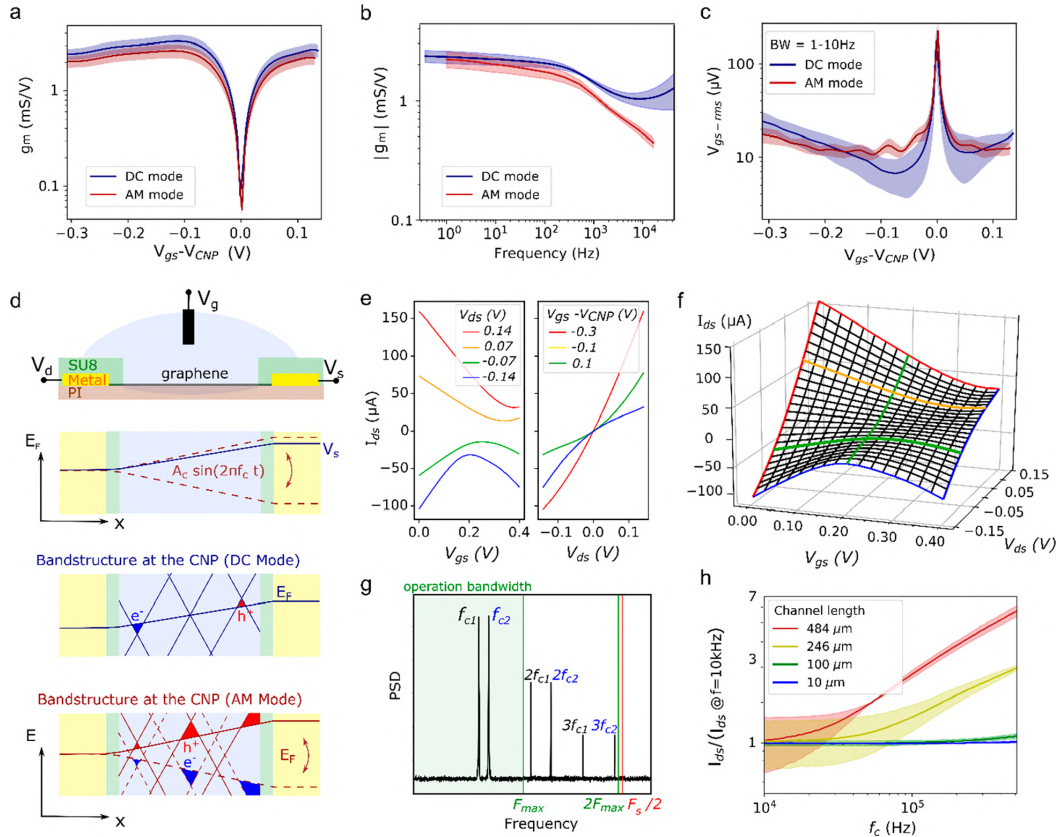
Figure 2. *In vitro* evaluation of g-SGFET performance in the AM mode. (a) g_m–V_{gs} relationship in the AM and DC modes, measured in a 3 × 3 g-SGFET array. (b) The magnitude of g_m over frequency of the signal applied at the gate is shown for the two modes. The response was measured in a 2 × 2 g-SGFET array. (c) V_{gs-rms} for an integration bandwidth of 1–10 Hz measured in the AM and DC modes; measurements performed with a 3 × 3 g-SGFET array. (d) Schematic representation of a g-SGFET and the Fermi energy in the graphene for the DC and AM mode (top). The band structure at the charge neutrality point (CNP) is shown along the graphene channel for the DC (middle) and AM (bottom) modes. (e) Dependence of I_{ds} on V_{gs} and V_{ds}, revealing the shift in the CNP, as well as the nonlinearities in the I_{ds}–V_{ds} produced by the effective gating. (f) Three-dimensional representation of the I_{ds} dependence on V_{gs} and V_{ds}. The relation between shifts of I_{ds}–V_{gs} along the V_{gs} axis and nonlinearities introduced in the I_{ds}–V_{ds} curves can be observed. (g) Two carrier signals and their second and third order harmonics are represented in the frequency domain. The frequency which defines the bandwidth of operation (F_{max}) and the position of the Nyquist frequency ($F_s/2$) with respect to F_{max} are indicated by the vertical lines. (h) The I_{ds} normalized by its value at 10 kHz is shown for different channel lengths. The filled area represents the standard deviation ($n = 3$).

achieved by the elimination of switches and the use of graphene electronics, opens the door to the implementation of high-count flexible neural probes as a readily available technology for neuroscientific studies as well as clinical applications.

■ FREQUENCY-DIVISION MULTIPLEXING OF G-SGFET ARRAYS

g-SGFETs have been proposed as signal transducers in the field of biosensing and bioelectronics,[15,26−28] presenting unique properties for the detection of full-band neural signals from infraslow to high-frequency components with a high spatial resolution.[29] Besides, as active sensors g-SGFETs provide an intrinsic preamplification of the signal and can be arranged in a column/row addressable matrix due to their two terminal (i.e., drain and source) configuration (see Figure 1a,b). These properties, combined with their remarkable

frequency response,[30] make g-SGFETs an ideal technology for the implementation of frequency-division sensor arrays.

In g-SGFETs, the graphene channel is placed in contact with an electrolyte gate, that is, the brain tissue in the case of neural sensing applications. Electrical potential fluctuations in the environment influence the conductivity of the transistor channel through the gate capacitance. The constant of proportionality between drain-source conductance (G_{ds}) and the electrical potential at the interface (V_{gs}) is referred to as the transconductance[31] (g_m). g-SGFETs can be modeled by the equivalent circuit shown in Figure 1a. Its stationary response to a constant bias (V_{gs-DC}) is described by the voltage dependent term G_{ds-DC}, while its dynamic response to a small-amplitude, time-dependent signal (V_{sig}) is characterized by the term $V_{sig}g_m$. In the typical operation mode (DC mode), the drain-source bias V_{ds} is constant; thus, the only time variations in the drain-source current (I_{ds}) are caused by variations in G_{ds}
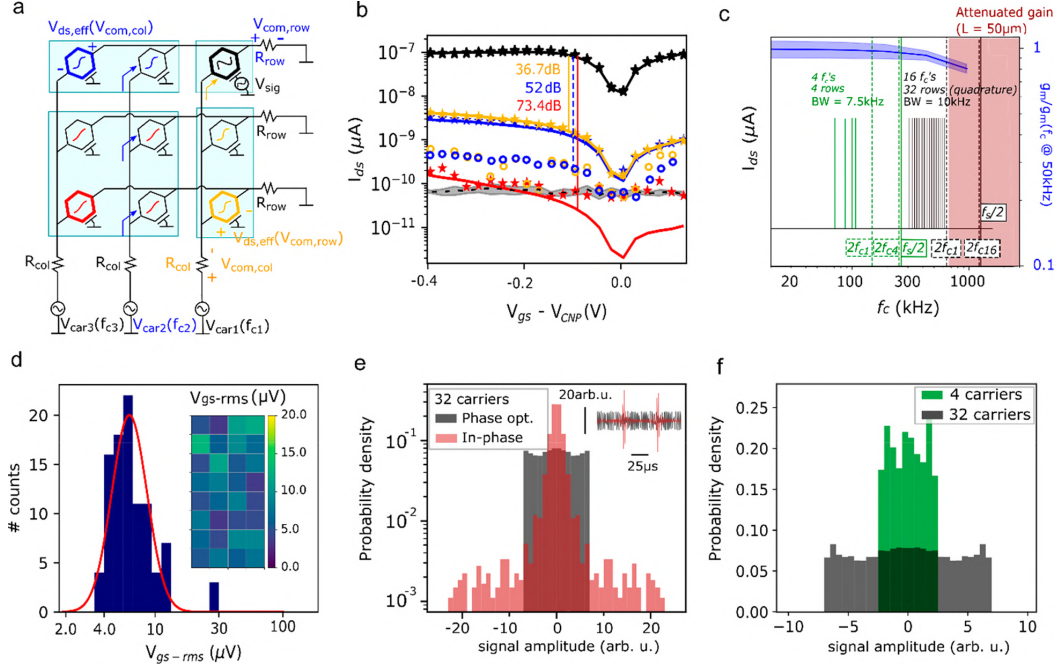
Figure 3. Scalability of g-SGFET arrays multiplexed in the frequency-domain: (a) Equivalent circuit of a 3 × 3 g-SGFET array. The metal track resistance of the columns and rows is modeled by R_{col} and R_{ow} respectively. Each column is biased with a different carrier (V_{car1}, V_{car2}, and V_{car3}). Common voltage oscillations ($V_{com,coll}$ and $V_{com,row}$) produce changes in $V_{ds,eff}$. The light blue area indicates the position of four polyelectrolyte gates printed on a 3 × 3 array. (b) Response to a 5 Hz signal measured in different g-SGFETs on a 3 × 3 array for different V_{gs} values. The color of the symbols and lines indicate the position of the corresponding g-SGFET in the 3 × 3 array shown in panel a. The solid lines indicate the fitting by the analytical model. The noise (dashed black line) was measured at 7 Hz. The empty blue and orange circles indicate the crosstalk level after correction. The signal-to-crosstalk values (in dB) corresponding to uncorrected, corrected, and second order crosstalk are marked by the vertical lines. (c) The right axis indicates the normalized transconductance for g-SGFETs of (50 μm x 50 μm, n = 4). The carrier frequencies selected for the *in vivo* proof of concept (4 × 8 array) are shown in green and those proposed for a 32 × 32 sensor array are indicated in black. High order harmonics are indicated together with the required sampling frequency. (d) Histograms of V_{gs-rms} from htree neural probes of 32 g-SGFETs integrated in the 1−10 Hz frequency. The log-normal distribution indicates the mean and standard deviation of V_{gs-rms}. The values from the specific neural probe which was implanted is shown in the inset. (e) Histogram of 32 superposed carriers with phase optimization to minimize the peak-to-peak amplitude (black) and with all carriers in phase (red). The inset shows a fragment of the resulting signals. (f) Histogram of the 4 superposed carriers used for the *in vivo* proof of concept compared to the amplitude of a 32-carrier signal with phase optimization.

(Figure 1c). On the other hand, in FDM (or amplitude modulation- AM mode), the drain-source bias is typically a pure tone signal ($V_{carrier}(t)$). Therefore, I_{ds} results from the product of $V_{carrier}(t)(g_m V_{sig}(t) + G_{ds-DC})$ (see Figure 1c).

The multiplication of $V_{carrier}$ and V_{sig} produces the folding of their frequencies. In the frequency-domain representation of $V_{carrier}(t) * V_{sig}(t)$ (Figure 1d, left), a peak at the carrier frequency (f_c) can be observed, which is proportional to G_{ds-DC}. In addition, two side bands (at $f_c - f_{sig}$ and $f_c + f_{sig}$) appear, the amplitude of which is proportional to $g_m V_{sig}$. This mixed signal can then be demodulated by a lock-in amplifier (see Figure 1d, middle) producing the folding of the side bands back to the baseband frequency (see Figure 1d, right) with the DC-offset corresponding to the stationary component of I_{ds}. This demodulation can be repeated for different carrier frequencies to recover the neural signals detected in each of the graphene sensors. The schematic in Figure 1e represents the FDM of a 2 × 2 sensor array. Carrier signals with different frequencies (f_c) are applied at each column of the array and independent data-acquisition channels are connected to each of the drains to reliably recover the information from the

multiplexed sensors. Here, we present frequency-division multiplexed arrays of up to 4 × 8 graphene sensors fabricated on a flexible polyimide (PI) substrate (see Figure 1b and Supporting Information for more details of the fabrication method). For the characterization of the FDM sensor arrays and their operation *in vivo*, we have developed a recording system based on a PXIe for high sampling speed and a custom built front-end amplifier for current−voltage conversion (see Supporting Information).

■ *IN VITRO* CHARACTERIZATION OF FDM GRAPHENE NEURAL PROBES

In order to validate the suitability of g-SGFETs for frequency-division multiplexing, their sensitivity in the AM mode must be characterized and compared with the sensitivity in the DC mode. The characterization of g_m can be performed of the following two approaches: from the derivative of the stationary $G_{ds}-V_{gs}$ curve or from the dynamic response of g-SGFETs to signals with various frequency components applied at the gate (see Figure 1c). Figure 2a shows the g_m-V_{gs} curves extracted following the first approach for a 3 × 3 g-SGFET array,

demonstrating the equivalence of the stationary response in the DC and AM operation modes. Figure 2b presents the frequency dependence of g_m measured following the second approach. The magnitude of g_m presents similar values in both modes for frequencies <1 kHz, above which the effect of capacitive currents contributes significantly in the DC mode (see Supporting Information). In addition to the transconductance, the intrinsic electrical noise of the graphene transistors shall be considered in order to fully characterize the sensitivity of the graphene sensors. In Figure 2c, the equivalent noise at the gate (V_{gs-rms}), defined as the RMS current noise (I_{ds-rms}) normalized by the transconductance, is represented under different V_{gs} bias conditions for a transistor area of 50 μm × 50 μm. Figure 2c demonstrates that the sensitivity of g-SGFETs, defined by their noise performance, does not differ dramatically in both modes, showing only slight changes in its V_{gs} dependence.

These slight discrepancies presumably arise from the differences in the drain-source bias in both modes. The gradient in the work function of graphene along the channel induced by this bias causes a nonhomogeneous effective gating of the transistor (see Figure 2d and Supporting Information). In the DC mode, this gradient is constant over time, producing a constant offset in the channel doping for a certain V_{ds} bias. Changing V_{ds} produces a shift of the transfer curves of the g-SGFETs along the V_{gs} axis (see Figure 2e). This effective gating is also responsible for the dependence of G_{ds} on V_{ds}, which introduces nonlinearities in the output characteristics shown in Figure 2e. Figure 2f shows a three-dimensional representation of the $I_{ds}-V_{gs}$ and $I_{ds}-V_{ds}$ characteristic curves of the g-SGFETs. In the DC mode, the g-SGFETs are operated at a stationary point in the $V_{gs}-V_{ds}$ plane but in the AM mode the drain-source bias oscillates along the V_{ds} axis. In this way, nonlinearities in the $I_{ds}-V_{ds}$ curves will lead to distortion of the carrier signal, introducing harmonics at frequencies multiple of f_c (see Figure 2g and Supporting Information). Harmonic distortion constrains the selection of carrier frequencies that can be used for AM: high order harmonics must not lie within the frequency band of operation dedicated to the carrier signals. Thereby, the frequency of all carriers must be below the second order harmonic of the carrier of lowest frequency (see Figure 2g). In addition, the Nyquist frequency ($f_s/2$) must be above the second order harmonic of the highest carrier frequency in order to prevent folding of third order harmonics into the band of operation by aliasing.

Another important aspect affecting the selection of carrier frequencies is the frequency response of g-SGFETs. The graphene−electrolyte interface exhibits a capacitive response, which at high frequencies allows a displacement current to flow from drain to source through the electrolyte,[30] degrading the device performance. The characteristic cutoff frequency of this phenomenon appears at relatively high frequencies due to the high ratio between mobility and interface capacitance in graphene. Other active sensors, such as organic electrochemical transistors, which present a lower mobility and a larger interface capacitance,[32] are expected to present a worse frequency response.[30] Figure 4e shows the frequency response of g-SGFETs for multiple channel lengths, demonstrating an approximately constant response for channels shorter than 100 μm and frequencies below 500 kHz at least.

■ SCALABILITY OF FDM GRAPHENE NEURAL PROBES

Considering the ultimate goal of enabling high-density, large-area sensor arrays, the scalability of the FDM graphene neural probes has to be thoroughly explored. Important aspects limiting the scalability of FDM are the crosstalk in the g-SGFET array, the constrains in the selection of carrier frequencies, and the requirements for the electronics used to operate the arrays.

In FDM, no switching among sensing sites is required. Although this feature bears a clear advantage for ease of fabrication of the neural probes, it prevents from doing on-site switching of the sensors and can therefore lead to an increased susceptibility to crosstalk. Crosstalk can appear between g-SGFETs in the same row (i.e., sharing a readout channel) as well as in the same column (i.e., biased by the same carrier) due to common-mode voltage (V_{com}) oscillations in the resistance of metal tracks in series with the drain (R_{row}) and source (R_{col}). By analyzing the equivalent circuit in Figure 3a, an analytical expression can be derived, which indicates that crosstalk among rows and among columns is proportional to R_{row} and R_{col}, respectively (see Figure 3a and Supporting Information). Additionally, crosstalk signals couple with g-SGFETs that are out of the same column and row, causing a second order crosstalk (see Supporting Information S4). In order to experimentally determine the crosstalk level, we have patterned multiple polyelectrolyte gates on the graphene sensor arrays by inkjet printing (see Figure 3a and Supporting Information S5). Figure 3b shows the signal measured by an individually gated g-SGFET (black) and the crosstalk it induced on sensors in the same column (orange), the same row (blue), and on the rest of g-SGFETs (red), together with the fitting of the experimental data using the analytical expression presented in the Supporting Information. A crosstalk of ∼36 dB/∼73 dB is observed for g-SGFETs within/outside the same column or row, which corresponds to a $R_{row} \approx R_{col} = 50$ Ω. In order to reduce the crosstalk to the level achieved using on-site switches (∼65 dB),[33] the resistance of the tracks should be reduced to the range of few ohms. This target could be met by increasing the width of the metal lines, which can be implemented easily when translating this technology from rodents research into human clinical applications (see Supporting Information S8). Moreover, knowing the mechanism of crosstalk generation and the coupling parameters among all sensors, it is possible to define a mathematical method for crosstalk cancelation (see Supporting Information S8). Using such calibration, a mitigation of crosstalk by an additional ∼15 dB was achieved (see Figure 3b).

Another important aspect related to the scalability of FDM graphene neural probes is the selection of the carrier frequencies, which are constrained by the frequency response of g-SGFETs and the harmonic distortion of the carrier signals. The $g_m(f_c)$ was characterized by sweeping f_c and measuring the dynamic response of the graphene sensors to pure tone signals applied at the gate. Figure 3c shows that g_m remains approximately constant for carrier frequencies up to at least $F_{max} = 600$ kHz and a channel length of 50 μm, while the current noise remains approximately constant (see Supporting Information S10). This bandwidth limitation is presumably caused by the capacitive leakage through the electrolyte characterized in Figure 2h and could therefore be expanded by
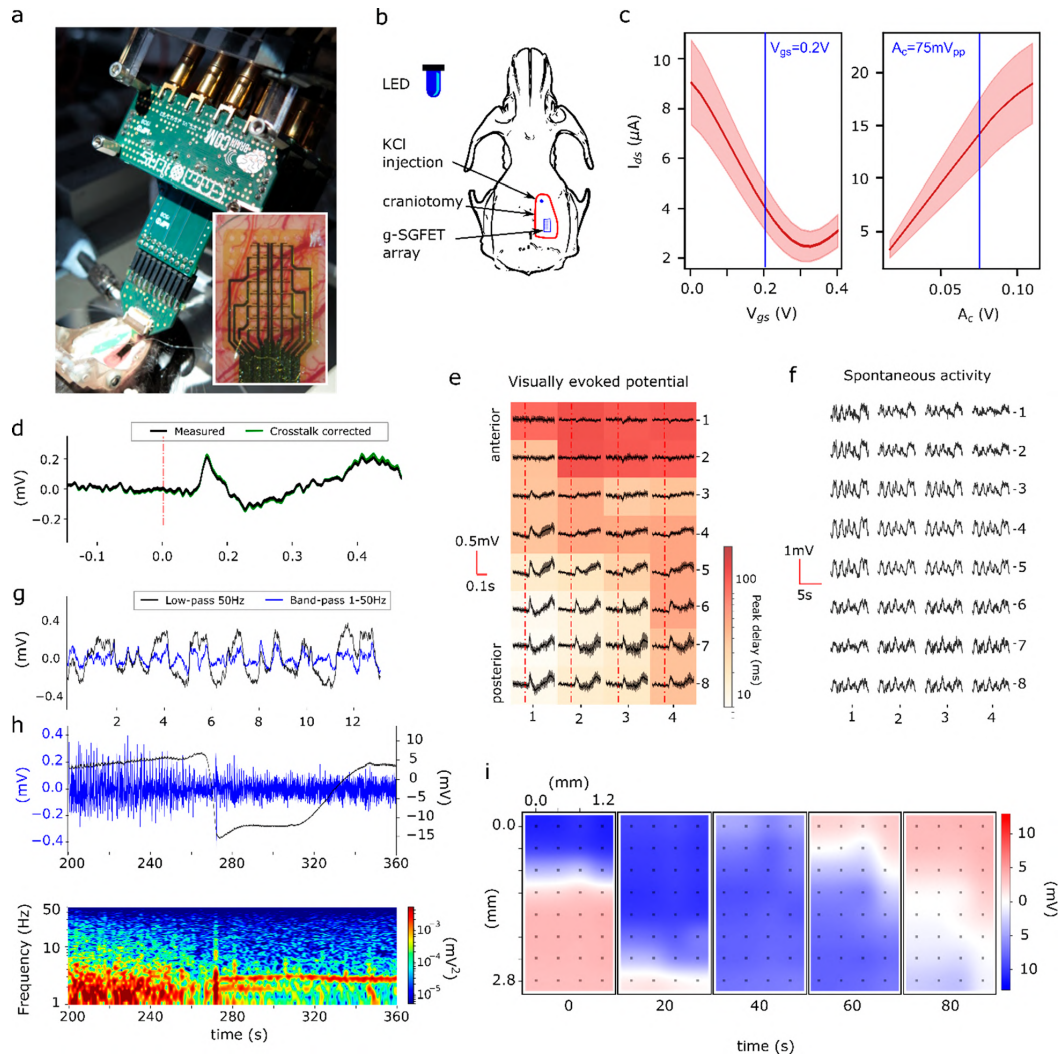
Figure 4. *In vivo* validation of FDM graphene neural probes for brain recordings. (a) Acute experiment setting. The g-SGFET array interfaces the brain with the custom-built front-end amplifier. (b) Illustration of a rat skull indicates the position of the craniotomy, the g-SGFET array, the LED, and the place of KCl injection. (c) Average and standard deviation of the $I_{ds}-V_{gs}$ and $I_{ds}-A_c$ curves obtained *in vivo* for the 32 channels. (d) The visually evoked potential averaged over 10 consecutive events is shown for the g-SGFET placed on the lower-left corner of the array before (black) and after (green) crosstalk correction. (e) Visually evoked potential averaged over 10 consecutive events for all g-SGFETs on the 4 × 8 array. The color map represents the delay between stimulus and the peak of the response. (f) Map of spontaneous activity under anesthesia. (g) Spontaneous activity filtered in two different bands indicates the presence of low-frequency components (<1 Hz) for channel in position (4,5). (h) CSD event recorded in a single g-SGFET. The top graph shows the activity in the 1−50 Hz band (blue, left axis) and the wide-band activity (0.001−50 Hz) (black, right axis). The corresponding spectrogram in the 1−50 Hz band is shown below. (i) The color maps indicate the signal amplitude in each of the g-SGFETs on the array at different times during the CSD propagation.

shortening the channel length of g-SGFET. Sampling at four times this F_{max} (i.e., $F_s \geq 4F_{max} = 2.4$ MHz) allows the use of carriers of up to ~600 kHz. Figure 3c shows a combination of carrier frequencies which meets all the requirements to allow the operation of 32 × 32 graphene sensor arrays. In this configuration, operation in quadrature AM[34] can be used to maximize the frequency bandwidth of each sensor to 10 kHz (see Figure 3c). The demodulated signals can then be high-pass filtered in the digital domain above ~5 kHz, given that

neural activity does not present significant power above such frequency. Importantly, the demodulated signals are still sampled in the megahertz range, allowing for an arbitrarily high oversampling. In this way, a 10 kHz guard-band between carriers can be kept to ensure a correct channel discrimination.

The discrete electronics system designed for the validation of the technology *in vivo* is limited to operate arrays of up to 4 × 8 g-SGFETs. This limitation comes from the constrained scalability of discrete electronics in opposition to ASICs.

Figure 3c shows the combination of carrier frequencies used for the in vivo proof of concept. The V_{gs-rms} from three probes of 4 × 8 g-SGFET arrays operated with this carrier's configuration is shown in Figure 3d, demonstrating a mean sensitivity of 6.29 μV with a standard deviation of 1.37 μV and a yield of 100%. This high sensitivity can eventually degrade due to the superposition of a large number of carrier signals, the large amplitude of which might challenge the resolution of the data acquisition (DAQ) system. The quantization error of the analog-to-digital converter (ADC), given by its less-significant bit (LSB), must be low enough to ensure signal integrity. When increasing the number of carriers, their amplitude (A_c) must be reduced in order to prevent saturation of the ADC (see Supporting Information S11). This decrease in A_c implies an attenuation of the transconductance (i.e., $A_c g_m$) of the g-SGFETs, while the LSB of the ADC remains unchanged. To minimize the amplitude of the carriers superposition for a certain A_c, the phase of the carriers can be adjusted. Figure 3e shows the improvement obtained by phase optimization for the combination of 32 carrier signals defined in Figure 3c, revealing a three-fold attenuation in the amplitude of the carrier superposition. The comparison with the superposition of the 4 carriers used for this proof of concept shows that upscaling to 32 carriers causes an increase in the amplitude by a factor of 2.8, which could be compensated by increasing the resolution of the ADC by 1–2 bits.[35] These results, together with the evaluation of crosstalk and the high frequency response of g-SGFETs, demonstrate the potential of this technology for high-count flexible neural probes.

IN VIVO EVALUATION OF FDM GRAPHENE NEURAL PROBES

Previous works have shown that g-SGFETs operated in the DC mode present a high sensitivity for the recording of neural activity.[15,26] Moreover, g-SGFETs have demonstrated a unique capability for the recording of infraslow neural activity with a high spatial resolution.[29] The FDM operation of g-SGFETs is not only expected to preserve their sensitivity for infraslow signals but to enhance their performance by eliminating flicker noise from the amplifiers due to the lock-in amplification in the AM mode. In addition, due to the low power consumption of g-SGFETs, heating of the tissue is not expected to be significant even for large scale arrays (see Supporting Information S12). To validate the in vivo functionality of FDM graphene probes, we have recorded electrical activity from the cortex of a Long Evans rat in an acute setting using a 4 × 8 FDM graphene neural probe (see Figure 4a,b and Supporting Information). The optimum V_{gs}, which maximizes g_m, and the highest carriers amplitude (A_c), which fills the dynamic range of the amplifiers, were determined in vivo (see Figure 4c).

The sensitivity of the sensors to high-frequency LFP activity was evaluated by measuring visually evoked potentials[36] triggered by a blue LED emitting light-pulses of 100 ms every 5 s. The sensors directly placed on the primary visual cortex V1 (lower left) exhibit a sharp response with 50 ms delay and 250 μV peak amplitude lasting until 100 ms after the initial trigger (Figure 4d). Sensors placed further away from the V1 show a distance-dependent suppressed response of smaller amplitude and extended delay (Figure 4e). This result is in full agreement with previously reported values,[36] demonstrating the preserved sensitivity of g-SGFETs in this

frequency band in the FDM operation mode. Besides, the crosstalk correction method discussed above showed the low impact of crosstalk in these signals (see Figure 4d and Supporting Information).

Similarly, the distortion-free recording of infraslow activity using g-SGFET has been previously shown in the DC mode by the recording of cortical spreading depression (CSD) events.[29] CSDs are a slowly propagating wave of depolarizing neurons and astrocytes, which has been clinically related to stroke, brain injury, and migraine.[37,38] CSDs can be easily triggered by injecting KCl into the brain cortex and present a propagation speed of approximately 5 mm per minute across the cortex. Figure 4f shows the spontaneous activity under anesthesia where highly coherent transitions from up to down states can be observed. Figure 4g shows the signal from channel in position (4,5) filtered in the 1−50 Hz frequency band (blue) together with the signal filtered in the 0.001−50 Hz band. This spontaneous activity is strongly suppressed during the depolarization wave, which results in a large infraslow signal drift with a duration over 70 s. Figure 3h shows the propagating front of the CSD wave across the array, demonstrating the capabilities of FDM graphene neural probes to study topography of wide-band oscillatory dynamics in the brain.

DISCUSSION

In summary, we have presented the concept of frequency-division multiplexing of graphene active sensor arrays to reduce the number of wires required for high sensor-count neural probes. This novel approach presents two main advantages over time-division multiplexing resulting from its switchless operation. First, the elimination of switches implies an enormous simplification of the technological complexity, eliminating the need for high-mobility and wide band gap flexible materials, such as ultrathin SiO_2. Second, FDM operates in a continuous mode, fully circumventing the problems derived from limited switching speed and artifacts in TDM, which ultimately limit the scalability of the arrays. Moreover, the signals from all sensors are continuously sampled at high speed in the megahertz range. Although the frequency separation between carriers determines the bandwidth of the sensors, the high sampling speed allows one to acquire the neural signals with an arbitrarily high oversampling. Finally, the modulation and subsequent demodulation of the signals in the FDM mode is based on a lock-in amplification scheme, which eliminates flicker noise from the amplifiers and improves the sensitivity of the system in the infraslow frequency band.

Our results demonstrate the high performance of g-SGFETs as mixers to perform on-site amplitude modulation of neural signals. We have shown their high sensitivity for wide-band neural signals both in the beaker as well as in vivo. Besides, we have also demonstrated the outstanding drain-source frequency response of solution-gated graphene sensors, validating their performance for high carrier frequencies, required for the operation of large-scale arrays. In addition, we have evaluated the crosstalk among sensing sites, which could reach the same level as for TDM with on-site switches when translating this technology to human scale neural probes. In order to maintain the sensitivity of the system for large arrays with up to 32 superposed carriers, we have described the use of carrier phase optimization as well as the requirements for the DAQ system, which could be met by an ASIC.[35]

The viability of large arrays controlled by an ASIC allows one to envision the realization of a new generation of high-density and large-area sensor arrays. The simplicity and robustness of the switchless, FDM methodology compared to state-of-the-art alternatives,[33,39] together with the high sensitivity, flexibility and biocompatibility of graphene active sensors make the implementation of these technologies very promising for both neuroscientific research as well as clinical applications.

■ ASSOCIATED CONTENT

Ⓢ Supporting Information

The Supporting Information is available free of charge at https://pubs.acs.org/doi/10.1021/acs.nanolett.0c00467.

> Fabrication process of the graphene sensor arrays; electrical setup hardware and software for device characterization and *in vivo* proof of concept; animal handling and device implantation; high-frequency response in DC-mode; nonhomogeneous doping of graphene transistors; carriers and baseband harmonic distortion; crosstalk modeling; crosstalk cancelation and scalability; validation of polyelectrolyte gating and frequency response in the DC-mode; dynamic range; frequency response of electrical noise and crosstalk; Power consumption and tissue heating; comparison of FDM graphene neural probes with state of the art technologies (PDF)

■ AUTHOR INFORMATION

Corresponding Authors

Jose A. Garrido − *Catalan Institute of Nanoscience and Nanotechnology (ICN2), CSIC and BIST, 08193 Bellaterra, Barcelona, Spain; ICREA, 08010 Barcelona, Spain;* ◉ orcid.org/0000-0001-5621-1067; Email: joseantonio.garrido@icn2.cat

Anton Guimerà-Brunet − *Instituto de Microelectrónica de Barcelona, IMB-CNM (CSIC), 08193 Bellaterra, Spain; Biomateriales y Nanomedicina (CIBER-BBN), Centro de Investigación Biomédica en Red en Bioingenieria, 08193 Madrid, Spain;* Email: anton.guimera@imb-cnm.csic.es

Authors

Ramon Garcia-Cortadella − *Catalan Institute of Nanoscience and Nanotechnology (ICN2), CSIC and BIST, 08193 Bellaterra, Barcelona, Spain;* ◉ orcid.org/0000-0002-1506-6534

Nathan Schäfer − *Catalan Institute of Nanoscience and Nanotechnology (ICN2), CSIC and BIST, 08193 Bellaterra, Barcelona, Spain*

Jose Cisneros-Fernandez − *Instituto de Microelectrónica de Barcelona, IMB-CNM (CSIC), 08193 Bellaterra, Spain*

Lucia Ré − *Instituto de Microelectrónica de Barcelona, IMB-CNM (CSIC), 08193 Bellaterra, Spain; Biomateriales y Nanomedicina (CIBER-BBN), Centro de Investigación Biomédica en Red en Bioingenieria, 08193 Madrid, Spain*

Xavi Illa − *Instituto de Microelectrónica de Barcelona, IMB-CNM (CSIC), 08193 Bellaterra, Spain; Biomateriales y Nanomedicina (CIBER-BBN), Centro de Investigación Biomédica en Red en Bioingenieria, 08193 Madrid, Spain*

Gerrit Schwesig − *Bernstein Center for Computational Neuroscience Munich, Munich Cluster of Systems Neurology (SyNergy), Faculty of Medicine, Ludwig-Maximilians Universität München, Planegg-Martinsried, Germany 80539*

Ana Moya − *Instituto de Microelectrónica de Barcelona, IMB-CNM (CSIC), 08193 Bellaterra, Spain;* ◉ orcid.org/0000-0001-6793-9133

Sara Santiago − *Departament de Química, Universitat Autònoma de Barcelona, 08193 Bellaterra, Barcelona, Spain*

Gonzalo Guirado − *Departament de Química, Universitat Autònoma de Barcelona, 08193 Bellaterra, Barcelona, Spain*

Rosa Villa − *Instituto de Microelectrónica de Barcelona, IMB-CNM (CSIC), 08193 Bellaterra, Spain; Biomateriales y Nanomedicina (CIBER-BBN), Centro de Investigación Biomédica en Red en Bioingenieria, 08193 Madrid, Spain*

Anton Sirota − *Bernstein Center for Computational Neuroscience Munich, Munich Cluster of Systems Neurology (SyNergy), Faculty of Medicine, Ludwig-Maximilians Universität München, Planegg-Martinsried, Germany 80539*

Francesc Serra-Graells − *Instituto de Microelectrónica de Barcelona, IMB-CNM (CSIC), 08193 Bellaterra, Spain*

Complete contact information is available at:
https://pubs.acs.org/10.1021/acs.nanolett.0c00467

Author Contributions

R.G.C. contributed to the design and fabrication of the neural sensor arrays. He characterized the devices and contributed to the software development and *in vivo* experiments. N.S. contributed to the design of the sensor arrays, DAQ system design, and *in vivo* experiments. J.C. designed the front-end and contributed to the characterization of the DAQ system. L.R. contributed to the software development and devices characterization. X.I. contributed to the design and fabrication of the neural sensor arrays. G.S. did the surgery for the acute experiment. A.M. developed the inkjet printing procedure to evaluate the crosstalk. S.S. and G.G. developed the polyelectrolytes used for crosstalk determination. A.S. led the team for the *in vivo* proof of concept. F.S.G. contributed to the concept of frequency-division multiplexing of graphene sensor arrays and the design of the front-end. R.V. provided support for the development of the software and harware. A.G.B. contributed to the experimental design, development of the software and hardware, as well as *in vivo* proof of concept. J.A.G. led the team for development of the graphene sensor arrays and contributed to the experimental design. R.G.C., A.G.B., and J.A.G. wrote the manuscript.

Author Contributions

∇R.G.C. and N.S contributed equally to this work.

Notes

The authors declare the following competing financial interest(s): Patent application (no. EP18382593) filled by UAB, CSIC and ICN2; entitled Circuit for the multiplexing and read-out of variable-resistance sensor arrays (pending); inventors who are co-authors in the present article are A.G.B., F.S.G., and J.A.G.

■ REFERENCES

(1) Jeannerod, M. *Motor Cognition: What Actions Tell the Self*; Oxford University Press, 2006.

(2) Georgopoulos, A. P.; Kettner, R. E.; Schwartz, A. B. Primate Motor Cortex and Free Arm Movements to Visual Targets in Three-Dimensional Space. II. Coding of the Direction of Movement by a Neuronal Population. *J. Neurosci.* **1988**, *8* (8), 2928−2937.

(3) Wilson, S. M.; Saygin, A. P.; Sereno, M. I.; Iacoboni, M. Listening to Speech Activates Motor Areas Involved in Speech Production. *Nat. Neurosci.* **2004**, *7* (7), 701−702.

(4) Galantucci, B.; Fowler, C. A.; Turvey, M. T. The Motor Theory of Speech Perception Reviewed. *Psychon. Bull. Rev.* **2006**, *13* (3), 361−377.

(5) Capogrosso, M.; Milekovic, T.; Borton, D.; Wagner, F.; Moraud, E. M.; Mignardot, J.-B.; Buse, N.; Gandar, J.; Barraud, Q.; Xing, D.; et al. A Brain−Spine Interface Alleviating Gait Deficits after Spinal Cord Injury in Primates. *Nature* **2016**, *539* (7628), 284−288.

(6) Anumanchipalli, G. K.; Chartier, J.; Chang, E. F. Speech Synthesis from Neural Decoding of Spoken Sentences. *Nature* **2019**, *568* (7753), 493−498.

(7) Averbeck, B. B.; Latham, P. E.; Pouget, A. Neural Correlations, Population Coding and Computation. *Nat. Rev. Neurosci.* **2006**, *7* (5), 358−366.

(8) Khodagholy, D.; Gelinas, J. N.; Thesen, T.; Doyle, W.; Devinsky, O.; Malliaras, G. G.; Buzsáki, G. NeuroGrid: Recording Action Potentials from the Surface of the Brain. *Nat. Neurosci.* **2015**, *18* (2), 310−315.

(9) Chang, E. F. Towards Large-Scale, Human-Based, Mesoscopic Neurotechnologies. *Neuron* **2015**, *86* (1), 68−78.

(10) Stringer, C.; Pachitariu, M.; Steinmetz, N.; Reddy, C. B.; Carandini, M.; Harris, K. D. Spontaneous Behaviors Drive Multidimensional, Brainwide Activity. *Science (Washington, DC, U. S.)* **2019**, *364* (6437), No. eaav7893.

(11) Chung, J. E.; Joo, H. R.; Fan, J. L.; Liu, D. F.; Barnett, A. H.; Chen, S.; Geaghan-Breiner, C.; Karlsson, M. P.; Karlsson, M.; Lee, K. Y.; et al. High-Density, Long-Lasting, and Multi-Region Electrophysiological Recordings Using Polymer Electrode Arrays. *Neuron* **2019**, *101* (1), 21−31.

(12) Jun, J. J.; Steinmetz, N. A.; Siegle, J. H.; Denman, D. J.; Bauza, M.; Barbarits, B.; Lee, A. K.; Anastassiou, C. A.; Andrei, A.; Aydın, Ç.; et al. Fully Integrated Silicon Probes for High-Density Recording of Neural Activity. *Nature* **2017**, *551* (7679), 232−236.

(13) Ferro, M. D.; Proctor, C. M.; Gonzalez, A.; Zhao, E.; Slezia, A.; Pas, J.; Dijk, G.; Donahue, M. J.; Williamson, A.; Malliaras, G. G. NeuroRoots, a Bio-Inspired, Seamless Brain Machine Interface Device for Long-Term Recording. *bioRxiv* **2018**, 460949.

(14) Musk, E. Neurolink. An Integrated Brain-Machine Interface Platform with Thousands of Channels. *bioRxiv* **2019**, 703801.

(15) Kostarelos, K.; Vincent, M.; Hebert, C.; Garrido, J. A. Graphene in the Design and Engineering of Next-Generation Neural Interfaces. *Adv. Mater.* **2017**, *29* (42), 1700909.

(16) Abbott, J.; Ye, T.; Qin, L.; Jorgolli, M.; Gertner, R. S.; Ham, D.; Park, H. CMOS Nanoelectrode Array for All-Electrical Intracellular Electrophysiological Imaging. *Nat. Nanotechnol.* **2017**, *12* (5), 460−466.

(17) Eversmann, B.; Jenkner, M.; Hofmann, F.; Paulus, C.; Brederlow, R.; Holzapfl, B.; Fromherz, P.; Merz, M.; Brenner, M.; Schreiter, M.; et al. A 128 × 128 CMOS Biosensor Array for Extracellular Recording of Neural Activity. *IEEE J. Solid-State Circuits* **2003**, *38*, 2306−2317.

(18) Tsai, D.; Sawyer, D.; Bradd, A.; Yuste, R.; Shepard, K. L. A Very Large-Scale Microelectrode Array for Cellular-Resolution Electrophysiology. *Nat. Commun.* **2017**, *8* (1), 1−11.

(19) Kook, G.; Lee, S. W.; Lee, H. C.; Cho, I.-J.; Lee, H. J. Neural Probes for Chronic Applications. *Micromachines* **2016**, *7* (10), 179.

(20) Andersen, R. A.; Musallam, S.; Pesaran, B. Selecting the Signals for a Brain−Machine Interface. *Curr. Opin. Neurobiol.* **2004**, *14* (6), 720−726.

(21) Chao. Long-Term Asynchronous Decoding of Arm Motion Using Electrocorticographic Signals in Monkey. *Front. Neuroeng.* **2010**. DOI: 10.3389/fneng.2010.00003.

(22) Yeager, J. D.; Phillips, D. J.; Rector, D. M.; Bahr, D. F. Characterization of Flexible ECoG Electrode Arrays for Chronic Recording in Awake Rats. *J. Neurosci. Methods* **2008**, *173* (2), 279−285.

(23) Obien, M. E. J.; Deligkaris, K.; Bullmann, T.; Bakkum, D. J.; Frey, U. Revealing Neuronal Function through Microelectrode Array Recordings. *Frontiers in Neuroscience*; Frontiers Media: S.A., 2015; p 423.

(24) Lee, W.; Kim, D.; Rivnay, J.; Matsuhisa, N.; Lonjaret, T.; Yokota, T.; Yawo, H.; Sekino, M.; Malliaras, G. G.; Someya, T. Integration of Organic Electrochemical and Field-Effect Transistors for Ultraflexible, High Temporal Resolution Electrophysiology Arrays. *Adv. Mater.* **2016**, *28* (44), 9722−9728.

(25) Viventi, J.; Kim, D.-H.; Vigeland, L.; Frechette, E. S.; Blanco, J. A.; Kim, Y.-S.; Avrin, A. E.; Tiruvadi, V. R.; Hwang, S.-W.; Vanleer, A. C.; et al. Flexible, Foldable, Actively Multiplexed, High-Density Electrode Array for Mapping Brain Activity in Vivo. *Nat. Neurosci.* **2011**, *14* (12), 1599−1605.

(26) Hébert, C.; Masvidal-Codina, E.; Suarez-Perez, A.; Calia, A. B.; Piret, G.; Garcia-Cortadella, R.; Illa, X.; Del Corro Garcia, E.; De la Cruz Sanchez, J. M.; Casals, D. V.; et al. Flexible Graphene Solution-Gated Field-Effect Transistors: Efficient Transducers for Micro-Electrocorticography. *Adv. Funct. Mater.* **2018**, *28*, 1703976.

(27) Blaschke, B. M.; Tort-Colet, N.; Guimerà-Brunet, A.; Weinert, J.; Rousseau, L.; Heimann, A.; Drieschner, S.; Kempski, O.; Villa, R.; Sanchez-Vives, M. V.; et al. Mapping Brain Activity with Flexible Graphene Micro-Transistors. *2D Mater.* **2017**, *4* (2), 025040.

(28) Hess, L. H.; Seifert, M.; Garrido, J. A. Graphene Transistors for Bioelectronics. *Proc. IEEE* **2013**, *101*, 1780.

(29) Masvidal-Codina, E.; Illa, X.; Dasilva, M.; Calia, A. B.; Dragojević, T.; Vidal-Rosas, E. E.; Prats-Alfonso, E.; Martínez-Aguilar, J.; De la Cruz, J. M.; Garcia-Cortadella, R.; et al. High-Resolution Mapping of Infraslow Cortical Brain Activity Enabled by Graphene Microtransistors. *Nat. Mater.* **2019**, *18* (3), 280−288.

(30) Drieschner, S.; Guimerà, A.; Cortadella, R. G.; Viana, D.; Makrygiannis, E.; Blaschke, B. M.; Vieten, J.; Garrido, J. A. Frequency Response of Electrolyte-Gated Graphene Electrodes and Transistors. *J. Phys. D: Appl. Phys.* **2017**, *50* (9), 095304.

(31) Mackin, C.; Hess, L. H.; Hsu, A.; Song, Y.; Kong, J.; Garrido, J. A.; Palacios, T. A Current−Voltage Model for Graphene Electrolyte-Gated Field-Effect Transistors. *IEEE Trans. Electron Devices* **2014**, *61* (12), 3971−3977.

(32) Rivnay, J.; Inal, S.; Salleo, A.; Owens, R. M.; Berggren, M.; Malliaras, G. G. Organic Electrochemical Transistors. *Nature Reviews Materials*; Nature Publishing Group, January 16, 2018. DOI: 10.1038/natrevmats.2017.86.

(33) Viventi, J.; Kim, D.-H.; Vigeland, L.; Frechette, E. S.; Blanco, J. A.; Kim, Y.-S.; Avrin, A. E.; Tiruvadi, V. R.; Hwang, S.-W.; Vanleer, A. C.; et al. Flexible, Foldable, Actively Multiplexed, High-Density Electrode Array for Mapping Brain Activity in Vivo. *Nat. Neurosci.* **2011**, *14* (12), 1599−1605.

(34) Chaparro, L. Fourier Analysis in Communications and Filtering. In *Signals and Systems Using MATLAB*; Elsevier, 2015; pp 449−490.

(35) Cisneros-Fernandez, J.; Dei, M.; Teres, L.; Serra-Graells, F. Switch-Less Frequency-Domain Multiplexing of GFET Sensors and Low-Power CMOS Frontend for 1024-Channel MECoG. In *2019 IEEE International Symposium on Circuits and Systems (ISCAS)*; IEEE, 2019; pp 1−5.

(36) Hébert, C.; Masvidal-Codina, E.; Suarez-Perez, A.; Calia, A. B.; Piret, G.; Garcia-Cortadella, R.; Illa, X.; Del Corro Garcia, E.; De la Cruz Sanchez, J. M.; Casals, D. V.; et al. Flexible Graphene Solution-Gated Field-Effect Transistors: Efficient Transducers for Micro-Electrocorticography. *Adv. Funct. Mater.* **2018**, *28* (12), 1703976.

(37) Dreier, J. P.; Reiffurth, C. The Stroke-Migraine Depolarization Continuum. *Neuron* **2015**, *86* (4), 902−922.

(38) Lauritzen, M.; Dreier, J. P.; Fabricius, M.; Hartings, J. A.; Graf, R.; Strong, A. J. Clinical Relevance of Cortical Spreading Depression in Neurological Disorders: Migraine, Malignant Stroke, Subarachnoid and Intracranial Hemorrhage, and Traumatic Brain Injury. *J. Cereb. Blood Flow Metab.* **2011**, *31* (1), 17−35.

(39) Fang, H.; Yu, K. J.; Gloschat, C.; Yang, Z.; Song, E.; Chiang, C.-H.; Zhao, J.; Won, S. M.; Xu, S.; Trumpis, M.; et al. Capacitively Coupled Arrays of Multiplexed Flexible Silicon Transistors for Long-Term Cardiac Electrophysiology. *Nat. Biomed. Eng.* **2017**, *1* (3), 0038.

S1. Device fabrication

In a first step 10um thick biocompatible Polyimide (PI-2611 HD MicroSystems) was spun on 4'' Si/SiO$_2$ support wafers and cured under nitrogen atmosphere at 350 °C. The perpendicular metal lines of the array (columns/ rows) were patterned in two standard lift-off steps (negative photoresist AZ5214E, Clariant, Germany) with the metal deposited by e-beam evaporation (30nm Ti/ 300nm Au, 10nm Ti/ 100nm Au) and separated by a 2um PI spacer layer (as in step 1). Interconnecting via-holes through the spacer layer were etched by oxygen plasma asher (Tepla Gigabatch 360M, 200W, 200 sccm O2, 40 sccm CF4) using a photolithographically defined protective aluminum mask (AZ5214E, 300nm Al). Then, single layer graphene, grown and transferred by Graphenea, is patterned by photolithography (HiPR6512 photoresist, FujiFilm) and etched by oxygen-based Reactive-Ion-Etching (Alcatel AMS110-DE, 150W for 1min) to form the transistor channel area. A third metal layer (20nm Ni/ 200nm Au) is added to form sandwich contacts improving the g-SGFET's durability and lowering its contact resistance due to work function matching [9, 10]. A subsequent thermal annealing step at 300°C was conducted in ultra-high vacuum. To passivate the metal leads, a 2um thick layer of SU8 epoxy photoresist (SU-8 2005 MicroChem) was deposited, leaving open windows in the channel regions to allow a direct electrolyte graphene interface. In a final step, the polyimide was structured by deep reactive ion etching using a photoresist etching mask (AZ9260, Clariant) and the flexible probes were mechanical peeled from the support wafer.

S2. Electrical setup hardware and software

For the characterization of graphene active sensor arrays in the amplitude modulation mode (AM-mode) as well as for the *in-vivo* proof of concept we developed a discrete electronics system based on both commercial and custom built components. In order to meet the demanding requirements in terms of high sampling speed and high number of inputs a commercial PXIe system (PXIe-1071 chassis with one PXIe-5105 scope module implementing 8 high speed input channels) was used. For the current-voltage conversion, a custom built circuit was used, which also provided the driver to bias the g-SGFETs. The carrier signals were provided by two PXIe-5413 modules with 2 signal generators each.

Together with the hardware, a custom software based on Python was developed for controlling the data acquisition systems. The aim of this software is to provide tools for the characterization of the g-SGFETs as well as for real-time data acquisition and visualization of electrophysiological recordings. **Table 1.1** summarizes the main specifications of the developed software, which includes a graphical user interface to tune the operation parameters and for real-time visualization of the signals in both the time and frequency domains.

	FDM
Repository	https://github.com/aguimera/Pyxi
Columns	4
Rows	8
De-multiplexed Channels	32
De-multiplexed Sampling Frequency	At least 5KHz bandwidth with oversampling of up to 500kHz
Input Sampling Frequency	500 kHz in Real-Time 10 MHz for testing

Table S1. Summary of the main specifications of the data acquisition system.

S3. Animal handling and device implantation

Experiments were performed in accordance with the European Union Directive 2010/63/EU and the German Law for Protection of Animals (TierSchG), and approved by the local authorities (ROB-55.2-2532.Vet_02-16-170). Long Evans rats (Charles River) were housed under controlled standard conditions (room temperature 22 ± 2 °C, 12:12 h light–dark cycle, lights on at 10:00) and provided food and water ad libitum.

In order to perform electrophysiological measurements rats were deeply anaesthetized with MMF (Midazolam 2mg/kg), Medetomidin 0.15 mg/kg, Fentanyl 0.005 mg/kg). About 1h into the surgery the initial MMF injection was supplemented with Isoflurane 0.5%-1% and 110 mg/kg Metamizol. The dorsal surface of the head was shaved and Bupivacain injected subcutaneously in the exposed area. Subsequently a dorsal midline cut was done and the dorsal skull surface cleaned from overlying tissue. In the next step craniotomies were performed

bilaterally with a maximum lateral width of 5 mm each while their anterior and posterior maxima were located ca. +2 mm and -8mm from bregma respectively. After careful resection of the dura mater the brain surface was covered with prepolymerized PDMS (mixing ratio 1:10, Sylgard 184, Dow Corning) and Vetbond (3M) was used to fasten the edge of the PDMS cover to the skull. After temporarily lifting the polymer cover the gSGFET array was placed on the right hemisphere partially overlying the primary visual area. After careful placement of the surface array, the PDMS covers were refastened to the skull with Vetbond to constrain brain movement and preventing drying of the brain surface.

Spontaneous activity was recorded at 0.5% Isoflurane and isolated events of cortical spreading depression (CSD) were induced by local application of 1 uL KCL (3mMol) with a Nanoject II micropipette injection device (Drummond Scientific). The CSD induction point was located about 4 mm anterior to bregma (approximately 7 mm from nearest site on recording array). Optical evoked responses were recorded at 2% Isofluran and triggered with 100 msec short light pulses delivered at 0.2 Hz to the contralateral visual field.

Signals of the gSGFET array were referenced to an Ag/Ag-Cl wire, positioned in either the temporal muscle and acquired with custom build electronics described in supplementary information S2.

S4. Frequency response at high frequencies

The frequency response of the g-SGFETs (i.e. $G_m(f)$) for signals applied at the gate differs between the DC and AM operation modes as described in the main text. The difference occurs at high frequencies, for which capacitive currents through the gate and parasitic capacitances flow into drain and source (see Fig. S2a). Fig. S2b shows the frequency response in the DC mode, indicating the contribution from capacitive currents. In the AM mode, these

fluctuations in the measured drain-to-source current do not contribute to G_m because they are not multiplied by the carrier signal. Therefore, when demodulating the drain-to-source current, this contribution is folded with the carrier frequency out of the bandwidth of sensing.
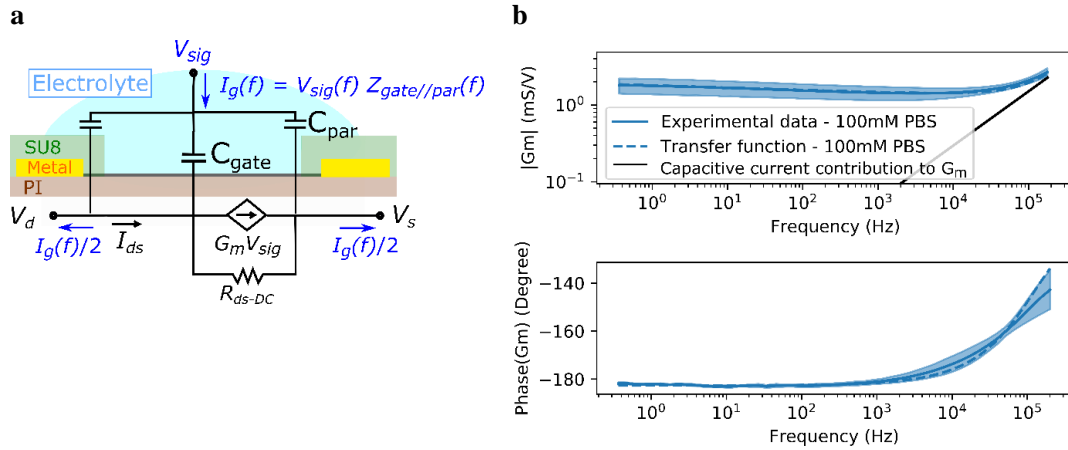

Figure S1| Frequency response at high frequencies in the DC mode. a. Equivalent circuit of the g-SGFET, including parasitic capacitances through the insulation layer. The gate current $I_g(f)$ flows into the drain and source. **b.** Bode representation of $G_m(f)$, The increase in the magnitude at high frequencies can be explained by the contribution from capacitive currents through the gate (black line). The phase at high frequencies increases and tends towards $-\pi/2$. Filled area indicates the standard deviation (n=4).

S5. Electrical doping of graphene along the channel

The drain-to-source bias produces a change in the Fermi level of the graphene with respect to the vacuum level (Fig. S2a-top). When brought in contact with the electrolyte gate, the Fermi energy in the graphene and electrolyte equalises. This would typically lead to band bending in a conductor-semiconductor interface. In the case of graphene, band bending does not occur, but a shift in the Dirac energy with respect to the Fermi energy can be observed[3].

This shift translates into an accumulation of charges at the graphene-electrolyte interface due to effective gating (see Fig. S2a). This effective gating causes a shift in the CNP for different V_{ds} values in the DC-operation mode (see Fig. S2b). This shift however is not observable in the AM-mode because of the oscillatory drain-to-source voltage applied. Fig. S2c shows the $I_{ds} - V_{gs}$ curves obtained in the AM-mode for different carrier amplitudes in the same range as in Fig. S2b.
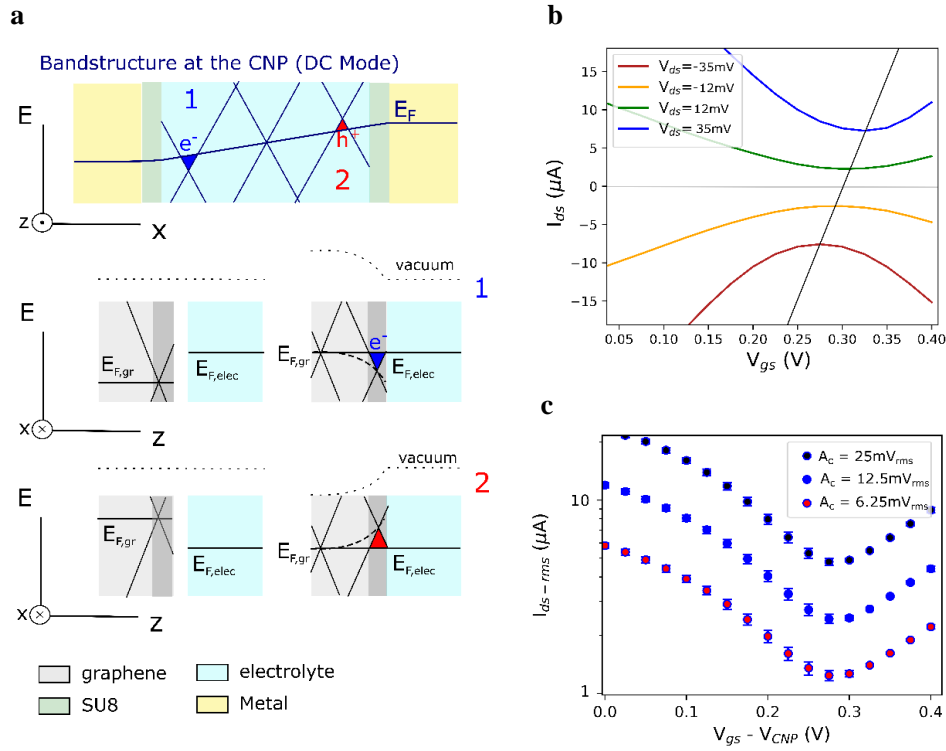

Figure S2| Effective gating induced by the drain-to-source bias. a. The gradient in the Fermi energy induced in the channel by the drain-to-source bias is shown together with the energy of the bandstructure in graphene. The effective doping induced results in a non-homogenous charge density along the channel. The bottom schematics represent the bandstructure of graphene before and after getting in contact with the electrolyte gate at two positions along the graphene channel. **b.** The $I_{ds} - V_{gs}$ curves for different V_{ds} values in the DC mode are plotted.

The shift in the CNP is marked with the straight black line. **c.** The $I_{ds} - V_{gs}$ curves for different carrier amplitudes in the AM mode are plotted.

S6. Harmonic distortion of signals at the gate and carrier signals

The effective gating induced by V_{ds} on the graphene channel does not produce a measurable shift in the CNP in the AM mode. However, it might produce slight changes in the shape of the $I_{ds} - V_{gs}$ curves. This changes can be quantified by comparing the harmonic distortion of the signals applied at the gate measured in the AM mode and calculated from the Taylor expansion of the $I_{ds} - V_{gs}$ curves in the DC mode. Fig. S3a shows this comparison, which demonstrates that although the 1st order harmonic, corresponding to the transconductance term, matches with the measured response, the 2nd and 3rd order harmonics are significantly lower in the AM-case. This deviation can be attributed to slight changes in the curvature of the transfer characteristics due to the different effective gating in both modes.

On the other hand, the harmonic distortion introduced in the carrier signal can also be compared to the values expected from the Taylor expansion of the output characteristics (i.e. the $I_{ds} - V_{ds}$ curves). Fig. S3b shows the comparison of measured and calculated amplitudes for the 1st, 2nd and 3rd harmonics of the carrier. The measured amplitude of the 2nd and 3rd order harmonics is clearly below the expected values from the non-linearities in the $I_{ds} - V_{ds}$ curves. We attribute this deviation to the fact that non-linearities arise from the effective doping in the graphene channel produced by the drain-to-source bias. At the high frequencies used for the carriers, the response of the graphene-electrolyte interface is attenuated, thus reducing the impact of effective gating.
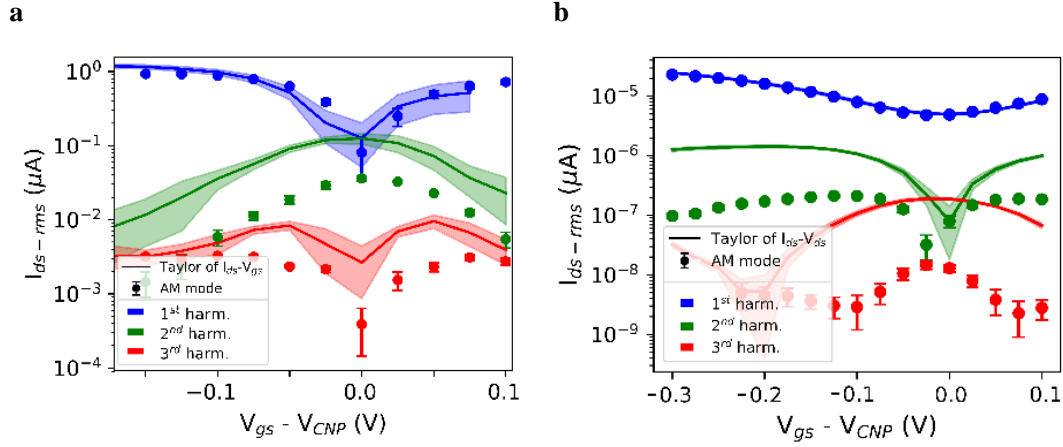
Figure S3| Harmonic distortion in the baseband. a. The 1st, 2nd and 3rd order harmonics introduced by the g-SGFET on a signal applied at the gate are shown for different V_{gs} bias conditions (dots). The terms derived from the Taylor expansion of the stationary transfer characteristics are also shown (lines). **b.** The 1st, 2nd and 3rd order harmonics introduced by the g-SGFET on a carrier signal are shown for different V_{gs} bias conditions (dots). The terms derived from the Taylor expansion of the output characteristics are also shown (lines). The filled area and error bars indicate the standard deviation (n=4).

S7. Crosstalk analytical modelling

The crosstalk level induced by common mode oscillations (V_{com}) at the resistance of the metal tracks, connectors, wires, etc in series with the transistors in row j ($R_{row,j}$) and in column i ($R_{col,j}$) can be expressed by an analytical expression. This expression can be derived by calculating how signals applied on a specific g-SGFET modify the effective drain-to-source bias ($V_{ds,eff}$) of g-SGFETs at different positions on the array. For a g-SGFET on position (i,j) (see Fig. S4).

$$V_{ds,eff,ij} = V_{carrier,i} - V_{com,row,j} - V_{com,col,i}$$

Eq. S1a

213

$$+V_{com,row,j} = \left[\sum_i \frac{V_{ds,eff,ij}}{R_{GFET,ij}} + \sum_i V_{ds,eff,ij} \, g_{m,ij} \, V_{sig,ij} \right] R_{row,j}$$

Eq. S1b

$$V_{com,col,i} = \left[\sum_j \frac{V_{ds,eff,ij}}{R_{GFET,ij}} + \sum_j V_{ds,eff,ij} \, g_{m,ij} \, V_{sig,ij} \right] R_{col,i}$$

Eq. S1c

In a zeroth order approximation, $V_{ds,eff,ij}(O^0)$ can be considered equal to $V_{carrier,i}$ in Eq. S1b and S1c, because $V_{com} \ll V_{carrier,i}$, i.e.:

$$\frac{R_{col,i}}{R_{GFET,ij} + R_{col,i} + R_{row,j}} \ll 1 \qquad \text{Eq. S2a}$$

$$\frac{R_{row,i}}{R_{GFET,ij} + R_{col,i} + R_{row,j}} \ll 1 \qquad \text{Eq. S2b}$$

and,

$$V_{carrier,i} \, g_{m,ij} \, V_{sig,ij} R_{col,i} \ll V_{carrier,i} \qquad \text{Eq. S2c}$$

$$V_{carrier,i} \, g_{m,ij} \, V_{sig,ij} R_{col,i} \ll V_{carrier,i} \qquad \text{Eq. S2d}$$

Following this approximation, Eq. S1a describing a first order approximation of the effective drain-source voltage can be defined as:

$$V_{ds,eff,ij}(O^1) = V_{carrier,i} - V_{com,row,j}(O^1) - V_{com,col,i}(O^1)$$

Eq. S3a

where:

$$V_{com,row,j}(O^1) = \left[\sum_i \frac{V_{carrier,i}}{R_{GFET,ij}} + \sum_i V_{carrier,i} \, g_{m,ij} \, V_{sig,ij} \right] R_{row,j}$$

$$V_{com,col,i}(O^1) = \left[\sum_j \frac{V_{carrier,i}}{R_{GFET,ij}} + \sum_j V_{carrier,i}\, g_{m,ij}\, V_{sig,ij} \right] R_{col,i}$$

In this way, the current flowing through a specific g-SGFET e.g. at position (1,1), can be estimated:

$$I_{ds,11}(O^1) = \frac{V_{ds,eff,11}(O^1)}{R_{GFET,11}} + V_{ds,eff,11}(O^1)\, g_{m,11}\, V_{sig,11}$$

If a signal is applied on g-SGFET on position (1,1), $I_{ds,11}(O^1)$ presents the multiplication of the main component $V_{carrier1}$ by $V_{sig,11}$ in the second term of Eq. S4. After demodulation, the signal of interest $G_m V_{sig,11}$ is determined from this product. Besides, $V_{ds,eff,11}(O^1)$ in the second term of Eq. S4 also includes the term $V_{com,row,1}(O^1)$, which contains a component at all carrier frequencies attenuated by a factor $R_{row,1}/R_{GFET,i1}$ as described by Eq. S3b. The product of $V_{sig,11}$ with $V_{com,row,1}(O^1)$ therefore causes a wrong attribution of $V_{sig,11}$, attenuated by a factor $R_{row,1}/R_{GFET,i1}$, to all g-SGFETs in row 1. On the other hand, regarding crosstalk among transistors in the same column; the signal applied ($V_{sig,11}$) causes a change in $V_{com,col,1}(O^1)$ as described in Eq. S3c. The current through all j transistors in column 1 ($I_{ds,1j}$) then presents a term proportional to $g_{m,11} V_{sig,11}$ attenuated by the factor $R_{col,1}/R_{GFET,1j}$.

Finally, a 2nd order crosstalk appears in $I_{ds,ij}(O^2)$:

$$I_{ds,ij}(O^2) = \frac{V_{carrier,i} - V_{com,row,j}(O^2) - V_{com,col,i}(O^2)}{R_{GFET,11}}$$

$$+ \left(V_{carrier,i} - V_{com,row,j}(O^2) - V_{com,col,i}(O^2)\right) g_{m,11} V_{sig,11}$$

Eq. S4

where $V_{com,col,i}(O^2)$:

$$V_{com,col,i}(O^2) = \left[\sum_j \frac{V_{carrier,i} - V_{com,col,i}(O^1) - V_{com,row,i}(O^1)}{R_{GFET,ij}} \right.$$

$$\left. + \sum_j \left(V_{carrier,i} - V_{com,col,i}(O^1) - V_{com,row,i}(O^1)\right) g_{m,ij} V_{sig,ij} \right] R_{col,i}$$

Eq. S5

Also presents a component at all carrier frequencies (i.e. $V_{com,row,i}(O^1) \approx \sum_i \frac{V_{carrier,i}}{R_{GFET,ij}} R_{row,j}$ in the first term of Eq. S5). This term, translates the crosstalk from the transistors in the same column to all the rest of columns. This 2nd order crosstalk affects all g-SGFETs out of the same column and row, and presents an attenuation by a factor $R_{col,1} R_{row,1} / (R_{GFET,1j})^2$, which is basically the squared attenuation factor. For the fitting of the experimental crosstalk, the aforementioned attenuation factors have been used. Leading to a $R_{col,1} \approx R_{row,1} \approx 50\Omega$.
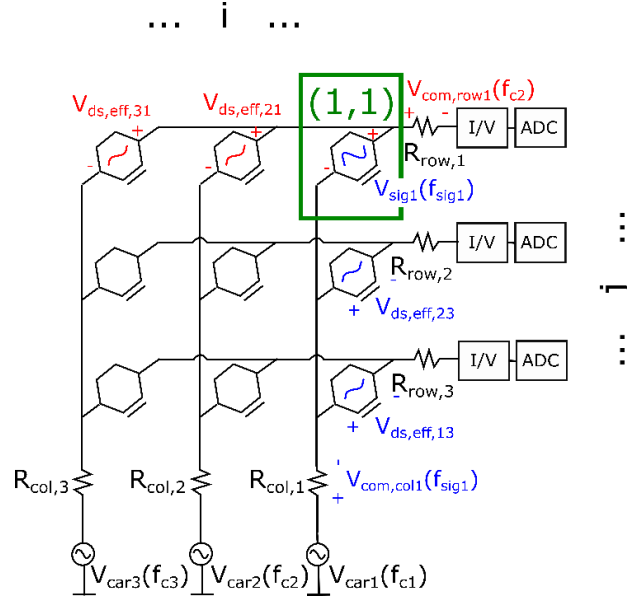
Figure S4: Equivalent circuit of a 3x3 g-SGFET array. The dimensions corresponding to index *i* and *j* used in Eq. S1 are indicated as well as the position of index (1,1), where a signal at the gate is applied. In red, the crosstalk induced in g-SGFET in row 1 is illustrated, which is caused by changes in $V_{ds,eff,i1}$. The crosstalk induced in g-SGFETs in column 1 is illustrated in blue, which is caused by changes in $V_{ds,eff,1j}$.

S8. Crosstalk cancelation and scalability

The experimental determination of crosstalk by individually gating g-SGFETs allowed determining the mechanism responsible for crosstalk generation. The experimental results show that a simple model of voltage oscillations in the metal tracks (R_{track}) explains the magnitude and the gate voltage dependence of the crosstalk. In order to mathematically eliminate the effects of crosstalk, the information about the coupling factors ($k = R_{track}/R_{g-SGFET}$, see Figure S4) is sufficient.

Due to crosstalk, the signals measured for one specific sensor are the linear superposition of multiple devices, with each contribution weighted by the specific coupling factor $k_{ij-i'j'}$ between the g-SGFETs in positions ij and another position $(i'j')$. Knowing all coupling factors and the measured signals from all N sensors we have a system of N linear equations and N variables (i.e. the actual biological signals from the N sensors). Expressed in matrix form:

$$\begin{bmatrix} k_{11-11} & \cdots & k_{11-mn} \\ \vdots & \ddots & \vdots \\ k_{mn-11} & \cdots & k_{mn-mn} \end{bmatrix} \begin{bmatrix} M_{11} \\ \vdots \\ M_{mn} \end{bmatrix} = \begin{bmatrix} S_{11} \\ \vdots \\ S_{mn} \end{bmatrix}$$

Eq. S6

where $n \times m = N$. M_{ij} represents the measured signal in sensor i, j and S_{ij} the actual electrophysiological signal without crosstalk effects in sensor i, j. The array of variables S can be determined by multiplying the inverse of the coupling coefficients matrix (k) by the array of measured signals (M):

$$S = k^{-1}M$$

Eq. S7

The coupling matrix k can be directly determined from the resistance values of the metal tracks and the g-SGFETs, which can be estimated with a high accuracy from the probe layout, a measurement of the metal sheet resistance using test structures and the I_{ds-DC} measured. Following this approach, the crosstalk in our proof-of-concept can be determined and mitigated. We have validated the method using the signals detected by individually gating the g-SGFETs using polyelectrolyte gates. The results show a dramatic decrease in the crosstalk, which is shown in Fig. S5a and Fig. 4b in the main text. Besides, we have used this method to estimate the actual effect of crosstalk on the signals detected *in-vivo.* Fig. S5b and S5c below show the map of visually evoked response with and without the crosstalk correction, revealing that only a very small crosstalk is present in the measurements.

However, crosstalk might become more severe if the density of the sensors is increased, due to reduced space for the metal tracks or due to high correlation among signals detected in multiple sites. The experimental determination and modelling of crosstalk presented in our manuscript demonstrate that crosstalk originates from common-mode voltage oscillations induced by non-zero resistance of the metal tracks. Therefore, reducing R_{track} as well as increasing the resistance of the g-SGFETs will mitigate the effect of crosstalk (see supporting information S7). For the R_{track}=50Ω and width to length ratio (W/L=1) presented in our proof of concept, a crosstalk level of ~1.5% (i.e. 36.7dB) is determined. However, this value does not represent the ultimate limit of the technology: it has been determined in a non-optimized test device for the sole purpose of demonstrating the origin of crosstalk. The g-SGFET array can be designed to meet rigorous constrains in terms of crosstalk, minimizing the tracks resistance and adjusting the W/L of the g-SGFET. Fig. S5d below represents the crosstalk-to-signal ratio (CTSR) calculated for different R_{track} and W/L values using the crosstalk factor (R_{track}/R_{GFET}) derived in supporting information S7. Given this map, it is possible to define a design rule for specific applications. For the mapping of local field potentials (LFP) using surface probes, as demonstrated in our manuscript, the density of the array does not need to be particularly high; instead, a high-count probe covering large areas is typically required[4]. For relatively low densities, the metal tracks can be wide, therefore enabling to reduce the tracks resistance to ~10Ω, which decreases the CTSR to the range of -50dB for a W/L=1 or -60dB for a W/L =1/3. Moreover, using the crosstalk correction method described above an additional attenuation of the CTSR of ~15dB can be achieved (see Fig. 4b in the main text), which would strongly relax the design rules shown in Fig. S5d.
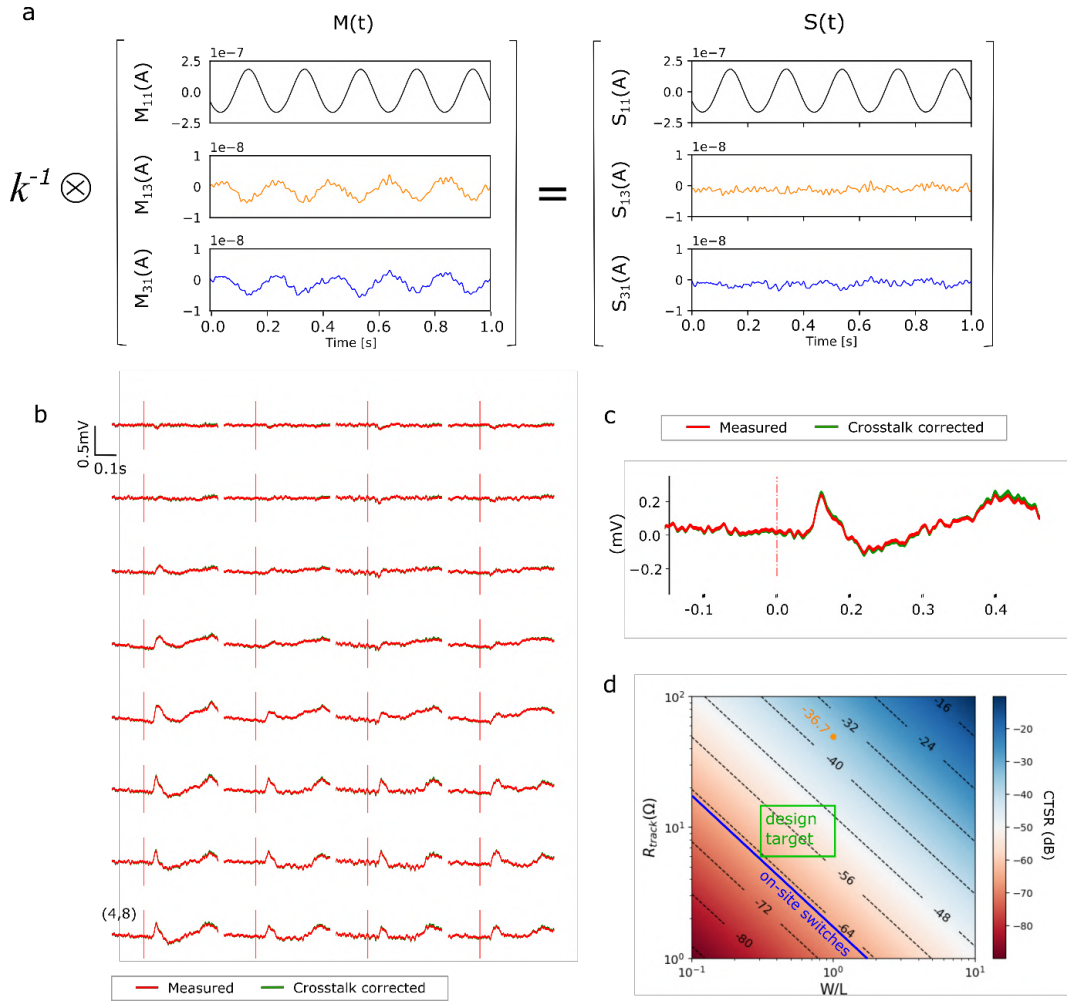
Figure S5: Validation of crosstalk cancelation method. a. Signal measured in different g-SGFETs before (left) and after (right) crosstalk mitigation. The black line corresponds to the g-SGFET where the signal was applied using printed polyelectrolyte gates. The orange and blue line correspond to g-SGFETs in the same column and row respectively. **b.** Spatial map of visually evoked response averaged for 10 stimulus. The red line represents the measured signal and the green line represents the signal after correction. **c.** Signal corresponding to the bottom-left position (i.e. 4,8) on the array. **d.** Map of CTSR for different R_{track} and W/L values. The experimentally determined crosstalk level is indicated in orange. A realistic design target is

indicated in green while crosstalk level for technologies with on-site switches is indicated by the blue line. Note that the effect of the crosstalk mitigation method is not considered in this figure.

S9. Validation of polyelectrolyte gating and frequency response in the DC-mode

Polyelectrolytes consist of immobile charged polymer chains with mobile counter-ions. This solid electrolytes present a high electrochemical stability[5,6], which minimizes electrochemical reactions at the interface and ensures field-effect operation. Polyelectrolytes have been recently attracting increasing interest for the gating of flexible field-effect transistors due to the high interface capacitance that can be achieved[7,8]. This high capacitance is in the same range as for solution-gated devices, therefore it represents a suitable material to model the response of g-SGFETs with a solid gate. Therefore, we have patterned the polyelectrolyte on different groups of graphene FETs on the array in order to apply signals on specific sites and measure the crosstalk induced on the rest of the array. The electrical potential in the polyelectrolyte has been controlled by coplanar gold gates as illustrated in Fig. S6a.

For the patterning of polyelectrolyte gates, inkjet printing has been chosen as an alternative to photolithographic methods. Photolithographic definition of spin-coated or dip-coated polymers is highly scalable, however, the patterned polymers must be photodefinable[9] or compatible with photodefinable resists and resist developers. Inkjet printing allows to circumvent this limitation, with the only constrains being the strict rheological properties that inks must meet[10].

The polyelectrolyte solution used here was specifically formulated to be compatible with a drop-on-demand piezoelectric printer. The ink was prepared by dissolving poly(vinylidene fluoride-*co*-hexafluoropropylene) (PVDF-HFP) pellets ($M\overline{w}$ = 400000, d = 1.78g/mL) and ion liquid 1-butyl-3-methylimidazolium tetrafluoroborate [BMIM][BF$_4$] with
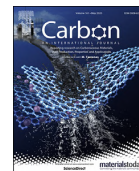
Chapter 7

Appendix B: complementary articles

Contents

Improved metal-graphene contacts for low-noise, high-density microtransistor arrays for neural sensing

Nathan Schaefer [a, b, 1], Ramon Garcia-Cortadella [a, b, 1], Andrea Bonaccini Calia [a, b, 1], Nikolaos Mavredakis [b], Xavi Illa [c, d], Eduard Masvidal-Codina [c], Jose de la Cruz [a], Elena del Corro [a], Laura Rodríguez [a], Elisabet Prats-Alfonso [c, d], Jessica Bousquet [a], Javier Martínez-Aguilar [c, d], Antonio P. Pérez-Marín [a], Clement Hébert [e], Rosa Villa [c, d], David Jiménez [b], Anton Guimerà-Brunet [c, d], Jose A. Garrido [a, f, *]

[a] Catalan Institute of Nanoscience and Nanotechnology (ICN2), CSIC and The Barcelona Institute of Science and Technology, Campus UAB, Bellaterra, Spain
[b] Departament d'Enginyeria Electrònica, Escola d'Enginyeria, Universitat Autònoma de Barcelona, Bellaterra, Spain
[c] Instituto de Microelectrónica de Barcelona IMB-CNM (CSIC), Esfera UAB, Bellaterra, Spain
[d] Centro de Investigación Biomédica en Red en Bioingeniería, Biomateriales y Nanomedicina (CIBER-BBN), Madrid, Spain
[e] Inserm and Université Grenoble Alpes, Saint Martin d'Hères, France
[f] ICREA, Barcelona, Spain

A R T I C L E   I N F O

A B S T R A C T

Poor metal contact interfaces are one of the main limitations preventing unhampered access to the full potential of two-dimensional materials in electronics. Here we present graphene solution-gated field-effect-transistors (gSGFETs) with strongly improved linearity, homogeneity and sensitivity for small sensor sizes, resulting from ultraviolet ozone (UVO) contact treatment. The contribution of channel and contact region to the total device conductivity and flicker noise is explored experimentally and explained with a theoretical model. Finally, in-vitro recordings of flexible microelectrocorticography (μ-ECoG) probes were performed to validate the superior sensitivity of the UVO-treated gSGFET to brain-like activity. These results connote an important step towards the fabrication of high-density gSGFET μ-ECoG arrays with state-of-the-art sensitivity and homogeneity, thus demonstrating the potential of this technology as a versatile platform for the new generation of neural interfaces.

1. Introduction

With its exceptional properties such as high mobility [1], biocompatibility [2], transparency [3] and mechanical strength [4], graphene has been extensively investigated for application in numerous fields such as electonics [5], photonics and optoelectronics [6], and more recently biomedical engineering [7–9]. Despite the vast potential of graphene, graphene-based devices often fall short of demonstrating their full capabilities, as large metal-graphene contact resistance [10], inhomogeneity among devices [11] and high 1/f noise [12] still hamper their performance.

* Corresponding author. Catalan Institute of Nanoscience and Nanotechnology (ICN2), CSIC and The Barcelona Institute of Science and Technology, Campus UAB, Bellaterra, Spain.
*E-mail address:* joseantonio.garrido@icn2.cat (J.A. Garrido).
[1] These authors contributed equally to this work.

Hence, great efforts have been undertaken to properly understand the source of noise and of the high contact resistance as well as to find ways to minimize their impact on the device performance.

In a graphene-based field-effect transistor (FET), we can distinguish several contributions to low-frequency noise [12]. For instance, variations in the scattering cross-section of lattice defects generate mobility fluctuations which ultimately cause changes in the resistance of graphene. In addition, charge trap states in the graphene channel or in the surrounding materials such as the substrate, gate dielectrics or encapsulation layers can cause fluctuations in the number of charge carriers. Due to the 2-dimensional nature of graphene, the latter is expected to be dominant, as shown for certain transistor configurations [13]. The use of buffer layer materials such as hexagonal boron nitride (hBN) [14] or engineering free-standing graphene channels [15] has been proposed to decouple the graphene sheet from the environment, and thus reduce flicker noise. Degradation of the electrical properties due to

e closer environment the is not restricted to graphene but has en also observed for other two-dimensional materials such as insition-metal-dichalcogenites (e.g. MoS_2) [16] and layered III-VI miconductors (i.e. InSe) [17].

High contact resistance, resulting from the work function smatch between graphene and metals as well as from the low nsity of states of graphene, has a negative impact on the performance of graphene FETs, resulting in a poor charge transfer and us in a low conductance of graphene FETs [10,18,19]. Common ategies to reduce contact resistance include the use of metals nich interact strongly with graphene [20—22] or the creation of fects in the graphene lattice; for instance, the introduction of ngling bonds can enhance the graphene-metal interaction. pical ways to create defects in graphene include, patterning the aphene sheet beneath the metal contacts, increasing the graene edge length [23—25], as well as treating the contacted graene with oxygen plasma [26] or ozone [27]. Despite the vast mber of available techniques to provide low contact resistance, e goal of most published studies focuses on setting new performance benchmarks for a single device by using nanofabrication chniques and exfoliated graphene [14,28], and only very few of em address the technique's scalability for wafer-size fabrication)]. Since the success of 2D materials will ultimately depend on eir translation from the laboratory to industry, demonstration of ge-scale fabrication processes with high homogeneity and high eld are of critical importance. In addition to their impact on the rrent-voltage characteristics of the transistor, metal-graphene

contacts have also been reported to exhibit time-dependent resistance fluctuations [30], thus contributing to the low-frequency noise. Although significant efforts have been devoted to a better understanding of the electrical noise in graphene [12], no consensus has been reached yet on whether channel or contact noise is dominant in graphene FETs, what the underlying noise-generating mechanisms are and how noise depends on channel and contact geometry [28,31—35].

Here we use wafer-processed graphene solution-gated field-effect transistors (gSGFETs) to demonstrate the effect of the contact resistance on the sensing performance of these devices. gSGFETs have been widely explored for application in micro-electrocorticography (μ-ECoG) arrays to record neural activity [9,36,37]. As neural signals are usually extremely small in amplitude (typically below 100 μV), having devices with good signal-to-noise ratio (SNR) is of paramount importance for high-quality recordings. Previous work investigated the bias-dependence of low-frequency noise in gSGFETs and demonstrated that carrier density fluctuations can generate low-frequency noise in the channel [13]. However, the impact of contact noise in g-SGFETs has not been addressed so far. In this work, in addition to present a fundamental noise study, we also explore the impact of low contact resistance on the actual recording quality of neural sensor-arrays considering factors such as signal-to-noise ratio, sensor homogeneity and linearity of signal transduction.
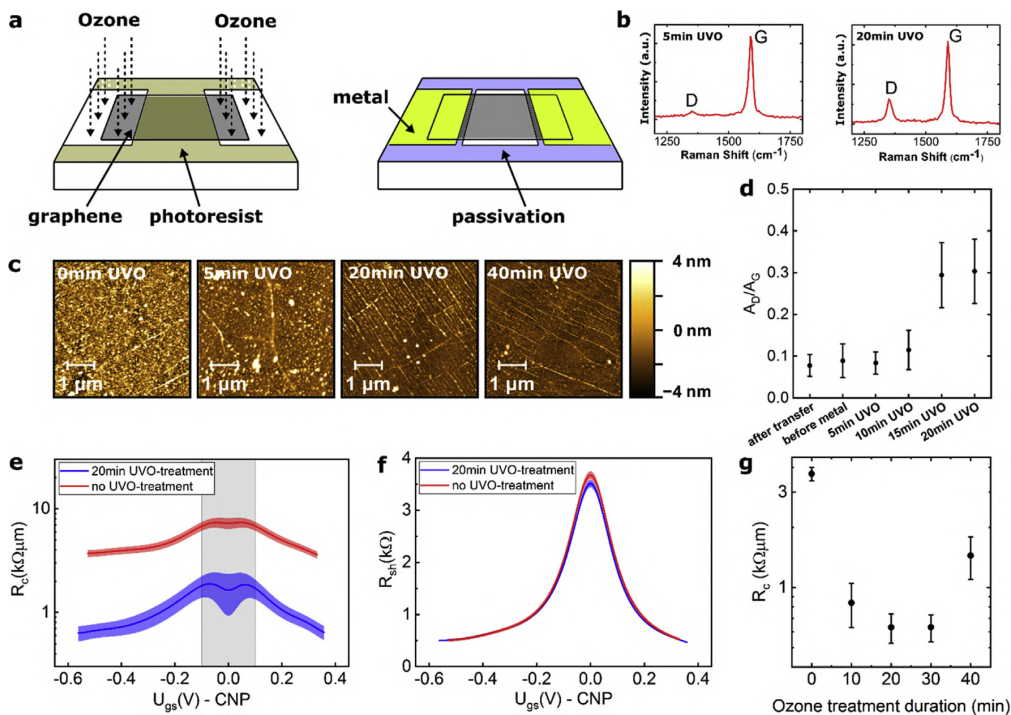
. 1. Improving contact resistance by surface cleaning and defect creation. a. Schematic of device fabrication with UVO applied to the graphene contact region prior to the tal deposition. b. Raman spectra after 5 min and 20 min treatment, indicating an increase of the D-peak with treatment duration. c. Surface roughness of the graphene layers asured by AFM. The lowering of the root-mean-square values with longer UVO treatments (2.1 nm, 1.3 nm, 1.1 nm and 0.8 nm, for 0 min, 5 min, 20 min, and 40 min duration, spectively) indicates the continuous cleaning of surface residues. d. Ratio of peak intensities of the D-band and G-band of single-layer graphene used as an indicator for the ount of residues and defects in the graphene sheet. R_c (e) and R_{sh} (f) measured as a function of applied gate bias for UVO-treated and non-treated devices. The shaded region se to the charge neutrality point (CNP) does not yield reliable values for R_c, as here the applied gate bias reaches similar values than the drain-source bias ($U_{ds} = 20$ mV), leading n non-constant R_{sh} along the channel. g. R_c at U_{gs} - CNP $= -0.5$ V as a function of UVO-treatment duration, showing optimal results for 20 min—30 min UV ozone exposure. (A ›ur version of this figure can be viewed online).

2. Experimental

2.1. Graphene CVD growth and wet transfer

The copper foil used for the chemical vapor deposition of graphene (25 μm thick Alfa Aesar coated of size 4.5 cm × 7 cm) was first electropolished for 5 min in a solution (1 L of H_2O, 0.5 L of H_3PO_4, 0.5 L of ethanol, 0.1 L of isopropanol and 10 g of urea) at a fixed current density of 62 mA/cm2 and subsequently loaded into a planar quartz tube (length of 160 cm and diameter of 6 cm) heated by a three-zone oven. A thermal annealing was performed for 1 h at 1050 °C (under 400 sccm Argon flow at 100 mbar pressure) to stabilize the temperature prior to the 10 min graphene growth step (gas mixture of 1000 sccm of Argon, 200 sccm of hydrogen and 2 sccm of methane, at 12 mbar pressure). The sample is then quenched down to room temperature by removing the tube from the heating zone. To transfer the graphene film, poly(methyl methacrylate) (PMMA A4) was spun onto the sample and dried at room temperature for 12 h. Afterwards, the backside graphene was removed by oxygen plasma and the sample was kept floating for at least 6 h in solution of $FeCl_3$/HCl to remove the copper. Subsequently, the sample was cleaned several times in deionized water, before being transferred onto the substrate. The wafer was then dried and thermally annealed in ultra-high vacuum (30 min at 40 °C, then gradually ramped up to 180 °C), before the PMMA was dissolved in acetone and isopropanol. Right after the growth, the quality and uniformity of the graphene monolayer is assessed by scanning electron microscopy (SEM) and Raman Spectroscopy (30 μm × 30 μm mapping). As detailed in the supplementary information, the graphene layers exhibit a domain size between 10 μm and 20 μm, a low defect density and high uniformity across the entire sample. The averaged full-width-half-maximum of the 2D Raman peaks of the used samples is around 33 cm^{-1}, indicating a low percentage of second nucelation.

2.2. Device fabrication

The devices for the transfer length method (TLM) study were fabricated by contact photolithography on 4 inch Si/SiO_2 wafers. In a first step, graphene was transferred, patterned (HiPR6512 photoresist, FujiFilm) and etched by deep reactive-ion etching (DRIE) for 1 min at 150 W in oxygen plasma. Subsequently, the photoresist for the contact metal layer was deposited, illuminated through a chromium mask and developed. Before evaporating 20 nm Ni and 200 nm Au (using an e-beam evaporator) the wafer was exposed to UV-ozone [Jelight Model 42] [27]. After lift-off, a 2 μm passivation layer (SU8-2005 MicroChem) is deposited with open windows in the channel region.

The flexible ECoG-probes were processed following the same protocol; however, a 7 μm layer of polyimide (PI-2611 HD Micro-Systems) was spun onto the Si wafer prior to fabrication to serve as the flexible substrate and structured via DRIE to allow individual peeling of each probe after all steps are finished. Due to the higher mechanical stress in the flexible probes, an additional metal layer (20 nm Ti and 200 nm Au) was used to improve adhesion between the top metal layer and the substrate, yet not directly contacting the graphene channel.

2.3. Device characterization and recording setup

Transfer characteristics and noise were measured with custom-built electronics, performing current-to-voltage conversion, filtering and bias-control of up to 16 transistors simultaneously. To allow sensitivity towards large DC currents and high gain for noise detection, the converted signals are split into DC (frequency < 0.1 Hz) and AC (0.1 Hz < frequency < 5 kHz) components. A commercial data acquisition system (National Instruments USB-6363) was used to provide the applied biases and record the voltage signals after conversion [36].

2.4. Raman spectroscopy and atomic force microscopy

The Raman spectra were acquired with a Witec spectrometer in backscattering configuration, using a 600 gr/nm grating which provided a spectral resolution of 3 cm^{-1}/pixel. A 488 nm excitation laser (1 mW power) was focused on the sample with a 50x objective leading to a spatial resolution below 0.8 μm. The integrated peak intensity ratio A_D/A_G is calculated by fitting each peak with a Lorentzian after previously substrating the background. Each data point shown in Fig. 1a was obtained from the statistical analysis of Raman mappings of 15 μm × 40 μm contact region. An Asylum MFP-3D atomic force microscope (AFM) was used to characterize the surface in standard air-tapping mode (Fig. 1c).

2.5. Contact resistance from transfer length method

The contact resistance (R_c) and the sheet resistance (R_{sheet}) values shown in Fig. 1e–g have been extracted by applying the TLM to different devices of 2.5 μm, 5 μm, 8 μm, 10 μm, 20 μm and 40 μm channel length and 40 μm channel width. For each length, the resistance value has been extracted from the mean value of several measurements and fitted with a linear regression model to extract the values for R_c and R_{sheet}. To further improve the accuracy of this approach, outlier resistance values which strongly deviate from the median of each transistor type (outside the 25th and 75th percentile) were not used in the analysis.

3. Results and discussion

3.1. Low contact resistance by surface cleaning and defect creation

Ultraviolet ozone (UVO) treatment has been previously reported as an efficient way to reduce contact resistance in graphene FETs [27,29]. Part of the effect is attributed to removal of fabrication residues which leads to a decrease of the intensity ratio of the D-peak to the G-peak (A_D/A_G). However, longer treatment durations are known to break up the sp^2-bonds and cause defects, which increases A_D/A_G. During the initial phase of defect creation, UVO exposure predominately leads to the formation of sp^3-bonds through the attachment of oxygen containing groups [38]. On the other hand, in the case of high defect density (n_D/n_C above 10^{-3}) due to long UVO treatment durations or increased sample temperature during the treatment, it has been shown that a transition from sp^3-type towards vacancy-type dominated defects takes place [42,43]. In our study, the UVO has been applied at room temperature and due to the relatively small size of the exposed contact region, surrounded by areas covered with photoresist, defects in the graphene film at the contacts are induced at a slow rate. In the case of the 20 min UVO duration, the resulting low A_D/A_G-ratio (0.3) together with the absence of a noticeable D' band indicates a low defect density, predominantly with a sp^3-type nature [42,43]. Since the sp^2 orbitals hinder charge injection along the z-plane [44,45], the creation of defects by long UVO-treatments further decreases the contact resistance.

Fig. 1d shows the evolution of A_D/A_G as a function of treatment duration. The results are comparable to the ones presented in literature [27], with the exact duration depending on the experimental conditions of the UVO-treatment. The accompanying change in surface topology was analyzed by AFM. Fig. 1c illustrates the surface roughness before and after treatments of varying
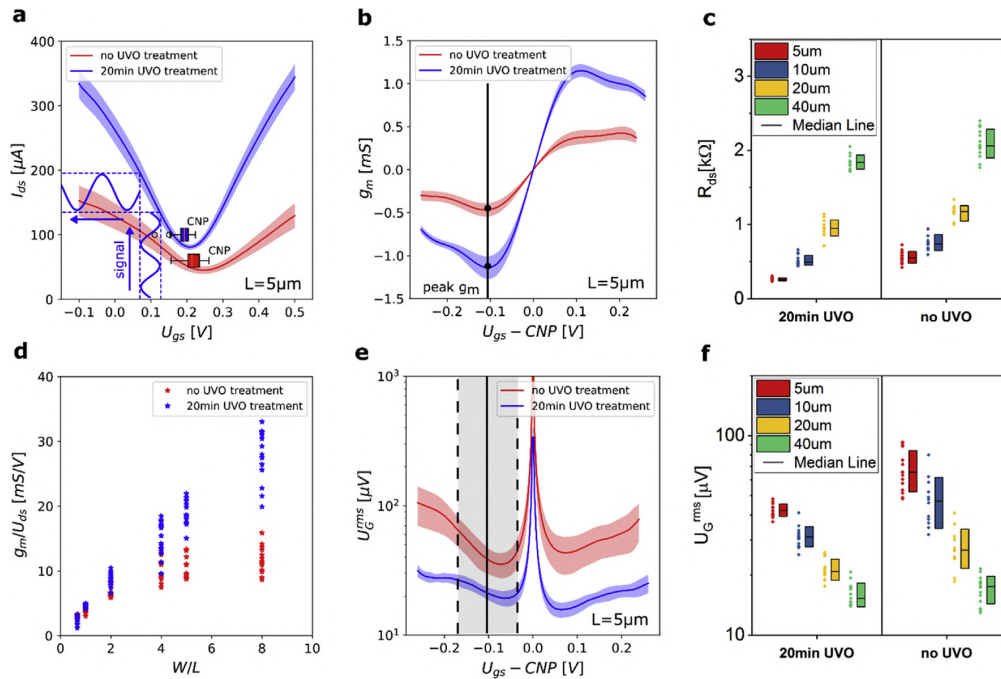
. 2. Effect of contact resistance on linearity of signal transduction, homogeneity and signal-to-noise ratio of gSFGETs. Average value and standard deviation of transfer ves for **a.** drain-source current I_{ds}, **b.** transconductance g_m and **e.** effective gate noise U_G^{rms} for devices of 5 μm channel length and 40 μm channel width. **d.** Normalized nsconductance g_m/U_{ds} (values within 25th and 75th percentile) versus width-to-length ratio of the channel. The statistical variation of the R_{ds} (**c**) and U_G^{rms} (**f**) values at peak nsconductance (U_{gs} = CNP - 0,1 V) for devices of different length are also shown. (A colour version of this figure can be viewed online).

ration, revealing the continuous cleaning of surface residues; s results in a lowering of the measured roughness (from a root-ean-square value of 2.1 nm for no treatment, down to 0.8 nm for min of UVO treatment) and a better visualization of the wrinkled rface of the graphene sheet. Fig. 1e and 1f shows the UVO in-ence on the contact resistance and sheet resistance of the gra-ne channel. The symmetric decrease (for electrons and holes) of away from the charge neutrality point (CNP) has been previously orted for back-gated graphene FETs using Ni contacts [18,21] d has been associated to the poor charge screening in 2D mate-ls with low charge carrier densities [46]. It is important to note t the TLM assumes a constant sheet resistance per unit area ross the whole transistor channel. However, this assumption is ly correct for cases in which the applied gate bias is much larger an the drain-source bias. While this is mostly true for field-effect-nsistors that usea relatively thick dielectrics, solution-gated FETs e normally operated at much lower gate voltages. In this case, the tential difference between channel and gate is not constant but anges gradually along the channel, which leads to a non-uniform eet resistance and can result in unreliable values for R_c in the ey shaded region of Fig. 1e. Values for R_c far away from the CNP g. 1g), yield around 3-4 kΩμm for the case of a pristine Ni/Au top-ntact structure and reach a minimum as low as 600 Ωμm for a –30 min UVO treatment duration. Longer treatments result in an crease of contact resistance, as a high defect density in the UVO-ated graphene sheet eventually hampers charge conduction. On e other hand, the sheet resistance remains independent of the O treatment as expected, since the channel region is protected the photoresist.

3.2. Improved linearity of signal transduction, homogeneity and signal-to-noise ratio in short channel transistors

When planning the use of gSGFETs as a transducer for neural activity, there are several factors to be considered to obtain distortion-free, high-resolution recordings. Fig. 2 illustrates how contact resistance influences the sensing performance of gSGFETs, by comparing devices (of varying channel length and 40 μm channel width) with low (20 min UVO treatment) and high contact resistance (no UVO treatment). The suitability of the gSGFET for sensing applications, in which the device converts the voltage variation of a signal at the gate into a current modulation between the drain and source terminals, depends on the linearity of its transfer characteristics. A high contact resistance at the metal-graphene interface causes a flattening of the transfer curve away from the CNP (Fig. 2a), limiting the range of linear operation. The resulting non-linearities can cause distortions in the transduced signal, thus degrading the recording quality of the graphene tran-sistors. Furthermore, a flattening of the transfer curve also limits the gSGFET's transconductance, defined as the change of drain-source current induced by a changing gate bias ($g_m = dI_{ds}/dU_{gs}$), which is a measure for the device's sensitivity. The gSGFET is commonly operated at the bias conditions which provide peak transconductance (illustrated in Fig. 2b). Fig. 2d shows how the normalized peak-transconductance value changes for devices of varying channel length (L = 5 μm, 8 μm, 10 μm, 20 μm, 40 μm, 60 μm) and constant channel width (W = 40 μm). In case of low R_c (i.e. for UVO-treated devices) the g_m/U_{ds} exhibits a near-linear in-crease with W/L, while for devices with high R_c (non-treated) it is increasingly limited for short channels. As a high transconductance is generally desirable for sensing applications to allow for best
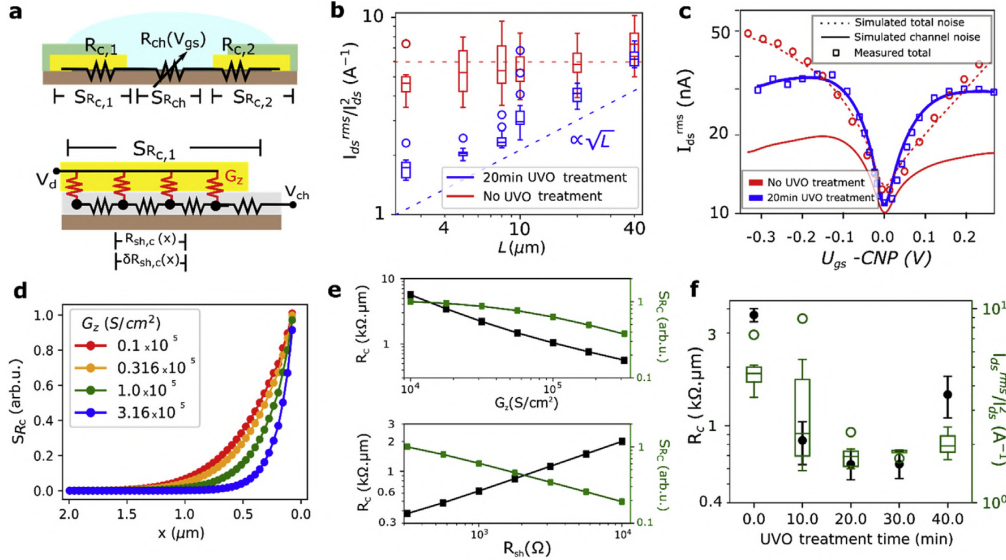
Fig. 3. Geometrical dependence of contact and channel noise in gSGFETs. a. Top: schematic of a gSGFET showing the contact resistance ($R_c = R_{c,1} + R_{c,2}$), channel resistance (R_{ch}) and the noise contributions from the contacts ($S_{R_c} = S_{R_{c,1}} + S_{R_{c,2}}$) and channel ($S_{R_{ch}}$). Bottom: Schematic of the equivalent circuit of the transmission-line contact at the graphene-metal interface. The distributed elements representing the sheet resistance of graphene along the contact ($R_{sh,c}$(x)) are defined together with the local fluctuations in the sheet resistance ($\delta R_{sh,c}$(x)). The drain voltage (V_d) and the potential at the channel/contact interface (V_{ch}) are also defined. b. Dependence of the normalized noise (I_{ds}^{rms} / I_{ds}^2) versus the channel length (L) for devices with non-treated contacts and for devices with contacts treated with UVO for 20 min ($U_{gs} = CNP - 0.1\ V$). A change from an approximately L-independent regime to a $\propto \sqrt{L}$ regime is observed. c. Experimentally obtained integrated noise I_{ds}^{rms} versus U_{gs}, plotted for non-treated contacts and contacts treated with UVO for 20 min and channel length of 5 μm. The lines correspond to the fitting of the experimental data with a model that considers the contributions of the channel noise (solid line) only and of the channel plus contact noise (dashed line). In UVO-treated devices the channel noise model fully describes the U_{gs} dependence of I_{ds}^{rms} (both curves exactly overlap). d. Local contribution of resistance fluctuations to S_{R_c} along the contact, shown for different values of conductance across graphene-metal interface (G_z), according to the FEM model described in the main text. e. Evolution of R_c (left axis) and S_{R_c} (right axis) with G_z (top) and $R_{sh,c}$ (bottom). f. Experimentally obtained R_c (left axis) and I_{ds}^{rms} / I_{ds}^2 (right axis) shown for different UVO treatment durations and channel length of 5 μm. (A colour version of this figure can be viewed online).

signal transduction, the influence of the contact resistance has to be considered for the choice of the sensor channel geometry.

Arguably, one of the most critical performance indicators of the gSGFET is its equivalent rms gate noise U_G^{rms} (Fig. 2e), which relates the intrinsic rms current noise I_{ds}^{rms} (integrated current noise over the frequency bandwidth of interest; here filtered between 1 and 100 Hz) of the transistor with its transconductance ($U_G^{rms} = I_{ds}^{rms} / g_m$), and represents the detection threshold for signals applied to the gate. At peak-g_m a significant reduction of the effective gate noise can be seen in the UVO-treated devices, which is most striking for short channel lengths. This difference becomes more pronounced when moving further away from the CNP: U_G^{rms} remains fairly constant in the case of low R_c and increases rapidly for devices with high R_c. This is particularly interesting when operating the gSGFET in-vivo, which typically requires using a common bias point for all devices. However, local changes in doping across the different recording sites, as well as electrochemical drifts of the reference electrode during long-lasting chronic recordings make it virtually impossible to operate all devices simultaneously at their ideal bias condition. As neural interfaces are mainly considered for long-term recordings, ranging from several days up to months or even years of implantation time, stable recording quality is mandatory. Consequently, having a constant SNR in a large bias window, resulting from a voltage-independent U_G^{rms}, is crucial to providing optimal sensing capabilities across the sensor array throughout long recording times. In addition to the positive effect of the UVO treatment on the contact resistance and noise of the devices, Fig. 2f shows that the dispersion across different recording sites is significantly reduced in the case of devices with the UVO treatment. This suggests that poor contact interfaces are

responsible for the dispersion observed in the array in terms of noise (Fig. 2f) and conductance (Fig. 2c), possibly overruling the contribution of the dispersion in graphene quality in the channel.

3.3. Noise contribution from contact and channel

The improvement in device performance resulting from the contact treatment directly leads to two questions: i) What is the contribution from the contact noise compared to the channel noise?, and ii) What is the reason for the contact noise improvement? Answering these questions is critical for knowing to which extent contact noise mitigation will affect the total noise in g-SGFETs, and to understand how to optimize the contact treatment procedure. The total normalized noise S_I/I_{ds}^2 generated in a gSGFET includes the contribution from the contacts (S_{R_c}) and from the channel ($S_{R_{ch}}$) (see Fig. 3a-top). The contributions of these terms to the measured current noise can be added linearly with the proper normalization:

$$\frac{S_I}{I_{ds}^2} = \frac{S_{R_c} + S_{R_{ch}}}{R_T^2} \tag{1}$$

where R_T is the total resistance of the transistor. The dependence of each of these terms on the channel width (W) and length (L) will determine their relative contribution to the total noise for different geometries and sizes. The dependence on geometry of S_{R_c} and S_{R_c} can be expressed explicitly:
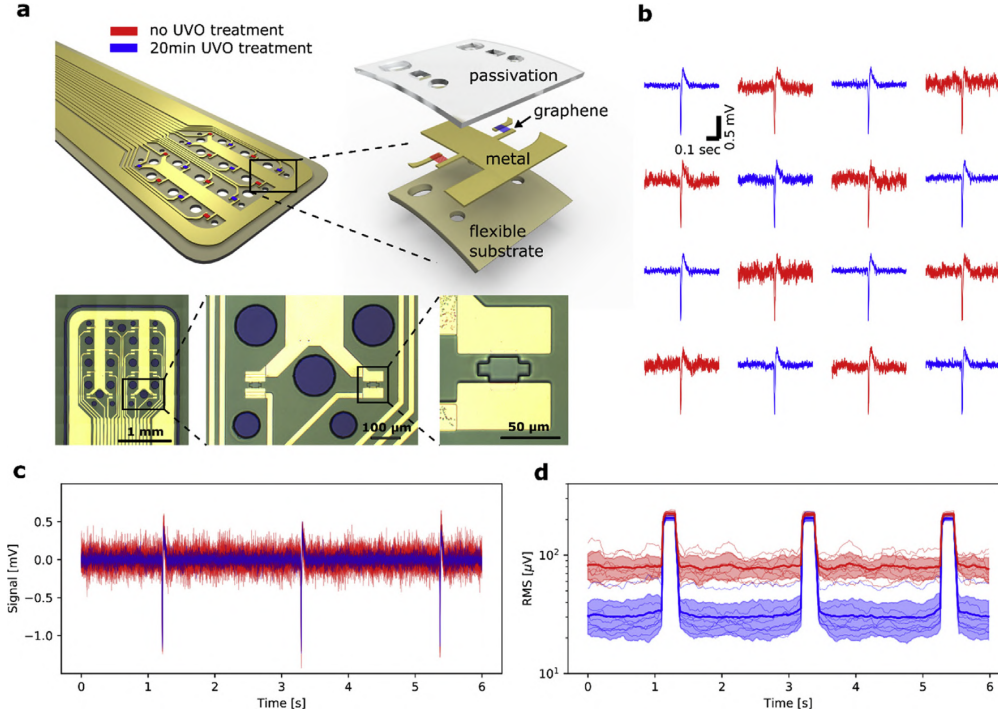
. 4. In-vitro assessment of recording quality of gSGFETs using hippocampal population spike-like signals. a. Schematic and optical images of a flexible epicortical probe with gSGFET sensors (20 μm × 20 μm channel area), with UVO-treated and non-treated sensors arranged in a chessboard layout. b. Map of a single spike event recorded by each nsistor of the array. c. Overlapped presentation of all recordings for several spike events. d. The root-mean-square (rms) value of the recorded signal (for each point integrated r a timespan of 200 ms) and its standard deviation are shown for each individual gSGFET as well as the mean value of all devices, revealing a significant improvement of the nal-to-noise ratio. (A colour version of this figure can be viewed online).

$$\frac{}{} = \left[k_{R_c} \big/ W^3 + k_{R_{ch}} L \big/ \left(W^3 \right) \right] \Big/ V_{ds}^2 \tag{2}$$

here k_{R_c} and $k_{R_{ch}}$ include all the constants which are independent the channel dimensions for S_{R_c} and $S_{R_{ch}}$ respectively (see sup- ementary information). The relative contribution of each term n therefore be identified by evaluating the dependence of noise L. Fig. 3b shows the normalized integrated current noise, $I_{ds}{}^{rms}$/ ^{2} (where $I_{ds}^{rms} \propto \sqrt{S_I}$), for different channel lengths. As demon- ated above, the measured noise is reduced for devices with the ʼO treatment. Interestingly, the derived dependence of the easured noise on L reveals the transition from a regime domi- ted by contact noise to a regime dominated by channel noise. The annel length for which the two terms contribute equally is proximately 60 μm. For devices with shorter channel length the ʼO treatment results in a significant improvement on the total ise of the g-SGFETs. It is important to note that the improvement U_G^{rms} is not only caused by the increase in g_m (Fig. 2), but also by e reduction of the intrinsic noise of the contact S_{R_c}. The transition m a regime dominated by contact noise to one dominated by annel noise can be confirmed by modelling the U_{gs}–dependence the measured current noise. Following the model presented in f. [13], which describes the U_{gs}-dependence of I_{ds}^{rms} when channel ise dominates, and including the contribution of the contact ise using Eq. (1) (assuming a constant R_c), we have fitted the perimental data to separate the contributions of contact and annel to the total noise. Fig. 3c compares the measured $I_{ds}^{rms} - U_{gs}$ · g-SGFETs with UVO-treated and non-treated contacts. In the

case of the non-treated devices the contribution from the contacts dominates the total transistor noise in most of the U_{gs} range. Conversely, for UVO-treated devices the U_{gs} dependence of the channel noise presents a characteristic M-shape, which has been attributed to the dominance of channel noise [13]. Note that in Fig. 3c the I_{ds}^{rms} is not normalized, therefore it does not directly represent the noise sources S_{R_c} and $S_{R_{ch}}$.

We turn now to discussing the cause of the contact noise improvement by the UVO treatment. To this end, we start by modelling the contact in graphene with the transmission-line model equivalent circuit shown in Fig. 3a, with G_z representing the conductance through the metal-graphene interface z-plane and $R_{sh,c}(x)$ representing the local values of the graphene sheet resis- tance at the contact. In this type of contacts, the current crowding [47] effect causes a non-homogenous current injection into the graphene sheet, with the highest current flowing next to the metal edge and the lowest at the end of the contact (see supplementary information). This attenuation of the current density at the contact is characterized by the transfer length L_T, at which the current density has decreased by a factor e. We suggest that the UVO treatment causes an increase in G_z, possibly due to elimination of fabrication residues and/or the creation of defects in graphene [27]. Such defects also produce an increase in the sheet resistance of graphene ($R_{sh,c}$) at the contacts, see Fig. 3a and [48]. Note that both the increase of G_z and increase of R_{sh} promote the current crowding effect, producing the shortening of L_T (see supplementary infor- mation). Following previous work [14], we assume that the noise originates from resistance fluctuations in the graphene sheet under the metal contacts. These fluctuations can be caused by mobility

228

653

fluctuations or by changes in the number of charge carriers trapped in the graphene substrate. Considering the equivalent circuit shown in Fig. 3a, the power of local fluctuations in the sheet resistance of graphene $\delta R_{sh,c}$ adds up linearly. However, in this distributed elements circuit the resistance fluctuations at different positions along the contact contribute differently to the overall contact noise. The contribution of each local noise source can be calculated by weighting its noise power with the term $dR_C/dR_{sh,c}(x)$ and integrating over the whole contact length (L_c) (see supplementary information). To perform this calculation, we have modelled the transmission-line contact using the finite elements method (FEM), as detailed in the supplementary information. Fig. 3d shows the calculated local contribution from each section of the contact for different values of conductance across the z-plane (G_z). When the current crowding effect is enhanced, the contribution to noise from local sources is confined closer to the metal edge. Similarly, when $R_{sh,c}$ is increased the same effect occurs (see supplementary information). The total integrated contact noise S_{R_c} is shown in Fig. 3e together with R_c as a function of G_z and $R_{sh,c}$, revealing that the simultaneous drop in R_c and in S_{R_c} can only be caused by an increase in G_z . Fig. 3f shows the measured R_c and S_{R_c} of the gSGFETs for different UVO treatment durations. It is possible to observe a monotonic decrease of both parameters until 20 min treatment duration, indicating that the contact noise mitigation in this range of UVO treatment is caused by an increase in G_z, rather than by an increase in $R_{sh,c}$. For UVO treatments above 30 min, however, the trend changes: R_c increases with the treatment duration, while S_{R_c} remains approximately constant (see supplementary information). We tentatively explain the increase in R_c as a result of the creation of defects on the graphene sheet at the contact, that causes a significant increase in $R_{sh,c}$ [39]. These results demonstrate the reduction of the noise contributions from the contacts by UVO treatment and offer an explanation to understand the origin and limits of this improvement.

3.4. Enhanced performance of flexible gSGFET ECoG-array for neural interfaces

After the above discussion on the effect of contact resistance on overall gSGFET performance and its low-frequency noise, we examine now how this improved performance is translated to the application of flexible gSGFET probes for neural activity recordings. Fig. 4a shows an illustration of this technology, combining several metal and passivation layers on a flexible polyimide substrate (fabrication described in the experimental section), corresponding to an array of 16 microtransistors. A squared channel geometry of 20 μm × 20 μm for each transistor is used to validate the performance of the flexible probe. The distance between transistors is 400 μm.

To exclude the variability due to the use of different graphene samples, the graphene transfer procedure or local changes of electronic properties in the graphene sheet, UVO-treated and non-treated gSGFETs are distributed in a chessboard arrangement on the same array (see transfer curves in Fig. S4 in supplementary information). A reliable comparison of recording quality across different recording sites is difficult in-vivo, as locally recorded signals depend on many factors such as the underlying brain tissue and the adhesion of each sensor to it. Therefore, a periodically generated artificial hippocampal population spike (Multi Channel Systems signal generator ME-W-SG) was applied to a phosphate-buffered saline solution (PBS, 10 mM). Fig. 4b displays one spike event recorded by each transistor of the array. Fig. 4c overlaps all the recordings for several events, demonstrating the improvement of SNR for the UVO-treated devices. To better quantify the SNR, the root-mean-square value of the recording in Fig. 4c and its standard deviation are plotted in Fig. 4d, showing average noise values around 80 μV for non-treated and 30 μV for UVO-treated devices. This presents an over twofold improvement of signal resolution for such sensor geometry, due to the improved metal-graphene contacts and compares very favorably to previously reported noise values in gSGFETs [36] (see Fig. S4d in supplementary information). Significantly reduced noise values due to the contact treatment have been reproduced across several probes on a single wafer and between different batches, validating the high reliability of this technique (see Fig. S4c in supplementary information). Small dispersion in noise values can be explained by minor variations in graphene quality and by the amount of surface residues between different devices.

4. Summary

Here we have shown the critical importance of the contact resistance for the performance of graphene solution-gated field-effect transistors in neural sensing applications. Poor contacts reduce the linearity of the transfer characteristics causing signal distortions, lower the signal-to-noise ratio of the recorded signal and limit the sensor homogeneity. Exposing the contact region of the graphene channel to UV-ozone before deposition of the contacting metal, is shown to significantly improve charge injection at the contacts by a combination of surface cleaning and defect creation. A theoretical model is used to understand the transition from contact-dominated to channel-dominated noise as a consequence of low contact resistance, and to assess its effect on the total noise of gSGFETs with different channel geometries. Finally, the compatibility of the contact improvement treatment with flexible substrates is validated, demonstrating the fabrication of flexible ECoG-arrays of gSGFETs exhibiting high signal-to-noise ratio.

The development of a novel class of brain-machine interfaces capable of providing further insights into the working paradigms of the brain and granting accurate control of neuro-prostheses might eventually require integrating brain-machine interfaces (BMIs) with single-neuron resolution (cell-body only several μm in size). Considering the increasing dominance of poor contacts on the SNR with decreasing sensor size, improved contact interfaces will become indispensable when moving the gSGFET technology towards this goal. Our work demonstrates a scalable technique to provide high-quality metal-graphene interfaces with low contact resistance, paving the way for low noise, high-density neural interfaces based on graphene transistors.

CRediT authorship contribution statement

Nathan Schaefer: Investigation, Conceptualization, Formal analysis, Writing - original draft. **Ramon Garcia-Cortadella:** Conceptualization, Methodology, Formal analysis, Writing - original draft. **Andrea Bonaccini Calia:** Investigation, Conceptualization. **Nikolaos Mavredakis:** Formal analysis, Methodology. **Xavi Illa:** Resources. **Eduard Masvidal-Codina:** Resources. **Jose de la Cruz:** Resources. **Elena del Corro:** Writing - review & editing. **Laura Rodríguez:** Resources. **Elisabet Prats-Alfonso:** Resources. **Jessica Bousquet:** Formal analysis, Writing - review & editing. **Javier Martínez-Aguilar:** Software. **Antonio P. Pérez-Marín:** Resources. **Clement Hébert:** Writing - review & editing. **Rosa Villa:** Supervision. **David Jiménez:** Supervision. **Anton Guimerà-Brunet:** Software, Supervision, Writing - review & editing. **Jose A. Garrido:** Supervision, Writing - review & editing, Project administration, Funding acquisition.

Appendix A. Supplementary data

Supplementary data to this article can be found online at https://doi.org/10.1016/j.carbon.2020.01.066.

References

[1] L. Banszerus, M. Schmitz, S. Engels, J. Dauber, M. Oellers, F. Haupt, K. Watanabe, T. Taniguchi, B. Beschoten, C. Stampfer, Ultrahigh-mobility graphene devices from chemical vapor deposition on reusable copper, Sci. Adv. 1 (2015) 1—7, https://doi.org/10.1126/sciadv.1500222.

[2] J. Conroy, N.K. Verma, R.J. Smith, E. Rezvani, G.S. Duesberg, J.N. Coleman, Y. Volkov, Biocompatibility of pristine graphene monolayers, nanosheets and thin films, ArXiv. http://arxiv.org/abs/1406.2497, 2014.

[3] R.R. Nair, P. Blake, A.N. Grigorenko, K.S. Novoselov, T.J. Booth, T. Stauber, N.M.R. Peres, A.K. Geim, Fine structure constant defines visual transparency of graphene, Science 320 (2008) 1308, https://doi.org/10.1126/science.1156965, 80.

[4] D.G. Papageorgiou, I.A. Kinloch, R.J. Young, Progress in Materials Science Mechanical properties of graphene and graphene-based nanocomposites, Prog. Mater. Sci. 90 (2017) 75—127, https://doi.org/10.1016/j.pmatsci.2017.07.004.

[5] F. Schwierz, Graphene transistors, Nat. Publ. Gr. 5 (2010) 4—5, https://doi.org/10.1038/nnano.2010.89.

[6] F. Bonaccorso, Z. Sun, T. Hasan, A.C. Ferrari, Graphene photonics and opto-electronics, Nat. Photon. 4 (2010) 611—622, https://doi.org/10.1038/nphoton.2010.186.

[7] C. Bussy, D. Jasim, N. Lozano, D. Terry, K. Kostarelos, The current graphene safety landscape-a literature mining exercise, Nanoscale 7 (2015) 6432—6435, https://doi.org/10.1039/c5nr00236b.

[8] T. Kuila, S. Bose, A.K. Mishra, P. Khanra, N.H. Kim, J.H. Lee, Chemical functionalization of graphene and its applications, Prog. Mater. Sci. 57 (2012) 1061—1105, https://doi.org/10.1016/j.pmatsci.2012.03.002.

[9] K. Kostarelos, M. Vincent, C. Hebert, J.A. Garrido, Graphene in the design and engineering of next-generation neural interfaces, Adv. Mater. 29 (2017) 1—7, https://doi.org/10.1002/adma.201700909.

[10] F. Giubileo, A. Di Bartolomeo, The role of contact resistance in graphene field-effect devices, Prog. Surf. Sci. 92 (2017) 143—175, https://doi.org/10.1016/j.progsurf.2017.05.002.

[11] Y. Zhang, V.W. Brar, C. Girit, A. Zettl, M.F. Crommie, Origin of spatial charge inhomogeneity in graphene, Nat. Phys. 5 (2009) 722—726, https://doi.org/10.1038/nphys1365.

[12] A.A. Balandin, Low-frequency 1/f noise in graphene devices, Nat. Nanotechnol. 8 (2013) 549—555, https://doi.org/10.1038/nnano.2013.144.

[13] N. Mavredakis, R. Garcia Cortadella, A. Bonaccini Calia, J.A. Garrido, D. Jiménez,

Understanding the bias dependence of low frequency noise in single layer graphene FETs, Nanoscale 10 (2018) 14947—14956, https://doi.org/10.1039/c8nr04939d.

[14] P. Karnatak, T.P. Sai, S. Goswami, S. Ghatak, S. Kaushal, Current crowding mediated large contact noise in graphene field-effect transistors, Nat. Commun. 7 (2016) 1—8, https://doi.org/10.1038/ncomms13703.

[15] Z. Cheng, Q. Li, Z. Li, Q. Zhou, Y. Fang, Suspended graphene sensors with improved signal and reduced noise, Nano Lett. 10 (2010) 1864—1868, https://doi.org/10.1021/nl100633g.

[16] X. Cui, G. Lee, Y.D. Kim, G. Arefe, P.Y. Huang, C. Lee, D.A. Chenet, X. Zhang, L. Wang, F. Ye, F. Pizzocchero, B.S. Jessen, K. Watanabe, T. Taniguchi, D.A. Muller, T. Low, P. Kim, J. Hone, Multi-terminal transport measurements of MoS2 using a van der Waals heterostructure device platform, Nat. Nanotechnol. (2015) 1—7, https://doi.org/10.1038/nnano.2015.70.

[17] W. Feng, W. Zheng, W. Cao, P. Hu, Back gated multilayer InSe transistors with enhanced carrier mobilities via the suppression of carrier scattering from a dielectric interface. https://doi.org/10.1002/adma.201402427, 2014, 6587-6593.

[18] S.M. Song, J.K. Park, O.J. Sul, B.J. Cho, Determination of work function of graphene under a metal electrode and its role in contact resistance, Nano Lett. 12 (2012) 3887—3892, https://doi.org/10.1021/nl300266p.

[19] A. Allain, J. Kang, K. Banerjee, A. Kis, Electrical contacts to two-dimensional semiconductors, Nat. Mater. 14 (2015) 1195—1205, https://doi.org/10.1038/nmat4452.

[20] Low contact resistance metals for graphene based devices, Diam. Relat. Mater. 24 (2012) 171—174, https://doi.org/10.1016/J.DIAMOND.2012.01.019.

[21] W.S. Leong, C.T. Nai, J.T.L. Thong, What does annealing do to metal—graphene contacts? Nano Lett. 14 (2014) 3840—3847, https://doi.org/10.1021/nl500999r.

[22] A. Gahoi, V. Passi, S. Kataria, S. Wagner, A. Bablich, M.C. Lemme, Systematic comparison of metal contacts on CVD graphene, in: 2015 45th Eur. Solid State Device Res. Conf., IEEE, 2015, pp. 184—187, https://doi.org/10.1109/ESSDERC.2015.7324744.

[23] W.S. Leong, H. Gong, J.T.L. Thong, Low-contact-resistance graphene devices with nickel-etched-graphene contacts, ACS Nano 8 (2014) 994—1001, https://doi.org/10.1021/nn405834b.

[24] H.Y. Park, W.S. Jung, D.H. Kang, J. Jeon, G. Yoo, Y. Park, J. Lee, Y.H. Jang, J. Lee, S. Park, H.Y. Yu, B. Shin, S. Lee, J.H. Park, Extremely low contact resistance on graphene through n-type doping and edge contact design, Adv. Mater. 28 (2016) 864—870, https://doi.org/10.1002/adma.201503715.

[25] J.T. Smith, A.D. Franklin, D.B. Farmer, C.D. Dimitrakopoulos, Reducing contact resistance in graphene devices through contact area patterning, ACS Nano 7 (2013) 3661—3667, https://doi.org/10.1021/nn400671z.

[26] X. Yan, K. Jia, Y. Su, Y. Ma, J. Luo, H. Zhu, Y. Wei, Edge-contact formed by oxygen plasma and rapid thermal annealing to improve metal-graphene contact resistance, ECS J. Solid State Sci. Technol. 7 (2018) M11—M15, https://doi.org/10.1149/2.0251802jss.

[27] L. Wei, Y. Liang, D. Yu, L. Peng, K.P. Pernstich, T. Shen, A.R. Hight Walker, G. Cheng, C.A. Hacker, C.A. Richter, Q. Li, D.J. Gundlach, X. Liang, Ultraviolet/ozone treatment to reduce metal-graphene contact resistance, Appl. Phys. Lett. 102 (2013), https://doi.org/10.1063/1.4804643.

[28] G. Liu, S. Rumyantsev, M. Shur, A.A. Balandin, Graphene thickness-graded transistors with reduced electronic noise, Appl. Phys. Lett. 100 (2012), https://doi.org/10.1063/1.3676277.

[29] W. Li, C.A. Hacker, G. Cheng, Y. Liang, B. Tian, A.R. Hight Walker, C.A. Richter, D.J. Gundlach, X. Liang, L. Peng, Highly reproducible and reliable metal/graphene contact by ultraviolet-ozone treatment, J. Appl. Phys. 115 (2014), https://doi.org/10.1063/1.4868897.

[30] G. Liu, S. Rumyantsev, M. Shur, A.A. Balandin, Graphene Thickness-Graded Transistors with Reduced Low-Frequency 1/f Noise, (n.d.).

[31] G. Liu, S. Rumyantsev, M.S. Shur, A.A. Balandin, Origin of 1/f noise in graphene multilayers: surface vs. volume, Appl, Phys. Lett. 102 (2013), https://doi.org/10.1063/1.4794843.

[32] G. Xu, C.M. Torres, Y. Zhang, F. Liu, E.B. Song, M. Wang, Y. Zhou, C. Zeng, K.L. Wang, Effect of spatial charge inhomogeneity on 1/f noise behavior in graphene, Nano Lett. 10 (2010) 3312—3317, https://doi.org/10.1021/nl100985z.

[33] Y. Zhang, E.E. Mendez, D. Xu, Mobility-Dependent Low-Frequency Noise in Graphene Field-E Ff Ect Transistors, 2011, pp. 8124—8130.

[34] A.K.M. Newaz, Y.S. Puzyrev, B. Wang, S.T. Pantelides, K.I. Bolotin, Probing charge scattering mechanisms in suspended graphene by varying its dielectric environment, Nat. Commun. 3 (2012) 734—736, https://doi.org/10.1038/ncomms1740.

[35] S. Chatoor, I. Heller, J.B. Oostinga, A.F. Morpurgo, S.G. Lemay, C. Dekker, J. Männik, M.A.G. Zevenbergen, Charge noise in graphene transistors, Nano Lett. 10 (2010) 1563—1567, https://doi.org/10.1021/nl903665g.

[36] C. Hébert, E. Masvidal-Codina, A. Suarez-Perez, A.B. Calia, G. Piret, R. Garcia-Cortadella, X. Illa, E. Del Corro Garcia, J.M. De la Cruz Sanchez, D.V. Casals, E. Prats-Alfonso, J. Bousquet, P. Godignon, B. Yvert, R. Villa, M.V. Sanchez-Vives, A. Guimerà-Brunet, J.A. Garrido, Flexible graphene solution-gated field-effect transistors: efficient transducers for micro-electrocorticography, Adv. Funct. Mater. 28 (2018) 1—15, https://doi.org/10.1002/adfm.201703976.

[37] E. Masvidal-Codina, X. Illa, M. Dasilva, A.B. Calia, T. Dragojević, E.E. Vidal-Rosas, E. Prats-Alfonso, J. Martínez-Aguilar, J.M. De la Cruz, R. Garcia-Cortadella, P. Godignon, G. Rius, A. Camassa, E. Del Corro, J. Bousquet, C. Hébert,

T. Durduran, R. Villa, M.V. Sanchez-Vives, J.A. Garrido, A. Guimerà-Brunet, High-resolution mapping of infraslow cortical brain activity enabled by graphene microtransistors, Nat. Mater. 18 (2019) 280—288, https://doi.org/10.1038/s41563-018-0249-4.

[38] G.H. Ryu, J. Lee, D. Kang, H.J. Jo, H.S. Shin, Z. Lee, Effects of Dry Oxidation Treatments on Monolayer Graphene, 2012, pp. 1—10.

[39] N. Leconte, J. Moser, P. Ordejón, H. Tao, A. Lherbier, A. Bachtold, F. Alsina, C.M. Sotomayor Torres, J.C. Charlier, S. Roche, Damaging graphene with ozone treatment: a chemically tunable metal - insulator transition, ACS Nano 4 (2010) 4033—4038, https://doi.org/10.1021/nn100537z.

[42] M. Seifert, J.E.B. Vargas, M. Bobinger, M. Sachsenhauser, A.W. Cummings, S. Roche, J.A. Garrido, Role of grain boundaries in tailoring electronic properties of polycrystalline graphene by chemical functionalization, 2D Mater. 2 (2015) 1—10, https://doi.org/10.1088/2053-1583/2/2/024008.

[43] A. Eckmann, A. Felten, A. Mischenko, L. Britnell, R. Krupke, K.S. Novoselov, C. Casiraghi, Probing the nature of defects in graphene by Raman spectroscopy, Nano Lett. 12 (2012) 3925—3930, https://doi.org/10.1021/nl300901a.

[44] Y. Matsuda, W.Q. Deng, W.A. Goddard, Contact resistance for "end-contacted" metal-graphene and metal-nanotube interfaces from quantum mechanics, J. Phys. Chem. C 114 (2010) 17845—17850, https://doi.org/10.1021/jp806437y.

[45] W.S. Leong, H. Gong, J.T.L. Thong, Low-contact-resistance graphene, ACS Nano (2014), https://doi.org/10.1021/nn405834b.

[46] H. Yu, A. Kutana, B.I. Yakobson, Carrier delocalization in two-dimensional coplanar p-n junctions of graphene and metal dichalcogenides, Nano Lett. 16 (2016) 5032—5036, https://doi.org/10.1021/acs.nanolett.6b01822.

[47] P. Zhang, Y.Y. Lau, R.M. Gilgenbach, Analysis of current crowding in thin film contacts from exact field solution, J. Phys. D Appl. Phys. 48 (2015) 475501, https://doi.org/10.1088/0022-3727/48/47/475501.

[48] D.C. Kim, D.Y. Jeon, H.J. Chung, Y. Woo, J.K. Shin, S. Seo, The structural and electrical evolution of graphene by oxygen plasma-induced disorder, Nanotechnology 20 (2009), https://doi.org/10.1088/0957-4484/20/37/375703.

Improved metal-graphene contacts for low-noise, high-density microtransistor arrays for neural sensing

Nathan Schaefer[a,b†], Ramon Garcia-Cortadella[a,b†], Andrea Bonaccini Calia[a,b†], Nikolaos Mavredakis[b], Xavi Illa[c,d], Eduard Masvidal-Codina[c], Jose de la Cruz[a], Elena del Corro[a], Laura Rodríguez[a], Elisabet Prats-Alfonso[c,d], Jessica Bousquet[a], Javier Martínez-Aguilar[c,d], Antonio P. Pérez-Marín[a], Clement Hébert[e], Rosa Villa[c,d], David Jiménez[b], Anton Guimerà-Brunet[c,d] and Jose A. Garrido[a,f*]

[a] Catalan Institute of Nanoscience and Nanotechnology (ICN2), CSIC and The Barcelona Institute of Science and Technology, Campus UAB, Bellaterra, Spain
[b] Departament d'Enginyeria Electrònica, Escola d'Enginyeria, Universitat Autònoma de Barcelona, Bellaterra, Spain
[c] Instituto de Microelectrónica de Barcelona IMB-CNM (CSIC), Esfera UAB, Bellaterra, Spain
[d] Centro de Investigación Biomédica en Red en Bioingeniería, Biomateriales y Nanomedicina (CIBER-BBN), Madrid, Spain
[e] Inserm and Université Grenoble Alpes, Saint Martin d'Hères, France
[f] ICREA, Barcelona, Spain

† These authors contributed equally to this work

Supplementary Material

Expansion of S_{R_c} and $S_{R_{ch}}$ terms

Expanding the terms in Eq. 1 in the main text, the following general expression can be written for both contact and channel noise if homogeneous noise generation along the graphene sheet is not assumed.

$$S_R f = \int \frac{R_{sh}^2 k}{W^3} dx$$

<div align="right">Eq. S1</div>

When k is assumed independent of x, the right hand side of Eq. S1 becomes kR^2/A, which can also be expressed as $k'L/W^3$ as in Eq. 2 of the main text. The error made with this approximation for the channel noise term decreases away from the charge neutrality point [1]

(CNP) where charge is approximately homogenously distributed along the channel. In this case, $k_{R_{ch}}$ can take different values, depending on whether mobility fluctuations dominate or charge noise does. If noise is considered to follow Hooge's law, then $k_{R_{ch}} = \alpha_H R_{sh}^2$. On the other hand, if charge trapping-detrapping noise dominates, as previously shown for gSGFETs [1];

$$k_{R_{ch}} \approx \frac{K_B T\, N_T\, R_{sh}^2}{4\alpha\, n^2}$$

<div align="right">Eq. S2</div>

where k_B and T are the Boltzman constant and temperature, respectively, N_T the volumetric density of traps in the environment surrounding the channel, α is a tunneling constant and n the density of charge carriers in the channel [1,2].

For the case of contact noise, the approximation of homogeneous noise generation along the graphene sheet is not valid unless most of the current is injected at the graphene edge, as it migh occur for graphene-metal edge contacts [3,4]. Otherwise, the contribution from each local noise source along the contact has a significantly different contribution to the total contact noise. The dependence of contact noise on the charge transfer length (L_T) is derived in a following section. In any case, k_{R_c} is independent of the length of the channel, therefore Eq. 2 in the main text can be derived.

Finite Elements Method modelling of the metal-graphene contact

The potential distribution in a transmission line model can be solved numerically using finite elements method (FEM). Figure S1a-top shows the potential distribution in a model of such a contact. The three domains of the model shown in figure S1a correspond to the metal (top-domain), the graphene sheet under the metal (bottom-domain) and the metal-graphene interface resistance (middle-domain), as illustrated by the equivalent circuit shown in figure S1a-bottom. This non-homogeneous potential distribution leads to a non-homogeneous charge injection through the z-plane (i.e. metal-graphene interface). Figure S1b shows the current density in the z-direction (J_z) along the contact for different conductance values across the interface (G_z). It can be observed how the current density is larger in the vicinity of the metal edge, and this feature is more pronounced for higher G_z values. Similarly, the current density is more inhomogeneous for increasing R_{sh} values.
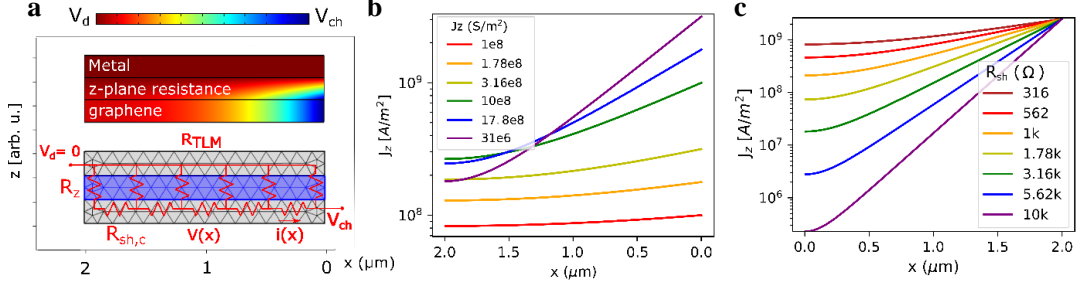
Figure S1: Finite elements method modelling of a transmission line metal-graphene contact. a. The FEM model of the TLM contacts is shown. The model consists of three domains accounting for the metal (top) for the metal graphene resistance (middle) and graphene (bottom). In the top image the voltage gradient in the contact is shown. A larger gradient is present in the vicinity of the channel (with potential V_{ch}). The schematic in the bottom shows the equivalent distributed elements circuit on top of the FEM model. R_z and $R_{sh,c}$ stand for the metal-graphene resistance and the graphene sheet resistance at the contact respectively. **b.** $J_z - x$ relationship for different values of conductance through the graphene-metal interface (G_z). **c.** $J_z - x$ relationship for different sheet resistance values for the graphene under the metal contacts.

Modelling the dependence of k_{R_c} on L_T

In the transmission line model (TLM) describing the metal-graphene interface, the charge injection is distributed non-homogeneously, as shown previously. This implies that changes in the resistance of the graphene sheet at different positions along the contacts have a different effect on the total resistance of the transmission line. Thus, R_c is a function of $R_{sh}(\mathbf{x})$. If R_{sh} is homogenous along the contact, the differential equation defining their relation can be solved analytically [5]. However, the differential equations defining the current flow through the graphene-metal interface, including fluctuations in R_{sh} at x=l (i.e. $\delta R_{sh}\,[\delta_{Dirac}(l = x)]$):

$$\frac{R_{sh} + \delta R_{sh}\,[\delta_{Dirac}(l = x)]}{W}\, i(l) = -\frac{dU(l)}{dl}$$

$$\frac{W}{R_g}\, U(l) = -\frac{di(l)}{dl}$$

Eq. S3a and S3b

which leads to:

$$U(l) - \frac{R_g}{R_{sh} + \delta R_{sh}\,[\delta_{Dirac}(l = x)]}\frac{d^2 U(l)}{dl^2} = 0$$

234

has, to our knowledge, no analytical solution. Therefore, the term $R_c(R_{sh}(x))$ must be determined numerically. For this purpose, we have modelled the transmission-line contact using finite elements method (FEM). The contact was divided in 50 parts and the effect of fluctuations in R_{sh} of each partition on R_c was evaluated to estimate $dR_c/dR_{sh}(x)$. The model was validated by doubling the number of parts and comparing the results (showing only a 1.1% difference). Having determined this term for different positions along the contact, it is possible to calculate how local fluctuations in the resistance of graphene propagate to resistance fluctuations in the total contact resistance. The power of the local contributions, weighted by the term $(dR_c/dR_{sh}(x))^2$, can be integrated along the contact length to determine S_{R_c}.

$$S_{R_c}f = \int_0^{L_c} \frac{kR_{sh}^2 dx}{W^3} \left(\frac{dR_c}{dR_{sh}(x)} \right)^2$$

Eq. S4

where k stands for the geometry independent terms, which depend on the origin of noise. If noise is caused by charge trapping-detrapping events, $k = \frac{K_B T \, N_T}{4\alpha \, n^2}$. In this way, local fluctuations in the sheet resistance in the vicinity of the metal edge cause a stronger contribution to the total contact noise as shown for different G_z values in figure 3d in the main text. It can be observed that the more confined the current density to the metal edge, the lower the integrated contributions to contact noise. Similarly, Figure S2 shows the effect of local fluctuations to total contact noise for different sheet resistance values. Again, higher resistance values, which lead to a more confined current density (i.e. smaller L_T) lead to a smaller total contact noise.
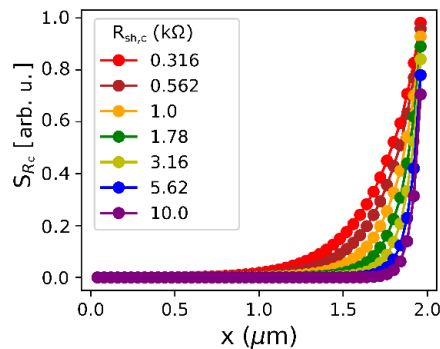

Figure S2: Local contributions to total contact noise along the contact length. The local contributions to contact noise are calculated using a discrete approximation of Eq. S3. The terms $(dR_c/dR_{sh}(x))^2$ are calculated using the FEM model shown in supplementary information S2, discretizing the contact in 50 parts.

Dominance of channel noise in gSGFETs with high R_{sh}

Contact resistance increases after reaching a minimum for excessively long UVO treatment times. This increase can be attributed to the creation of defects on the graphene sheet under the metal contacts. Nevertheless, this increase in R_{sh} is expected to further reduce the contact noise as described above. Figure S3a shows the dependence of the normalized integrated noise on the channel length for gSGFETs with contacts treated with UVO for 40 min, which led to an increased contact resistance. It is possible to validate that the relationship with L corresponds to a channel noise dominated regime. These results can be further supported by the bias dependence of the integrated noise in Figure S3b, which can be explained by the noise contribution from the channel in opposition to the contacts. The fact that contact noise does not increase with the density of defects in the graphene sheet at the contacts implies that noise origins in trapping-detrapping events. Nevertheless, the improvement of contact noise with the density of defects in the graphene sheet must have a limit, which is likely to be the rise of mobility noise for large density of defects.
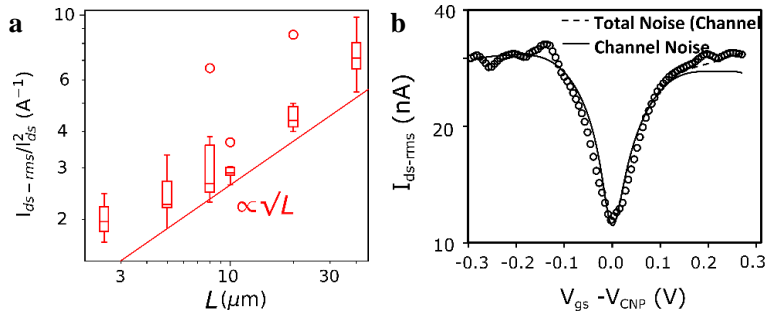

Figure S3: Dominance of channel noise in gSGFETs with increased contact resistance. a. The normalized integrated noise I_{ds-rms}/I_{ds}^2 for gSGFETs with contacts treated with UVO for 40 min is shown for different channel lengths. The red straight line indicates the $\propto \sqrt{L}$ trend corresponding to channel dominated noise. **b.** The V_{gs} bias dependence of I_{ds-rms} is shown for gSGFETs with a 5 μm long channel and contacts treated for 40 min with UVO.

Performance, repeatability and benchmarking of UVO treated gSGFET-array

Figure S4a and b show the transconductance G_m and the effective gate noise U_G^{rms} as a function of applied gate bias for the gSGFET array shown in figure 4 of the main text. Both represent the most important parameters for the gSGFET's performance, as the transconductance specifies the device's sensitivity and the effective gate noise sets it into

comparison with its current noise I_{ds}^{rms}. Both show a clear improvement with the UVO contact treatment, resulting in a strongly improved detection limit of the device. As repeatability is an essential criterium when introducing technology improvements for large-scale device fabrication, we also assessed the reliability of the UVO treatment to provide low contact resistance and reduced contact noise in gSGFETs. Therefore, the procedure has been applied to independent wafers undergoing identical process flows. Figure S4c compares the effective gate noise of UVO-treated and non-treated gSGFETS (all channel size of 20 μm x 20 μm) of several devices on independent wafers.
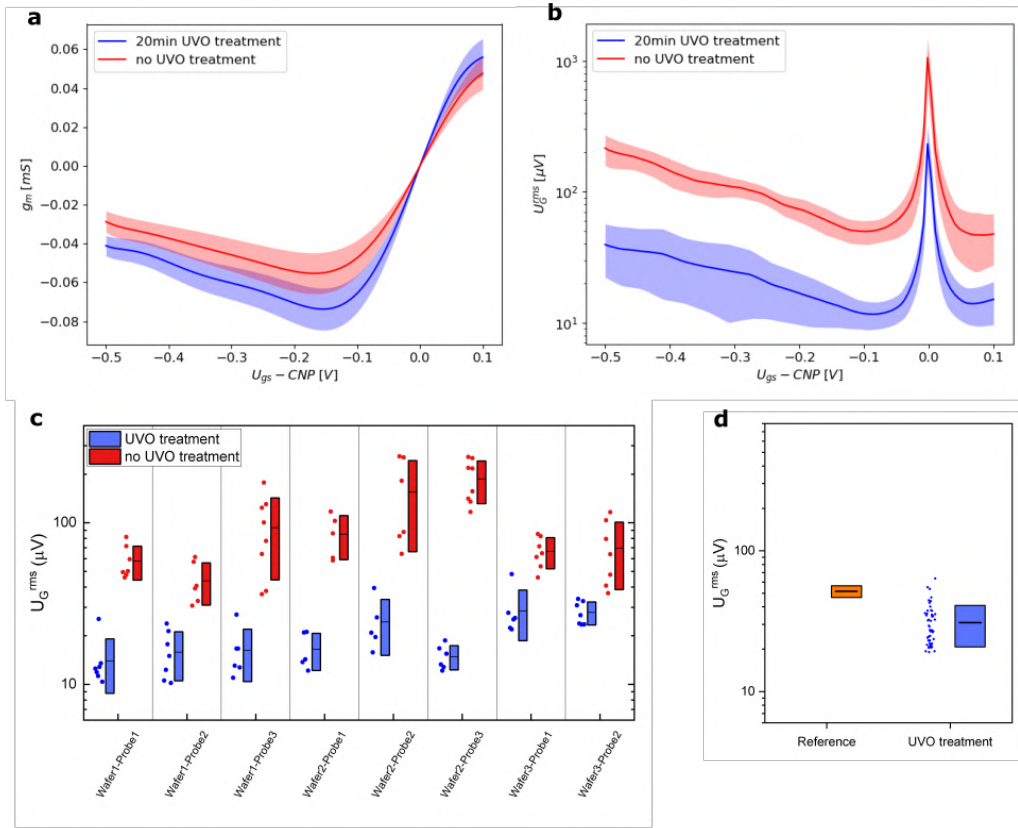

Figure S4: Repeatability of UVO treatment and comparison to previously reported noise values. Transconductance g_m (**a.**) and effective gate noise U_G^{rms} (**b.**) as a function of applied gate bias U_{gs} of the flexible gSGFET array in figure 4 of the main text. **c.** Comparison of the effective gate noise U_G^{rms} (integrated from 1 Hz to 100 Hz) for different gSGFET-arrays (all size 20 μm x 20 μm) across several wafers indicates the high repeatability of the technique. For each device group the mean value and standard deviation as well as the individual data points are shown. **d.** U_G^{rms} mean value (integrated from 1 Hz to 5 kHz) and standard deviation obtained with the UVO contact improvement presented in this work compared to previously reported noise values for gSGFETs with a sandwich contact configuration [6].

While small variations in measured noise values can be seen between different devices, which are attributed to non-identical graphene quality and changes in the amount of surface residues, the mean noise value of the UVO-treated gSGFETs always compares highly favorably towards the one of the untreated devices. In previous work [6], a mean effective gate noise value of 21 $\mu V \pm 2\ \mu V$ (integrated from 1 Hz to 5 kHz) has been reported for gSGFETs of size 30 μm x 80 μm. To compare this value to the one obtained for UVO-treated gSGFETs it has to be renormalized by a surface ratio term to account for the $\mathbf{1/\sqrt{A}}$ dependence of flicker-noise, yielding an expected mean effective gate noise of 52 $\mu V \pm 5\ \mu V$ for devices of size 20 μm x 20 μm. Figure S4d compares this predicted noise value to the ones measured for gSGFETs with the UVO contact improvement, showing the clear impact the treatment has on the noise performance

Graphene quality and homogeneity

The graphene quality has been characterized by Raman spectroscopy and scanning electron microscopy (SEM) on the sample on copper right after growth. Figure S5a and b shows SEM images of an open graphene layer for short growth time (2 min) and of a closed layer for the full growth duration (10 min). Domain sizes around 10 μm to 20 μm are clearly visible and result in a homogeneous single layer film with only minor amount of second nucleation.

Figure S5c compares the Raman spectra for regions of monolayer graphene and regions with second nucleation. Figure S5d displays the histogram of the 2D Raman peak width, Γ_{2D}, of a 30 μm x 30 μm mapping area, resulting in a median value of 30.4 cm^{-1}. To more carefully assess the homogeneity of the graphene film across the entire substrate, Raman maps in 3 different regions (left, center, right) of the 4.5 cm x 7 cm substrate have been collected periodically over many samples, resulting in a median Γ_{2D} of 33 cm^{-1} with a 6% increase towards the edges of the sample compared to the central region. A small Γ_{2D} value with a high homogeneity across the entire sample confirms the consistently low percentage of second nucleation and thus the high quality of the graphene film.
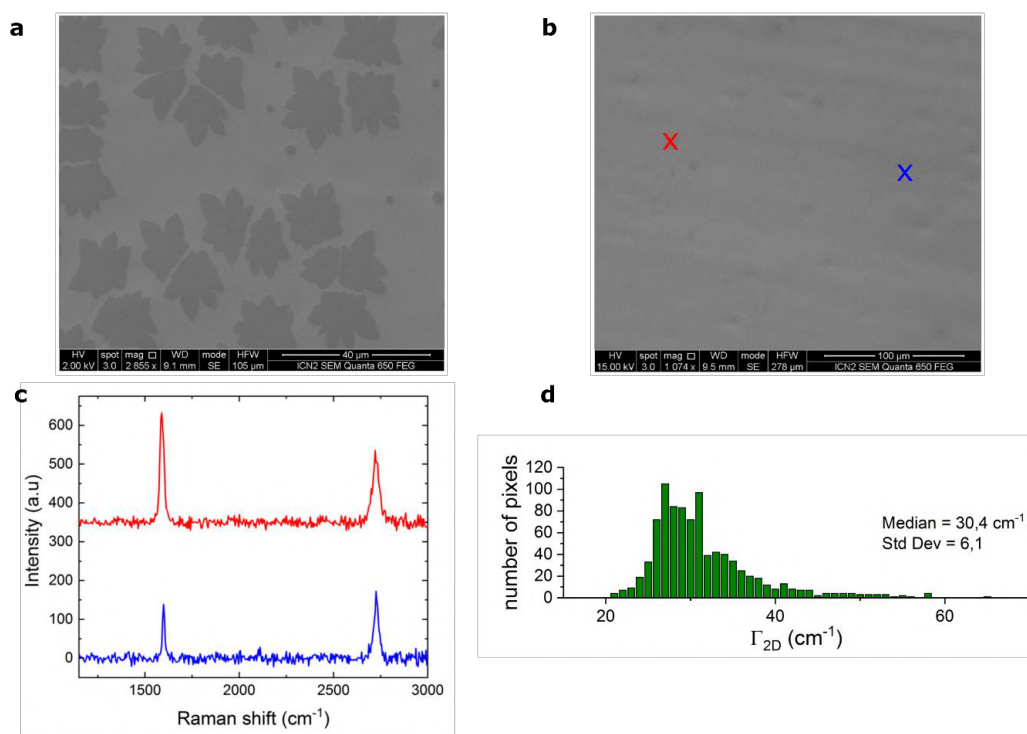
Figure S5: Raman and SEM analysis of graphene layer on copper. a. SEM picture of an open graphene layer after short growth time (2 min) showing domain sizes around 10 μm to 20 μm. **b.** SEM picture of a closed graphene layer after a full growth cycle (10 min). **c.** Typical Raman spectra for a region of single layer graphene (blue) and a region with second nucleation (red), crosses in figure S5b indicate positions. **d.** Histogram of the full-width half-maximum of the 2D Raman peak Γ_{2D} over an area of 30 μm x 30 μm in the center of the sample.

References

[1]   N. Mavredakis, R. Garcia Cortadella, A. Bonaccini Calia, J.A. Garrido, D. Jiménez, Understanding the bias dependence of low frequency noise in single layer graphene FETs, Nanoscale. 10 (2018) 14947–14956. https://doi.org/10.1039/C8NR04939D.

[2]   J.T. Smith, A.D. Franklin, D.B. Farmer, C.D. Dimitrakopoulos, Reducing Contact Resistance in Graphene Devices through Contact Area Patterning, ACS Nano. 7 (2013) 3661–3667. https://doi.org/10.1021/nn400671z.

[3]   D.W. Yue, C.H. Ra, X.C. Liu, D.Y. Lee, W.J. Yoo, Edge contacts of graphene formed by using a controlled plasma treatment, Nanoscale. 7 (2015) 825–831. https://doi.org/10.1039/c4nr05725b.

[4]   L. Wang, I. Meric, P.Y. Huang, Q. Gao, Y. Gao, H. Tran, T. Taniguchi, K. Watanabe, L.M. Campos, D.A. Muller, J. Guo, P. Kim, J. Hone, K.L. Shepard, C.R. Dean, One-

dimensional electrical contact to a two-dimensional material., Science. 342 (2013) 614–7. https://doi.org/10.1126/science.1244358.

[5]   Y. Tsividis, J. Milios, A detailed look at electrical equivalents of uniform electrochemical diffusion using nonuniform resistance–capacitance ladders, J. Electroanal. Chem. 707 (2013) 156–165. https://doi.org/10.1016/J.JELECHEM.2013.08.017.

[6]   C. Hébert, E. Masvidal-Codina, A. Suarez-Perez, A.B. Calia, G. Piret, R. Garcia-Cortadella, X. Illa, E. Del Corro Garcia, J.M. De la Cruz Sanchez, D.V. Casals, E. Prats-Alfonso, J. Bousquet, P. Godignon, B. Yvert, R. Villa, M. V. Sanchez-Vives, A. Guimerà-Brunet, J.A. Garrido, Flexible Graphene Solution-Gated Field-Effect Transistors: Efficient Transducers for Micro-Electrocorticography, Adv. Funct. Mater. 28 (2018) 1–15. https://doi.org/10.1002/adfm.201703976.

Nanoscale

Check for updates

Understanding the bias dependence of low frequency noise in single layer graphene FETs†

Nikolaos Mavredakis, [ID] *[a] Ramon Garcia Cortadella,[b] Andrea Bonaccini Calia,[b] Jose A. Garrido[b] and David Jiménez[a]

This letter investigates the bias-dependent low frequency noise of single layer graphene field-effect transistors. Noise measurements have been conducted with electrolyte-gated graphene transistors covering a wide range of gate and drain bias conditions for different channel lengths. A new analytical model that accounts for the propagation of the local noise sources in the channel to the terminal currents and voltages is proposed in this paper to investigate the noise bias dependence. Carrier number and mobility fluctuations are considered as the main causes of low frequency noise and the way these mechanisms contribute to the bias dependence of the noise is analyzed in this work. Typically, normalized low frequency noise in graphene devices has been usually shown to follow an M-shape dependence *versus* gate voltage with the minimum near the charge neutrality point (CNP). Our work reveals for the first time the strong correlation between this gate dependence and the residual charge which is relevant in the vicinity of this specific bias point. We discuss how charge inhomogeneity in the graphene channel at higher drain voltages can contribute to low frequency noise; thus, channel regions nearby the source and drain terminals are found to dominate the total noise for gate biases close to the CNP. The excellent agreement between the experimental data and the predictions of the analytical model at all bias conditions confirms that the two fundamental 1/f noise mechanisms, carrier number and mobility fluctuations, must be considered simultaneously to properly understand the low frequency noise in graphene FETs. The proposed analytical compact model can be easily implemented and integrated in circuit simulators, which can be of high importance for graphene based circuits' design.

Introduction

The outstanding characteristics of graphene such as its high carrier mobility and saturation velocity have attracted significant interest to use this material in future high-performance, high frequency electronics. Although its gapless nature renders it inappropriate for digital circuitry, it can result in a

[a]*Departament d'Enginyeria Electrònica, Escola d'Enginyeria, Universitat Autònoma de Barcelona, Bellaterra 08193, Spain. E-mail: nikolaos.mavredakis@uab.es*
[b]*Catalan Institute of Nanoscience and Nanotechnology (ICN2), CSIC, Barcelona Institute of Science and Technology, Campus UAB, Bellaterra, Barcelona, Spain*

†Electronic supplementary information (ESI) available: At first, a more detailed description of the theoretical derivation of both carrier number and mobility fluctuation models is provided. Then, Fig. S1 illustrates the behavior of graphene channel charge at every position of the channel under different bias conditions. After that, the analytical extraction of noise models without considering the residual charge is shown with Fig. S2 showing the local ΔN and $\Delta \mu$ noise contributions after neglecting ρ_0. Fig. S3 is shown which presents the 1/f noise results for the rest of channel lengths and drain voltages available. Then, the simplified $\sim(g_m/I_D)^2$ carrier number fluctuation model with and without correlated mobility fluctuation effect is derived for graphene and is presented in Fig. S4. Finally, Fig. S5 represents the $B = f \times \text{Area} \times S_{ID}/I_D{}^2$ factor which is crucial for comparison with other works. See DOI: 10.1039/c8nr04939d

tremendous performance boost in both analog and radio frequency (RF) applications.[1,2] In addition, graphene could also be successfully used in chemical and biological sensors[3–9] as well as in optoelectronic devices.[10] Such applications, though, are extremely prone to Low Frequency Noise (LFN) which can limit the sensitivity of sensors and can also be up-converted to undesired phase noise in voltage controlled oscillators. Furthermore, LFN is a very powerful tool for characterizing the quality and reliability of graphene devices.[11,12]

LFN is also referred to as 1/f (flicker) noise when its Power Spectral Density (PSD) is inversely proportional to frequency, which is usually the case in devices with channel lengths typically longer than few hundreds of nanometres. The capture and subsequent emission of charges at border traps near the dielectric interface of oxide semiconductors is the main effect responsible for the generation of LFN.[13] Each carrier that gets trapped causes a Random Telegraph Signal (RTS) in time domain, corresponding to a Lorentzian spectrum determined by a time constant. The high number of such Lorentzians in large devices and the uniform spatial distribution of these traps that results in a uniform distribution of time constants, are responsible for the 1/f behavior of noise. This noise

mechanism is called carrier number fluctuation effect (ΔN) and was first proposed by McWhorter.[14] This phenomenon is adequately described by a number of basic LFN models for metal–oxide–semiconductor field-effect transistors (MOSFETs) available in bibliography.[15–19] In addition to carrier number, mobility fluctuation ($\Delta\mu$) is also considered a main contribution to LFN in semiconductor devices and can be generated due to fluctuations in the scattering cross-section of scattering centres. This effect is described by the empirical Hooge formula.[20]

In this letter we focus on the effect of LFN on single layer graphene devices (GFETs) and more specifically on long channel solution-gated transistors,[21] which are broadly used in biosensing and bioelectronics applications (Fig. 1a) (details on the fabrication of these devices can be found in Experimental data section). A map of the 2D/G Raman bands intensity ratio and the average Raman spectrum over the graphene channel are shown in Fig. 1b and c respectively. According to the values of the 2D/G band intensity map, a low second nucleation density as well as a relatively good SLG homogeneity can be derived. The D/G ratio in the average spectrum indicates a low density of defects in the graphene channel. Flicker noise which prevails in these transistors, is of high interest because of its unique characteristics.[22] As a semimetal, graphene presents mobility fluctuations which can generate $1/f$ noise. On the other hand, single-layer graphene (SLG), as a 2D material is extremely prone to trapping effects leading to high amplitude carrier number fluctuations. In fact, a recent study illustrated that LFN can either be dominated by carrier number fluctuations (surface noise) or mobility fluctuations (volume noise) effect depending on the number of Graphene layers;[23] the lower this number the more dominant the surface LFN is. The addition of these two contributions, combined with the unusual transfer characteristics of graphene FETs and the noise originated at the contacts[24] leads to a rather complex dependence of noise on the gate voltage. More specifically, it has been stated that $1/f$ noise follows a V-shape dependence close to the Dirac or charge neutrality point (CNP) with the minimum of the V-shape at this gate voltage; this behavior can turn into an M-shape in case the gate bias is extended.[4,25–33] The gate dependence has been shown to strongly depend on the spatial charge inhomogeneity related to the presence of both electron and hole puddles near the CNP[31] and it has been observed in both top-gated[4,25–30] and back-gated[26–28,31–33] devices. We will also show that the charge inhomogeneity induced in graphene devices at higher drain voltage values, which is more intense at CNP, has a significant effect on the LFN. In case of GFETs on particular substrates such as boron nitride, not only $1/f$ noise is reduced in comparison to standard SiO_2 substrates but also the M-shape is eliminated or almost disappears.[31,32] It will be shown that the latter occurs in cases where less charge is induced by impurities near CNP, also known as residual charge.[34] Furthermore, flicker noise is shown to be reduced after the effect of electron-beam
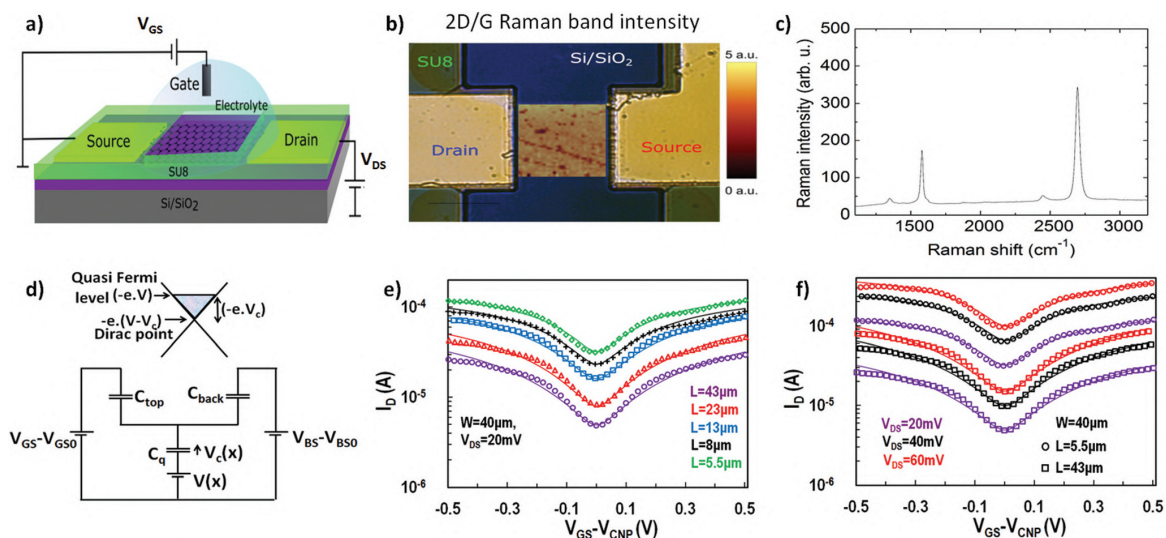

Fig. 1 (a) Schematic of a solution-gated GFET, (b) the colour scale indicates the 2D/G Raman band intensity ratio. The colour map overlapped with the optical image of the graphene transistor, represents the local value of the 2D/G ratio measured in the channel area. (c) Average Raman spectrum over the whole graphene channel. (d) Energy dispersion relation of a single layer GFET (top) and its capacitive network are shown with C_q: quantum capacitance, C_{top}, C_{back}: top and back oxide capacitances, $V_c(x)$: chemical potential, $V(x)$: quasi-Fermi channel potential, $V_{G(B)S} - V_{G(B)S0}$: top and back gate source voltage overdrives (back gate is not active in devices under test of (a) but is included in the capacitive network of (d) to support the generalizability of the model). Drain current I_D vs. top gate voltage ($V_{GS} - V_{CNP}$) measured in solution-gated GFETs with (e) $W = 40$ μm for different channel length values (L = 43, 23, 13, 8, 5.5 μm) at V_{DS} = 20 mV and (f) V_{DS} = 20, 40, 60 mV for L = 43, 5.5 μm. Symbols: Experimental data, solid lines: model.

irradiation[35] while the introduction of graded thickness throughout the graphene channel, with a single layer in the middle and two or more layers close to the contacts, also reduces 1/f noise whereas it still ensures a high mobility.[36] Classical Hooge formula alone cannot predict such M-shape behavior since residual charge does not play a significant role as it will be shown and this can only lead to a Λ-shape gate bias dependence.[37] On the other hand, V and M shapes can be explained in terms of carrier number fluctuations due to charge trapping/detrapping processes.[26,28]

There have been several attempts to model 1/f noise in GFETs considering either carrier number fluctuations[4,38–42] (ΔN) or mobility fluctuations effects[27] ($\Delta \mu$), while in some cases both effects have been taken into account simultaneously.[28] Usually noise models are taken from conventional Si devices[4,28,41,42] assuming that noise is homogeneously generated over the channel. This assumption is consequence of considering charge to be homogeneously distributed along the channel leading to a carrier number noise which is proportional to the transconductance.[4] In few reports, detailed formulas are derived; however, they are not compact[38–40] and, thus, they cannot be solved analytically by a circuit simulator. Finally, in some cases there is no validation of the proposed models with experimental data.[39–41] It is clear that there is still missing a complete approach that combines physics validity with analytical equations that can be easily integrated in a circuit simulator and provide fast and robust solutions.

Results and discussion

Thus, the main goal of this work is to propose a physics-based model which accounts for both carrier number and mobility fluctuation noise sources inhomogeneously distributed over the graphene channel and which can be solved analytically. Furthermore, we validate that the developed model can accurately capture the experimentally obtained M-shape gate dependence of 1/f noise data measured in solution-gated GFETs at different bias conditions and for several channel lengths. Residual charge, which is dominant near CNP, will be shown to be responsible for the M-shape dependence, however channel charge inhomogeneity is also found to be significant to the LFN minimum at CNP. As well as this, ΔN model is the main 1/f noise contributor for SLG FETs as it was expected[23] but $\Delta \mu$ also contributes near CNP. The contact resistance has a significant effect on 1/f noise at high gate voltages because of the increased and bias dependent contact resistance experimentally observed in this regime.[24] The model also works properly for data from solid-gated GFETs taken from bibliography.[30,32,33]

The basic methodology for the derivation of the physics-based 1/f noise equations in this work is based on a procedure developed for MOSFET devices.[15,19,43,44] The implementation of a correct 1/f noise model requires the existence of a reliable current–voltage (I–V) model that can qualitatively capture the bias dependence of the drain current of the device. Since LFN

expresses the fluctuation of current, thus the absolute current has to be well described. The model for 1/f noise in GFETs has been implemented considering the chemical potential based compact model reported in ref. 45 and 46. According to this model, a GFET can be represented by the equivalent capacitive circuit shown in Fig. 1d. Graphene charge Q_{gr} is stored in the quantum capacitance (C_q); the chemical potential $V_c(x)$ represents the voltage drop across C_q at position x. $V_c(x)$ is defined as the difference between the potential at quasi-Fermi level and the potential at the CNP, as shown in the energy dispersion relation scheme of graphene in Fig. 1d where $V_c(0) = V_{cs}$ at the source end ($x = 0$) and $V_c(L) = V_{cd}$ at the drain end ($x = L$). $V_{GS} - V_{GS0}$, $V_{BS} - V_{BS0}$ are the top and back gate source voltage overdrives while C_{top} and C_{back} are the top and back gate capacitances, respectively. The quasi-Fermi potential $V(x)$ is the voltage drop in the graphene channel at position x, which is equal to zero at the source end ($x = 0$) and equal to V_{DS} at the drain end ($x = L$).

Drain-to-source current and 1/f noise spectra were measured in single layer, top liquid-gated GFETs with $W = 40$ μm and five different channel lengths ($L = 43, 23, 13, 8, 5.5$ μm) (see Experimental data section). Data were obtained from 4 samples for $L = 5.5, 8, 23$ μm, 3 samples for $L = 13$ μm and 2 samples for $L = 43$ μm, at three different drain voltage levels ($V_{DS} = 20, 40$ and 60 mV). Top gate potential was swept from $V_{GS} = -0.4$ to 0.6 V with a step of 20 mV, covering the whole range from strong p-type conduction to strong n-type conduction. These extended bias conditions allowed a thorough examination of 1/f noise at all the operation regimes. The measured frequency range from 1.5 Hz up to 1.5 kHz. Fig. 1e and f confirm the excellent agreement of the drain current model and the experiment for all bias and geometry conditions. The compact model reported in ref. 45 and 46 was used to fit the experimental data obtained from the investigated solution-gated FETs. The values of the model parameters extracted from the fitting of the experimental data are shown in Table 1. The fundamental parameters which are going to be used in noise equations are the carrier mobility (μ), the residual charge density (ρ_0), the top gate capacitance (C_{top}), the contact resistance (R_c) and the flat band top gate voltage (V_{GS0}). One parameter set is used for all bias conditions at each channel length; even for different channel lengths, the parameters are quite close to each other. Fig. 2a shows the measured spectra of the $L = 23$ μm devices at $V_{DS} = 40$ mV where it can be observed the 1/f dependence of noise amplitude. LFN can be originated by the local random fluctuations of the carriers' density and of the mobility which correspond to the above described ΔN and $\Delta \mu$ effects, respectively. We develop a physics-based analytical model describing these effects, considering the channel of the device divided into elementary slices.[43] Here, the chemical potential based analytical current model will be used to define the conditions at each channel slice. The fluctuations generating LFN are always small and, consequently, the analysis of the propagation of the noise sources to the voltages or currents at the contact terminals reduces to linear analysis. Therefore, the principle of

Table 1 Drain current and 1/f noise model parameters

| Parameter	Units	$L = 43$ μm	$L = 23$ μm	$L = 13$ μm	$L = 8$ μm	$L = 5.5$ μm	Ref. 30	Ref. 32	Ref. 33
μ	cm^2 (V s)$^{-1}$	3400	3250	3400	3400	3600	950	3000	4500
C_{top}	μF cm^{-2}	1.9	1.9	2.05	2.05	2.2	0.65	$C_{back} = 1,9.10^{-2}$	$C_{back} = 1.15 \times 10^{-2}$
V_{GS0}	V	0.09	0.09	0.095	0.095	0.095	0	$V_{BS0} = 7,75$	$V_{BS0} = 4$
ρ_0	cm^{-2}	$5 \cdot 10^{11}$	4.6×10^{11}	5.3×10^{11}	5×10^{11}	4.8×10^{11}	5.9×10^{12}	1.3×10^{13}	1.2×10^{11}
R_c	Ω	120	120	120	120	120	—	—	—
N_T	eV^{-1} cm^{-3}	1.3×10^{20}	1.1×10^{20}	1×10^{20}	9×10^{19}	5.5×10^{19}	3×10^{20}	3.5×10^{21}	2×10^{20}
α_H	—	1.5×10^{-3}	1.3×10^{-3}	1.3×10^{-3}	1.2×10^{-3}	1.1×10^{-3}	3×10^{-3}	7×10^{-3}	3×10^{-4}
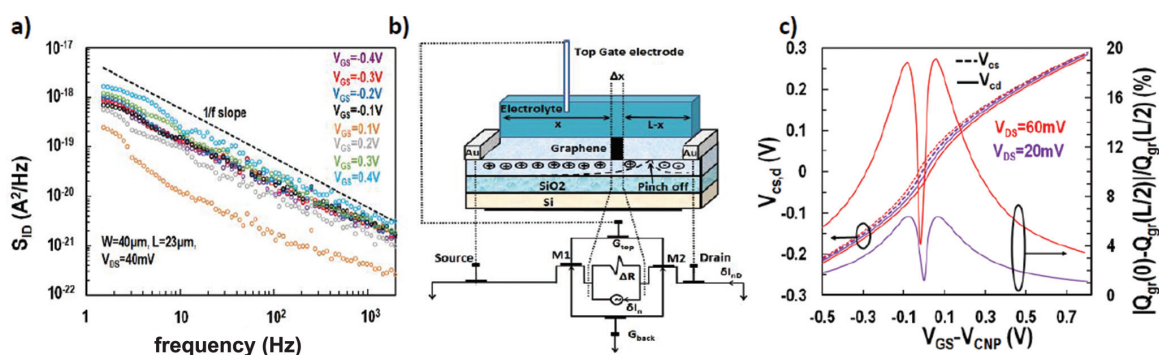
Fig. 2 (a) Relative power spectral density of drain current noise S_{ID} for solution top-gated GFETs with $W = 40$ μm and $L = 23$ μm at $V_{DS} = 40$ mV for different top gate voltage values ($V_{GS} = -0.4, -0.3, -0.2, -0.1, 0.2, 0.3, 0.4$ V); the dashed line corresponds to a 1/f slope. (b) Device cross-section. The equivalent circuit for a local current noise contribution to the total noise is illustrated. Each noise-generating slice of the channel is connected to two noiseless GFETs, M1 and M2 respectively. The local current noise source (δI_n) generates a δI_{nD} current fluctuation at the drain. (c) Chemical potential V_c (left y-axis) and the relative fluctuation of graphene charge $|Q_{gr}(0) - Q_{gr}(L/2)|/Q_{gr}(L/2)$ (right y-axis) from the beginning ($x = 0$) to the middle ($x = L/2$) of the channel are plotted vs. top gate voltage overdrive ($V_{GS} - V_{CNP}$) for two drain voltage values of 20 and 60 mV.

superposition can be used for adding the effects of the local noise sources along the channel.[43] These local fluctuations can be modeled by adding a random local current noise source δI_n with a PSD $S\delta I^2_n$ as shown in Fig. 2b. The local fluctuations propagate to the terminals resulting in fluctuations of the voltages and currents around the DC operating point. The local noise sources are assumed to be spatially uncorrelated and, therefore, their PSDs can be summed. For detailed explanation of the general methodology, see ESI A.†

The model considers a non-homogeneous charge distribution along the device channel, according to the physics of GFET, making this approach more realistic. Fig. 2c illustrates, in left y-axis, the chemical potential $V_{cs,d}$ at source and drain terminal respectively, calculated by the employed current model,[45,46] vs. top gate voltage overdrive at the lower and higher drain voltage values used in the experiments ($V_{DS} = 20$, 60 mV). As predicted by the model, V_{cd} approaches V_{cs} for low V_{ds} values. This effect can be justified from the larger charge homogeneity in the channel at low drain voltage; under these bias conditions V_c is approximately the same at every position in the graphene channel. At $V_{DS} = 60$ mV, the channel charge non-homogeneity increases with respect to a $V_{DS} = 20$ mV and as a result, V_{cd} differs more significantly from V_{cs} especially around CNP (see Fig. 2c). At high gate voltages the difference between V_{cd} and V_{cs} becomes less important even for the

higher drain voltages, which indicates that the non-homogeneity of the channel is more pronounced near CNP. In the right y-axis of Fig. 2c, the relative fluctuation of $Q_{gr}(x)$ from source terminal to the middle of the channel, $|Q_{gr}(0) - Q_{gr}(L/2)|/Q_{gr}(L/2)$ (%), is shown vs. top gate voltage overdrive for the same drain voltages ($V_{DS} = 20$, 60 mV). The homogeneity of the channel for the small V_{DS} away from V_{CNP} is clear since the observed relative fluctuation of $Q_{gr}(x)$ is insignificant (~1%). As we approach CNP, this fluctuation increases since the channel starts to become non-homogeneous even for this small V_{DS}. At abs($V_{GS} - V_{CNP}$) ≈ 0.1 V, the relative fluctuation of $Q_{gr}(x)$ reaches its maximum value (~6%) and then it starts to decrease leading to an M-shape behavior similar to that observed in LFN data. This can be justified in terms of the residual charge ($e \cdot \rho_0 = 8 \times 10^{-8}$ C cm^{-2}) which starts to contribute to $Q_{gr}(x)$ at this operating point. At V_{CNP}, ρ_0 is dominant at almost every position of the channel and this leads to the minimum of the relative fluctuation of $Q_{gr}(x)$ observed for the low V_{DS} value (~1%). For the higher V_{DS}, an M-shape is also observed for the relative fluctuation of $Q_{gr}(x)$ from source terminal to the middle of the channel but the more intense non-homogeneity leads to higher values. More specifically, the maximum values of the relative fluctuation at abs($V_{GS} - V_{CNP}$) ≈ 0.1 V are almost ~20%. At V_{CNP}, the effect of ρ_0 decreases the relative fluctuation at a minimum value of ~4% which is sig-

nificantly higher than the minimum observed at CNP for the lower V_{DS}. This also occurs because of the inhomogeneity of the channel at the higher V_{DS}. For detailed explanation of the behaviour and value of $Q_{gr}(x)$ at every channel position x under different bias conditions, see ESI B (Fig. S1†).

Considering the carrier number fluctuation effect, if a certain number of carriers is trapped at channel position x, the relative current fluctuation can be calculated as:

$$\frac{\delta I_D(x)}{I_D} = \frac{\delta N_{gr}}{N_{gr}} = \frac{1}{N_{gr}}\frac{\delta Q_{gr}}{\delta Q_t}\delta N_t \tag{1}$$

for $V_{cs,cd} > 0$,

$$KD\bigg|_{\Delta N} = \frac{1}{(\alpha k + C^2)}\left[\alpha k \ln(\alpha + kV_c^2) - 2\alpha k \ln(\alpha) + 2C^2 \ln(C + kV_c) - 4C^2 \ln(C) - 2\sqrt{\alpha k}C\cdot \arctan\left(\sqrt{\frac{k}{a}}V_c\right)\right]_{V_{cd}}^{V_{cs}}$$

for $V_{cs,cd} < 0$,

$$KD\bigg|_{\Delta N} = \frac{1}{(\alpha k + C^2)}\left[-\alpha k \ln(\alpha + kV_c^2) - 2C^2 \ln(C - kV_c) - 2\sqrt{\alpha k}C\cdot \arctan\left(\sqrt{\frac{k}{a}}V_c\right)\right]_{Vcd}^{V_{cs}} \tag{2}$$

where N_{gr} is the graphene carrier density and Q_t, N_t are the trapped charge and density respectively; charges and number of carriers are expressed per unit area since they are referred to a channel slice. Fluctuations of the trapped charge δQ_t can cause a variation in the chemical potential δV_c which can lead to a change of charges that depend directly on the chemical potential such as the graphene charge, the top gate and the back gate charge. By applying charge conservation law and by considering a linear dependence of the quantum capacitance C_q and the chemical potential $V_c(C_q = k\cdot/V_c/)$,[45,46] with k defined in ESI A,† the following expression is derived:

$$\frac{\delta I_D(x)}{I_D} = \frac{e}{Q_{gr}}\frac{C_q}{C_q + C_{top} + C_{back}}\delta N_t \tag{3}$$

and the PSD of the local noise source normalized by squared drain current can then be calculated as (see ESI A†):

$$\frac{S_{\delta I_n^2}}{I_D^2}\bigg|\Delta N = \left(\frac{e}{Q_{gr}}\frac{C_q}{C_q + C_{top} + C_{back}}\right)^2\frac{KT\lambda N_T}{W\Delta x f} \tag{4}$$

where N_T is the dielectric volumetric trap density per unit energy (in $eV^{-1} cm^{-3}$) which is used as a fitting parameter, K is the Boltzmann constant, T is the absolute temperature, e the electron charge, $\lambda \sim 0.1$ nm is the tunneling attenuation distance since the trapping/detrapping mechanism is considered a tunneling process. The analysis of this process is difficult at atom level, thus the best possible approach is to model the capture cross-section according to $P(z) = \exp(-z/\lambda)$, where P is the tunnelling probability of a carrier to get captured by a trap located at a barrier depth z into the dielectric. C_{back} is not defined for the measured devices in this work but is included in the equations for better generalizability of the proposed model. By integrating the PSD of the local noise source in the entire channel length[41] and by changing the integration vari-

able from length to chemical potential at source and drain terminals,[45,46] it is possible to derive the following analytical formula for the relative PSD of the total fluctuation of the drain current resulting from a carrier density fluctuation ΔN:

$$\frac{S_{I_D}}{I_D^2}f|\Delta N = \frac{SD|\Delta N\cdot KD|\Delta N}{[g(V_C)]_{V_{cs}}^{V_{cd}}} \tag{5}$$

$SD/_{\Delta N} = 2\cdot KT\cdot\lambda\cdot N_T\cdot e^2/(C\cdot WL\cdot k)$ is a bias independent term representing the amplitude of the ΔN effect noise, where $C = C_{top} + C_{back}$. $KD/_{\Delta N}$ is a bias dependent term of the ΔN model and is defined by eqn (2), where $\alpha = 2\cdot\rho_0\cdot e$. Finally, $g(V_c)$ is a bias dependent term proportional to the drain current[45,46] (see also ESI A†). As far as the mobility fluctuation effect is concerned, by using a methodology identical to the presented above, the following analytical formula is obtained:

$$\frac{S_{I_D}}{I_D^2}f|\Delta\mu = \frac{SD|\Delta\mu\cdot KD|\Delta\mu}{[g(V_C)]_{V_{cs}}^{V_{cd}}} \tag{6}$$

$$\text{for } V_{cs,cd} > 0, KD\bigg|_{\Delta\mu} = \left[CV_c + \frac{kV_c^2}{2}\right]_{V_{cd}}^{V_{cs}}$$

$$\text{for } V_{cs,cd} < 0, KD\bigg|_{\Delta\mu} = \left[CV_c - \frac{kV_c^2}{2}\right]_{V_{cd}}^{V_{cs}} \tag{7}$$

(see ESI A†). The bias dependent term $KD/_{\Delta\mu}$ is given by eqn (7) where residual charge related term α does not play any role and $SD/_{\Delta\mu} = 2\cdot\alpha_H\cdot e/(C\cdot WL\cdot k)$ where α_H is the unitless Hooge parameter which is used as a fitting parameter. In order to calculate the total $1/f$ noise of the device, the two different contributions have to be added as:

$$\frac{S_{I_D}}{I_D^2} = \frac{S_{I_D}}{I_D^2}\bigg|_{\Delta N} + \frac{S_{I_D}}{I_D^2}\bigg|_{\Delta\mu}. \tag{8}$$

The strong dependence of $1/f$ noise on both residual charge and channel charge inhomogeneity makes it essential to thoroughly investigate these phenomena. Fig. 3a illustrates the dependence of the two $1/f$ noise models, ΔN and $\Delta\mu$, on the residual charge and Fig. 3b on the drain voltage. In Fig. 3a the contributions of both noise mechanisms ΔN and $\Delta\mu$ are shown for different values of the residual charge density ρ_0 at $V_{DS} = 20$ mV. The value $(4.6 \times 10^{11} cm^{-2})$ corresponds to the value experimentally extracted from fitting the $I-V$ data (see Fig. 1e and f). In addition, the model is tested at three other lower values of ρ_0 $(3 \times 10^{11}, 4.6 \times 10^{10}, 0 cm^{-2})$. It can be con-
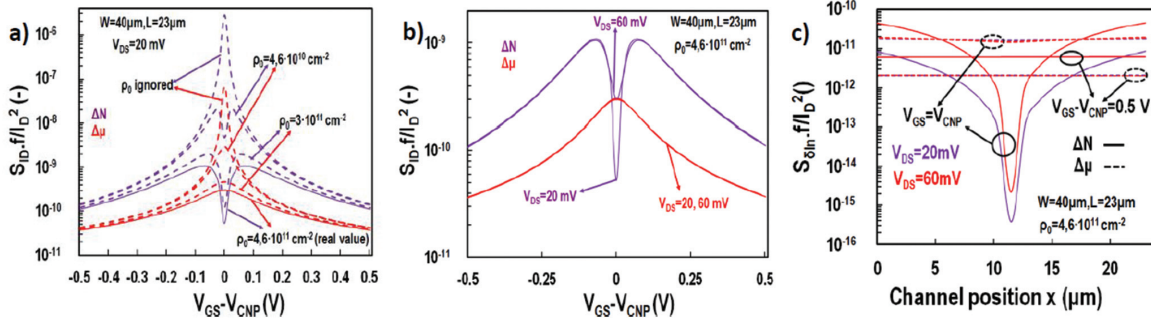
Fig. 3 Output current noise divided by squared drain current, S_{ID}/I_D^2, referred to 1 Hz, *vs.* top gate voltage overdrive $V_{GS} - V_{CNP}$ for solution top-gated GFETs. (a) ΔN and $\Delta\mu$ effects at $V_{DS} = 20$ mV for four different values of residual charge (ρ_0) and for $W/L = 40$ μm/23 μm. (b) ΔN and $\Delta\mu$ contributions for two V_{DS} values (20, 60 mV). The experimental ρ_0 value (4.6×10^{-11} cm^{-2}) extracted from the current data is used for the calculations. (c) Normalized PSD of the local noise, $S_{\delta In}/I_D^2$, referred to 1 Hz, *vs.* channel position x.

cluded from Fig. 3a that the ΔN effect is responsible for the M-shape bias dependence in case of relatively high ρ_0 values are considered (see Fig. 2c) while for low ρ_0 values, a Λ shape behavior is obtained. $\Delta\mu$ model always provides an Λ shape behavior with an increased maximum at CNP as ρ_0 decreases since ρ_0 only affects normalized drain current term $g(V_c)$ in eqn (6) and not the bias dependent term $KD/_{\Delta\mu}$ of eqn (7) (for more information, see ESI C†). Regarding the drain voltage dependence, Fig. 3b indicates that the increase of V_{DS} (20, 60 mV) increases the contribution of the ΔN noise near the CNP resulting from the increased graphene charge inhomogeneity observed at higher V_{DS} (see Fig. 2c) while $\Delta\mu$ noise remains unaffected. At higher gate voltages no drain voltage dependence can be observed by any of the noise mechanisms confirming that Q_{gr} is homogeneous at high V_{GS} values. According to Fig. 2c, V_{cs}, V_{cd} are very close for higher V_{GS} values and since eqn (2), (5)–(7) show that the bias dependence of both noise mechanisms ΔN and $\Delta\mu$, is exclusively expressed in terms of chemical potentials V_{cs}, V_{cd}, the drain voltage independence of both ΔN and $\Delta\mu$ noise mechanisms for higher gate voltages can be explained. In Fig. 3c, the local noise at each channel position x is shown at $V_{GS} = V_{CNP}$ and at $V_{GS} - V_{CNP} = 0.5$ V for both noise mechanisms ΔN and $\Delta\mu$, as it is calculated by eqn (4) and (A12)† respectively for $V_{DS} = 20$, 60 mV. At V_{CNP}, the total noise ΔN propagated to the terminals is mainly determined by the local noise at the source/drain ends while away from CNP, all the points along the channel contributes equally. This proves the homogeneity of the channel at higher gate voltages while the different contributions of the charge distributed along the channel at V_{CNP} indicate the channel inhomogeneity close to CNP, especially for the higher V_{DS}, as described in Fig. 2c. Regarding $\Delta\mu$ noise, all the points of the channel contribute similarly at every bias condition. By summing the local ΔN and $\Delta\mu$ noise sources throughout the channel, we can accurately obtain the values of the total ΔN and $\Delta\mu$ noise PSD as calculated by eqn (5) and (6) and as shown in Fig. 3b for the operating conditions under study. The effect of ρ_0 in the local LFN is shown in ESI C.†

Fig. 4 shows the experimental noise data averaged in the bandwidth of 10–40 Hz, referred to 1 Hz. The data are fitted using the same parameters extracted from the current compact model and adjusting only the N_T and α_H values. Fig. 4a and b present the normalized noise data for transistors with two different channel lengths, $L = 43$ μm and $L = 5.5$ μm, respectively, at two drain voltage values (20 and 60 mV). Fig. 4c shows the fitted normalized noise data for two other channel lengths (23 and 8 μm) at all the drain voltage values (20, 40, 60 mV) (see Fig. S3 in ESI D† for the complete set of data). The symbols correspond to the experimental data and the solid lines represent the total $1/f$ noise model. The well-known M-shape trend is observed in our data near the CNP. The change in the minimum value at the CNP with V_{DS} caused by the charge inhomogeneity is also properly described. Away from the CNP, the measured noise is independent on the drain voltage and the model follows this trend as well. Dashed lines representing the different $1/f$ noise contributors in Fig. 4a and b, provide additional insights on the contributions of the different noise mechanisms. The dotted lines in Fig. 4a present the simplified $(g_m/I_D)^2$ model[16,17] (see ESI E, Fig. S4†) for both drain voltages available. It is apparent that the specific approach cannot capture the drain voltage dependence of LFN near CNP since it considers a uniform charge along the channel. The ΔN mechanism is responsible for the M-shape, as it was shown previously in Fig. 3a. Despite the fact that the ΔN model can predict the drain voltage dependence near CNP, it significantly underestimates the minimum of noise near the CNP. On the other hand, the $\Delta\mu$ model predicts a Λ-shape dependence with the gate bias which is independent on the drain voltage. This term can have a significant effect near CNP, setting a minimum noise value that helps to fit better the experimental data (see Fig. 4a and b). The distinction of the ΔN and $\Delta\mu$ contributions near the CNP is shown in this work for the first time. The normalized noise increases with decreasing device area, as it is apparent in Fig. 4c; this is expected since $1/f$ noise is known to scale inversely proportional with the device dimensions. As it can be derived
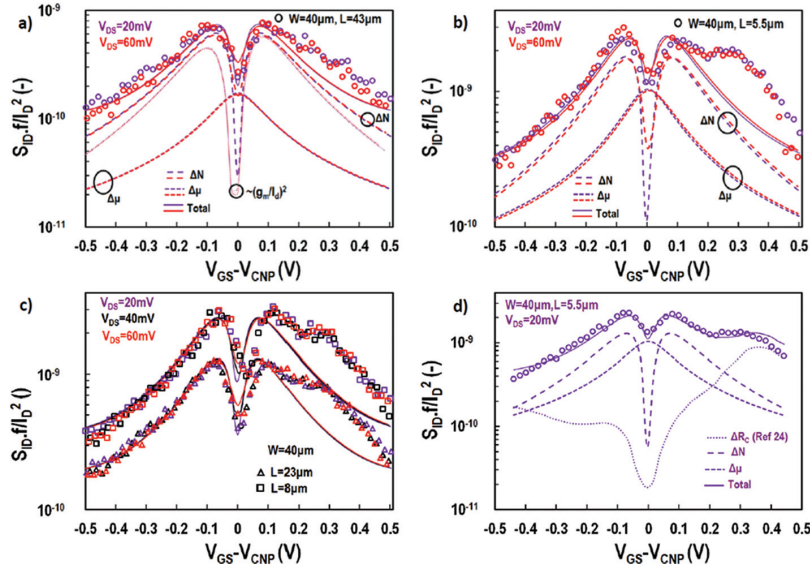
Fig. 4 Output noise divided by squared drain current S_{ID}/I_D^2, referred to 1 Hz, *vs.* top gate voltage overdrive ($V_{GS} - V_{CNP}$), for solution top-gated GFETs with W = 40 μm. (a) Data from transistors with a channel length L = 43 μm and V_{DS} = 20 and 60 mV. The experimental data is fitted with the derived compact model (the ΔN and $\Delta \mu$ contributions are displayed separately). The simplified $(g_m/I_D)^2$ noise model[4,16,17] (ESI E, eqn (A24)),† which considers charge homogeneous along the channel is plotted with dotted lines for both V_{DS} values. (b) Data from transistors with an L = 5.5 μm and V_{DS} = 20 and 60 mV. A fitting of the data and the individual contributions from ΔN and $\Delta \mu$ are also plotted. (c) Data from transistors with a channel length L = 23 μm and 8 μm at V_{DS} = 20, 40 and 60 mV is plotted together with the fitting provided by the analytical model. (d) Experimental data from transistors with L = 5.5 μm and V_{DS} = 20 mV is shown. A contact noise term[23] (dotted line) is added to the compact model to correct the deviations from experimental data away from the CNP.

from eqn (5) and (6). The higher noise measured in the n-type conduction regime, more pronounced at higher gate voltages and at shorter channel lengths, is tentatively attributed to the bias dependent contact resistance experimentally observed in this bias regime.[24] Fig. 4d shows the model corrected to include a contact noise contribution[24] as reported previously. To calculate the magnitude of this contribution, the contact resistance has been calculated using a transmission line method (TLM) analysis. The contact noise model used to refine the fitting of the experimental noise also proves that contact noise is negligible near the CNP. All the extracted $1/f$ noise parameters are shown in Table 1; it is important to highlight that for a fixed channel length, the same parameters are used to fit the whole range of bias conditions. Regarding the level of normalized $1/f$ noise, the values of the extracted noise parameters are in the same order of magnitude or lower than what is available in bibliography for graphene devices. The α_H parameter is lower than many reports[28,30,37] even considering that the Hooge model underestimates $1/f$ noise, since the ΔN effect is more dominant as shown in Fig. 4. In some reports,[4,42] the N_T parameter is also derived and it is quite comparable with the values in Table 1; still, N_T is higher than its typical range at Si devices ($N_T \sim 10^{16} - 10^{18}$ eV^{-1} cm^{-3}).[19,43] The noise amplitude $B = f \cdot \text{area} \cdot S_{ID}/I_D^2$, can be easily found to range from $10^{-7} - 10^{-6}$ μm^2 in the present work (see Fig. S5 in ESI F†), which is similar or lower in comparison with other works.[4,28,29,33,37,38]

In order to confirm the generalizability of the proposed model, we have tested it with datasets of three solid gated GFETs taken from literature.[30,32,33] Fig. 5a shows the S_{ID}/I_D^2 noise data for a top-gated device with W/L = 12 μm/0.35 μm from ref. 30 (Fig. 4b, T = 300 K) at V_{DS} = 0.2 V, Fig. 5b presents the S_{ID}/I_D^2 noise data for a back-gated device with W/L = 6.3 μm/2.1 μm from ref. 32 (Fig. 4a, Si/SiO$_2$ data) at V_{DS} = 0.01 V and Fig. 5c illustrates the S_{VD}/V_D^2 $1/f$ noise data for a back-gated GFET with W/L = 12.7 μm/11 μm from ref. 33 (Fig. 3b, T = 1.6 K) at V_{DS} ∼ 0.6 mV. The two different representations of normalized noise displayed in Fig. 5 (S_{ID}/I_D^2 and S_{VD}/V_D^2) are equivalent. The symbols represent the measurements and the total model is shown by the solid lines, the ΔN and $\Delta \mu$ contributions are also shown with dashed and dotted lines respectively. Regarding Fig. 5a where the M-shape dependence of noise is also observed, the total model behavior is acceptable. Additionally, both ΔN and $\Delta \mu$ effects have a significant contribution especially near CNP, similarly as in Fig. 4. In Fig. 5b, the M-shape dependence of noise is intense probably due to a higher residual charge value and our model captures well this shape. ΔN effect is the dominant noise source while $\Delta \mu$ effect has a small contribution near CNP. The LFN data in Fig. 5b are asymmetrical with an increased value at p-type region while our model is equivalent in both n- and p-regions. We extracted the noise parameters by targeting a better performance in n-type conduction but we could achieve an overall
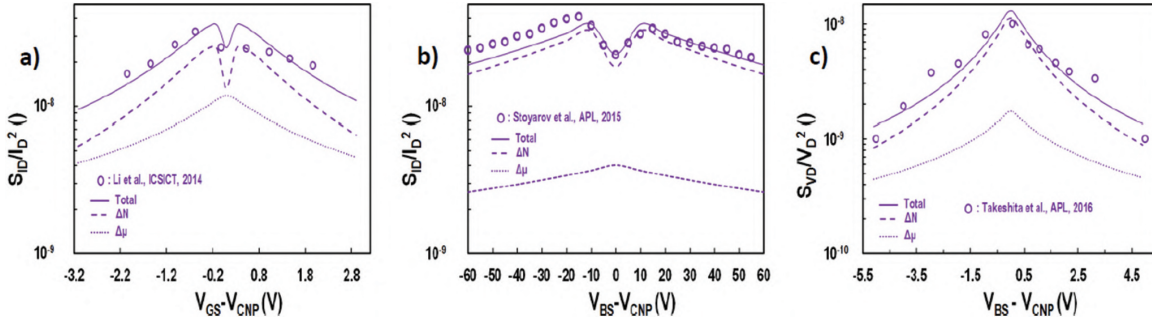
Fig. 5 (a) Output current noise divided by squared drain current S_{ID}/I_D^2, referred to 1 Hz, *vs.* top gate voltage overdrive ($V_{GS} - V_{CNP}$), for a top-gated GFETs with W/L = 12 μm/0.35 μm at V_{DS} = 0.2 V (ref. 30). (b) Output current noise divided by squared drain current S_{ID}/I_D^2, referred to 1 Hz, *vs.* back gate voltage overdrive ($V_{BS}-V_{CNP}$), for a back-gated GFETs with W/L = 6.3 μm/2.1 μm at V_{DS} = 0.01 V (ref. 32). (c) Output voltage noise divided by squared voltage potential S_{VD}/V_D^2, referred to 1 Hz, *vs.* back gate voltage overdrive ($V_{BS}-V_{CNP}$), for a back-gated GFETs with W/L = 12.7 μm/11 μm at V_{DS} ~ 0.6 mV (ref. 33). Symbols: Data,[30,32,33] solid line: model, dashed lines: different noise contributions, ΔN and $\Delta\mu$.

better fitting by using different LFN parameters below and above CNP. Finally, Fig. 5c shows that the 1/f normalized noise follows a Λ-shape behavior. By fitting the noise curve with our model, it is possible to distinguish between the ΔN and the $\Delta\mu$ effects due to the different slopes of their curves. This finding can be explained by the relatively small value of the residual charge ρ_0 = 1.2 × 10^{11} cm^{-2} in this device. The parameters extracted are also presented in the last three columns of Table 1. For all devices, the N_T parameter is a little higher than the ones extracted for our dataset. Regarding the α_H parameter, it is in the same level as in our data set for the plot in Fig. 5a while it is quite lower in the Fig. 5b but in this case the error of the fitting can be quite significant.

Conclusions

In conclusion, this paper investigates the bias-dependence of 1/f noise in liquid gated, single layer GFETs. An analytical compact model is developed considering both carrier number and mobility fluctuation mechanisms. According to this procedure, the noise in an elementary slice of the channel is calculated based on physical laws; after integrating along the channel, the local noise sources are propagated to the terminals and the final formulas are derived. In this compact format the model can be easily implemented in Verilog-A code and integrated in circuit simulators, which could be instrumental to bridge the gap between device and circuit levels. The model is capable of quantitatively capture the experimental M-shape of normalized output noise which is observed for all channel lengths and drain voltages available. The simultaneous contribution of the ΔN and $\Delta\mu$ noise mechanisms significantly improves the prediction accuracy of the model, confirming that both noise contributions are needed to properly model noise in graphene FETs. Additionally, a previously reported contact noise term based on carrier number fluctuations proved to be effective to account for such contribution. An analytical solution of the LFN generated by contact resis-

tance is an essential future step so as our model to be capable of capturing additional behaviours of LFN mentioned in bibliography such as an extended V-shape *vs.* gate voltage and thus, to be considered complete. The analytical model presented in this work encompasses all the main contributions to 1/f noise in graphene FETs, taking into account the non-homogeneities in the channel. Such an analytical and yet complete model can be of high interest to identify and understand the main causes of noise as well as for boosting the design of integrated circuits based on graphene.

Experimental data

Graphene CVD growth and transfer

Graphene is synthesized by chemical vapour deposition (CVD) technique on a copper foil. A chemical wet transfer method is used to transfer the graphene from the Cu foil to the SiO$_2$ substrate. First, the graphene is protected with a sacrificial poly (methyl meth-acrylate) PMMA layer. Subsequently, the back side graphene is removed by oxygen plasma treatment. The Cu foil is then placed in FeCl$_3$ 0.5 M/HCl 2 M (1 : 2) etchant solution until all the Cu is chemically dissolved. Before the final transfer onto the desired SiO$_2$ substrate, the graphene/PMMA stack is placed several times in DI water to rinse the residual etchant solution away. The wafer is dried for 30 minutes at 40 °C on a hot plate and then gradually increased up to 180 °C in a vacuum oven. Finally, the PMMA is removed in acetone and IPA.

Devices fabrication

Arrays of graphene transistors are fabricated on 4-inch S_i/S_iO_2 wafer with a 285 nm thick layer of thermal silicon oxide. A first metal layer of Ti/Au is deposited by electron-beam evaporation and structured by a lift-off process. Afterwards, the CVD-gown graphene is transferred as previously described. The graphene transistor active area is protected by a photo definable resist HIPR 6512. Thus, graphene is patterned by oxygen plasma in a

reactive ion etching (RIE) system. Top contacts of Ni/Au are deposited by evaporation and defined by lift-off. In order to prevent any damage of graphene, the lift-off is performed by leaving the wafer 1 hour in acetone and flushing it with a syringe. After 2 hours annealing step at 300 °C in ultra-high vacuum, a 2 μm thick SU8 negative epoxy resist (SU-8 2005 MicroChem) layer is spin coated and structured such that only the graphene between source and drain contact is exposed to the electrolyte.

Electrical characterization

The liquid-gated graphene-transistor characteristics are measured in a 10 mM PBS electrolyte. The gate voltage is applied *versus* an Ag/AgCl reference electrode. At each polarization, the drain-to-source current signal is measured with a custom-made current-to-voltage converter with two parallel inputs for DC (low-pass filter at 0.1 Hz for I–V characteristics) and AC (band-pass filter from 0.1 Hz to 7 kHz for noise characterization). The data acquisition is performed using a National Instruments DAQ-card system (NI 6363). In order to stabilize the I_{DS} current value at each gate bias, the sampling condition is $dI_{DS}/dt < 1 \times 10^7$ A s^{-1} before each recorded point. For the noise characterization, the sampling frequency was set to 50 kHz for a period of time of 13 seconds choosing the Welch's method in which 10 segments overlap by 50%.

Data availability

The data that support the findings of this study are available from Ramon Garcia Cortadella and Andrea Bonaccini Calia. Please, address your requests to ramon.garcia@icn2.cat and andrea.bonaccini@icn2.cat.

Conflicts of interest

There are no conflicts to declare.

Acknowledgements

References

1 F. Schwierz, *Nat. Nanotechnol.*, 2010, **5**, 487–496.

2 Y. M. Lin, K. A. Jenkins, A. Valdes-Garcia, J. P. Small, D. B. Farmer and P. Avouris, *Nano Lett.*, 2009, **9**(1), 422–426.

3 F. Schedin, A. K. Geim, S. V. Mozorov, E. W. Hill, M. I. Blake, M. I. Katsnelson and K. S. Novoselov, *Nat. Mater.*, 2007, **16**, 652–655.

4 I. Heller, S. Chatoor, J. Mannik, M. A. G. Zevenbergen, J. B. Oostinga, A. F. Morpurgo, C. Dekker and S. G. Lemay, *Nano Lett.*, 2010, **10**(5), 1563–1567.

5 L. H. Hess, M. Seifert and J. A. Garrido, *Proc. IEEE*, 2013, **101**(7), 1780–1792.

6 C. Herbert, E. Masvidal-Codina, A. Suarez-Perez, A. Bonaccini-Calia, G. Piret, R. Garcia-Cortadella, X. Illa, D. E. Corro Garcia, J. M. De la Cruz Sanchez, D. V. Casals, E. Prats-Alfonso, J. Bousquet, P. Godignon, B. Yvert, R. Villa, M. V. Sanchez-Vives, A. Guimera-Brunet and J. A. Garrido, *Adv. Funct. Mater.*, 2017, 1703976.

7 S. Rumyantsev, G. Liu, M. S. Shur, R. A. Potyrailo and A. A. Balandin, *Nano Lett.*, 2012, **12**(5), 2294–2298.

8 S. Rumyantsev, G. Liu, R. A. Potyrailo, A. A. Balandin and M. S. Shur, *IEEE Sens. J.*, 2013, **13**(8), 2818–2822.

9 R. Samnakay, C. Jiang, S. Rumyantsev, M. S. Shur and A. A. Balandin, *Appl. Phys. Lett.*, 2015, **106**(2), 23115.

10 F. Bonaccorso, Z. Sun, T. Hasan and A. C. Ferrari, *Nat. Photonics*, 2010, **4**, 611–622.

11 L. Vandamme, *IEEE Trans. Electron Devices*, 2002, **41**(11), 2176–2187.

12 S. K. Lee, C. G. Kang, Y. G. Lee, C. Cho, E. Park, H. J. Chung, S. Seo, H. D. Lee and B. H. Lee, *Carbon*, 2012, **50**(11), 4046–4051.

13 M. J. Uren, D. J. Day and M. J. Kirton, *Appl. Phys. Lett.*, 1985, **47**(11), 1195–1197.

14 A. L. McWhorter, *Semiconductor Surface Physics*, 1957, pp. 207–228.

15 G. Reimbold, *IEEE Trans. Electron Devices*, 1984, **31**(9), 1190–1194.

16 G. Ghibaudo, *Solid-State Electron.*, 1989, **32**(7), 563–565.

17 G. Ghibaudo, O. Roux, Ch. Nguyen-Duc, F. Balestra and J. Brini, *Phys. Status Solidi*, 1991, **124**, 571.

18 K. K. Hung, P. K. Ko, C. Hu and Y. C. Cheng, *IEEE Trans. Electron Devices*, 1990, **37**(3), 654–665.

19 N. Mavredakis, A. Antonopoulos and M. Bucher, 5th IEEE Europ. Conf. on Circuits & Systems for Communications (ECCSC), 2010, 86–89.

20 F. N. Hooge, *Phys. B*, 1976, **83**, 14–23.

21 M. B. Blaschke, N. Tort-Colet, A. Guimera-Brunet, J. Weinert, L. Rousseau, A. Heimann, S. Drieschner, O. Kempski, R. Villa, V. M. Sanchez-Vives and J. A. Garrido, *2D Mater.*, 2017, **4–2**, 025040.

22 A. A. Balandin, *Nat. Nanotechnol.*, 2013, **8**, 549–555.

23 G. Liu, S. Rumyantsev, M. S. Shur and A. A. Balandin, *Appl. Phys. Lett.*, 2013, **102**(9), 93111.

24 G. R. Cortadella, C. A. Bonaccini, G. A. Brunet, M. E. Codina and J. A. Garrido, Submitted 2018.

25 G. Liu, W. Stillman, S. Rumyantsev, Q. Shao, M. Shur and A. A. Balandin, *Appl. Phys. Lett.*, 2009, **95**(3), 033103.

26 G. Xu, C. M. Torres, Y. Zhang, F. Liu, E. B. Song, M. Wang, Y. Zhou, C. Zeng and K. L. Wang, *Nano Lett.*, 2010, **10**(9), 3312–3317.

27 Y. Zhang, E. E. Mendez and X. Du, *ACS Nano*, 2011, **5**(10), 8124–8130.

28 A. N. Pal, S. Ghatak, V. Kochat, A. Sneha, A. Sampathkumar, S. Raghavan and A. Ghosh, *ACS Nano*, 2011, **5**(3), 2075–2081.

29 S. Rumyantsev, G. Liu, W. Stillman, M. Shur and A. A. Balandin, *J. Phys.: Condens. Matter*, 2010, **22**(39), 395302.

30 T. Li, Q. Gao, Z. Wei, X. Li, Y. Fu and Y. Wu, 12th IEEE Int. Conf. on Solid-State and Integrated Circuit Technology (ICSIT), 2014, China.

31 M. Kayyala and Y. P. Chen, *Appl. Phys. Lett.*, 2015, **107**(23), 113101.

32 M. A. Stolyarov, G. Liu, S. Rumyantsev, M. Shur and A. A. Balandin, *Appl. Phys. Lett.*, 2015, **107**(23), 023106.

33 S. Takeshita, S. Matsuo, T. Tanaka, S. Nakaharai, K. Tsukagoshi, T. Moriyama, T. Ono, T. Arakawa and K. Kobayashi, *Appl. Phys. Lett.*, 2016, **108**(10), 103106.

34 J. Xia, J. L. Cheng and N. Tiao, *Nat. Nanotechnol.*, 2009, **4**(8), 505–509.

35 M. Z. Hossain, S. Rumyantsev, M. S. Shur and A. A. Balandin, *Appl. Phys. Lett.*, 2013, **102**(15), 153512.

36 G. Liu, S. Rumyantsev, M. S. Shur and A. A. Balandin, *Appl. Phys. Lett.*, 2012, **100**(3), 33103.

37 H. N. Arnold, V. K. Sangwan, S. W. Schmucker, C. D. Cress, K. A. Luck, A. L. Friedman, J. T. Robinson, T. J. Marks and M. C. Hersam, *Appl. Phys. Lett.*, 2016, **108**(7), 073108.

38 N. Sun, K. Tahy, H. Xing, D. Jena, G. Arnold and S. T. Ruggiero, *J. Low Temp. Phys.*, 2013, **172**(3–4), 202–211.

39 B. Pellegrini, *Eur. Phys. J. B*, 2013, **86**, 373.

40 B. Pellegrini, P. Marconcini, M. Macucci, G. Fiori and G. Basso, *J. Stat. Mech.: Theory Exp.*, 2016, 054017.

41 C. Mukherjee, J. D. Aguirre-Morales, S. Fregonese, T. Zimmer, C. Maneux, H. Happy and W. Wei, 45th IEEE Europ. Solid State Dev. Res. Conf. (ESSDERC), 2015, 176–179.

42 S. Peng, Z. Jin, D. Zhang, J. Shi, D. Mao, S. Wang and G. Yu, *ACS Appl. Mater. Interfaces*, 2017, **9**(8), 6661–6665.

43 C. Enz and E. Vitoz, *Charge-based MOS Transistor Modeling*, John Wiley and Sons, 2006.

44 A. S. Roy, Thesis No 3921, EPFL, 2007.

45 D. Jiménez and O. Moldovan, *IEEE Trans. Electron Devices*, 2011, **58**(11), 4377–4383.

46 G. M. Landauer, D. Jiménez and J. L. Gonzalez, *IEEE Trans. Nanotechnol.*, 2014, **13**(5), 895–904.

Supplementary Information for:

Understanding the Bias Dependence of Low Frequency Noise in Single Layer Graphene FETs

Nikolaos Mavredakis*[a], Ramon Garcia Cortadella[b], Andrea Bonaccini Calia[b], Jose A. Garrido[b] and David Jiménez[a]

[a] Departament d'Enginyeria Electrònica, Escola d'Enginyeria, Universitat Autònoma de Barcelona, Bellaterra 08193, Spain

[b] Catalan Institute of Nanoscience and Nanotechnology (ICN2), CSIC, Barcelona Institute of Science and Technology, Campus UAB, Bellaterra, Barcelona, Spain

* nikolaos.mavredakis@uab.es

A. Supplementary Information: Thorough theoretical procedure for equations extraction

Generalized Noise Modeling methodology:

Under the assumption that the channel of the device is noiseless apart from an elementary slice between positions χ and $\chi+\Delta\chi$ as it is shown in Fig. 2b in the manuscript, the microscopic noise coming from this slice of the channel can be modeled as a local current source δI_n with a PSD $S_{\delta I^2_n}$ which is connected between χ and $\chi+\Delta\chi$ in parallel with the resistance of the slice ΔR (Norton equivalent) [43]. The transistor then can be split into two noiseless transistors M1 and M2 on each side of the local current noise source, at the source and drain side ends with channel lengths equal to χ and $L-\chi$ respectively. Since the voltage fluctuations on parallel resistance ΔR are small enough compared to thermal voltage U_T, small signal analysis can be used in order to extract a noise model according to which, M1 and M2 can be replaced by two simple conductances G_S on the source side and G_D on the drain side. The total channel conductance comes from the series connection of G_S and G_D as: $1/G_{CH}=1/G_S+1/G_D$ [43]. The fluctuation of the current due to the local current noise source at the drain side δI_{nD} and its corresponding PSD $S_{\delta I^2_{nD}}$ are given by the following equations [43]:

$$\delta I_{nD} = G_{CH}\Delta R\delta I_n \tag{Eq. A1}$$

$$S_{\delta I^2_{nD}}\left(\omega,x\right)= G^2_{CH}\Delta R^2 S_{\delta I^2_n}\left(\omega,x\right) \tag{Eq. A2}$$

The PSD of the total noise current fluctuation at the drain side S_{ID} due to all different sections along the channel is obtained by summing their elementary contributions $S_{\delta I^2_{nD}}$ assuming that the contribution of each slice at different positions along the channel remains uncorrelated [43]:

$$S_{ID} = \int_0^L G_{CH}^2 \Delta R^2 \frac{S_{\delta I_n^2}(\omega,x)}{\Delta x} dx = \frac{1}{L^2} \int_0^L \Delta x S_{\delta I_n^2}(\omega,x) dx, \quad where \; G_{CH}^2 \Delta R^2 = \left(\frac{\Delta x}{L}\right)^2 \qquad \text{(Eq. A3)}$$

Carrier Number Fluctuation Effect:

As mentioned in the manuscript, the fluctuation of the trapped charge δQ_t can cause a variation in the chemical potential δV_c which can lead to a change to all charges that depend directly on chemical potential such as the graphene charge, the top gate and the back gate charge. The application of the charge conservation law gives:

$$\delta Q_{gr} + \delta Q_{top} + \delta Q_{back} + \delta Q_t = 0 \qquad \text{(Eq. A4)}$$

These induced fluctuations of the graphene, top gate and back gate charges can be related to the fluctuation of the chemical potential δV_c as[15, 43-46]:

$$\delta Q_{gr} = -C_q \delta V_c$$
$$\delta Q_{top} = -C_{top} \delta V_c \qquad \text{(Eq. A5)}$$
$$\delta Q_{back} = -C_{back} \delta V_c$$

If eqns (A4, A5) are taken into account then eqn (1) is transformed in eqn (3) in the manuscript. If the linear relationship between quantum capacitance and chemical potential mentioned in the manuscript, is integrated, charge of graphene can be calculated as:

$$Q_{gr} = \frac{k \cdot V_c^2}{2} + \rho_0 \cdot e \qquad \text{(Eq. A6)}$$

The PSD of the local noise source is calculated by eqn (4) in the manuscript. Taking the integral of this from Source to Drain in order to calculate the total 1/f noise PSD as in eqn (A3)[15, 43], we have:

$$\left. \frac{S_{I_D}}{I_D^2} f \right|_{\Delta N} = \frac{1}{L^2} \int_0^L \left(\frac{e}{Q_{gr}}\right)^2 \left(\frac{C_q}{C_{top} + C_{back} + C_q}\right)^2 \cdot \frac{KT \lambda N_T}{W} dx \qquad \text{(Eq. A7)}$$

In order to express this integral in terms of chemical potential V_c, we have to change the integral variable as[45-46]:

$$\frac{dx}{dV_c} = \frac{-\mu W Q_{gr}}{I_D} \frac{C_q + C_{top} + C_{back}}{C_{top} + C_{back}} \qquad \text{(Eq.A8)}$$

Where drain current is given as[45-46]:

$$I_D = \frac{\mu W k}{2L} \left[g\left(V_C\right) \right]_{V_{cs}}^{V_{cd}} \qquad \text{(Eq.A9)}$$

With $k = 2 \cdot e^3 / (\pi \cdot h^2 \cdot v^2 f)$[45-46] where vf is the Fermi velocity ($=10^6$ m/s) and h the reduced Planck constant ($=1,05 \cdot 10^{-34}$ J·s). Bias dependent term $g(V_c)$ is calculated as[45-46]:

$$\left[g\left(V_C\right) \right]_{V_{cs}}^{V_{cd}} = \frac{V_{cs}^3 - V_{cd}^3}{3} + \frac{k}{4\left(C_{top} + C_{back}\right)} \left[\mathrm{sgn}\left(V_{cd}\right)V_{cd}^4 - \mathrm{sgn}\left(V_{cs}\right)V_{cs}^4 \right] + \frac{2\rho_0 e V_{DS}}{k} \qquad \text{(Eq.A10)}$$

eqn (A7) is transformed because of eqns (A8, A9, A10) to:

$$\frac{S_{I_D}}{I_D^2} f \bigg|_{\Delta N} = \frac{4KT\lambda N_T e^2 k}{WL \left[g\left(V_c\right) \right]_{V_{cs}}^{V_{cd}} \left(C_{top} + C_{back}\right)} \int_{V_{cd}}^{V_{cs}} \frac{V_c^2}{\left(kV_c^2 + 2\rho_0 e\right)\left(C_{top} + C_{back} + k|V_c|\right)} dV_c \qquad \text{(Eq.A11)}$$

The integral in eqn (A11) can be solved analytically and gives the eqns (2, 5) in the manuscript.

Mobility Fluctuation Effect:

In the empirical Hooge model, the PSD of the local noise source is expressed as[43]:

$$\frac{S_{\delta I_n^2}}{I_D^2} \bigg|_{\Delta\mu} = \frac{\alpha_H e}{Q_{gr} W \Delta x f} \qquad \text{(Eq.A12)}$$

If eqn (A12) is integrated along the channel as eqn (A3), the total noise PSD due to mobility fluctuations effect can be calculated as[43]:

$$\frac{S_{I_D}}{I_D^2} f \bigg|_{\Delta\mu} = \frac{\alpha_H e}{WL^2} \int_0^L \frac{1}{Q_{gr}} dx \qquad \text{(Eq. A13)}$$

If eqn (A8) is applied in order to change the integration variable from x to V_c:

$$\frac{S_{I_D}}{I_D^2} f \bigg|_{\Delta\mu} = \frac{\alpha_H e}{L^2 W \left(C_{top} + C_{back}\right)} \int_{V_{cd}}^{V_{cs}} \frac{\mu W Q_{gr}}{Q_{gr} I_D} \left(k|V_c| + C_{top} + C_{back}\right) dV_c \qquad \text{(Eq.A14)}$$

Where Q_{gr} is simplified in eqn (A14) and does not play a role in mobility fluctuation effect. If eqns (A9, A10) are also taken into account, then:

$$\frac{S_{I_D}}{I_D^2} f \bigg|_{\Delta\mu} = \frac{2\alpha_H e}{WLk \left[g\left(V_c\right) \right]_{V_{cs}}^{V_{cd}} \left(C_{top} + C_{back}\right)} \int_{V_{cd}}^{V_{cs}} \left(k|V_c| + C_{top} + C_{back}\right) dV_c \qquad \text{(Eq.A15)}$$

The integral in eqn (A12) can be solved analytically and gives the eqns (6, 7) in the manuscript.
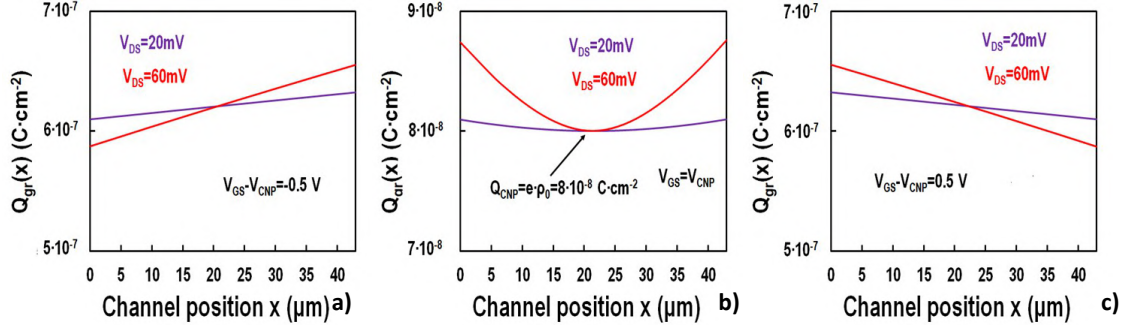
B. Supplementary Information Figure S1: Detailed examination of graphene charge along the channel.

Figure S1. Graphene charge $Q_{gr}(x)$ vs. channel position x, for V_{GS}-V_{CNP} = -0,5 V (a), 0 V (CVP) b) and 0,5 V (c) at V_{DS} = 20, 60 mV for W/L=40 μm/43 μm.

Away from CNP (Fig. S1a-S1c), $Q_{gr}(x)$ is ~6-6.5·10^{-7} C.cm^{-2} all along the channel for both drain voltage values. Considering the relative fluctuation of $Q_{gr}(x)$ from source terminal to the middle of the channel shown in Fig. 2c of the manuscript, the homogeneity of the channel is shown at high gate voltages for both V_{DS} values. Near CNP (Fig. S1b), $Q_{gr}(x)$ is equal to residual charge, $e \cdot \rho_0$, at x=L/2 for both high and low V_{DS}. This value remains almost constant throughout the channel for V_{DS}=20 mV but it is increased significantly for V_{DS}=60 mV confirming the inhomogeneous channel under these conditions.

C. Supplementary Information: Detailed examination of effect of residual charge in the M-shape bias dependence of 1/f noise.

If the procedure of the extraction of the theoretical equations regarding carrier number fluctuation effect takes place without considering residual charge, this can lead to very significant conclusions regarding the effect of residual charge on noise behavior. If residual charge is considered insignificant, then it must be eliminated in eqns (A6, A10). This results in the extraction of the following equation regarding 1/f noise due to carrier number fluctuation effect if the equivalent integral of eqn (A8) is solved:

$$\frac{S_{I_D}}{I_D^2} f \bigg|_{\Delta N} = \frac{SD\big|_{\Delta N} \cdot KD\big|_{\Delta N}}{\big[g(V_c)\big]_{V_{cs}}^{V_{cd}}}, \quad SD\big|_{\Delta N} = \frac{2KT\lambda N_T e^2}{\big(C_{top}+C_{back}\big)kWL} \qquad \text{(Eq.A16)}$$

and *KD/$_{\Delta N}$* is now given as:

$$\text{for } V_{cs,d} > 0, \quad KD\big|_{\Delta N} = \Big[\, 2\ln\big(C_{top} + C_{back} + kV_c\big) - 4\ln\big(C_{top} + C_{back}\big) \Big]_{V_{cd}}^{V_{cs}}$$

$$\text{for } v_{cs,d} < 0, \quad KD\big|_{\Delta N} = \Big[\, -2\ln\big(C_{top} + C_{back} - kV_c\big) \Big]_{V_{cd}}^{V_{cs}}$$

(Eq.A17)

eqn (A17) is much simpler that eqn (2) of the manuscript. Regarding Hooge model, residual charge plays a role only in $g(V_c)$ factor in eqn (A10). As it can be seen in Fig. 3a of the manuscript, the omission of the residual charge lead to a Λ – shape behavior even for the carrier number fluctuation effect while the less the residual charge, the steeper Λ – shape trend with a higher maximum is observed for both carrier number and mobility fluctuation effects.

It would be very useful to observe how the absence of the residual charge affects both noise mechanisms *ΔN* and *Δμ* locally in the transistor channel. Regarding *ΔN* local noise model described by eqn (4) of the manuscript and *Δμ* local noise model described by eqn (A12), residual charge has an effect only in Q_{gr} as this is defined in eqn (A6). As it can be seen in Fig. S2, residual charge does not affect local noise at higher gate voltages for both noise mechanisms as it was expected (see Fig. 3a of the manuscript) since there ρ_0 does not affect significantly Q_{gr}. On the contrary at CNP, where ρ_0 approximately dominates Q_{gr}, the effect on local noise mechanisms is important. Fig. S2a shows the increase of *ΔN* local noise when ρ_0 is ignored leading to the Λ-shape of Fig. 3a of the manuscript. Similarly Fig. S2b shows the increase of *Δμ* local noise when ρ_0 is ignored.
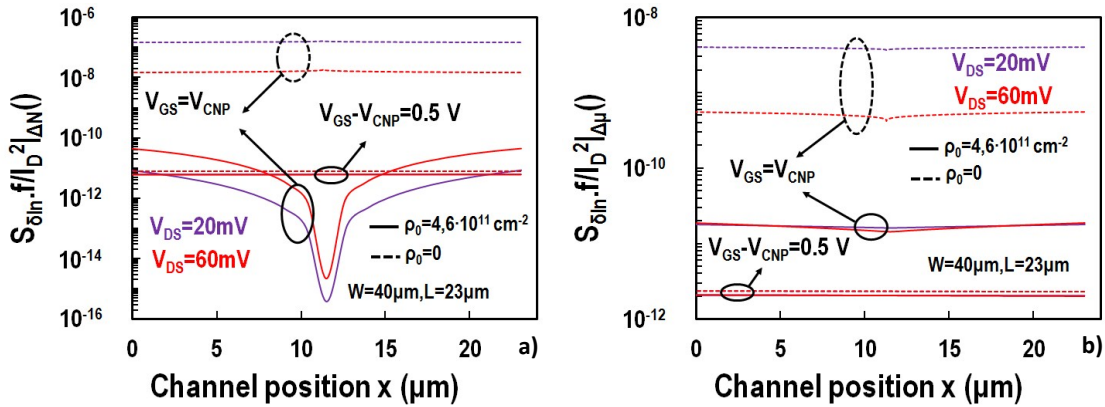

Figure S2. Normalized PSD of the local noise, $S_{\delta in}/I_D{}^2$, referred to *1 Hz*, vs. channel potential *x* for *ΔN* (a) and *Δμ* (b) noise mechanisms.

D. Supplementary Information Figure S3: similar analysis with Fig. 4a and 4b of the manuscript but for the rest of the channel lengths
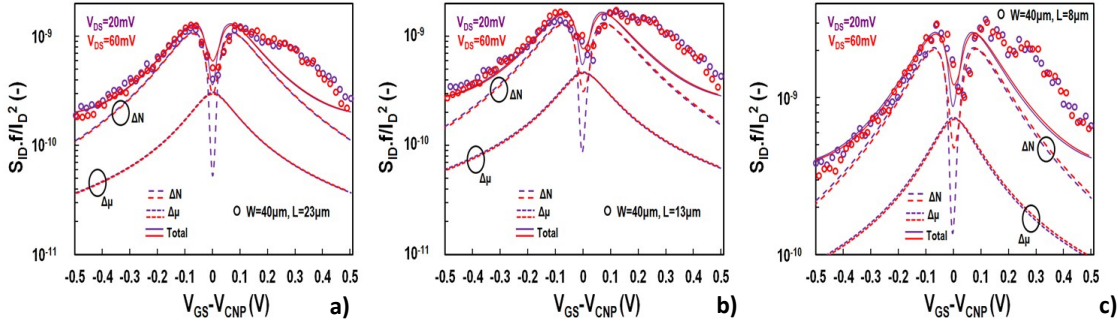

Figure S3. Output noise divided by squared drain current S_{ID}/I_D^2, referred to *1 Hz*, vs. top gate voltage overdrive $V_{GS} - V_{CNP}$, for liquid top-gated GFETs with *W=40 μm* for channel length *L=23 μm* (a), *L=13 μm* (b) and *L=8 μm* (c) at V_{DS} = *20, 60 mV*. markers: measured, solid lines: model, dashed lines: different noise contributions.

E. Supplementary Information: Derivation of an *$(g_m/I_D)^2$* related LFN model with and without correlated mobility fluctuations

A very common approximation for modeling LFN in Si MOSFETs relates the output noise divided by squared drain current S_{ID}/I_D^2, with the squared transconductance to current ratio *$(g_m/I_D)^2$* [15-16]. Despite the fact that this model is widely used in circuit simulators, is valid only under uniform channel conditions. This method has also been applied in Graphene FETs[4] and has been found to underestimate LFN at CNP where the channel is non-uniform even for a small V_{DS} as shown in Figure 2c of the main manuscript. In this section we will follow a similar approach as in References 15-17 in order to show how this model is extracted for Graphene FETs with and without the effect of correlated mobility fluctuations. For reasons of simplicity and since back gate voltage is not active in the devices used in this work, both back gate voltage and capacitance will be ignored.

Initially, we will show that the model proposed in Reference 16 ($S_{ID}/I_D^2 = (g_m/I_D)^2 \cdot S_{Vfb}$) can be also applied in SLG FETs. From basic GFET electrostatics and if back gate is ignored we have:

$$Q_{gr}(x) = -C_t \left(V_{GS} - V_{GS0} + V_c(x) \right)$$ (Eq. A18)

From Drift-Diffusion theory[43-45], we can assume that:

$$\Delta I_D = \frac{\mu W}{L} \int_{V_S}^{V_D} \Delta Q_{gr}(x) dV = \frac{\mu W}{L} \int_0^L \frac{dQ_{gr}(x)}{dV_{GS}} \frac{dV_{GS}}{dQ_t} \Delta Q_t \frac{dV}{dx} dx \qquad \text{(Eq. A19)}$$

From eqn (A18) we can conclude that $dV_{GS}/dQ_{gr}(x) = -1/C_t$ while if we assume that $KV_c >> qT$ which means that we are away from CNP and thus $C_q >> C_t$ then from eqns (1, 3) of the main manuscript we have $dQ_{gr}(x)/dQ_t = 1$. So eqn (A19) becomes:

$$\Delta I_D = \frac{-\mu W}{L} \int_0^L \frac{dQ_{gr}(x)}{dV_{GS}} \frac{1}{C_t} \Delta Q_t \frac{dV}{dx} dx = \frac{-\mu W}{L} \int_0^L \frac{dQ_{gr}(x)}{dI_{DS}} \frac{dI_D}{dV_{GS}} \frac{1}{C_t} \Delta Q_t \frac{dV}{dx} dx \qquad \text{(Eq. A20)}$$

Again from Drift-Diffusion theory we have:

$$I_D = \mu W Q_{gr}(x) \frac{dV}{dx} \Rightarrow Q_{gr}(x) = \frac{-I_D}{\mu W \frac{dV}{dx}} \qquad \text{(Eq. A21)}$$

Under the assumption of a uniform channel where the graphene charge Q_{gr} and the electric field dV/dx are constant along it we have:

$$\frac{dQ_{gr}}{dI_D} = \frac{-1}{\mu W \frac{dV}{dx}} \qquad \text{(Eq. A22)}$$

From eqns (A20, A22) and since $d_{ID}/dV_{GS} = g_m$ we conclude:

$$\Delta I_D = \frac{1}{LC_t} g_m . e \int_0^L \Delta N_t dx \qquad \text{(Eq. A23)}$$

Which leads to:

$$\frac{S_{I_D}}{I_D^2} f \bigg|_{\Delta N} = \left(\frac{g_m}{I_D}\right)^2 \cdot \frac{q^2 KT \lambda N_T}{WLC_t^2} \qquad \text{(Eq. A24)}$$

The above eqn is exactly the same with eqn (9) of Reference 16 with the constant term to represent the flat band voltage fluctuations S_{VFb}. As we proved before, this model is valid only under uniform channel conditions and away from the CNP.

According to Reference 17, the model of eqn (A24) can be expanded including the correlated mobility fluctuations as:

$$\frac{S_{I_D}}{I_D^2} f \bigg|_{\Delta N} = \left(\frac{g_m}{I_D} + \alpha_c \mu C_t\right)^2 \cdot \frac{q^2 KT \lambda N_T}{WLC_t^2} \qquad \text{(Eq. A25)}$$

where α_c is the Coulomb scattering coefficient in *V.s/C* and μ is the mobility of the device. Figure S4 below presents the behavior of this simple approach described above with (eqn A25) and without (eqn A24) the effect of correlated mobility fluctuations for the shortest device with *L=5.5 µm* at V_{DS}=20 mV and V_{DS}=60 mV.
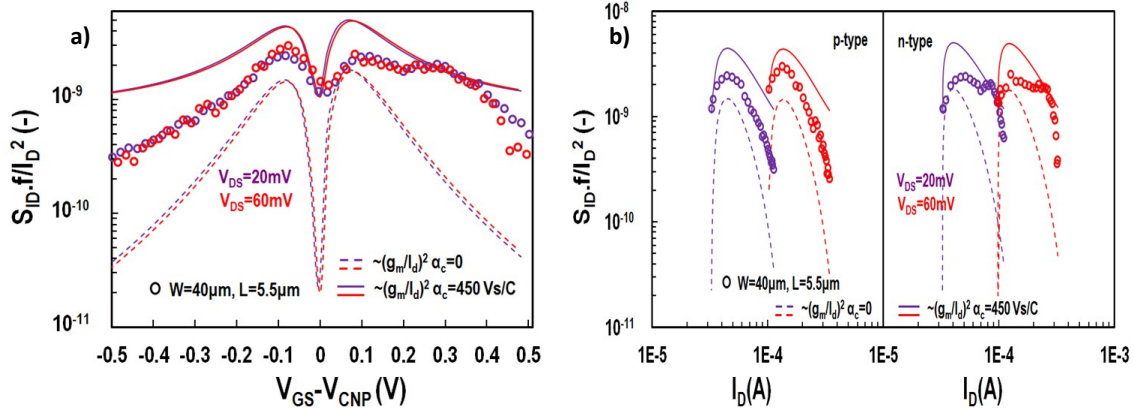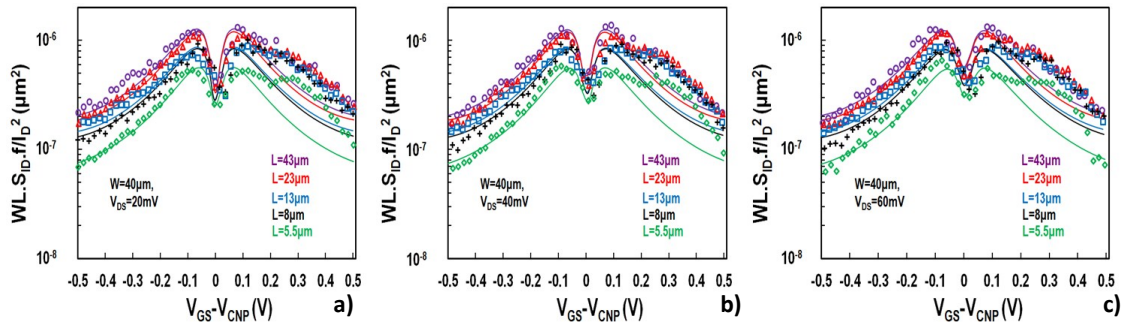

Figure S4. Output noise normalized with area and divided by squared drain current $S_{ID}/I_D{}^2$, referred to *1 Hz,* vs. top gate voltage overdrive $V_{GS} - V_{CNP}$ (a) and vs. drain current in both p- and n-type region (b) for liquid top-gated GFETs with *W/ L=40 µm / 5.5 µm* at V_{DS}=20 mV and V_{DS}=60 mV. markers: measured, solid lines: eqn (A25) model, dashed lines: eqn (A24) model.

Figure S4a presents the normalized $S_{ID}/I_D{}^2$ LFN vs top gate voltage overdrive $V_{GS} - V_{CNP}$ and what can be observed is that the model of eqn (A24) (α_c=0) underestimates LFN as it is also shown in Figure 4a of the manuscript for the longest device. Furthermore it is clear that the behavior of LFN is independent of V_{DS} even at the CNP because of the consideration of a uniform channel. If correlated mobility fluctuations model of eqn (A25) is activated then for a value of α_c=450 Vs/C the model captures the level of LFN at CNP still with no drain voltage dependence. But simultaneously the model overestimates LFN at higher gate voltages. Even if we assume that with an appropriate combination of α_c and α_H parameters we could achieve a better fitting, still the model would be independent of V_{DS} due to the homogeneous channel consideration.

Figure S4b presents the results of Figure 4a versus drain current I_D in log scale. Since I_D is symmetrical below (p-type) and above (n-type) CNP as it is shown in Figure 1c of the main manuscript, the two regions should be shown separately in log-scale. In an illustration similar to Figure S4b for Si MOSFETs, $S_{ID}/I_D{}^2$ LFN is maximum and constant in weak inversion region and decreases as we get deeper in strong inversion (See Figure 6 of Reference 17). Regarding weak inversion regime, this occurs because g_m/I_D

term is maximum and constant in the specific region and thus, eqn (A24) becomes equivalent to eqn (A25) since α_c is negligible. Consequently, N_T parameter which is included in S_{Vfb} term is extracted. As the drain current gets higher, LFN decreases and α_c parameter is extracted from this higher current regime. This is not the case in GFET though as it can be seen from Figure S4b since $(g_m/I_D)^2$ is not constant in lower current regime.

F. Supplementary Information Figure S5: normalized output noise with device area - WLS_{ID}/I_D^2

Figure S5. Output noise normalized with area and divided by squared drain current WLS_{ID}/I_D^2, referred to *1 Hz,* vs. top gate voltage overdrive $V_{GS} - V_{CNP}$ for liquid top-gated GFETs with *W=40 µm* for different channel length values (*L=43, 23, 13, 8, 5.5 µm*) at V_{DS}=*20 mV* (a), V_{DS}=*40 mV* (b) and V_{DS}=*60 mV* (c). markers: measured, solid lines: model.

259

Multiplexed Neural Sensor Array of Graphene Solution-Gated Field-Effect Transistors

Nathan Schaefer[1,2], Ramon Garcia-Cortadella[1,2], Javier Martínez-Aguilar[3,4], Gerrit Schwesig[5], Xavi Illa[3,4], Ana Moya Lara[3,4], Sara Santiago[6], Clement Hébert[7], Gonzalo Guirado[6], Rosa Villa[3,4], Anton Sirota[5], Anton Guimerà-Brunet[3,4] and Jose A. Garrido[1,8]

[1]Catalan Institute of Nanoscience and Nanotechnology (ICN2), CSIC and the Barcelona Institute of Science and Technology, Campus UAB, Bellaterra, Spain
[2]Departament d'Enginyeria Electrònica, Escola d'Enginyeria, Universitat Autònoma de Barcelona, Bellaterra, Spain
[3]Instituto de Microelectrónica de Barcelona IMB-CNM (CSIC), Esfera UAB, Bellaterra, Spain
[4]Centro de Investigación Biomédica en Red en Bioingeniería, Biomateriales y Nanomedicina (CIBER-BBN), Madrid, Spain
[5]Bernstein Center for Computational Neuroscience, Ludwig-Maximilians-University Munich, Planegg-Martinsried, Germany
[6]Departament de Química, Universitat Autònoma de Barcelona, Bellaterra, Barcelona, Spain
[7]Inserm and Université Grenoble Alpes, Saint Martin d'Hères, France
[8]ICREA, Barcelona, Spain

E-mail: joseantonio.garrido@icn2.cat

Abstract

Electrocorticography (ECoG) is a well-established technique to monitor electrophysiological activity from the surface of the brain and has proved crucial for the current generation of neural prostheses and brain-computer interfaces. However, existing ECoG technologies still fail to provide the resolution necessary to accurately map highly localized activity across large brain areas, due to the rapidly increasing size of connector footprint with sensor count. This work demonstrates the use of a flexible array of graphene solution-gated field-effect transistors (gSGFET), exploring the concept of multiplexed readout using an external switching matrix. This approach does not only allow for an increased sensor count, but due to the use of active sensing devices (i.e. transistors) over microelectrodes it makes additional buffer transistors redundant, which drastically eases the complexity of device fabrication on flexible substrates. The presented results pave the way for upscaling the gSGFET technology towards large-scale, high-density µECoG-arrays, eventually capable of resolving neural activity down to a single neuron level, while simultaneously mapping large brain regions.

Keywords: Multiplexed µECoGs, graphene solution-gated field-effect transistor, flexible probes, neurosensing

1. Introduction

Exploration of novel materials and improved micro- and nano-fabrication techniques are bringing up a new class of brain-computer interfaces (BMIs) which promise to revolutionize neuroprosthetics and unveil the underlying vast functionalities of the brain. Impressive breakthroughs have been recently achieved in motor control rehabilitation, understanding the mechanisms for learning and formation of memory, treating neuropsychiatric disorders (e.g. depression) and synthesizing audible speech using machine learning algorithms, emphasizing the immense potential BMIs have.[1–10] While the presented capabilities to interface with the brain are already very impressive, they mostly rely on relatively simple epi-cortical electrode arrays with low number of recording sites and large inter-site spacing, and are unsuitable for long chronic implantation. Higher cognitive functions do typically arise from a complex interplay of activity in several brain regions at once, therefore a detailed analysis of the neural activity underlying such functions would require sensor arrays recording from all involved areas with high local resolution in each of them. Current commercially available neural sensor arrays fail to provide the high sensor counts necessary for such endeavor, mostly due to the technologic challenge of excessive wiring with increasing array size, which could only

be overcome by the employment of multiplexed read-out circuitry. Multiplexing strategies are not new to the field of neuro-sensing and have previously been used as a versatile tool to manage large amounts of recording sites. Most of the emerged technologies are based on a CMOS-compatible monolithic integration of recording electrodes and read-out electronics to minimize connection distance for preserving signal integrity and maximizing the density of recording sites. Using rigid silicon substrates, however, restricts such concepts to applications in which device flexibility is expendable such as depth-probes or MEAs for ex-vivo recordings.[11–14] Yet, considering the extensive damage rigid depth-probes cause to the brain tissue, sets a clear limitation to the amount of insertable shanks and thus the simultaneously mappable brain regions. Here, electrocorticography offers a minimally invasive alternative with clear advantage on sensor resolution over large areas by using flexible μECoG arrays to record from the surface of the cortex.[15] Still, so far only very few examples of multiplexed μECoG arrays have been realized, due to the scarcity of durable materials for low-noise, high-performance switches compatible with flexible substrates as well as the high level of complexity such device fabrication requires. An example is the work of Rodgers which utilizes a combination of buffer and addressing transistor (ultrathin Si) to process the signals of an array of 360 passive platinum electrodes.[16, 17] Using passive elements, i.e. electrodes, as sensors requires the implementation of an additional transducer (buffer transistor) to decouple the electrode from the read-out circuitry, which otherwise would lead to load currents affecting the electrodes performance. This additional complexity can be avoided by directly using active elements i.e. transistors to interface with the brain. Such approach has recently been explored for organic electrochemical transistors (OECTs) with the conductive polymer poly(3,4-ethylenedioxythiophene):poly(styrenesulfonate) (PEDOT:PSS) as channel material.[18, 19] However, it has only been used to selectively address different sites, but not yet to actually acquire signals in multiplexed operation, which might be due to the relatively low carrier mobility in PEDOT:PSS prohibiting the rapid switching needed for multiplexing.

As the brain consists of corrugated soft tissue moving at every heartbeat, highly flexible probes are imperative to create intimate interfaces for best signal quality and to avoid gradual cicatrizing of the neural tissue. In this work, we present flexible multiplexed μ-ECoG arrays based on active sensing devices, namely graphene solution-gated field-effect transistors (gSGFETs). The gSFGET has emerged as one of the most promising technologies for brain-machine interfaces (BMIs) as it provides essential properties such as biocompatibility, chemical stability, mechanical flexibility and high signal-to-noise ratio.[20, 21] In particular, it has shown great potential for application in μ-ECoG arrays with its high sensitivity over a broad frequency range (0.001Hz up to 10kHz), making it an efficient transducer of both infra-slow and fast neural activity.[20, 22] While the gSGFETs suitability to provide high-quality recordings has already been proven for up to 16 recording sites in previous publications, its potential has never been evaluated for high-density arrays of large sensor count. Graphene is commonly considering as an ideal material for high-frequency application, as its reported mobilities up to 350 000 $cm^2V^{-1}s^{-1}$ for CVD grown graphene, can easily surpass materials such as Si and PEDOT:PSS with respective mobilities of 1400 $cm^2V^{-1}s^{-1}$ and 0.01 $cm^2V^{-1}s^{-1}$, which makes it an interesting candidate to consider for multiplexed devices.[23, 24] Moreover, we demonstrate that by using active sensing devices, the integration of multiplexing circuitry, i.e. buffer and switching transistors, is unnecessary, thus drastically easing the complexity of fabricating flexible multiplexed sensor arrays.

2. Methods

2.1 Probe fabrication

In a first step 10um thick biocompatible Polyimide (PI-2611 HD MicroSystems) was spun on 4'' Si/SiO2 support wafers and cured under nitrogen atmosphere at 350 °C. The perpendicular metal lines of the array (columns/ rows) were patterned in two standard lift-off steps (negative photoresist AZ5214E, Clariant, Germany) with the metal deposited by e-beam evaporation (30nm Ti/ 300nm Au, 10nm Ti/ 100nm Au) and separated by a 2 μm PI spacer layer. Interconnecting via-holes through the spacer layer were etched by oxygen plasma using a photolithographically defined protective aluminum mask (AZ5214E, 300nm Al). Then, single layer graphene, grown and transferred by Graphenea, is patterned by photolithography (H6512 photoresist) and etched by oxygen-based reactive ion etching (100W for 1min) to form the transistor channel area. A third metal layer (20nm Ni/ 200nm Au) is added to form sandwich contacts improving the gSGFET's durability and lowering its contact resistance due to work function matching. A subsequent thermal annealing step at 300°C in ultra-high vacuum has been found to reduce surface contamination from photoresist residues and improving the conformality of the Ni-graphene interface, thus improving contact resistance and device performance. To passivate the metal leads, a 2 μm thick layer of SU8 epoxy photoresist (SU-8 2005 MicroChem) was deposited, leaving open windows in the channel regions to allow a direct electrolyte graphene interface. In a final step, the polyimide

was structured by deep reactive ion etching using a photoresist etching mask (AZ9260, Clariant) and the flexible probes were mechanical peeled from the support wafer.

2.2 Characterization and multiplexing setup

Custom-build electronics were used for bias control and to convert the drain source current signal into voltage by a transimpedance amplifier (10k gain). The voltage signal was split into DC (frequency < 0.1 Hz) and AC (0.1 Hz < frequency > 5 kHz) components. The AC signal is amplified by an additional factor of 100 for the noise evaluation. The voltage read out was done by a standard data acquisition system (National Instruments DAQ-Card, USB-6363). For the multiplexed data acquisition, a similar system was used as for the probe characterization, however the gain of the AC stage was reduced by a factor of 10 to prevent saturation of the amplifier's dynamic range due to mismatch in transistor resistance. The digital output lines were used to address the n-type MOSFET switching matrix by applying either +5V for ON- and 0V for OFF-state. All software to control the DAQ-Card and handle data acquisition is based on self-built python code.

2.3 In-vivo experiments

Long Evans rats (Charles River) were kept under standard conditions (room temperature $22 \pm 2\,°C$, 12:12 h light–dark cycle, lights on at 10:00). Food and water were provided ad libitum. All experiments were performed in accordance with the European Union Directive 2010/63/EU as well as the German Law for Protection of Animals (TierSchG) and approved by the local authorities (ROB-55.2-2532.Vet_02-16-170). Three adult rats (2 males, 1 female), 3-8 month of age, weighing in the range of 400-600g were used in this study. In preparation of electrophysiological measurements, they were deeply anaesthetized with MMF (Midazolam 2mg/kg), Medetomidin 0.15 mg/kg, Fentanyl 0.005 mg/kg) and supplemented after 1h with Isoflurane 0.5%-1% and Metamizol at 110 mg/kg. After subcutaneous infiltration with Bupivacain the skin above the cranium was incised and the dorsal skull surface exposed. Craniotomies were performed bilaterally, with a maximum width of 5 mm and extending anterior-posteriorly between +2 mm and -8mm with respect to bregma. The dura mater was opened and carefully resected. The craniotomies were subsequently covered with prepolymerized PDMS (Sylgard 184, Dow Corning) with mixing ratio 1:10 and fastened with Vetbond (3M). In one rat an additional 1x1 mm craniotomy was performed over the cerebellum for the placement of a reference wire. For placement of the recording arrays the PDMS covers were flapped open partially and the gSGFET array was placed on the right hemisphere while the NeuroNexus array (E32-600-10-100) was symmetrically positioned on the left hemisphere, (between ca -7 to -3 mm from bregma) each partially covering the primary visual cortex. Subsequently the PDMS covers were flapped back to cover arrays and craniotomies. A reference wire (Ag/Ag-Cl) was inserted either in the cerebellar craniotomy (n=1) or temporal muscle (n=2). Data from the NeuroNexus array was acquired at 25 kHz using the eCube recording system (WhiteMatter LLC) while data from the gSGFET was acquired using custom build electronics described in the previous section. Anesthesia was kept at 0.5% isoflurane during the recordings of spontaneous activity and cortical spreading depression (CSD) and 2% isoflurane for the recording of optically evoked activity with reduced spontaneous activity. The CSD event was triggered by application of 1uL KCl (3 mMol) with a glass-micropipette and Nanoject II injection device (Drummond Scientific) at ca 4 mm anterior to bregma, approximately 7 mm anterior to the closest site on the recording array. The optically evoked response was triggered by a contralaterally placed blue LED in front of the left eye, which delivered 100 msec light pulses every 5 seconds.

3. Results and discussion

3.1 Device performance and multiplexing methodology

Scalable thin-film technology of 8x8 gSGFET sensor arrays was fabricated on 7um-thick flexible polyimide (PI) using 4-inch support wafers. The layout of the probe can be seen in Figure 1a and consists of a stack of two metal layers constructing the perpendicular lines of the sensor grid with a separating PI layer in between. The 64 gSGFET sensors have single-layer graphene channels of 50μm x 50μm dimension and 400μm inter-site separation (detailed description of probe fabrication in experimental section). A picture of the final probe, after releasing it from the Si support wafer is shown in Figure 1c. In contrast to their solid-state counterparts, solution-gated transistors are being modulated through the creation of a charge double layer at the interface between transistor channel and an electrolyte solution. Potential fluctuations in the surroundings (e.g. neural activity) can modulate this double layer and result, in turn, in a shift of the Fermi level of the channel material, which is detectable as a current fluctuation. Graphene's ability to create a stable interface with aqueous solutions in combination with its high transconductance, resulting from its large interfacial capacitance and carrier mobility, makes the gSGFET an ideal device for bio-sensing.[20–22, 25–28]
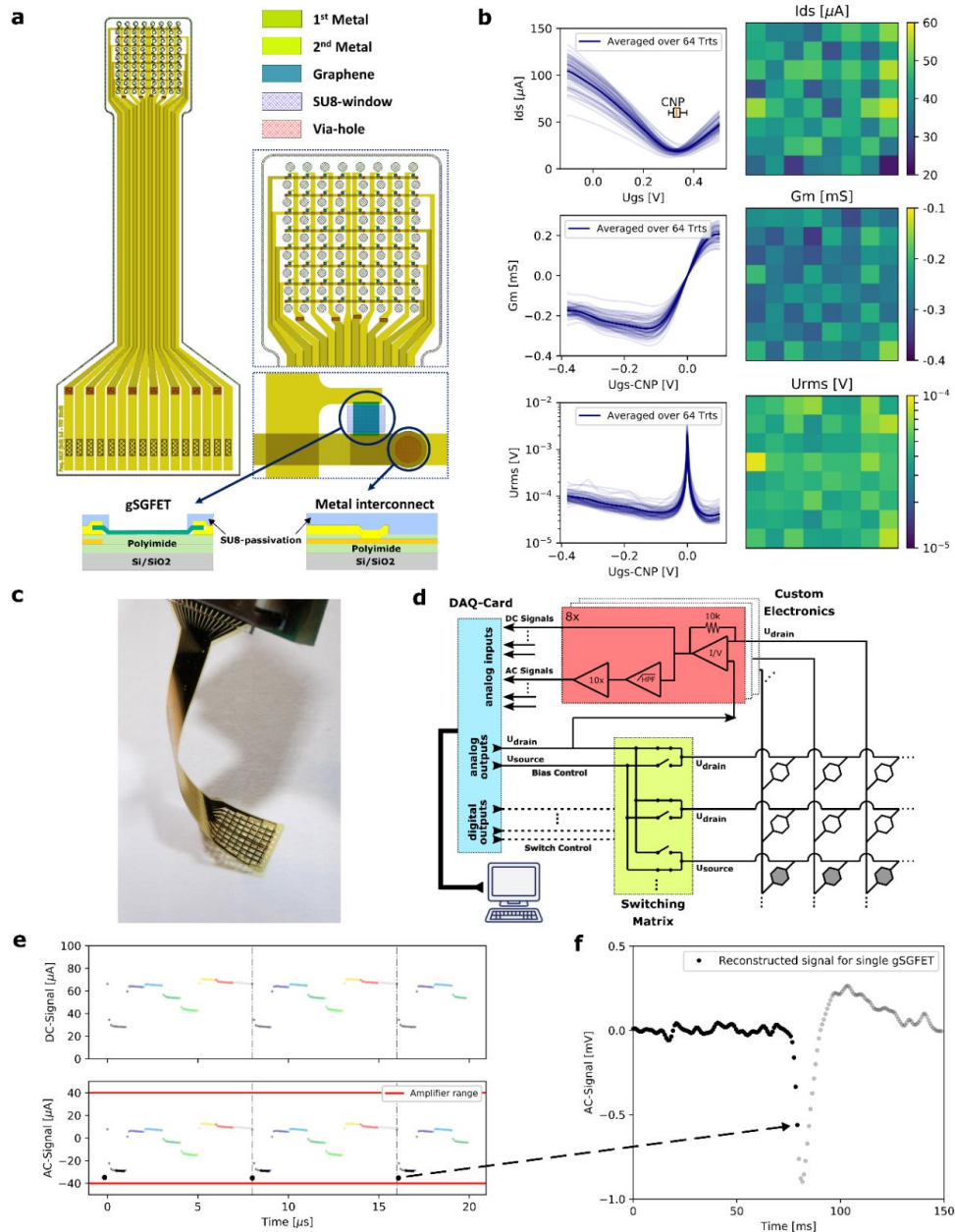
Figure 1. Multiplexed gSGFET µECoG-array: a. Layout and cross section of flexible ECoG array with 64 gSGFETs showing the grid construction with two metal layer and tapered via-holes (Figure S1 in supporting information) crossing the PI interlayer. **b.** gSGFET's transfer curve showing the change of drain-source current with applied gate bias (I_{ds}-U_{gs}, measured at U_{ds}=100mV), its transconductance (G_m-U_{gs}) and the device's equivalent gate noise (U_{rms}-V_{gs}). Also, the respective distribution of each parameter at peak G_m (bias point yielding highest absolute transconductance) across the array is being shown in the adjacent color map. **c.** Picture of flexible probe after release from Si support wafer. **d.** Schematic of discrete multiplexing setup using a DAQ-card for bias control and read-out (blue) and a custom-build PCB board for switching (yellow), filtering and current-to-voltage conversion (red). **e.** Acquired DC and AC raw signal for one column showing eight distinct current levels corresponding to the transistors in each row, which repeat for every cycle (grey dashed line). Due to the high gain (100k) applied to the AC component of the signal, the dynamic amplifier range sets a limit to the allowable current mismatch between devices, before amplifier saturation occurs (solid red line). **f.** From the 10 data points taken for each transistor per cycle, an average value of the last 5 points is taken, to yield one sample in the final reconstructed signal for each sensor.

Figure 1b shows a performance and homogeneity assessment of the gSGFET array. The transfer curve, namely the change of drain-source current I_{ds} with applied gate bias U_{gs} is presented as an averaged value and for all 64 individual devices, with the boxplot indicating the variation of charge neutrality point (CNP). Also, the transconductance Gm is shown (normalized to each transistor's CNP), which is defined as the first derivative of I_{ds} over U_{gs}. Of crucial importance to any sort of sensor array is the signal-to-noise ratio (SNR) and its homogeneity across recording sites. The SNR in the gSGFET is mainly affected by two physical parameters: the transconductance, which sets the transistor's sensitivity to signal fluctuations at the gate and the intrinsic device noise integrated over the relevant frequency range I_{rms}. A common figure of merit to quantify the gSGFET's SNR is the U_{rms} value (I_{rms}/G_m), which represents the equivalent gate noise below which signals are undetectable. As can be seen, the U_{rms} values of the gSGFETs on the array, are around 40 μV_{rms} (for the frequency band from 1Hz to 100Hz), which allows the detection of local field potentials (typical amplitude above 100μV) from the surface of the brain. The distribution across the array of each parameter (I_{ds}, G_m, U_{rms}), calculated at the bias point of highest absolute transconductance (peak-G_m), where the device shows lowest U_{rms}, is shown in the corresponding color maps. With yields above 90% on a 4-inch wafer (each wafer carrying 14 probes) and large, evenly distributed SNR across all recording sites, the gSGFET technology shows high maturity and homogeneity, which is a key requirement to enable multiplexed addressing schemes.

The most common type of multiplexing is time-division multiplexing (TDM), which refers to a technique of sequentially addressing the columns of a sensor array, while continuously measuring from its rows. Such addressing is normally being achieved by switches, which can be placed either directly on the array or externally.[14, 17, 18] While placing the switches directly on the array has the advantage of reducing inter-site crosstalk it requires complex fabrication of flexible switching technology, as previously mentioned.[17] Complementing arrays of passive sensing elements (i.e. electrodes) with an external addressing configuration is challenging, as their recorded voltage signal is prone to pick up noise; if the preamplifier is placed far from the electrode, additional buffer transistors are required to convert the signal into current and feed it to the read-out circuitry. The use of active sensing elements (i.e. transistors) offers a great benefit here, as they feature an intrinsic voltage-to-current conversion, making the recorded signal more robust to noise. A schematic representation of the addressing and acquisition methodology is shown in Figure 1d. For this purpose, a custom-build PCB board consisting of two main functional

blocks has been developed using discrete electronics. One functional block performs the filtering and amplification of the simultaneously acquired AC and DC signals; the other block selects the row to which the bias difference is applied to, using the external switching matrix for addressing. Figure 1e illustrates the acquired AC and DC raw input signals for a column of eight gSGFETs and how they can subsequently be used to reconstruct the original signal at each site (Figure 1f). Resistance mismatch between different transistors leads to current jumps when switching between transistors, which results in the different DC levels in the acquired signal (each gSGFET corresponds to one color in Figure 1e). The vertical dashed grey line in Figure 1e indicates the point at which all eight rows were addressed and a new readout cycle begins. At each site a total of 10 points is taken at 100 kHz sampling speed; we discard the first 5 to avoid any switching artefacts and average the rest to a single data point resulting in 1.25 kHz effective sampling rate. It should be here emphasized that array homogeneity carries an additional importance in multiplexed operation owing to two reasons. First, the trade-off between applicable AC signal gain and transistor resistance mismatch; as previously mentioned, current jumps can exceed the dynamic range of the amplifier (indicated in Figure 1e) leading to saturation and signal loss. Second, the switching artefacts scale with the level of mismatch between devices, requiring longer stabilization times before reliable data points can be collected.

3.2 Scalability and in-vitro assessment

With the goal of creating a high-density, large-scale sensor array, an important discussion to undertake is the one on scalability of this technology. The most important aspects to consider here are the transient response of the transistor, which limits the achievable switching speeds, and the increase of inter-site crosstalk with array size and track resistance. To obtain distortion-free, high-quality recordings in multiplexed operation, it is important to allow sufficient stabilization time after switching, for the transistor to adjust to the changed drain-source bias conditions. This stabilization time is device specific and generally scales with channel length and carrier mobility. Owing to the high carrier mobility of graphene, which is for our devices 1000-2000 $cm^2V^{-1}s^{-1}$ but can potentially reach up to 350 000 $cm^2V^{-1}s^{-1}$, the transient response of the gSGFET is extremely short (Figure 2a) compared to other technologies (e.g. transistors based on silicon or conducting polymers).[23] The ON-state is reached before 1μs, which is the time resolution of the used measurement equipment (NI DAQ-Card X-Series 6363); for a channel length of 50μm and a carrier mobility of 2000 $cm^2V^{-1}s^{-1}$ the actual stabilization time from a time-of-flight

estimation is expected to be in the range of hundred nanoseconds. Such fast device stabilization can eventually allow switching speeds beyond 1MHz (our current configuration is limited by the electronics to 10kHz). Thus, much larger arrays could be operated this way while maintaining enough sampling speed (>10kHz) to record even high frequency activity such as spikes. Due to the solution-gated nature of the device, a small drift occurs during the ON-state of the device which is tentatively associated to the migration of ions when the bias conditions in the channel change under switching. This phenomenon happens at a much slower time scale due to the low ionic mobility; however, it does only create a minor inaccuracy in the measured DC current and does not impact the AC recordings.

As previously stated, the use of external switches bears the disadvantage of not allowing to cut the connections to non-addressed sensors within the array, which leads to the so-called crosstalk. The lack of on-site switches opens alternative current pathways leading to current contribution from adjacent sites which carry signals from the respective gates and are wrongly attributed to the measured sensor (see Figure 2b). Such crosstalk can be strongly reduced and, in the ideal case of vanishing track resistance, even fully suppressed by setting the bias point of the non-addressed rows to the same voltage as the data lines, thus preventing any current flow through non-addressed lines.[18] However, in real-world applications the issue of finite track resistance cannot be completely avoided, as the requirements of high sensor density and probe flexibility limit the allowed width and thickness of the metal lines. The presence of these additional resistances create local potential drops, driving current through otherwise suppressed pathways whose amplitude depends on the ratio between track resistance (R_{track}) and transistor resistance (R_{gSGFET}) as well as the number n of columns and rows in the array. To quantify crosstalk in the gSGFET array experimentally, lateral Ag-gates and confined pads of solid polyelectrolyte were placed at each gSGFET of a 2x2 array by means of inkjet printing (Figure 2c). This approach allows for selective gate control, which is not possible in a shared liquid electrolyte. Figure 2d shows the measured signal at each of the transistors, with a test signal (sine wave of 10Hz frequency and 30mV amplitude) only being applied to one of them (black circle in Figure 2c). Sensors on the same column (red curve in Figure 2d) or row (dark-red curve in Figure 2d) as the applied signal are the ones with the largest impact of crosstalk, showing a

crosstalk level of -40dB at peak transconductance compared to the signal amplitude.

Diagonally placed sensors (orange curve in Figure 2d) are much less affected; however, in the latter case the exact level of crosstalk cannot be extracted with accuracy because the signal lies below the floor noise of the electronics. To validate this estimation of the crosstalk, we compared the experimental data with the results obtained from a PSpice simulation of a gSGFET array in which we used a standard p-type MOSFET element tailored to fit the gSGFET's transfer curve (Figure S2a-b in supporting information). Figure 2e shows the aggregated crosstalk on a single site depending on the track resistance and the array size, assuming identical signals on all remaining sites of the array which sum up to the total crosstalk value. The PSpice model validates the expected near-linear relation with both track resistance and array size. For a 2x2 array with 20Ω track resistance and a gSGFET resistance of 1,25kΩ, both the experiment and the simulation model yield a crosstalk of -40dB. Extrapolating to an array of size 32x32 (1024 sensors), a crosstalk lower than -20dB can be obtained by reducing the track resistance below 5 Ω or by increasing the resistance of the gSGFET. Such track resistance reduction could be achieved by increasing metal track thickness, using higher number of stacked metal layers and, most importantly, relaxing constraints on probe dimensions. While the ECoG array in this work was designed for application in rodents, which imposes strict size restrictions due to the dimensions of the craniotomy, many other application (e.g. neural probes for large animals or humans) would loosen those significantly.

To validate the fidelity of the gSGFET recordings in the multiplexed operating mode, the recording quality must be compared to the one obtained in steady, non-multiplexed operation. For instance, the rapid switching between devices can potentially increase the noise or generate artefacts in the multiplexed operation mode. Figure 2f compares recordings of an artificially generated electrocardiogram signal (ME-W-SG, Multichannel Systems), containing components of different frequencies. The multiplexed and non-multiplexed representation of both test signals are nearly identical, suggesting that the rapid sequential addressing by the multiplexed mode does not generate any visible artefacts, neither in the low nor in the mid frequency band. The root-mean-square value of both recordings is also compared, showing equivalent SNR ratio (Figure 2g) in both acquisition modes.
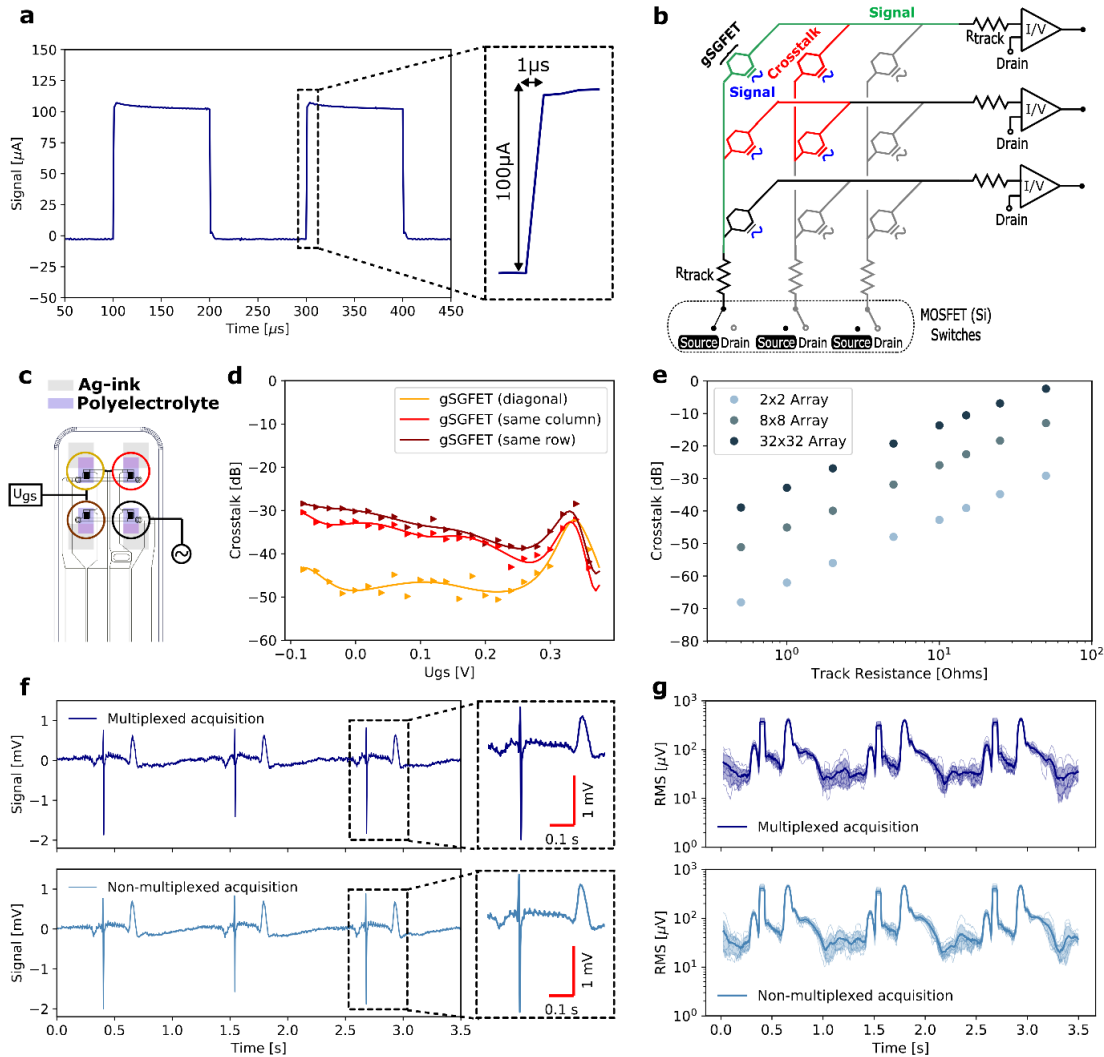
Figure 2. Scalability and in-vitro assessment: a. Transient response of gSGFET when switched between ON and OFF state, showing short stabilization time of the device. Response below 1µs cannot be resolved due to sampling rate limitation of the setup (1MHz). **b.** Origin of crosstalk in array without on-site switches and finite track resistance. Biasing to U_{drain} of non-addressed columns significantly decreases the amount of crosstalk. **c.** Location of measured gSGFETs on a 2x2 probe for crosstalk evaluation, utilizing inkjet printing to pattern confined gates consisting of Ag and polyelectrolyte pads. **d.** Crosstalk versus gate bias when applying a test signal (sinewave 30mV, 10Hz) to a single gSGFET and measuring the signal on each of the adjacent sensors. The devices in the same column and row as the one, to which the test signal is applied to, show a crosstalk of -40dB while the device on the diagonal shows crosstalk lower than -50dB (below floor noise of electronics). **e.** Simulated (PSpice) crosstalk for a 2x2, 8x8 and 32x32 arrays in dependence of the track resistance. The aggregated crosstalk value is presented assuming a superposition of identical signals on all but the probed sensor. **f.** Recordings of one gSGFET on the same 8x8 µECoG-array, acquired in either multiplexed or steady (non-multiplexed) acquisition. An artificial electrocardiogram signal was used to compare the fidelity of both acquisition modes. In both cases, the same averaging method was applied (cycles of 10 points, discarding first 5 points and averaging last 5 points), to ensure comparability. **g.** For each acquisition mode, the root-mean-square (RMS) value is calculated as the mean value of all 8 gSGFETs on one column, indicating the signal-to-noise ratio of the recorded signal.

3.3 In-vivo validation

Having confirmed the recording fidelity of the gSGFET in the multiplexed operation compared to the standard non-multiplexed acquisition mode, we demonstrate the unimpaired sensitivity of the multiplexed µECoG-array towards biological signals. Electrocortiography is primarily used to record local field potentials (LFPs) from the surface of the brain, which originate from spatio-temporal summation of transmembrane-currents generated by synaptic and active conductances, excluding the action potentials.[29, 30] The characteristic spectral content of the LFP signal reflects the time scale of network synchronization and ranges from <1Hz to hundreds of Hz. Figure 3a shows a time trace of spontaneous LFP activity in an anesthetized Long Evans rat, recorded in an acute in-vivo experiment using an array of gSGFETs operated in the multiplexed mode (more details in methods section). Under deep anaesthesia, such cortical LFP reflects slow oscillations that are highly coherent across the whole cortical mantle; indeed, no significant differences in signal shape can be seen across all the 64 sensors in the array.[31] To benchmark the recording capabilities of the gSGFET array against other state-of-the-art technologies, a NeuroNexus ECoG array (with 32 circular platinum electrodes of 100µm diameter) was simultaneously placed on the opposite hemisphere (Figure S3 in supporting information). Figure 3c-d show recordings and corresponding spectrograms from an electrode and a gSGFET, displaying the expected synchronicity in activity of both hemispheres. Filtering the signals from 0.1Hz to 200Hz (dark-blue and red curve in Figure 3c), a clear difference in signal shape can be noticed. This difference reflects the high-pass filter of the AC-coupled headstage used for passive ECoG recordings (see Experimental Section), which is necessary to prevent amplifier saturation due to drifts; also the high impedance of passive ECoG electrodes at low frequency leads to reduced gain in such signals, which results in an attenuation of the infraslow frequency content in the LFP signal.[22] Removing these low-frequency components from the gSGFET signal (green curve in Figure 3c), it is possible to validate that both technologies show very similar recordings of the LFP activity as can also be seen in the corresponding spectrograms.

Visually evoked LFP activity exhibits a well-defined spatial topography and thus can be used for validating the mapping capabilities of the multiplexed gSGFET technology.[32] Figure 3b shows the averaged response over 10 consecutive evoked events recorded with an array of gSGFETs in the multiplexed mode. Visually evoked activity typically exhibits a clear response with a delay of 40 ms after both the ON- and OFF-switching of the stimulus (Figure 3e). The recordings show a main peak (ON response) lasting until 70 ms after the stimulation with and peak amplitude of 500 µV. Hence, signal shape and amplitude are in nice agreement with previously reported results of non-multiplexed gSGFETs.[20] Further, Figure 3f presents the spatial distribution of both amplitude and time-delay of the ON-peak. The earliest response is detected on the lower end of the array which represents sensors directly placed on the primary visual cortex (V1) where the activity originates, and spreads then radially towards other higher visual cortical areas. However, highest peak-amplitude is measured in the centre-left region (secondary visual cortex, V2) which likely reflects a different magnitude and proximity current dipole, that gives rise to the surface LFP (LGN input to LIV in V1 vs V1 input to L2/3 pyramidal cells in V2).[33]

In addition, to its capability to record LFPs, the gSGFETs exhibit a unique sensitivity towards slow and infra-slow (below 0.1Hz) signals, which in the case of passive electrode recordings are hidden by baseline drifts and the impedance-related loss of gain at low frequency.[22] In order to confirm that multiplexed acquisition preserves signal quality in this frequency band, we have investigated recordings of a cortical spreading depression (CSD). CSDs emerge due to a cellular depolarization of neurons and astrocytes which is associated to brain injury and migraines among others.[34] Here, the CSD was artificially triggered by injecting KCl into the cortex that caused a slowly propagating wave moving across the cortex. Figure 3g depicts the recording of a gSGFET in the array. The DC component of the signal shows the characteristic large shift of 15mV amplitude. The AC component and its corresponding spectrogram (Figure 3h) reveals a silencing of the high-frequency activity during the event, caused by the cellular depolarization and which is characteristic for the CSD. The maps below (Figure 3i) show the respective position of the depolarising wave at different times after KCL injection, moving from the top right to the bottom left at about 7mm per minute speed.
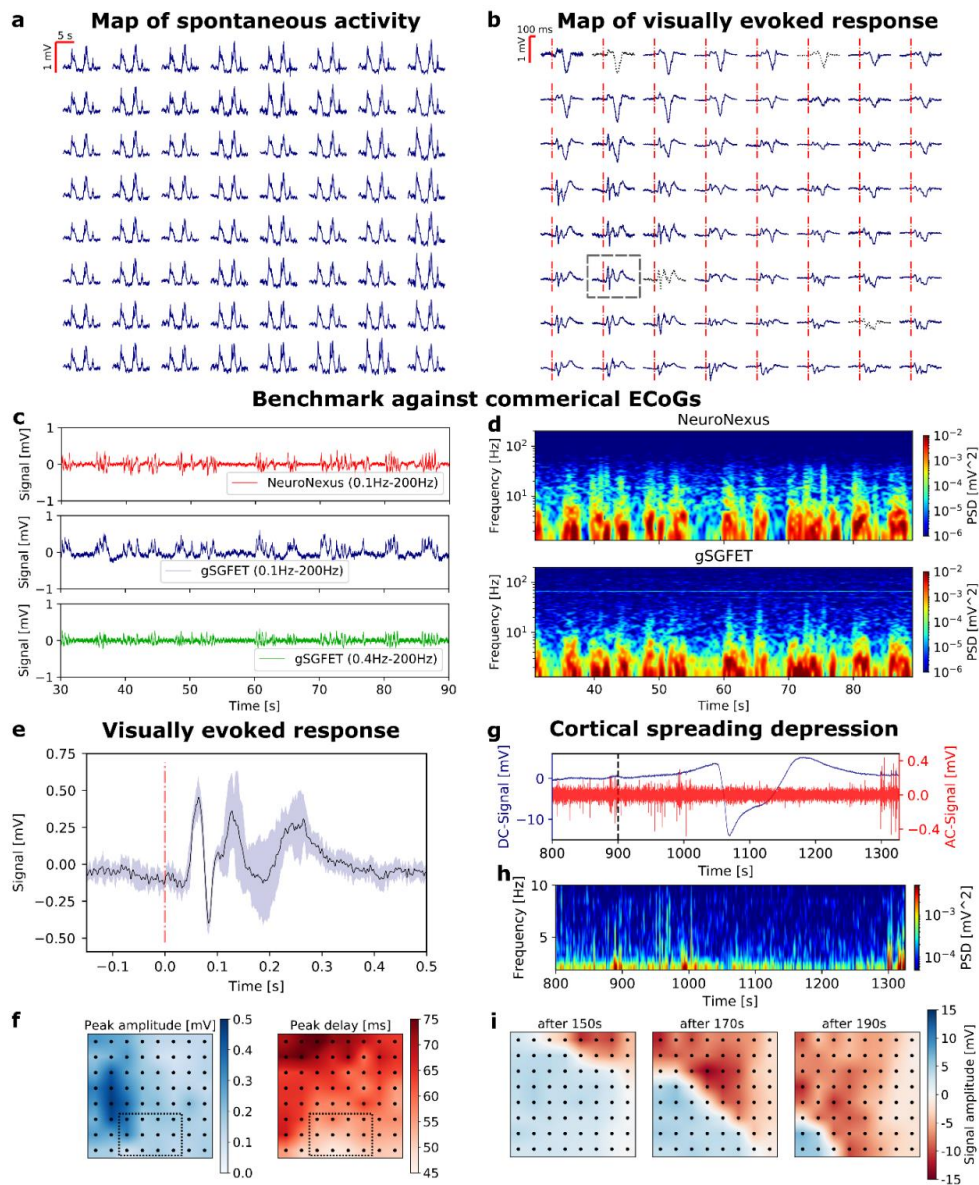
Figure 3. In-vivo validation of multiplexed gSGFET µECoG-array: a. Map of spontaneous LFP activity showing near identical shape across all sites. **b.** Map of visually evoked activity averaged over 10 consecutive events (dashed red line indicates timing of optical stimulus; dashed black curves are interpolated values from neighbouring sites for non-functioning sensors. **c.** Recording trace derived from AC-coupled passive ECoG-array (NeuroNexus, platinum electrode) as well as DC and AC-filtered gSGFET's. Note prominent infraslow oscillations (0.1-0.4Hz), which are not visible in the AC electrode recordings. **d.** Corresponding spectrograms of both, NeuroNexus and gSGFET recordings. **e.** Visually evoked response recorded on a single sensor (dashed grey box in Figure 3b), with an ON- and OFF-response of 50 ms delay and 500µV peak amplitude. **f.** Array maps displaying the distribution of amplitude and time-delay of the ON-peak response across all sites. While the shortest delay is measured for the sensors placed directly on the primary visual cortex (V1), the highest peak-amplitude is seen in the secondary visual cortex (V2). **g.** DC-signal (blue, lowpass-filtered below 20Hz) and AC signal (red, bandpass-filtered between 1-20Hz) of a single gSGFET during the cortical spreading depression (CSD). A strong DC shift of -15mV occurs simultaneously with a silencing of high-frequency activity, which is characteristic for a CSD. **h.** Corresponding spectrogram of CSD event to validate the silencing. **i.** Array map showing the propagating front of the spreading depolarization wave across the array from the right upper to the left lower corner.

4. Conclusion

This work demonstrates the compatibility of graphene solution-gated field-effect transistors (gSGFETs) with time-division multiplexed acquisition mode, utilizing a strongly simplified addressing concept to overcome the hurdle of excessively complex device fabrication. The superiority of graphene over silicon and organic polymers for high-speed applications makes the gSGFET an ideal device for multiplexed sensor arrays. In-vitro and in-vivo assessments confirm the fidelity of broad-band signal representation (infra-slow oscillations and local field potentials) in multiplexed operation, with signal quality comparable to the state-of-the-art of commercially available neuro-sensors. Consequently, next to their potential as efficient transducers of neural activity, gSGFETs show great promise as a building block for multiplexed brain-machine interfaces of high sensor count. Thus, this work represents an important cornerstone in the development of large-scale, flexible gSGFET μECOG arrays capable of providing high resolution mappings of neural activity to control neuroprosthetics and to help exploring the operation and functionalities of the brain.

References

1. Lee B, Kramer D, Salas MA, Kellis S, Brown D, Dobreva T, Klaes C, Heck C, Liu C, Andersen RA (2018) Engineering artificial somatosensation through cortical stimulation in humans. Front Syst Neurosci 12:1–11

2. Ajiboye AB, Willett FR, Young DR, et al (2017) Restoration of reaching and grasping movements through brain-controlled muscle stimulation in a person with tetraplegia: a proof-of-concept demonstration. Lancet 389:1821–1830

3. Moxon KA, Foffani G (2015) Brain-machine interfaces beyond neuroprosthetics. Neuron 86:55–67

4. Orsborn AL, Pesaran B (2017) Parsing learning in networks using brain–machine interfaces. Curr Opin Neurobiol 46:76–83

5. Clancy KB, Koralek AC, Costa RM, Feldman DE, Carmena JM (2014) Volitional modulation of optically recorded calcium signals during neuroprosthetic learning. Nat Neurosci 17:807–809

6. Shanechi MM (2019) Brain–machine interfaces from motor to mood. Nat Neurosci 22:1554–1564

7. Mayberg HS, Lozano AM, Voon V, Mcneely HE, Seminowicz D, Hamani C, Schwalb JM, Kennedy SH (2005) Deep Brain Stimulation for Treatment-Resistant Depression ing electrical stimulation of the subgenual cingulate. Neuron 45:651–660

8. Holtzheimer PE, Husain MM, Lisanby SH, et al (2017) Subcallosal cingulate deep brain stimulation for treatment-resistant depression: a multisite, randomised, sham-controlled trial. The Lancet Psychiatry 4:839–849

9. Dagamseh AMK, Wiegerink RJ, Lammerink TSJ, Krijnen GJM (2012) Towards a high-resolution flow camera using artificial hair sensor arrays for flow pattern observations. Bioinspiration and Biomimetics. https://doi.org/10.1088/1748-3182/7/4/046009

269

10. Anumanchipalli GK, Chartier J, Chang EF (2019) Speech synthesis from neural decoding of spoken sentences. Nature 568:493–498

11. Raducanu BC, Yazicioglu RF, Lopez CM, et al (2016) Time multiplexed active neural probe with 678 parallel recording sites. Eur Solid-State Device Res Conf 2016-Octob:385–388

12. Jun JJ, Steinmetz NA, Siegle JH, et al (2017) Fully integrated silicon probes for high-density recording of neural activity. Nature 551:232–236

13. Angotzi GN, Boi F, Lecomte A, Miele E, Malerba M, Zucca S, Casile A, Berdondini L (2019) SiNAPS: An implantable active pixel sensor CMOS-probe for simultaneous large-scale neural recordings. Biosens Bioelectron 126:355–364

14. Eversmann B, Jenkner M, Hofmann F, et al (2003) A 128 x 128 CMOS Biosensor Array for Extracellular\rRecording of Neural Activity. Ieee J Solid-State Circuits, 38:2306–2317

15. Khodagholy D, Gelinas JN, Thesen T, Doyle W, Devinsky O, Malliaras GG, Buzsáki G (2015) NeuroGrid: Recording action potentials from the surface of the brain. Nat Neurosci. https://doi.org/10.1038/nn.3905

16. Escabi MA, Read HL, Viventi J, et al (2014) A high-density, high-channel count, multiplexed ECoG array for auditory-cortex recordings. J Neurophysiol 112:1566–1583

17. Viventi J, Kim DH, Vigeland L, et al (2011) Flexible, foldable, actively multiplexed, high-density electrode array for mapping brain activity in vivo. Nat Neurosci 14:1599–1605

18. Lee W, Kim D, Matsuhisa N, Nagase M, Sekino M, Malliaras GG, Yokota T, Someya T (2017) Transparent, conformable, active multielectrode array using organic electrochemical transistors. Proc Natl Acad Sci 201703886

19. Lee W, Kim D, Rivnay J, Matsuhisa N, Lonjaret T, Yokota T, Yawo H, Sekino M, Malliaras GG, Someya T (2016) Integration of Organic Electrochemical and Field-Effect Transistors for Ultraflexible, High Temporal Resolution Electrophysiology Arrays. Adv Mater 28:9722–9728

20. Hébert C, Masvidal-Codina E, Suarez-Perez A, et al (2018) Flexible Graphene Solution-Gated Field-Effect Transistors: Efficient Transducers for Micro-Electrocorticography. Adv Funct Mater 28:1–15

21. Kostarelos K, Vincent M, Hebert C, Garrido JA (2017) Graphene in the Design and Engineering of Next-Generation Neural Interfaces. Adv Mater 29:1–7

22. Masvidal-Codina E, Illa X, Dasilva M, et al (2019) High-resolution mapping of infraslow cortical brain activity enabled by graphene microtransistors. Nat Mater 18:280–288

23. Banszerus L, Schmitz M, Engels S, Dauber J, Oellers M, Haupt F, Watanabe K, Taniguchi T, Beschoten B, Stampfer C (2015) Ultrahigh-mobility graphene devices from chemical vapor deposition on reusable copper. Sci Adv 1:1–7

24. Stavrinidou E, Leleux P, Rajaona H, Khodagholy D, Rivnay J, Lindau M, Sanaur S, Malliaras GG (2013) Direct measurement of ion mobility in a conducting polymer. Adv Mater 25:4488–4493

25. Dankerl M, Hauf M V., Lippert A, et al (2010) Graphene solution-gated field-effect transistor array for sensing applications. Adv Funct Mater 20:3117–3124

26. Li X, Cai W, An J, et al (2009) Large-area synthesis of high-quality and uniform graphene films on copper foils. Science (80-) 324:1312–1314

27. Hess LH, Hauf M V., Seifert M, Speck F, Seyller T, Stutzmann M, Sharp ID, Garrido JA (2011) High-transconductance graphene solution-gated field effect transistors. Appl Phys Lett 99:2009–2012

28. Hess LH, Jansen M, Maybeck V, Hauf M V., Seifert M, Stutzmann M, Sharp ID, Offenhäusser A, Garrido JA (2011) Graphene transistor arrays for recording action potentials from electrogenic cells. Adv Mater 23:5045–5049

29.   Buzsáki G, Anastassiou CA, Koch C (2012) The origin of extracellular fields and currents-EEG, ECoG, LFP and spikes. Nat Rev Neurosci 13:407–420

30.   Pesaran B, Vinck M, Einevoll GT, Sirota A, Fries P, Siegel M, Truccolo W, Schroeder CE, Srinivasan R (2018) Investigating large-scale brain dynamics using field potential recordings: Analysis and interpretation. Nat Neurosci 21:903–919

31.   Sirota A, Buzsáki G (2005) Interaction between neocortical and hippocampal networks via slow oscillations. Thalamus Relat Syst 3:245–259

32.   Katzner S, Nauhaus I, Benucci A, Bonin V, Ringach DL, Carandini M (2009) Local Origin of Field Potentials in Visual Cortex. Neuron 61:35–41

33.   Michalareas G, Vezoli J, van Pelt S, Schoffelen JM, Kennedy H, Fries P (2016) Alpha-Beta and Gamma Rhythms Subserve Feedback and Feedforward Influences among Human Visual Cortical Areas. Neuron 89:384–397

34.   Cozzolino O, Marchese M, Trovato F, Pracucci E, Ratto GM, Buzzi MG, Sicca F, Santorelli FM (2018) Understanding spreading depression from headache to sudden unexpected death. Front Neurol 9:1–13

Multiplexed Neural Sensor Array of Graphene Solution-Gated Field-Effect Transistors

Nathan Schaefer, Ramon Garcia-Cortadella, Javier Martínez-Aguilar, Gerrit Schwesig, Xavi Illa, Ana Moya Lara, Sara Santiago, Clement Hébert, Gonzalo Guirado, Rosa Villa, Anton Sirota, Anton Guimerà-Brunet and Jose A. Garrido
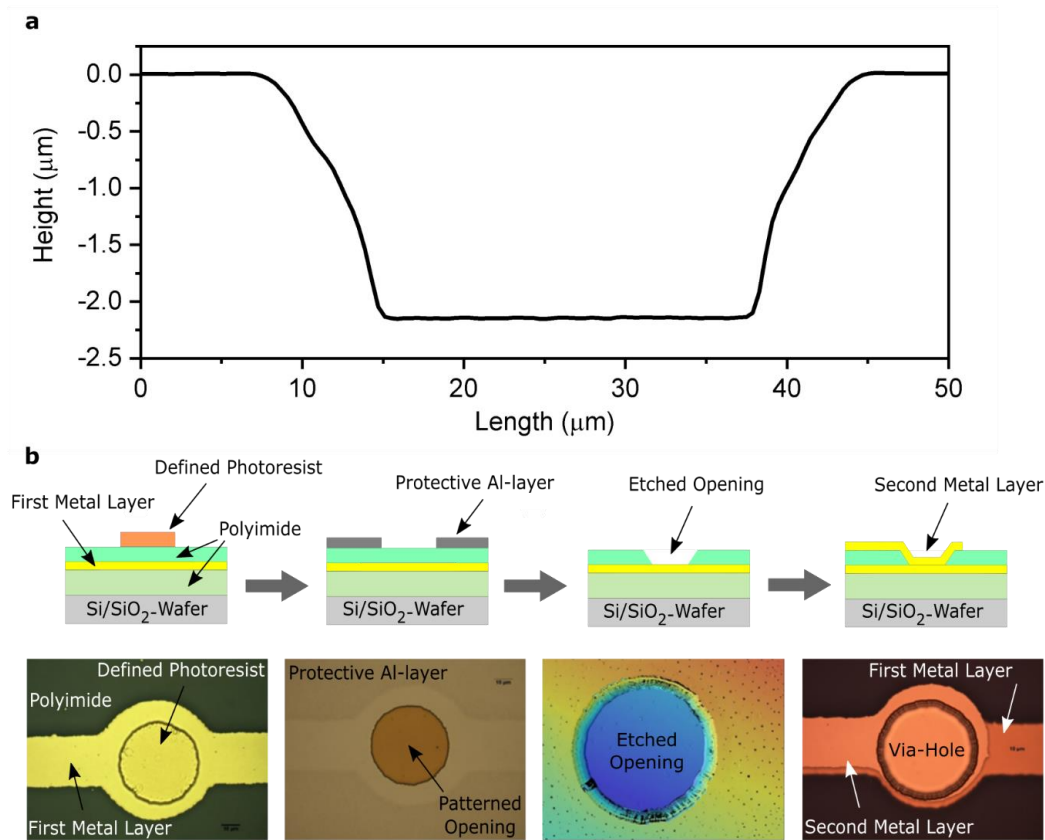

Figure S1. Tapered via-hole technology: a. Profile of a polyimide via-hole from a profilometer measurement, showing a smooth slope enabling reliable metal-metal interconnections. **b.** Fabrication steps for via-holes through patterning of photoresist to define the protective aluminium mask, etching of the tapered profile with isotropic oxygen plasma and deposition of top metal layer. Microscopic images after each step illustrate the procedure.
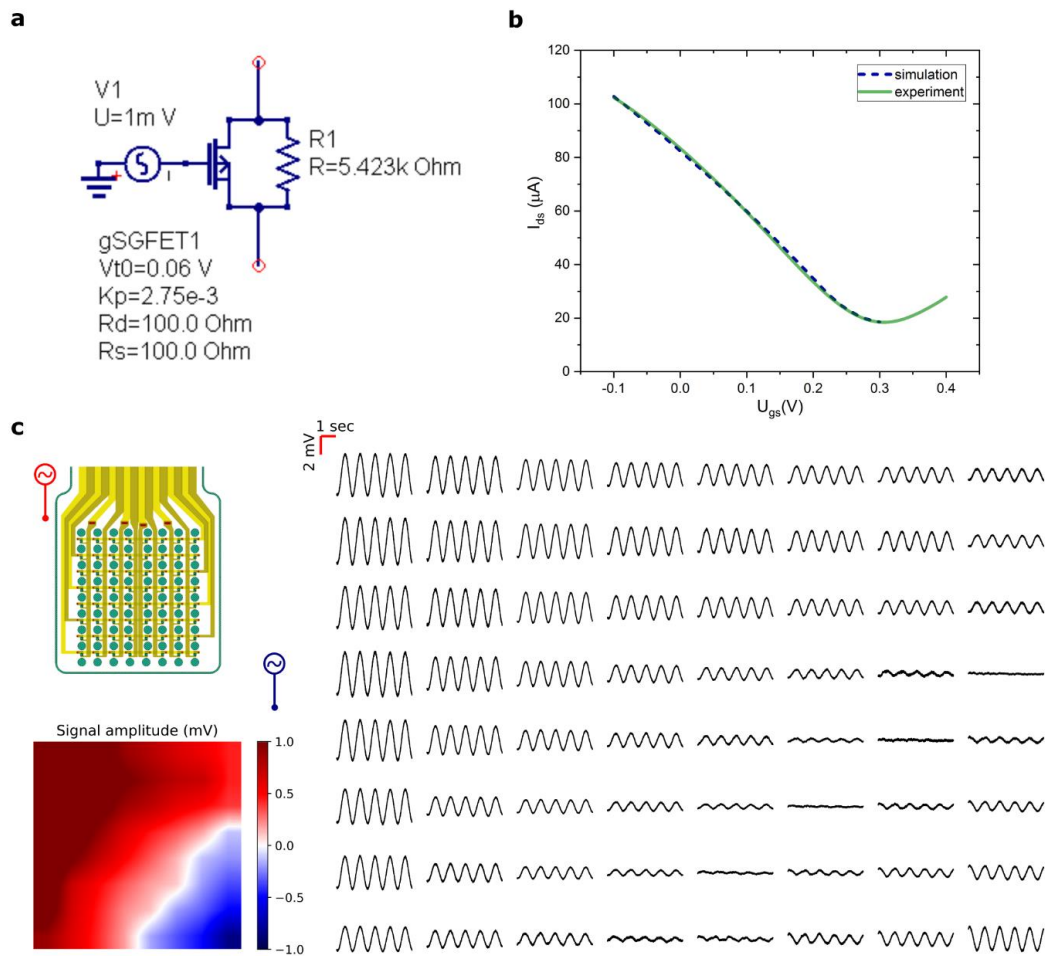
a

b

c

Figure S2. Crosstalk evaluation: a. Schematic of tailored PSpice MOSFET element used to simulate the crosstalk in the gSGFET array. **b.** Drain-source current as a function of applied gate voltage for the PSpice model and for the experimentally measured gSGFET showing near-identical transfer characteristics. **c.** In-vivo measured gradient in signal amplitude when a bipolar current stimulation is applied across the sensor-array (Multichannel Systems STG4002). Centric between both stimulating electrodes, the opposite polarity of both waves leads to destructive interference. This serves as a final validation, that no significant crosstalk is observed in the 8x8 array, as this would otherwise prohibit full amplitude cancelation in the recorded signal.
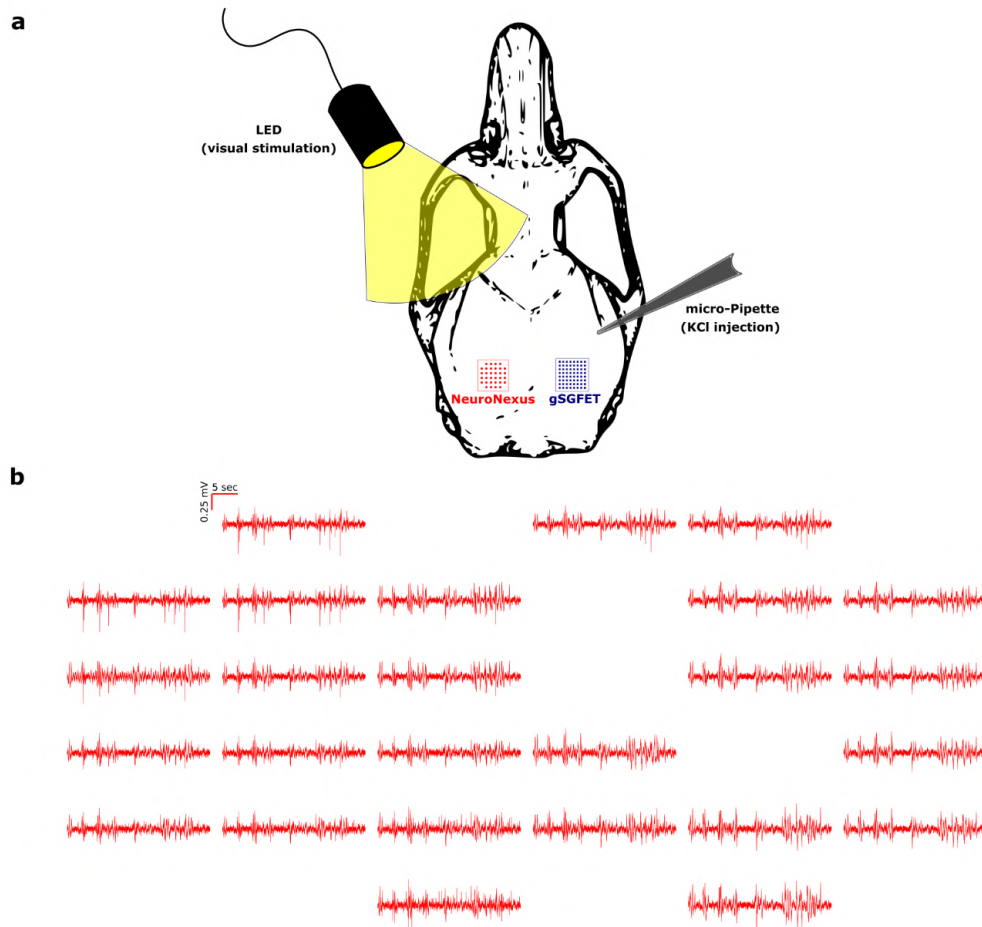
Figure S3. Setup of acute in-vivo experiments a. Positioning of both, the gSGFET (right hemisphere) and the NeuroNexus ECoG array (left hemisphere) during the in-vivo recordings. The visually evoked response is triggered by a contralaterally placed LED in front of the left eye. Also, the location of the KCl injection (micro-pipette) which is triggering the cortical spreading depression is indicated. **b.** Time trace of spontaneous activity for each electrode on the NeuroNexus ECoG array.
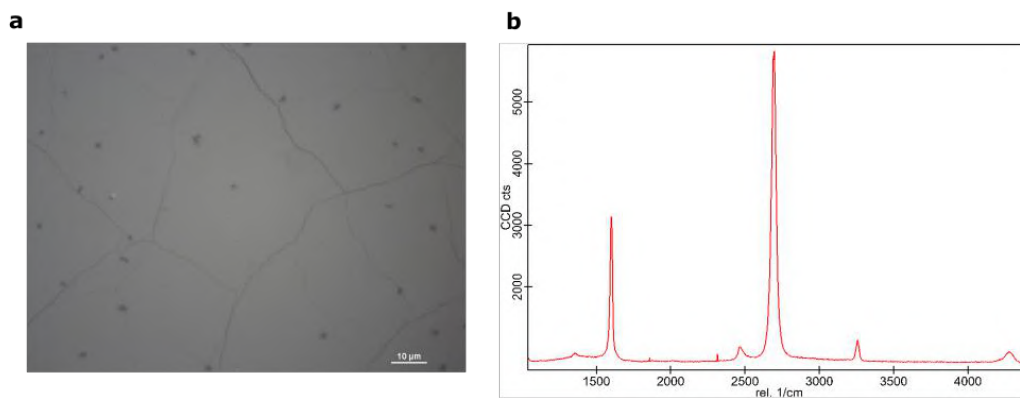
Figure S4. Quality of graphene films a. Optical image of typical graphene film on Si/SiO$_2$ wafer (90 nm oxide thickness) showing the density of multilayer graphene (around 3% of surface area) and of cracks in the film. b. Raman spectrum of graphene on Si/SiO$_2$ wafer (90 nm oxide thickness) showing a full-width half-maximum of the 2D-peak of 39.92 cm^{-1}, a I$_{2D}$/I$_{G}$-ratio of 2 and an I$_{D}$/I$_{G}$-ratio of 0.05.

Declaration of Originality

I hereby declare that this thesis is my own work, and that I have not used any sources and aids other than those stated in the thesis.

Bellaterra, 19.03.2021